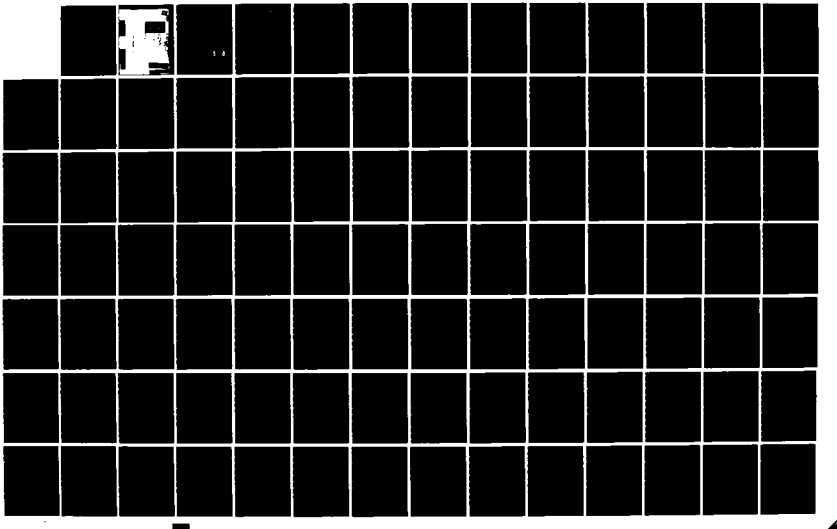
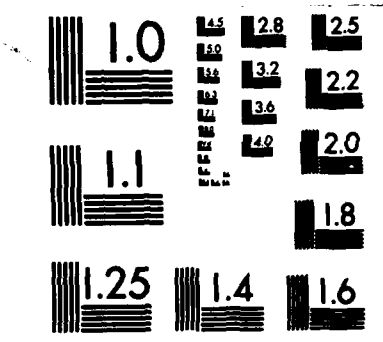
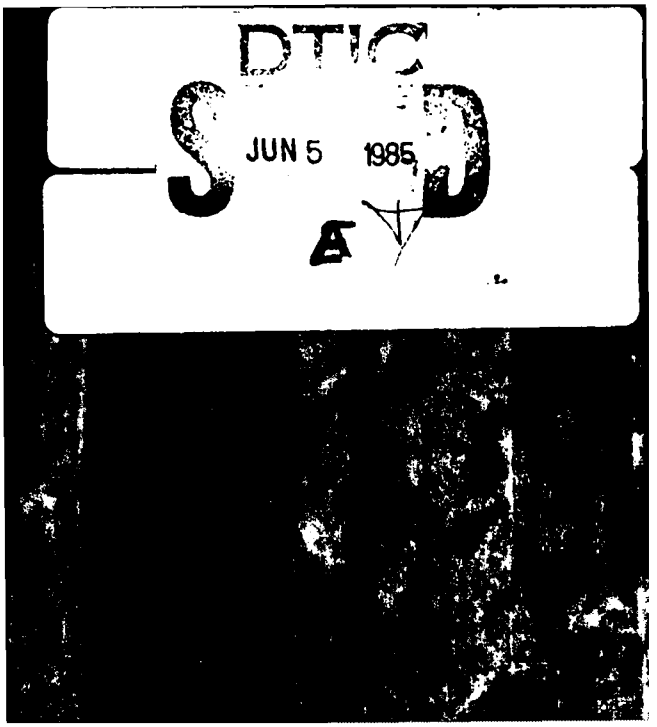
AD-A154 708 NONLINEAR SPECTROSCOPY(U) IBM RESEARCH LAB SAN JOSE CA 1/6
R G BREWER 20 MAR 85 N00014-78-C-0246

UNCLASSIFIED F/G 20/6 NL





MICROCOPY RESOLUTION TEST CHART
NATIONAL BUREAU OF STANDARDS-1963-A


DTIC
JUN 5 1985
S
D
A

(4)

NONLINEAR SPECTROSCOPY

Richard G. Brewer

IBM Research Laboratory
San Jose, California 95193

March 20, 1985

Final Report for Period 1 January 1978 - 31 December 1984

Contract N00014-78-C-0246

Sponsored by the Office of Naval Research

Approved for public release; distribution unlimited

Accession For
NTIS GRA&I
DTIC TAB
Unannounced
Justification
By
Distribution/
Availability Codes
Dist | Avail and/or Special
A/1

DTIC
SELECTE
JUN 5 1985
S D
E

DTIC COPY INSPECTED

SECURITY CLASSIFICATION OF THIS PAGE *(When Data Entered)*

REPORT DOCUMENTATION PAGE		READ INSTRUCTIONS BEFORE COMPLETING FORM
1. REPORT NUMBER	2. GOVT. ACCESSION NO. A154 708	3. RECIPIENT'S CATALOG NUMBER
4. TITLE *(and Subtitle)* Nonlinear Spectroscopy		5. TYPE OF REPORT & PERIOD COVERED Final Report 1 January 1978 through 31 December 1984 6. PERFORMING ORG. REPORT NUMBER
7. AUTHOR(s) Richard G. Brewer		8. CONTRACT OR GRANT NUMBER(s) N00014-78-C-0246
9. PERFORMING ORGANIZATION NAME AND ADDRESS IBM San Jose Research Laboratory 5600 Cottle Road San Jose, CA 95193		10. PROGRAM ELEMENT, PROJECT, TASK AREA & WORK UNIT NUMBERS
11. CONTROLLING OFFICE NAME AND ADDRESS Office of Naval Research 800 N. Quincy Street Arlington, Virginia 22217		12. REPORT DATE 20 March 1985 13. NUMBER OF PAGES
14. MONITORING AGENCY NAME & ADDRESS *(if different from Controlling Office)*		15. SECURITY CLASS. *(of this report)* UNCLASSIFIED 15a. DECLASSIFICATION/ DOWNGRADING SCHEDULE

16. DISTRIBUTION STATEMENT *(of this Report)*

Approved for public release;
distribution unlimited.

17. DISTRIBUTION STATEMENT *(of the abstract entered in Block 20, if different from Report)*

18. SUPPLEMENTARY NOTES

19. KEY WORDS *(Continue on reverse side if necessary and identify by block number)*

coherent optical transients, laser spectroscopy, photon echoes, free induction decay, Bloch equations, relaxation mechanisms, decay time, molecular collisions, solids.

20. ABSTRACT *(Continue on reverse side if necessary and identify by block number)*

This research includes the development of novel laser techniques which allow precise and fundamental studies of atoms, molecules and solids, especially relaxation phenomena in the time domain.

DD FORM 1 JAN 73 1473 EDITION OF 1 NOV 65 IS OBSOLETE

SECURITY CLASSIFICATION OF THIS PAGE *(When Data Entered)*

I. Research Summary

During the period 1978-1984, work continued in the general area of Laser Spectroscopy, the emphasis being on coherent optical transients and precision spectroscopy. Both theoretical and experimental studies were conducted. The most notable experimental accomplishments include the development of new experimental techniques: (1) the laser frequency switching technique of observing coherent optical transients such as optical free induction decay and photon echoes for studying the dynamic properties of solids or gas phase collisions; (2) the extension of these ideas to the picosecond time scale using a novel traveling wave electro-optic phase modulator; (3) the frequency stabilization of dye lasers to a linewidth of ≈ 100 Hertz for precision spectroscopic measurements; and (4) the Raman heterodyne detection method for observing nuclear magnetic resonance with a sensitive optical probe.

One of the interesting applications of ultrastable dye lasers has been in the area of solid state laser spectroscopy where the optical homogeneous linewidths are of the order of 1 kilohertz or less. Here, the need for laser stability is clearly evident in coherent optical transient phenomena such as free induction decay or in steady state measurements such as hole burning. Using a 100 Hertz linewidth stabilized dye laser to excite an impurity ion crystal, it was discovered that the optical Bloch equations (the basic equations of motion for describing coherent emission) are violated when the optical transition is saturated, i.e., the T_2 dephasing time is not a true constant, as is commonly assumed, but instead depends on the field strength. These experimental findings lead to a series of theoretical studies in our own laboratory and around the world in an attempt to find a microscopic understanding, work which continues today.

Cont'd

Other theoretical studies include §1) a generalized theory of two-photon processes; §2) oscillatory free induction decay which lead to a prediction of a new phenomenon that was later verified both in the optical and radio frequency regions; §3) an elegant theorem on coherent transients which sets a rigorous limit on the duration of any coherent transient emission signal; and §4) a theory of cumulative two-pulse photon echoes. Originator Supplied Keywords include:

The results of these studies have been published in the papers attached in the Appendix.

See DD1473 (Block 19)

II. Personnel

R. G. Brewer: Principal Investigator

R. G. DeVoe

K. L. Foster

A. Schenzle

A. Z. Genack

R. M. Macfarlane

S. S. Kano

S. C. Rand

A. Wokaun

A. Szabo

N. C. Wong

J. Mlynek

E. S. Kintzer

M. Mitsunaga

E. L. Hahn

III. APPENDIX

1. Generalized Two Photon Theory
   A. Schenzle and R. G. Brewer, Physics Reports 43, 456 (1978)
   Festschrift for Willis E. Lamb, Jr., edited by D. ter Haar and M. O. Scully (North-Holland, 1978), p. 455.

2. Optical Free Induction Decay of the F_3^+ Center in NaF
   R. M. Macfarlane, A. Z. Genack and R. G. Brewer, Physical Review B17, 2821 (1978).

3. Optical Coherent Transients by Laser Frequency Switching: Subnanosecond Studies
   R. G. DeVoe and R. G. Brewer, Physical Review Letters 40, 862 (1978).
   Picosecond Phenomena (Springer-Verlag, N.Y. 1978), edited by C. V. Shank, E. P. Ippen and S. L. Shapiro, p. 199.

4. Optical FID Measurement of Low Temperature Dephasing in Pr^{3+}:LaF_3
   R. M. Macfarlane, A. Z. Genack, S. Kano and R. G. Brewer, Journal of Luminescence 18/19, 933 (1979).

5. Subnanosecond Optical Free Induction Decay
   R. G. DeVoe and R. G. Brewer, IBM Journal of Research and Development 23, 527 (1979).

6. Subnanosecond Optical Free Induction Decay II
   R. G. DeVoe and R. G. Brewer, Physical Review A20, 2449 (1979).

7. Magic Angle Line Narrowing in Optical Spectroscopy
   S. C. Rand, A. Wokaun, R. G. DeVoe and R. G. Brewer, Physical Review Letters 43, 1868 (1979).
   Beijing/Shanghai Proceedings of an International Conference on Lasers (Wiley-Interscience, 1983), p. 65.

8. Ultraslow Optical Dephasing of Pr^{3+}:LaF_3
   R. G. DeVoe, A. Szabo, S. C. Rand and R. G. Brewer, Physical Review Letters 42, 1560 (1979).

9. Optical Dephasing in Molecular Iodine
   R. G. Brewer and S. S. Kano, in Nonlinear Behavior of Molecules, Atoms and Ions in Electric, Magnetic or Electromagnetic Fields, edited by L. Neal (Elsevier, Amsterdam, 1979), p. 45.

10. Optical Rotary Echoes
N. C. Wong, S. S. Kano and R. G. Brewer, Physical Review A21, 260 (1980).

11. Oscillatory Free Induction Decay
A. Schenzle, N. C. Wong and R. G. Brewer, Physical Review A21, 887 (1980).

12. Theorem on Coherent Transients
A. Schenzle, N. C. Wong and R. G. Brewer, Physical Review A22, 635 (1980).

13. Monte Carlo Theory of Optical Dephasing in $LaF_3:Pr^{3+}$
R. G. DeVoe, A. Wokaun, S. C. Rand and R. G. Brewer, Physical Review B23, 3125 (1981).

14. Anticrossings in Solid State Laser Spectroscopy
A. Wokaun, S. C. Rand, R. G. DeVoe and R. G. Brewer, Physical Review B23, 5733 (1981).

15. Theorem on Coherent Transients: Response to a Comment
A. Schenzle, N. C. Wong and R. G. Brewer, Physical Review A24, 2250 (1981).

16. New Phenomena in Coherent Optical Transients
R. G. Brewer, R. G. DeVoe, S. C. Rand, A. Schenzle, N. C. Wong, S. S. Kano and A. Wokaun, Proceedings of the Fifth International Laser Spectroscopy Conference, Jasper, 1981 (Springer-Verlag, 1981), p. 219.
NATO Advanced Study Institute on Advances in Laser Spectroscopy, San Miniato, 1981 (Plenum Press, 1983), p. 365.

17. Phase Modulation Laser Spectroscopy
A. Schenzle, R. G. DeVoe and R. G. Brewer, Physical Review A25, 2606 (1982).

18. Coherence Phenomena in Phase Modulation Laser Spectroscopy
R. G. DeVoe and R. G. Brewer, Physical Review A, Rapid Communications, 26, 705 (1982).

19. Laser Spectroscopy of Solids
R. G. Brewer and R. G. DeVoe, International Conference on Photochemistry and Photobiology, Alexandria, Egypt, January 5-10, 1983 (Harwood Academic Publishers, New York, 1983), edited by A. Zewail, p. 21.
NATO Workshop on Coherence and Energy Transfer in Glasses, Cambridge University, England, 1982 (Plenum Press, New York, 1984), edited by P. Fleury and B. Golding, p. 171.

20. Raman Heterodyne Detection of NMR
J. Mlynek, N. C. Wong, R. G. DeVoe, E. S. Kintzer and R. G. Brewer, Physical Review Letters 50, 993 (1983).
Laser Spectroscopy VI, edited by H. P. Weber and W. Lüthy (Springer-Verlag, Berlin, 1983), p. 60.

21. Experimental Test of the Optical Bloch Equations for Solids
R. G. DeVoe and R. G. Brewer, Physical Review Letters 50, 1269 (1983).

22. Raman Heterodyne Detection of Nuclear Magnetic Resonance
N. C. Wong, E. S. Kintzer, R. G. DeVoe, J. Mylnek and R. G. Brewer, Physical Review B, 4993 (1983).

23. Microscopic Theory of Optical Line Narrowing of a Coherently Driven Solid
A. Schenzle, M. Mitsunaga, R. G. DeVoe and R. G. Brewer, Physical Review A30, 325 (1984).

24. Raman Heterodyne Interference of Inequivalent Nuclear Sites
M. Mitsunaga, E. S. Kintzer and R. G. Brewer, Physical Review Letters 52, 1484 (1984).

25. Cumulative Two-Pulse Photon Echoes
A. Schenzle, R. G. DeVoe and R. G. Brewer, Physical Review A30, 1866 (1984).

26. Laser Frequency Division and Stabilization
R. G. DeVoe and R. G. Brewer, Physical Review A30, 2827 (1984).

27. Atomic Memory
R. G. Brewer and E. L. Hahn, Scientific American, page 50, December 1984.

Appendix - Item 1

PHYSICS REPORTS (Section C of Physics Letters) 43, No. 12 (1978) 455–484. NORTH-HOLLAND PUBLISHING COMPANY.

GENERALIZED TWO PHOTON THEORY*†

Axel SCHENZLE** and Richard G. BREWER

IBM Research Laboratory, San José, California 95193, U.S.A.

Received November 1977

Contents:

1. Introduction	457	6.1. Geometric solutions	472
2. The Hamiltonian	458	6.2. Analytic solutions	473
3. Formulation of the basic equations	459	6.3. The general three-level problem	476
3.1. Outline of the theory	459	7. Eigenfunctions of the stationary Hamiltonian	478
3.2. Diagrammatic representation	461	7.1. $N + 2$ level case	478
3.3. Formal solution and approximations	462	7.2. Three level case	479
4. Perturbation theory	464	8. A simplified application: the Raman beat experiment	479
4.1. Raman process	465	Appendix A	482
5. Perturbation theory including nonresonant terms	468	Appendix B	483
5.1. Raman process	469	References	483
6. Nonperturbative eigenvalues	470		

Abstract:

Recent laser experiments and theoretical discussions of coherent two photon transient phenomena have prompted us to develop a generalized theory for the case of an $N + 2$ level quantum system interacting with two optical fields. New perturbation solutions, derived from an effective two level Hamiltonian, are presented in the form of a continued fraction expansion where the leading term agrees with earlier treatments. The theory applies to homogeneously broadened systems where the intermediate transitions are far off resonance. When inhomogeneous broadening plays a role, the expansion parameter is no longer unique and the theory breaks down. Nonperturbative solutions are then required which are also capable of explaining other features not appearing in the perturbative approach. An important example is intensity-dependent dephasing. Exact and approximate solutions of this kind are derived.

Single orders for this issue

PHYSICS REPORT (Section C of PHYSICS LETTERS) 43, No. 12 (1978) 455–484.

Copies of this issue may be obtained at the price given below. All orders should be sent directly to the Publisher. Orders must be accompanied by check.

Single issue price Dfl. 15.00, postage included.

* Contribution to the Festschrift of Professor Willis Lamb Jr. on the occasion of his sixty-fifth birthday.

† Work supported in part by the U.S. Office of Naval Research.

** On leave from the Department of Physics, Universität Essen, Gesamthochschule, Essen, West Germany.

Appendix - Item 1

GENERALIZED TWO PHOTON THEORY

Axel SCHENZLE and Richard G. BREWER

IBM Research Laboratory,
San José, California 95193, U.S.A.



NORTH-HOLLAND PUBLISHING COMPANY AMSTERDAM

1. Introduction

Two photon resonances in atomic and molecular systems have interested theorists over the years beginning with the earliest calculations by M. Göppert-Mayer in 1931 [1]. Figure 1(a) shows such a transition for the case where two photons are absorbed simultaneously. The related Raman effect [2] in fig. 1(b), which is a two photon process also, has been known experimentally since 1927 and involves the absorption of one photon and the emission of another. However, verification of the first case, had to await the invention of the laser before its observation in 1961 [3].

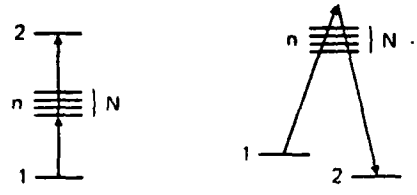


Fig. 1. Two photon processes for an $N + 2$ level system showing (a) two photon absorption and (b) the Raman process.

Within the last few years, other novel two photon experiments have been performed with laser light. For example, a counter propagating laser beam geometry can yield ultrahigh resolution two photon spectra where the Doppler broadening is eliminated [4]. Coherent two photon transients have been monitored also in the time domain [5–10] and have stimulated theoretical discussions which attack the problem from different points of view.

Particular attention has been given to explaining two photon transient effects such as the Raman beat [6]. This experiment is described in section 8 and arises in coherently prepared molecular samples when the level degeneracy is suddenly removed by Stark switching. In the calculation of Brewer and Hahn [11], a three level model is assumed where the pulse preparative stage yields an exact solution when the two photon resonance condition is maintained. The solutions are valid for either adiabatic or nonadiabatic transients. The transient Raman beat signal which follows is described by a perturbation theory [12].

A different approach was taken by Takatsuji [13] and also by Grischkowsky, Loy and Liao [14]. They performed a perturbation calculation suggested by Heitler [15] using a canonical transfo nation. The $N + 2$ level structure of fig. 1(a) is assumed where the N intermediate transitions are esonance. The problem then reduces to an effective two level calculation where the solutions liabatic in character and display a slowly varying time dependence.

The paper of et al. [16] extends an earlier perturbation treatment of Brewer and Hahn [12] and also that of Hopf, Shea and Scully [17]. It includes all terms of the polarization up to third order in the optical field.

In this article, we treat the general problem of two photon transients where two radiation fields interact with $N + 2$ atomic levels as suggested in fig. 1. In its most general form, this problem cannot be solved analytically as the Schrödinger wave equation leads to an infinite hierarchy of coupled equations. Even if the hierarchy is cut by an approximation, there still remains the difficulty of solving a characteristic equation of order $N + 2$. Clearly, approximations are required. We show that the terms appearing in the equations of motion can be understood physically by means of Feynman-like diagrams and provide a simple way of identifying the important terms.

case $N = 1$. For the $N + 2$ level problem, we assume for the sake of simplicity two photon resonance while for the 3-level problem where this assumption would make the solution trivial, we do not assume resonance at all.

As already mentioned, the two principle obstacles in solving this problem are

1) The use of nonresonant terms as well as several external fields leads to an infinite hierarchy of equations.

2) A multilevel problem leads to a multidimensional characteristic equation that cannot be solved in general.

The purpose of the preceding discussion was to deal with both problems simultaneously in a perturbative approach. The idea of this section is to neglect the nonresonant terms totally while attempting to derive nonperturbative solutions for the characteristic equation. We treat the two photon process for the case of $N + 2$ levels. Assume that the transition frequencies are quite different so that we can neglect in eq. (8) the simultaneous interaction of the frequencies Ω_2 (or Ω_1) with the transitions $\omega_n - \omega_1$ and $\omega_2 - \omega_n$. This eliminates half of the terms contained in (8). We further neglect all counterrotating or antiresonant and nonresonant contributions. Then, by applying the transformation

$$\tilde{c}_1(z) = c_1(z + \mathrm{i}\Omega_1), \qquad \tilde{c}_2(z) = c_2(z - \mathrm{i}\Omega_2),$$

we are left with the following set of coupled equations appropriate to the two photon process:

$$\left[z + \mathrm{i}\omega_1 + \mathrm{i}\Omega_1 + \tfrac{1}{4}\sum_n \frac{(\chi^1_{1n})^2}{z + \mathrm{i}\omega_n}\right]\tilde{c}_1(z) = I_1(z) - \tfrac{1}{4}\sum_n \frac{\chi^1_{1n}\chi^2_{2n}}{z + \mathrm{i}\omega_n}\tilde{c}_2(z),$$

$$\left[z + \mathrm{i}\omega_2 - \mathrm{i}\Omega_2 + \tfrac{1}{4}\sum_n \frac{(\chi^2_{2n})^2}{z + \mathrm{i}\omega_n}\right]\tilde{c}_2(z) = I_2(z) - \tfrac{1}{4}\sum_n \frac{\chi^2_{2n}\chi^1_{1n}}{z + \mathrm{i}\omega_n}\tilde{c}_1(z),$$

$$(z + \mathrm{i}\omega_n)c_n(z) = c_n(0) - \frac{\mathrm{i}}{2}\chi^1_{n1}\tilde{c}_1(z) - \frac{\mathrm{i}}{2}\chi^2_{2n}\tilde{c}_2(z),$$

where

$$I_1(z) = c_1(0) - \frac{\mathrm{i}}{2}\sum_n \chi^1_{1n}\frac{c_n(0)}{z + \mathrm{i}\omega_n}, \qquad I_2(z) = c_2(0) - \frac{\mathrm{i}}{2}\sum_n \chi^2_{2n}\frac{c_n(0)}{z + \mathrm{i}\omega_n}.$$

The characteristic equation of this problem reads

$$(z+\mathrm{i}\omega_1+\mathrm{i}\Omega_1)(z+\mathrm{i}\omega_2-\mathrm{i}\Omega_2)+\tfrac{1}{4}\sum_n(\chi^1_{1n})^2\frac{z+\mathrm{i}\omega_2-\mathrm{i}\Omega_2}{z+\mathrm{i}\omega_n}+\tfrac{1}{4}\sum_n(\chi^2_{2n})^2\frac{z+\mathrm{i}\omega_1+\mathrm{i}\Omega_1}{z+\mathrm{i}\omega_n}$$

$$+\tfrac{1}{32}\sum_{nn'}\frac{(\chi^1_{1n}\chi^2_{2n'}-\chi^1_{1n'}\chi^2_{2n})^2}{(z+\mathrm{i}\omega_n)(z+\mathrm{i}\omega_{n'})}=0. \tag{39}$$

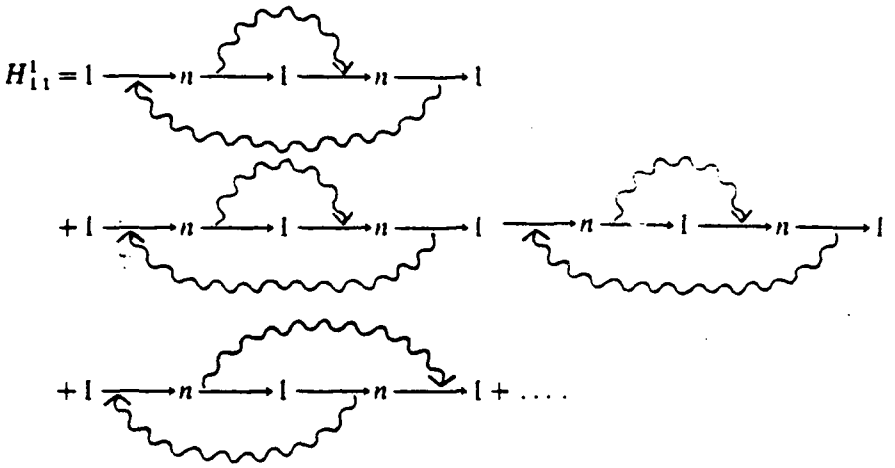
When we recognize that the diagonal elements of the double sum vanish, then it is obvious that the characteristic equation is of order $(N + 2)$ defining $N + 2$ eigenvalues.

Let us abbreviate the last term in eq. (39) by L. We notice that L vanishes exactly in the following three cases:

1) $L = 0$ for $N = 1$ (3-level system).

2) $L = 0$ when the dipole matrix elements do not depend on the level index n so that

$$g_{1n} = g_1, \qquad g_{2n} = g_2.$$



+ time-reversed diagrams. It is obvious from our earlier discussion that these graphs have been neglected before.

Let us now compare the corrections derived in the preceding paragraph with the results obtained here. The term $\Gamma^0_{11}(-i\omega_1 \pm (\Omega_2 - \Omega_1))$ is of the order

$$\Gamma^0_{11} \sim \chi^2 \Delta_n \qquad \text{with} \qquad \Delta_n = \omega_n - \omega_1 - \Omega_1, \quad \text{and therefore}$$

$$H^1_{11} \sim \hbar \frac{\chi^2}{\Delta_n}\left(1 + \frac{\Delta \cdot \Delta_n}{\chi^2}\right)^{-1}, \qquad \Delta = \Omega_2 - \Omega_1.$$

We then have

1. $\Delta \ll \chi$, $\quad \frac{1}{\hbar} H^1_{11} = \mathcal{O}\left(\frac{\chi^2}{\Delta_n} \cdot 1\right)$,

2. $\Delta \approx \chi$, $\quad \frac{1}{\hbar} H^1_{11} = \mathcal{O}\left(\frac{\chi^2}{\Delta_n} \cdot \frac{\chi}{\Delta_n}\right)$.

3. $\Delta \gg \chi$, $\quad \frac{1}{\hbar} H^1_{11} = \mathcal{O}\left(\frac{\chi^2}{\Delta_n} \cdot \left(\frac{\chi}{\Delta_n}\right)^2\right)$.

Therefore the contribution of the nonresonant terms may be of the same order as the resonant corrections when the difference in the two optical frequencies is less than the power broadening of the levels.

6. Nonperturbative eigenvalues

In a great number of examples the perturbation results are not applicable. For inhomogeniously broadened lineshapes wider than the power broadening contribution, assumptions like $\Delta_n \gg \chi$ are no longer valid because the off-resonance parameter Δ_n can vary from $-\infty \to 0 \to +\infty$. Therefore an approximate result has to be derived in these cases such that the expansion parameter does not contain the molecular velocity.

We will derive in this paragraph approximate results which are not limited to a power series expansion in χ/Δ_n. We will do this for the $(N + 2)$ level system for general N as well as for the specia

where $\hat{\Sigma}$ contains the odd products of the translation operators

$$T^{\pm}(\nu)T^{\pm}(\nu') = T^{\pm}(\nu \pm \nu') \qquad \nu \pm \nu' \neq 0.$$

Taking the c-number contributions only and dropping in this step of approximation $\hat{\Sigma}$, we find

$$\{z + i\omega_1 - \Gamma^0_{11}(z) - \sum_{\nu}(z + \nu + i\omega_1 - \Gamma^0_{11}(z+\nu))^{-1}\Gamma^{\nu}_{11}{}^{+}(z)\Gamma^{\nu}_{11}{}^{-}(z+\nu)$$
$$- \sum_{\nu}(z - \nu + i\omega_1 - \Gamma^0_{11}(z-\nu)^{-1}\Gamma^{\nu}_{11}{}^{-}(z)\Gamma^{\nu}_{11}{}^{+}(z-\nu)\}c_1(z)$$
$$= [1 + \Gamma^1_{11}(z)(z + i\omega_1 - \Gamma^0_{11}(z))^{-1}][I_1(z) + \Gamma_{12}c_2(z)]. \tag{35}$$

The same arguments can be used to handle the nondiagonal contributions as well.

5.1. *Raman process*

To make this approximation more clear, we show how these results can be derived in a Raman-process with two close lying frequencies Ω_2 and Ω_1. Under the assumption $|\Omega_2 - \Omega_1| \ll \Omega$, we collect only the terms $\nu = i\Delta = i(\Omega_2 - \Omega_1)$ and drop all further off-resonant terms like $\nu = 2i\Omega_{1,2}$ etc. for convenience. Then we get, as can be seen from Appendix A,

$$\Gamma^0_{11}(z) = -\tfrac{1}{4}\sum_n \frac{(\chi^1_{1n})^2}{z + i\omega_n - i\Omega_1} + \frac{(\chi^1_{1n})^2}{z + i\omega_n + i\Omega_1} + \frac{(\chi^2_{1n})^2}{z + i\omega_n - i\Omega_2} + \frac{(\chi^2_{1n})^2}{z + i\omega_n + i\Omega_2} \tag{36}$$

as well as the translation terms of (8a)

$$\Gamma^1_{11}(z + i\Omega_1) = -\tfrac{1}{4}\sum_n \left(\frac{\chi^1_{1n}\chi^2_{1n}}{z + i\omega_n} + \frac{\chi^2_{1n}\chi^1_{1n}}{z + i\omega_n + i(\Omega_2 + \Omega_1)}\right)T^{+}(i(\Omega_2 - \Omega_1))$$
$$- \tfrac{1}{4}\sum_n \left(\frac{\chi^1_{1n}\chi^2_{1n}}{z + i\omega_n + 2i\Omega_1} + \frac{\chi^2_{1n}\chi^1_{1n}}{z + i\omega_n - i(\Omega_2 - \Omega_1)}\right)T^{-}(i(\Omega_2 - \Omega_1)). \tag{37}$$

With (35) transformed as in (17)

$$c_{1,2} \to \tilde{c}_{1,2} = c_{1,2}(z + i\Omega_{1,2}),$$

we find for the diagonal terms of the effective Hamiltonian

$$H_{11} = H^0_{11} + H^1_{11},$$

where H^0_{11} is the perturbation result obtained in eq. (24). The nonresonant correction H^1_{11} is given by

$$H^1_{11} = \frac{\hbar}{16}(i(\Omega_2 - \Omega_1) - \Gamma^0_{11}(-i\omega_1 + i\Omega_2 - i\Omega_1))^{-1}\left[\sum_n (\chi^1_{1n})(\chi^2_{1n})\left(\frac{1}{\omega_n - \omega_1 - \Omega_1} + \frac{1}{\omega_n - \omega_1 + \Omega_2}\right)\right]^2$$
$$+ \frac{\hbar}{16}(-i(\Omega_2 - \Omega_1) - \Gamma^0_{11}(-i\omega_1 - i\Omega_2 + i\Omega_1))^{-1}\left[\sum_n (\chi^1_{1n})(\chi^2_{1n})\left(\frac{1}{\omega_n - \omega_1 + \Omega_1} + \frac{1}{\omega_n - \omega_1 - \Omega_2}\right)\right]^2 \tag{38}$$

This correction includes a group of diagrams that has been neglected above. The diagrams leading to H^1_{11} are the iteration of nonresonant processes that can be made into closed loops in 4th order:

5. Perturbation theory including nonresonant terms

Nonresonant interactions are important when calculating energy shifts. Therefore in calculating the eigenvalues of eqs. (13) and (14) the contributions from nonresonant terms should be included. In a perturbation approach we can include nonresonant terms in the following way. Starting from eq. (12),

$$(z + i\omega_1 - \Gamma_{11})c_1(z) = I_1(z) + \Gamma_{12}(z)c_2(z), \tag{28}$$

we can write

$$\begin{aligned} &c_1(z) = ()^{-1}\Gamma^1_{11}c_1(z) + ()^{-1}I_1(z) + ()^{-1}\Gamma_{12}c_2(z), \\ &()^{-1} = (z + i\omega_1 - \Gamma^0_{11}(z))^{-1}. \end{aligned} \tag{29}$$

Notice that the inverse $(z + i\omega_1 - \Gamma^0_{11})^{-1}$ exists because $\Gamma^0_{11}(z)$ is only a c-number. Multiplying this equation by $\Gamma^1_{11}(z)$ gives

$$\begin{aligned} \Gamma^1_{11}(z)c_1(z) = {} & \Gamma^1_{11}(z)(z + i\omega_1 - \Gamma^0_{11}(z))^{-1}\Gamma^1_{11}c_1(z) + \Gamma^1_{11}(z)(z + i\omega_1 - \Gamma^0_{11}(z))^{-1}I_1(z) \\ & + \Gamma^1_{11}(z)(z + i\omega_1 - \Gamma^0_{11}(z))^{-1}\Gamma_{12}(z)c_2(z). \end{aligned} \tag{30}$$

Inserting this expression into eq. (28) leads to

$$\begin{aligned} &[z + i\omega_1 - \Gamma^0_{11}(z) - \Gamma^1_{11}(z + i\omega_1 - \Gamma^0_{11}(z))^{-1}\Gamma^1_{11}]c_1(z) \\ &\qquad = [1 + \Gamma^1_{11}(z)(z + i\omega_1 - \Gamma^0_{11}(z))^{-1}][I_1(z) + \Gamma_{12}(z)c_2(z)]. \end{aligned} \tag{31}$$

The operators $\Gamma^1_{ij}(z)$ can be expanded into a finite series with structure

$$\Gamma^1_{ij}(z) = \sum_\nu \Gamma^\nu_{ij}{}^+(z)T^+(\nu) + \Gamma^\nu_{ij}{}^-(z)T^-(\nu), \tag{32}$$

where the functions $\Gamma^\nu_{ij}{}^\pm(z)$ contain the c-number prefactors of the various translation operators $T^\pm(\nu)$.

Let us calculate the correction to the diagonal terms of the effective Hamiltonian H. In eq. (31), we have

$$\begin{aligned} &\Gamma^1_{11}(z)(z + i\omega_1 - \Gamma^0_{11}(z))^{-1}\Gamma^1_{11}(z) \\ &\qquad = \sum_\nu \Gamma^\nu_{11}{}^+(z)(z + \nu + i\omega_1 - \Gamma^0_{11}(z + \nu))^{-1}T^+(\nu)\Gamma^1_{11}(z) \\ &\qquad + \sum_\nu \Gamma^\nu_{11}{}^-(z)(z - \nu + i\omega_1 - \Gamma^0_{11}(z - \nu))^{-1}T^-(\nu)\Gamma^1_{11}(z). \end{aligned} \tag{33}$$

Extracting the c-number part out of this expression and using the identity

$$T^+(\nu)T^-(\nu) = T^-(\nu)T^+(\nu) = 1,$$

we find for the right hand side of (33)

$$\begin{aligned} &\sum_\nu \Gamma^\nu_{11}{}^+(z)\Gamma^\nu_{11}{}^-(z + \nu)(z + \nu + i\omega_1 - \Gamma^0_{11}(z + \nu))^{-1} \\ &\qquad + \sum_\nu \Gamma^\nu_{11}{}^-(z)\Gamma^\nu_{11}{}^+(z - \nu)(z - \nu + i\omega_1 - \Gamma^0_{11}(z - \nu))^{-1} + \hat{\Sigma}, \end{aligned} \tag{34}$$

Inspecting this perturbation approach we find that the parameter of expansion is of the form

$$\lambda = \chi/\Delta$$

where Δ is an off resonance tuning parameter.

The expansion is supposed to be valid if the individual one photon processes are far from resonance, compared to the Rabi-flopping frequencies χ. But carrying out this perturbation further and further cannot lead to the exact result because we already neglected the nonresonant terms in (13) and (14). Especially when we have to assume that the one-photon transitions have to be far from resonance, neglecting non-resonant terms can be inconsistent.

We can explore this question by comparing for example the two cases shown in fig. 3 where the shady region indicates power broadening of the transitions 1 and 2. In case (a) where Ω_2 is far from resonance with transition 1 and Ω_1 with transition 2, we may well neglect these interactions. Under this assumption and the neglect of the counter rotating fields, the hierarchy is easily truncated (see section 6). The more interesting example is represented by case (b), where these interactions play an increasingly important role, the closer Ω_1 and Ω_2 lie together. In the following section we want to show how these interactions can be dealt with in an approximate way.

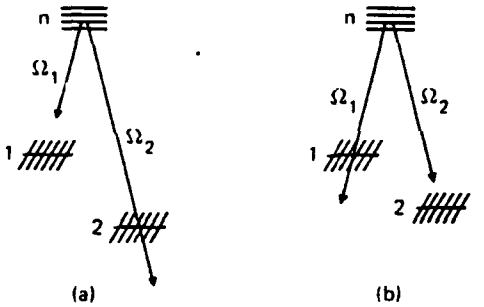
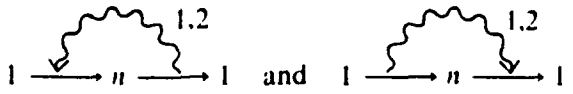
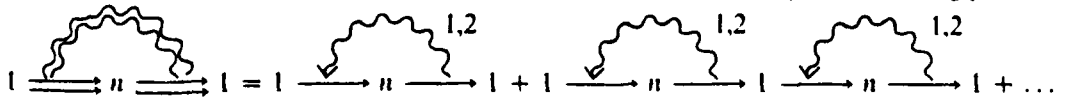


Fig. 3. In case (a) Ω_2 is near resonant with the $n \rightarrow 2$ transition (transition 2) only and Ω_1 with the $n \rightarrow 1$ transition (transition 1) only. The cross-hatched lines on levels 1 and 2 indicate power broadening. In (b) both frequencies are near resonant with both transitions.

Our solution of the coupled equations (12) and (13) is equivalent to a time-dependent perturbation calculation of the wave function where the elementary processes constitute a partial sum carried out to infinite order. By iterating



up to infinite order we approximate the exact diagional matrix element by the following partial sum



From this diagrammatic representation, we can easily make contact to a variety of standard problems in solid state physics where the above "one photon" approximation is frequently used, namely, any vertical line drawn through the diagrams of the approximation cut at most through one wavy photon line. More complex diagrams where two or more photons are present at the same time have been neglected.

After these approximations, (18) and (19) become

$$[z+i\omega_1+i\Omega_1-\Gamma^0_{11}(z_1+i\Omega_1)]\tilde{c}_1(z)=I_1(z_1+i\Omega_1)+\tfrac{1}{2}(\Gamma_{12}(z_1+i\Omega_1)+\Gamma_{12}(z_2+i\Omega_1))\tilde{c}_2, \tag{20}$$

$$[z+i\omega_2+i\Omega_2-\Gamma^0_{22}(z_2+i\Omega_2)]\tilde{c}_2(z)=I_2(z_1+i\Omega_2)+\tfrac{1}{2}(\Gamma_{21}(z_1+i\Omega_2)+\Gamma_{21}(z_2+i\Omega_2))\tilde{c}_1. \tag{21}$$

The problem is now two dimensional and is totally equivalent to a two-level-problem (Appendix B) described by the following effective Hamiltonian matrix elements

$$H_{jj}=\hbar(\omega_j+\Omega_j+i\Gamma_{jj}(z_j+i\Omega_j)), \qquad j=1,2 \tag{22}$$

and

$$H_{12}=i\tfrac{1}{2}\hbar(\Gamma_{12}(z_1+i\Omega_1)+\Gamma_{12}(z_2+i\Omega_1))=H_{21}. \tag{23}$$

Written out explicitly, we have for the Raman process

$$H_{11}=\hbar(\omega_1+\Omega_1)+\tfrac{1}{2}\hbar\sum_n(\chi^1_{1n})^2\frac{(\omega_n-\omega_1)}{\Omega_1^2-(\omega_n-\omega_1)^2}+\tfrac{1}{2}\hbar\sum_n(\chi^2_{1n})^2\frac{(\omega_n-\omega_1)}{\Omega_2^2-(\omega_n-\omega_1)^2} \tag{24}$$

and

$$H_{12}=-\tfrac{1}{8}\hbar\sum_n(\chi^1_{n1})(\chi^2_{2n})(2\omega_n-\omega_1-\omega_2)\times\left[\frac{1}{(\omega_n-\omega_2-\Omega_2)(\omega_n-\omega_1+\Omega_2)}+\frac{1}{(\omega_n-\omega_1-\Omega_1)(\omega_n-\omega_2+\Omega_1)}\right]. \tag{25}$$

These results are identical with those derived by Grischkowsky et al. [14] using the Heitler [15] perturbation approach.

To obtain the energy to various orders, we iterate eqs. (19) and (20). This leads to a continued fraction expansion for the elements of the equivalent Hamiltonian: e.g.

$$\begin{aligned}H^{(0)}_{jj}/\hbar&=\omega_j+\Omega_j,\\ H^{(1)}_{jj}/\hbar&=\omega_j+\Omega_j+i\Gamma^0_{jj}(-iH^{(0)}_{jj}/\hbar+i\Omega_j),\\ H^{(n)}_{jj}/\hbar&=\omega_j+\Omega_j+i\Gamma^0_{jj}(-iH^{(n-1)}_{jj}/\hbar+i\Omega_j).\end{aligned} \tag{26}$$

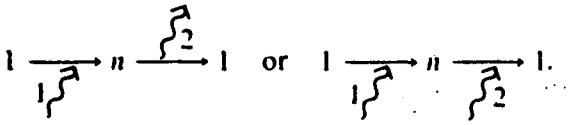
The second order contributions are e.g.

$$H^{(2)}_{11}/\hbar=\omega_1+\Omega_1+\tfrac{1}{2}\sum_n(\chi^1_{1n})^2\frac{(\omega_n-\omega_1-\Omega_1-i\Gamma^0_{11}(-i\omega_1)}{\Omega_1^2-(\omega_n-\omega_1-\Omega_1-i\Gamma^0_{11}(-i\omega_1))^2}+\tfrac{1}{2}\sum_n(\chi^2_{1n})^2\frac{(\omega_n-\omega_1-\Omega_1-i\Gamma^0(-i\omega_1)}{\Omega_2^2-(\omega_n-\omega_1-\Omega_1-i\Gamma^0_{11}(-i\omega_1))^2}. \tag{27}$$

This procedure leads to a continued fraction expansion as can easily be seen by expanding the terms on the right side of eq. (27) into partial fractions. Then the terms $\Gamma^0_{11}(z_1)$ cancel in the numerator and remain only in the denominators.

It is worth mentioning that this approximation contains all antiresonant interactions, as well as all cross-interactions of the field Ω_2 with the transitions $\omega_n-\omega_1$ etc. – as long as they conserve energy in second order.

while $\Gamma^1_{11}(z)$ contains diagrams of the form



These diagrams cannot be deformed into closed loops because they do not conserve energy.

4.1. Raman process

For the nondiagonal parts this expansion depends on the specific process we have in mind. Let's consider for the moment the Raman process and use for convenience the transformation

$$c_1(z + i\Omega_1) = \tilde{c}_1(z), \qquad c_2(z + i\Omega_2) = \tilde{c}_2(z). \tag{17}$$

Then the equations read

$$(z + i\omega_1 + i\Omega_1 - \Gamma_{11}(z + i\Omega_1))\tilde{c}_1(z) = I_1(z + i\Omega_1) + \Gamma_{12}(z + i\Omega_1)\tilde{c}_2(z), \tag{18}$$

$$(z + i\omega_2 + i\Omega_2 - \Gamma_{22}(z + i\Omega_2))\tilde{c}_2(z) = I_2(z + i\Omega_2) + \Gamma_{21}(z + i\Omega_2)\tilde{c}_1(z). \tag{19}$$

See Appendix A for the explicit terms used in (18) and (19) leading to the derivation of eqs. (22)–(25). The transformation (17) makes the following discussion easier because now the c-number terms in $\Gamma_{12}(z + \Omega_1)$ and $\Gamma_{21}(z + i\Omega_2)$ are the resonant interactions for the Raman-type process, as we shall see.

The simpliest approximation to the equations can be found by neglecting the operator contributions totally,

$$\Gamma_{ij}(z) \to \Gamma^0_{ij}(z) \quad \text{and} \quad \Gamma^1_{ij}(z) \to 0.$$

This radical procedure solves for the moment the first problem mentioned above, but we still struggle with the $(N + 2)$nd order eigenvalue equation. We solve this problem by a perturbation approach considering the coupling terms Γ^0_{ij} as the expansion parameter.

In zero order – setting the Γ^0_{ij} equal to zero after all – we first find the undisturbed poles of (18) and (19),

$$z_1 = -i(\omega_1 + \Omega_1) \qquad \text{and} \qquad z_2 = -i(\omega_2 + \Omega_2).$$

In the next step, we assume that the coupling between (18) and (19) can be neglected, i.e.,

$$|\Gamma_{12}| \ll |z_1|, |z_2|.$$

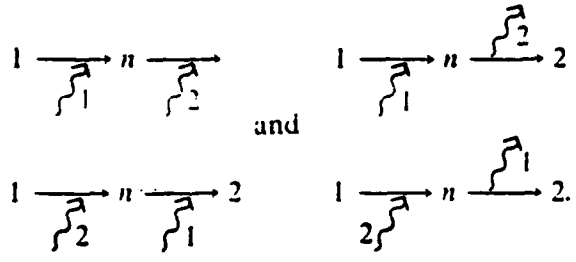
Next, the diagonal matrix elements in first order are found by replacing

$$\Gamma_{11}(z) \to \Gamma_{11}(z_1) \qquad \text{and} \qquad \Gamma_{22}(z) \to \Gamma_{22}(z_2).$$

For the coupling terms $\Gamma_{12}(z)$, we have to insert both poles $z_{1,2}$ simultaneously and get the symmetrized expression

$$\Gamma_{ij}(z) \to \tfrac{1}{2}(\Gamma_{ij}(z_1) + \Gamma_{ij}(z_2)), \qquad i \neq j.$$

twice this process can be made "resonant" and can be an important contribution. The nondiagonal terms depend on the special process considered, for example,



4. Perturbation theory

Let us forget for the moment that the coefficients in eqs. (12) and (13) are operators. Then we could solve this problem by diagonalizing the 2-by-2 matrix. The zero's of the determinant of the matrix would give the "eigen-energies" of the complete problem. From eq. (14) we find the eigenvalues by solving the equation

$$(z + i\omega_1 - \Gamma_{11}(z))(z + i\omega_2 - \Gamma_{22}(z)) - \hat{\Gamma}_{12}(z)\Gamma_{21}(z) = 0. \tag{15}$$

This equation determines a series of values for the poles $z = z_i$.

There are two obstacles in proceeding this way:

1) The $\Gamma_{ij}(z)$ are operators.

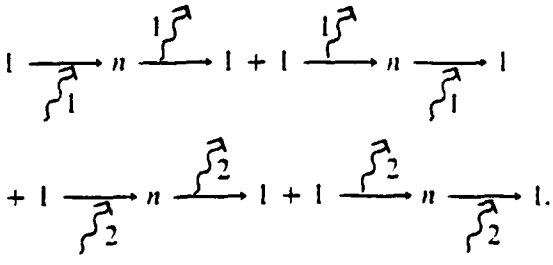
2) Equation (15) is a linear equation of high order and no exact solution exists even if the Γ_{ij} would be c-numbers.

We can find a way out of this predicament when we realize that the Γs can be split into two parts

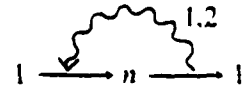
$$\Gamma_{ij}(z) = \Gamma^0_{ij}(z) + \Gamma^1_{ij}(z) \tag{16}$$

where $\Gamma^0_{ij}(z)$ contains the c-number part (the resonant terms) while $\Gamma^1_{ij}(z)$ contains all the translation operators (the nonresonant terms). This is quite obvious, e.g. the diagonal parts in diagrammatic form are

$\Gamma^0_{11}(z)$:



To indicate that these diagrams are resonant we can draw them in a modified form closing the in and outgoing photon lines into a closed loop



$c_1(z \pm i\Delta)$. A similar equation with $c_1(z \pm i\Delta)$ on the left can be generated from (8a) by translating $c_1(z) \to c_1(z \pm i\Delta)$. The right hand terms now include $c_1(z + 2i\Delta)$ and $c_1(z)$ (see fig. 2). Continuing in this way, an infinite hierarchy of coupled equations can be generated. This difficulty is removed by retaining only the leading resonant terms, a step which is equivalent to the rotating wave approximation. Even if we find a way to cut the hierarchy by an approximation into a finite number of equations, we are still left with the problem of solving a characteristic equation of order $(N + 2)$.

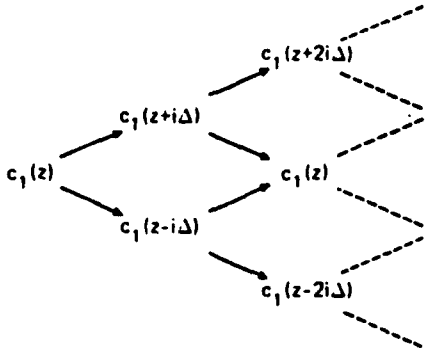
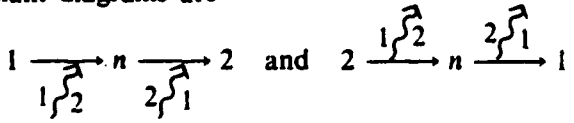


Fig. 2. Diagrammatic representation of an infinite hierarchy of coupled equations in $c_1(z)$, $c_1(z \pm i\Delta)$, ...

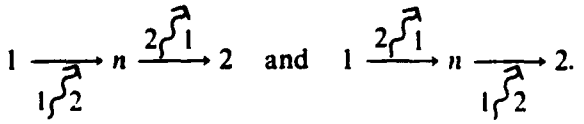
Therefore an approximation would require the following two steps:

1) Restriction to a special level structure. Then we have to neglect all terms that are far from resonance in second order.

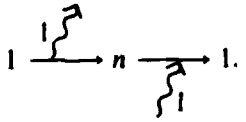
2) The resulting $(N + 2)$ order characteristic equation has to be solved in an approximate way. As an example of point 1), we take the two photon case with level 1 as the ground state. The relevant resonant diagrams are



while the Raman-process with levels 1 and 2 as the lower states can be approximated by the following resonant diagrams

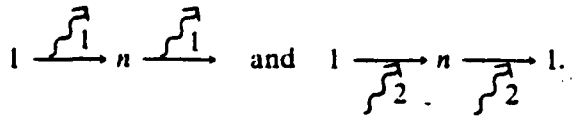


It is important to notice that the above second order terms can be resonant even when they contain nonresonant first order terms. A typical example is



When level 1 is lower than level n, the individual processes $1 \longrightarrow n$ and $n \longrightarrow 1$ are antiresonant (the upward process involves emission). But in second order by "violating" energy conservation

look at the graphs



There is no level arrangement for finite frequencies Ω_1, Ω_2 where these graphs could be of the resonant type. We therefore expect that the contributions from these graphs are of minor importance in any case.

3.3. Formal solution and approximations

The general procedure to approach this complex problem would be the formal solution by the introduction of translation operators

$$T^{\pm}(a)f(z) = f(z \pm a). \tag{10}$$

Then, eq. (8) could be written in the following way

$$(z+i\omega_1)c_1(z) = I_1(z) - \tfrac{1}{2}\sum_n \left[\frac{\chi^1_{1n}}{z+i\omega_n - i\Omega_1} \begin{Bmatrix} [\chi^1_{1n}(1+T^-(2i\Omega_1)) + \chi^2_{1n}(T^+(i\Delta)+T^-(i\Sigma))]c_1(z) \\ +[\chi^1_{2n}(1+T^-(2i\Omega_1)) + \chi^2_{2n}(T^+(i\Delta)+T^-(i\Sigma))]c_2(z) \end{Bmatrix} + \dots \right], \tag{11}$$

and a similar relation for $c_2(z)$. Collecting the individual terms, the formal expressions result

$$(z + i\omega_1 - \Gamma_{11}(z))c_1(z) = I_1(z) + \Gamma_{12}(z)c_2(z) \tag{12}$$

and

$$(z + i\omega_2 - \Gamma_{22}(z))c_2(z) = I_2(z) + \Gamma_{21}(z)c_1(z) \tag{13}$$

where we have to keep in mind that the coefficients $\Gamma_{ij}(z)$ actually are operators of the form (10) acting on any function on the right that depends on z. The translation operators themselves do fulfill relations of Abelian groups – but the operators $\Gamma_{ij}(z)$ no longer commute. The explicit expressions for $\Gamma_{ij}(z)$ can easily be written down by comparing eqs. (12) and (8).

The formal solution can be written down immediately in the form

$$[(z+i\omega_2-\Gamma_{22}(z))(z+i\omega_1-\Gamma_{11}(z)) - \hat{\Gamma}_{12}(z)\Gamma_{21}(z)]c_1(z) = (z+i\omega_2-\Gamma_{22}(z))I_1(z) + \hat{\Gamma}_{12}(z)I_2(z) \tag{14}$$

where we use

$$\hat{\Gamma}_{12}(z) = (z + i\omega_2 - \Gamma_{22})\Gamma_{12}(z)(z + i\omega_2 - \Gamma_{22})^{-1},$$

provided the inverse operator can be defined. An equivalent formal expression results for the variable $c_2(z)$. Equation (14) and the corresponding equation for $c_2(z)$ give the final result in a very compact form, but as long as the matrix-operators $\Gamma_{ij}(z)$ cannot be replaced in some manner by c-numbers this result is useless.

There is no way to find a general solution of the problem without introducing specific assumptions and approximations. The two equations (12) and (13) actually represent an infinite hierarchy of coupled equations. The nature of the hierarchy is more clearly evident by inspection of (8a) where we see that $c_1(z)$ on the left hand side is a function of various terms on the right, such as

These are the most general equations we can write for the system considered as long as the external fields are given parameters.

As is clear from the definition of the basic Hamiltonian and from the structure of eq. (8), our treatment thus far contains all possible resonant and antiresonant interactions. It also includes the interaction of the field Ω_2 with the set of intermediate transitions $\omega_n - \omega_1$ and Ω_1 with $\omega_2 - \omega_n$ as well as Ω_1 with $\omega_n - \omega_1$ and Ω_2 with $\omega_2 - \omega_n$.

3.2. Diagrammatic representation

Each element of the numerous contributions to eq. (8) can be characterized by Feynman-type diagrams which make the physical interpretation more transparent. For example,

$i \xrightarrow[1]{} j$ stands for a transition from level i to j by absorption of a photon of the frequency Ω_1, and

$i \xrightarrow{2} j$ stands for a transition from level i to j by emission of a photon of frequency Ω_2.

Let us write down the contributions to eq. (8a) in diagrammatic form. The first bracket is represented by

$$1 \xrightarrow[1]{} n \xrightarrow{1} 1+1 \xrightarrow[1]{} n \xrightarrow[1]{} 1+1 \xrightarrow[1]{} n \xrightarrow{2} 1+1 \xrightarrow[1]{} n \xrightarrow[2]{} 1$$

$$+1 \xrightarrow[1]{} n. \xrightarrow{1} 2+1 \xrightarrow[1]{} n \xrightarrow[1]{} 2+1 \xrightarrow[1]{} n \xrightarrow{2} 2+1 \xrightarrow[1]{} n \xrightarrow[2]{} 2.$$

Exchanging Ω_1 by $-\Omega_1$ is identical to a time reversal so that emission and absorption processes involving frequency Ω_1 are exchanged. We find the second bracket of (8a) by exchanging in the diagrams above only the Ω_1 processes $1 \xrightarrow[1]{} n \to 1 \xrightarrow{1} n$ and keep the Ω_2 as they are.

The identification of a specific graph and the corresponding contribution to the equations of motion is evident. For example

$$\left[i \xrightarrow[1]{} n \xrightarrow{2} j \right] \equiv \frac{\chi^1_{in}\chi^2_{nj}}{z + i\omega_n - i\Omega_1} c_j(z - i\Omega_1 + i\Omega_2),$$

$$\left[i \xrightarrow{2} n \xrightarrow[1]{} j \right] \equiv \frac{\chi^2_{in}\chi^1_{nj}}{z + i\omega_n + i\Omega_2} c_j(z + i\Omega_2 - i\Omega_1). \tag{9}$$

The index i indicates that the terms are contributions to the equation for $c_i(z)$. With this mnemonic method we could write down the equations for the amplitudes c_1 and c_2 without deriving each term explicitly. From symmetry arguments we easily can check if all possible terms are collected. With the physical interpretation of the individual terms we are able to pick out the relevant terms for a special arrangement of levels and a particular resonance condition. As an example, let's

can be derived then from Maxwell's wave equation

$$\partial \vec{E}_c/\partial z = 2\pi i k N \langle \tilde{p} \rangle$$

when the sample is optically thin, N being the molecular number density. The slowly varying part of the polarization

$$\langle \tilde{p}(t) \rangle = h \,\mathrm{Tr} \langle g \tilde{\rho}(t) \rangle$$

follows from the above wavefunctions where

$$\rho_{ij}(t) = c_i(t) c_j^*(t).$$

The bracket $\langle\rangle$ denotes an average over the Doppler lineshape, and hg is the dipole magnitude. After performing the Laplace transformation we find

$$(z + i\omega_1)c_1(z) = c_1(0) - i \sum_n \tfrac{1}{2}\chi^1_{1n}(c_n(z - i\Omega_1) + c_n(z + i\Omega_1)) - i \sum_n \tfrac{1}{2}\chi^2_{1n}(c_n(z - i\Omega_2) + c_n(z + i\Omega_2)). \tag{6}$$

The equation for $c_2(z)$ is easily found by exchanging the sub-indices 1 and 2. The form of $c_n(z)$ is

$$\begin{aligned}(z + i\omega_n)c_n(z) = c_n(0) &- \tfrac{1}{2}i\chi^1_{1n}(c_1(z + i\Omega_1) + c_1(z - i\Omega_1)) - \tfrac{1}{2}i\chi^2_{1n}(c_1(z + i\Omega_2) + c_1(z - i\Omega_2)) \\ &- \tfrac{1}{2}i\chi^1_{2n}(c_2(z + i\Omega_1) + c_2(z - i\Omega_1)) - \tfrac{1}{2}i\chi^2_{2n}(c_2(z + i\Omega_2) + c_2(z - i\Omega_2)).\end{aligned} \tag{7}$$

By substituting eq. (7) into (6) and the corresponding equation for $c_2(z)$, we are left with two coupled equations for $c_1(z)$ and $c_2(z)$ where

$$\begin{aligned}(z+i\omega_1)c_1(z) = I_1(z) - \tfrac{1}{4}\sum_n \Bigg[&\frac{\chi^1_{1n}}{z+i\omega_n - i\Omega_1}\Big\{\chi^1_{1n}(c_1(z)+c_1(z-2i\Omega_1))+\chi^2_{1n}(c_1(z+i\Delta)+c_1(z-i\Sigma)) \\ &+\chi^1_{2n}(c_2(z)+c_2(z-2i\Omega_1))+\chi^2_{2n}(c_2(z+i\Delta)+c_2(z-i\Sigma))\Big\} \\ &+\frac{\chi^1_{1n}}{z+i\omega_n + i\Omega_1}\Big\{\chi^1_{1n}(c_1(z)+c_1(z+2i\Omega_1))+\chi^2_{1n}(c_1(z-i\Delta)+c_1(z+i\Sigma)) \\ &+\chi^1_{2n}(c_2(z)+c_2(z+2i\Omega_1))+\chi^2_{2n}(c_2(z-i\Delta)+c_2(z+i\Sigma))\Big\} \\ &+\frac{\chi^2_{1n}}{z+i\omega_n - i\Omega_2}\Big\{\chi^1_{1n}(c_1(z-i\Delta)+c_1(z-i\Sigma))+\chi^2_{1n}(c_1(z)+c_1(z-2i\Omega_2)) \\ &+\chi^1_{2n}(c_2(z-i\Delta)+c_2(z-i\Sigma))+\chi^2_{2n}(c_2(z)+c_2(z-2i\Omega_2))\Big\} \\ &+\frac{\chi^2_{1n}}{z+i\omega_n + i\Omega_2}\Big\{\chi^1_{1n}(c_1(z+i\Delta)+c_1(z+i\Sigma))+\chi^2_{1n}(c_1(z)+c_1(z+2i\Omega_2)) \\ &+\chi^1_{2n}(c_2(z+i\Delta)+c_2(z+i\Sigma))+\chi^2_{2n}(c_2(z)+c_2(z+2i\Omega_2))\Big\}\Bigg]\end{aligned} \tag{8a}$$

with $\Delta = \Omega_2 - \Omega_1$ and $\Sigma = \Omega_1 + \Omega_2$.

$I_1(z)$ is the collection of inhomogenities which depend on the $c_i(0)$ terms, and is not needed explicitly at the moment. The corresponding equation in $c_2(z)$ is

$$\begin{aligned}(z+i\omega_2)c_2(z) = I_2(z) - \tfrac{1}{4}\sum_n \Bigg[&\frac{\chi^1_{2n}}{z+i\omega_n - i\Omega_1}\Big\{\chi^1_{1n}(c_1(z)+c_1(z-2i\Omega_1))+\chi^2_{1n}(c_1(z+i\Delta)+c_1(z-i\Sigma)) \\ &+\chi^1_{2n}(c_2(z)+c_2(z-2i\Omega_1))+\chi^2_{2n}(c_2(z+i\Delta)+c_2(z-i\Sigma))\Big\} \\ &+\frac{\chi^1_{2n}}{z+i\omega_n + i\Omega_1}\Big\{\chi^1_{1n}(c_1(z)+c_1(z+2i\Omega_1))+\chi^2_{1n}(c_1(z-i\Delta)+c_1(z+i\Sigma)) \\ &+\chi^1_{2n}(c_2(z)+c_2(z+2i\Omega_1))+\chi^2_{2n}(c_2(z-i\Delta)+c_2(z+i\Sigma))\Big\} \\ &+\frac{\chi^2_{2n}}{z+i\omega_n - i\Omega_2}\Big\{\chi^1_{1n}(c_1(z-i\Delta)+c_1(z-i\Sigma))+\chi^2_{1n}(c_1(z)+c_1(z-2i\Omega_2)) \\ &+\chi^1_{2n}(c_2(z-i\Delta)+c_2(z-i\Sigma))+\chi^2_{2n}(c_2(z)+c_2(z-2i\Omega_2))\Big\} \\ &+\frac{\chi^2_{2n}}{z+i\omega_n + i\Omega_2}\Big\{\chi^1_{1n}(c_1(z+i\Delta)+c_1(z+i\Sigma))+\chi^2_{1n}(c_1(z)+c_1(z+2i\Omega_2)) \\ &+\chi^1_{2n}(c_2(z+i\Delta)+c_2(z+i\Sigma))+\chi^2_{2n}(c_2(z)+c_2(z+2i\Omega_2))\Big\}\Bigg].\end{aligned} \tag{8b}$$

The open parameter v appears in the tuning parameters which are of the form $\Delta_i = \Omega_i + \omega_n - \omega_i$ ($i = 1, 2$ and $n \geq 3$) and is carried through the whole calculation. Only in the final results do we average over a thermal velocity distribution. Later, we shall see that some solutions depend critically on the velocity while others do not. In general, all parameters containing kv are undetermined and any expansion parameter we use for approximations has to be independent of kv when the Doppler-broadening is larger than all other system parameters. For example, the description with two optical fields propagating parallel or antiparallel contains the tuning parameter sum $\Delta_1 \pm \Delta_2$ where the Doppler shifts cancel. These are just the two-photon resonances that have been exploited so successfully in recent Doppler free spectroscopy studies [4].

3. Formulation of the basic equations

3.1. Outline of the theory

The wave function of the system is

$$\psi(t) = \sum_n c_n(t)\,|n\rangle. \tag{2}$$

The time-dependent Schrödinger-equation leads to the following system of linear first-order differential equations for the expansion coefficients $c_n(t)$:

$$\dot{c}_1(t) = -i\omega_1 c_1 - i\sum_n g_{1n} c_n (E_1(t) + E_2(t)), \tag{3}$$

$$\dot{c}_2(t) = -i\omega_2 c_2 - i\sum_n g_{2n} c_n (E_1(t) + E_2(t)), \tag{4}$$

$$\dot{c}_n(t) = -i\omega_n c_n - i g_{n1} c_1 (E_1(t) + E_2(t)) - i g_{n2} c_2 (E_1(t) + E_2(t)). \tag{5}$$

These constitute a set of $N + 2$ coupled equations. We can assume without specializing the problem that

$$g_{ij} = g_{ji} \qquad \text{and define} \qquad g_{in} E_j = \tfrac{1}{2}\chi^j_{in}.$$

For solving the system of equations (3)–(5) we use the standard procedure of Laplace-transformation where

$$c(z) = \int_0^\infty e^{-zt} c(t)\,dt, \qquad c(t) = \frac{1}{2\pi i}\int_{-i\infty}^{+i\infty} e^{izt} c(z)\,dz \qquad \text{and} \qquad c(0) = c(t = 0).$$

It should be mentioned that a linear system of differential equations with time-dependent coefficients can be transformed into algebraic equations only when the coefficients can be expanded into a series of exponentials. The coupled differential equations are then transformed into a set of coupled difference equations.

The major portion of this article is concerned with finding the $N + 2$ poles z_i which satisfy the characteristic equation associated with the $N + 2$ $c(z)$ equations of motion. The solutions, which are obtained in various degrees of approximation, yield the coefficients $c_n(t)$ after application of the inverse Laplace transform, given above. Coherent optical transient signals of the form

$$E_c(z, t) = \tilde{E}_c(z, t)\, e^{-i(\Omega t - kz)} + \text{c.c.}$$

In section 4, we retain resonant terms to second order and find an effective Hamiltonian which is equivalent to a two level quantum problem. Higher orders are obtained in a continued fraction expansion where the expansion parameter χ/Δ is the ratio of the Rabi frequency to the off resonance tuning parameter. The leading term in this series is the result given by Takatsuji [13] and by Grischkowsky et al. [14]. In section 5, nonresonant terms are included in the above calculation, as is necessary when the two optical frequencies Ω_1 and Ω_2 are sufficiently close that $|\Omega_1 - \Omega_2| \sim \chi$.

An important aspect of these perturbative calculations is the underlying assumption that $\chi/\Delta \ll 1$, or an equivalent approximation, that must be maintained. This condition will prevail when the line is homogeneously broadened. When inhomogeneous broadening plays a role, the tuning parameter Δ is not unique and in fact can vary from $-\infty \to 0 \to +\infty$. This point appears not to have been considered in earlier work. In section 6, new nonperturbative solutions are presented where the singularity $\Delta \to 0$ does not appear. Solutions are found for the $N + 2$ and the three level problems, either in exact or approximate form.

Another important characteristic of two photon transients is that they exhibit intensity-dependent dephasing [12]. This property does not appear in the earlier perturbation calculations [12–14, 16, 17]. A nonperturbative treatment is required, and an example of this effect is given in section 8 for the Raman beat effect.

2. The Hamiltonian

We treat a multilevel quantum system, with $N + 2$ levels, interacting with two optical fields

$$E_i(t) = 2E_i \cos \Omega_i t \qquad i = 1, 2$$

in a two photon or Raman process. Dipole interactions are assumed. We have in mind the level configurations of fig. 1 where the initial state is level 1, the final state is level 2 and there are N intermediate states. To distinguish case (a) from case (b) in fig. 1, hereafter we will refer to case (a) as the "two photon process" and to case (b) as the Raman process.

The fundamental Hamiltonian of the problem is

$$\begin{aligned} H = &\sum_n \hbar\omega_n a_n^\dagger a_n \\ &+ \sum_n \hbar g_{n1} a_n^\dagger a_1 (E_1(t) + E_2(t)) + \text{hermitian conjugate} \\ &+ \sum_n \hbar g_{n2} a_n^\dagger a_2 (E_1(t) + E_2(t)) + \text{hermitian conjugate} \end{aligned} \tag{1}$$

where $\hbar\omega_n$ = the eigenvalue of the undisturbed atomic level n, and $\hbar g_{ij}$ = a dipole matrix element. The quantities $a^\dagger$ and a are the atomic creation and annihilation operators which satisfy the Fermi commutation relation $a_n a_m^\dagger + a_m^\dagger a_n = \delta_{n,m}$. The level index n of the intermediate levels runs from $n = 3$ to $N + 2$.

For this $N + 2$ dimensional problem, wave function solutions of the Schrödinger equation are to be found. Phenomenological damping terms are neglected in the equations of motion as they affect population decay only and do not modify the nature of the solutions.

For an inhomogeneous system which is Doppler-broadened the external frequencies have to be corrected according to the longitudinal velocity v of the absorber where

$$\Omega_{1,2} \to \Omega_{1,2}^0 + k_{1,2} v.$$

3) $L = 0$ when the transition matrix elements from level 1 to n and from n to 2 are equal, but may still depend on n so that
$g_{1n} = g_{2n}$.

In general, L is not zero, but is of 4th order in the coupling constant q. Therefore, it is very tempting to drop this term for one of the above reasons. For the discussion of the $(N-2)$ level system with $N > 1$, we further assume two-photon resonance

$$\omega_2 - \omega_1 = \Omega_2 + \Omega_1 .$$

With the transformation

$$z = i(S - \omega_1 - \Omega_1), \qquad z = i(S - \omega_2 + \Omega_2),$$

we find for the characteristic equations (39)

$$S\left[S - \sum_{n=1}^{N} \frac{G_n^2}{S - \Delta_n}\right] = 0 \tag{40}$$

where $G_n^2 = \frac{1}{4}[(\chi_{1n}^1)^2 + (\chi_{2n}^2)^2]$ and $\Delta_n = \Omega_1 - \omega_n + \omega_1 = \omega_2 - \omega_n - \Omega_2$. The trivial pole $S = 0$ follows from the two-photon resonance assumption, i.e.,

$$S_0 = 0 \rightarrow z_0 = -i\omega_1 .$$

6.1. Geometric solutions

The nontrivial solutions of (40) can be given a geometrical interpretation. The solutions of

$$S = \sum_{n=1}^{N} \frac{G_n^2}{S - \Delta_n} \tag{41}$$

as shown in fig. 4, are the intersections of various curves with a straight line of 45° slope.
From the graphical representation we already can draw a number of general conclusions:

1) If all Δ_n are positive, we find in the limit $\chi \rightarrow 0$

$$S_1 \rightsquigarrow 0^-$$

$$S_l \rightsquigarrow \Delta_{l-1}, \qquad l = 2, 3 \ldots N + 1.$$

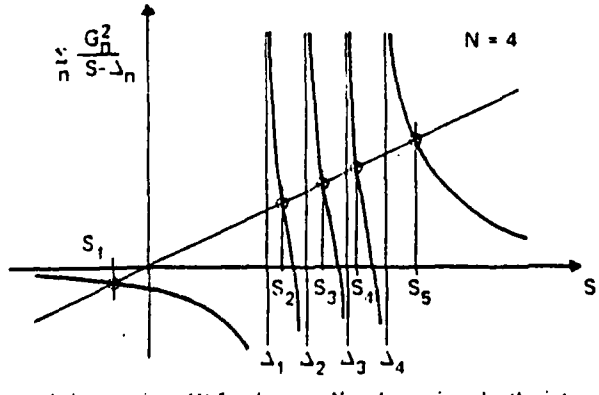


Fig. 4. The solutions of the characteristic equation (41) for the case $N = 4$ are given by the intercepts of a line of 45° slope with the $\sum_n G_n^2/(S - \Delta_n)$ versus S curves.

2) If all Δ_n are negative, we find in the limit $\chi \to 0$

$$S_l \rightsquigarrow \Delta_l, \qquad l = 1, 2 \ldots N$$

$$S_{N+1} \rightsquigarrow 0^+.$$

3) In the limit $\chi \to \infty$ there remains a band of solutions still close to the free solutions Δ_n. Two solutions S_1 and S_{N+1} split far apart from the undisturbed values.

4) In the limit $|\Delta_n| \gg \chi$, N solutions lie close to Δ_n while one solution is split apart lying close to zero.

From the definition

$$\Delta_n = \Omega_1 - (\omega_n - \omega_1),$$

we see that in a Doppler-broadened system the longitudinal molecular velocity v appears as an open parameter through the relation $\Omega_1 = \Omega_1^0 + kv$. Varying v from $-\infty$ to $+\infty$ means that we move all the vertical asymptotes together from $-\infty$ to $+\infty$, shifting the exact eigenvalues

$$\begin{aligned} -\infty \leftarrow v \quad &\rightarrow +\infty \\ \Delta_l \quad \leftarrow S_l \quad &\rightarrow \Delta_{l-1}, \qquad l = 2, 3, \ldots N \\ \Delta_1 \quad \leftarrow S_1 \quad &\rightarrow 0^- \\ 0^+ \quad \leftarrow S_{N+1} &\rightarrow \Delta_N. \end{aligned} \tag{42}$$

From (42) we conclude that a simple perturbation theory cannot give satisfactory results for the whole variation of v because even for small χ a single pole can approach different limiting values for large positive and negative values of v.

6.2. *Analytic solutions*

We can find approximate eigenvalues in analytic form in the case $|\Delta_{n+1} - \Delta_n| \gg \chi$ for all n as this relation is independent of the molecular velocity. Under this assumption it is straightforward to derive the following approximate results, where we use for convenience $\Delta_n < \Delta_{n+1}$ for all n. The poles are

$$\begin{aligned} S_1 &= \tfrac{1}{2}(\Delta_1 - \sqrt{\Delta_1^2 + 4G_1^2}), \\ S_{n+1} &= \tfrac{1}{2}(\Delta_n + \Delta_{n+1} + \sqrt{\Delta_n^2 + 4G_n^2} - \sqrt{\Delta_{n+1}^2 + 4G_{n+1}^2}) \qquad \text{for } n = 1, 2, 3, \ldots N-1, \\ S_{N+1} &= \tfrac{1}{2}(\Delta_N + \sqrt{\Delta_N^2 + 4G_N^2}). \end{aligned} \tag{43}$$

These solutions are not perturbation results and therefore can fulfill the requirements (42). It is worth mentioning that the exact solutions do not have unique limiting values when $\chi_{in} \to 0$ in contrast to the perturbation solution of section 4. These unique properties are well represented by the above approximate solutions, e.g.

$$\begin{aligned} S_1 &\to 0^- \qquad \Delta_1 > 0 \qquad G_1 \to 0 \\ S_1 &\to \Delta_1 \qquad \Delta_1 < 0 \qquad G_1 \to 0 \end{aligned}$$

and

$$S_l \to \Delta_{l-1} \qquad \Delta_{l-1}, \Delta_l > 0 \qquad G_{l-1}, G_l \to 0$$
$$S_l \to \Delta_l \qquad \Delta_{l-1}, \Delta_l < 0 \qquad G_{l-1}, G_l \to 0$$
$$S_l \to 0 \qquad \Delta_{l-1} < 0, \Delta_l > 0 \qquad G_{l-1}, G_l \to 0.$$

That the exact solutions approach these limiting values can be verified easily using the graphical construction above.

Let us briefly discuss some other limiting results.

1) In the case $G_n \to \infty$, each of the intermediate $N-1$ solutions are constrained to lie between its two neighboring poles. The two outer solutions are separated far apart from this band. They are given by

$$S_{1,N+1} = \tfrac{1}{2}(\Delta_{1,N+1} \mp \sqrt{\Delta_{1,N+1}^2 + 4\sum_n G_n^2}),$$
$$S_n = (G_{n+1}^2\Delta_n + G_n^2\Delta_{n+1})/(G_{n+1}^2 + G_n^2) \qquad \text{for } 2 \geq n \geq N \tag{44}$$

if $\sum_n G_n^2 \gg |\Delta_N - \Delta|^2$.

2) In the case of symmetry where

$$\Delta_n = -\Delta_{N-n+1}, \qquad G_n^2 = G_{N-n+1}^2,$$

it follows that $\sum_n G_n^2/\Delta_n = 0$ and $S = 0$ is a two-fold degenerate pole.

3) The case of degeneracy $\Delta_n = \Delta$ for all n is equivalent to the 3-level problem. We find there are $N-1$ degenerate solutions

$$S_l = \Delta \quad \text{and}$$
$$S_{1,N+1} = \tfrac{1}{2}(\Delta \mp \sqrt{\Delta^2 + 4\sum_n G_n^2}). \tag{45}$$

Compared with the 3-level results in two-photon resonance, we realize that the multiplicity of the intermediate levels increases the power-broadening N times, i.e.,

$$G^2 \to \sum_n G_n^2 \to NG^2.$$

4) If the intermediate levels are numerous, we might assume the levels to be continuously distributed and replace the sum in eq. (41) by an integral

$$S = \sum_n \frac{G_n^2}{S - \Delta_n} \to \int_{\xi_1}^{\xi_2} D(\xi)\frac{G^2(\xi)}{S - \xi}\,d\xi, \tag{46}$$

where

$$D(\xi) = \lim_{\delta_n \to 0} \frac{\delta n}{\Delta_{n+\delta n} - \Delta_n}.$$

The function $D(\xi)$ characterizes the density of states. Assuming $D(\xi)$, $G(\xi)$ to be regular functions, we can write

$$S = \mathrm{P}\int_{\xi_1}^{\xi_2} \frac{D(\xi)G^2(\xi)}{S - \xi}\,d\xi + i\pi \begin{cases} D(s)G^2(s) & \text{if } \xi_1 < s < \xi_2 \\ 0 & \text{otherwise.} \end{cases} \tag{47}$$

In the special case of $D(\xi)G^2(\xi) = D(0)G^2(0)$ we find

$$S = -D(0)G^2(0) \begin{cases} \ln\dfrac{\xi_2 - S}{S - \xi_1} - i\pi & \xi_1 < S < \xi_2 \\ \ln\dfrac{\xi_2 - S}{\xi_1 - S} + 0 & \text{otherwise.} \end{cases} \tag{48}$$

If we first drop the imaginary parts, we can solve eq. (48) graphically (see fig. 5). Two solutions S_1 and S_3 lie outside the region $\xi_1 - \xi_2$, and therefore, dropping the imaginary parts is allowed so that these solutions are real. However, the third solution lies inside this region and is complex. Under the assumption that the imaginary part is small, we can approximate the solution S_2 by deriving its real part from

$$S_2^R = -D(0)G^2(0)\ln\frac{\xi_2 - S_2^R}{S_2^R - \xi_1}. \tag{49}$$

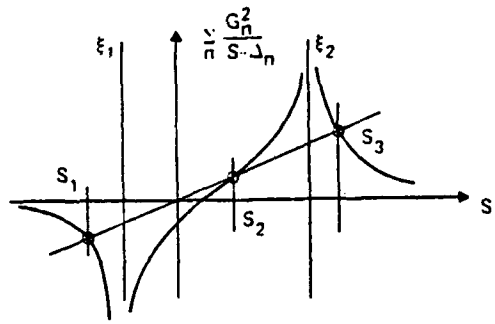


Fig. 5. Graphical solution of the characteristic equation (46) for the case where the density of intermediate states is continuous.

The imaginary part then is given by

$$S_2^I = \pi D(0)G^2(0).$$

Summarizing we find

$S_1 < \xi_1$ and real

$S_3 > \xi_2$ and real

$S_2 = S_2^R + iS_2^I$ where $\xi_1 < S_1^R < \xi_2$.

This means that we have replaced the N-level system by an equivalent 3-level system. The multitude of intermediate levels is reflected in the broadening of one of the eigenvalues. The finite lifetime of this pole is proportional to the intensity of the optical field (intensity-dependent dephasing). We note that this complicated problem simplifies when the density of states is high for the intermediate levels and therefore could be of importance in solid state problems.

6.3. The general three-level problem

The general 3-level problem, making use only of the rotating wave approximation in (39), leads to the following characteristic equation

$$(z + i\omega_1 + i\Omega_1)(z + i\omega_2 - i\Omega_2) + \tfrac{1}{4}(\chi_{13}^1)^2 \frac{z + i\omega_2 - i\Omega_2}{z + i\omega_3} + \tfrac{1}{4}(\chi_{23}^2)^2 \frac{z + i\omega_1 + i\Omega_1}{z + i\omega_3} = 0. \quad (50)$$

In contrast to the $N + 2$ level problem, the two-photon resonance condition $\omega_2 - \omega_1 = \Omega_2 + \Omega_1$ is not required in obtaining an analytic result. Using the transformation $z = iS - i\omega_3$ to symmetrize the equation, we end up with

$$S = \tfrac{1}{4}\left(\frac{(\chi_{13}^1)^2}{S + \omega_1 - \omega_3 + \Omega_1} + \frac{(\chi_{23}^2)^2}{S + \omega_2 - \omega_3 - \Omega_2}\right). \quad (51)$$

With the abbreviations

$$w_1 = \omega_3 - \omega_1 - \Omega_1, \qquad w_2 = \omega_3 - \omega_2 + \Omega_2,$$

we arrive at a characteristic equation

$$S = \tfrac{1}{4}\left(\frac{(\chi_{13}^1)^2}{S - w_1} + \frac{(\chi_{23}^2)^2}{S - w_2}\right) \quad (52)$$

that in a formal way is identical to the 4-level problem for two-photon resonance (41). With the resonance conditions used, the labeling χ_{13}^1, χ_{23}^2 is now redundant and we shall use χ_1, χ_2 instead.

Exact solutions of this equation exist in the following cases:

$$\begin{aligned}
&1)\ \chi_1 = \chi_2 = 0: && S_{1,2} = w_{1,2};\quad S_3 = 0\\
&2)\ w_1 = w_2 = w: && S_1 = w;\quad S_{2,3} = \tfrac{1}{2}(w \pm \sqrt{w^2 + (\chi_1)^2 + (\chi_2)^2})\\
&3)\ w_1 = -w_2 = w \quad \text{and} \quad \chi_1 = \chi_2 = \chi: && S_1 = 0;\quad S_{2,3} = \pm\sqrt{w^2 + \tfrac{1}{2}\chi^2} \qquad (53)\\
&4)\ \chi_2^2 - \chi_1^2 = w_1^2 - w_2^2: && S_1 = \tfrac{1}{2}(w_1 + w_2);\\
& && S_{2,3} = \tfrac{1}{4}(w_1 + w_2 \pm \sqrt{(w_1 + w_2)^2 + (\chi_1)^2 + (\chi_2)^2}).
\end{aligned}$$

It will now be evident that cases 2) and 3) above for the two photon process are independent of molecular velocity with the following laser beam geometry

(a) $w_1 = w_2 \to \omega_2 - \omega_1 = \Omega_2 + \Omega_1 = \Omega_1^0 + \Omega_2^0 + (k_1 + k_2)v$
$k_1 = -k_2$, antiparallel beams

(b) $w_1 + w_2 = 0 \to 2\omega_3 - \omega_1 - \omega_2 = \Omega_1 - \Omega_2$, the beams are parallel.
In addition, for the Raman process, we have

(c) $w_1 = w_2 \to \omega_2 - \omega_1 = \Omega_1 - \Omega_2 = \Omega_1^0 - \Omega_2^0 + (k_1 - k_2)v$
$k_1 = k_2$, parallel beams

(d) $w_1 + w_2 = 0 \to 2\omega_n - \omega_1 - \omega_2 = \Omega_1 + \Omega_2$, the beams are antiparallel where now $w_1 = \omega_3 - \omega_1 - \Omega_1$ and $w_2 = \omega_3 - \omega_2 - \Omega_2$. We see that in all four cases, the tuning parameter is velocity independent. When $\Omega_1 = \Omega_2$, cases (b) and (c) become degenerate while the other cases remain unspecialized. We note that case (a) corresponds to the familiar two-photon Doppler free resonance and case (c) to Doppler free forward Raman scattering, as in the Raman beat effect. Cases (b) and (d) are unusual nonresonant contributions.

These exact solutions can be used as a starting point for perturbation results of various kinds. Expanding around these solutions leads to the following cases:

1) $\chi_{1,2} \ll w_{1,2}$

$$S_1 = w_1 + \tfrac{1}{4}(\chi_1)^2/w_1, \qquad S_2 = w_2 + \tfrac{1}{4}(\chi_2)^2/w_2$$
$$S_3 = -\tfrac{1}{4}((\chi_1)^2/w_1 + (\chi_2)^2/w_2). \tag{54}$$

2) $|w_1 - w_2| \ll \chi$,

$$S_1 = \tfrac{1}{2}\left(w_1 + w_2 - \frac{w_1^2 - w_2^2 + (\chi_1)^2 - (\chi_2)^2}{(\chi_1)^2 + (\chi_2)^2}(w_1 - w_2)\right)$$
$$S_{2,3} = \tfrac{1}{4}(w_1 + w_2 \pm \sqrt{\ })\left(1 \pm \tfrac{1}{2}\frac{w_1 + w_2 \pm \sqrt{\ }}{\sqrt{((\chi_1)^2 + (\chi_2)^2)}}(w_1 - w_2)^2\right) \tag{55}$$

where

$$\sqrt{\ } = [(w_1 + w_2)^2 + 4(\chi_1)^2 + 4(\chi_2)^2]^{1/2}.$$

3) $|\chi_1 - \chi_2| \ll \chi_{1,2}$ and $w_1 + w_2 \ll \chi_{1,2}$,

$$S_1 = \frac{(\chi_1)^2 w_2 + (\chi_2)^2 w_1}{(w_1 - w_2)^2 + (\chi_1)^2 + (\chi_2)^2}$$
$$S_{2,3} = \pm \tfrac{1}{2}\sqrt{(w_1 - w_2)^2 + (\chi_1)^2 + (\chi_2)^2} - \tfrac{1}{4}\left(1 + \frac{(w_1 - w_2)^2}{(w_1 - w_2)^2 + (\chi_1)^2 + (\chi_2)^2}\right)^2. \tag{56}$$

Nonperturbative results can be derived also in the limit $|w_1 - w_2| \gg \chi_1, \chi_2$. Here, we derive results that are analogous to those for the general $N + 2$ level problem which are given in (43). From the graphical representation, it is obvious in the limit $|w_1 - w_2| \gg \chi$ that the mutual interference of the poles w_1 and w_2 can be made small, and we find with $w_1 < w_2$ that

$$S_1 = \tfrac{1}{2}(w_1 - \sqrt{w_1^2 + \chi_1^2}), \qquad S_2 = \tfrac{1}{2}(w_2 + \sqrt{w_2^2 + \chi_2^2}). \tag{57}$$

Dividing the characteristic equation (52) by $(S - S_1) \cdot (S - S_2)$ leads to an approximate result for the third pole

$$S_3 = \tfrac{1}{2}(w_1 + w_2 + \sqrt{w_1^2 + \chi_1^2} - \sqrt{w_2^2 + \chi_2^2}). \tag{58}$$

All the limiting values above are reasonably approximated by these expressions. It is important to notice that the values S_i are not perturbation results that approach the undisturbed eigenvalues in a unique way. One eigenvalue can approach different undisturbed eigenvalues, depending on the signs of w_1 and w_2. This is an important property of the exact results as well.

In the opposite limit $|w_1 - w_2| \ll \chi$ where the levels overlap due to power-broadening, we find

$$S_{1,2} = \tfrac{1}{2}(\Delta \pm \sqrt{\Delta^2 + \chi_1^2 + \chi_2^2}) \qquad \text{with} \quad \Delta = \tfrac{1}{2}(w_1 + w_2)$$

and

$$S_3 = \frac{w_1 \chi_2^2 + w_2 \chi_1^2}{\chi_1^2 + \chi_2^2} + \ldots, \tag{59}$$

which corresponds to eq. (44).

7. Eigenfunctions of the stationary Hamiltonian

Once a solution is obtained in the resonance approximation, the poles can then be inserted into eq. (8) for the amplitudes $c_1(z)$ and $c_2(z)$. The inverse Laplace-transformation is a trivial procedure and gives explicitly the general results

$$c_n(t) = c_n(t, c_1(0), c_2(0), \ldots c_{N+2}(0)), \tag{60}$$

which then can be used to derive various optical transients. At this point the problem is solved, but it still might be of interest in comparison with other treatments to deduce the eigenfunctions from the general result. In doing so, we have to remember that a complete set of eigenfunctions exists only for a stationary problem. It is necessary therefore to invoke the rotating wave approximation so that the Hamiltonian and the eigenfunctions are time-independent in the rotating frame where

$$c_1(z) = \tilde{c}_1(z \pm i\Omega_1), \qquad c_2(z) = \tilde{c}_2(z \pm i\Omega_2),$$

and the signs have to be chosen equal for the Raman and opposite for the two-photon process.

7.1. $N + 2$ level case

For the $(N + 2)$ level system under the assumption of two photon resonance and $L = 0$ in (39) we can write the unnormalized eigenfunction as

$$|n\rangle = \left\{S_n - \tfrac{1}{4}\sum_k \frac{(\chi_{2k}^2)^2}{S_n - \Delta_k}\right\}|1\rangle + \tfrac{1}{4}\sum_k \frac{\chi_{1k}^1\chi_{2k}^2}{S_n - \Delta_k}|2\rangle - \tfrac{1}{2}\sum_k \frac{\chi_{1k}^1 S_n}{S_n - \Delta_k}|k\rangle. \tag{61}$$

Here, we have taken the initial conditions to be $c_1(0) = 1$, $c_2(0) = c_n(0) = 0$ so that $I_1 = 1$ and $I_2 = 0$. Inserting the eigenvalues derived in the different approximations in (61) gives the corresponding eigenfunctions of the interacting system. For simplicity, we assume $\chi_{1n}^1 = \chi_{2n}^2$. The assumption of resonance leads to the exact eigenfunction

$$|0\rangle = \tfrac{1}{2}(|1\rangle - |2\rangle); \qquad S_0 = 0 \tag{62}$$

and reduces the dimensionality of the problem by 1. In the case of a 3-level system the assumption of two photon resonance reduces the problem to an effective 2-level system, as in the Brewer-Hahn treatment [11].

In the limit $\chi \ll \Delta_n$ we find e.g.

$$|l\rangle = N_l(|1\rangle + |2\rangle - 2\frac{\Delta_l}{\chi}|l\rangle) \qquad S_n \approx \Delta_n + \tfrac{1}{2}\chi^2/\Delta_n$$

$$|N+1\rangle = N_{N+1}(|1\rangle + |2\rangle + \sum_k \frac{\chi}{\Delta_k}|k\rangle) \qquad S_{N+1} \approx -\tfrac{1}{2}\sum_n \frac{\chi^2}{\Delta_n} \tag{63}$$

where the factor N_l takes care of the normalization of the eigenfunctions. Note that the eigenfunctions $|l\rangle$ where $l = 0, 1, 2, \ldots N + 1$ are mutually orthogonal as can be seen in (62) and (63), as expected. In the limit $\chi \to 0$ the above eigenfunctions are

$$|0\rangle = \frac{1}{\sqrt{2}}(|1\rangle - |2\rangle), \qquad |l\rangle = |l\rangle, \qquad |N+1\rangle = \frac{1}{\sqrt{2}}(|1\rangle + |2\rangle). \tag{64}$$

Thus, we get the linear combinations

$$|1\rangle \pm |2\rangle$$

and not $|1\rangle, |2\rangle$. This is quite obvious when we remember that the assumption of two photon resonance makes the noninteracting system degenerate in the energy level splitting $\Delta_n = \Omega_1 - \omega_n + \omega_1 = \omega_2 - \omega_n - \Omega_2$ in the rotating frame. Therefore in zeroth order the even and odd linear combinations are the proper eigenfunctions.

7.2. *Three level case*

For the general 3-level problem, without invoking a resonance assumption, we find for the two photon process

$$|I\rangle = N_I\{(S_I(S_I - w_2) - \tfrac{1}{4}(\chi_{23}^2)^2)|1\rangle + \tfrac{1}{4}(\chi_{13}^1)^2(\chi_{23}^2)^2|2\rangle + \tfrac{1}{2}\chi_{23}^2(S_I - w_2)|3\rangle\}. \tag{65}$$

Setting for simplicity $\chi_{13}^1 = \chi_{23}^2$ and using the approximate eigenvalues (57) and (58), there results

$$\begin{aligned}
|1\rangle &= N_1\{\tfrac{1}{2}\Delta(\Delta - w_2 - \sqrt{w_1^2 + \chi^2})|1\rangle + \tfrac{1}{4}\chi^2|2\rangle + \tfrac{1}{4}\chi^2(\Delta - w_2 - \sqrt{w_1^2 + \chi^2})|3\rangle\} \\
|2\rangle &= N_2\{\tfrac{1}{4}\chi^2|2\rangle - \tfrac{1}{4}\chi(w_2 - \sqrt{w_2^2 + \chi^2})|3\rangle\} \\
|3\rangle &= N_3\{(w_1 + \sqrt{w_1^2 + \chi_2})(w_1 + \sqrt{w_1^2 + \chi^2} - 2\sqrt{w_2^2 + \chi^2})|1\rangle + \chi^2|2\rangle + \chi(\Delta + \sqrt{w_1^2 + \chi^2} \\
&\quad - \sqrt{w_2^2 + \chi^2})|3\rangle\}.
\end{aligned} \tag{66}$$

In the limit $\chi \to 0$, the eigenfunctions reduce to three possible cases

$$\begin{aligned}
&|1\rangle \to |3\rangle, \quad |1\rangle, \quad |1\rangle \\
&|2\rangle \to |2\rangle, \quad |2\rangle, \quad |3\rangle \\
&|3\rangle \to |1\rangle, \quad |3\rangle, \quad |2\rangle,
\end{aligned}$$

corresponding to $w_1, w_2 > 0$, $w_1 < 0$, $w_2 > 0$ and $w_1, w_2 < 0$. As we did not assume resonance for the 3-level system, the eigenfunctions for vanishing coupling parameters are the undisturbed functions themselves and are not linear combinations as in the $N + 2$ level problem above.

8. A simplified application: the Raman beat experiment [6, 11, 12]

We consider a 3-level Raman configuration, continuously driven by a single monochromatic field as in fig. 6. The lower two levels are assumed to be degenerate initially. At time $t = 0$, the two lower levels are split by a Stark pulse and coherent Raman scattering commences. The off diagonal matrix element $\rho_{12} = c_1 c_2^*$ established in the preparative phase can be monitored then as a low frequency beat. An important consequence of this experiment is that the Raman beat, observed after switching the lower levels, shows only very weak power broadening. In the lowest order of approximation of (66) this can be understood very easily because the level splitting $\omega_1 - \omega_2$ does not depend on the longitudinal velocity. Perturbation theory in first order, therefore, gives no power broadening at all. There has been an attempt [16] to do conventional perturbation

theory to higher orders by iterating the underlying integral equation of the density matrix

$$\rho(t) = e^{iL_0 t}\rho(0) + i\int_0^t e^{iL_0(t-t')}L_1\rho(t')\,dt' \tag{67}$$

where the Louville commutators for the free and interaction Hamiltonians are

$$L_0 = [H_0, \ ] \qquad \text{and} \qquad L_1 = [H_1, \ ].$$

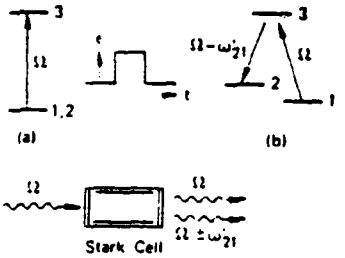


Fig. 6. Molecular energy level diagrams illustrate (a) coherent preparation of a three level quantum system during a Stark pulse when the levels 1 and 2 are degenerate ($\omega_{21} = 0$); and (b) transient forward scattering following the pulse because of the coherent Raman beat effect. A second frequency component $\Omega - \omega_{21}$ not shown in (b) is also emitted.

We conclude immediately since L_0 does not depend on intensity, that power broadening of intensity-dependent dephasing cannot appear. Indeed, the claim [16] that no power broadening has been found up to third order is certainly correct because power broadening will not be found up to any finite order using this kind of perturbation theory.

Let us consider next how the nonperturbative results (57), (58) for the 3-level system predict power broadening or an intensity-dependent dephasing. For the time span $t < 0$ the two lower levels are degenerate and the problem is exactly solvable. For times $t > 0$, we can assume that the level splitting is large compared to the Rabi frequency, and therefore we can use the approximate result (57).

The general wave function as derived above reads formally

$$\Psi(t) = \sum_{n,m} \Lambda_{n,m}(\{c_l(0)\})\, e^{iS_n t}\,|m\rangle. \tag{68}$$

The expectation value of the dipole moment operator $p = g_{13}\,|1\rangle\langle 3| + g_{23}\,|2\rangle\langle 3|$ then can be given in the form

$$\langle p\rangle_t = g_{13}\sum_{nn'} \Lambda^*_{n'1}\Lambda_{n3}\exp\{i(S_n - S_{n'})t\} + (1 \to 2). \tag{69}$$

We do not want to treat this example to full generality but rather show for a typical term how dephasing comes about. A typical contribution to the dipole moment for $t > 0$ is of the form

$$\langle p\rangle \sim \frac{1}{w^2 + \chi^2}\exp\{i(S_1 - S_2)t\}. \tag{70}$$

The resonance denominator is established during the preparation of the system at $t < 0$ for

$w_1 = w_2 = w$ and we assume for simplicity that $\chi_1 = \chi_2$. For $t > 0$, the resulting poles then become

$$\begin{aligned} S_1 &= \tfrac{1}{2}(w_1 - \sqrt{w_1^2 + \chi^2}), \qquad w_1 = w + \delta_1 \\ S_2 &= \tfrac{1}{2}(w_2 + \sqrt{w_2^2 + \chi^2}), \qquad w_2 = w + \delta_2, \end{aligned} \tag{71}$$

where $\delta_{1,2}$ describes the shifts of levels 1 and 2 from their initial position, and

$$w = (\omega_3 - \omega_1 - \Omega) = \omega_3 - \omega_1 - \Omega^0 - kv = \Delta^0 - kv.$$

Without loss of generality we can set $\Delta^0 = 0$. Then we find

$$S_1 - S_2 = \tfrac{1}{2}(\delta_1 - \delta_2) - \tfrac{1}{2}(\sqrt{(\delta_1 - kv)^2 + \chi^2} + \sqrt{(\delta_2 - kv)^2 + \chi^2}). \tag{72}$$

In the limit $\chi \to 0$ and for $\delta_1 < 0$, $\delta_2 > 0$ the difference of the eigenvalues S_1 and S_2 approaches the nondifferentiable function

$$(S_1 - S_2) = \begin{cases} -\delta_2 + kv, & kv < \delta_1 \\ \delta_1 - \delta_2, & \delta_1 < kv < \delta_2 \\ \delta_1 - kv, & \delta_2 < kv. \end{cases} \tag{73}$$

Besides the regions $kv \approx \delta_1$ and $kv \approx \delta_2$ the function is rather smooth. The resonance denominator limits the variation of kv to $|kv| \lesssim \chi$. Therefore we can expand the function $(S_1 - S_2)$ around zero, if none of the parameters δ_1, δ_2 are zero.

We find

$$(S_1 - S_2) = \delta_1 - \delta_2 + \tfrac{1}{4}\chi^2(1/\delta_1^2 - 1/\delta_2^2)kv + \tfrac{1}{4}\chi^2(1/\delta_1^3 - 1/\delta_2^3)(kv)^2. \tag{74}$$

The following special cases emerge:

1) $\delta_1 = \delta_2$ The Raman beat does not occur.
2) $\delta_1 = -\delta_2$ The linear term in kv drops out.
3) $\delta_1 \neq -\delta_2$ The kv dependence remains linear around $kv = 0$.

In case 3, we find, assuming the Doppler-width to be large compared with all other parameters that

$$p \rightsquigarrow \exp\left[\mathrm{i}(\delta_1 - \delta_2)t - \tfrac{1}{4}\frac{\chi^2}{\delta^2}\chi t\right] \tag{75}$$

where

$$1/\delta^2 = |1/\delta_1^2 - 1/\delta_2^2|.$$

If δ is of the order δ_1, δ_2, we conclude that the intensity-dependent dephasing of the Raman beat is drastically reduced by the factor χ^2/δ^2.

The Doppler average of the induced polarization for case 2) is of the form

$$p \rightsquigarrow \exp\{\mathrm{i}(\delta_1 - \delta_2)t\} \int_{-\infty}^{\infty} \frac{\exp[\tfrac{1}{4}\mathrm{i}(\chi^2/\delta_1^3)(kv)^2 t]}{(kv)^2 + \chi^2}\, \mathrm{d}(kv). \tag{76}$$

The integral can be evaluated analytically and leads to an expression containing the Fresnel sin and cos integrals. Because we are interested in the dephasing behavior, we do not write down the

full expression but rather its asymptotic expansion for $t \to \infty$

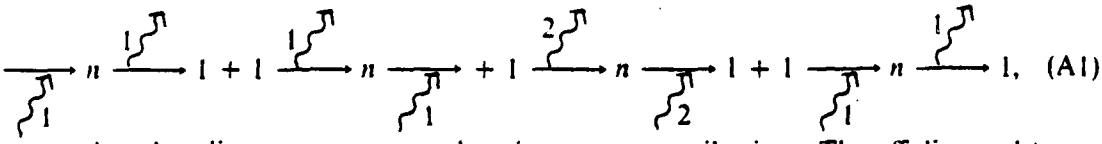
$$p \sim \exp\{i(\delta_1 - \delta_2)t\}\frac{\delta_1^2}{\chi^3}\sqrt{\frac{2\pi}{\delta_1 t}}, \qquad p \sim 1/\sqrt{t}.$$

We see, that the dephasing is reduced to the slow decay of a fractional power law.

The results above are the only evident analytic expressions for the Raman beat. For more general expressions, the Doppler integration must be handled numerically. Here, we confined ourselves to cases where χ is a small parameter. The nonanalytic behavior of $(S_1 - S_2)$ for the limit $\chi \to 0$ in the neighborhood of δ_1, δ_2 does not allow us to expand the roots in the case where one of the lower-levels remains at resonance (magnetic state $M = 0$) for $t > 0$. It seems that this case has to be treated numerically as well.

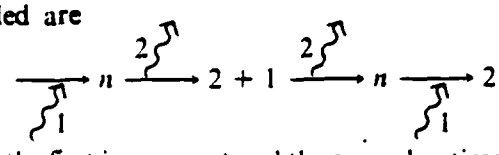
Appendix A

The formal eqs. (18) and (19) contain all of the terms indicated in (8). Since Γ_{ij} is an operator, it may not be immediately evident which terms are being retained in (18) and (19), leading to the derivation of equations (22)–(25). For the Raman process, we intend that (18) include the diagonal terms



(A1)

which as mentioned earlier are resonant and antiresonant contributions. The off-diagonal terms included are



(A2)

where the first is resonant and the second antiresonant. These diagrams correspond to the following terms in eq. (8a) which are given in the same order as (A1) and (A2),

$$(z + i\omega_1)c_1(z) = I_1(z) - \tfrac{1}{4}\sum_n\left[\frac{(\chi^1_{n1})^2}{z + i\omega_n - i\Omega_1}c_1(z) + \frac{(\chi^1_{1n})^2}{z + i\omega_n + i\Omega_1}c_1(z)\right.$$
$$\left. + \frac{(\chi^2_{1n})^2}{z + i\omega_n + i\Omega_2}c_1(z) + \frac{(\chi^2_{1n})^2}{z + i\omega_n - i\Omega_2}c_1(z) + \frac{\chi^1_{1n}\chi^2_{n2}}{z + i\omega_n - i\Omega_1}c_2(z + i\Delta) + \frac{\chi^2_{1n}\chi^1_{n2}}{z + i\omega_n + i\Omega_2}c_2(z + i\Delta)\right]. \tag{A3}$$

Other resonant terms such as $c_1(z + 2i\Omega_1)$ and $c_1(z + i\Omega_1 + i\Omega_2)$ are neglected. A similar equation for $c_2(z)$ can be derived from (A3) by the sub-index interchange $1 \leftrightarrow 2$. After the transformation (17), $c_1(z + i\Omega_1) = \tilde{c}_1(z)$, we can write (A3) in the form of eq. (18) where

$$\Gamma_{11}(z + i\Omega_1) = -\tfrac{1}{2}i\sum_n\left[(\chi^1_{n1})^2\frac{\omega_n - \omega_1}{\Omega_1^2 - (\omega_n - \omega_1)^2} + (\chi^2_{n1})^2\frac{\omega_n - \omega_1}{\Omega_2^2 - (\omega_n - \omega_1)^2}\right]$$
$$\Gamma_{12}(z + i\Omega_1) = -\tfrac{1}{4}\sum_n\left[\frac{\chi^1_{1n}\chi^2_{n2}}{z + i\omega_n} + \frac{\chi^2_{1n}\chi^1_{n2}}{z + i\omega_n + i\Omega_1 + i\Omega_2}\right]. \tag{A4}$$

Selection of the terms in (A1) and (A2) thus allows us to truncate the hierarchy of equations, as Γ_{12} is a c number rather than a translation operator and the coupled $c_1(z)$ and $c_2(z)$ eqs. (20) and (21) are now in closed form. Equations (22)–(25) are derived easily from (A4).

Appendix B

Even though the two-level atomic quantum problem is well known, we include it here for easy comparison with eqs. (22)–(23). We assume that an electromagnetic wave resonantly excites a two level quantum system in the transition $1 \rightarrow 2$ where the lower level is labeled 1. The atomic wave function

$$\psi(t) = c_1(t)|1\rangle + c_2(t)|2\rangle \tag{B1}$$

satisfies the Schrödinger equation

$$i\hbar\dot{\psi} = H\psi \tag{B2}$$

where the Hamiltonian

$$H = H_0 + H_1 \tag{B3}$$

contains the free atom and atom-field interaction terms. The equations of motion

$$\begin{aligned} \dot{c}_1(t) &= -i\frac{H_{11}}{\hbar}c_1(t) - i\frac{H_{12}}{\hbar}c_2(t), \\ \dot{c}_2(t) &= -i\frac{H_{22}}{\hbar}c_2(t) - i\frac{H_{21}}{\hbar}c_1(t), \end{aligned} \tag{B4}$$

subject to the Laplace transform become

$$\begin{aligned} (z + iH_{11}/\hbar)c_1(z) &= c_1(0) - i\frac{H_{12}}{\hbar}c_2(z), \\ (z + iH_{22}/\hbar)c_2(z) &= c_2(0) - i\frac{H_{21}}{\hbar}c_1(z). \end{aligned} \tag{B5}$$

Comparison of (B5) with (20) and (21) leads directly to the effective Hamiltonian matrix elements H_{jj} and H_{12}, eqs. (22) and (23).

References

[1] M. Göppert-Mayer, Ann. Physik 9 (1931) 273.
[2] C.V. Raman, Ind. Journ. Phys. 2 (1928) 387.
[3] W. Kaiser and C.G.B. Garrett, Phys. Rev. Lett. 7 (1961) 229.
[4] N. Bloembergen and M.D. Levenson, Doppler-free two photon absorption spectroscopy, in: High Resolution Laser Spectroscopy Vol. 13, ed. K. Shimoda (Springer-Verlag, New York, 1976) p. 315.
[5] R.G. Brewer, Physics Today (May 1977) p. 50.
[6] R.L. Shoemaker and R.G. Brewer, Phys. Rev. Lett. 28 (1972) 1430.
[7] P.F. Liao, J.E. Bjorkholm and J.P. Gordon, Phys. Rev. Lett. 39 (1977) 15.

[8] M.M.T. Loy, Phys. Rev. Lett. 39 (1977) 187.
[9] D.G. Gold and E.L. Hahn, Phys. Rev. A16 (1977) 324.
[10] H. Hatanaka and T. Hashi, J. Phys. Soc. Japan 39 (1975) 1139;
H. Hatanaka, T. Ozawa and T. Hashi, J. Phys. Soc. Japan 42 (1977) 2069.
[11] R.G. Brewer and E.L. Hahn, Phys. Rev. A11 (1975) 1641.
[12] R.G. Brewer and E.L. Hahn, Phys. Rev. A8 (1973) 464.
[13] M. Takatsuji, Phys. Rev. A11 (1975) 619.
[14] D. Grischkowsky, M.M.T. Loy and P.F. Liao, Phys. Rev. A12 (1975) 2514;
see also D. Grischkowsky and R.G. Brewer, Phys. Rev. A15 (1977) 1789.
[15] W. Heitler, The Quantum Theory of Radiation (third ed., Oxford University Press, London 1954) p. 146.
[16] J.R.R. Leite, R.L. Sheffield, M. Ducloy, R.D. Sharma and M.S. Feld, Phys. Rev. A14 (1976) 1151; see their footnote 20 in particular.
[17] F.A. Hopf, R.F. Shea and M.O. Scully, Phys. Rev. A7 (1973) 2105.

PHYSICAL REVIEW B VOLUME 17, NUMBER 7 1 APRIL 1978

Optical free-induction decay of the F_3^+ center in NaF*

R. M. Macfarlane, A. Z. Genack,* and R. G. Brewer
IBM Research Laboratory, San Jose, California 95193
(Received 20 October 1977)

We have measured the optical dephasing time T_2 of the $^1A_1 \rightarrow {}^1E$ zero-phonon transition of the F_3^+ color center in NaF by optical free-induction decay. In this way we eliminate the effect of the 54-GHz inhomogeneous broadening, and find a homogeneous linewidth of 20 ± 5 MHz ($T_2 = 16 \pm 4$ nsec). We have also measured a spontaneous emission lifetime of $T_1 = 10 \pm 2$ nsec. In the range 1.5–4 K, our results are consistent with the relation $T_2 = 2T_1$, indicating that optical dephasing is limited by population-decay processes. This relation was even more clearly demonstrated by performing the same experiment on the D lines of sodium vapor at 3×10^{-5} Torr, where the effects of collisions are negligible. We find that the dephasing is again limited by radiative decay, and that $T_2(32 \pm 3$ nsec$) = 2T_1(16.3 \pm 0.4$ nsec).

I. INTRODUCTION

Color centers in alkali halides have been studied spectroscopically for many years,[1] and have recently attracted renewed interest because of their promise as materials for tunable cw lasers.[2] In spite of this, there appear to have been few studies of their homogeneous linewidths.[3] In this paper we apply high-resolution laser techniques to the problem.

A number of color centers, especially aggregate centers, exhibit relatively sharp zero-phonon lines,[3] in addition to the strong broad multiphonon sidebands which give rise to the "color" of the materials. Relaxation of these sidebands is dominated by the fast relaxation of the vibrational states. Therefore, in order to observe the homogeneous dephasing of the purely electronic state of the centers, it is necessary to investigate the zero-phonon lines. Spectroscopy of color centers has, in the past, been limited by the inhomogeneous (strain) broadening of these lines, whereas at the lowest temperatures it should be possible to observe a linewidth limited only by the population decay rate. Such a result is demonstrated here.

We have recently shown[4] that the optical free-induction decay[5] (FID) can be used to eliminate the effects of inhomogeneous broadening in solids at low temperatures. In our FID experiments, a coherent polarization is induced in the sample by resonant excitation with a narrow-band laser. The sample then exhibits the FID effect when the laser frequency is abruptly switched outside the homogeneous linewidth.[6] The resulting FID beat signal under these conditions is given by[7]

$$V \propto [1 - \Gamma/(\Gamma^2 + \hat{\Gamma}^2)^{1/2}] \times \exp\{-[\Gamma + (\Gamma^2 + \hat{\Gamma}^2)^{1/2}]t\} \cos\Delta\omega t \quad . \tag{1}$$

Here, $\Delta\omega$ is the laser frequency shift and the FID damping rate

$$\Gamma_{\mathrm{FID}} = \Gamma + (\Gamma^2 + \hat{\Gamma}^2)^{1/2} \tag{2}$$

is a function of the dipole dephasing time

$$\Gamma \equiv 1/T_2 \tag{3}$$

and a power broadening term

$$\hat{\Gamma}^2 = (\chi^2\Gamma/2\Gamma_1\Gamma_2)(\Gamma_1 + \Gamma_2 - \gamma) \quad . \tag{4}$$

For this two-level quantum problem, the upper level (labeled 2) depopulates at a rate Γ_2 and the lower level (labeled 1) at a rate Γ_1. The radiative spontaneous emission decay rate for the transition $2 \rightarrow 1$ is γ and $\chi = (\vec{\mu}\cdot\vec{E})/\hbar$ is the Rabi frequency, $\vec{\mu}$ being the transition dipole moment and $\vec{E}$ the electric-field vector of the laser. Note that when the upper state depopulates solely from radiative spontaneous emission, i.e., $\Gamma_2 = \gamma$, then $\hat{\Gamma}^2 = \chi^2\Gamma/2\Gamma_2$ independent of the value of Γ_1. At low laser powers ($\hat{\Gamma}^2 \ll \Gamma^2$), the polarization decays in a time $\frac{1}{2}T_2$, and this gives the homogeneous linewidth $(\pi T_2)^{-1}$. In our earlier measurements on solids[4] we investigated the dephasing of the $^1D_2 \rightarrow {}^3H_4$ transition of LaF_3: Pr^{3+}, where $T_2 \approx 1$ μsec. Here we have extended the technique to much higher speeds in order to apply it to the color center system and to atomic sodium, where radiative decay times are rather fast ($\sim$10 nsec).

II. LINEWIDTH CONTRIBUTIONS

Before presenting the measurements, we will discuss contributions to the homogeneous linewidth in terms of a two-level quantum model and compare some limiting examples of the optical case with the well known magnetic resonance and infrared cases. In general, the total dephasing rate is made up of lifetime and phase interrupting effects. In the latter,

*Work supported in part by the U.S. Office of Naval Research.

REFERENCES

1. R. G. Brewer and A. Z. Genack, Phys. Rev. Lett. 36, 959 (1976); ibid, Phys. Rev. A, April 1978.

2. A. Z. Genack, R. M. Macfarlane and R. G. Brewer, Phys. Rev. Lett. 37, 1073 (1976); A. H. Zewail et al., Proc. of the Society of Photo-Optical Instrumentation Engineers 113, 42 (1977); H. de Vries, P. de Bree and D. A. Wiersma, Chem. Phys. Lett. 52, 399 (1977).

3. R. M. Macfarlane, A. Z. Genack and R. G. Brewer, Phys. Rev. B, April 1978.

4. R. G. Brewer and R. L. Shoemaker, Phys. Rev. A6, 2001 (1972).

5. K. L. Foster, S. Stenholm and R. G. Brewer, Phys. Rev. A10, 2318 (1974).

6. P. F. Liao, J. E. Bjorkholm and J. P. Gordon, Phys. Rev. Lett. 39, 15 (1977).

7. M. Abramowitz and I. A. Stegun, Handbook of Mathematical Functions (Dover, N.Y.), p. 297.

8. I. P. Kaminow, An Introduction to Electrooptic Devices, (Academic Press, N.Y., 1974), p. 213-237.

9. For a review see S. Haroche in High-Resolution Laser Spectroscopy, (Springer-Verlag, 1977), edited by K. Shimoda, p. 253.

In the case of extreme homogeneous broadening when $\Gamma/\sigma \gg \sigma t$, Eq. (1) simplifies to give the NMR result

$$E_b^2(L,t) = KE_o^2 \, e^{-t/T_2} \, e^{-i(\omega_{21}-\Omega')t} \, \frac{1/T_2 - i\delta}{\Gamma^2+\delta^2} + \text{c.c.}, \qquad (5)$$

and then T_2 may be obtained in the absence of the above interference phenomena.

In extending this subnanosecond technique, it is evident that other coherent transients involving pulse preparation such as adiabatic rapid passage and photon echoes can be applied in quantitative optical dephasing studies where the time scale may be reduced even further.

The technical assistance of D. E. Horne and K. L. Foster proved most valuable and is acknowledged with pleasure. Conversations with A. Z. Genack are appreciated also.

Doppler peak, as in Fig. 2(d) where $(\omega_{21}-\Omega)/2\pi = -1$ GHz, in agreement with (3) and Fig. 1(d). Furthermore, the first order FID beat frequency of 6.5 GHz in Fig. 2(a) is given by $\omega_{21}-\Omega'$, and is confirmed in other experiments by varying Ω'.

On the other hand, the nonlinear FID becomes more prominent when $\omega_{21}-\Omega$ is small, as it is in Figures 2(b)-(d), due to the large amplitude preparation of the *resonant velocity group*. Compare with Figs. 1(b)-(d). The decay, which persists beyond the first order FID, is exponential in agreement with Eq. (2), being given by $\sim e^{-\chi t}$ in this power-broadened regime with $\chi=0.8$ GHz. Note that the decay is faster in Fig. 1 as $\chi=2.3$ GHz. The observed beat frequency of 5 GHz is given by the laser frequency jump $(\Omega-\Omega')/2\pi$ and is verified in other experiments where this quantity is varied. These signals are also absorptive since their phase is invariant to laser tuning. In Fig. 2(c) where $\omega_{21}-\Omega=0$, a dramatic interference between the linear and nonlinear FID occurs near the time origin, as in Fig. 1(c). Thus, all of the predictions of Eq. (1) seem to be obeyed.

In addition, in Fig. 2(d) where $\omega_{21}-\Omega=-1.0$ GHz, the laser is tuned midway between the two hyperfine components producing a modulated pattern, not present in Fig. (1), due to a 1.8 GHz interference beat of the ground state hyperfine splitting. The origin of this beat is being studied further through its Fourier transform spectrum. Quantum beats have been observed previously in the upper state by spontaneous emission, in the lower or upper state by modulated photon echoes, and in superfluorescence but at frequencies which are at least one order of magnitude smaller.[9]

refractive index from n_o to n_1. Since the propagation velocities of the optical (c) and dc (v) waves differ, the light will experience a time-varying refractive index and hence a frequency shift

$$\Omega-\Omega' = \Omega \frac{n_1-n_o}{n_o} \cdot \frac{v}{c\mp v} \tag{4}$$

where the waves may travel either in the same direction (minus sign) or opposite direction (plus sign). Frequency shifts in the range 0 to 10 GHz have been achieved with a duration of 1.5 nsec, a rise time of ~100 psec, and at a rate of 17 MHz/volt.

In testing the above FID theory, we examined the behavior of the sodium D_1 line at 16,956.16 cm^{-1} using a 10 cm path length of Na vapor at $\sim 2\times10^{-6}$ Torr with 5% of the laser beam being absorbed. Figure 2 shows the observed FID heterodyne beat signals for different values of $\omega_{21}-\Omega$ where the frequency jump $(\Omega-\Omega')/2\pi=5$ GHz and the laser power density is 3 W/cm^2 ($\eta=0.055$). Note that the large frequency switch makes it possible for the first time to switch completely outside the Doppler linewidth, which for Na is 0.77 GHz. We see that as the initial laser frequency Ω is tuned through the Doppler lineshape, the FID changes remarkably, displaying a rich assortment of new effects, in agreement with the results of Eqs. (1)-(3) and Fig. 1. Thus, in Fig. 2(a) where $(\omega_{21}-\Omega)/2\pi= 1.5$ GHz the detuning is large enough so that only the first order FID is evident and only the *off resonant velocity groups* contribute. The decay, which obviously is nonexponential, is complete in 500 psec, as expected since $T_2^*=340$ psec. Due to the high laser intensity, the signal is dispersive and thus reverses sign when the laser is tuned to the other side of the

and a dispersive part, which depends on the initial laser frequency through the factor $(\omega_{21}-\Omega)$. Here, the decay is a Gaussian, $e^{-(\sigma t/2)^2}$. Consequently, at short times the first and higher order FID terms interfere in a variety of interesting ways, dependent on the particular conditions of light intensity and laser tuning. Numerical solutions of the general expression (1) are obtained using an error function subroutine, and the results of computer plots are given in Fig. (1) for the Na D_1 line where $(\Omega-\Omega')/2\pi$=5 GHz, σ=5.8 GHz, Γ=1.6 GHz, χ=2.3 GHz, T_2=32 nsec and η=0.019. At lower light intensity when χ=0.8 GHz, the interferences are less striking and more closely resemble the observations of Fig. 2, which we now consider.

In the present optics, light from a Coherent 599 cw dye laser is frequency switched by a travelling wave electro-optic phase modulator[8] that is external to the laser cavity. This beam excites a sample resonantly and with the forward FID emission strikes a fast GaAs photodiode. The photo-detector of 2 mil diameter has a 30 psec response time or less and is mounted directly on an S-4 Sampling Head (25 psec response) of a Tektronix 7904 oscilloscope with a 7S11 sampling unit. The time-averaged transient signals are then sampled and stored digitally using a local computer.

The optical phase modulator is a lithium tantalate crystal ($0.5\times0.65\times50$ mm^3) mounted in a stripline microwave transmission line. A square wave dc voltage pulse (Tektronix 109 pulser with a 700 Hz repetition rate) applied to this configuration propagates with the light wave down the length of the crystal in a time of 1.5 nsec, changing the optical

matrix element; and the saturation parameter $\eta \equiv 1/(T_2\Gamma)$. This expression is nearly exact within the rotating wave approximation and the slowly varying envelope approximation for an optically thin sample of length L.

In the asymptotic limit[7] as $t \to \infty$, Eq. (1) yields

$$E_b^2(L,t) = 4(\eta-1)E_o^2 K\, e^{-t/T_2}\, e^{-\Gamma t}\, e^{-\delta^2/\sigma^2}\, \cos(\Omega-\Omega')t, \qquad (2)$$

the anticipated nonlinear FID transient[4,5] where the emission occurs at the initial laser frequency Ω and produces with the laser beam a heterodyne beat of frequency $\Omega-\Omega'$. Note that the signal is nonlinear in the laser intensity due to the factor $E_o^2(\eta-1)$, the signal is absorptive, and the decay is an exponential with decay rate $1/T_2+\Gamma$.

In the short time limit $t<2\Gamma/\sigma^2$, we expand the error function[7]

$$w(z) = 1 + \frac{2iz}{\sqrt{\pi}} + \ldots \qquad \text{for} \quad z<1,$$

retaining only the first two terms to obtain the initial behavior of the first order FID

$$E_b^2(L,t) \cong 4E_o^2 K\, e^{-t/T_2}\, e^{-(\sigma t/2)^2}$$

$$\times \left\{ \frac{1}{T_2} \left(\frac{1}{\Gamma} - \frac{2}{\sqrt{\pi}\sigma}\right) \cos(\omega_{21}-\Omega')t - \frac{2}{\sqrt{\pi}} \frac{(\omega_{21}-\Omega)}{\sigma} \sin(\omega_{21}-\Omega')t \right\}. \qquad (3)$$

This radiation peaks at the Doppler line center at frequency ω_{21} and produces with the laser beam a beat of frequency $\omega_{21}-\Omega'$. The signal amplitude is linear in the laser intensity and contains both an absorptive

switching. The well-known nonlinear FID[4] may be long-lived with a decay time determined by the power-broadened homogeneous linewidth. We view these two forms of FID as the transient analogs of steady-state linear and nonlinear (hole-burning) laser spectroscopy of an inhomogeneously broadened transition. Furthermore, the increased time resolution permits the first observations of very high frequency interference beats, for example due to the 1.8 GHz hfs splitting of the sodium ground state.

The above properties of FID follow from a density matrix solution[5] of the Schrödinger wave equation where we assume that a Doppler-broadened atomic transition 1→2 with center frequency ω_{21} is coherently prepared in steady-state by a cw laser beam. The system then radiates the FID transient when the laser frequency is suddenly switched from $\Omega \to \Omega'$. We make use of an earlier derivation[5] of the Doppler-averaged polarization and express the FID heterodyne beat signal E_b^2 in terms of an error function of complex argument $w(x+iy)$,[6,7]

$$E_b^2(L,t) = KE_o^2 e^{-t/T_2}\, e^{-(\sigma t/2)^2}\, e^{-i(\omega \quad ')t}$$

$$\times \left\{(1+\eta)w\left(\frac{i\sigma t}{2} + \frac{i\Gamma-\delta}{\sigma}\right) + (\eta-1)w\left(\frac{-i\sigma t}{2} + \frac{i\Gamma+\delta}{\sigma}\right)\right\} + \text{c.c.} \qquad (1)$$

Here, all frequencies are in angular units; the dipole dephasing time is T_2; the population decay time T_1; the Doppler linewidth is σ; we define the inhomogeneous dephasing time $T_2^* \equiv 2/\sigma$; the quantity $\delta \equiv \omega_{21} - \Omega$; the power-broadened linewidth is $\Gamma \equiv \sqrt{1/T_2^2 + \chi^2 T_1/T_2}$; the Rabi frequency is $\chi \equiv \mu_{12}E_o/\hbar$ where E_o is the laser field amplitude and μ_{12} the transition

The method of *laser frequency switching*,[1] utilized recently in generating coherent optical transients, has provided new ways for examining the dynamic interactions occurring in molecules,[1] solids,[2] and atoms.[3] In this work, the frequency of a cw dye laser is abruptly switched by means of voltage pulses applied to an intracavity electro-optic phase modulator. A resonant sample in the path of this light exhibits coherent transients which are detected in the forward beam, allowing dephasing and population decay times to be measured thus far in the range 1 microsecond to 5 nanoseconds.

In the present study, laser frequency switching is extended to a time scale of 100 picoseconds. This fifty-fold increase in time resolution is achieved without sacrificing the previous advantages of heterodyne detection, high sensitivity, and the ability to monitor the entire class of coherent optical transients by preselecting the voltage pulse sequence. Hence, quantitative studies of coherent optical transients in this time domain are now feasible.

New coherence effects may also arise at these short times as illustrated here for the optical free induction decay[4] of an inhomogeneously broadened transition. This transient displays a polarization containing both a first order and a nonlinear laser field dependence having different decay times, heterodyne beat frequencies, and laser tuning characteristics. The first order FID, which was predicted[5], decays rapidly in the time of an inverse inhomogeneous linewidth T_2^* and is observed in the time domain for the first time by laser frequency

RJ2207(30160)3/22/78
Physics (General)

OPTICAL COHERENT TRANSIENTS BY LASER FREQUENCY SWITCHING: SUBNANOSECOND STUDIES*

Ralph G. DeVoe
Richard G. Brewer

IBM Research Laboratory
San Jose, California 95193

ABSTRACT: By extending the laser frequency switching technique to a 100 psec time scale, we have observed for the Na D_1 line the first order free induction decay (FID), its inhomogeneous dephasing time T_2^*, its interference with the nonlinear FID, and a 1.8 GHz quantum beat of the ground state hfs. Detailed theoretical predictions of these new coherence effects are faithfully observed.

*Work supported in part by the U.S. Office of Naval Research.

13, 8, 72 (1977).
[20]L. R.Sarles and R. M. Cotts, Phys. Rev. 111, 85 (1958).
[21]B. P. Kibble, G. Copley, and L. Krause, Phys. Rev. 153, 9 (1967).
[22]S. Völker, R. M. Macfarlane, A. Z. Genack, H. P. Trommsdorff, and J. H. van der Waals, J. Chem. Phys. 67, 1759 (1977); H. de Vries and D. A. Wiersma, Chem. Phys. Lett. 51, 565 (1977).

this temperature range. At higher temperatures this will certainly no longer be true, and phonon scattering will provide the dominant contribution.

We have seen that under our experimental conditions, Γ_ϕ is very small for the color center, and this provides a nice example of the limiting case of Sec. IIC, viz., $T_2 = 2T_1$. It is expected that a low-pressure gas, in which collisions are negligible—the classical system where $\Gamma_\phi \approx 0$ would provide an even clearer illustration of this. We have therefore studied the optical FID of the D lines of atomic sodium. The experimental apparatus is the same as used for the FID in the F_3^+ center, but the signal-to-noise ratio was sufficiently high so that the data were not averaged, and Fig. 4 shows a typical single oscilloscope trace. At a pressure of 3×10^{-5} Torr, we find for the $3p\ ^2P_{3/2} \rightarrow 3s\ ^2S_{1/2}$ transition at 5889.95 Å, $T_2 = 32 \pm 3$ nsec, which is twice the radiative decay time T_1 of 16.3 ± 0.4 nsec.[21]

The case $T_2 \approx 2T_1$ has also been observed recently in photochemical hole-burning experiments.[22] It contrasts with our earlier measurement of FID in $LaF_3:Pr^{3+}$,[4] where the forbidden $^1D_2 \rightarrow {}^3H_4$ transition gave a long T_1 (500 μsec), and $\Gamma_\phi >> \Gamma_2$.

VI. CONCLUSION

We have measured both the population decay time (T_1) and the dephasing time (T_2) for the zero-phonon transition of the F_3^+ center in NaF at 5456 Å.

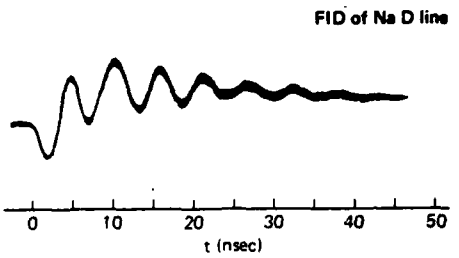


FIG. 4. FID of the D line ($^2P_{1/2} \rightarrow {}^2S_{1/2}$ at 5889.95 Å) of atomic sodium at 3×10^{-5} Torr.

Below 4 K the dephasing is limited by population-decay processes. Our data are consistent with the relationship $T_2 = 2T_1$, and correspond to a homogeneous linewidth of 16–20 MHz which is much narrower than the inhomogeneous width of 54 GHz. This suggests the possibility of very high resolution spectroscopy of color centers, to study for example, the effect of applied perturbations. The regime of population decay limited dephasing was further explored by optical FID measurements on the D lines of sodium vapor.

ACKNOWLEDGMENTS

We wish to thank Professor F. Lüty for supplying the F_3^+ NaF samples, and Dr. Axel Schenzle for helpful discussions.

*Present address: Exxon Research and Engineering Co., Linden, N.J. 07036.

[1](a) See for example, C. J. Delbecq and P. Pringsheim, J. Chem. Phys. 21, 794 (1953); (b) P. Pringsheim, Z. Phys. 136, 573 (1954); (c) F. Seitz, Rev. Mod. Phys. 26, 7 (1954); (d) C. Z. Van Doorn, Philips Res. Rept. Suppl. No. 4, 1 (1962); (e) W. D. Compton and H. Rabin, *Solid State Physics*, edited by F. Seitz and D. Turnbull (Academic, New York, 1964), Vol. 16, p. 121, and references therein.

[2]B. Fritz and E. Menke, Solid State Commun. 3, 61 (1965); L. F. Mollenauer and D. H. Olson, Appl. Phys. Lett. 24, 386 (1974); J. Appl. Phys. 46, 3109 (1975).

[3]D. B. Fitchen, R. H. Silsbee, T. A. Fulton, and E. L. Wolf, Phys. Rev. Lett. 11, 275 (1963).

[4]A. Z. Genack, R. M. Macfarlane, and R. G. Brewer, Phys. Rev. Lett. 37, 1078 (1976).

[5]R. G. Brewer and R. L. Shoemaker, Phys. Rev. A 6, 2001 (1972).

[6]R. G. Brewer and A. Z. Genack, Phys. Rev. Lett. 36, 959 (1976).

[7]A. Schenzle and R. G. Brewer, Phys. Rev. A 14, 1756 (1976).

[8]See, for example, M. Sargent III, M. O. Scully, and W. E. Lamb, Jr., *Laser Physics* (Addison-Wesley, London, 1974), p. 87.

[9]N. Bloembergen, E. M. Purcell, and R. V. Pound, Phys. Rev. 73, 27 (1948).

[10]P. R. Berman, J. M. Levy, and R. G. Brewer, Phys. Rev. A 11, 1668 (1975).

[11]P. R. Berman, Appl. Phys. 6, 283 (1975).

[12]C. Z. van Doorn, Philips Res. Rept. 12, 309 (1957); and in Ref. 1d; R. Pick, Z. Phys. 159, 69 (1960); I. Schneider and H. Rabin, Phys. Rev. 140, A1983 (1965).

[13]G. Baumann, F. Lanzl, W. von der Osten, and W. Waidelich, Z. Phys. 197, 367 (1966).

[14]L. F. Stiles and D. B. Fitchen, Phys. Rev. Lett. 17, 689 (1966).

[15]G. Johannson, W. von der Osten, R. Piehl, and W. Waidelich, Phys. Status Solidi 34, 699 (1969).

[16]J. A. Davis and D. B. Fitchen, Solid State Commun. 7, 1363 (1969).

[17]H. Modl, F. Lanzl, W. von der Osten, and W. Waidelich, International Symposium on Color Centers in Alkali Halides, Rome (1968) (unpublished), p. 199.

[18]A. Z. Genack and R. G. Brewer, Phys. Rev. A 4, 1463 (1978).

[19]D. Anafi, R. Goldstein, and J. Machewirth, Laser Focus

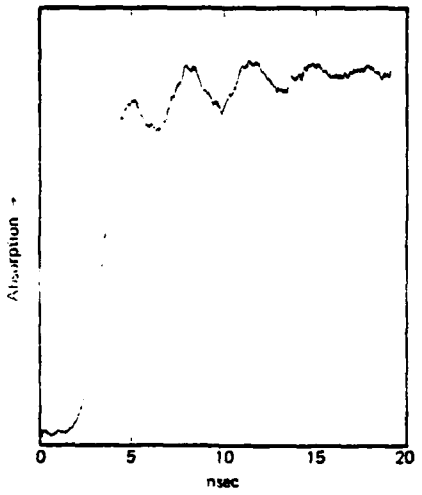


FIG. 3. Optical FID measured in the zero-phonon line at 5456 Å using a 500-V switching pulse.

that which would produce saturation [$\Gamma^2 >> \hat{\Gamma}^2$ see Eq. (2)]. The laser frequency is then switched to ω_1 by applying a voltage across an electro-optical modulator in the cavity, and the sample freely radiates at ω_0. The light beams from the sample and the laser interfere, producing beats at $\omega_0 - \omega_1$ which are detected by the p-i-n photodiode. The AD^*P modulator was supplied by Lasermetrics[19] and had a switching coefficient in our laser of 0.6 MHz/V. To observe the FID signal it is necessary to switch the frequency in a time less than T_2 and by an amount greater than the homogeneous linewidth so that the laser does not continue to interact with the original group of centers. It is further advisable to shift the laser frequency by several linewidths, since then several beats will be observed in a time T_2. We used a high-voltage Huggins pulser, which is a charged cable discharged by a mercury relay at a 60-Hz rate. This low repetition rate gave us a relatively poor signal to noise ratio (e.g., compared to Ref. 4). Signal averaging was performed with a Tektronix sampling oscilloscope, using a 100-sec scan with an integrating time constant of 1.5 sec. A rise time of 3.5 nsec was observed across the phase modulator and terminating 50-Ω resistor. The signal observed with 500 V switched across the modulator, is shown in Fig. 3, the beat frequency corresponding to the 300-MHz laser-frequency switch. The phase of the beat $\theta(t)$ is equal to the additional phase imposed on the laser light by the voltage across the modulator. The beat signal decays because of (i) dephasing processes affecting the individually excited isochromats and (ii) the homogeneous linewidth ($\sim T_2^{-1}$) excited in the steady-state preparation process. Hence the observed rate is twice the intrinsic rate, i.e., $2/T_2$. As seen from Eq. (1) with $\hat{\Gamma} = 0$, the signal measured is

$$V_s = \text{const} \cos\theta(t) \exp(-2t/T_2) \ , \tag{7}$$

the envelope of the beats giving $\frac{1}{2}T_2$. The dephasing time ($T_2 = 16 \pm 4$ nsec) was obtained from the data by computer fit to Eq. (7), including a shift in baseline (see Fig. 3) after the frequency switch.

V. DISCUSSION

We begin by discussing the effect of the fast frequency switch on the observed signal. The voltage rise time in this experiment is only slightly longer than the round-trip time of light in the cavity $t_c = 2.5$ nsec. Consequently, light in different parts of the cavity at a given time will not have experienced an equivalent phase-frequency modulation by the voltage across the modulator. A general discussion of the phase-frequency modulation of the laser for arbitrary applied voltage is given by Genack and Brewer.[18] We merely note that the laser-frequency shift here is in contrast to previous experiments[4] where the rise time (~10 nsec) of the voltage was considerably longer than t_c and the rate of phase advance was fairly uniform. The fast frequency switch introduces sidebands on the laser whose amplitudes increase with increasing voltage.[18] The jump in absorption in Fig. 3 then appears as a consequence of the increase in spectral width of the laser which reduces the degree of saturation.

We now turn to the experimental data, viz., $T_2 = 16 \pm 4$ nsec (i.e., a homogeneous linewidth of 20 ± 5 MHz) and $T_1 = 10 \pm 2$ nsec. These suggest that the dephasing time Γ_ϕ^{-1} is greater than 50 nsec, and are consistent with the relation $T_2 = 2T_1$ obtained in Sec. II C with $\Gamma_\phi = 0$. At the lowest temperatures, population-decay limited dephasing occurs because the optical transition is allowed, so the $\Gamma_2 >> \Gamma_\phi$. Several measurements are relevant to the smallness of Γ_ϕ in the F_3^+ center. From the measured decay time, the oscillator strength of the $^1A_1 - {}^1E$ band is $f \simeq 0.1$, and since the integrated absorption in our sample is $\simeq 10^3$ cm^{-2}, we estimate the concentration of centers to be $\simeq 10^{16}$ cm^{-3}. At this low concentration energy transfer is improbable, especially since the zero-phonon line has only about 10^{-3} of the total oscillator strength. The g value of the ^1E level of ($g = 0.04$) (Ref. 16) is small, so the hyperfine field of the F^- ions which is less than 10 G, would produce less than 0.[illegible] of broadening. In any case only a small fraction of this contributes to the homogeneous width, since nuclear T_2 processes due to mutual spin flips (≈20 μsec),[20] are slower than the optical dephasing. Finally since we found T_2 to be independent of temperature from 2 to 4 K we conclude that phonon scattering does not contribute to dephasing in

temperatures or molecular concentrations $\Gamma_* \neq 0$ and T_1 and T_2 are unrelated.

III. F_3^+ CENTER IN NaF

The F_3^+ center in NaF which we study here is an aggregate center composed of two electrons localized around three adjacent F^--ion vacancies lying in a (111) plane [see Fig. 1(a)].[12] Our samples were prepared by Professor F. Lüty, by x-ray irradiation of NaF for about 12 h at room temperature. In addition to the F_3^+ center, there are expected to be other active centers. In particular, there is some background absorption from M centers.[13] The inhomogeneous width of the 5456-Å zero-phonon line in our samples, measured at 2 K, is 54 GHz (1.8 cm^{-1}), and the concentration of centers was such that we had 52% absorption at the peak of the line, in a sample 4 mm thick.

Previous absorption and emission studies under applied stress[13,14] led to the assignment of the ground state as an orbital singlet and the excited state as an orbital doublet, and they were consistent with a trigonal symmetry for the center. The orbital degeneracies were confirmed by Stark-effect measurements[15] and the center was shown to have C_{3v} symmetry. A simple theoretical model[14] predicts that the ground state is a spin singlet and hence that the observed strong optical absorption arises from a singlet-singlet transition (i.e., $^1A_1 \rightarrow {}^1E$). Davis and Fitchen[16] confirmed the singlet-spin nature of the states by magnetic circular dichroism measurements, and further found that the orbital moment of the ^1E level is quenched, probably due to the dynamic Jahn-Teller effect. We came to the same conclusion from our Zeeman measurements on the zero-phonon line in fields up to 70 kG, which gave $|g(^1E)| < 0.1$.

IV. RELAXATION MEASUREMENTS

A. Spontaneous emission

The population decay (T_1) of the ^1E excited state was studied by observing the fluorescence decay in the phonon sideband around 5800 Å after pulsed excitation of the sample using a nitrogen-pumped dye laser with a pulse width of 5 nsec. The quantum efficiency of the transition is very high, so a high speed (HP5082-4227) p-i-n photodiode could be used to detect the fluorescence. After 30 dB of amplification, the signal was displayed on an oscilloscope. The total electronic bandwidth of the apparatus is estimated to be 350 MHz. A Corning 3-66 filter was used to eliminate laser light scattered from the exciting pulse. The data were taken from photographs of the oscilloscope trace.

The zero-phonon line of the $^1A_1 \rightarrow {}^1E$ transition rides on top of the phonon sideband of the M center[13] which is also present in the sample. In order to obtain T_1 for the zero-phonon transition, we subtracted the fluorescence signal in the case of near-resonant excitation (5461 Å), from the signal obtained in the case of resonant excitation (5456 Å). This involved approximately a 30% correction to T_1. The results at a temperature of 1.8 K are shown in Fig. 2, and give an exponential decay with $T_1 = 10 \pm 2$ nsec, which is close to the value of $T_1 = 8$ nsec obtained by Modl *et al.*[17] for the F_3^+ center in LiF at 4874 Å. The time origin was taken to be 6 nsec after the onset of fluorescence by which time the exciting pulse had terminated. As we have seen, T_1 is still defined in terms of a two level system even though the dominant decay path is to vibronic levels of the ground state.

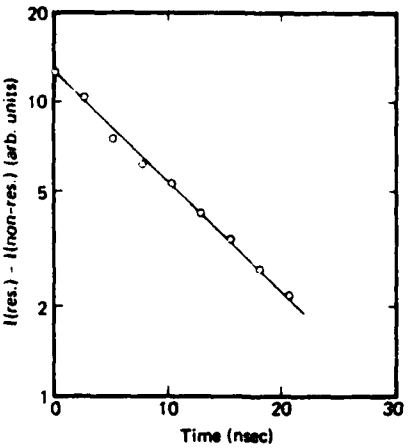


FIG. 2. Decay of the fluorescence intensity (I) of the $^1A_1 \rightarrow {}^1E$ transition measured at the peak of vibronic band around 5800 Å. The ordinate measures the difference in intensity under resonant I (res.) and nonresonant I (non. res.) excitation. The sample temperature was 1.8 K.

B. Dephasing time (T_2)

The value of T_2 at 1.8 K was obtained from the FID observed by the method of laser-frequency switching which has been described elsewhere.[6,18] Here we will briefly outline the experiment and emphasize differences from previous experiments which are introduced because of the short time-scale of the present measurement.

The sample is coherently prepared by irradiation at a frequency ω_0 with a Spectra-Physics single-frequency dye laser. This is in resonance with a set of F_3^+ centers within the inhomogeneous line, and it induces a polarization with a width determined by Γ and the frequency width of the laser. The laser width was less than 1 MHz, i.e., negligible here, and the power used of up to 10 mW unfocused was far below

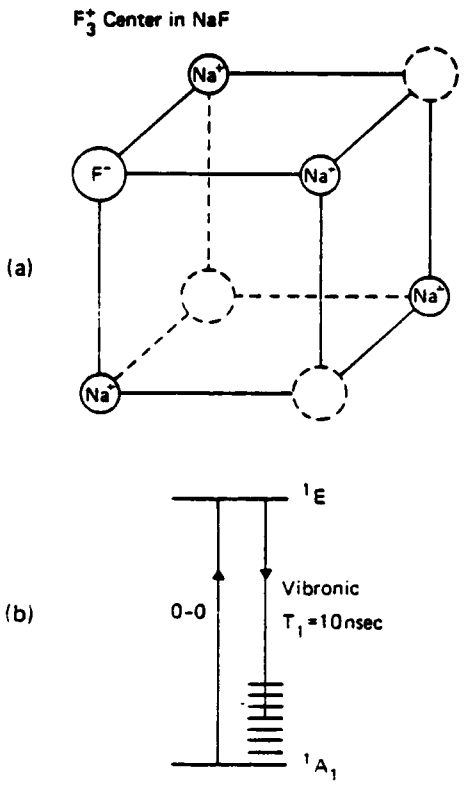


FIG. 1. (a) Model for the F_3^+ center in NaF. Two electrons are localized around three adjacent F^- vacancies in the (111) plane. (b) Energy-level diagram for the $^1A_1 - {}^1E$ transition at 5456 Å. Most of the intensity of the transition is in the multiphonon vibronic band which peaks about 1000 cm^{-1} from the zero-phonon line.

the level populations are unchanged, but a random jump is introduced in the relative phase of the amplitudes of the coherently prepared states in the wave function. The total dipole dephasing rate is given by[8]

$$\Gamma = \tfrac{1}{2}(\Gamma_1 + \Gamma_2) + \Gamma_\phi \ , \tag{5}$$

where Γ_ϕ is the rate of phase interruptions. The rates Γ_1 and Γ_2 can often be simply related to the relaxation time T_1 as we see below. The factor of $\frac{1}{2}$ in Eq. (5) arises since dephasing (Γ_ϕ) reflects the randomization in the relative phase of two amplitudes, whereas Γ_1 and Γ_2 are the decay rates of populations which are given by the square of the amplitudes. Hence the populations decay at twice the rate of the corresponding amplitudes. There are some interesting limiting cases of Eq. (5).

A. Magnetic resonance

The normal case is $kT >> E$ (the energy-level difference), so that the thermally induced upward and downward transition rates are equal ($\Gamma_1 = \Gamma_2$). Since T_1 is defined as the rate at which the population difference relaxes to equilibrium (in this case $n_1 - n_2 \cong 0$) it can easily be shown that $T_1 = \frac{1}{2}\Gamma_2^{-1}$. Further, when the mechanism for population relaxation and pure dephasing is the same (e.g., fluctuating dipole-dipole interactions),[9] there is a definite relation between T_1 and T_2. For dipole-dipole interactions it has been shown[9] that the dephasing and population decay contributions to T_2 are equal. This gives $T_2 = T_1$ which is an unusually simple relationship in the presence of nonvanishing Γ_ϕ.

B. Infrared transitions in a gas

Here the initial and final states are relaxed by collisions into nearby rotational levels. In the usual case these rates are equal,[10] and there are no purely dephasing terms,[11] i.e., $\Gamma_1 = \Gamma_2$, $\Gamma_\phi = 0$, $T_1 = \Gamma_2^{-1}$, and $T_2 = T_1$.

C. Optical transitions

For this case $kT << E$, so that the upper level is not thermally populated. In a low-pressure atomic gas with a dominant relaxation path (e.g., Na) we again have a true two-level system as in Sec. II A. The lower state is normally the ground state so $\Gamma_1 = 0$. The excited state population decay is limited by spontaneous emission. At low pressure $\Gamma_\phi = 0$ so that $\Gamma = \frac{1}{2}\Gamma_2$. Now T_1 measures the rate at which the population difference relaxes to the condition $n_2 = 0$, $n_1 = N$, where N is the total population. This rate is given by

$$\dot{n}_2 - \dot{n}_1 = -\Gamma_2[(n_2 - n_1) - N] \tag{6}$$

and $T_1 = \Gamma_2^{-1}$. We now have $T_2 = 2T_1$, in contrast to the cases in Secs. II A and II B. Note that for a two level system it is only when $\Gamma_1 = 0$ (this case) or $\Gamma_1 = \Gamma_2$ in Secs. II A and II B, that T_1 is defined.

In solids, phase interruptions are usually caused by phonon scattering, fluctuating hyperfine fields, or ion-ion interactions. At low temperatures, phonon scattering and absorption can be frozen out. In the special case where the other contributions to Γ_2 can be neglected, then again $T_2 = 2T_1$. Note, however, that a common situation in solids is for the dominant radiative pathway to terminate on excited phonon levels of the ground state [see Fig. 1(b), for example]. When, as is almost always the case, these phonon levels relax to the ground state in a time that is short compared to the decay from level 2; it is possible to replace the complicated level structure by the two levels 1 and 2.

The simple relations between T_1 and T_2 discussed above do not, of course, hold in general. At high

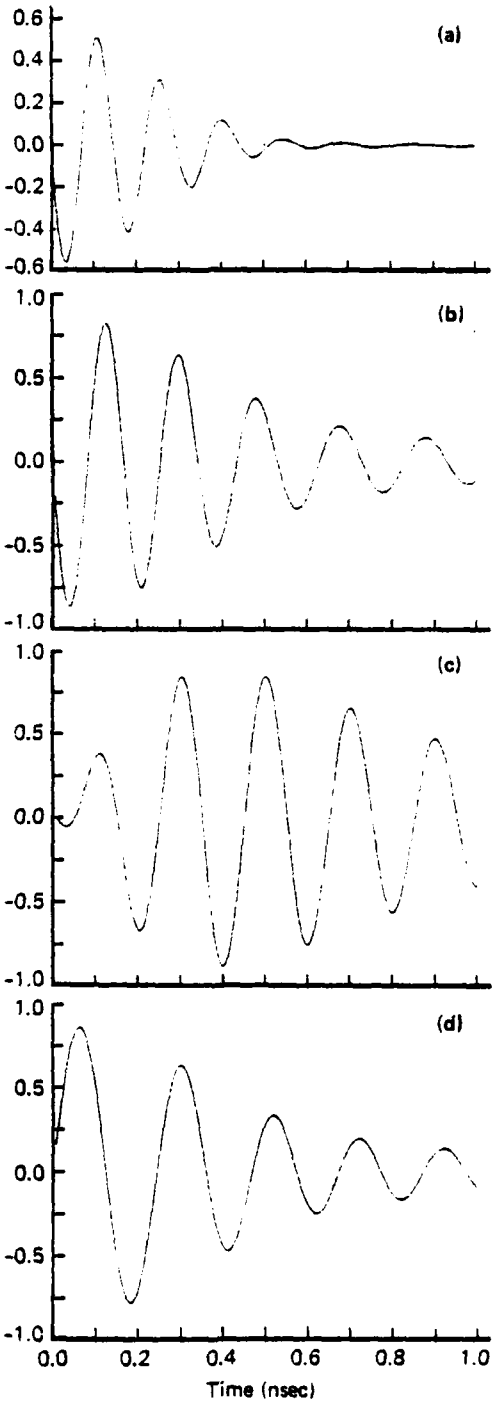


Figure 1. Numerical solutions of the FID heterodyne beat signal $E_0^2(L,t)$ of Eq. (1) where χ=2.3 GHz, $(\Omega-\Omega')/2\pi$=5 GHz, and $(\omega_{21}-\Omega)/2\pi$ in GHz equals (a) 1.5, (b) 1.0, (c) 0.0, and (d) -1.0. See text for other parameters.

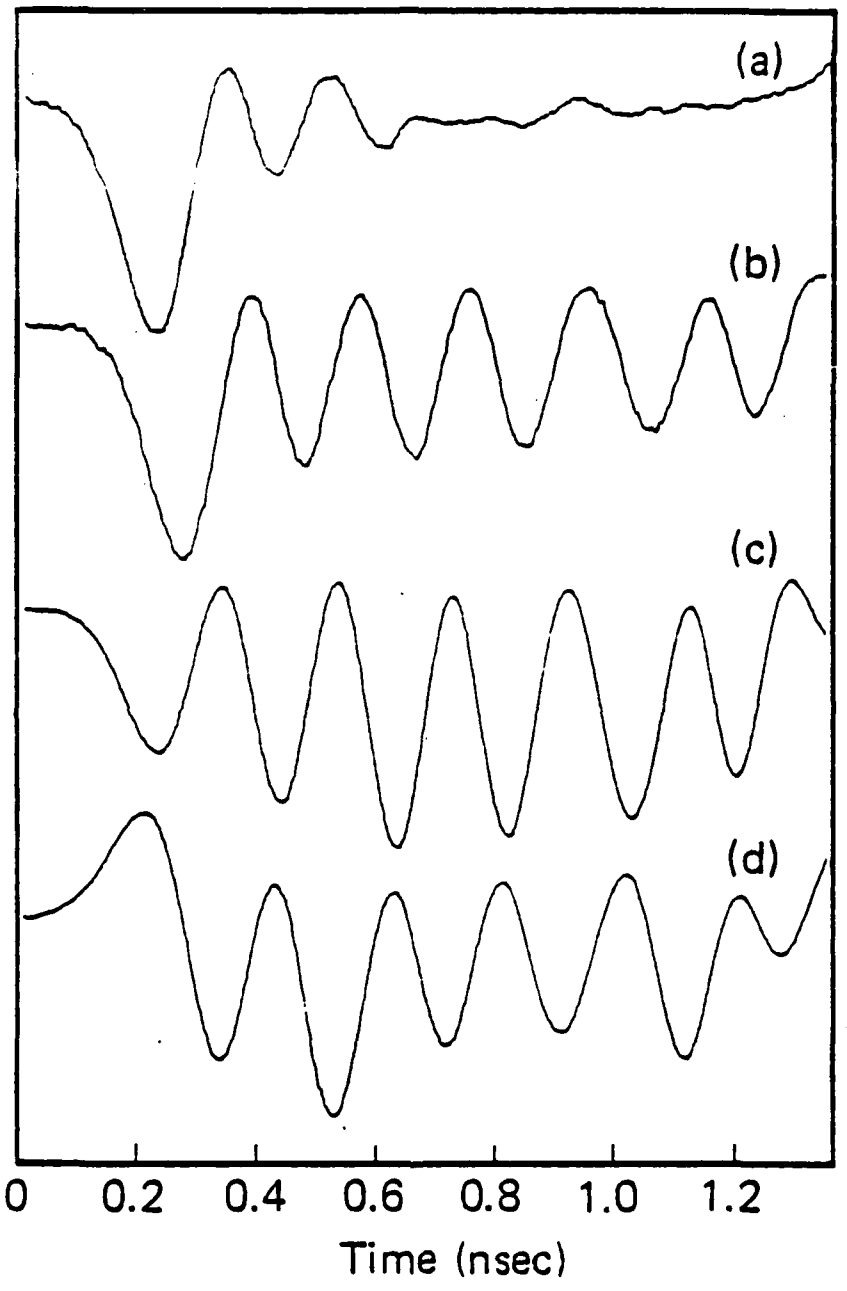


Figure 2. Experimental FID heterodyne beat signals where χ= 0.8 GHz and $(\omega_{21}-\Omega)/2\pi$ in GHz equals (a) 1.5, (b) 0.7, (c) 0.0, and (d) -1.0. The laser frequency shift is $(\Omega-\Omega')/2\pi$=5 GHz, corresponding to a 335 volt dc square wave pulse. The gain in (a) is 2×.

RJ2288(31030)7/7/78
Physics (General)

OPTICAL FID MEASUREMENT OF LOW TEMPERATURE DEPHASING IN $Pr^{3+}:LaF_3$*

R. M. Macfarlane
A. Z. Genack†
S. Kano
R. G. Brewer

IBM Research Laboratory
San Jose, California 95193

ABSTRACT: The temperature dependence of the dephasing rate of the $^1D_2 \leftrightarrow {}^3H_4$ transition in 0.05% $Pr^{3+}:LaF_3$ has been measured between 1.8K and 4.5K by optical free induction decay. One-phonon absorption between the two lowest crystal field components of $^1D_2$ is the dominant relaxation mechanism above ~3K.

---

† Present address: Exxon Research and Enginnering Co., Linden, NJ 07036.

*Work supported in part by the U.S. Office of Naval Research.

Optical dephasing of the $^1D_2 \leftrightarrow {}^3H_4$ transition of dilute (.05%) Pr^{3+} in LaF_3 at 1.5K has been reported [1], and recent measurements have explored the temperature dependence in the range 1.8K to 4.5K [2]. The transition studied at 5925.2A is that from the lowest crystal field component of $^3H_4$ (the ground state) to the lowest component of $^1D_2$. These are electronic singlet states which couple to the Pr^{3+} nuclear spin I=5/2, via quadrupolar, and second order dipolar interactions to give Kramers' doublets separated by ~10MHz (see Fig. 1).

The dephasing times were measured by optical free induction decay (FID) following frequency switching of a cw dye laser [3]. The effect of depleting the ground state population by optical pumping [4] was minimized by scanning the laser slowly through the inhomogeneous lineshape. To some extent, this allowed time for the hyperfine levels to relax, but more importantly it reverse-pumped the hyperfine levels by sweeping successively through the resonances a,b,c of Fig. 1. The degree of saturation between $^3H_4\Gamma_1$ and $^1D_2\Gamma_1$, which occurs on a time scale of the excited state lifetime of 520μsec [4], has been reduced by amplitude gating the laser as described below.

At temperatures where T≈0 we expect two contributions to the intrinsic dephasing to persist. The first is due to the spontaneous emission lifetime (T_1=520μsec) of the $^1D_2\Gamma_1$ state which contributes a linewidth of $1/\pi T_2$(FWHM)=300Hz, where $T_2=2T_1$. The second arises from the fluctuating magnetic fields at the Pr^{3+} site due to mutual spin-flips of the surrounding fluorine nuclei, the time scale for this being 17μsec [5],

and the corresponding linewidth 17kHz. At present the frequency jitter of our laser prevents measuring these small effects, but it has been possible to determine when phonon induced relaxation dominates the dephasing process.

In our earlier measurements of the dephasing rate at 1.5K [1] an optical linewidth of Γ=830kHz was obtained but its origin was not clear. We have now made careful FID studies of the dephasing of the 5895.84A line of I_2 vapor and these indicate that most of this linewidth is instrumental and arises from laser frequency jitter. For example, the linewidth of this iodine line extrapolated to zero pressure and zero laser power is 780kHz, and the FID decay is exponential (i.e., the jitter contributes a Lorentzian lineshape). In the absence of laser frequency jitter the width is expected to be 160kHz corresponding to the measured I_2 radiative lifetime of 1.02μsec. The difference of 620kHz we attribute to laser jitter.

Other sources of line broadening which we found to contribute about 150kHz arise from saturation effects, and to a lesser extent heating by the absorbed laser energy. These were eliminated as follows. Instead of uniformly reducing the laser power P, with a consequent large decrease in FID amplitude ($\propto P^2$), we gated the amplitude of the 12mW laser so that it was on for 10μsec and off for 500μsec ($\approx T_1$). This maintained a high peak power for the FID, but low average power to reduce saturation and also heating, since heat is released to the lattice on a time scale of T_1. Laser frequency switching occurs in the middle of the laser 'on' period,

which lasts ~$10T_2$ [6]. The data obtained in this way are shown in Fig. 2. As is shown in Fig. 3, the FID signal at the lowest temperature of 1.8K is exponential, and corresponds to a linewidth of 660kHz which as we have seen is mostly laser frequency jitter [7]. The residual width at $T\simeq 0$ was subtracted from the other measured points to obtain the temperature dependence of the intrinsic dephasing. This is shown by the solid points in Fig. 2.

The temperature dependence of the homogeneous linewidth of the $^1D_2 \leftrightarrow {}^3H_4$ transition has been studied at higher temperatures by conventional spectroscopy [8] and by fluorescence line narrowing (FLN) [9]. The FLN linewidth was fit by the expression [9]:

$$\Gamma = 0.7\ \bar{n}(23) + 50\ \bar{n}(57) + 125\ \bar{n}(76) \quad \text{GHz}$$

where $\bar{n}(\omega)=[\exp(\hbar\omega/kT)-1]^{-1}$ is the phonon occupation number. This expression is derived from a model [5] in which a single phonon is absorbed, either in the ground or excited state, and induces transitions between the low lying crystal field levels ($23cm^{-1}$ in the excited state, $57cm^{-1}$ and $76cm^{-1}$ in the ground state). In the temperature range of interest to us here, only the first term survives with any appreciable magnitude, i.e., the fit to the high temperature data extrapolates to $\Gamma=7\times10^5\bar{n}(23)$kHz. This is shown by the solid curve in Fig. 2, and is seen to be in very good agreement with the experimental points. This provides additional evidence that the dephasing above ~3K is dominated by 1-phonon absorption between the lowest two crystal field components of $^1D_2$ separated by $23cm^{-1}$.

REFERENCES

† Present address: Exxon Research and Engineering Co., Linden, NJ 07036.

[1] A. Z. Genack, R. M. Macfarlane and R. G. Brewer, Phys. Rev. Lett. 37, (1976) 1078.

[2] A preliminary report was given in R. M. Macfarlane, A. Z. Genack and R. G. Brewer, Bull. Am. Phys. Soc. 23, (1978) 75.

[3] R. G. Brewer and A. Z. Genack Phys. Rev. Lett. 36, (1976) 959; A. Z. Genack and R. G. Brewer, Phys. Rev. A17, (1978) 1463.

[4] L. E. Erickson, Phys. Rev. B16, (1977) 4731.

[5] L. Shen, Phys. Rev. 172, (1968) 259.

[6] This is distinct from the acousto-optic amplitude gating experiments given the acronym LADS by A. H. Zewail, Chem. Phys. Lett., (to be published). We refer to our experiment as Gated Amplitude Laser Spectroscopy or GALS.

[7] Erickson (Ref. 4) measured absorption hole-widths of 800kHz at 2K from which he deduced a 200kHz homogeneous linewidth, allowing for his laser jitter. He noted that this is consistent with the fluorine hyperfine field of ~10gauss acting on the Pr^{3+} g-value of 23kHz/gauss. However because of the slow spin-flip rate on the F^- ions we consider this to be inhomogeneous broadening, the homogeneous width being much less.

[8] W. M. Yen, W. C. Scott and A. L. Schawlow, Phys. Rev. 136, (1964) A271.

[9] L. E. Erickson, Opt. Comm. 15, (1975) 246.

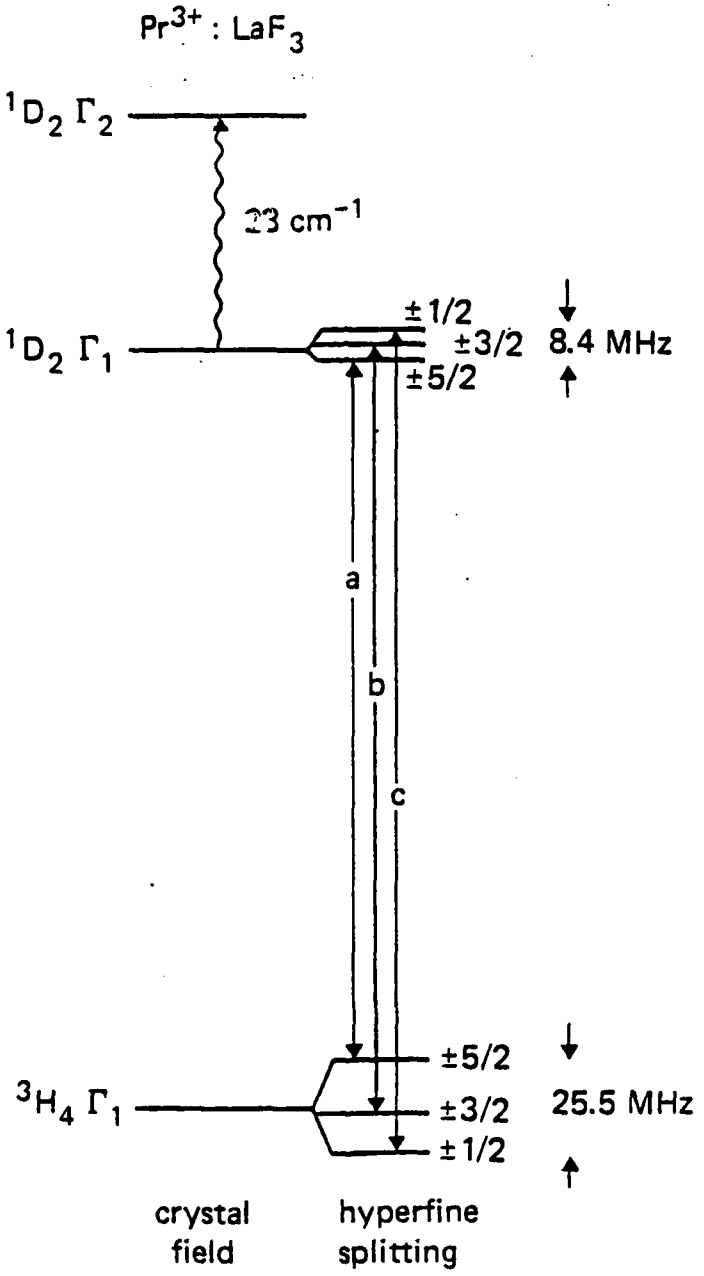


Fig. 1 Energy level diagram for Pr^3:LaF_3 showing the 5925.2A transition and the lowest excited component of the $^1D_2$ term. Temperature dependent dephasing at low temperatures arises from 1-phonon absorption $^1D_2(\Gamma_1 \rightarrow \Gamma_2)$.

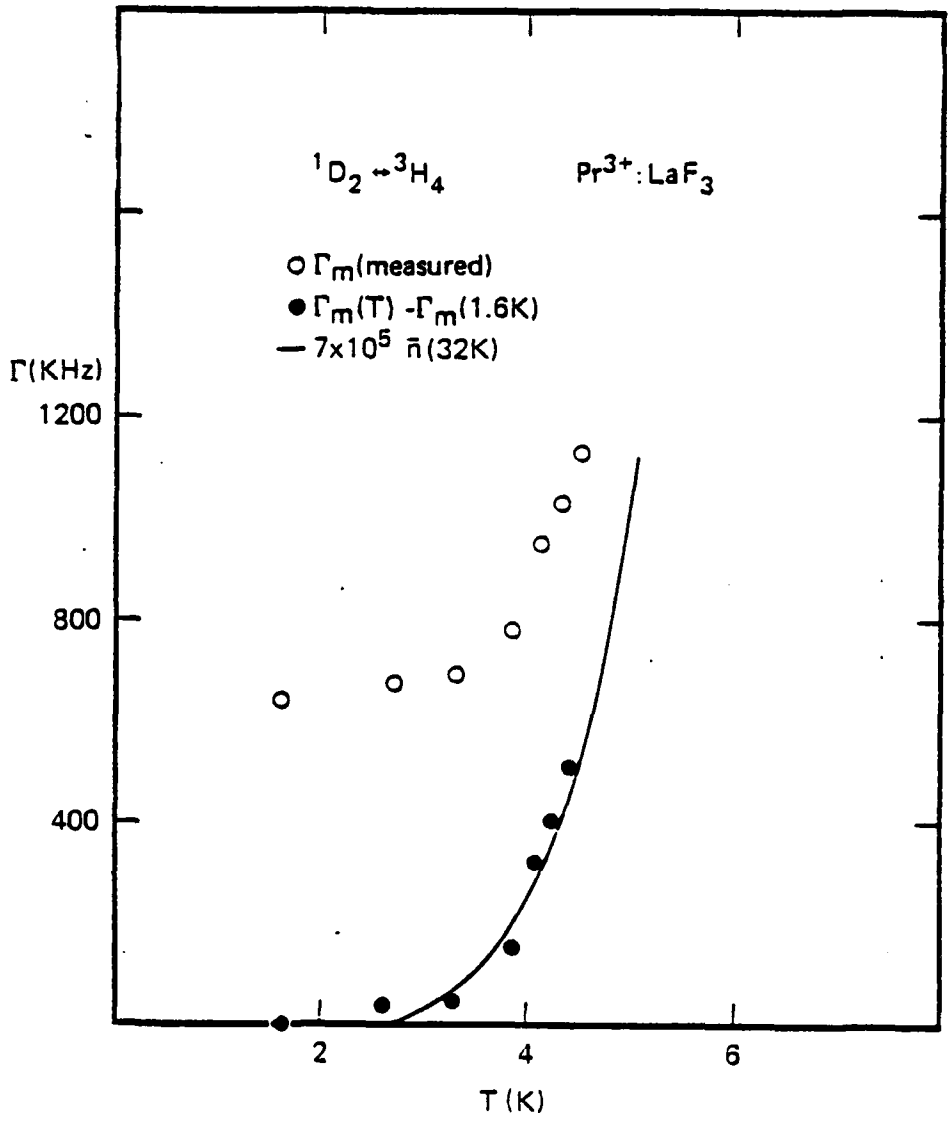


Fig. 2 Temperature dependent dephasing of the 5925.2A transition of Pr^3:LaF_3 measured by optical FID. Below 3K the width is dominated by laser jitter. The solid curve is extrapolated from a fit to the high temperature data of Refs. [8] and [9].

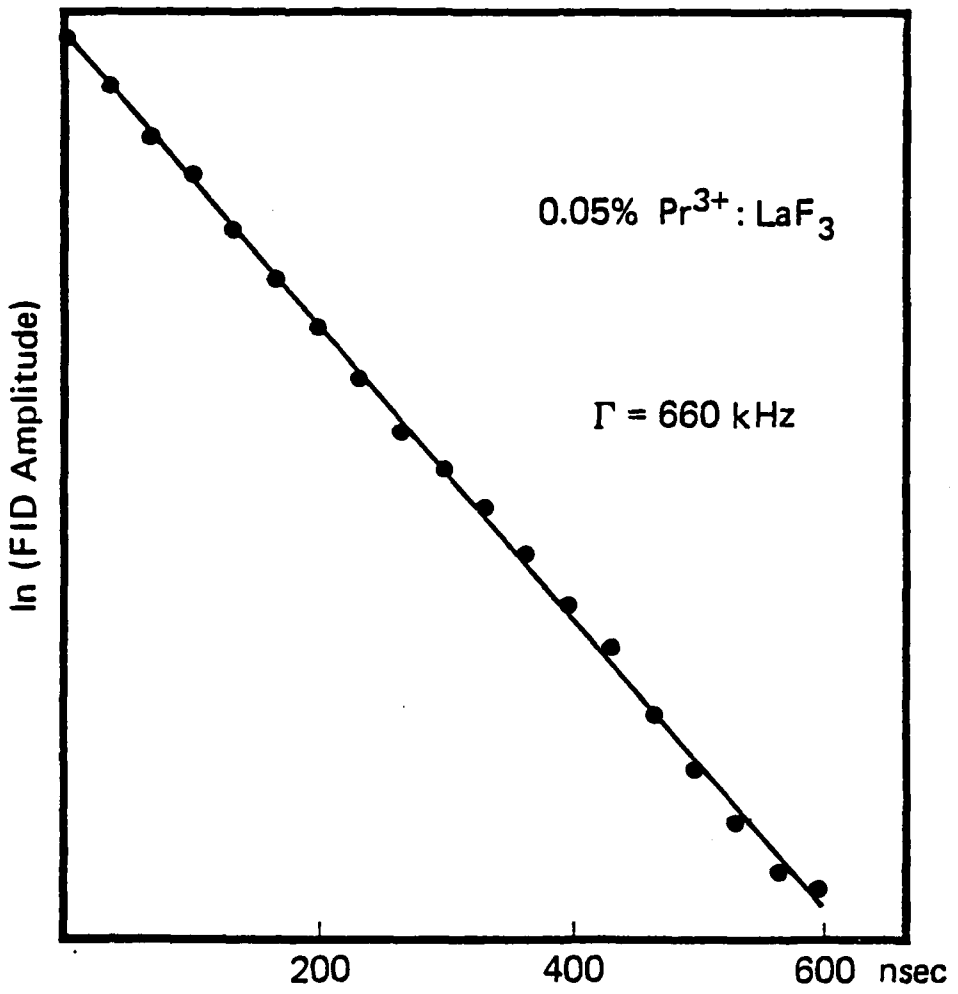


Fig. 3 Decay of the envelope of the FID beat signal at 1.8K, limited by laser frequency jitter.

RJ2483(32432)3/7/79
Physics

Appendix - Item 5

SUBNANOSECOND OPTICAL FREE INDUCTION DECAY *

Ralph G. DeVoe
Richard G. Brewer

IBM Research Laboratory
San Jose, California 95193

ABSTRACT: A novel form of laser frequency switching is devised which extends coherent optical transient studies to a 100 picosecond time scale, the measurements being performed in real time. Free induction decay on a subnanosecond time scale reveals new features such as a first order FID which dephases with the inhomogeneous dephasing time T_2^* and interferes with the well-known nonlinear FID. A complete analytical expression for optical FID is derived and supports our FID observations for the sodium D_1 transition.

*Work supported in part by the U.S. Office of Naval Research.

I. INTRODUCTION

Coherent optical transient phenomena, such as the free induction decay (FID) effect, have been detected recently on a 100 picosecond time scale using a novel form of laser frequency switching.[1] This development represents a fifty fold improvement in temporal resolution over our initial version[2] of laser frequency switching which incorporated an intracavity electro-optic phase modulator. The present device is a traveling wave electro-optic phase modulator that is external to the laser cavity where the earlier advantages are still preserved, namely, heterodyne detection, high sensitivity, and the ability to monitor the entire class of coherent optical transients by preselecting the voltage pulse sequence. Hence, quantitative coherent transient measurements in this time domain are now feasible.

New aspects of optical coherence become evident as the time scale is reduced. This article explores additional properties of optical FID which are noticeable in the subnanosecond region for the sodium D line transitions. Our observations confirm a complete density matrix solution of the Schrödinger wave equation which we consider first.

II. THEORY

A general expression for optical FID is presented here along with its physical interpretation. The detailed derivation will appear elsewhere.[3] Theoretically, the appearance or nonappearance of first order FID depends on the manner in which the optically induced dipole is averaged over the atomic velocity distribution. In earlier theories[4-6] where the laser

frequency or Stark switching is assumed small compared to the Doppler broadening, the Gaussian lineshape was assumed to be constant over the region of integration, and therefore could be factored outside the Doppler integral. Foster, Stenholm, and Brewer[6] first predicted a rapid transient arising from the entire inhomogeneous line by retaining the Gaussian in the integral and evaluating the result approximately. Indeed an exact analytical evaluation of their Equation (10) forms the basis of this work where we adopt the same notation.

Let us write down Eq. (10) of Foster, Stenholm, and Brewer and examine the consequences of an analytical evaluation of the Doppler integral. Here $\tilde{\rho}_{12}$ is the familar off-diagonal density matrix element of the transition levels 1 and 2, expressed in a frame rotating at the preparative laser frequency Ω. The Doppler-averaged density matrix element is given by

$$\langle\tilde{\rho}_{12}(t)\rangle = \frac{1}{u\sqrt{\pi}}\int_{-\infty}^{+\infty}\tilde{\rho}_{12}(v_z,t)e^{-v_z^2/u^2}dv_z$$

$$= \frac{i\chi}{2\sqrt{\pi}u}\cdot\Delta\rho_{21}^{o}\ e^{-t/T2}\int_{-\infty}^{+\infty}\frac{i\Delta(v_z)+\gamma}{\Delta^2(v_z)+\Gamma^2}\ e^{i\Delta(v_z)t}\ e^{-v_z^2/u^2}\ dv_z \qquad (2.1)$$

where the tuning parameter $\Delta(v_z)=-\Omega+\omega_{21}-kv_z$, the power-broadened homogeneous linewidth $\Gamma=\sqrt{1/T_2^2+\chi^2T_1/T_2}$, the Doppler width $\sigma\equiv ku$, $\gamma\equiv 1/T_2$, the Rabi frequency $\chi=\mu_{ij}E/h$, and $\Delta\rho_{21}^{o}$ is the level population difference in the absence of excitation. This integral is just the convolution of the Lorentzian susceptibility of each velocity group with the Gaussian velocity distribution. The phase factor $e^{i\Delta(v_z)t}$ corresponds to the free transient decay of each velocity group; i.e., regardless of the excitation frequency, each velocity group decays at its own free resonant frequency.

We change the variable of integration from v_z to $x \equiv \Delta(v_z)$ and define

$$\delta \equiv \omega_{21} - \Omega \ .$$

Then the integral in (2.1) becomes

$$I = \int_{-\infty}^{+\infty} \frac{ix+\gamma}{x^2+\Gamma^2} e^{ixt} e^{-\frac{(x-\delta)^2}{\sigma^2}} dx \ . \qquad (2.2)$$

This integral can be expressed analytically in terms of the error function $W(z)$ of complex argument,[7,8] taking the form for $t<2\Gamma/\sigma^2$,

$$I = \frac{\pi}{2} e^{-(\sigma t/2)^2} e^{i\delta t} \times \left\{ (\eta+1) W\left[\frac{\delta}{\sigma} + i\left(\frac{\sigma t}{2} + \frac{\Gamma}{\sigma}\right)\right] + (\eta-1) W\left[-\frac{\delta}{\sigma} + i\left(-\frac{\sigma t}{2} + \frac{\Gamma}{\sigma}\right)\right] \right\} . \qquad (2.3a)$$

For $t>2\Gamma/\sigma^2$,

$$I = \pi(\eta-1) e^{-\left(\frac{i\Gamma-\delta}{\sigma}\right)^2} e^{-\Gamma t} + \frac{\pi}{2} e^{-(\sigma t/2)^2} e^{i\delta t} \left\{ (\eta+1) W\left(\frac{i\sigma t}{2} + \frac{i\Gamma+\delta}{\sigma}\right) - (\eta-1) W\left(\frac{i\sigma t}{2} + \frac{-i\Gamma+\delta}{\sigma}\right) \right\} \qquad (2.3b)$$

where the saturation parameter

$$\eta \equiv \gamma/\Gamma \ .$$

It then follows in a sample of length L and atomic number density N that the FID heterodyne beat signal[9] is

$$E_b^2 = K e^{-t/T_2} e^{i(\Omega-\Omega')t} \times \begin{cases} I = \text{Eq. (2.3a)}, & t<2\Gamma/\sigma^2 \\ I = \text{Eq. (2.3b)}, & t>2\Gamma/\sigma^2 \end{cases} + \text{c.c} \qquad (2.4)$$

REFERENCES

1. R. G. DeVoe and R. G. Brewer, Phys. Rev. Lett. 40, 862 (1978).

2. R. G. Brewer and A. Z. Genack, Phys. Rev. Lett. 36, 959 (1976); A. Z. Genack and R. G. Brewer, Phys. Rev. A17, 1463 (1978).

3. R. G. DeVoe and R. G. Brewer (to be published).

4. R. G. Brewer and R. L. Shoemaker, Phys. Rev. A6, 2001 (1972).

5. F. A. Hopf, R. F. Shea, and M. O. Scully, Phys. Rev. A7, 2105 (1973).

6. K. L. Foster, S. Stenholm, and R. G. Brewer, Phys. Rev. A10, 2318 (1974).

7. Handbook of Mathematical Functions, National Bureau of Standards Applied Mathematics Series 55 (U.S. Government Printing Office, 1964), edited by M. Abramowitz and I. A. Stegun, p. 297.

8. P. F. Liao, J. E. Bjorkholm, and J. P. Gordon, Phys. Rev. Lett. 39, 15 (1977).

9. R. G. Brewer in Frontiers in Laser Spectroscopy (North-Holland, 1977), edited by R. Balian, S. Haroche, and S. Liberman, p. 341.

10. E. L. Hahn, Phys. Rev. 77, 297 (1950).

11. W. W. Rigrod and I. P. Kaminow, Proc. IEEE 51, 137 (1963); I. P. Kaminow, Phys. Rev. Lett. 6, 528 (1961).

12. An Introduction to Electrooptic Devices (Academic, N.Y., 1974), edited by I. P. Kaminow, p. 213-237.

13. H. Kogelnik and T. Li, Proc. IEEE, 1312 (1966).

14. See reference 12, p. 182.

15. See reference 12, p. 92, Eq. (10).

16. See for example R. C. Eden, Proc. IEEE 63, 32 (1975).

coherence effects are faithfully observed. It is evident that other coherent transients can be observed in this way where the time scale may be reduced even further.

ACKNOWLEDGMENT

The technical assistance of D. E. Horne and K. L. Foster proved most valuable and is acknowledged with pleasure. This work was supported in part by the U.S. Office of Naval Research.

order term manifests itself as a Gaussian build-up of the nonlinear FID. The corresponding theoretical result in Fig. 4c where $\delta=0$ shows this interference effect again but in a more dramatic way since $\chi=2.3$ GHz.

In Fig. 3d, $\delta/2\pi=-1$ GHz and we see that tuning the laser from the low to the high frequency side of the transition reverses the phase of the first order FID. Compare the theoretical curves Figs. 4b and 4d where $\delta/2\pi=1$ and -1 GHz, respectively, which shows the same phase reversal.

Figure 3d also gives evidence of a hyperfine interference beat because the laser is now tuned midway between the two pairs of lines so that all four transitions are prepared. The FID is now modulated at ~1.8 GHz, which is the ground state hyperfine splitting of Na. The mechanism for this process is very likely a coherent Raman beat effect,[17] but further studies are needed in testing this idea. In any event, it now becomes possible to detect microwave splittings by a transient method where the beat frequency exceeds quantum beat[18] measurements by at least one order of magnitude.

V. SUMMARY

We have described a laser frequency switching technique which permits coherent optical transient investigations on a subnanosecond time scale. A key feature of these measurements is that they are highly reproducible and lend themselves to quantitative analysis. This point is illustrated by optical FID which shows new characteristics when the temporal resolution is ~100 picoseconds. Detailed theoretical predictions of these new

A more physical explanation of the frequency dependence of first order FID is that it behaves like the dispersive part of a Lorentzian lineshape in which Doppler broadening has been ignored. For example, a Lorentzian $(\gamma+ix)/(\Delta^2+x^2)$ approaches i/x at large detuning and yields the slow tuning behavior described above. For small detuning, we also expect the first order FID signal to change sign as we pass through resonance, and furthermore to equal zero exactly at resonance. These characteristics are evident in Figs. 3 and 4.

Figure 3a shows the observed FID signal for the laser tuned 1.5 GHz below the transition frequency ($\delta/2\pi$=1.5 GHz). The nonlinear FID is reduced by a factor of e^2 and does not appear. The observed decay is obviously nonexponential and is completed in 500 psec as expected since T_2^* is 340 psec. A careful analysis shows that the beat frequency is ~6.5 GHz, which is equal to $(\omega_{21}-\Omega')/2\pi$ rather than $(\Omega-\Omega')/2\pi$=5 GHz.

Figure 3b shows the FID for $\delta/2\pi$=0.7 GHz. Here there is a large amplitude preparation due to the saturation of a resonant velocity group. The decay, which persists beyond the first order FID, is exponential in agreement with Eq. (2.6), being given by $e^{-\chi t}$ in this power broadened regime with χ=0.8 GHz. The observed beat frequency is equal to the laser frequency switch of 5 GHz. These signals are also absorptive since their phase is invariant to laser tuning.

Figure 3c shows the FID for $\omega_{21}-\Omega$=0. Note that here the first order and nonlinear FID cancel at the time origin, and the decay of the first

downward by 5 GHz. This procedure avoids sweeping the laser frequency through the remaining two lines at higher frequency.

Figure 3 shows the observed FID heterodyne beat signals for different values of the initial laser frequency Ω or $\delta \equiv \omega_{21} - \Omega$, where ω_{21} is the frequency of one of the transitions of the low frequency pair. The numerical solutions of Eq. (2.4) are shown in Fig. 4 where for the Na D_1 line $(\Omega - \Omega')/2\pi = 5$ GHz, $\sigma = 5.8$ GHz, $\Gamma = 1.6$ GHz, $\chi = 2.3$ GHz, $T_2 = 32$ nsec, and $\eta = 0.019$. The laser power density is $3 W/cm^2$ ($\eta = 0.055$), and 5% of the beam is absorbed in a 10 cm path of Na at a pressure of 2×10^{-6} Torr. Note that the large frequency switch makes it possible for the first time to switch completely outside the Doppler linewidth, which is 0.77 GHz for Na.

As shown in Fig. 3, first order FID and nonlinear FID can be distinguished by varying the preparative laser frequency Ω. This is because the intensity of nonlinear FID depends on the optical dipole induced in a *single velocity group*. Since the density of any given velocity group is a Gaussian $e^{-(\delta/\sigma)^2}$, the nonlinear FID signal will decrease rapidly with laser detuning (see Eq. (2.6)). First order FID, however, is primarily a nonresonant phenomenon in which all velocity groups participate weakly. Examining Eq. (2.8) one can see that the first order FID varies slowly with laser tuning δ. By tuning off resonance, therefore, one should see a slow reduction in first order FID, and a rapid disappearance of nonlinear FID.

directly on an S-4 sampling head (25 psec response) of a Tektronix 7904 oscilloscope with a 7S11 sampling unit. Because the photodiode has a low cw power rating, a Pockel's cell optical shutter blocks the laser light except for a 2 μsec interval, immediately before and after the frequency switch so that the FID signal can be seen during this period.

The step function dc modulating voltage is generated at a 700 Hz repetition rate by a Tektronix 109 reed relay pulser, where the output is delayed by 75 nsec to permit triggering the Pockel's cell and the 7T11 sampling time base.

IV. MEASUREMENTS

Coherent transients on a 100 psec time scale were detected for both I_2 vapor and atomic sodium. However, the large number of closely spaced hyperfine transitions in I_2, which are distributed over one Doppler width, produce heavily modulated FID signals and at present are difficult to interpret. Therefore to avoid unnecessary complications in these initial studies, experiments were performed on atomic sodium vapor which permits a quantitative test of the above FID theory.

The transition monitored is the sodium D_1 line $^2P_{1/2} \leftrightarrow {}^2S_{1/2}$ at 16,956.16 cm^{-1}. As is well known its hyperfine splitting, 192 MHz ($^2P_{1/2}$) and 1.772 GHz ($^2S_{1/2}$), produces two pairs of lines. The initial laser frequency Ω is tuned to the center of the low frequency pair, and the traveling wave modulator voltage adjusted to shift the laser frequency

inversely proportional to the electrode spacing. The crystal therefore is chosen to be as narrow as possible up to the optical diffraction limit. Kogelnik[13] has calculated the optimum focusing arrangement for such a case. We used a 10 cm lens which produces a 1/e field spot diameter of 150 microns at the crystal apertures. The crystal must consequently be aligned to an angle of ~1 mrad and to a position of 50μ to avoid beam distortion. A second 10 cm lens recollimates the beam before entering the sample cell.

The ratio of height to width of the crystal (0.65mm to 0.50mm) was chosen so that, given the microwave dielectric constant of lithium tantalate (ε=43), the crystal appears to be a 50Ω transmission line. The electrical rise time of the crystal and the quality of the impedance match to an external 50Ω line were tested with a time domain reflectometer which revealed 100 psec rise times. Using the known electro-optic coefficient[14] of lithium tantalate $r_{33}=3.04\times10^{-9}$ cm/volt, we calculate $\Delta n/\text{volt}=-2.43\times10^{-7}$/volt using standard techniques.[15] Inserting this into Eq. (3.4) we obtain $\Omega-\Omega'/2\pi=13.9$ MHz/volt which agrees with our experimental value to within 10%.

The beam from a single mode cw dye laser (Coherent 599) passes through a focusing lens in the $LiTaO_3$ modulator crystal, a collimating lens, and a sample cell containing sodium vapor. It emerges together with the forward FID emission and is focused to a 40 micron diameter spot on a fast GaAs-GaAlAs photodiode (Rockwell International Corp.)[16] The photodetector of 50μ diameter has a response time of 30 psec or less and is mounted

harmonics. Therefore, the modulation efficiency is often low. In our arrangement with dc voltage pulses, all of the light is shifted uniformly.

Fourth, as already stated, intracavity switching,[2] which requires the application of a transverse field, will not satisfy our requirements either. For example, electro-optic AD*P crystals cannot be frequency switched fast enough or far enough. The electro-optic coefficient is too low for gigahertz frequency shifts with available voltages. Furthermore, these crystals are not easily matched to a 50 ohm driver impedance since their characteristic capacitance of ~40 picofarads implies an RC rise time of 2 nsec. More importantly, the modulating voltage takes at least 500 psec to travel across the crystal. *However, in our traveling wave modulator, rather than trying to overcome the transit time problem, we have used it as the operating principle of our device.*

The unique features of our traveling wave modulator therefore facilitates rapid FID measurements and also other coherent transient effects by a variation of the pulse sequence.

B. Apparatus

The optical phase modulator consists of two lithium tantalate crystals 0.5mm×0.65mm×25mm as in Fig. 2. The end faces are polished and anti-reflection coated, and gold electrodes are deposited on opposite faces to form a parallel plate transmission line. A voltage between the electrodes produces an electric field parallel to the c-axis. For a given applied voltage, the electric field, and hence the frequency shift, is

where the minus sign corresponds to copropagating fields. By a similar argument, for counter propagating fields the plus sign follows. The singularity in (3.4) for v=c is artificial and results from our neglecting the pulse rise time, which for the above step function is zero. For typical values of these parameters, to be discussed, gigahertz shifts are easily accomplished, particularly in the visible or ultraviolet region due to the large factor $\Omega \sim 10^{15}$ Hertz. Of course, once the dc pulse reaches the end of the crystal $d\varphi/dt=0$ and the frequency shift is zero.

This technique possesses several advantages over more conventional traveling wave modulators.[12] First, conventional devices do not employ dc square wave pulses and require additional microwave techniques to phase match the microwave wave velocity to the light wave velocity. This matching is never perfect and degrades the rise time of the crystal. In our design the rise time is determined primarily by the crystal connections which we believe can approach 20 picoseconds. Second, a conventional traveling wave modulator when driven by a dc voltage ramp, where $v(t) \propto t$ can produce a frequency shift but it is impractical. Producing a ramp with constant slope, a sharp corner at t=0, and no ringing appears to be a formidable task in the 100 picosecond region. Also, in our design once the modulating wave is launched into the crystal, it will attenuate slowly, and the frequency shift will be highly uniform.

Third, previous devices require microwave sources which generate a distribution of optical sidebands corresponding to the various microwave

order of magnitude more favorable. The principle of operation is the following. An electro-optic crystal, which constitutes an integral part of a microwave transmission line, allows a cw laser beam and a direct current voltage pulse to simultaneously propagate longitudinally along one crystal axis as shown in Fig. 2. As the dc field advances down the crystal, it produces a zone of increasing refractive index, $n_0 \rightarrow n_1$, which shifts the phase φ of the light wave uniformly in time and hence its angular frequency Ω where

$$\Omega - \Omega' = \frac{d\varphi}{dt} . \tag{3.1}$$

This behavior is easily derived by noting that the phase of the light wave emerging from a crystal of length ℓ at time t is

$$\begin{aligned} \varphi(\ell,t) &= \int_0^{\ell} kn(z)dz \\ &= \int_0^{vt'} kn_1 dz + \int_{vt'}^{\ell} kn_o dz \end{aligned} \tag{3.2}$$

where $\vec{k}$ is the optical propagation vector and v and c are the velocities of the dc field and light wave in the crystal medium. Consider first the case of copropagating fields. If a step function dc field pulse enters the crystal at z=0 at time t=0, then at the intermediate time t' when the light wave is just at the boundary of n_o and n_1, the obvious relation

$$vt' + c(t-t') = \ell \tag{3.3}$$

holds. Inserting $t'=(\ell-ct)/(v-c)$ into (3.2), the frequency shift according to (3.1) is

$$\Omega - \Omega' = \Omega \frac{n_1-n_o}{n_o} \frac{v}{c \mp v} \tag{3.4}$$

advantageous to place the electro-optic modulator inside the laser cavity as in the past,[2] since the transient dies away before the laser beam completes one round trip through the optical cavity. On the other hand, when the modulator is external to the laser cavity, the modulator design can be varied easily while still retaining the advantages of undiminished laser intensity and stability. A novel traveling wave electro-optic modulator is described here which permits such measurements.

Two requirements must be satisfied in laser frequency switching to insure the generation of intense coherent transient signals. First, the laser frequency switch must exceed the homogeneous linewidth $1/\pi T_2$, and second, the switching time should be less than the dephasing time T_2. Therefore, measurements on a subnanosecond time scale imply a shift of several gigahertz with a ~100 picosecond rise time. A schematic diagram of our apparatus is shown in Fig. 1. It consists of a stable cw dye laser, a traveling wave electro-optic modulator, the sample, a fast photodiode detector, and a sampling oscilloscope. The frequency shifted laser beam produces in the sample coherent transients which are detected in the forward direction in real time. All emission signals, such as the FID or the photon echo, appear as heterodyne beat signals, as discussed previously.[4,9]

The traveling wave electro-optic modulator was invented initially by Kaminow in 1961.[11] When suitably modified, this device allows subnanosecond coherent transient studies. Compared to intracavity frequency switching, the rise times and frequency shifts are at least one

preparation. We view these two forms of FID as the transient analogs of steady-state linear and nonlinear (hole burning) laser spectroscopy of an inhomogeneously broadened transition.

(3) *Limit of no inhomogeneous broadening*. In the limit $\sigma \to 0$, the Doppler integral for $\langle \tilde{\rho}_{12}(t) \rangle$, Eq. (2.1), must reduce to a form identical to $\tilde{\rho}_{12}(v_z=0,t)$, thus checking our calculation. As $\sigma \to 0$, $2\Gamma/\sigma^2 \to \infty$ so the short time form of the integral must be used. The argument of the $W(z)$ function approaches $z = \frac{\pm\delta+i\Gamma}{\sigma}$ and its modulus approaches ∞ as $\sigma \to 0$, so we may again use the asymptotic form[7]

$$W(z) = \frac{i}{\sqrt{\pi}z} + \ldots, \quad |z| \to \infty, \quad \mathrm{Im}z > 0$$

In this limit,

$$E_b^2 = \frac{2K\sigma\sqrt{\pi}}{\Gamma^2+\delta^2} e^{-t/T_2} \left(\gamma \cos(\omega_{21}-\Omega')t - \delta \sin(\omega_{21}-\Omega')t\right) \qquad (2.9)$$

where $\delta = \omega_{21}-\Omega$ and $K\sigma = \frac{\sqrt{\pi}}{2} k\bar{n}NL\chi^2\Delta\rho_{21}^o$.

As expected, Eq. (2.9) can be derived[9] directly from $\tilde{\rho}_{12}(t)$ without Doppler averaging when $v_z=0$. The radiation now occurs at the atomic transition frequency ω_{21} regardless of the laser excitation frequency Ω, with an identical amplitude, frequency and relaxation dependence to that of $\tilde{\rho}_{12}(v_z=0,t)$. The FID again exhibits a linear intensity dependence. Equation (2.9) also agrees with the well-known FID theory of nuclear magnetic resonance.[10]

III. EXPERIMENTAL TECHNIQUE

A. Traveling Wave Modulator

To study subnanosecond coherent transients by laser frequency switching, new techniques are required. At such speeds, it is no longer

$$W(z) = \sum_{n=0}^{\infty} \frac{(iz)^n}{\Gamma\left(\frac{n}{2}+1\right)}$$

$$= 1 + \frac{2iz}{\sqrt{\pi}} + \ldots , \quad z<1 .$$

In addition to the condition

$$z = \left| i\left(\frac{\Gamma}{\sigma} \pm \frac{\sigma t}{2}\right) \pm \frac{\delta}{\sigma} \right| < 1 , \tag{2.7}$$

we require that

$$t << 2\Gamma/\sigma^2 ,$$

thereby allowing the $\sigma t/2$ term to be dropped in (2.7). With these conditions, Eq. (2.4) reduces to

$$E_b^2 = 2\pi K e^{-t/T_2} e^{-(\sigma t/2)^2} \times \left\{ \gamma\left(\frac{1}{\Gamma} - \frac{2}{\sqrt{\pi}\sigma}\right) \cos(\omega_{21}-\Omega')t - \frac{2}{\sqrt{\pi}} \frac{(\omega_{21}-\Omega)}{\sigma} \sin(\omega_{21}-\Omega')t \right\} . \tag{2.8}$$

We refer to (2.8) as the first order FID since $E_b^2 \propto \chi^2$. Furthermore, the decay is now Gaussian, $e^{-(\sigma t/2)^2}$, where the characteristic dephasing time $T_2^* \equiv 2/\sigma$. This signal contains both an absorptive and dispersive part which depends on the initial laser frequency through the factor $(\omega_{21}-\Omega)/\sigma$. From (2.8), it is evident that the atomic sample radiates at the Doppler peak ω_{21}, independent of the initial laser frequency Ω, and produces a heterodyne beat of frequency $\omega_{21}-\Omega'$. We conclude, therefore, that in first order FID the various velocity packets destructively interfere, except at Doppler line center. By contrast, the nonlinear FID radiates at the initial laser frequency and therefore possesses memory of its

where

$$K = \frac{\sqrt{\pi}}{2u} \hbar N L \chi^2 \Delta\rho_{21}^{o} \ .$$

This general expression reduces to the following limiting cases.

(1) *Long time limit.* For decay times longer than the inverse Doppler width such that $\sigma t >> 1$, we may use the asymptotic form[7] of the error function

$$W(z) = \frac{i}{\sqrt{\pi} z} + \ldots \quad (z \to \infty) \ ,$$

and Eq. (2.4) yields a heterodyne beat signal

$$E_b^2(t) = K\pi(\eta-1) e^{-(1/T_2+\Gamma)t} \ e^{i(\Omega-\Omega')t} \ e^{-\left(\frac{i\Gamma-\delta}{\sigma}\right)^2} + \text{c.c.} \qquad (2.5)$$

where $\sigma t >> 1 > 2\Gamma/\sigma$. The imaginary part of the term $e^{-\left(\frac{i\Gamma-\delta}{\sigma}\right)^2}$ introduces a small phase shift in E_b^2 for $\Gamma/\sigma << 1$ and therefore makes E_b^2 slightly dispersive. However, we neglect it here and obtain

$$E_b^2(t) = 2K\pi(\eta-1) e^{-(1/T_2+\Gamma)t} \ e^{-(\delta/\sigma)^2} \cos(\Omega-\Omega')t \ . \qquad (2.6)$$

This result is identical to earlier approximate derivations[4-6] where the Gaussian was factored outside the Doppler integral. We shall refer to Eq. (2.6) as the nonlinear FID signal since $E_b^2 \propto \chi^4$ at low light intensities when $\chi^2 T_1 T_2 << 1$. As has already been verified by experiment,[4,6,9] the long time limit of FID displays the properties predicted by (2.6). First, the sample radiates at the initial laser frequency Ω and produces a heterodyne beat signal of frequency $\Omega-\Omega'$ which is absorptive, and second, it decays at the rate $1/T_2+\Gamma$ due to the preparative and post preparative stages.

(2) *Short time limit.* For short times, we retain the first two terms of the power series expansion[7]

17. R. L. Shoemaker and R. G. Brewer, Phys. Rev. Lett. 28, 1430 (1972); R. G. Brewer and E. L. Hahn, Phys. Rev. A8, 464 (1973); ibid., A11, 1641 (1975).

18. S. Haroche in High Resolution Laser Spectroscopy (Springer, Berlin, 1977), edited by K. Shimoda, p. 253.

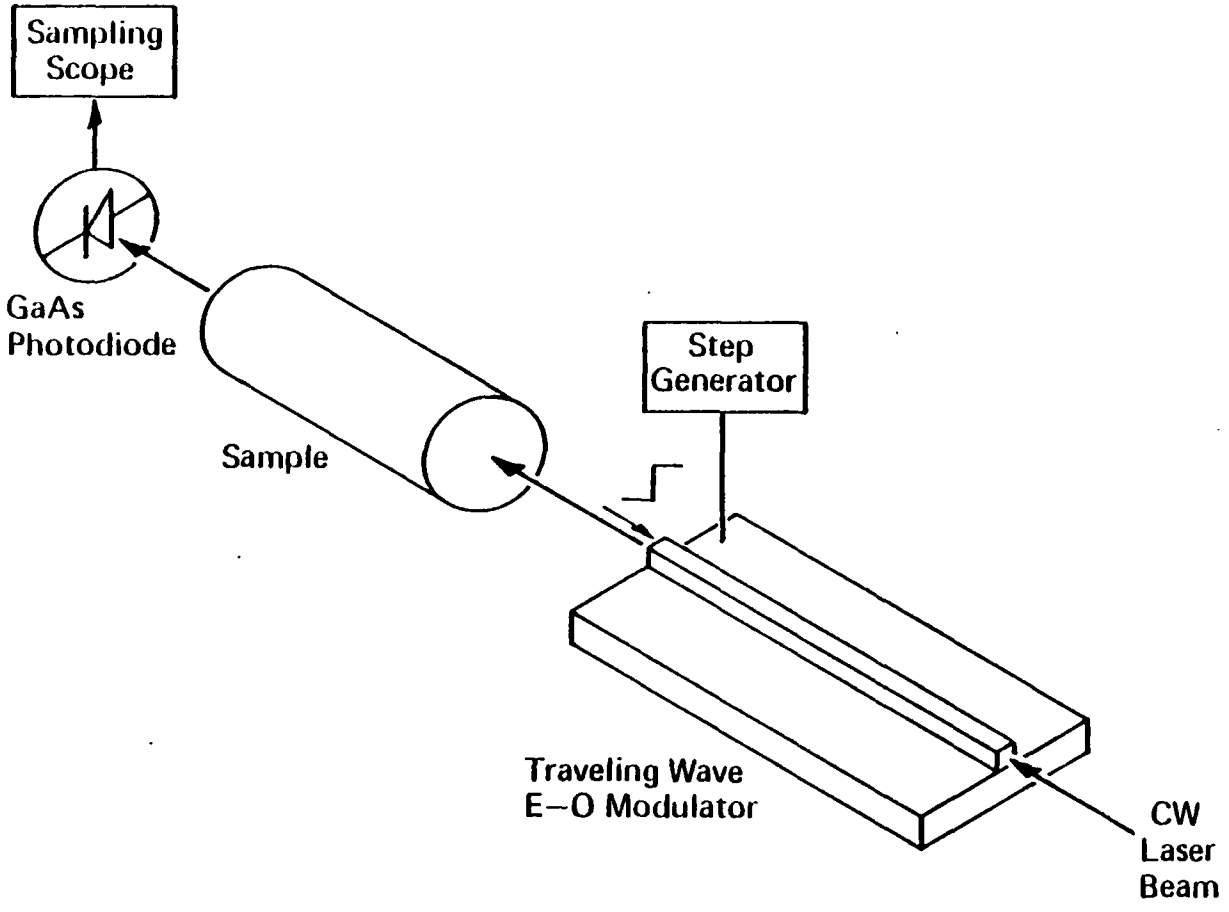


Figure 1. Schematic of the optical layout for detecting subnanosecond coherent optical transients with a traveling wave electro-optic phase modulator. The microwave guide is greatly simplified to show the crystal element and the focusing and collimating lens to either side of it are not shown.

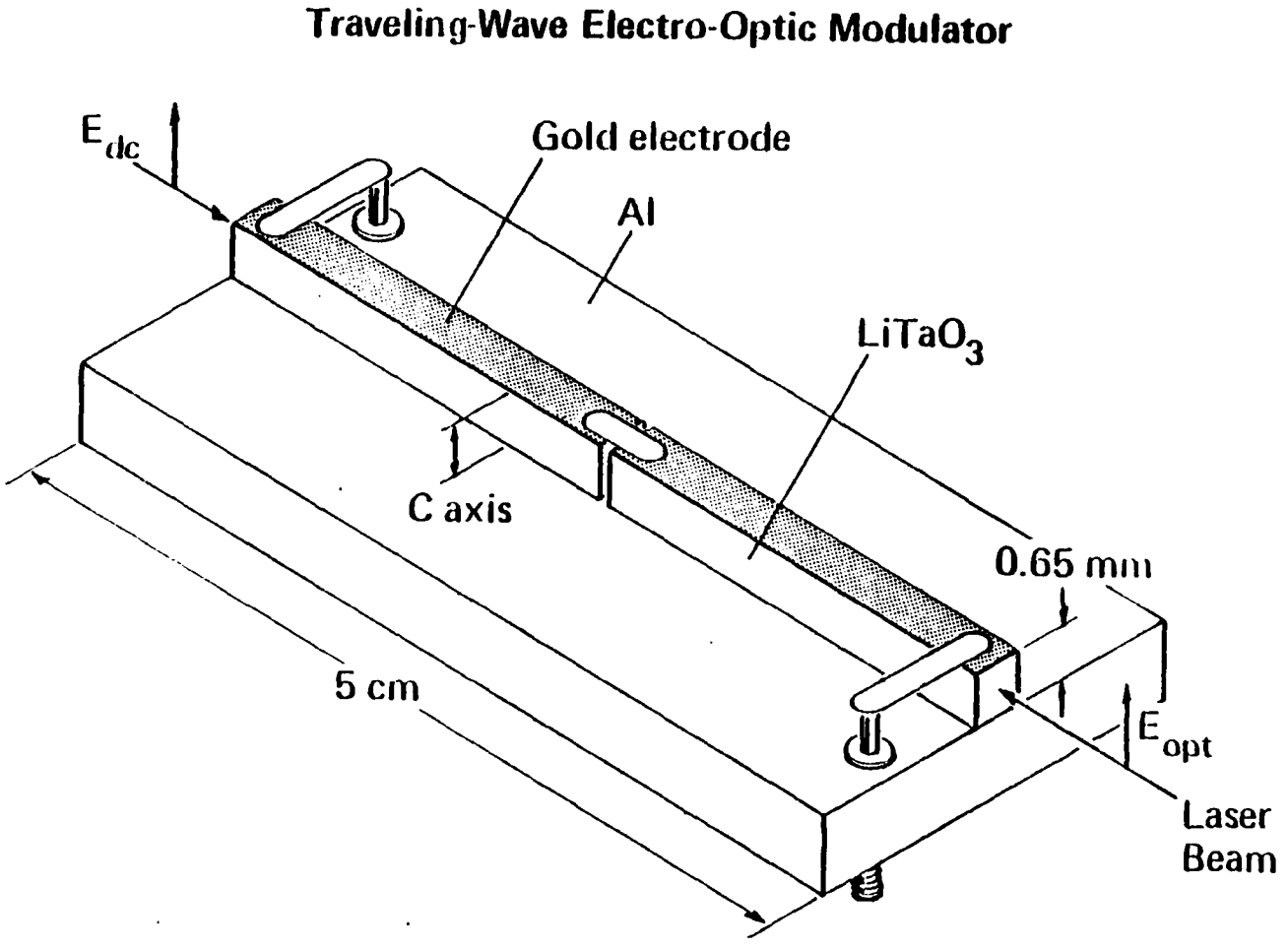


Figure 2. Detailed drawing of the $LiTaO_3$ modulator crystal elements mounted on an aluminum substrate of the microwave guide.

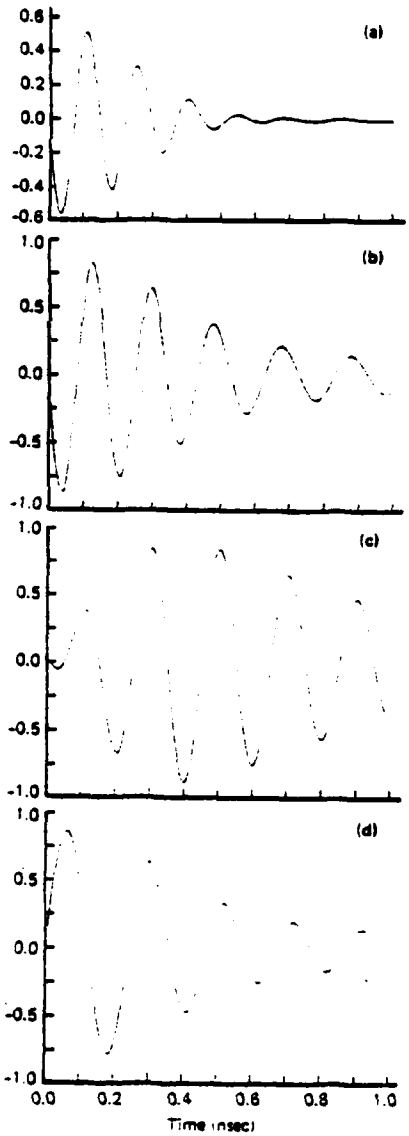


Figure 4. Numerical solution of the FID heterodyne beat signal $E_b^2(L, t)$ of Eq.(2.4) where χ=2.3 GHz, $(\Omega-\Omega')/2\pi$=5 GHz and $(\omega_{21}-\Omega)/2\pi$ in GHz equals (a) 1.5, (b) 1.0, (c) 0.0, and (d) -1.0.

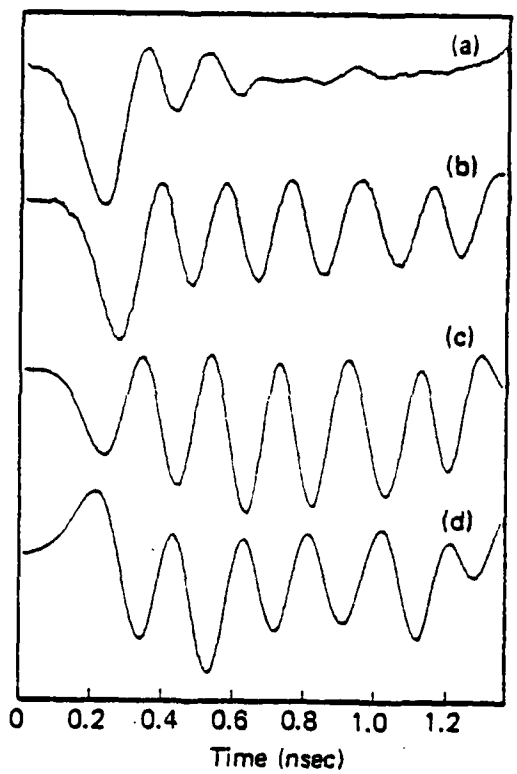


Figure 3. Experimental FID heterodyne beat signals where χ=0.8 GHz and $\delta\equiv(\omega_{21}-\Omega)/2\pi$ in GHz equals (a) 1.5, (b) 0.7, (c) 0.0, and (d) -1.0. The laser frequency shift is $(\Omega-\Omega')/2\pi$=5 GHz corresponding to a 335 V dc square wave pulse. The gain in (a) is 2x.

RJ2535(33075)5/9/79
Physics

SUBNANOSECOND OPTICAL FREE INDUCTION DECAY II*

Ralph G. DeVoe
Richard G. Brewer

IBM Research Laboratory
San Jose, California 95193

ABSTRACT: A novel form of laser frequency switching is devised which extends coherent optical transient studies to a 100 picosecond time scale. The technique incorporates a traveling wave electro-optic element which imposes with unit efficiency a uniform time varying phase and thus a frequency shift on a cw laser beam. In contrast to earlier optical traveling wave modulators which are driven by a microwave oscillator, here the optical phase change is induced rapidly and easily by a dc electric field pulse that propagates in a microwave guide either parallel or antiparallel to the light wave. This advance enables optical free induction decay (FID) studies on a subnanosecond time scale and reveals new features such as a rapid first order FID that dephases with the inhomogeneous dephasing time T_2^*. The well-known nonlinear FID can interfere with the first order component at short times and decays over the much longer period $T_2/(1+\sqrt{1+\chi^2 T_1 T_2})$ where χ is the Rabi frequency. A complete analytical expression is derived for optical FID of a transition subject to homogeneous and inhomogeneous broadening and supports detailed observations of the sodium D_1 line.

*Work supported in part by the U.S. Office of Naval Research.

I. INTRODUCTION

Optical free induction decay (FID) was detected recently on a time scale of 100 picoseconds using a new form of laser frequency switching.[1] This development represents a fifty fold improvement in temporal resolution over an earlier version[2] of laser frequency switching which utilized an intracavity electro-optic phase modulator. The present device (Fig. 1), which is a traveling wave electro-optic phase modulator, is located external to the laser cavity and retains the previous advantages of heterodyne detection, high sensitivity, and the ability to monitor the entire class of coherent optical transients by preselecting the voltage pulse sequence. Hence, quantitative coherent optical transient measurements in the subnanosecond range are now feasible.

As the time scale is reduced, optical coherence phenomena can display new characteristics. This article explores features of optical FID which only become evident in the subnanosecond region when the transition is homogeneously and inhomogeneously broadened. We detect for the sodium D line a rapid first order FID which dephases in an inhomogeneous dephasing time T_2^* and a much longer-lived nonlinear FID[3,4] with a decay time $T_2/(1+\sqrt{1+\chi^2 T_1 T_2})$ where T_2 is the dipole dephasing time, χ is the Rabi frequency, and T_1 is the population decay time. These two forms of FID (Fig. 2) exhibit other important differences which are predicted by theory in Section II and verified by experiment in Section IV. We view these two types of FID as the transient counterpart of steady-state linear and nonlinear (hole burning) laser spectroscopy.

The first order FID had been suggested[5] earlier, but escaped detection because of instrumental limitations. In fact, only the nonlinear FID has been observed in the past, either in the infrared[3] or visible[2] regions. Our discussion thus far implies that the homogeneous linewidth is much narrower than the inhomogeneous broadening. In the event that the homogeneous broadening exceeds the inhomogeneous width, the FID becomes first order again, but now the decay is exponential rather than Gaussian. This is just the domain encountered previously in nuclear magnetic resonance.[6] In the next section, we present a general density matrix solution of the Schrödinger wave equation for optical FID which reduces in the appropriate limit to the above cases.

II. THEORY

We derive a general expression for optical FID assuming the transition to be homogeneously and inhomogeneously broadened. It is assumed also that the sample is prepared continuously with a cw laser (Fig. 1) and that FID occurs when the laser frequency is switched suddenly by several homogeneous linewidths (Fig. 2).

A. Density Matrix in the Rotating Frame

Theoretically, the appearance or nonappearance of first order FID depends on how the optically induced dipole is averaged over the atomic velocity distribution. In earlier work[2,3] where the laser frequency or Stark switching is small compared to the Doppler broadening, the Gaussian Doppler lineshape is assumed constant over the principle region of integration and therefore can be factored outside the Doppler integral.

Foster, Stenholm, and Brewer[5] first predicted a rapid transient arising from the entire inhomogeneous line by retaining the Gaussian in the integral and evaluating the result approximately. Indeed, an exact analytical evaluation of their equation (A1) forms the theoretial basis of this article.

Consider a two level quantum system interacting with an optical field

$$E(t) = E_o \cos(\Omega t - kz)$$

through a dipole perturbation

$$H' = -\vec{\mu} \cdot \vec{E} ,$$

the total Hamiltonian being

$$H = H_o + H' .$$

We label the upper level 2 and the lower level 1. The density matrix equation

$$i\hbar\dot{\rho} = [H,\rho] + \text{relaxation terms}$$

then takes the explicit form[7]

$$\dot{\rho}_{12} = i\chi(\rho_{22}-\rho_{11})\cos(\Omega t-kz) - (i\omega_{12}+1/T_2)\rho_{12} \qquad (2.1)$$

$$\dot{\rho}_{22} = -i\chi(\rho_{21}-\rho_{12})\cos(\Omega t-kz) - (\rho_{22}-\rho_{22}^o)/T_1 \qquad (2.2)$$

$$\dot{\rho}_{11} = i\chi(\rho_{21}-\rho_{12})\cos(\Omega t-kz) - (\rho_{11}-\rho_{11}^o)/T_1 . \qquad (2.3)$$

Here, the Rabi frequency

$$\chi = \mu_{12} E_o/\hbar ,$$

the free molecule eigenenergies are

$$\langle 1|H_o|1\rangle \equiv \hbar\omega_1 ,$$
$$\langle 2|H_o|2\rangle \equiv \hbar\omega_2 ,$$
$$\omega_{21} \equiv \omega_2 - \omega_1 ,$$

and T_2 and T_1 are the phenomenological dipole and population decay times. The rapidly varying components are removed with the substitution

$$\tilde{\rho}_{12} = \rho_{12}\, e^{-i(\Omega t - kz)}$$

and by neglecting second harmonic terms. Therefore, the tilde denotes a reference frame rotating at the optical frequency Ω. Equations (2.1)-(2.3) become

$$\left(\frac{d}{dt} - i\Delta(v_z) + 1/T_2\right)\tilde{\rho}_{12} = \frac{i\chi\Delta\rho_{21}}{2} \qquad (2.4)$$

$$\Delta\dot{\rho}_{21} = -i\chi(\tilde{\rho}_{21} - \tilde{\rho}_{12}) - \frac{\Delta\rho_{21} - \Delta\rho_{21}^o}{T_1} \qquad (2.5)$$

where

$$\Delta(v_z) = -\Omega + \omega_{21} + kv_z ,$$

$$\Delta\rho_{21} = \rho_{22} - \rho_{11} .$$

For times $t<0$, these lead to the steady state preparative solution

$$\tilde{\rho}_{12}(v_z,0) = \frac{i\chi}{2} \cdot \Delta\rho_{21}^o \cdot \frac{i\Delta(v_z)+\gamma}{\Delta^2+\Gamma^2} \qquad (2.6)$$

where

$$\Gamma^2 \equiv \frac{1}{T_2^2} + \chi^2 \frac{T_1}{T_2} \quad \text{and} \quad \gamma \equiv \frac{1}{T_2} . \qquad (2.7)$$

At time t=0, the laser frequency is suddenly switched from Ω to Ω', and for t>0, the density matrix equations (still expressed in the frame rotating at Ω) are

$$\left(\frac{d}{dt} - i\Delta(v_z) + \frac{1}{T_2}\right)\tilde{\rho}_{12}(t) = \frac{i\chi}{2}\,\Delta\rho_{21}\, e^{i(\Omega'-\Omega)t} \tag{2.8}$$

and

$$\Delta\dot{\rho}_{21} = -i\chi\left[\tilde{\rho}_{21}\, e^{i(\Omega'-\Omega)t} - \tilde{\rho}_{12}\, e^{-i(\Omega'-\Omega)t}\right] - \frac{\Delta\rho_{21}-\Delta\rho^{o}_{21}}{T_1}\,. \tag{2.9}$$

In general, we must solve both equations simultaneously. However, this is unnecessary for FID as can be seen by formally integrating (2.8) so that

$$\tilde{\rho}_{12}(t) = \tilde{\rho}_{12}(0)\, e^{(i\Delta-1/T_2)t} + e^{(i\Delta-1/T_2)t}\int_0^t \frac{i\chi}{2}\,\Delta\rho_{21}\, e^{i(\Omega'-\Omega)t'}\, e^{(-i\Delta+1/T_2)t'}dt'\,. \tag{2.10}$$

The FID part of (2.10) is

$$\tilde{\rho}_{12}(t) = \tilde{\rho}_{12}(0)\, e^{(i\Delta-1/T_2)t}\,, \tag{2.11}$$

and the remaining term, which expresses the off-resonance driving effect, can be ignored. This result has an important physical meaning which is evident by considering $\rho_{12}(t)$ in the laboratory frame where

$$\rho_{12}(v_z,t) = \tilde{\rho}_{12}(v_z,t)\, e^{i(\Omega t-kz)} = \frac{i\chi}{2}\,\Delta\rho^{o}_{21}\cdot\frac{i\Delta(v_z)+\gamma}{\Delta^2(v_z)+\Gamma^2}\cdot e^{i(\omega_{21}+kv_z-1/T_2)t-ikz}\,. \tag{2.12}$$

Note that although each Doppler velocity group v_z was prepared at the same laser frequency Ω, during free induction decay each radiates at its own natural resonant frequency $\omega_{21}+kv_z$.

B. Doppler Velocity Average

A straightforward average over the Doppler velocity v_z substantiates this last point in a precise analytic way and makes evident the various effects of inhomogeneous broadening on FID. The exact Doppler-averaged solution allows us to extract various limiting cases, including a comparison with free induction decay in pulsed NMR.

Calculating the Doppler average $\langle\tilde{\rho}_{12}\rangle$ in the rotating frame Ω, we obtain

$$\langle\tilde{\rho}_{12}(t)\rangle = \frac{1}{u\sqrt{\pi}}\int_{-\infty}^{+\infty}\tilde{\rho}_{12}(v_z,t)e^{-v_z^2/u^2}dv_z$$

$$= \frac{i\chi\Delta\rho_{21}^{o}}{2\sqrt{\pi}u}\,e^{-t/T_2}\int_{-\infty}^{+\infty}\frac{i\Delta(v_z)+\gamma}{\Delta^2(v_z)+\Gamma^2}\,e^{+i\Delta(v_z)t}\,e^{-v_z^2/u^2}dv_z \qquad (2.13)$$

We change the variable of integration from v_z to $x\equiv\Delta(v_z)\equiv-\Omega+\omega_{21}-kv_z$ and define

$$\delta \equiv \omega_{21} - \Omega \ ,$$

$$\sigma \equiv ku \ .$$

Then, the integral in (2.13) becomes

$$I = \int_{-\infty}^{+\infty}\frac{ix+\gamma}{x^2+\Gamma^2}\,e^{+ixt}\,e^{-\left(\frac{x-\delta}{\sigma}\right)^2}dx \ . \qquad (2.14)$$

This integral, which is the complex conjugate of Eq. (A1) of Foster, Stenholm and Brewer,[5] is most easily evaluated by observing that it is in the form of a Fourier convolution integral[8]

$$\int_{-\infty}^{+\infty} f(x)g(\delta-x)dx = \int_{-\infty}^{+\infty} F(u)G(u)e^{-i\delta u}du$$

where

$$F(u) = \frac{1}{\sqrt{2\pi}} \int_{-\infty}^{+\infty} f(x)e^{iux}dx \ ,$$

and similarly for G(u). Now choose

$$g(\delta-x) = e^{-\left(\frac{\delta-x}{\sigma}\right)^2}$$

and

$$f(x) = \frac{ix+\gamma}{x^2+\Gamma^2} e^{ixt} \ .$$

Then, both Fourier transforms F(u) and G(u) are elementary,

$$G(u) = \frac{\sigma}{\sqrt{2}} e^{-u^2\sigma^2/4}$$

and

$$F(u) = \begin{cases} \sqrt{\frac{\pi}{2}}\left(\frac{\gamma}{\Gamma} - 1\right)e^{-\Gamma(t+u)}, & u>-t \\ \sqrt{\frac{\pi}{2}}\left(\frac{\gamma}{\Gamma} + 1\right)e^{\Gamma(t+u)}, & u<-t \ . \end{cases}$$

The integral (2.14) becomes

$$I = \frac{\sigma\sqrt{\pi}}{2}(\eta+1)\int_{-\infty}^{-t} e^{\Gamma(t+u)} \ e^{-u^2\sigma^2/4} \ e^{-i\delta u}du$$

$$+ \frac{\sigma\sqrt{\pi}}{2}(\eta-1)\int_{-t}^{+\infty} e^{-\Gamma(t+u)} \ e^{-u^2\sigma^2/4} \ e^{-i\delta u}du$$

here the saturation parameter is defined by $\eta \equiv \gamma/\Gamma$. Note that the integrands are at most quadratic functions of u in the exponent. By completing the square in the exponent, they may be expressed as error functions[9]

$$\operatorname{erfc}(z) = \frac{2}{\sqrt{\pi}} \int_z^\infty e^{-t^2} dt$$

of complex argument so that

$$I = \frac{\pi}{2}(\eta+1) e^{\left(\frac{\Gamma-i\delta}{\sigma}\right)^2} e^{\Gamma t} \operatorname{erfc}\left(\frac{\sigma t}{2} + \frac{\Gamma-i\delta}{\sigma}\right)$$

$$+ \frac{\pi}{2}(\eta-1) e^{\left(\frac{\Gamma+i\delta}{\sigma}\right)^2} e^{-\Gamma t} \operatorname{erfc}\left(-\frac{\sigma t}{2} + \frac{\Gamma+i\delta}{\sigma}\right) . \qquad (2.15)$$

This is the same result obtained by Liao, Bjorkholm and Gordon.[10] The physical implications of this solution, however, remain obscure because the erfc functions vary rapidly in magnitude and phase for typical values of the argument. Fortunately, it is always possible to express the erfc(z) function in terms of a simpler error function

$$W(z) = e^{-z^2} \operatorname{erfc}(-iz) .$$

This is a tabulated quantity which is slowly varying when the condition Imz>0 is satisfied and Rez<0 or Rez>0. When Imz>0, it has the asymptotic behavior[9]

$$W(z) \to \frac{i}{\sqrt{\pi} z} \quad (z \to \infty) ,$$

and limiting value

$$W(0) = 1 .$$

owever, when Imz<0, $W(z)$ is rapidly varying, but then it can be expressed onveniently in terms of the tabulated function $W(z)$ through the relation[9]

$$W(-z) = 2e^{-z^2} - W(z) \ . \tag{2.16}$$

n Eq. (2.15) the first erfc has the real part of its argument >0 for all ime. The second erfc, however, has the real part of its argument change rom a positive to a negative value at $t=2\Gamma/\sigma^2$. Thus there is a short ime and a long time form for this integral. For $t<2\Gamma/\sigma^2$,

$$I = \frac{\pi}{2} e^{-(\sigma t/2)^2} e^{i\delta t} \times \left\{(\eta+1)W\left[\frac{\delta}{\sigma} + i\left(\frac{\sigma t}{2} + \frac{\Gamma}{\sigma}\right)\right] + (\eta-1)W\left[-\frac{\delta}{\sigma} + i\left(-\frac{\sigma t}{2} + \frac{\Gamma}{\sigma}\right)\right]\right\} . \tag{2.17}$$

or $t>2\Gamma/\sigma^2$,

$$I = \pi(\eta-1)e^{-\left(\frac{i\Gamma-\delta}{\sigma}\right)^2} e^{-\Gamma t} + \frac{\pi}{2} e^{-(\sigma t/2)^2} e^{i\delta t}\left\{(\eta+1)W\left(\frac{i\sigma t}{2} + \frac{i\Gamma+\delta}{\sigma}\right) - (\eta-1)W\left(\frac{i\sigma t}{2} + \frac{-i\Gamma+\delta}{\sigma}\right)\right\} . \tag{2.18}$$

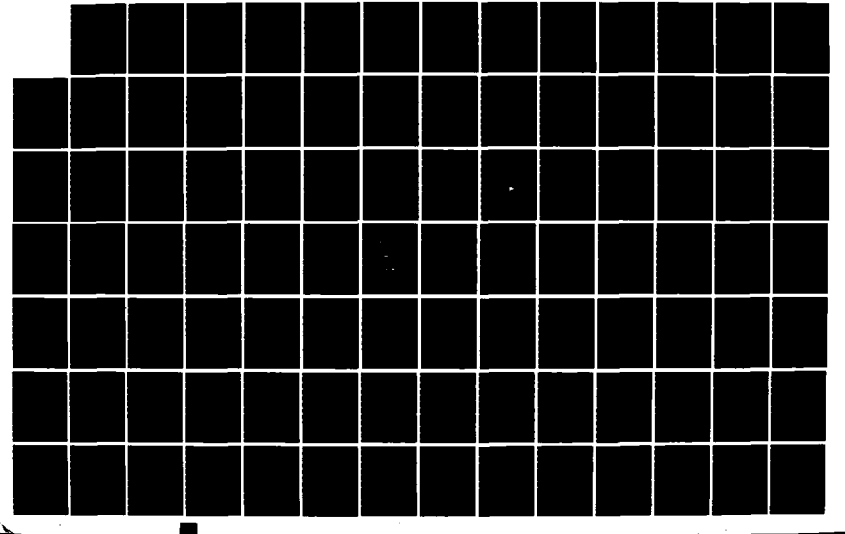
hus, we obtain

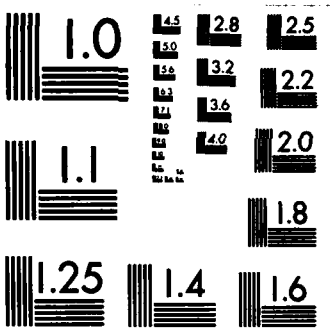
$$\langle\tilde{\rho}_{12}(t)\rangle = \frac{i\chi\Delta\rho^o_{21}}{2\sqrt{\pi}\sigma} e^{-t/T_2} \times \begin{cases} I = \text{Eq. (2.17)}, & t<2\Gamma/\sigma^2 \\ I = \text{Eq. (2.18)}, & t>2\Gamma/\sigma^2 \end{cases} . \tag{2.19}$$

s we shall see, the two temporal regions indicated by (2.17) and (2.18) orrespond physically to a short-time behavior where the first order FID ominates and a long-time behavior where the nonlinear FID prevails.

AD-A154 708 NONLINEAR SPECTROSCOPY(U) IBM RESEARCH LAB SAN JOSE CA 2/6
R G BREWER 20 MAR 85 N00014-78-C-0246

UNCLASSIFIED F/G 20/6 NL





MICROCOPY RESOLUTION TEST CHART
NATIONAL BUREAU OF STANDARDS-1963-A

C. Field Dependence

In the experimental configuration of Fig. 1, the total field striking the photodetector is

$$E_T(z,t) = E_{12}(z,t) + E(z,t) \ .$$

Here, the frequency switched laser field amplitude

$$E(z,t) = E_o \cos(\Omega' t - k'z)$$

is assumed constant. The FID field

$$E_{12}(z,t) = \tilde{E}_{12}\, e^{i(\Omega t - kz)} + c.c.$$

is generated by the induced polarization

$$p = N\mu_{12}\, e^{i(\Omega t - kz)} \langle\tilde{\rho}_{12}\rangle + c.c. \ ,$$

and in the thin sample approximation can be calculated from Maxwell's equation in the form

$$\frac{\partial \tilde{E}_{12}}{\partial z} = -2\pi i k N \mu_{12} \langle\tilde{\rho}_{12}\rangle$$

where N is the molecular number density. At the end of a sample of length L, the field intensity E_T^2 contains beat cross terms of the form

$$E_b^2 = \frac{E_o \tilde{E}_{12}}{2}\, e^{i(\Omega - \Omega')t} + c.c.$$

such that

$$\tilde{E}_{12} = -2\pi i k L N \mu_{12} \langle\tilde{\rho}_{12}\rangle \ ,$$

and $\langle\tilde{\rho}_{12}\rangle$ is given by (2.19). Collecting terms, we obtain

$$E_b^2 = Ke^{-t/T_2} e^{i(\Omega-\Omega')t} \times \begin{Bmatrix} I = \text{Eq. (2.17)}, & t<2\Gamma/\sigma^2 \\ I = \text{Eq. (2.18)}, & t>2\Gamma/\sigma^2 \end{Bmatrix} + \text{c.c.} \qquad (2.20)$$

where

$$K = \frac{\sqrt{\pi}}{2u} \hbar NL\chi^2 \Delta\rho_{21}^{o} \ .$$

D. Physical Interpretation

Since Eq. (2.19) was derived without approximations placed on t, χ, δ, Γ, σ and η, we may take various limits and compare to previous results. In particular, we hope to find which features of optical free induction decay appear when inhomogeneous broadening dominates the lineshape. In the other extreme, when homogeneous broadening dominates, we encounter the case which is prevalent in nuclear magnetic resonance.

(1) *Long time limit.* For decay times longer than the inverse Doppler width such that $\sigma t \gg 1$, we may use the asymptotic form of the error function[9]

$$W(z) = \frac{i}{\sqrt{\pi} z} + \ldots \quad (z \to \infty) \ ,$$

and Eq. (2.20) reduces to

$$E_b^2(t) = K\pi(\eta-1)e^{-(1/T_2+\Gamma)t} e^{i(\Omega-\Omega')t} e^{-\left(\frac{i\Gamma-\delta}{\sigma}\right)^2} + \text{c.c.}$$

where $\sigma t \gg 1 > 2\Gamma/\sigma$. The imaginary part of the term $e^{-\left(\frac{i\Gamma-\delta}{\sigma}\right)^2}$ introduces a small phase shift in E_b^2 for $\Gamma/\sigma \ll 1$ and therefore makes E_b^2 slightly dispersive. However, we neglect it here and obtain

$$E_b^2(t) = 2K\pi(\eta-1)e^{-(1/T_2+\Gamma)t} e^{-(\delta/\sigma)^2} \cos(\Omega-\Omega')t \ . \qquad (2.21)$$

This result is identical to an earlier approximate derivation[3,4] where the Gaussian was factored outside the Doppler integral. We shall refer to Eq. (2.21) as the *nonlinear FID* signal since $E_b^2 \propto \chi^4$ at low light intensities when $\chi^2 T_1 T_2 \ll 1$. As has already been verified by experiment,[2,3] the long time limit of FID displays the properties predicted by (2.21). First, the sample radiates at the initial laser frequency Ω and produces a heterodyne beat signal of frequency $\Omega-\Omega'$ which is absorptive, and second, it decays at the rate $1/T_2+\Gamma$ due to the preparative and post preparative stages.

(2) *Short time limit.* For short times, we retain the first two terms of the power series expansion[9]

$$W(z) = \sum_{n=0}^{\infty} \frac{(iz)^n}{\Gamma\left(\frac{n}{2}+1\right)}$$

$$= 1 + \frac{2iz}{\sqrt{\pi}} + \ldots , \quad |z|<1 .$$

In addition to the condition

$$|z| = \left| i\left(\frac{\Gamma}{\sigma} \pm \frac{\sigma t}{2}\right) \pm \frac{\delta}{\sigma} \right| < 1 , \tag{2.22}$$

we require that

$$t \ll 2\Gamma/\sigma^2 ,$$

thereby allowing the $\sigma t/2$ term to be dropped in (2.22). With these conditions, Eq. (2.20) reduces to

$$E_b^2 = 2\pi K e^{-t/T_2} e^{-(\sigma t/2)^2}$$

$$\times \left\{ \gamma\left(\frac{1}{\Gamma} - \frac{2}{\sqrt{\pi}\sigma}\right) \cos(\omega_{21}-\Omega')t \right.$$

$$\left. - \frac{2}{\sqrt{\pi}} \frac{(\omega_{21}-\Omega)}{\sigma} \sin(\omega_{21}-\Omega')t \right\} . \qquad (2.23)$$

We refer to (2.23) as the *first order FID* since $E_b^2 \propto \chi^2$. Furthermore, the decay is now Gaussian, $e^{-(\sigma t/2)^2}$, where the characteristic dephasing time

$$T_2^* \equiv 2/\sigma .$$

This signal contains both an absorptive and dispersive part which depends on the initial laser frequency through the factor $(\omega_{21}-\Omega)/\sigma$. From (2.23), it is evident that the atomic sample radiates at the Doppler peak ω_{21}, independent of the initial laser frequency Ω, and produces a heterodyne beat of frequency $\omega_{21}-\Omega'$. We conclude, therefore, that in first order FID the various velocity packets destructively interfere, except at Doppler line center. By contrast, the nonlinear FID radiates at the initial laser frequency and therefore possesses memory of its preparation. These two forms of FID are the transient analogs of steady-state linear and nonlinear laser spectroscopy of an inhomogeneously broadened transition.

(3) *Limit of no inhomogeneous broadening*. In the limit $\sigma \to 0$, the Doppler integral (2.13) for $\langle\tilde{\rho}_{12}(t)\rangle$ must reduce to a form identical to $\tilde{\rho}_{12}(v_z=0,t)$, thus checking our calculation. As $\sigma \to 0$, $2\Gamma/\sigma^2 \to \infty$ so the short time form of the integral must be used. The argument of the $W(z)$ function approaches $z = \frac{\pm\delta+i\Gamma}{\sigma}$ and its modulus approaches ∞ as $\sigma \to 0$, so we may again use the asymptotic form

$$W(z) = \frac{i}{\sqrt{\pi}z} + \ldots, \quad |z| \to \infty, \quad \mathrm{Im}z > 0 .$$

In this limit,

$$E_b^2 = \frac{2K\sigma\sqrt{\pi}}{\Gamma^2+\delta^2} e^{-t/T_2} \left(\gamma \cos(\omega_{21}-\Omega')t - \delta \sin(\omega_{21}-\Omega')t\right) \qquad (2.24)$$

where $\delta=\omega_{21}-\Omega$ and $K\sigma = \frac{\sqrt{\pi}}{2} k\hbar NL\chi^2\Delta\rho_{21}^o$.

As expected, Eq. (2.24) can be derived directly from (2.12) without Doppler averaging when $v_z=0$. The radiation now occurs at the atomic transition frequency ω_{21} regardless of the laser excitation frequency Ω, with an identical amplitude, frequency and relaxation dependence to that of $\tilde{\rho}_{12}(v_z=0,t)$. The FID again exhibits a linear intensity dependence. Equation (2.24) also agrees with the well-known FID theory of nuclear magnetic resonance.[6]

III. EXPERIMENTAL TECHNIQUE

A. Traveling Wave Modulator

To study subnanosecond coherent transients by laser frequency switching, new techniques are required. At such speeds, it is no longer advantageous to place the electro-optic modulator inside the laser cavity as in the past,[2] since the transient dies away before the laser beam completes one round trip through the optical cavity. On the other hand, when the modulator is external to the laser cavity, the modulator design can be varied easily while still retaining the advantages of undiminished laser intensity and stability. A novel traveling wave electro-optic modulator is described here which permits such measurements.

Two requirements must be satisfied in laser frequency switching to insure the generation of intense coherent transient signals. First, the laser frequency switch must exceed the homogeneous linewidth $1/(\pi T_2)$, and second, the switching time should be less than the dephasing time T_2. Therefore, measurements on a subnanosecond time scale imply a shift of several gigahertz with a ~100 picosecond rise time. A schematic diagram of our apparatus[1] is shown in Fig. 1. It consists of a stable cw dye laser, a traveling wave electro-optic modulator, the sample, a fast photodiode detector, and a sampling oscilloscope. The frequency shifted laser beam produces in the sample coherent transients which are detected in the forward direction in real time. All emission signals, such as the FID or the photon echo, appear as heterodyne beat signals, as discussed previously.[3,7]

The traveling wave electro-optic modulator was invented initially by Kaminow[11] in 1961. We have used it in a new configuration. Compared to intracavity frequency switching,[2] the rise times and frequency shifts are at least one order of magnitude more favorable. The principle of operation of our configuration is the following. An electro-optic crystal, which constitutes an integral part of a microwave transmission line, allows a cw laser beam and a direct current voltage pulse to simultaneously propagate longitudinally along one crystal axis as shown in Fig. 1. As the dc field advances down the crystal, it produces a zone of increasing refractive index, $n_0 \rightarrow n_1$, which shifts the phase φ of the light wave uniformly in time and hence its angular frequency Ω where

$$\Omega - \Omega' = \frac{d\varphi}{dt} . \tag{3.1}$$

This behavior is easily derived by noting that the phase of the light wave emerging from a crystal of length ℓ at time t is

$$\varphi(\ell,t) = \int_0^{\ell} kn(z)dz$$

$$= \int_0^{vt'} kn_1 dz + \int_{vt'}^{\ell} kn_o dz \qquad (3.2)$$

where $\vec{k}$ is the optical propagation vector and v and c are the velocities of the dc field and light wave in the crystal medium. Consider first the case of copropagating fields. If a step function dc field pulse enters the crystal at z=0 at time t=0, then at the intermediate time t' when the light wave is just at the boundary of n_o and n_1, the obvious relation

$$vt' + c(t-t') = \ell \qquad (3.3)$$

holds. Inserting $t'=(\ell-ct)/(v-c)$ into (3.2), the frequency shift according to (3.1) is

$$\Omega - \Omega' = \Omega \frac{n_1-n_o}{n_o} \frac{v}{c\mp v} \qquad (3.4)$$

where the minus sign corresponds to copropagating fields. By a similar argument, for counter propagating fields the plus sign follows. The singularity in (3.4) for v=c is artificial and results from our neglecting the pulse rise time, which for the above step function is zero. For typical values of these parameters, to be discussed, gigahertz shifts are easily accomplished, particularly in the visible or ultraviolet region due to the large factor $\Omega \sim 10^{15}$ Hertz. Of course, once the dc pulse reaches the end of the crystal $d\varphi/dt=0$ and the frequency shift is zero.

This technique possesses several advantages over more conventional traveling wave modulators.[12] First, conventional devices do not employ dc square wave pulses but require additional microwave techniques to phase match the microwave wave velocity to the light wave velocity. This matching is never perfect and degrades the rise time of the crystal. In our design the rise time is determined primarily by the crystal connections which we believe can approach 20 picoseconds. Second, frequency shifting could also be accomplished by a conventional traveling wave modulator using a dc ramp voltage where $V(t) \propto t$ but such a device is impractical. Producing a ramp with constant slope, a sharp corner at t=0, and no ringing appears to be a formidable task in the 100 picosecond region. Also, in our design once the modulating wave is launched into the crystal, it will attenuate slowly, and the frequency shift will be highly uniform.

Third, many devices[12] require microwave sources which generate a distribution of optical sidebands corresponding to the various microwave harmonics. Therefore, the modulation efficiency is often low. In our arrangement with dc voltage pulses, all of the light is shifted uniformly.

Fourth, as already stated, intracavity laser frequency switching,[2] which requires application of a transverse field, will not satisfy our requirements either. For example, electro-optic AD*P crystals cannot be frequency switched fast enough or far enough. The electro-optic coefficient is too low for gigahertz frequency shifts with available voltages. Furthermore, these crystals are not easily matched to a 50 ohm driver impedance since their characteristic capacitance of ~40 picofarads

implies an RC rise time of 2 nsec. More importantly, the modulating voltage takes at least 500 psec to travel across the crystal. *However, in our traveling wave modulator, rather than try to overcome the transit time problem, we have used it as the operating principle of our device.*

The unique features of this traveling wave modulator therefore facilitates rapid FID measurements and also other coherent transient effects by a variation of the pulse sequence.

B. Apparatus

Modulator Design: The optical phase modulator consists of two lithium tantalate crystals 0.5mm×0.65mm×25mm as in Fig. 3. The end faces are polished and anti-reflection coated, and gold electrodes are deposited on opposite faces to form a parallel plate transmission line. A voltage between the electrodes produces an electric field parallel to the c-axis. For a given applied voltage, the electric field and hence the frequency shift are inversely proportional to the electrode spacing. The crystal therefore is chosen to be as narrow as possible up to the optical diffraction limit. Kogelnik and Li[13] have calculated the optimum focusing arrangement for such a case. We used a 10 cm lens which produces a 1/e field spot diameter of 150 microns at the crystal apertures. The crystal must consequently be aligned to an angle of ~1 mrad and to 50μ in position to avoid beam distortion.

The ratio of height to width of the crystal (0.65mm to 0.50mm) was chosen so that, given the microwave dielectric constant of lithium

tantalate (ε=43), the crystal appears to be a 50Ω transmission line.[14] The electrical rise time of the crystal and the quality of the impedance match to an external 50Ω line were tested with a time domain reflectometer which revealed 100 psec rise times. Using the known electro-optic coefficient[15] of lithium tantalate $r_{33}=3.04\times10^{-9}$ cm/volt, we calculate $\Delta n/\text{volt}=-2.43\times10^{-7}$/volt using standard techniques.[16] Inserting this into Eq. (3.4), we obtain $\Omega-\Omega'/2\pi=13.9$ MHz/volt which agrees with our experimental value of 15.0 MHz/volt.

Modulator Construction: Two different mechanical designs were successfully employed. In one, a Lasermetrics Model 2033 phase matched traveling wave modulator was used with the phase matching elements removed. The electrical rise time of the modulator was measured with a 40 psec time domain reflectometer (Tektronix 7S12), and found to be about 150 psec. The optical rise time should be about half this value since it is limited by the inductance of the input connection alone. A second modulator was constructed from crystals supplied by Crystal Technology. The mechanical layout was such that the crystal connections were reduced to several millimeters in length resulting in an electrical rise time of 100 psec.

Beam Configuration: The beam from a single mode cw dye laser (Coherent 599) passes through a 10 cm focusing lens, the $LiTaO_3$ modulator, a 10 cm collimating lens, and sample cell containing sodium vapor. The sample cell was differentially heated so as to make the cell windows (of aluminosilicate glass) its hottest part.

Detection: The emerging laser beam together with the forward FID emission are focused to a 40 micron diameter spot on a fast GaAs-GaAlAs photodiode (Rockwell International Corp).[17] The photodetector of 50 micron

diameter is mounted directly on an S-4 sampling head (25 psec response) of a Tektronix 7904 oscilloscope with a 7S11 sampling unit. The photodiode's response time of less than 30 psec was too fast to deconvolve it from the response of the sampling unit. It is known, however, that the S-4 photodiode combination recorded FID signals at 11 GHz, compared to the nominal 3 db point of 14 GHz for the sampler alone. We have estimated that the modulator produced FID signals with a 40 GHz beat but we are unable to detect them. Because the photodiode can be destroyed by several milliwatts of cw power, a Pockel's cell optical shutter blocks the laser light except for a 2 μsec interval immediately before and after the frequency switch so that the FID signal can be seen.

Pulser: The step function dc modulating voltage is generated at a 700 Hz repetition rate by a Tektronix type 109 reed relay pulser. Despite much lower ratings, this unit could produce pulses of up to 1000 volts into 50Ω for short periods of time, which would yield 15 GHz shifts. The pulser's output is delayed by 75 nsec before reaching the modulator to permit triggering the Pockel's cell and a 7T11 sampling time base. A low loss microwave cable was required to preserve the rise time of the pulser (Andrews LDF-50).

IV. MEASUREMENTS

We have detected FID on a 100 psec time scale for both I_2 vapor and atomic sodium. Since the hyperfine splittings in I_2 give rise to a large number of closely spaced lines within one Doppler width, the FID signals are strongly modulated and at present are difficult to interpret. To

avoid unnecessary complications in these initial studies, experiments are restricted to Na which permits a quantitative test of the above FID theory.

The transition monitored is the sodium D_1 line $^2P_{1/2} \leftrightarrow ^2S_{1/2}$ at 16,956.18 cm^{-1}. As is well known, its hyperfine splitting, 192 MHz ($^2P_{1/2}$) and 1.772 GHz ($^2S_{1/2}$), produces two pairs of lines. The initial laser frequency Ω is tuned to the center of the low frequency pair, and the traveling wave modulator voltage is adjusted to shift the laser frequency downward by ~5 GHz. This procedure avoids sweeping the laser frequency through the remaining two lines at higher frequency.

Figure 4 shows the observed FID heterodyne beat signals for different values of the initial laser frequency Ω or $\delta \equiv \omega_{21} - \Omega$ where ω_{21} is the frequency of one of the transitions of the lower pair of lines. Here the laser power density is $3 W/cm^2$ (η=0.055) and 5% of the beam is absorbed in a 10 cm path of Na vapor at a pressure of 2×10^{-6} Torr. Note that the large frequency shift of ≥5 GHz makes it possible for the first time to switch completely outside the Doppler linewidth, which is 0.77 GHz for Na.

Correspo[illegible] computer solutions of Eq. (2.20) are shown in Fig. 5 for the Na D_1 line as [illegible] function of δ where $(\Omega - \Omega')/2\pi$=5 GHz, σ=5.8 GHz, Γ=1.6 GHz, χ=2.3 GHz, T_2=32 nsec and η=0.019. The saturation parameter is chosen smaller than in Fig. 4 (0.019 versus 0.055) to emphasize the interference of linear and nonlinear FID, an effect which becomes more conspicuous at elevated optical fields.

MAGIC ANGLE LINE NARROWING IN OPTICAL SPECTROSCOPY*

S. C. Rand
A. Wokaun
R. G. DeVoe
R. G. Brewer

IBM Research Laboratory
San Jose, California 95193

ABSTRACT: Spin decoupling and line narrowing are observed for the first time in an optical transition, $^3H_4 \leftrightarrow {}^1D_2$ of Pr^{3+} in LaF_3 at 2°K, using optical FID. The ^{19}F nuclei, when irradiated by an appropriate rf field, undergo forced precession about an effective field at the magic angle in the rotating frame. The fluctuating ^{19}F-^{19}F dipolar interaction is thereby quenched and the optical linewidth drops from ~10 to ~2 kHz, as predicted in a theory of spin diffusion.

*Work supported in part by the U.S. Office of Naval Research

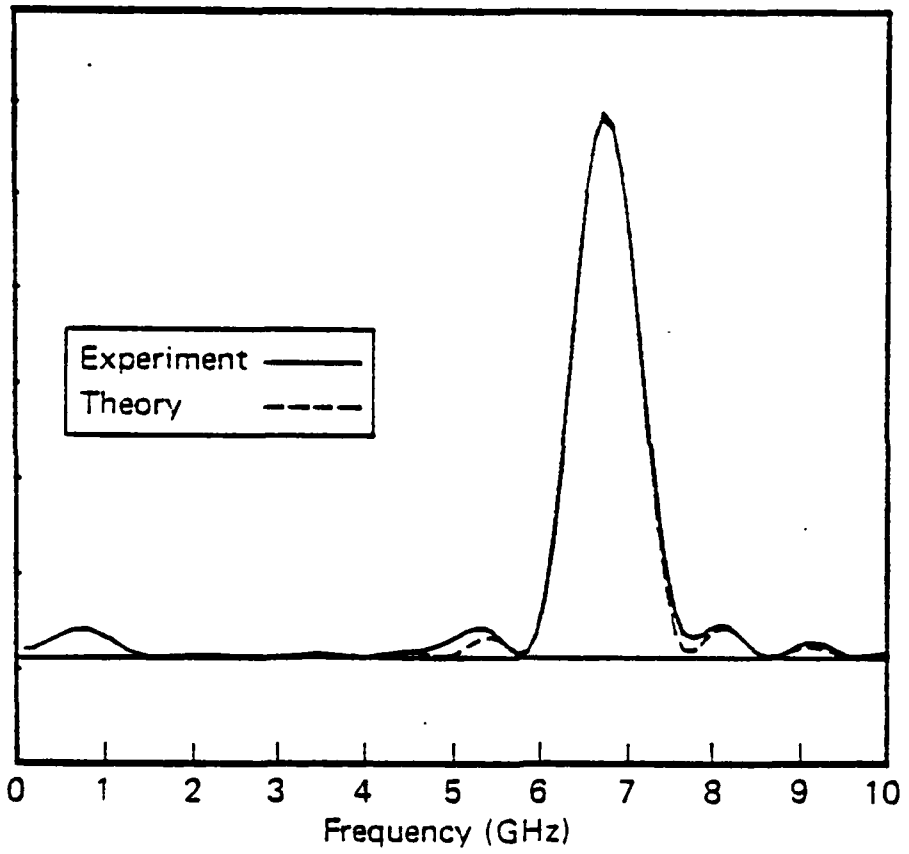


Figure 7. Power spectrum obtained by a digital Fourier transform of the experimental and theoretical data of Fig. 6.

Figure 6. Overlay of the experimental FID of the Na D_1 line with a computer fit where $(\Omega-\Omega')/2\pi=6.7$ GHz, $\delta=0$, and $\eta=0.055$. The switching pulse has an amplitude of 439 volts.

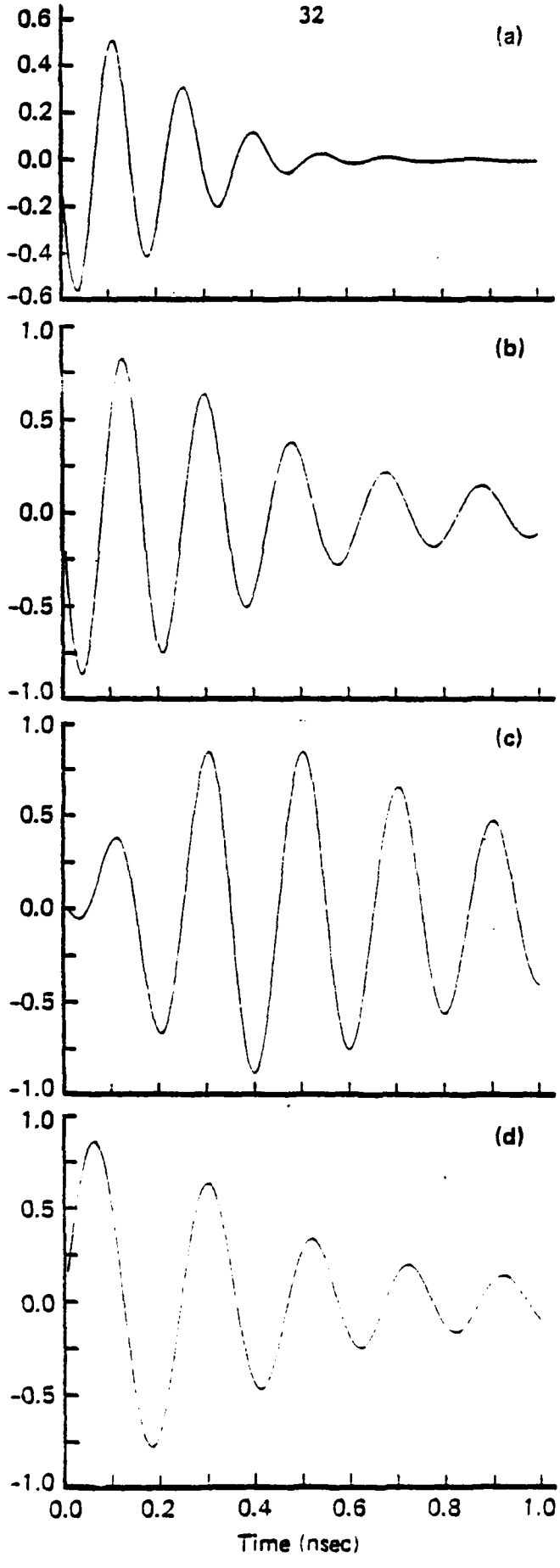


Figure 3. Computer plot of numerical solution of the FID heterodyne beat signal $E_5^2(L,t)$ of Eq. (2.20) where χ=2.3 GHz, η=0.019, σ=5.8 GHz, T_2=32 nsec, $(\Omega-\Omega')/2\pi$=5 GHz, and $\delta\equiv(\omega_{21}-\Omega)/2\pi$ in GHz equals (a) 1.5, (b) 1.0, (c) 0.0, and (d) -1.0

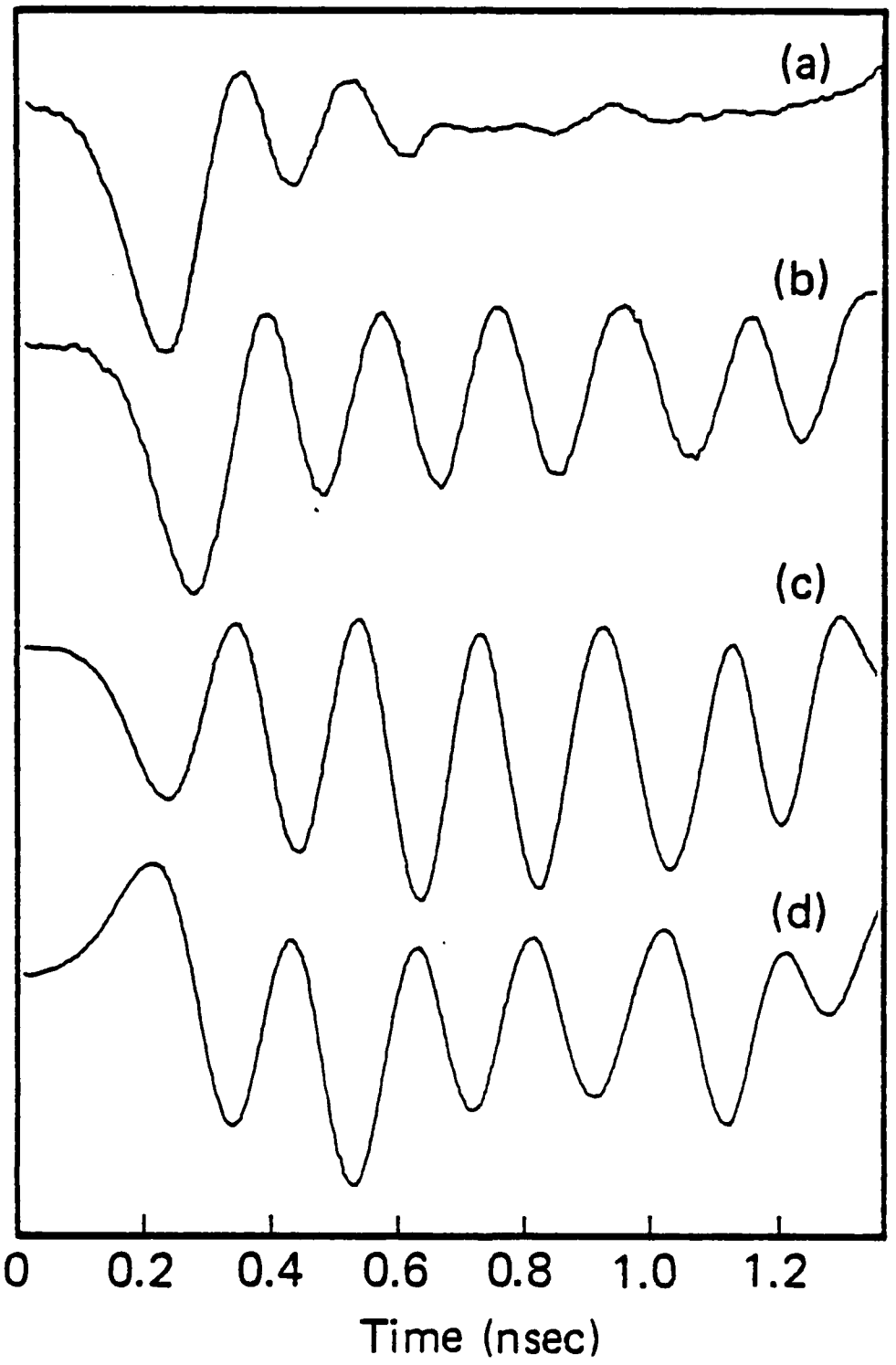


Figure 4. Experimental FID heterodyne beat signals of the Na D_1 line where χ=0.8 GHz and $\delta \equiv (\omega_{21}-\Omega)/2\pi$ in GHz equals (a) 1.5, (b) 0.7, (c) 0.0, and (d) -1.0. The laser frequency shift is $(\Omega-\Omega')/2\pi$=5 GHz corresponding to a 335 V dc square wave pulse. The gain in (a) is 2×.

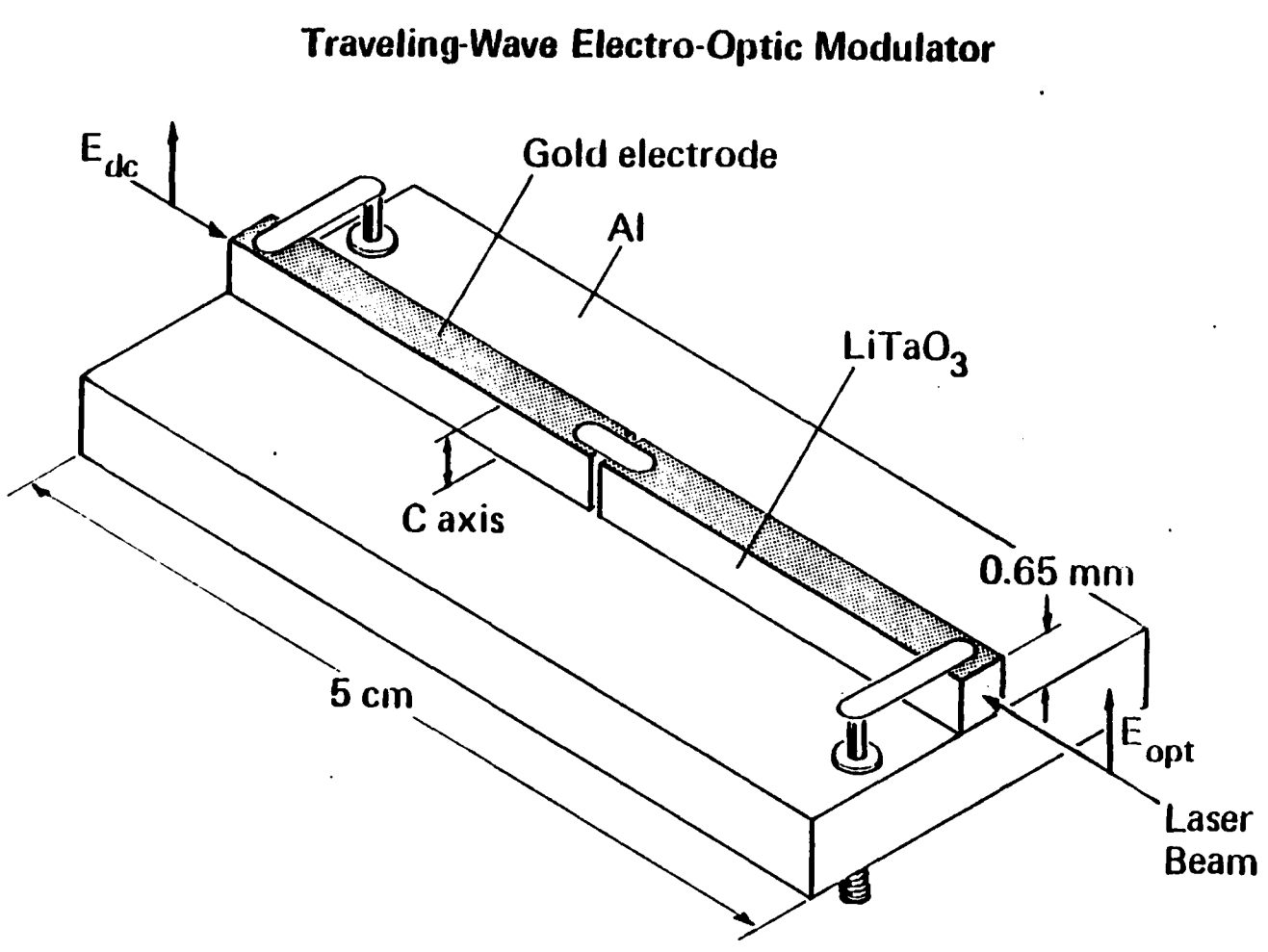


Figure 3. Detailed drawing of the $LiTaO_3$ modulator crystal elements mounted on an aluminum substrate of the microwave guide.

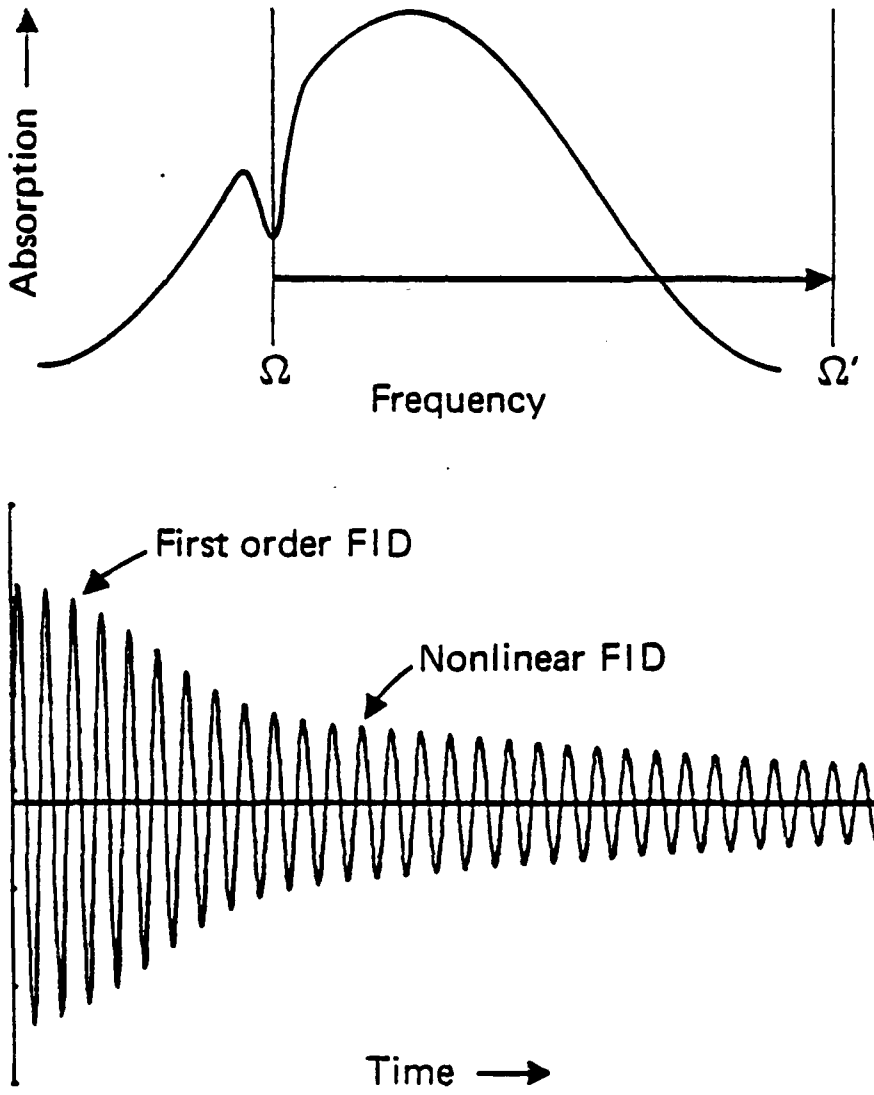


Figure 2. The upper curve shows a hole burnt into an inhomogeneously broadened lineshape due to the steady-state preparation by a laser with initial frequency Ω. The lower curve is a computer plot of Eq. (2.20) giving the transient response of the entire lineshape when the laser frequency is suddenly switched from Ω to Ω'.

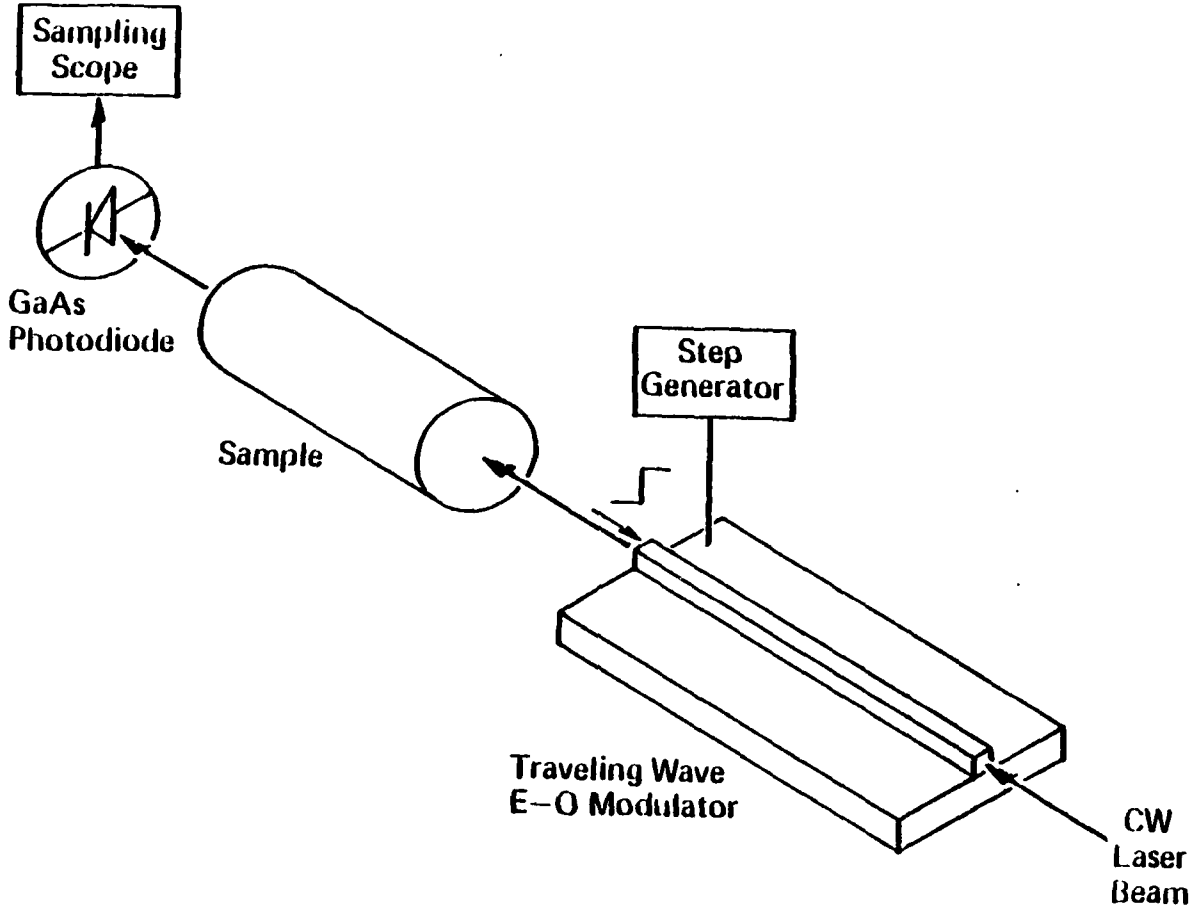


Figure 1. Schematic of the optical layout for detecting subnanosecond coherent optical transients with a traveling wave electro-optic phase modulator. The microwave guide is greatly simplified to show the crystal element and the focusing and collimating lens to either side of it are not shown.

17. See for example K. C. Eden, Proc. IEEE 63, 32 (1975).

18. R. L. Shoemaker and R. G. Brewer, Phys. Rev. Lett. 28, 1430 (1972); R. G. Brewer and E. L. Hahn, Phys. Rev. A8, 464 (1973); ibid., A11, 1641 (1975).

19. S. Haroche in High Resolution Laser Spectroscopy (Springer, Berlin, 1977), edited by K. Shimoda, p. 253.

REFERENCES

1. R. G. DeVoe and R. G. Brewer, Phys. Rev. Lett. 40, 862 (1978).
2. R. G. Brewer and A. Z. Genack, Phys. Rev. Lett. 36, 959 (1976); A. Z. Genack and R. G. Brewer, Phys. Rev. A17, 1463 (1978).
3. R. G. Brewer and R. L. Shoemaker, Phys. Rev. A6, 2001 (1972).
4. F. A. Hopf, R. F. Shea, and M. O. Scully, Phys. Rev. A7, 2105 (1973).
5. K. L. Foster, S. Stenholm, and R. G. Brewer, Phys. Rev. A10, 2318 (1974).
6. E. L. Hahn, Phys. Rev. 77, 297 (1950).
7. R. G. Brewer in Frontiers in Laser Spectroscopy (North-Holland, 1977), edited by R. Balian, S. Haroche, and S. Liberman, p. 341.
8. I. N. Sneddon, Fourier Transforms (McGraw-Hill, 1951), p. 24.
9. Handbook of Mathematical Functions, National Bureau of Standards Applied Mathematics Series. 55 (U.S. Government Printing Office, 1964), edited by M. Abramowitz and I. A. Stegun, p. 297.
10. P. F. Liao, J. E. Bjorkholm, and J. P. Gordon, Phys. Rev. Lett. 39, 15 (1977).
11. W. W. Rigrod and I. P. Kaminow, Proc. IEEE 51, 137 (1963); I. P. Kaminow, Phys. Rev. Lett. 6, 528 (1961).
12. An Introduction to Electrooptic Devices (Academic, N.Y., 1974), edited by I. P. Kaminow, p. 213-237.
13. H. Kogelnik and T. Li, Proc. IEEE, 1312 (1966).
14. G. White and G. M. Chin, Opt. Commun. 5, 374 (1972).
15. See reference 12, p. 182.
16. See reference 12, p. 92, Eq. (10).

coherence effects are faithfully observed. It is evident that other coherent transients can be observed in this way where the time scale may be reduced even further.

ACKNOWLEDGMENT

The technical assistance of D. E. Horne and K. L. Foster proved most valuable and is acknowledged with pleasure. The cooperation of D. Anafi of Lasermetrics in modifying their traveling wave modulator is appreciated. One of us (R.G.D.) acknowledges discussions with Axel Schenzle on Fourier transform theory. This work was supported in part by the U.S. Office of Naval Research.

order term manifests itself as a Gaussian build-up of the nonlinear FID. The corresponding theoretical result in Fig. 5c where $\delta=0$ and $\chi=2.3$ GHz shows this interference effect again but in a more dramatic way.

In Fig. 4d, $\delta/2\pi=-1$ GHz and we see that tuning the laser from the low to the high frequency side of the transition reverses the phase of the first order FID. Compare the theoretical curves Figs. 5b and 5d where $\delta/2\pi=1$ and -1 GHz, respectively, which shows the same phase reversal.

Figure 4d also gives evidence of a hyperfine interference beat because the laser is now tuned midway between the two pairs of lines so that all four transitions are prepared. The FID is now modulated at ~1.8 GHz, which is the ground state hyperfine splitting of Na. The mechanism for this process is very likely a coherent Raman beat[18] effect, but further studies are needed in testing this idea. In any event, it now becomes possible to detect microwave splittings by a transient method where the beat frequency exceeds quantum beat[19] measurements by at least one order of magnitude.

V. SUMMARY

We have described a laser frequency switching technique which permits coherent optical transient investigations on a subnanosecond time scale. A key feature of these measurements is that they are highly reproducible and lend themselves to quantitative analysis. This point is illustrated by optical FID which shows new characteristics when the temporal resolution is ~100 picoseconds. Detailed theoretical predictions of these new

A more physical explanation of the frequency dependence of first order FID is that it behaves like the dispersive part of a Lorentzian lineshape in which Doppler broadening has been ignored. For example, at large detuning a Lorentzian $(\gamma+ix)/(\Gamma^2+x^2)$ approaches i/x and yields the slow tuning behavior described above. For small detuning, we also expect the first order FID signal to change sign as we pass through the Doppler peak, and furthermore to equal zero exactly at resonance. These characteristics are evident in Figs. 4 and 5.

Figure 4a shows the observed FID signal for the laser tuned $\delta/2\pi$=1.5 GHz below the transition frequency. The nonlinear FID is reduced by a factor of e^2 and does not appear. The observed signal is the linear FID and obviously is nonexponential; it is complete in 500 psec, as expected since T_2^*=340 psec. A careful analysis shows that the beat frequency is ~6.5 GHz, which is equal to $(\omega_{21}-\Omega')/2\pi$ rather than $(\Omega-\Omega')/2\pi$=5 GHz.

Figure 4b shows the FID for $\delta/2\pi$=0.7 GHz. Here there is a large amplitude preparation due to the saturation of a resonant velocity group. The decay, which persists beyond the first order FID, is exponential in agreement with Eq. (2.21), being given by $e^{-\chi t}$ in this power broadened regime with χ=0.8 GHz. The observed beat frequency is equal to the laser frequency switch of 5 GHz. These signals are also absorptive since we find that their phase is invariant to laser tuning.

Figure 4c shows the FID for $\omega_{21}-\Omega$=0. Note that here the first order and nonlinear FID cancel at the time origin, and the decay of the first

In Fig. 6, the experimental FID signal for the sodium D_1 line is compared to a theoretical computer fit in time where now the parameters $(\Omega-\Omega')/2\pi=6.7$ GHz, $\delta=0$, and $\eta=0.055$. Considering the fast time scale, the fit is quite good. The slight deviation in amplitude and frequency at 0.6 nsec results from a minor impedance mismatch caused by an air gap separating the two $LiTaO_3$ crystals (Fig. 3). The power spectrum of Fig. 7 is the digital Fourier transform of Fig. 6 and indicates an even closer fit because low frequency components are displaced from the central line at 6.7 GHz, which obviously is the nonlinear FID. The quantities $T_2=32$ nsec and $\eta=0.055$ imply a power-broadened homogeneous linewidth of 0.19 GHz FWHM (see Eq. (2.21)) whereas the broader 0.87 GHz linewidth of Fig. 7 reflects the ~1 nsec duration of the FID signal.

Now consider Fig. 4 where first order and nonlinear FID can be distinguished by varying the preparative laser frequency Ω. This can be seen by first noticing that the nonlinear component is associated with the resonant excitation of a single velocity group. Since the density of the velocity distribution is a Gaussian $e^{-(\delta/\sigma)^2}$, the nonlinear FID decreases rapidly with laser detuning as in Eq. (2.21). The first order component, however, is primarily a nonresonant phenomenon where all velocity groups participate weakly. This can be seen in Eq. (2.23) where the first order FID varies slowly with laser tuning δ. By tuning off the Doppler peak, therefore, one should see a slow reduction in first order FID, and a rapid disappearance of nonlinear FID.

In the field of nuclear magnetic resonance (NMR), there exist several ways of reducing the time-dependent magnetic dipolar interaction between spins. Examples are motional narrowing,[1,2] macroscopic sample rotation,[3] spontaneous spin flip-flop processes,[4] and forced spin precession.[5-10] In this article, we report the first observation of this kind in an optical transition of a low temperature solid, $LaF_3:Pr^{3+}$, where the dilute nuclear spin (I) is praseodymium and the abundant spin (S) is fluorine. The Pr^{3+} ions are coherently prepared by a laser field and thereafter exhibit nonlinear optical free induction decay (FID). The Pr^{3+} dephasing time, as suggested in earlier work,[11] is limited by spin diffusion among the ^{19}F nuclei which undergo resonant flip-flops and impress weak fluctuating fields on the ^{141}Pr nuclei. This action adiabatically modulates the Pr^{3+} optical transition frequency through the dipolar I-S interaction and broadens the line. We now show that the half-width half-maximum (HWHM) optical linewidth is reduced from ~10 to ~2 kHz when the fluorine spin diffusion process is quenched by application of suitable magnetic static and rf fields, causing the ^{19}F nuclei to precess about an effective magnetic field at the *magic angle* in the rotating frame. This observation enables us to identify in an unambiguous way that the ^{19}F-^{19}F dipolar interaction is the dominant optical line broadening mechanism and provides the first test of spin diffusion theory in an optical transition. As we shall see, the behavior at optical and rf frequencies is different.

Imagine that the Pr^{3+} ions are coherently prepared by a laser field in the optical transition $1 \leftrightarrow 2$ and then experience nonlinear FID when the laser frequency is switched outside the Pr^{3+} homogeneous linewidth. The

novelty of this technique[11] is that a single homogeneous packet ($\lesssim$10 kHz width) can be selected from the much broader inhomogeneous lineshape (5 GHz width). The FID signal, expressed in terms of the induced polarization, is of the form

$$\langle p(t)\rangle = \left\langle p(0)e^{i(\omega_{12}t+\int_0^t \delta\omega_{12}(t')dt')}\right\rangle \qquad (1)$$

where $\delta\omega_{12}(t')$ represents the fluctuation in the optical transition frequency ω_{12} due to the nuclear dipolar S-S and I-S interactions. The bracket denotes an average over the optical inhomogeneous lineshape, the geometric variables of the I-S interaction, and the S-S spin fluctuations. With the assumption of Markoffian spin statistics, we apply the spin diffusion theory of Klauder and Anderson[12] and find that (1) predicts a Lorentzian homogeneous lineshape having a HWHM linewidth

$$\Delta\nu = \frac{4\pi\hbar}{9\sqrt{3}} \left|\left(\gamma_I''I_z''-\gamma_I'I_z'\right)\gamma_S S_z\right| n_S \frac{r}{R} . \qquad (2)$$

Here, γ_I (~23 kHz/G) denotes the enhanced gyromagnetic ratio of $^{141}Pr^{3+}$ for the lower (double prime) or upper (single prime) electronic state. The fluorine spin S has a gyromagnetic ratio γ_S (4 kHz/G), number density n_S, flips at the intrinsic rate r and has a macroscopic rate parameter R, introduced by Klauder and Anderson[12] to assure stationarity.

Now consider the application of a static magnetic field B_o and a radio frequency field $B(t)=2B_x\cos\omega t$ which is detuned from the fluorine Larmor frequency $\gamma_S B_o$ by $\Delta_S=\gamma_S B_o-\omega$. In a frame rotating at the frequency ω, the effective field $B_e=\sqrt{B_x^2+(\Delta_S/\gamma_S)^2}$ is stationary and makes an angle $\beta=\tan^{-1}(\gamma_S B_x/\Delta_S)$ with the static field B_o. When the ^{19}F precession

frequency $\gamma_S B_e$ exceeds the square root of the S-S second moment, the ^{19}F precessional motion at the angle β will tend to be uninterrupted, and it is then advantageous to perform a transformation to a second rotating frame where the axis of quantization is parallel to $\vec{B}_e$.[8-10] In this tilted rotating frame, the secular part of the dipolar Hamiltonian $\mathcal{H}=\mathcal{H}_{SS}+\mathcal{H}_{IS}$ contains the time-independent terms

$$\mathcal{H}_{IS}(\beta) = \cos\beta\mathcal{H}_{IS}^{(0)} \tag{3a}$$

$$\mathcal{H}_{SS}(\beta) = \frac{1}{2}(3\cos^2\beta-1)\mathcal{H}_{SS}^{(0)} \tag{3b}$$

where $\mathcal{H}_{IS}^{(0)} = \sum_j 2(b_j''-b_j')S_{jz}I_z$ and $\mathcal{H}_{SS}^{(0)} = \sum_{k<j} a_{kj}(3S_{kz}S_{jz}-\vec{S}_k\cdot\vec{S}_j)$ are the corresponding dipolar terms in the absence of an rf field, a_{kj} and b_j being the usual geometric factors.[8-10] We are now able to modify Eq. (2) by including the effect of an rf field on the Pr^{3+} optical linewidth. First, (3a) implies that $S_z(\beta)=\cos\beta S_z(0)$,[5] which replaces the heteronuclear term S_z in (2). Second, we associate the S spin flipping rate r in (2) with an inverse correlation time, $r(\beta)\equiv 1/\tau_c(\beta)=|\frac{1}{2}(3\cos^2\beta-1)|/\tau_c(0)$, derived previously by Mehring et al. for NMR[9] using the result (3b). Equation (2) now takes the form

$$\Delta\nu(\beta) = \Delta\nu(0)\left|\cos\beta \cdot \frac{1}{2}(3\cos^2\beta-1)\right| , \tag{4}$$

and gives the Pr^{3+} optical linewidth as a function of the off-resonance angle β. Equation (4), which is shown in Fig. 3, predicts that the linewidth vanishes at the magic angle $\beta=\cos^{-1}\sqrt{1/3}$ or 54.7° and also at $\beta=\pi/2$, the fluorine resonance condition.

The Pr^{3+} transition[11] examined, $^1D_2 \leftrightarrow {}^3H_4$ at 5925Å, involves the lowest crystal field components of each state. These are electronic singlet states that couple to the Pr^{3+} nuclear spin I=5/2 in second order, producing quadrupolar splittings of order 10 MHz and an enhanced nuclear gyromagnetic ratio γ_I. Three equally intense optical transitions occur, $I''_z \leftrightarrow I'_z = \pm 5/2 \leftrightarrow \pm 5/2$, $\pm 3/2 \leftrightarrow \pm 3/2$, and $\pm 1/2 \leftrightarrow \pm 1/2$, and overlap due to the large inhomogeneous strain broadening of ~5 GHz. We investigated the $\pm 1/2 \leftrightarrow \pm 1/2$ transition, which is easily identified because it appears as a long decay following the faster 5/2 and 3/2 components, consistent with Eq. (2) and a computer simulation of a triexponential decay.

Optical FID is monitored by laser frequency switching[11] using the pulse sequence of Fig. 1. An acousto-optic Bragg modulator, driven by a 110 MHz rf pulse generator, deviates the beam of a cw ring dye laser through a 1.5 mm aperture while imparting a 110 MHz laser frequency switch. Before and after the pulse the undeviated beam is blocked and since the pulse repetition rate is 1 Hz, complications due to optical pumping[11] are reduced. The transmitted beam propagates along the c axis (laboratory y axis) of a $5\times6\times7$ mm^3 crystal of $LaF_3:Pr^{3+}$(0.1% Pr^{3+}) before striking a p-i-n photodiode. The laser field is linearly polarized along the laboratory x axis and has a 1.0 mm diameter in the crystal at a power of 10 mW. In Fig. 1, we see that the Pr^{3+} ions are coherently prepared by the optical field during the initial 200 μsec of the pulse, and then FID occurs when the laser frequency shift is suddenly reduced from 110 to 108 MHz, the laser field remaining constant. Most important, broadening due to laser frequency jitter is

reduced by frequency_locking the ring laser to a passive external reference cavity, the laser stability being ~1 kHz over the duration of the measurement, ~50 μsec.

For the spin decoupling experiment, an rf coil oriented along the x axis is in close contact with the crystal and provides a pulse with a rotating component B_x=25 G which is variable over the frequency range 0 to 600 kHz and is time-coincident with the optical pulse of 400 μsec duration (Fig. 1). Both coil and crystal are immersed in liquid helium at 1.8°K. A static magnetic field B_o=130 Gauss is oriented either along the z or y laboratory axes ($\perp$ or $\parallel$ to the crystal c axis) and exceeds the local field so that the nonsecular dipolar terms are small. Individual FID signals, which appear at a 2.003 MHz beat frequency because of heterodyne detection with the laser field, are captured with a Biomation 8100 Transient Recorder for reproduction on an X-Y chart recorder (Fig. 2). In the absence of power broadening, the observed dephasing time is $T_2/2$.

A clear demonstration of optical line narrowing by spin decoupling is indicated in Fig. 2 for the case $B_o \perp$ c axis. In the absence of rf, trace (a), the linewidth at HWHM is 10.2 kHz (T_2=15.6 μsec). In the presence of rf, trace (b), the value is 2.4 kHz (T_2=66 μsec) where the rf frequency $\omega/2\pi$=450 kHz corresponds to the magic angle 54.7°. Additional confirmation is obtained by varying the rf frequency over the range from off-resonance, β=0, to on-resonance, $\omega/2\pi$=520 kHz or $\beta=\pi/2$. Figure 3 shows that the observed optical linewidth for the case $B_o \perp$ c axis follows the theoretical expectation Eq. (4), where a frequency offset of 3 kHz is added to account

for residual broadening. Furthermore, at frequencies above resonance ($\beta>\pi/2$), the experimental pattern repeats with the mirror symmetry predicted by (4). For the case $B_o \perp c$ axis, the behavior is similar but not identical to Fig. 3 because of the Pr^{3+} hyperfine anisotropy. Our theoretical model for spin decoupling therefore is confirmed in some detail and clearly exposes the magnetic origin of the optical line broadening mechanism.

On the other hand, spin decoupling in NMR has revealed different characteristics, partly because the FID observed in the rf region is a first order process and thus both dynamic and static interactions contribute to the linewidth. In systems such as AgF, the F spin diffusion process can motionally narrow the NMR ^{109}Ag resonance,[4] and when the spin diffusion process is suppressed as it is at the magic angle, the linewidth *broadens* rather than narrows.[9,10] Line narrowing[9,10] is observed, however, at the F resonance condition $\beta=\pi/2$.

At the magic angle, the optical linewidth of ~2 kHz appears to be limited by residual laser frequency jitter. Of course, a fundamental limit of 160 Hz is set by a $^1D_2$ radiative lifetime of 0.5 msec. We estimate that at 1.8°K the phonon broadening linewidth is only 7 Hz, and in the preparative FID stage, laser power broadening and the effect of a finite optical pulse width of 200 μsec are negligible. As the laser frequency stability is improved further, it will be possible to examine weaker interactions which otherwise would be obscured in the absence of spin decoupling, an example being the ^{141}Pr-^{141}Pr interaction. Thus, a new

family of spin decoupling experiments can be carried out for the first time at optical frequencies, allowing the manipulation and study of the basic dynamic processes.

The technical assistance of D. Horne and K. L. Foster are acknowledged.

REFERENCES

1. N. Bloembergen, E. M. Purcell and R. V. Pound, Phys. Rev. 73, 679 (1948).

2. A. Abragam, Prnciples of Nuclear Magnetism, (Oxford, London, 1961).

3. E. R. Andrew, A. Bradbury, and R. G. Eades, Nature 182, 1659 (1958).

4. A. Abragam and J. Winter, C.R. Acad.-Sci. (Paris) 249, 1633 (1959).

5. F. Bloch, Phys. Rev. 111, 841 (1958).

6. M. Lee and W. I. Goldburg, Phys. Rev. 140, A1261 (1965).

7. D. A. McArthur, E. L. Hahn, and R. E. Waldstedt, Phys. Rev. 188, 609 (1969).

8. J. S. Waugh, L. M. Huber, and U. Haeberlen, Phys. Rev. Lett. 20, 180 (1968); W-K. Rhim, A. Pines, and J. S. Waugh, Phys. Rev. B3, 684 (1971).

9. M. Mehring, G. Sinning, and A. Pines, Z. Phys. B24, 73 (1976).

10. M. Mehring and G. Sinning, Phys. Rev. B15, 2519 (1977).

11. R. G. DeVoe, A. Szabo, S. C. Rand, and R. G. Brewer, Phys. Rev. Lett. 42, 1560 (1979).

12. J. R. Klauder and P. W. Anderson, Phys. Rev. 125, 912 (1962).

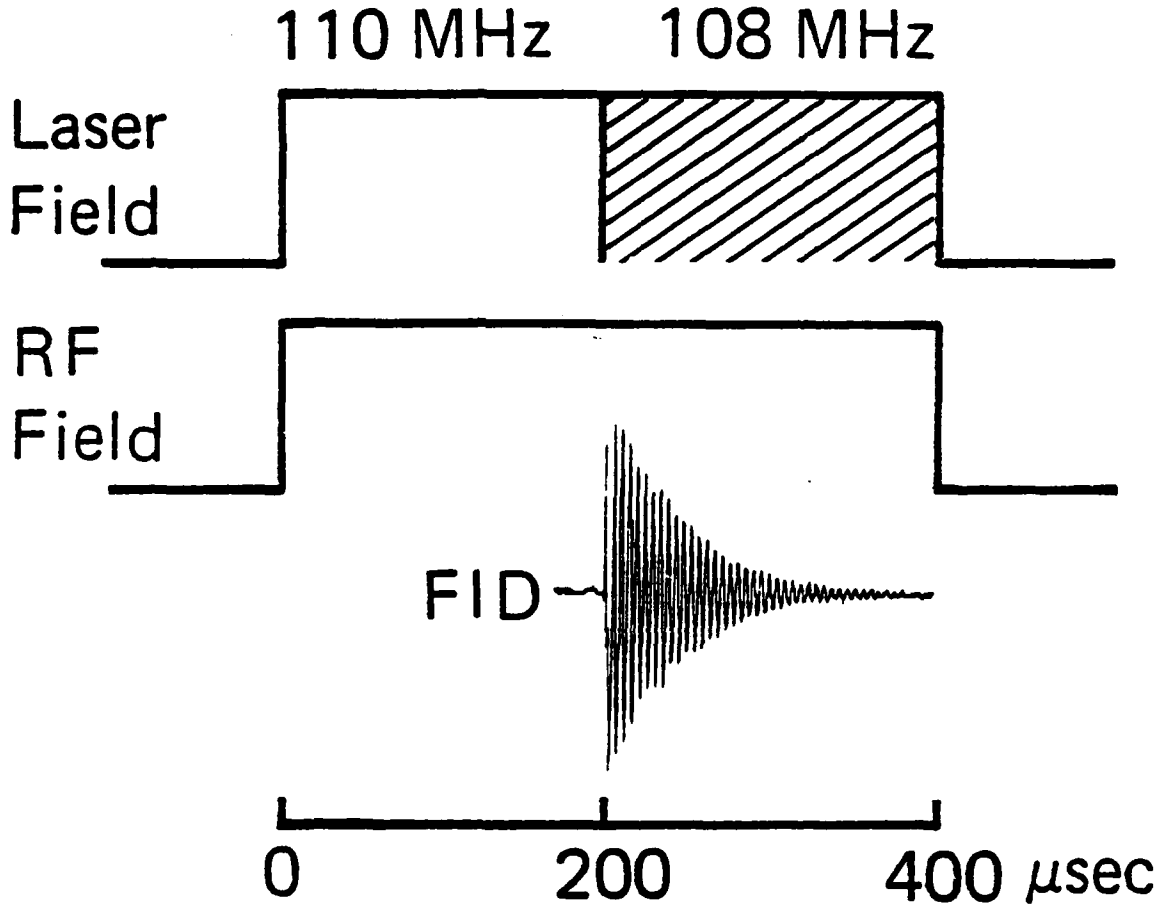


Figure 1. Pulse sequence showing the laser field and its frequency shift and the spin decoupling radio frequency with time. The Pr^{3+} ions are coherently prepared by the laser field in the initial 200 μsec interval and then exhibit optical FID when the laser frequency is suddenly switched 2 MHz at $\underline{t}$=200 μsec.

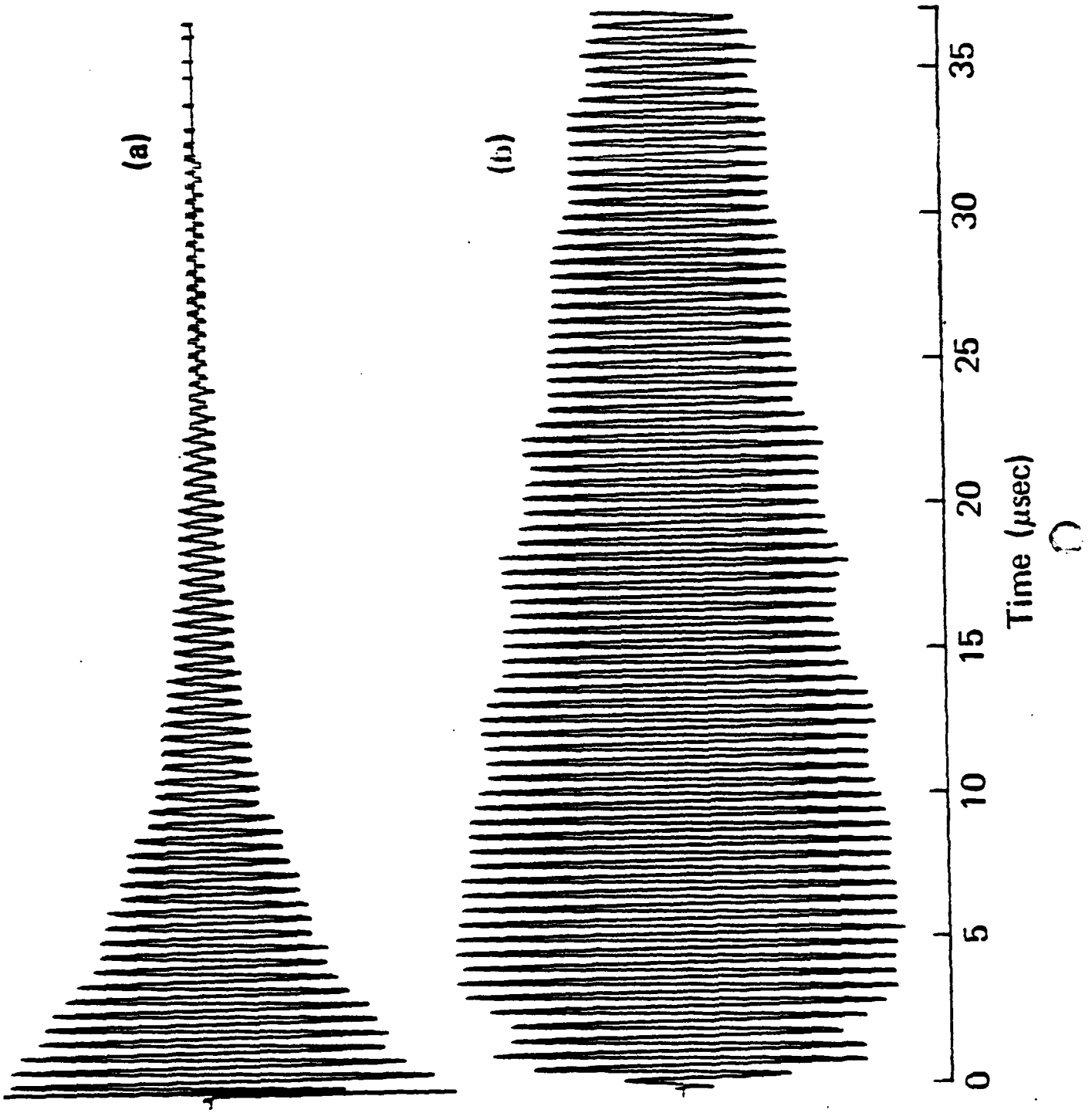


Figure 2. Optical free induction decay is $LaF_3:Pr^{3+}$ at 1.8°K in the presence of a static magnetic field B_o=130 G $\perp$c axis and (a) with no rf field where T_2=15.6 μsec (10.2 kHz) and (b) with an rf field B_x=25 G where T_2=66 μsec (2.4 kHz).

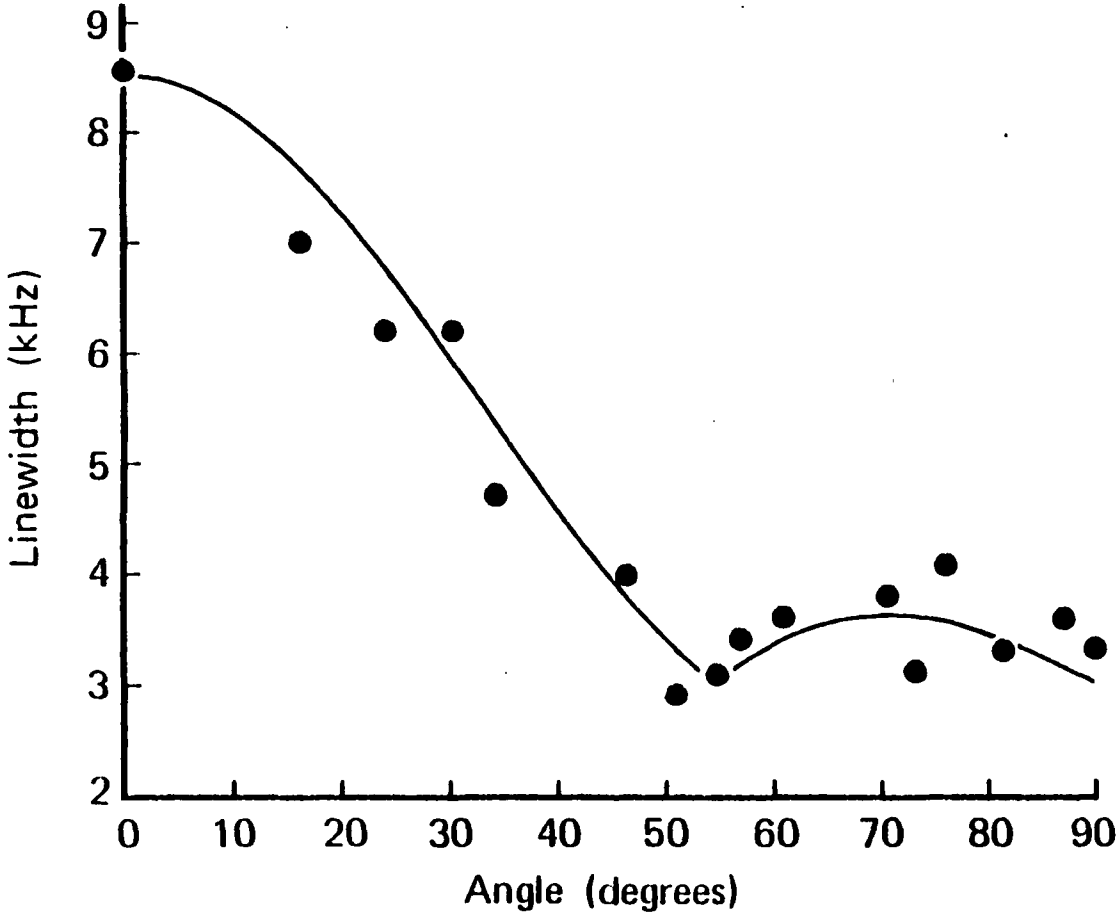


Figure 3. Pr^{3+} optical linewidth versus the angle $\beta=\tan^{-1}(\gamma_S B_x/\Delta_S)$ expressed in degrees. Solid circles •: experimental points for the case B_o=130G∥c axis and B_x=25 G. Solid curve —: Eq. (4) with frequency offset of 3 kHz included for residual broadening.

RJ2542(33082)5/15/79
Physics

Appendix - Item 8

ULTRASLOW OPTICAL DEPHASING OF Pr^{3+}:LaF_3*

R. G. DeVoe
A. Szabo†
S. C. Rand
R. G. Brewer

IBM Research Laboratory
San Jose, California 95193

ABSTRACT: Optical free induction dephasing times as long as 16 μsec, corresponding to an optical homogeneous linewidth of 10 kHz, have been observed for the $^3H_4 \leftrightarrow {}^1D_2$ transition of Pr^{3+} ions in LaF_3 at 2°K. Measurements are facilitated by a frequency-locked cw dye laser and a new form of laser frequency switching. Zeeman studies reveal a Pr-F dipole-dipole dephasing mechanism where the Pr nuclear moment is enhanced in both $^1D_2$ and $^3H_4$.

---

*Work supported in part by the U.S. Office of Naval Research

†On leave from the National Research Council of Canada, Ottawa

In this Letter, we report a new advance in the observation of extremely long optical dephasing times in a low temperature solid. Coherently prepared Pr^{3+} impurity ions in a LaF_3 host crystal exhibit optical free induction decay (FID) where the dephasing times correspond to an optical linewidth of only 10 kHz half-width half-maximum and a spectral resolution of 5×10^{10}. At this level of resolution, which represents a fifty fold increase over our previous measurements,[1] it is now possible to perform detailed optical studies of magnetic Pr-F dipole-dipole interactions in the ground and optically excited states. Heretofore, such weak relaxation effects could be detected only in the ground state by spin resonance techniques[2-4] or radio-frequency optical double resonance.[5,6]

The Pr^{3+} transition $^3H_4 \leftrightarrow {}^1D_2$ monitored at 5925Å involves the lowest crystal field components of each state. These are singlet states where the 2J+1 degeneracy is lifted by the crystalline field due to the low Pr^{3+} site symmetry, perhaps C_2 or C_{2v}. The nuclear quadrupole interaction[7] of Pr^{3+} (I=5/2) splits each Stark level into three hyperfine components which are each doubly degenerate ($\pm I_z$), and to a first approximation, three equally probable optical transitions connecting these states occur, namely, $I_z'' \leftrightarrow I_z' = \pm5/2 \leftrightarrow \pm5/2$, $\pm3/2 \leftrightarrow \pm3/2$, and $\pm1/2 \leftrightarrow \pm1/2$. All three transitions overlap and can be excited simultaneously by a monochromatic laser field since the Pr^{3+} hyperfine splittings of order 10 MHz are considerably less than the inhomogeneous crystalline strain broadening of ~5 GHz. Weaker transitions of the type $5/2 \leftrightarrow 1/2$, $5/2 \leftrightarrow 3/2$, ... also occur among these hyperfine states because of a nonaxial field gradient at the Pr^{3+} nucleus which mixes the $|I_z\rangle$ wavefunctions slightly. As noted previously,[1,8] the weaker transitions

redistribute the ground state hyperfine population distribution drastically in an optical pumping cycle, and play an important role in the optical dephasing measurements reported here.

Bleaney[9] has shown that when an electronic singlet of a rare earth ion admixes with close lying Stark split levels of a given J manifold, it produces in second order a pseudo-quadrupole moment and an enhanced nuclear magnetic moment

$$m_i = (g_N\beta_N - 2g_J\beta\Lambda_{ii})I_i \ , \qquad (1)$$

where the notation is that of Teplov.[4] Here, the principal axes are labeled i=x,y,z, the nuclear and electronic g values are g_N and g_J, the electronic matrix element $\Lambda_{ii}=\sum_{n\neq 0} A_J|\langle 0|J_i|n\rangle|^2/(E_n-E_0)$ connects the lower state $|0\rangle$ with an excited state $|n\rangle$ removed in energy by E_n-E_0, and A_J is the Pr^{3+} hyperfine constant. Now imagine that a fluctuating local magnetic field $\tilde{H}_z$ exists at the Pr^{3+} site due to distant pairs of F nuclei participating in mutual spin flips, and ignore other dephasing mechanisms for the moment. This field modulates the optical transition frequency randomly through a Pr-F dipole-dipole interaction and produces a HWHM homogeneous optical linewidth

$$\Delta\nu = |\gamma_z''I_z'' - \gamma_z'I_z'|\tilde{H}_z/2\pi \qquad (2)$$

where γ_z'' and γ_z' are the Pr^{3+} *enhanced* gyromagnetic ratios ($\gamma_z=m_z/\hbar I_z$) of $^3H_4$ and $^1D_2$. Because the Pr nuclear wavefunctions are mixed to some extent,[7] rigorously I_z is not a good quantum number. Nevertheless, to a good approximation[5,8] $I_z''\sim I_z'$ and as already mentioned, we expect three strong optical transitions $|\pm 5/2\rangle\rightarrow|\pm 5/2\rangle$, $|\pm 3/2\rangle\rightarrow|\pm 3/2\rangle$, and $|\pm 1/2\rangle\rightarrow|\pm 1/2\rangle$.

for collision-induced vibration-rotation transitions within the $B^3\Pi_{o^+u}$ state. The lower transition level can only decay to neighboring vibration-rotation levels via collisions at the rate

$$\Gamma_1 = \Gamma'_{v-r} \ . \tag{3}$$

On the other hand, the optical dipole dephasing rate is

$$\Gamma = \frac{1}{2}\,(\Gamma_1+\Gamma_2) + \Gamma_\phi \tag{4}$$

where $\Gamma \equiv 1/T_2$. The quantity Γ_ϕ represents the rate of phase interrupting *elastic* collisions caused by perturber-induced energy level shifts. The competition of other possible elastic collision mechanisms will be discussed later.

2.3 Two Pulse Delayed Nutation

Consider that two brief laser frequency switching pulses with delay time τ are produced. The first pulse induces nutation in I_2 vapor, which is contained in an evacuated and sealed off cell, and thereby creates a population imbalance among the transition levels. In the interval τ between the two pulses, the population difference is partially restored due to relaxation. The second pulse monitors the extent of population recovery through the magnitude of the resulting nutation signal. The envelope function of the second nutation signal is of the form [16]

$$S_{2N} \sim \left(1 + \frac{\gamma}{\Gamma_2-\Gamma_1}\right) e^{-\Gamma_2\tau} + \left(1 - \frac{\gamma}{\Gamma_2-\Gamma_1}\right) e^{-\Gamma_1\tau} \ , \tag{5}$$

and in principle it is possible to measure the population decay rates Γ_2 and Γ_1 where γ is the radiative decay rate for the 2→1 transition alone.

of 9 cm^{-1} while the v'=2 assignment follows from the appearance of two vibrational bands to the high frequency side of the transition frequency. The upper state v'=15 follows from a comparison of the observed transition energy 16,956.39 cm^{-1} with the calculated value 16,956.35 cm^{-1} using the spectroscopic constants of WEI and TELLINGHUISEN [14]. The transition wavelength is measured with a digital wavemeter, a travelling Michelson interferometer [15], using a frequency-locked He-Ne reference laser where the measurement is accurate to $1/10^6$ after correction to vacuum wavelength.

2.2 Relaxation Model and Notation

In what follows, we adopt the theoretical derivations and notation of SCHENZLE and BREWER [16] where a two-level quantum system interacts with a classical electromagnetic field while undergoing relaxation. The upper level is labeled 2 and the lower level 1. We assume that the optical excitation of the transition 1→2 does not modify the population distribution of the remaining n levels which act as a thermal reservoir. The upper level has the population decay rate

$$\Gamma_2 = \Gamma^r + \Gamma_e + \Gamma_{v-r} \qquad (1)$$

where the pressure-independent term

$$\Gamma^r = \hat{\gamma} + \gamma_{sp} \qquad (2)$$

consists of radiative decay $\hat{\gamma}$ to vibration-rotation levels of the ground electronic state and the term γ_{sp} accounts for spontaneous predissociation. The *inelastic* collision rate Γ_e applies to transitions to other electronic states including collision-induced predissociation. The rate Γ_{v-r} allows

a frequency switched cw dye laser, the broad tuning range permits general studies in atoms, molecules and solids--in a manner resembling the versatile pulsed NMR techniques. The apparatus [4] consists of a cw dye laser that is phase modulated by an electro-optic intracavity crystal, an X-cut ammonium dideutero-hydrogen phosphate (AD*P) crystal which is driven by a sequence of low voltage pulses. The laser frequency shift is 0.6 MHz/V. The frequency switched beam irradiates the sample before it and the coherent emission from the sample strike a photodetector. The FID and echo signals are easily detected because they produce a heterodyne beat with the laser which acts as a local oscillator, the beat frequency being $\Omega-\Omega'$.

2. COLLISION PHENOMENA

The relaxation behavior of electronically excited I_2 vapor has been studied extensively and exclusively in the past by fluorescence decay measurements [11-13]. With few exceptions, the observations have been confined to inelastic collision mechanisms which deplete the excited state population. In this section, we reexamine a number of these inelastic processes for I_2-I_2^* collisions using coherent transients. In addition, elastic collisions which were not detected in the older work are found to exhibit a profound optical dephasing in an FID or echo experiment.

2.1 Transition Assignment

Only one optical transition is studied here in detail, the R(59) line of $^1\Sigma_g^+ \longrightarrow B^3\Pi_{o^+u}$, $(v,J)=(2,59)\longrightarrow(15,60)$. From the fluorescence spectrum, the rotational assignment is confirmed by the P and R branch line splitting

1. LASER FREQUENCY SWITCHING

Consider a stable single mode cw laser of frequency Ω which initially excites an atomic two-level quantum system under steady-state conditions. For a dilute gas, the spectral lineshape will consist of a narrow homogeneous contribution and a much broader inhomogeneous Doppler lineshape. The atomic group having longitudinal velocity v_z will be excited resonantly at the laser frequency Ω and therefore will be coherently prepared since the upper and lower states will be in superposition. The entire collection of excited atoms constitutes a phased array of dipoles which can emit or absorb coherent light. The well known atom-field interaction is described by the Maxwell and Schrödinger wave equations, and the relevant theory is given elsehwere [7,9].

Now imagine that the laser frequency is abruptly switched from Ω to Ω'. The initial velocity group v_z, which is no longer resonant with the applied field, radiates a coherent beam of light in the forward direction--the free induction decay effect. Simultaneously, a second velocity group v_z' is excited coherently and exhibits Rabi oscillations, the nutation effect, where the atoms undergo alternating stimulated absorption and emission. If the laser is frequency switched twice in succession by two brief pulses, the velocity group v_z' emits a photon echo in the forward direction. Evidently, by varying the pulse sequence the entire class of coherent optical transients can be observed in this manner.

Laser frequency switching obviously resembles Stark switching [10]. However, the former is not restricted to Stark tunable systems, and with

Perhaps the oldest spectroscopic technique for studying time-dependent interactions in matter goes back to the turn of the century when MICHELSON [1] demonstrated that atomic collisions can broaden spectral lines. Some 55 years later, similar time-dependent interactions were pursued in more sophisticated and detailed ways by pulsed nuclear magnetic resonance--the difference being that the measurements were carried out more directly in the time domain using coherent radio frequency sources. The development of this field abounds with coherence effects such as the spin echo and the free induction decay (FID) effect introduced initially by HAHN [2], and thus has set an example of what might be done at optical frequencies using laser sources. Indeed, the optical analog of the spin echo was first reported [3] in 1964, and the field of *coherent optical transients* has progressed steadily since that time.

At IBM we have been using coherent optical transient methods to study (1) molecular collision mechanisms in I_2 vapor [4], (2) the optical dephasing behavior of Pr^{3+} impurity ion in a LaF_3 host crystal at liquid helium temperatures [5], and (3) novel coherence phenomena which occur in sodium vapor on a 100 picosecond time scale [6]. Here, the experimental techniques of *laser frequency switching* [4,6] are utilized. In this article, recent work on I_2 collisions is discussed. Theoretical derivations, other background material, and references not given here may be found in review articles [7-9].

RJ2356(31528)9/25/78
Physics(General)

Appendix - Item 9

OPTICAL DEPHASING IN MOLECULAR IODINE *

Richard G. Brewer
Satoru S. Kano

IBM Research Laboratory
San Jose, California 95193

ABSTRACT: Elastic and inelastic collision mechanisms occurring in molecular iodine are studied using novel coherent optical transient effects.

*Work supported in part by the U.S. Office of Naval Research.

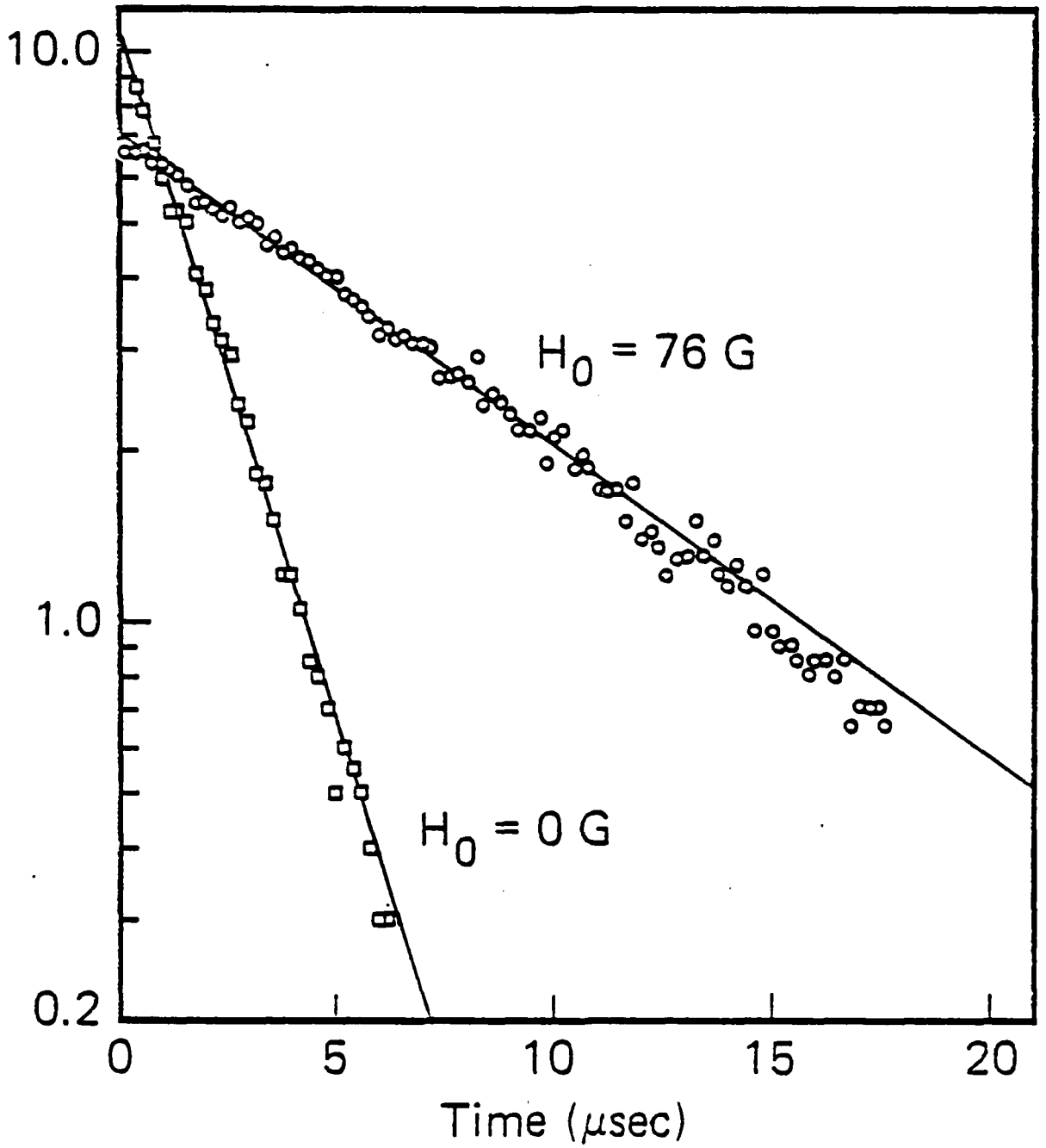


Figure 2. Semilog FID plots of the data of Figs. 1(a) and (c) showing a simple exponential decay.

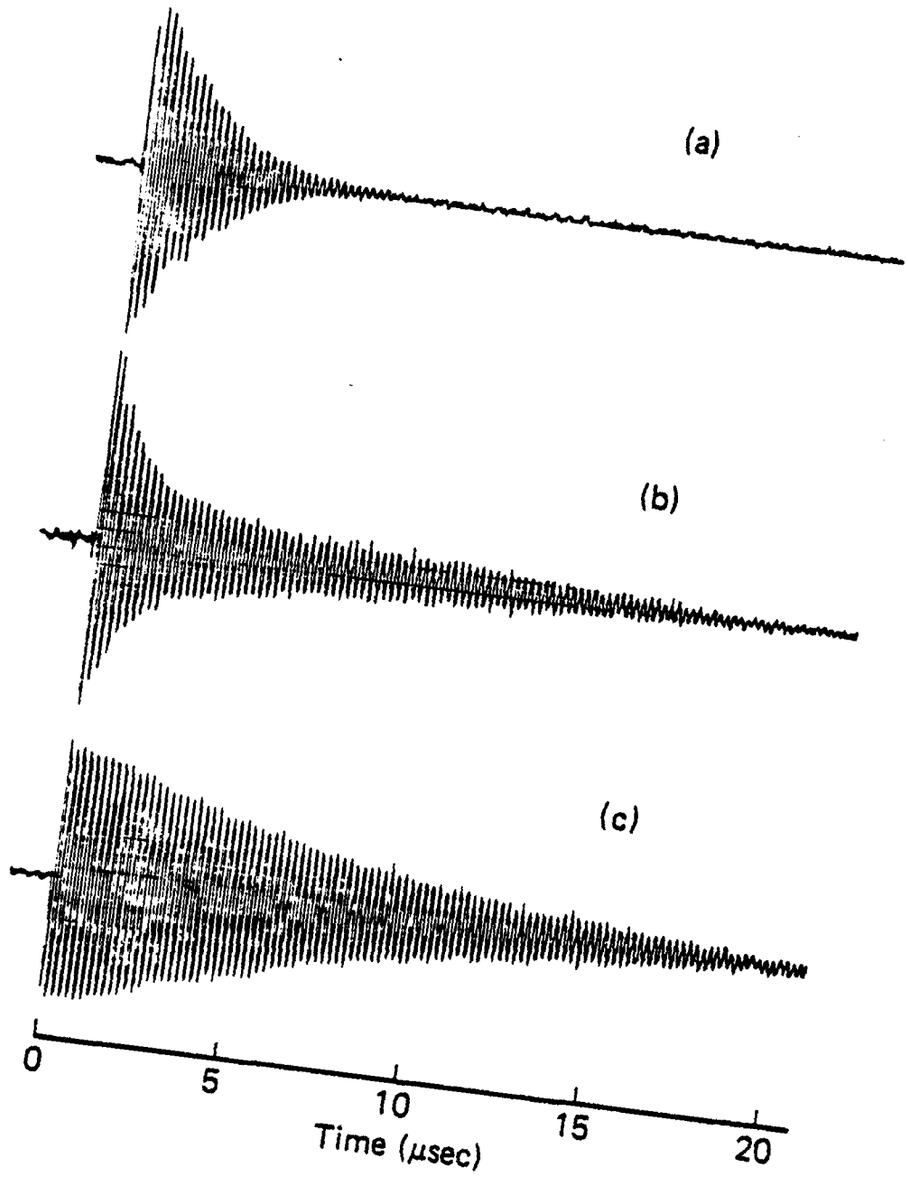


Figure 1. Free induction decay of 0.1 atomic % Pr^{3+} in LaF_3 at 2°K in the presence of an external magnetic field $H_o \perp c$ axis. H_o equals (a) 0.5G (earth's field), (b) 19G and (c) 76G. The optical heterodyne beat frequency is 5.005 MHz. Cases (a) and (c) are plotted in Fig. 2.

REFERENCES

1. A. Z. Genack, R. M. Macfarlane and R. G. Brewer, Phys. Rev. Lett. 37, 1078 (1976); R. M. Macfarlane, A. Z. Genack, S. Kano and R. G. Brewer, Journal of Luminescence 18/19, 933 (1979).

2. K. Lee and A. Shir, Phys. Rev. Lett. 15, 1027 (1965).

3. W. B. Mims in Electron Paramagnetic Resonance, ed. S. Geschwind (Plenum, NY, 1972), p. 263.

4. M. A. Teplov, Soviet Phys. JETP 26, 872 (1968).

5. L. E. Erickson, Opt. Comm. 21, 147 (1977).

6. R. M. Shelby, C. S. Yannoni and R. M. Macfarlane, Phys. Rev. Lett. 41, 1739 (1978).

7. T. P. Das and E. L. Hahn, Nuclear Quadrupole Resonance Spectroscopy, (Academic, 1958).

8. L. E. Erickson, Phys. Rev. 16B, 4731 (1977).

9. B. Bleaney, Physica 69, 317 (1973).

10. S. Matthies and D. Welsch, Phys. Status Solidi B, 68, 125 (1975).

11. E. Y. Wong, O. M, Stafsudd and D. R. Johnston, J. Chem. Phys. 39, 786 (1963); V. K. Sharma, J. Chem. Phys. 54, 496 (1971).

12. R. G. Brewer and A. Z. Genack, Phys. Rev. Lett. 36, 959 (1976); A. Z. Genack and R. G. Brewer, Phys. Rev. 17A, 1463 (1978).

13. M. J. Weber, J. Chem. Phys. 48, 4774 (1978).

Other broadening mechanisms we have considered appear to be negligible. They include a $^1D_2$ radiative decay time of 0.5 msec[13] (0.16 kHz) and phonon processes[8] (0.8 kHz). Our linewidths are also independent of Pr^{3+} concentration in the range 0.03 to 0.1 atomic % so that Pr^{3+}-Pr^{3+} interactions are excluded. Since the width is independent of laser power and a nutation signal is not detected, we estimate that the optical transition matrix element $\mu_{ij} \leq 4.5 \times 10^{-5}$ Debye. This implies that only 10^{-5} of the $^1D_2$ ions return directly by radiative decay to the ground $^3H_4$ state; the remainder radiate to excited Stark split states of $^3H_4$ and other states[13] followed by rapid spontaneous phonon emission processes to the ground state. Clearly, the optical pumping cycle is not simple. The contribution of laser frequency jitter to the linewidth appears to be small since the decay time varies with external magnetic field in a predictable manner. We expect that a significantly higher spectral resolution can be achieved in the near future and will further improve precision measurements of this kind where ultraslow optical dephasing processes occur.

We are indebted to D. Horne for the design and construction of the laser frequency locking circuit and to K. L. Foster for technical assistance. We are pleased to acknowledge conversations with E. Wong, L. E. Erickson, C. S. Yannoni, I. D. Abella, E. L. Hahn, W. B. Mims, and A. Wokaun.

modifies the optical pumping cycle and the $^3H_4$ population distribution in a sensitive way by mixing the nuclear wavefunctions $|I_z\rangle$ further since the $^1D_2$ Zeeman and quadrupole energies[8] can be comparable. This model is also consistent with the zero field rf-optical double resonance observation[6,8] that the $^3H_4$ quadrupole transition $|5/2\rangle\leftrightarrow|3/2\rangle$ is more intense than the $|3/2\rangle\leftrightarrow|1/2\rangle$. More detailed calculations of the nuclear wavefunctions are needed to test these ideas further and will require determining the orientation of the principal axes x, y, z for both $^3H_4$ and $^1D_2$.

We now turn to Eq. (2) to determine the $^1D_2$ enhanced gyromagnetic ratio γ_z'. A fluctuating local dipolar field of $\tilde{H}_z$=0.41G at the Pr^{3+} site due to the fluorine nuclei can be deduced from the ground state value[5] $\gamma_z''/2\pi$=23 kHz/G and a ground state linewidth[6] of 9.5 kHz for the $^3H_4$ quadrupole transition $|5/2\rangle\leftrightarrow|3/2\rangle$ at H_o=0G. The same local field modulates the optical transition frequency producing a considerably broader linewidth of 44 kHz (I_z=5/2) at H_o=0G. Therefore, we find from (2) that $\gamma_z'/2\pi$=20±4 kHz/G where we have taken the enhanced moments of $^3H_4$ and $^1D_2$ to be of opposite sign. This quantity is bounded by $1.29<\gamma_z'/2\pi<19$ kHz/G, the lower limit being derived from the first term of (1), i.e., with no enhancement. The upper limit follows from the second term of (1) where we assume in Λ_{zz} the maximum matrix element $\langle 1|J_z|0\rangle$=2, the lowest Stark level of $^1D_2$ mixes with the first excited state where E_1-E_0=23 cm^{-1}, g_J=1, and $A\sim1.093\times10^9$ Hz. If γ_z'' and γ_z' are assumed to be of the same sign, $\gamma_z'/2\pi$=66 kHz/G which exceeds the upper limit. In addition, ab initio calculations[10] of $\langle J_z\rangle$ are in serious disagreement with our experimental results.

hyperfine states excited (three packets) will be depleted and FID cannot be detected. However, by sweeping the laser frequency at a slow rate of ≤10 kHz/16 μsec so as not to influence the decay rate, the pumping cycle can be reversed[1] and the hyperfine population partially restored. The $^3H_4$ hyperfine population distribution which results depends on the sweep rate and the relative transition probability among the hyperfine states as they decay from $^1D_2$ to $^3H_4$ via intermediate states. Therefore, the pumping cycle dictates which of the three strong transitions can be prepared to yield FID.

In Fig. 1, a dramatic variation in the FID occurs when a weak external field H_o is applied perpendicular to the crystal c axis. The T_2 dephasing times for the three cases are (a) 3.6 μsec at H_o=0.5G (earth's field), (b) 3.5 and 15.6 μsec at H_o=19G, and (c) 15.8 μsec at H_o=76G. Note that case (c) corresponds to a 10 kHz HWHM linewidth which appears to be the *narrowest homogeneously broadened optical transition detected in a solid.* Its magnitude is comparable to NMR linewidths[2,4,6] which result from a magnetic dipole-dipole dephasing process. Cases (a) and (c) are single exponentials (Fig. 2), the ratio of the two decay times being 4.6. The intermediate case (b) is dominantly a biexponential and displays precisely the same two decay times found in (a) and (c). It is significant that the decay time ratio approximates 5 and that the magnitude of these decay times is essentially independent of magnetic field. These results are consistent with Eq. (2) where we expect three decay times in the ratio 5:3:1, and we conclude that case (a) represents dephasing due to the $|5/2\rangle$ state, case (c) to the $|1/2\rangle$ state, and case (b) to both of these states with possibly a small contribution from $|3/2\rangle$ as well. We conclude that application of a weak magnetic field

extra-cavity laser frequency switching is compatible with laser frequency locking which we now consider.

To detect ultraslow dephasing times by FID, the laser frequency must remain fixed within the sample's narrow homogeneous linewidth $\Delta\nu=1/(2\pi T_2)$ for an interval $\sim T_2$ - a stability condition which is less stringent than in a linewidth measurement. In the present work, a frequency stability of ~10 kHz in a time of ~16 μsec is required. To this end, our laser is locked to an external reference cavity which provides an error signal in a servo loop of high gain for correcting slow frequency drift and high frequency jitter. The noise spectrum as seen from the error signal or a spectrum analyzer is not flat but is dominated by isolated jumps of 30 to 100 kHz in a 10 μsec period. At such times, the sample is prepared at two (or more) discrete frequencies which result in a deeply modulated FID pattern. This behavior agrees with a computer simulation of FID which assumes a bimodal spectrum. However, at other times frequency jumps do not occur, and the free induction decays monotonically as in Fig. 1. Under these conditions, a laser jitter of <10 kHz permits a reliable decay time measurement of these *single events* which are considerably longer-lived than the time-averaged value of many decays. These signals are captured with a Biomation 8100 Transient Recorder and then reproduced on an X-Y chart recorder.

A key feature of the measurement is an optical pumping absorption-emission cycle which transfers population from any given hyperfine level of the $^3H_4$ ground state to its two neighbors, for example from $|3/2\rangle$ to $|5/2\rangle$ and $|1/2\rangle$ within the same inhomogeneous packet. As a result, each of the three $^3H_4$

Therefore, from (2) three different decay times should appear in an optical FID. We shall see that this idea is supported and that γ_z' for $^1D_2$ can be obtained since γ_z'' is known[5] and $\tilde{H}_z = 2\pi\Delta\nu_{rf}/\gamma_z''$ can be deduced from an rf-optical double resonance linewidth[6] of the $^3H_4$ state. Furthermore, these experiments offer a new way of testing ab initio calculations[10] of Λ_{ii} as well as the Pr^{3+} site symmetry, which remains controversial.[10,11]

The technique adopted for observing optical FID relies on laser frequency switching,[12] but in a new form. A cw dye laser radiates a beam at 5925Å which is linearly polarized at a power of ~4 mW. The beam passes through a lead molybdate acousto-optic modulator which is external to the laser cavity and oriented at the Bragg angle. The Bragg diffracted beam is focused to a 200 micron diameter in a 7×7×10 mm^3 crystal of Pr^{3+}:LaF_3 (0.1 or 0.03 atomic % Pr^{3+}) which is immersed in liquid helium at 2°K, and the emerging laser and FID light, which propagates parallel to the crystal c axis, then strikes a PIN diode photodetector. The Pr^{3+} ions are coherently prepared while the modulator is driven continuously and efficiently at 110 MHz. FID follows when the rf frequency is suddenly shifted (100 nsec rise time) from 110 to 105 MHz, the duration of the switching pulse being 40 μsec. Note that the laser is switched 500 homogeneous linewidths. Figure 1 shows FID signals produced in this way where the dephasing time $T_2/(1+\sqrt{1+\chi^2 T_1 T_2}) \sim T_2/2$ is independent of power broadening since $\chi^2 T_1 T_2 \ll 1$, χ being the Rabi frequency. The anticipated heterodyne beat of 5 MHz frequency is readily observed because the shifted laser and FID beams overlap due to the change in the Bragg angle (0.4 mrad) being less than the beam divergence (7 mrad). This type of

2.4 Spontaneous Emission

The quantities Γ^r and Γ_e are easily determined in the conventional way by monitoring the spontaneous emission decay time as a function of I_2 vapor pressure. The sample is excited by a 500 nsec optical pulse, due to a gated Pockels cell which briefly transmits a cw laser beam. The 90° emission is detected with a photomultiplier. Since the radiative decay time $\hat{\gamma}$ changes very slowly with excitation wavelength [11], collision-induced vibration-rotation transitions in the $B^3\Pi_{o+u}$ will not affect the measurement. However, the inelastic electronic quenching rate Γ_e will be detectable.

Combining the two pulse nutation measurement, which yields Γ_2, with the value $\Gamma^r+\Gamma_e$ derived from spontaneous emission, we obtain Γ_{v-r} using (1). Since it has not been possible to measure Γ_1 yet, we invoke the reasonable approximation

$$\Gamma_1 = \Gamma'_{v-r} \sim \Gamma_{v-r} . \tag{6}$$

2.5 Free Induction Decay

Here the I_2 molecules are prepared under steady-state conditions with a cw laser beam. When the laser frequency is switched to a new value, the optically induced dipoles radiate in the forward direction and exhibit the decay rate,

$$\bar{\Gamma} = \Gamma + \sqrt{\Gamma^2+\hat{\Gamma}^2} \tag{7}$$

where the dipole dephasing rate Γ is defined by (4) and

$$\hat{\Gamma}^2 = \frac{\chi^2\Gamma}{2\Gamma_1\Gamma_2}\left(\Gamma_1+\Gamma_2-\gamma\right) \tag{8}$$

reflects the intensity-dependent line broadening in the preparative step due to the Rabi frequency

$$\chi = \mu_{ij}E_o/\hbar \tag{9}$$

where μ_{ij} is the matrix element for the transition i→j and E_o is the peak laser field amplitude.

Thus, in the zero laser power limit (χ=0), the FID rate is 2Γ. Furthermore, once Γ_2 and Γ_1 are known, we obtain the rate of elastic collisions Γ_ϕ using (4). Since Γ, $\Gamma_2 >> \Gamma_{v-r}$, any error introduced in Γ_ϕ through the approximation (6) will be small. Alternatively, the FID measurement of Γ can be replaced by photon echo or rotary echo experiments which we find all agree to within an uncertainty of 1 to 2%.

2.6 Optical Nutation

We now show how the radiative decay rate $\hat{\gamma}$ can be derived from the optical nutation effect. Furthermore, the rate of spontaneous predissocation γ_{sp} then follows from (2) once Γ^r is known. In terms of the Einstein A coefficient, we have for the excited state $|e'v'J'M'\rangle$

$$\hat{\gamma} = \sum_{\substack{v''J''\\M''M'}} A(e'v'J'M', e''v''J''M'') = \frac{64\pi^4}{3h}\sum_{v''}|R^{e'e''}R^{v'v''}|^2/\lambda^3_{v'v''} \tag{10}$$

where the transition matrix element in (9) is

$$\mu_{ij} = R^{e'e''}R^{v'v''}R^{J'M'J''M'} \quad . \tag{11}$$

The neglect of hyperfine interactions in the limit of large J is justified elsewhere [17].

The optical nutation signal following a step function laser frequency switching pulse is of the form

$$S_N(t) = be^{-\Gamma t}\sum_{M'M''}\chi_{ij}^2 J_o(\chi_{ij}t) \tag{12}$$

where b is a scaling factor, the Rabi frequency is given by (9), and J_o is the zero order Bessel function. We include, in contrast to previous treatments [7], the degeneracy in the rotational magnetic quantum number M_J, which is large in this case as J'=60. When (12) is fitted by computer techniques to the observed nutation signal, we obtain

$$R^{e'e''}R^{v'v''} = 0.150 \pm 0.003 \text{ Debye} \tag{13}$$

for the $^1\Sigma_g^+ \rightarrow B^3\Pi_{o^+u}$, (v,J)=(2,59)→(15,60) transition. The electronic matrix element

$$R^{e'e''} = 0.740 \pm 0.015 \text{ Debye} \tag{14}$$

since the calculated vibrational overlap integral $R^{v'v''}$=0.2028 [18]. Note that the uncertainty is 2% or less. The evaluation of (12) also reveals that the degeneracy does not wash out the nutation effect since the most intense transitions are weighted the most [17].

By invoking the vibrational sum rule $\sum_{v''}|R^{v'v''}|^2=1$ in (10), we can estimate the radiative decay rate as

$$\hat{\gamma} = 0.88\ \mu sec^{-1} . \tag{15}$$

This compares with the observed pressure-independent decay rate

$$\Gamma^r = 0.93\ \mu sec^{-1} . \tag{16}$$

Utilizing (2), we conclude that the spontaneous predissociation decay rate $\gamma_{sp}=0.05\ \mu sec^{-1}$ is indeed very small for the v'=15 level. This result compares favorably with a molecular beam fluorescence study [13] which gives the dependence of the spontaneous predissociation rate on the excited state vibrational quantum number where Γ_{sp} reaches a minimum and very small value at v'=14 and 15.

3. SUMMARY

The various inelastic and elastic I_2-I_2^* collision cross-sections σ can be derived from the corresponding decay rates Γ through the relation $\Gamma=N\sigma v$ where N is the molecular density, the relative velocity $v=\sqrt{8kT/\pi m}$, and m is the reduced mass for $^{127}I_2$. The results listed in Table I are given, however, in terms of the collision diameter squared, $D^2=\sigma/\pi$, to facilitate a comparison where possible with earlier work. We see that the inelastic collision rate Γ_e for electronic transitions is in excellent agreement with CHUTJIAN et al. [11]. The vibration-rotation rate Γ_{v-r} is similar in magnitude to that of STEINFELD et al. [12] but presumably differs because different transitions were excited, namely, 43'0", P(12) and R(14).

It is interesting that the elastic collision cross-section associated with Γ_ϕ, which has not been determined heretofore, dominates all other collision mechanisms. We expect that this process results from perturber-induced frequency shifts of the molecular superposition state over the brief duraction of a collision, but other mechanisms must be considered as well. It appears unlikely that elastic velocity-changing collisions occur as observed in infrared vibration-rotation transitions [19]. We find that FID signals of I_2 are exponential and do not display a cubic decay law $\exp(-Kt^3)$ at short times (~10 nsec) which would be symptomatic of a classical state-independent scattering. This is expected since collisions of electronically excited molecules in a superposition state will be state-dependent [20]. Collisional reorientation is another elastic collision process, and its importance at the present time is unknown and awaits further study.

Table I I_2-I_2^* Collision Diameter^2 ($\AA^2$)

	This work	Other work
inelastic		
electronic	70.5	70.0 [11]
vibration	40	10 [12]
rotation		36 [12]
elastic		
phase interruptions	145	

REFERENCES

1. A. A. Michelson, The Astrophysical Journal II, 251 (1895).

2. E. L. Hahn, Phys. Rev. 80, 580 (1950); Phys. Rev. 77, 297 (1950).

3. N. A. Kurnit, I. D. Abella, and S. R. Hartmann, Phys. Rev. Lett. 13, 567 (1964).

4. R. G. Brewer and A. Z. Genack, Phys. Rev. Lett. 36, 959 (1976).

5. A. Z. Genack, R. M. Macfarlane, and R. G. Brewer, Phys. Rev. Lett. 37, 1078 (1976).

6. R. G. DeVoe and R. G. Brewer, Phys. Rev. Lett. 40, 862 (1978).

7. R. G. Brewer in Frontiers in Laser Spectroscopy, (North Holland, 1977), p. 341, edited by R. Balian, S. Haroche, and S. Liberman.

8. R. G. Brewer in Physics Today 30, 50 (1977).

9. R. G. Brewer in NATO Advanced Study Institute on Coherence in Spectroscopy and Modern Physics (Plenum Press, in press), edited by F. T. Arecchi.

10. R. G. Brewer and R. L. Shoemaker, Phys. Rev. Lett. 27, 631 (1971).

11. A. Chutjian, J. K. Link, and L. Brewer, J. Chem. Phys. 46, 2666 (1967).

12. R. B. Kurzel, J. I. Steinfeld, D. A. Hatzenbuhler, and G. E. Leroi, J. Chem. Phys. 55, 4822 (1971).

13. J. Vigué, M. Broyer, and J. E. Lehmann, J. Phys. B: Atom. Molec. Phys. 10, L379 (1977).

14. J. Wei and J. Tellinghuisen, J. Mole. Spectrosc. 50, 317 (1974).

15. F. V. Kowalski, R. T. Hawkins, and A. L. Schawlow, J. Opt. Soc. Am. 66, 965 (1976).

16. A. Schenzle and R. G. Brewer, Phys. Rev. A14, 1756 (1976).

17. S. Kano and R. G. Brewer (to be published).

18. J. Tellinghuisen, J. Quant. Spectrosc. Radiat. Transfer 19, 149 (1978).

19. J. Schmidt, P. R. Berman and R. G. Brewer, Phys. Rev. Lett. 31, 1103 (1973); P. R. Berman, J. M. Levy, and R. G. Brewer, Phys. Rev. A11, 1668 (1975).

20. P. R. Berman, Applied Physics 6, 283 (1975).

RJ2637(33925)9/6/79
Physics

Appendix - Item 10

OPTICAL ROTARY ECHOES*

N. C. Wong†
Satoru S. Kano
Richard G. Brewer

IBM Research Laboratory
San Jose, California 95193

and

Department of Applied Physics
Stanford University
Stanford, California 94305

ABSTRACT: The first observation of optical rotary echoes, the optical analog of rotary spin echoes, is reported. Rotary echoes are produced in a quantum mechanical two-level system which is driven resonantly (nutation effect) by a coherent field that suffers a sudden phase retardation. The initial nutation transient dephases, due to an inhomogeneity either in the driving field or the transition frequency of the sample, and then rephases to form an echo following the phase shifting pulse. Hence, optical rotary and photon echoes are similar processes - the former being an interference in nutation and the latter an interference in free precession. Perturbative solutions of the Bloch equations are derived for the case where inhomogeneous dephasing arises from Doppler broadening and the Rabi frequency exceeds the homogeneous damping rate. Observations of the optical rotary echo in I_2 vapor are facilitated by the technique of laser frequency switching which generates precise phase shifts in the optical field. The measurements corroborate detailed theoretical predictions.

---

*Supported in part by the U.S. Office of Naval Research.

†Hertz Foundation Graduate Fellow.

I. INTRODUCTION

In 1959, Solomon[1] reported a new coherent transient effect in nuclear magnetic resonance (NMR), *rotary spin echoes*. While this phenomenon resembles the usual spin echo,[2] important differences exist which make it particularly useful in the measurement of long relaxation times. Whereas the spin echo is a manifestation of free induction decay[3] (FID) and appears in the absence of a driving field, the rotary echo is a manifestation of spin nutation[4] and appears in the presence of a driving field. In this article, we report observations and a theory of *optical rotary echoes* which are the optical analog of rotary spin echoes.

A Bloch vector model[5] description of rotary spin echoes (Fig. 1) provides a simple introduction to the subject. Consider a two-level spin system in the rotating frame where a static magnetic field H_0 lies along the z axis and a radio frequency field H_1 lies along the x axis. We presume for the moment, as Solomon did, that the inhomogeneity in H_1 is much larger than that in H_0 and thus determines the spin nutation decay rate. In other words, the distribution in the Rabi frequency is much larger than the static inhomogeneous broadening. Here and in the discussion which follows assume the rf pulse sequence shown in Fig. 2 where the rf frequency Ω', which is initially out of resonance with the spin system, comes into resonance at time t=0 due to the frequency switch $\Omega' \rightarrow \Omega$. This pulse causes a magnetization M, which is assumed to be directed along the -z axis at t=0, to precess in the yz plane about the x axis where the angle of precession in time T is $\theta=\gamma H_1 T$. For an inhomogeneous distribution in H_1,

the magnetization vectors will precess at different rates and thus through different angles θ causing them to get out of phase.

Now assume that at time t=T the rf frequency is switched out of resonance, $\Omega \rightarrow \Omega'$, for a duration τ so that the rf field suffers a phase change

$$\phi = (\Omega' - \Omega)\tau \ .$$

For the case $\phi=\pi$, the direction of H_1 in the rotating frame is reversed. At the end of the pulse at $t=T+\tau$, the switch $\Omega' \rightarrow \Omega$ brings the rf field back into resonance with the spins, and they begin to execute precessional motions about the x axis in the opposite direction but at the same rate as before. The phase interruption thus acts as a mirror which reflects the initial nutation signal backward in time. Therefore, at time $t=2T+\tau$ all magnetization vectors will appear in phase along the -z axis producing an echo. A computer plot of this dephasing-rephasing behavior (see Section II for details) is shown also in Fig. 2.

It will be evident from the above argument that an rf phase shift of $\phi=0$ or $\phi=2\pi$ will not affect the spins, and consequently, the echo amplitude will be zero. In general, we can see that the

$$\begin{aligned} &\text{echo amplitude = a maximum} , && \phi = \pi, 3\pi, 5\pi \ldots . \\ &\text{echo amplitude = 0} , && \phi = 0, 2\pi, 4\pi \ldots . \end{aligned} \qquad (1.1)$$

Solomon noted that for liquids the envelope function of a rotary echo will be characterized by an exponential decay rate α which is the average value of the longitudinal and transverse components,

$$\alpha = \frac{1}{2}\,(1/T_1+1/T_2)\ . \qquad (1.2)$$

Furthermore, using a multiple pulse sequence consisting of π phase shift pulses, he showed that dephasing arising from self-diffusion can be minimized and very long dephasing times measured because errors in the π phase shift pulses are not cumulative as in a Carr-Purcell[6] experiment.

The possibility of observing optical rotary echoes had been suggested by Nurmikko and Schwarz,[7] and such an effect has been detected recently in the microwave region by Rohart et al.[8] for a molecular rotational transition using the method of Stark switching.[9]

Optical rotary echoes are observed here for the visible transition of I_2 using laser frequency switching.[10] This technique is ideally suited for producing well defined phase shifts in a coherent light wave, making the observation of optical rotary echoes a simple matter. In contrast to earlier NMR[1] and microwave[7] studies, our measurements are performed in the low intensity regime where the Rabi frequency is much smaller than the Doppler linewidth. The nature of the solutions to the Bloch equations for both low and high intensity limits is derived for an inhomogeneously broadened optical transition subject to population decay and homogeneous dephasing processes. We shall see that essentially all of the

characteristics described above for NMR apply to the optical region as well.

II. THEORY

A. Equations of Motion

It is not immediately evident that the optical rotary echo is described by the same theoretical treatment which has been applied in NMR.[1,11] For example, at optical frequencies, inhomogeneous broadening is often the dominant line broadening mechanism, the transition levels do not constitute an isolated system, and spontaneous radiative decay is usually important. However, for spins, the lines are frequently homogeneously broadened, the transition levels usually form an isolated system, and spontaneous decay can be ignored. These differences have prompted us to carry out a detailed calculation using the Bloch equations.

We assume a two-level quantum system, having upper level $|2\rangle$ and lower level $|1\rangle$, which interacts with a resonant laser field

$$\vec{E}_x(z,t) = \vec{e}_x E_o \cos(\Omega t - kz) , \tag{2.1}$$

polarized in the x direction and propagating along the z axis. This field undergoes laser frequency switching with the pulse sequence shown in Fig. 2 and produces a rotary echo. We seek solutions[12,13] of the density matrix equations of motion

$$i\hbar \frac{\partial \rho}{\partial t} = [H,\rho] + \text{damping terms} \tag{2.2}$$

where the Hamiltonian

$$H = H_o + H'$$

consists of the free molecule term H_o and the electric dipole interaction

$$H' = -\vec{\mu} \cdot \vec{e}_x E_o \cos(\Omega t - kz) \ .$$

For an optically thin sample of length L, the transient signal field

$$E_{12}(z,t) = \tilde{E}_{12}(z,t) e^{i(\Omega t - kz)} + c.c. \tag{2.3}$$

obeys Maxwell's wave equation

$$\frac{\partial \tilde{E}_{12}}{\partial z} = -2\pi i k N \mu_{12} \langle \tilde{\rho}_{12} \rangle \tag{2.4}$$

where the tilde denotes the slowly varying part and N is the molecular number density. The polarization

$$\langle \tilde{p}(t) \rangle = N \mathrm{Tr} \langle \mu \tilde{\rho}(t) \rangle \tag{2.5}$$

is to be averaged over the inhomogeneous lineshape, which is a Gaussian in the case of Doppler broadening. The brackets in (2.4) and (2.5) denote this average.

We introduce the phenomenological decay rates γ_1 and γ_2 to account for population loss from states $|1\rangle$ and $|2\rangle$ which are assumed to be in contact with a thermal reservoir. The rate γ_{21} describes radiative decay for the transition $|2\rangle \rightarrow |1\rangle$, and γ is the dipole dephasing rate.

With the definition

$$\rho_{12}(z,t) = \tilde{\rho}_{12}(t)e^{i(\Omega t-kz)} , \tag{2.6}$$

and the neglect of nonresonant terms, the equations of motion (2.2) become

$$\begin{aligned}
\dot{\rho}_{11} &= \tfrac{1}{2} i\chi(\tilde{\rho}_{21}-\tilde{\rho}_{12}) - \gamma_1(\rho_{11}-\rho_{11}^{o}) + \gamma_{21}\rho_{22} \\
\dot{\rho}_{22} &= \tfrac{1}{2} i\chi(\tilde{\rho}_{12}-\tilde{\rho}_{21}) - \gamma_2\rho_{22} \\
\dot{\tilde{\rho}}_{12} &= \tfrac{1}{2} i\chi(\rho_{22}-\rho_{11}) + (-\gamma+i\Delta)\tilde{\rho}_{12} .
\end{aligned} \tag{2.7}$$

Here, the Rabi frequency χ, the tuning parameter Δ, and the eigenenergies E_i of the free molecule are given by

$$\chi \equiv \mu_{12}E_o/\hbar$$

$$\Delta \equiv -\Omega + kv_z + \omega_{21}$$

$$E_i \equiv \hbar\omega_i , \qquad i = 1,2$$

where kv_z is the Doppler shift and $\omega_{21}\equiv\omega_2-\omega_1$.

As noted previously,[13] Eqs. (2.7) are not solved readily as they involve four coupled equations in the variables ρ_{11}, ρ_{22}, ρ_{12} and ρ_{21}, and therefore, approximations are required. To make the problem tractable and yet retain the essential characteristics expected for optical rotary echoes, we restrict this discussion to two cases of damping

$$\begin{aligned}
&\text{(i)} \quad \gamma_1 = \gamma_2 , \qquad \gamma_{21} = 0 \\
&\text{(ii)} \quad \gamma_1 = 0 , \qquad \gamma_{21} = \gamma_2 .
\end{aligned} \tag{2.8}$$

s rephased and agrees well with the predicted value $t=2T+\tau=0.65$ μsec
ere the pulse delay time $T=0.310$ μsec and the pulse width $\tau=0.030$ μsec.

Preliminary studies of the rotary echo damping rate yield

$$\alpha = 0.63 + 0.051p \text{ (mTorr) } \mu\text{sec}^{-1} \tag{3.1}$$

ere p is the I_2 vapor pressure, but it remains difficult at present to
st the relation (2.37) or (2.39).

In Fig. 5, the rotary echo $\sin^2\phi/2$ dependence in (2.35) is tested by
rying the pulse width τ. For $\tau=20$ nsec and a laser frequency shift
$-\Omega')/2\pi=26.7$ MHz, the phase retardation of the laser field $\phi=1.07\pi$.
early, the echo shape function is a maximum for odd multiples of π and
ids to zero for even multiples of π as predicted. Note that the
companying photon echo which consists of small-amplitude, high-frequency
illations (26.7 MHz) clustered about $t=2T+\tau$ exhibits a different behavior
h pulse width, which is well known.

Finally, we have observed rotary (and photon) echoes, using a two-pulse
er frequency switching sequence (Fig. 6). Now the velocity packet which
excited resonantly in steady state for times $t<0$ experiences an initial
se interruption arising from the first pulse. This procedure merely
ablishes an initial condition which differs from that used in Eq. (2.23).
reafter the rotary echo problem is precisely the same as the above
atment.

The second velocity packet is resonant with the laser field for $t<0$. It becomes nonresonant at $t=0$ and exhibits FID. The switching pulse which commences at $t=T$ causes this packet to be excited resonantly and generates an FID or photon echo at $t=2T+\tau$ (Fig. 5).

Thus, the rotary and photon echoes precisely overlap in time. They can be distinguished, however, because the shape functions are different. The rotary echo looks like a damped sinusoid where the oscillation frequency is $\sim\chi$, the Rabi frequency, and the FID echo displays a beat signal where the beat frequency is the shift $\Omega-\Omega'$. In addition, the FID echo can be suppressed by reducing the pulse width τ as in Fig. 4. The rotary echo can be suppressed by selecting a phase interrupting pulse with $\phi=0,2\pi,4\pi,\ldots$ as in Fig. 5. Finally, by switching completely outside the Doppler linewidth,[17] either rotary or photon echoes could be observed alone.

We wish to emphasize that optical rotary echoes will occur simultaneously with photon echoes in Stark or laser frequency switching whenever the frequency shift is less than the inhomogeneous linewidth. This point was not realized in previous studies.[9,10]

Now consider some of the other characteristics of the rotary echo which are revealed in Fig. 4. First, the echo has the shape of a damped sinusoid which assumes a zero value at $t=0.66$ μsec and resembles the theoretical result Fig. 3. This crossing point identifies when the echo

The I_2 transition selected, $(v,J)=2,59\rightarrow 15,60$ of $X'\Sigma_g^+ \rightarrow B^3\pi_{o+u}$, falls in the visible region at 16,956.43 cm^{-1}, the wavelength being determined to $1/10^6$ or better by a digital wavemeter. The I_2 vapor is contained in an evacuated cell of 20cm length having a thermoelectrically refrigerated cold finger for regulating the I_2 vapor pressure. Except for self-broadening studies, a 30 mTorr I_2 vapor pressure was maintained. A 580A Spectra-Physics dye laser (Rhodamine 6G) delivered to the sample cell ~30mW in a collimated beam of 0.5mm diameter. A laser frequency shift $(\Omega-\Omega')/2\pi \sim 30$ MHz resulted when a 50V dc square wave pulse, from a Hewlett-Packard 214A generator, was applied to the intracavity AD*P phase modulator. Additional details can be found elsewhere.[10]

A typical optical rotary echo is presented in Fig. 4 and as we shall see confirms our expectations. However, additional characteristics not discussed yet require explanation. First note that the frequency switch $(\Omega-\Omega')/2\pi=30$ MHz is adequate for observing coherent transients since it far exceeds the homogeneous width of ~3 MHz. Since the shift is much smaller than the I_2 Doppler width of 500 MHz, there will always be two relevant velocity packets, one which is resonant and one which is nonresonant with the laser field. Each packet will generate its own set of coherent transients throughout the pulse sequence. For example, the rotary echo arises from a packet which is nonresonant with the laser field for times $t<0$ preceding the initial switch. This velocity group becomes resonant at $t=0$ when the frequency switch takes place, exhibits nutation, and thereafter produces the nutation or rotary echo in the fashion already described.

$$\alpha_2' = \left[\gamma\Delta^2 + \frac{1}{2}\left(\gamma + \frac{\gamma_1+\gamma_2+\gamma_{21}}{2}\right)\chi^2\right]\Big/\beta^2 \qquad (2.38)$$

Therefore, the echo damping rate (2.37) becomes

$$\alpha_2' \cong \frac{1}{2}\left(\gamma + \frac{\gamma_1+\gamma_2+\gamma_{21}}{2}\right). \qquad (2.39)$$

It is worth mentioning that rotary echoes arising either from an optical field inhomogeneity or a Doppler linebroadening inhomogeneity are not fundamentally different processes. This point is suggested in the effective Rabi frequency parameter

$$\beta = \sqrt{\chi^2+\Delta^2}$$

where the Rabi frequency and the tuning parameter appear on an equal footing. Hence, we expect that a distribution in either χ or Δ will lead to the same transient behavior, which the above analysis shows.

III. DETECTION OF ROTARY ECHOES

Rotary echoes are observed by the method of laser frequency switching.[10] A cw dye laser is frequency-switched by an intracavity electro-optic phase modulator, an x-cut ammonium dideuterium phosphate crystal (AD*P) that is driven by a dc voltage pulse generator. The beam of this laser passes through a sample of I_2 vapor before striking a P-I-N diode photodetector (HP 5082-4227) where the transient signals are monitored with a 7904 Tektronix sampling oscilloscope and thereafter are displayed on an X-Y recorder.

A numerical calculation of the integral in (2.35) is shown in Fig. 3 which exhibits a damped Rabi oscillation with the expected crossing at the time origin. Numerical values of the parameters are given in the caption of Fig. 3. To understand the damping behavior first note that the $1/\beta^3$ factor is sharply peaked about $\Delta=0$ so that the principal part of the integral arises from the low frequency components. This observation suggests the approximation

$$\alpha_2 \cong \frac{1}{2}(\gamma+\gamma_2) \ . \qquad (2.37)$$

When (2.37) is included in (2.35), the dashed curve of Fig. 3 results. The close agreement in the two curves, particularly at long times, supports the approximation (2.37) which we now see is a valid description of the damping rate.

Notice that the damping rate (2.37) applies also in the strong field limit, the NMR case,[1] where

$$\chi^2 >> (k\omega)^2 \ .$$

This can be seen without numerical integration as α_2 reduces to Eq. (2.37) immediately. Therefore, our results yield the same decay rate as Eq. (1.2) which is the original result derived by Solomon for NMR.

If we relax the restriction (2.8), we are still able to obtain the echo damping rate for arbitrary γ_1, γ_2, γ_{21}, and γ. Employing the perturbative method as described in Section II.B, again assuming $\chi >> \gamma_1, \gamma_2, \gamma_{21}, \gamma$, Eq. (2.18) is replaced by

1. $\chi >> \gamma, \gamma_2$
2. $\Delta\tau << 1$ and $\gamma\tau << 1$
3. $\Omega = \omega_{21}$.

D. Characteristics

Before considering the Doppler integral in (2.35), which must be handled numerically, certain properties of (2.35) can be identified immediately. First, the factor $e^{i\phi}$ merely indicates that the signal field is retarded in phase to the same extent that the driving field (2.26) is.

The $\sin^2\phi/2$ factor in (2.35) supports (1.1) by revealing that the echo amplitude

$$\tilde{E}^e_{12} = \text{a maximum} , \qquad \phi = \pi, 3\pi, 5\pi, \ldots\ldots$$

$$\tilde{E}^e_{12} = 0 , \qquad \phi = 0, 2\pi, 4\pi, \ldots\ldots \tag{2.36}$$

Hence, the echo amplitude can be precisely controlled by adjusting the phase retardation ϕ. This precision is not ordinarily available with photon echoes,[16] unless $\chi >> ku$, as the laser field radial profile is Gaussian and hence the optical pulse area assumes a continuous distribution of values. Furthermore, for a rotary echo each transition of a degenerate set will experience the same phase shift, independent of the distribution of transition matrix elements.[7]

The $\sin\beta(t-2T-\tau)$ term of the integral shows that the echo appears at time $t=2T+\tau$, at which point the signal vanishes, $\tilde{E}^e_{12}(t=2T+\tau)=0$.

Now recall that the echo field amplitude in a sample of length L is given by (2.3)-(2.5),

$$\tilde{E}^e_{12}(L,t) = -2\pi ikNL\mu_{12}\langle\tilde{\rho}^e_{12}(t)\rangle \tag{2.32}$$

where the Doppler integral

$$\langle\tilde{\rho}^e_{12}(t)\rangle = \frac{1}{ku\sqrt{\pi}}\int_{-\infty}^{\infty}\tilde{\rho}^e_{12}(t)e^{-(\Delta/ku)^2}d\Delta\ , \tag{2.33}$$

u being the most probable molecular velocity. Expressing $\tilde{\rho}^e_{12}(t)$ in terms of (2.31), we find

$$\tilde{\rho}^e_{12}(t) = \frac{e^{i\phi}}{2}\left[u'_e(t)+iv'_e(t)\right]\ ,$$

and the echo amplitude is

$$\tilde{E}^e_{12}(L,t) = \frac{\sqrt{\pi}}{u}NL\mu_{12}e^{i\phi}w(0)\chi^3e^{-\gamma\tau}\left[\sin^2\phi/2+\frac{1}{2}\left(e^{(\gamma-\gamma_2)\tau}-1\right)\right]$$
$$\times\int_{-\infty}^{\infty}\frac{\sin\beta(t-2T-\tau)}{\beta^3}e^{-\alpha_2(t-\tau)}e^{-(\Delta/ku)^2}d\Delta\ . \tag{2.34}$$

Since the phase shifting pulse can be sufficiently brief that the decay will be insignificant, we can set $\gamma\tau<<1$ to obtain a slight simplification in (2.34). The final result is

$$\tilde{E}^e_{12}(L,t) = \frac{\sqrt{\pi}}{u}NL\mu_{12}e^{i\phi}w(0)\chi^3\sin^2\phi/2$$
$$\times\int_{-\infty}^{\infty}\frac{\sin\beta(t-2T-\tau)}{\beta^3}e^{-\alpha_2t}e^{-(\Delta/ku)^2}d\Delta\ , \tag{2.35}$$

where

$$\alpha_2 = [\gamma\Delta^2+\frac{1}{2}(\gamma+\gamma_2)\chi^2]/\beta^2\ .$$

It may be useful at this point to recall the assumptions and conditions which apply in obtaining (2.35), namely,

$$v'_e(t) = e^{-\alpha_2(t-T-\tau)}\left(u'(T+\tau)\,\frac{\Delta}{\beta}\sin\beta(t-T-\tau)\right.$$
$$+ v'(T+\tau)\cos\beta(t-T-\tau)$$
$$\left.+ w(T+\tau)\,\frac{\chi}{\beta}\sin\beta(t-T-\tau)\right) \qquad (2.29)$$

where the index e denotes "echo." It is apparent from (2.29) that we require the terms

$$u'(T+\tau) = \frac{1}{2}\left(u(T)+iv(T)\right)e^{-i\phi-\gamma\tau} + c.c.$$
$$v'(T+\tau) = \frac{i}{2}\left(u(T)-iv(T)\right)e^{i\phi-\gamma\tau} + c.c.\,, \qquad (2.30)$$

which are easily derived from the definitions (2.11) using the transformation (2.28) and with the aid of (2.24).

A further simplification results if we allow the initial laser frequency to match the Doppler line center,

$$\Omega = \omega_{21}\,.$$

This condition causes the echo terms which are odd in the tuning parameter Δ to vanish upon integration of the echo signal over the Doppler lineshape.

Inclusion of (2.23), (2.24) and (2.30) in (2.29) produces the resulting echo terms

$$u'_e(t) = 0$$
$$v'_e(t) = w(0)\,\frac{\chi^3}{\beta^3}\sin\beta(t-2T-\tau)e^{-\alpha_2(t-\tau)-\gamma\tau}$$
$$\times\left[\sin^2\phi/2 + \frac{1}{2}\left(e^{(\gamma-\gamma_2)\tau}-1\right)\right]\,, \qquad (2.31)$$

which we see assume a remarkably simple form.

For the sake of simplicity, we have introduced in (2.24) the approximation

$$\Delta\tau << 1 \ , \tag{2.25}$$

which will apply for sufficiently brief pulses.

At $t=T+\tau$, the laser field has now acquired the phase shift (2.22), and therefore, for $t>T+\tau$ it is necessary to replace (2.1) by

$$\vec{E}_x(z,t) = \vec{e}_x E_o \cos(\Omega t+\phi-kz) \ . \tag{2.26}$$

The equations of motion and the solutions are of the same form as (2.10) and (2.20) when we replace (2.6) by

$$\rho_{12}(z,t) = \tilde{\rho}'_{12}(t)e^{i(\Omega t+\phi-kz)} \ . \tag{2.27}$$

Thus, in the new representation, each off-diagonal density matrix element is transformed according to

$$\tilde{\rho}'_{12}(t) = \tilde{\rho}_{12}(t)e^{-i\phi} \ . \tag{2.28}$$

For times $t>2T+\tau$, we retain only those terms in (2.20) that rephase at $t=2T+\tau$, i.e., echo terms are retained. The solutions now take the form

$$u'_e(t) = e^{-\alpha_2(t-T-\tau)}\left(u'(T+\tau)\,\frac{\Delta^2}{\beta^2}\cos\beta(t-T-\tau)\right.$$
$$-v'(T+\tau)\,\frac{\Delta}{\beta}\sin\beta(t-T-\tau)$$
$$\left.+\,w(T+\tau)\,\frac{\Delta\chi}{\beta^2}\cos\beta(t-T-\tau)\right)$$

$$\tilde{\rho}_{12}(t) = \frac{1}{2}\,[u(t)+iv(t)] \tag{2.21}$$

in accordance with the laser frequency switching pulse sequence of Fig. 2. To reiterate, at time t=0 the laser field is suddenly switched from $\Omega' \rightarrow \Omega$, thereby exciting a group of molecules which exhibits damped Rabi oscillations. The excitation is interrupted over the interval $T<t<T+\tau$ due to the switch $\Omega \rightarrow \Omega'$, which introduces in time τ a phase shift

$$\phi = (\Omega'-\Omega)\tau \tag{2.22}$$

in the laser field. Rabi oscillations resume following the phase shift, and the rotary echo appears at time $t=2T+\tau$.

Beginning at time t=0, the initial conditions u(0)=0, v(0)=0, w(0)=-1 and w^o=-1 allow us to evaluate (2.20) at t=T, namely,

$$\begin{aligned}
u(T) &= w^o \frac{\gamma_2 \Delta\chi}{\alpha_1 \beta^2}\,(e^{-\alpha_1 t}-1) + w(0)\,\frac{\Delta\chi}{\beta^2}\,(e^{-\alpha_2 T}\cos\beta T - e^{-\alpha_1 T}) \\
v(T) &= w(0)\,\frac{\chi}{\beta}\,e^{\alpha_2 T}\sin\beta T \\
w(T) &= w^o \frac{\gamma_2 \Delta^2}{\alpha_1 \beta^2}\,(1-e^{-\alpha_1 T}) + w(0)\left(\frac{\Delta^2}{\beta^2}\,e^{-\alpha_1 T} + \frac{\chi^2}{\beta^2}\,e^{-\alpha_2 T}\cos\beta T\right) .
\end{aligned} \tag{2.23}$$

During the phase interruption pulse, FID solutions follow from (2.20) by letting χ=0. At $t=T+\tau$, we have

$$\begin{aligned}
u(T+\tau) &= u(T)e^{-\gamma\tau} \\
v(T+\tau) &= v(T)e^{-\gamma\tau} \\
w(T+\tau) &= w^o(1-e^{-\gamma_2\tau}) + w(T)e^{-\gamma_2\tau} .
\end{aligned} \tag{2.24}$$

Application of the inverse Laplace transformation

$$\rho(t) = \frac{1}{2\pi i}\int_{-i\infty+r}^{i\infty+r} e^{zt}\rho(z)dz \tag{2.19}$$

to (2.13) using the roots (2.17) yields the time-dependent behavior

$$\begin{aligned}
u(t) &= u(0)\left(\frac{\chi^2}{\beta^2}\, e^{-\alpha_1 t} + \frac{\Delta^2}{\beta^2}\, e^{-\alpha_2 t}\cos\beta t\right) - v(0)\,\frac{\Delta}{\beta}\, e^{-\alpha_2 t}\sin\beta t \\
&\quad + w(0)\,\frac{\Delta\chi}{\beta^2}\left(-e^{-\alpha_1 t} + e^{-\alpha_2 t}\cos\beta t\right) + w^o\,\frac{\gamma_2\Delta\chi}{\alpha_1\beta^2}\left(e^{-\alpha_1 t} - 1\right), \\
v(t) &= u(0)\,\frac{\Delta}{\beta}\, e^{-\alpha_2 t}\sin\beta t + v(0)e^{-\alpha_2 t}\cos\beta t \\
&\quad + w(0)\,\frac{\chi}{\beta}\, e^{-\alpha_2 t}\sin\beta t \\
&\quad + w^o\left(\frac{\gamma\gamma_2\chi}{\alpha_1\beta^2} + \frac{(\alpha_1-\gamma)\gamma_2\chi}{\alpha_1\beta^2}\, e^{-\alpha_1 t} - \frac{\gamma_2\chi}{\beta^2}\, e^{-\alpha_2 t}\cos\beta t\right), \\
w(t) &= u(0)\,\frac{\Delta\chi}{\beta^2}\left(-e^{-\alpha_1 t} + e^{-\alpha_2 t}\cos\beta t\right) - v(0)\,\frac{\chi}{\beta}\, e^{-\alpha_2 t}\sin\beta t \\
&\quad + w(0)\left(\frac{\Delta^2}{\beta^2}\, e^{-\alpha_1 t} + \frac{\chi^2}{\beta^2}\, e^{-\alpha_2 t}\cos\beta t\right) \\
&\quad + w^o\left(\frac{\gamma_2\Delta^2}{\alpha_1\beta^2}\left(1 - e^{-\alpha_1 t}\right) + \frac{\gamma_2\chi^2}{\beta^3}\, e^{-\alpha_2 t}\sin\beta t\right).
\end{aligned} \tag{2.20}$$

Here, we have consistently retained the leading terms in u(0), v(0), w(0) and w^o. Note that these solutions apply to optical nutation[14] or optical free induction decay[15] (with χ=0), providing the above approximations are satisfied, and constitute the principal result of this section.

C. Rotary Echoes

Armed with the solutions (2.20), it is a straightforward task to trace the evolution of the density matrix element

This condition means that many nutation cycles will appear in a dephasing time, and of course is a desirable case for monitoring optical rotary echoes. Setting $\gamma=\gamma_2=0$ in (2.14), we find the zeroth-order solutions

$$z_1^{(0)} = 0$$

$$z_{2,3}^{(0)} = \pm i\beta \tag{2.16}$$

where the effective Rabi frequency

$$\beta = \sqrt{\chi^2+\Delta^2} \ .$$

To first-order in γ/β, the first-order solutions are

$$z_1^{(1)} = -\alpha_1$$

$$z_2^{(1)} = i\beta - \alpha_2$$

$$z_3^{(1)} = z_2^{(1)*} \tag{2.17}$$

where

$$\alpha_1 \equiv (\gamma_2\Delta^2+\gamma\chi^2)/\beta^2$$

$$\alpha_2 \equiv [\gamma\Delta^2+ \tfrac{1}{2} (\gamma+\gamma_2)\chi^2]/\beta^2 \ . \tag{2.18}$$

These roots are obtained by equating first-order terms in (2.14) with corresponding terms in the approximate relation

$$D(z) \cong (z-z_1^{(1)})(z-z_2^{(1)})(z-z_3^{(1)}) \ .$$

$$\rho(z) = \int_0^\infty \rho(t) e^{-zt} dt$$

$$z\rho(z) - \rho(0) = \int_0^\infty \dot{\rho}(t) e^{-zt} dt$$

where $\rho(0)$ is the value at t=0. The transformed equations of (2.10) in matrix form read

$$\begin{pmatrix} z+\gamma & \Delta & 0 \\ -\Delta & z+\gamma & -\chi \\ 0 & \chi & z+\gamma_2 \end{pmatrix} \begin{pmatrix} u(z) \\ v(z) \\ w(z) \end{pmatrix} = \begin{pmatrix} u(0) \\ v(0) \\ w(0)+\frac{\gamma_2}{z} w^o \end{pmatrix} . \tag{2.12}$$

The inversion of (2.12) yields the solution

$$\begin{pmatrix} u(z) \\ v(z) \\ w(z) \end{pmatrix} = \frac{1}{D(z)} \begin{pmatrix} (z+\gamma)(z+\gamma_2)+\chi^2 & -\Delta(z+\gamma_2) & -\Delta\chi \\ \Delta(z+\gamma_2) & (z+\gamma)(z+\gamma_2) & \chi(z+\gamma) \\ -\Delta\chi & -\chi(z+\gamma) & (z+\gamma)^2+\Delta^2 \end{pmatrix} \begin{pmatrix} u(0) \\ v(0) \\ w(0)+\frac{\gamma_2}{z} w^o \end{pmatrix} \tag{2.13}$$

where the matrix determinant

$$D(z) = (z+\gamma_2)\left[(z+\gamma)^2+\Delta^2\right] + (z+\gamma)\chi^2 . \tag{2.14}$$

The solution to D(z)=0, which is a third order equation in z gives the three poles of the transformation needed to obtain u, v, and w. Rather than seek an exact solution to (2.14), which would be unnecessarily complex, we invoke the reasonable approximation that

$$\chi >> \gamma, \gamma_2 . \tag{2.15}$$

The first case corresponds to infrared molecular transitions where radiative decay can be neglected, and the second to atomic ultraviolet transitions where only a few decay channels exist. For both cases, there are only two decay parameters

$$\gamma_2 = 1/T_1$$

$$\gamma = 1/T_2 \ , \tag{2.9}$$

making it possible to express (2.7) in terms of the Bloch equations

$$\dot{u} + \Delta v + \gamma u = 0$$

$$\dot{v} - \Delta u - \chi w + \gamma v = 0$$

$$\dot{w} + \gamma_2(w-w^o) + \chi v = 0 \ . \tag{2.10}$$

In (2.10), we have defined

$$u \equiv \tilde{\rho}_{12} + \tilde{\rho}_{21} \ ,$$

$$v \equiv i(\tilde{\rho}_{21} - \tilde{\rho}_{12}) \ ,$$

$$w = \rho_{22} - \rho_{11} \ , \tag{2.11}$$

and $w^o \equiv \rho^o_{22} - \rho^o_{11}$ is the population difference at thermal equilibrium in the absence of the laser field.

B. Perturbative Solutions

Solutions of Eqs. (2.10) are facilitated by application of the Laplace transform[4,13]

REFERENCES

1. I. Solomon, Phys. Rev. Lett. 2, 301 (1959).

2. E. L. Hahn, Phys. Rev. 80, 580 (1950).

3. E. L. Hahn, Phys. Rev. 77, 297 (1950).

4. H. C. Torrey, Phys. Rev. 76, 1059 (1949).

5. F. Bloch, Phys. Rev. 70, 460 (1946).

6. H. Y. Carr and E. M. Purcell, Phys. Rev. 94, 630 (1954).

7. A. V. Nurmikko and S. E. Schwarz, Optics Comm. 2, 416 (1971).

8. F. Rohart, P. Glorieux and B. Macke, J. Phys. B: Atom. Molec. Phys. 10, 3835 (1977).

9. R. G. Brewer and R. L. Shoemaker, Phys. Rev. Lett. A6, 2001 (1972).

10. R. G. Brewer and A. Z. Genack, Phys. Rev. Lett. 36, 959 (1976); A. Z. Genack and R. G. Brewer, Phys. Rev. A17, 1463 (1978).

11. A. Abragam, The Principles of Nuclear Magnetism (Oxford, London, 1961).

12. R. G. Brewer in Frontiers in Laser Spectroscopy (North-Holland, Amsterdam, 1977) edited by R. Balian, S. Haroche and S. Liberman, p. 342.

13. A. Schenzle and R. G. Brewer, Phys. Rev. A14, 1756 (1976).

14. G. B. Hocker and C. L. Tang, Phys. Rev. Lett. 21, 591 (1968); C. L. Tang and B. D. Silverman in Physics of Quantum Electronics, eds. P. Kelley, B. Lax and P. E. Tannenwald (McGraw-Hill, New York, 1966), p. 280.

15. R. G. Brewer and R. L. Shoemaker, Phys. Rev. A6, 2001 (1972).

16. N. A. Kurnit, I. D. Abella and S. R. Hartmann, Phys. Rev. Lett. 13, 567 (1964); I. D. Abella, N. A. Kurnit and S. R. Hartmann, Phys. Rev. 141, 391 (1966).

17. R. G. DeVoe and R. G. Brewer, Phys. Rev. Lett. 40, 862 (1978).

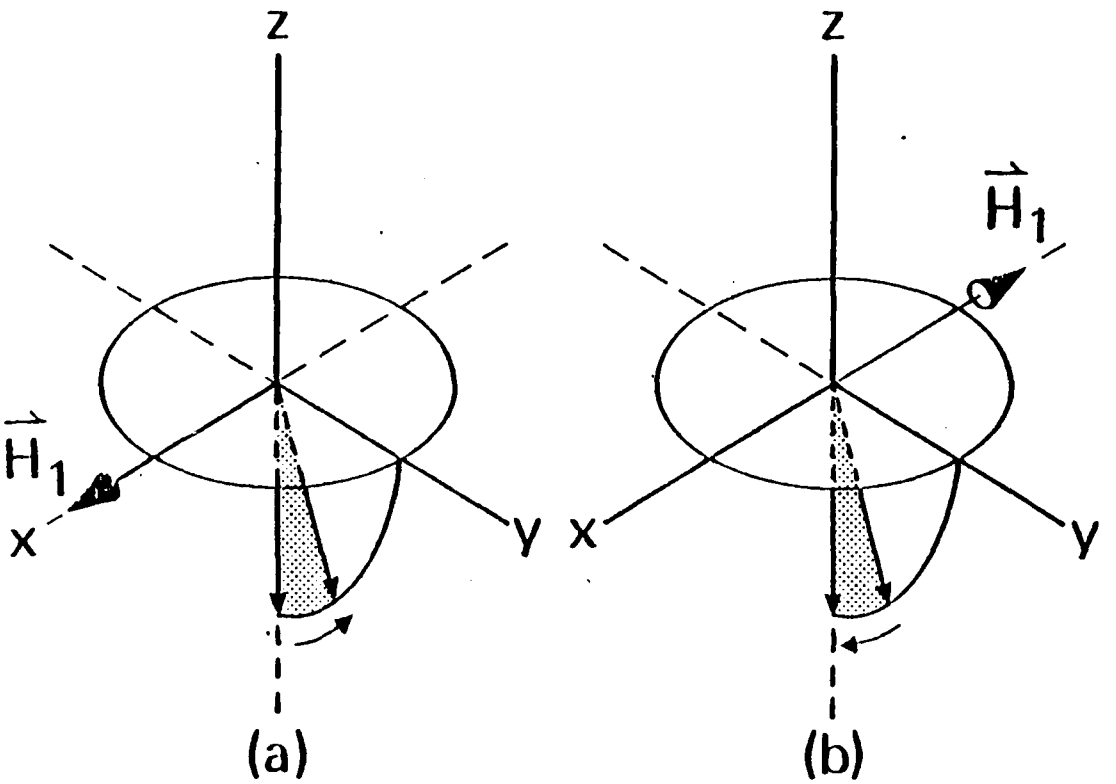


Figure 1. Bloch vector description of rotary echoes showing evolution of magnetization vectors M before and after the phase interruption. (a) The M vectors nutate at different rates in the initial direction and dephase. (b) After the $\vec{H}_1$ field reverses its direction, the M vectors nutate at the same rates as before but in the opposite direction and rephase to form an echo.

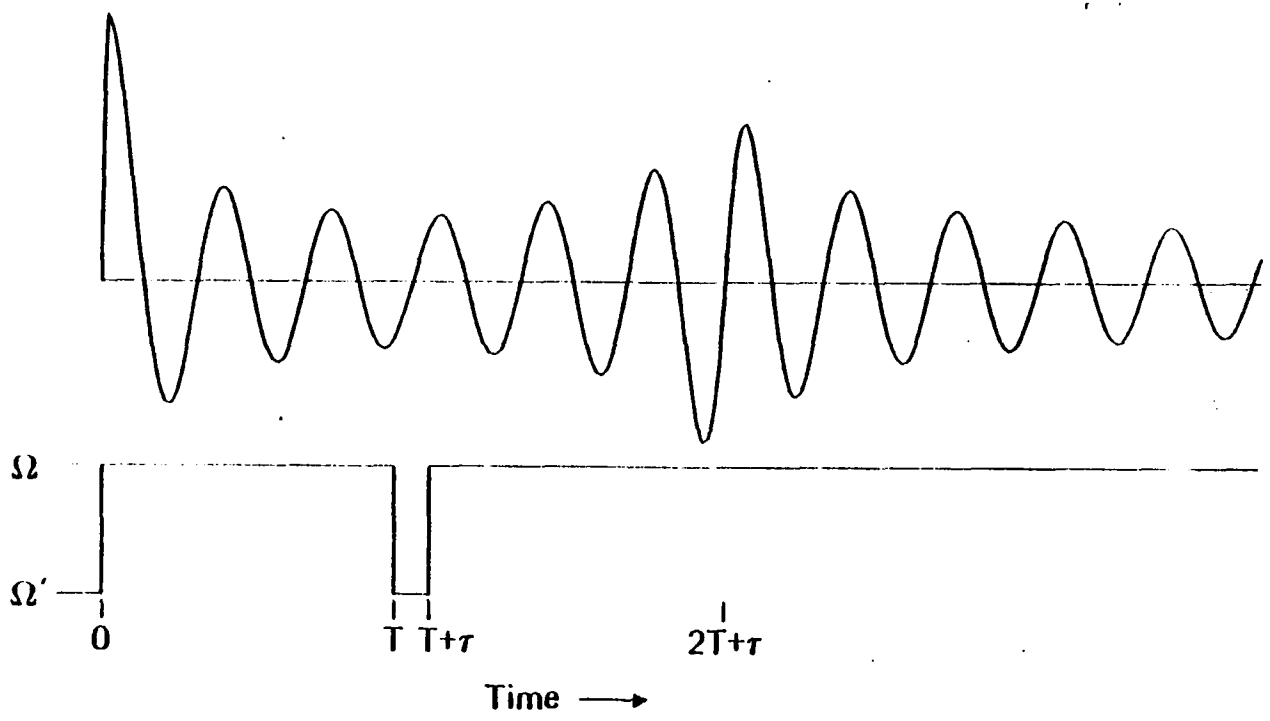


Figure 2. *Lower curve*: laser frequency switching pulse sequence for rotary echoes. *Upper curve*: computer plot of the transient response showing the nutation signal and the rotary echo formed at t=2T+τ.

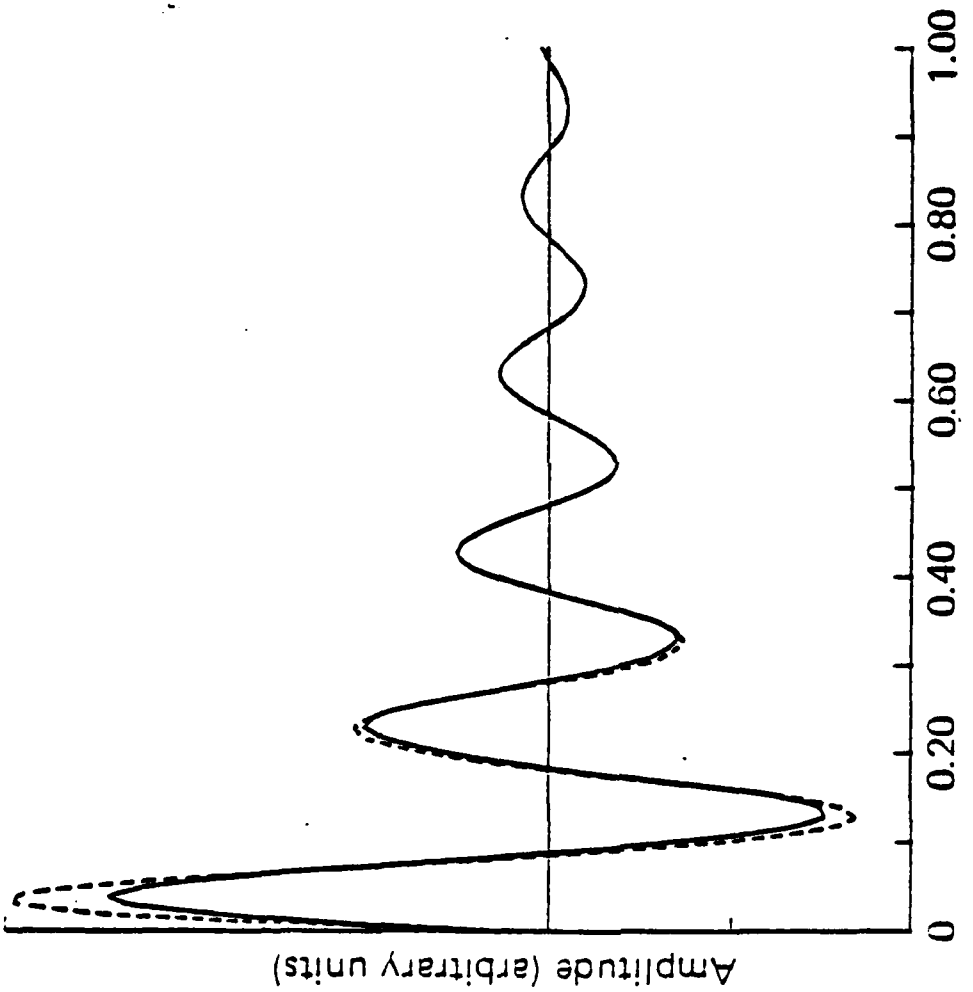


Figure 3. The solid line is a computer plot of the rotary echo solution of Eq. (2.35), while the dashed line is one of the same solution using the approximation Eq. (2.37) with $\kappa/2\pi$=500 MHz, $\chi/2\pi$=5 MHz, γ=3 μs^{-1}, γ_2=2 μs^{-1}, T=1μs, and $\phi=\pi$.

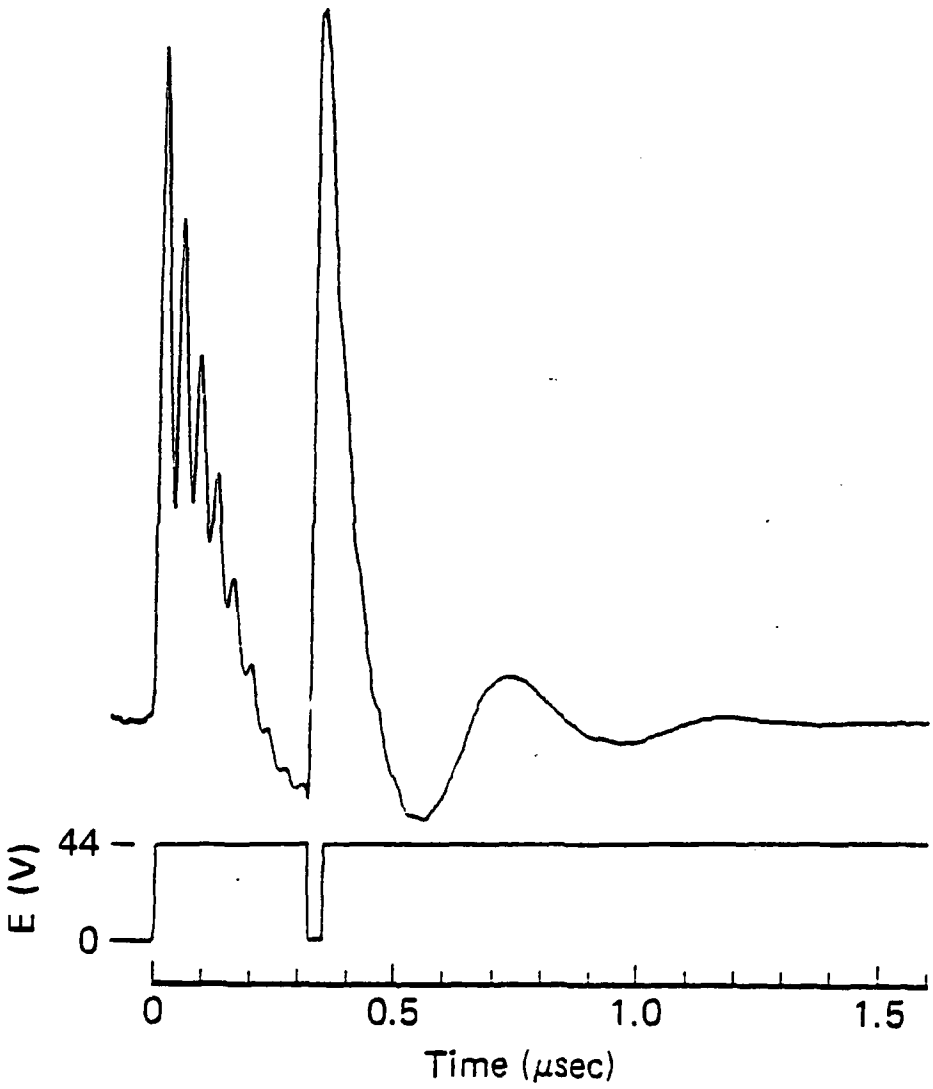


Figure 4. *Lower curve*: dc voltage pulse sequence. *Upper curve*: optical transient response of I_2 where the arrow marks the rephasing point of the rotary echo.

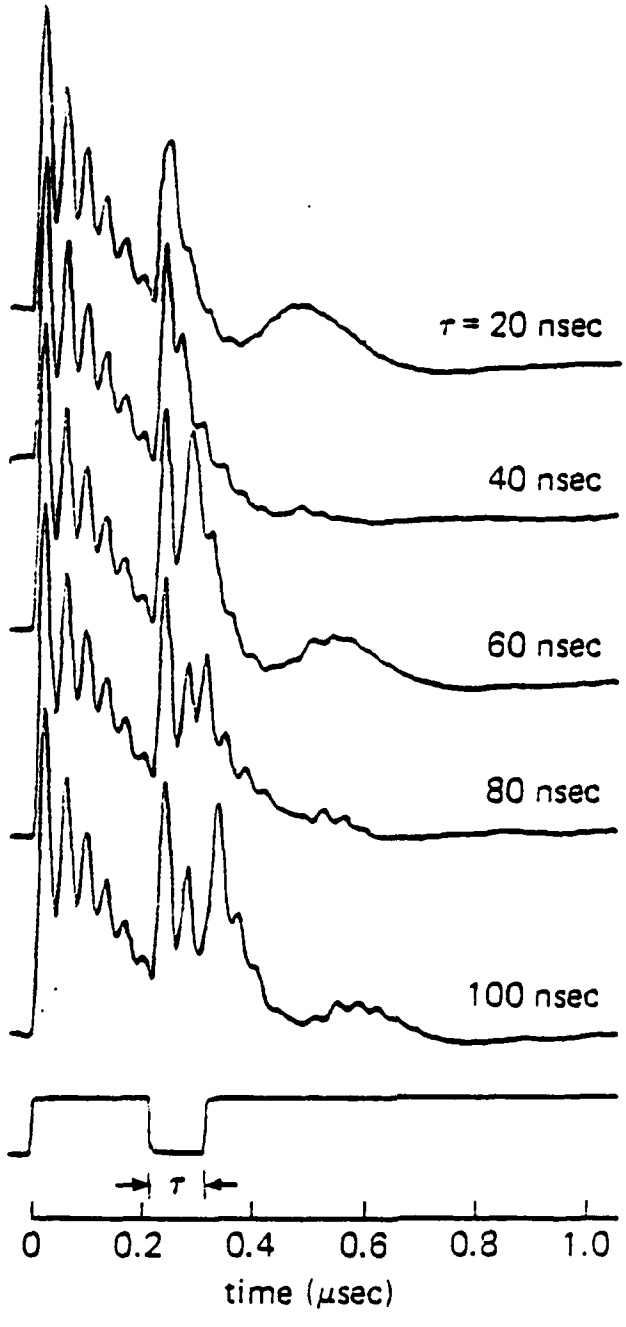


Figure 5. Dependence of the rotary echo amplitude on pulse width τ. These measurements support the $\sin^2(\phi/2)$ dependence of Eq. (2.35) where τ=20ns and a frequency shift of 26.7 MHz correspond to $\phi=1.07\pi$.

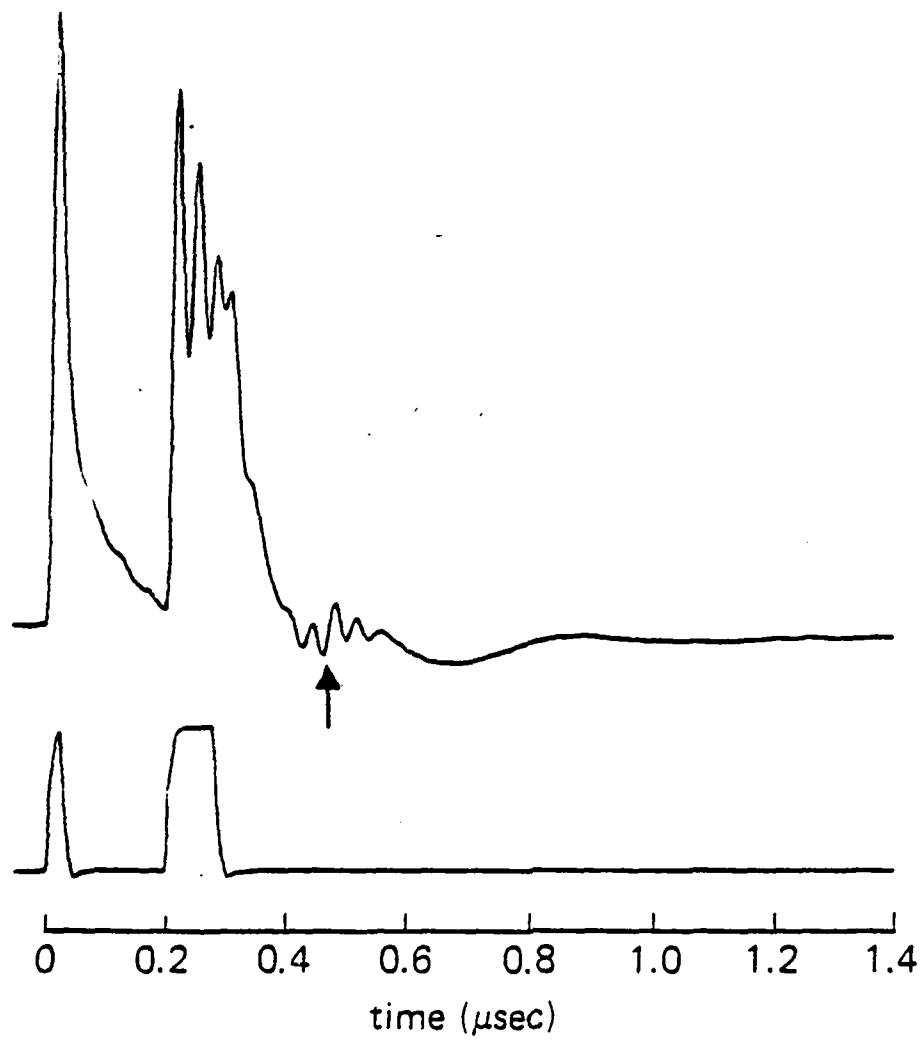


Figure 6. *Lower curve*: dc voltage pulse sequence for two-pulse echo. *Upper curve*: optical rotary and photon echoes superimposed where the arrow marks the rephasing point.

RJ2700(34595)11/30/79
Physics

Appendix - Item 11

OSCILLATORY FREE INDUCTION DECAY*

Axel Schenzle†
N. C. Wong‡
Richard G. Brewer

IBM Research Laboratory
San Jose, California 95193

and

Department of Applied Physics
Stanford University
Stanford, California 94305

ABSTRACT: Large amplitude oscillations are predicted in the free induction decay (FID) of atomic or spin two-level quantum systems that are coherently prepared by a resonant electromagnetic field in the form of a square amplitude pulse of duration T. The effect should be detectable in nuclear magnetic resonance (NMR) or in optical resonance experiments when the transition lineshape is inhomogeneously broadened ($T_2^* \ll T_2$) and the applied field is intense so that the pulse area $\chi T \geq 2\pi$, where χ is the Rabi frequency. Physically, the effect is due to Rabi oscillations which are generated in the preparative stage and are then reproduced because of atomic memory in the radiative period which follows. The atomic polarization derived from the Bloch equations assumes the form of an integral over the inhomogeneous lineshape, and can be evaluated numerically for arbitrary linewidth σ or analytically when $\sigma \to \infty$. The characteristics of the oscillation are unusual since the oscillation frequency, which is of order χ, increases with time while the oscillation envelope vanishes identically for times $t \geq 2T$. Coherent emission is confined therefore to one pulse width T immediately following the pulse. Previous NMR and infrared FID experiments with small area pulses ($\chi T \leq 4\pi$), interpreted erroneously in terms of an *edge echo* effect, support the oscillatory FID behavior described here. For the case $\chi T > 4\pi$, an experimental test would be even more decisive as the oscillations are more pronounced.

---

*Supported in part by the U.S. Office of Naval Research

†On leave from the Department of Physics, Universität Essen, Gesamthochschule, Essen, West Germany

‡Hertz Foundation Graduate Fellow

I. INTRODUCTION

In this article, we predict a novel oscillatory behavior which appears in the free induction decay (FID) effect and should be observable in inhomogeneously broadened transitions, either in nuclear magnetic resonance (NMR) or in optical resonance experiments. We assume a set of two-level quantum systems which are coherently prepared by a resonant driving field in the form of a square amplitude pulse of duration T. See Fig. 1. The transition lineshape is dominated by inhomogeneous broadening so that the inhomogeneous dephasing time T_2^* and the dipole dephasing time T_2 satisfy the inequality

$$T_2 >> T_2^* . \tag{1.1}$$

Following the pulse, FID occurs where the decay is smoothly varying for low field amplitudes. However, as the field intensity increases, we find that the decay exhibits a continuous train of large amplitude oscillations (Figs. 2 and 3) which have not been discussed heretofore. Oscillations appear when the pulse area satisfies

$$\chi T \geq 2\pi , \tag{1.2}$$

and in first approximation, the oscillation frequency is the Rabi frequency χ. We also show that the FID signal is exactly zero for times $t \geq 2T$, as in Figs. 2 and 3. These and other characteristics are considered further in the theoretical analysis which follows.

Oscillatory FID, therefore, differs significantly from previous observations[1-8] of FID in the optical region. In the earlier optical

studies, the sample is prepared under steady-state conditions by a cw laser beam, rather than by a pulse, and FID results when the transition frequency or the laser frequency is suddenly switched. The initial transient is dominated by the first order FID,[2,7] which is a Gaussian $e^{-(t/T_2^*)^2}$ that decays rapidly in a time T_2^*. The nonlinear FID survives the first order component by displaying a long-lived exponential signal S which, apart from unimportant factors, is of the form[1,9]

$$S \sim \left(\frac{1}{\sqrt{\chi^2 T_1 T_2+1}} - 1\right) e^{-t/T_2\left(1+\sqrt{\chi^2 T_1 T_2+1}\right)} . \qquad (1.3)$$

In this case, an increase in laser intensity only produces power broadening through the χ^2 term in the exponent, but no frequency shift and thus no oscillations. Of course, in the low power limit ($\chi^2 T_1 T_2 \ll 1$), the dephasing time is $T_2/2$ corresponding to preparation of a single homogeneous packet.

Oscillatory FID of this kind is not observed normally in NMR either. Because spin transitions often are homogeneously broadened, on-resonance pulse preparation can only yield FID signals which decay monotonically as e^{-t/T_2}, while off-resonance preparation produces oscillations but they have a different origin.[10] Furthermore, the oscillations described here have nothing to do with quantum[11] or Raman beats[12] in coupled multilevel quantum systems or with NMR interferences in the FID of two or more independent two-level transitions.

However, in 1955, Bloom[13] reported observations of interference effects in FID for the case when the static magnetic field is highly inhomogeneous

and the pulse area, $\chi T \sim 4\pi$, is relatively small. We believe that these interferences, which Bloom gave the name *edge echoes*, are not an echo phenomenon, but rather are an example of oscillatory FID. This paper clarifies the subject by providing the first detailed theoretical treatment of oscillatory FID.

II. THEORETICAL MODEL

A. Basic Equations

We shall adopt a model and the mathematical language commonly used in quantum optics,[14,15] namely, an atomic two-level quantum system which interacts for the period T with a resonant laser field

$$E_x(z,t) = E_o \cos(\Omega t - kz) \ . \tag{2.1}$$

The polarization and propagation directions are x and z, respectively. The upper quantum state is $|2\rangle$ and the lower $|1\rangle$. We assume that the field is turned on at t=0 and off at t=T. Equivalently, we could have also assumed a laser frequency switching[3,6] pulse as the solutions are virtually identical.

For times t>T following the pulse, the FID field

$$E_{12}(z,t) = \tilde{E}_{12}(z,t) e^{i(\Omega t - kz)} + \text{c.c.} \tag{2.2}$$

satisfies Maxwell's wave equation

$$\frac{\partial \tilde{E}_{12}}{\partial z} = -2\pi i k N \mu_{12} \langle \tilde{\rho}_{12} \rangle \tag{2.3}$$

or an optically thin sample. Here, N is the atomic number density, μ_{12} s the transition matrix element and the tilde denotes the slowly varying art. Hence, the problem reduces to one of calculating the polarization

$$\langle\tilde{p}(t)\rangle = N\mathrm{Tr}\langle\mu\tilde{\rho}(t)\rangle \tag{2.4}$$

here the off-diagonal density matrix element $\tilde{\rho}_{12}$ is to be averaged denoted by a bracket) over the inhomogeneous Doppler lineshape. We herefore seek solutions of the Bloch equations

$$\begin{aligned}
\dot{u} + \Delta v + u/T_2 &= 0 \ , \\
\dot{v} - \Delta u - \chi w + v/T_2 &= 0 \ , \\
\dot{w} + \chi v + (w-w^o)/T_1 &= 0 \ ,
\end{aligned} \tag{2.5}$$

here

$$\begin{aligned}
u &= \tilde{\rho}_{12} + \tilde{\rho}_{21} \ , \\
v &= i(\tilde{\rho}_{21}-\tilde{\rho}_{12}) \ , \\
w &= \rho_{22} - \rho_{11} \ .
\end{aligned} \tag{2.6}$$

he tuning parameter Δ, the Rabi frequency χ and the eigenenergies E_i are iven by

$$\begin{aligned}
\Delta &= -\Omega + kv_z + \omega_{21} \\
\chi &= \mu_{12}E_o/\hbar \\
E_i &= \hbar\omega_i \ , \qquad i = 1,2
\end{aligned} \tag{2.7}$$

ere kv_z is the Doppler shift and $\omega_{21}\equiv\omega_2-\omega_1$.

To avoid unnecessary complications, we assume that (1) the population
d dipole dephasing rates are equal, (2) the Rabi frequency is much larger
an the dipole dephasing rate, and (3) the laser frequency is tuned to
e transition line center, i.e.,

$$\gamma \equiv 1/T_1 = 1/T_2 \ , \tag{2.8}$$

$$\chi^2 >> \gamma^2 \ , \tag{2.9}$$

$$\Omega = \omega_{21} \ . \tag{2.10}$$

th the approximation (2.8) and the initial conditions v(t=0)=u(0)=0 and
0)=w^o, the solutions of (2.5) are

$$v(t) = \frac{\chi w(0) e^{-\gamma t}}{\chi^2+\Delta^2+\gamma^2} \left[-\gamma\cos\beta t+\beta\sin\beta t+\gamma e^{\gamma t}\right] ,$$

$$u(t) = \frac{\Delta\chi w(0) e^{-\gamma t}}{\chi^2+\Delta^2+\gamma^2} \left[\frac{\gamma\sin\beta t}{\beta} + \cos\beta t - e^{\gamma t}\right] . \tag{2.11}$$

uations (2.11) will be required when damping is to be included, but for
e present purpose, we invoke (2.9) and obtain the relevant solutions
r pulse preparation at time t=T,

$$v(T) = \chi w(0) e^{-\gamma t} \frac{\sin\beta T}{\beta}$$

$$u(T) = \frac{\Delta\chi w(0)}{\beta^2} \left(e^{-\gamma T}\cos\beta T - 1\right) \tag{2.12}$$

ere

$$\beta = \sqrt{\Delta^2+\chi^2} \ .$$

In the next stage t>T, χ=0 and the FID solutions of (2.5) apply,

$$u(t) = [u(T)\cos\Delta(t-T)-v(T)\sin\Delta(t-T)]e^{-\gamma(t-T)}$$

$$v(t) = [u(T)\sin\Delta(t-T)+v(T)\cos\Delta(t-T)]e^{-\gamma(t-T)} \quad . \qquad (2.13)$$

Inserting Eq. (2.12) into Eq. (2.13), we obtain the desired result t>T,

$$v(t) = \chi w(0)e^{-\gamma t}\left[\frac{\Delta}{\beta^2}(\cos\beta T-e^{\gamma T})\sin\Delta(t-T) + \frac{\sin\beta T}{\beta}\cos\Delta(t-T)\right] . \qquad (2.14)$$

dispersive term u(t) is not needed as it vanishes with Doppler gration due to its odd order dependence in Δ and the assumption (2.10).

The FID signal (2.2) therefore involves the Doppler integral I where

$$N\langle\tilde{\rho}_{12}(t)\rangle = \frac{i}{2}\int_{-\infty}^{\infty} g(\Delta)v(t)d\Delta \equiv \frac{i}{2} I(t) \quad , \qquad (2.15)$$

inhomogeneous lineshape function

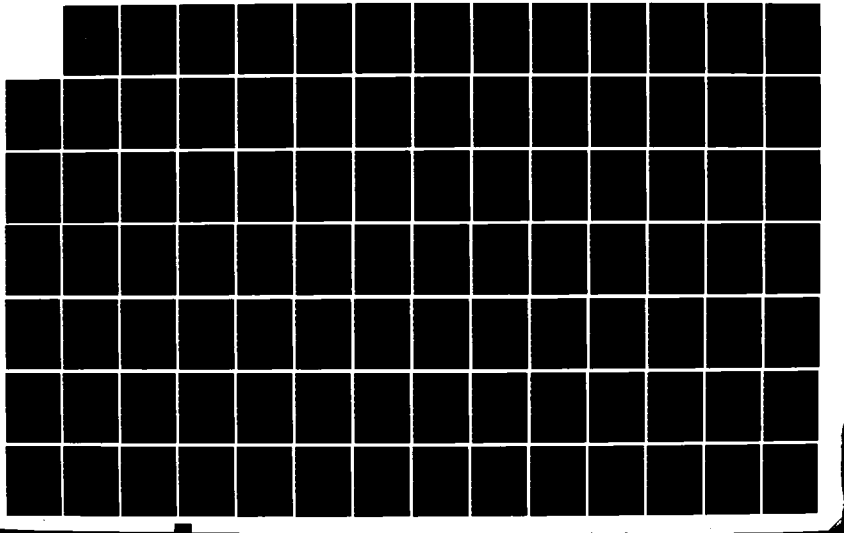
$$g(\Delta) = \frac{N}{\sqrt{\pi}\sigma} e^{-(\Delta/\sigma)^2} \quad , \qquad (2.16)$$

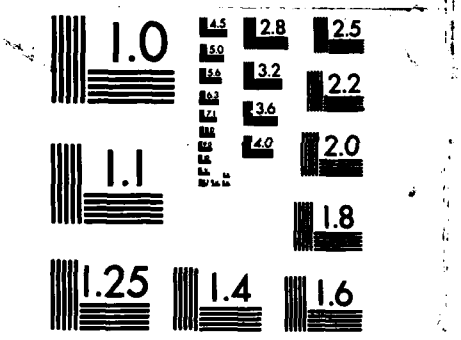
the Doppler width is σ.

The major challenge of this paper is the evaluation of the integral 5). Analytic results are not anticipated because of the Gaussian term ie integrand, and furthermore, the square root $\beta=\sqrt{\Delta^2+\chi^2}$ can introduce

AD-A154 708 NONLINEAR SPECTROSCOPY(U) IBM RESEARCH LAB SAN JOSE CA 3/6
R G BREWER 20 MAR 85 N00014-78-C-0246

UNCLASSIFIED F/G 20/6 NL





MICROCOPY RESOLUTION TEST CHART
NATIONAL BUREAU OF STANDARDS-1963-A

a branch cut in the complex plane which is troublesome. In Section IIB, (2.15) is evaluated by direct numerical integration and allows a preliminary understanding of the nature of oscillatory FID. The remaining sections uncover analytic results in the limit of an infinite Doppler linewidth ($\sigma \to \infty$), and give a more detailed and complete description of the phenomena involved. In Section IIIA, certain limiting cases are derived using a Laplace transform method. In Section IIIB, a general analytic expression of compact form is found by transforming the integral (2.15) to a differential equation.

B. Numerical Results

Figures 2 and 3 are computer plots of the normalized FID amplitude, E_{12}/χ, as a function of time (t-T) and for different pulse areas χT. The solid curves result from direct numerical integration of (2.15), while the dashed curves overlayed are analytic results of Section IIIB and will be discussed later.

The following values of parameters were assumed: $\sigma = 50\pi$ μsec^{-1}, T=1 μsec and $\gamma = 0$, and hence the desired inequalities $\sigma > \chi > 1/T > \gamma$ were maintained. Consideration is given in Section IIIA to the case $\gamma \neq 0$. Obviously, other time scales apply to these curves when an appropriate change is made in the time-frequency units. We find that about $100\sigma T$ integration points are needed to attain the required accuracy for the Doppler integration.

The first characteristic to notice in Figs. 2 and 3 is the initial fast rise beginning at t=T which appears on all solid curves. This is

the first order free induction decay effect which has been observed[7] and analyzed theoratically[2,7] for the case of steady-state preparation. For both pulse and steady-state preparation, the rise time is given by $T_2^*\equiv 2/\sigma$. The Doppler lineshape, being of finite width, allows the FID signal to rise smoothly from its initial value at t=T. In the limit of infinite Doppler width, the signal is discontinuous at t=T, as found in previous FID derivations[1,2,9] such as Eq. (1.3).

For times $(t-T)>T_2^*$, the decay is more slowly varying and exhibits oscillations which are clearly evident in Figs. 2 and 3 for pulse areas $\chi T\geq 2\pi$. Notice in particular the curve for $\chi T=4\pi$ as it closely resembles Bloom's NMR free decay[13] (his Fig. 4 where $\chi T\cong 4\pi$) in shape, the number of oscillations, and its vanishing at t=2T. We believe this observation strongly supports our calculation. However, the term *edge echo* coined by Bloom is inappropriate as the effect is not an echo phenomenon.

As the pulse area increases further, the number of oscillations increases, the number of periods being given by $\sim\chi T/2\pi$. Thus, for $\chi T=10\pi$, there are 5 periods where the last wiggle being of small amplitude is better seen on an expanded scale. These curves and the analysis of Section III show that in each case the last wiggle always approaches the time axis as $(2T-t)^2$ and from the positive direction as $t\to 2T$.

Another feature is that the oscillation frequency, while of order χ, is not constant but increases steadily with time. The envelope function

of these oscillations obeys approximately a linear time dependence such that the amplitude vanishes precisely at time t=2T. This remarkable behavior is an exact and general result which can be demonstrated by very general theoretical arguments and will be presented elsewhere.[16] An earlier optical FID measurement,[1] where $\chi T=1.5\pi$ corroborates this point and otherwise resembles the $\chi T=1.5\pi$ curve of Fig. 2.

Physical Interpretation

As a first approximation, we can say that during the preparative stage the driving field creates Rabi sidebands and thus new frequency components which would be observed in a spectrum of the sample. Following the pulse, the polarization retains memory of its preparation and produces a time-dependent signal which is the Fourier transform of this spectrum, and hence, oscillations will appear at the Rabi frequency. Of course, this picture neglects the mutual interference of packets distributed throughout the inhomogeneous lineshape.

We can summarize this section, perhaps in an oversimplified manner, by pointing out that there are three parameters (σ, χ and T) which characterize the temporal response of the atomic sample. The Doppler width σ gives rise to the initial rapid first order FID; the Rabi frequency χ determines the frequency of oscillation; and the pulse width T establishes when the free induction signal vanishes.

III. ANALYTIC RESULTS

A. Laplace Transform Method

1. Case $\gamma=0$

We now evaluate the Doppler integral I(t) defined in (2.15) using (2.14) for v(t) in the case $\gamma=0$. We apply the Laplace transform technique[17,18] because it yields the characteristic behavior for certain limiting cases very quickly. The case $\gamma\neq 0$ will be treated below as well. In the limit of infinite Doppler width ($\sigma\to\infty$), $e^{-(\Delta/\sigma)^2}\to 1$ while the spectral density N/σ is constant, and

$$I(t) = \chi w(0)g(0)\left\{\int_{-\infty}^{\infty}\frac{\sin\beta T}{\beta}\cos\Delta(t-T)d\Delta\right.$$

$$\left.+\int_{-\infty}^{\infty}\frac{\Delta}{\beta^2}\cos\beta T\sin\Delta(t-T)d\Delta-\int_{-\infty}^{\infty}\frac{\Delta}{\beta^2}\sin\Delta(t-T)d\Delta\right\},\quad t>T\ . \tag{3.1}$$

We identify the three integrals in the order given by

$$I(t) = \chi w(0)g(0)[F_1(t)+F_2(t)+F_3(t)]\ , \tag{3.2}$$

and perform the Laplace transform

$$F(z) = \int_0^{\infty}F(T)e^{-zT}dT \equiv \mathscr{L}F(T) \tag{3.3}$$

in the variables z and T with the quantity t-T held fixed. This operation yields

$$F_1(z) = \frac{\pi}{\sqrt{z^2+\chi^2}}\,e^{-\sqrt{z^2+\chi^2}\,(t-T)}\ , \tag{3.4}$$

$$F_2(z) = \frac{\pi}{z}\left(e^{-\chi(t-T)} - e^{-\sqrt{z^2+\chi^2}(t-T)}\right) , \tag{3.5}$$

$$F_3(z) = -\frac{\pi}{z} e^{-\chi(t-T)} . \tag{3.6}$$

Note that two of the terms cancel in the sum

$$I(z) = \chi w(0)g(0)\left[F_1(z)+F_2(z)+F_3(z)\right]$$

$$= -\pi\chi w(0)g(0)\frac{G(z)}{z} \tag{3.7}$$

where

$$G(z) = \left(1-\frac{z}{\sqrt{z^2+\chi^2}}\right) e^{-\sqrt{z^2+\chi^2}(t-T)} . \tag{3.8}$$

Recognizing that the inverse Laplace transform of (3.7) is given by

$$\mathscr{L}^{-1}\frac{G(z)}{z} = \int_0^T G(T')dT' , \tag{3.9}$$

we need

$$\mathscr{L}^{-1}G(z) = G(T)$$

$$= \begin{cases} 0 & 0<T<t-T \quad (3.10a) \\ \chi\left(\frac{T-(t-T)}{T+(t-T)}\right)^{1/2} J_1\left(\chi\sqrt{T^2-(t-T)^2}\right) , & T>t-T \quad (3.10b) \end{cases}$$

where this transformation is tabulated.[19] Combining (3.7)-(3.10), the integrals in (3.1) assume the compact form

$$I(t) = \begin{cases} 0 & t>2T \quad (3.11a) \\ -\pi w(0)g(0)\chi^2 \int_{t-T}^{T}\left[\frac{s-(t-T)}{s+(t-T)}\right]^{1/2} J_1\left(\chi\sqrt{s^2-(t-T)^2}\right)ds, & T<t<2T . \quad (3.11b) \end{cases}$$

Notice the interesting result (3.11a) which states that for times t>2T, coherent emission is identically zero. Stated otherwise, when a two-level

quantum system is coherently prepared in the interval $0<t<T$, it radiates coherently only in the interval $T<t<2T$. We have shown elsewhere[16] that this result is true under very general conditions, a theoretical result which apparently has gone unnoticed in NMR and quantum optics.

Limiting Cases

In order to see how the solution (3.11b) connects to the solutions for $t<T$ and $t>2T$, we consider the following limiting cases.

$t \to T$: In this limit, (3.11b) is given by

$$I(t \to T) = \pi w(0) g(0) \chi (J_0(\chi T) - 1) \ . \tag{3.12}$$

Since $J_0(\chi T)$ is the transient nutation amplitude at the end of the pulse, we recognize that the -1 term signifies a discontinuity at $t=T$ which we attribute to the first order FID for the case of infinite Doppler width. Additional attention is given below to first order FID when the Doppler width is finite.

$t \to 2T$: In this regime, since the argument α of the Bessel function[20] $J_1(\alpha)$ remains small throughout the range of integration,

$$J_1(\alpha) \sim \alpha/2 \ ,$$

and

$$I(t \to 2T) = - \frac{\pi}{4} w(0) g(0) \chi^3 (2T-t)^2 \ . \tag{3.13}$$

Because $w(0)=-1$, the FID signal approaches a zero value from the positive direction with a quadratic dependence in the time difference $(2T-t)$, independent of χT. Thus, $I(t)$ and its first derivative are continuous at

t=2T and exhibit no unusual characteristics such as an edge echo. Note that the numerical results of Section IIIB are verified therefore. In this connection, one should compare Bloom's[13] Fig. 4 for the case of a single pulse (which resembles our Fig. 3 for $\chi T=4\pi$) and his Fig. 5 for the case of a closely spaced multiple pulse train which produces a sharp interference near t=2T. The multiple pulse train is an entirely different situation from the single pulse calculations discussed in this paper.

First Order FID

To investigate the first order FID, also notice that the only term in (3.1) which possesses a singularity at t=T is $F_3(t)$. For the case of finite σ, we write

$$F_3'(t) = -\chi w(0) \int_{-\infty}^{\infty} g(\Delta) \frac{\Delta}{\beta^2} \sin\Delta(t-T) d\Delta \ . \tag{3.14}$$

For a Lorentzian inhomogeneous lineshape

$$g(\Delta) = N \frac{\sigma}{\pi} \frac{1}{\Delta^2+\sigma^2} \ , \tag{3.15}$$

instead of the Gaussian (2.16), we obtain an analytic expression in terms of elementary functions

$$F_3'(t) = -N \frac{\chi w(0)\sigma}{\sigma^2-\chi^2} \left(e^{-\chi(t-T)} - e^{-\sigma(t-T)}\right)$$

$$\sim \pi\chi |w(0)| g(0) e^{-\chi(t-T)} \left(1-e^{-\sigma(t-T)}\right) \ , \tag{3.16}$$

where the second line applies when $\sigma >> \chi$. Thus, immediately following the end of the pulse the FID signal rises rapidly but smoothly in a time $1/\sigma \sim T_2^*$, reaches a maximum at $(t-T)_{max} = 1/\sigma \ln(\sigma/\chi)$, and then decays in a time $1/\chi$

prior to going into oscillation. The initial fast rise is the first order FID[2,7] (which corresponds to the discontinuity at t=T in (3.12) and (1.3) when $\sigma\to\infty$) and is readily seen in all of the numerical results of Figs. 2 and 3 where a Gaussian lineshape of finite width σ is utilized.

2. Case $\gamma\neq 0$

To include damping in the above derivations, it is necessary to begin with the more general solutions (2.11) in place of (2.12). The calculation then proceeds as before to yield

$$I(t) = \begin{cases} 0 & t>2T \\ -\pi w(0)g(0)\chi^2 e^{-\gamma(t-T)}\displaystyle\int_{t-T}^{T}\left(\frac{s-(t-T)}{s+(t-T)}\right)^{1/2} J_1\left(\chi\sqrt{s^2-(t-T)^2}\right)e^{-\gamma s}ds\,, & T<t<2T\,. \end{cases} \tag{3.17}$$

Apart from damping factors, (3.17) maintains the same form as (3.11).

Limiting Cases

Infinite pulse width ($T\to\infty$): As the pulse width T increases, the solutions must approach the case of steady-state preparation.[1,2,7,9] This limit can be tested using (3.17), in contrast to (3.11), because damping is needed to restore the population during continuous excitation. The integral (3.17) can be written as

$$\tau\int_1^\infty\left(\frac{y-1}{y+1}\right)^{1/2} J_1\left(\chi\tau\sqrt{y^2-1}\right)e^{-\gamma y\tau}dy \tag{3.18}$$

and becomes analytic[21] as $T\to\infty$, where $\tau\equiv t-T$ remains finite and $y\equiv s/\tau$. The result is

$$I(t) = \pi w(0)g(0)\chi\left(\frac{1}{\sqrt{(\chi/\gamma)^2+1}} - 1\right)e^{-\gamma\left(1+\sqrt{(\chi/\gamma)^2+1}\right)(t-T)} , \qquad (3.19)$$

which we see agrees with earlier steady-state derivations such as Eq. (1.3).[1,2,7,9]

t→T: Equation (3.17) reduces in this instance to

$$I(t\to T) \sim \pi w(0)g(0)\chi(J_0(\chi T)-1)e^{-\gamma T} \qquad (3.20)$$

where for simplicity we have assumed that $\gamma\to 0$. As expected, (3.20) agrees with (3.12).

t→2T: In this regime, (3.17) becomes

$$I(t\to 2T) = -\frac{\pi}{4} w(0)g(0)\chi^3 e^{-\gamma T}(2T-t)^2 , \qquad (3.21)$$

and corresponds to the no damping case (3.13).

B. Differential Equation Method

In this section, we again evaluate the Doppler integral expression I(t) given in (3.1) assuming $\sigma\to\infty$ and $\gamma=0$. The derivation is more lengthy than the Laplace transform method, but it is also more instructive and reduces to a compact analytical form which is exact. For this purpose, the integral form of I(t) is transformed by differentiation with respect to the variable T and yields the second order differential equation

$$\frac{d^2I}{dT^2} - \chi^2 I = \left\langle \frac{2\chi^3}{\beta} \sin\beta T\cos\Delta(t-T) - \Delta\chi\sin\Delta(t-T) \right\rangle , \qquad (3.22)$$

where the bracket denotes a Doppler average and we have set w(0)=-1 throughout. The observation time t is treated as a constant.

We now show that

$$\frac{d^2I}{dT^2} - \chi^2 I = 0 , \qquad t>2T \qquad (3.23a)$$

$$\frac{d^2I}{dT^2} - \chi^2 I = 2\pi g(0)\chi^3 J_0\left(\chi\sqrt{t(2T-t)}\right) , \qquad T<t<2T . \qquad (3.23b)$$

Equation (3.23a) follows when a Lorentzian inhomogeneous lineshape (3.15)

$$g(\Delta) = g(0)\,\frac{\sigma^2}{\Delta^2+\sigma^2}$$

is substituted for the Gaussian (2.16) as then the integrals[21] in (3.22) are analytic and vanish in the limit $\sigma\to\infty$. Thus, we have

$$\left\langle \frac{2\chi^3}{\beta}\sin\beta T\cos\Delta(t-T)\right\rangle$$

$$= 2\pi g(0)\chi^3\,\frac{\sigma e^{-\sigma(t-T)}}{\sqrt{\sigma^2-\chi^2}}\sinh\sqrt{\sigma^2-\chi^2}\;T , \qquad t>2T$$

$$\to 0 \text{ as } \sigma\to\infty , \qquad (3.25)$$

and

$$\langle -\Delta\chi\sin\Delta(t-T)\rangle = -\pi g(0)\chi\sigma^2 e^{-\sigma(t-T)} , \qquad t>T$$

$$\to 0 \text{ as } \sigma\to\infty , \qquad (3.26)$$

where the initial conditions are

$$I(T=0) = 0$$

$$\frac{dI(T=0)}{dT} = \langle -\chi\cos\Delta t\rangle = -\pi g(0)\chi\sigma e^{-\sigma t}$$

$$\to 0 \text{ as } \sigma\to\infty \text{ for } t>0 . \qquad (3.27)$$

Thus, (3.23a) is derived. On the other hand, (3.23b) follows from (3.26) and

$$\left\langle \frac{2\chi^3}{\beta} \sin\beta T \cos\Delta(t-T) \right\rangle$$

$$= 2\pi g(0)\chi^3 J_0\left[\chi\sqrt{t(2T-t)}\right], \qquad T<t<2T \tag{3.28}$$

where g(0) has been factored outside the integral to enable its evaluation.

From (3.23a) and the initial conditions (3.27), we obtain the same result as (3.11a),

$$I(t) = 0, \qquad t>2T. \tag{3.29}$$

Therefore, the FID signal lasts as long as the pulse width itself and vanishes for t>2T.

Notice that the integrals (3.25) and (3.26) decay rapidly, as in first order FID, because of the $e^{-\sigma(t-T)}$ factor. In contrast to first order FID at the beginning of the pulse (Section IIIA), its amplitude is extremely small and is not evident in the numerical results of Figs. 2 and 3 where a finite Doppler width is assumed. Clearly, the use of a Lorentzian lineshape in place of a Gaussian does not change these arguments as $\sigma\to\infty$.

We now attempt to find the general solution of (3.23b)

$$I(\chi,t,T) = I_H(T) + I_p(T), \qquad T<t<2T \tag{3.30}$$

where the homogeneous solution is of the form

$$I_H(T) = Ae^{\chi T} + Be^{-\chi T}, \tag{3.31}$$

and a particular solution, using the method of variation of parameters,[22] is

$$I_p(T) = \pi g(0)\chi^2\left[\int_0^T e^{\chi(T-T')} J_0\left(\chi\sqrt{t(2T'-t)}\right) dT' - \int_0^T e^{-\chi(T-T')} J_0\left(\chi\sqrt{t(2T'-t)}\right) dT'\right] . \qquad (3.32)$$

Equation (3.32) can be written as

$$I_p(T) = 2\pi \frac{g(0)}{t} \int_0^z \sinh\left(\frac{z^2-z'^2}{2\chi t}\right) z' J_0(z') dz' \qquad (3.33)$$

where

$$z = \chi\sqrt{t(2T-t)} .$$

In the Appendix, we show that (3.33) reduces simply to a sum of even order Bessel functions

$$I_p(T) = 2\pi g(0)\chi \sum_{m=1}^{\infty} \left(\frac{z}{\chi t}\right)^{2m} J_{2m}(z) . \qquad (3.34)$$

Equation (3.34) and its derivative

$$\frac{dI_p}{dT} = 2\pi g(0)\chi \sum_{m=1}^{\infty} \left(\frac{z}{\chi t}\right)^{2m} J_{2m-1}(z) , \qquad (3.35)$$

yield the initial conditions

$$I_p(0) = \frac{dI_p(0)}{dT} = 0 . \qquad (3.36)$$

When (3.36) and (3.27) are combined, it follows that $I_H(T) \equiv 0$ and the solution (3.30) is

RJ2816(35962)5/7/80
Physics

Appendix - Item 12

THEOREM ON COHERENT TRANSIENTS*

Axel Schenzle†
N. C. Wong‡
Richard G. Brewer

IBM Research Laboratory
San Jose, California 95193

and

Department of Applied Physics
Stanford University
Stanford, California 94305

ABSTRACT: A fundamental theorem in NMR and quantum optics is derived for an atomic system subject to inhomogeneous broadening and coherent preparation by a pulsed electromagnetic field of arbitrary shape. We show that the coherent emission, free induction decay or echo, which follows is confined to an interval which precisely equals the duration of the applied pulse sequence. The theorem applies to two or multi-level transitions.

---

*Supported in part by the U.S. Office of Naval Research.

†On leave from the Department of Physics, Universität Essen, Gesamthochschule, Essen, West Germany.

‡Hertz Foundation Graduate Fellow.

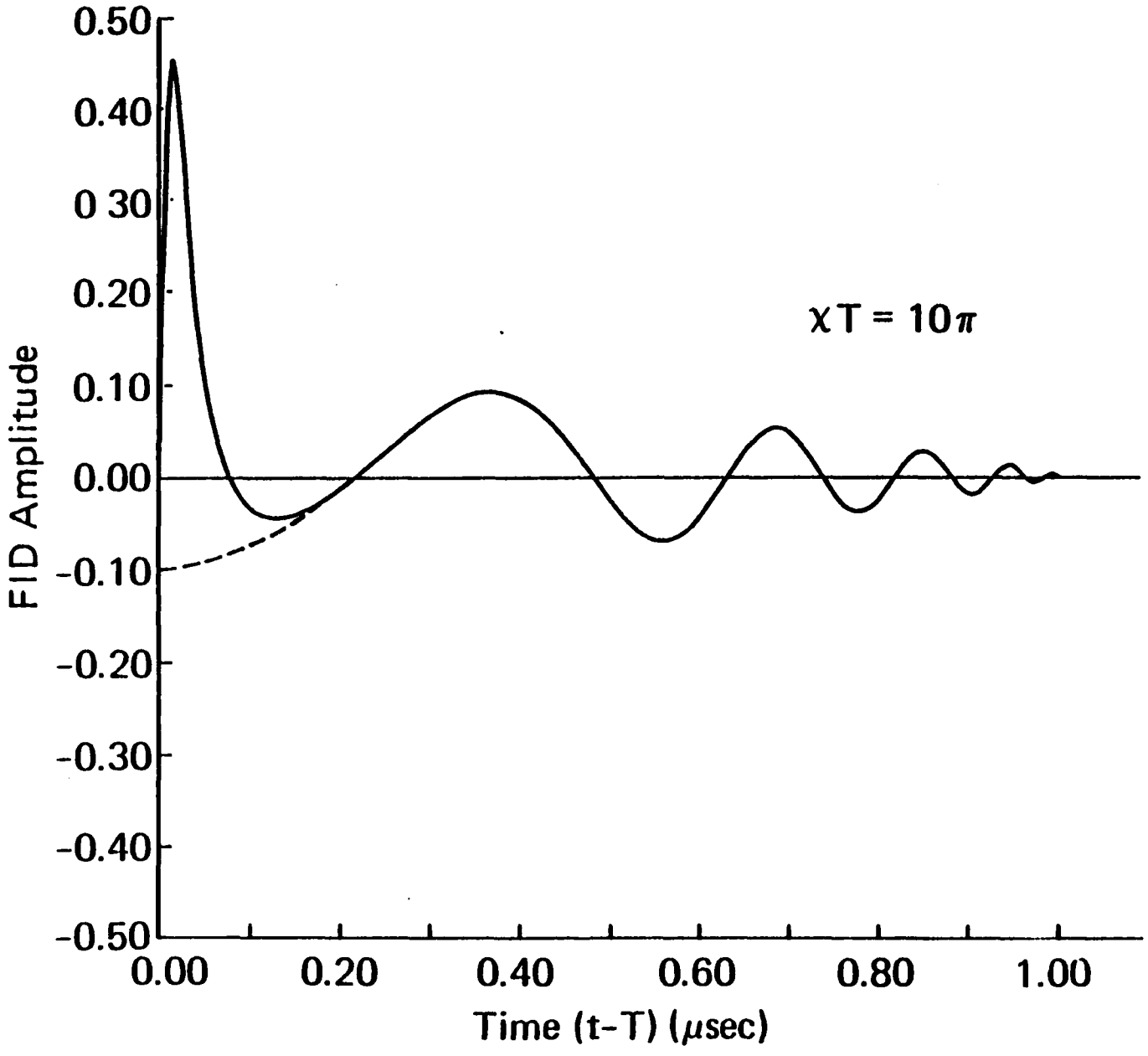


Figure 5. Computer plot of FID versus time for a pulse area $\chi T=10\pi$ μsec^{-1}. Solid curve: Direct numerical integration of Eq. (2.15) where $\sigma=50\pi$ μsec^{-1}, $\chi=10\pi$ μsec^{-1}, and T=1 μsec. Dashed curve: Asymptotic function Eq. (3.39).

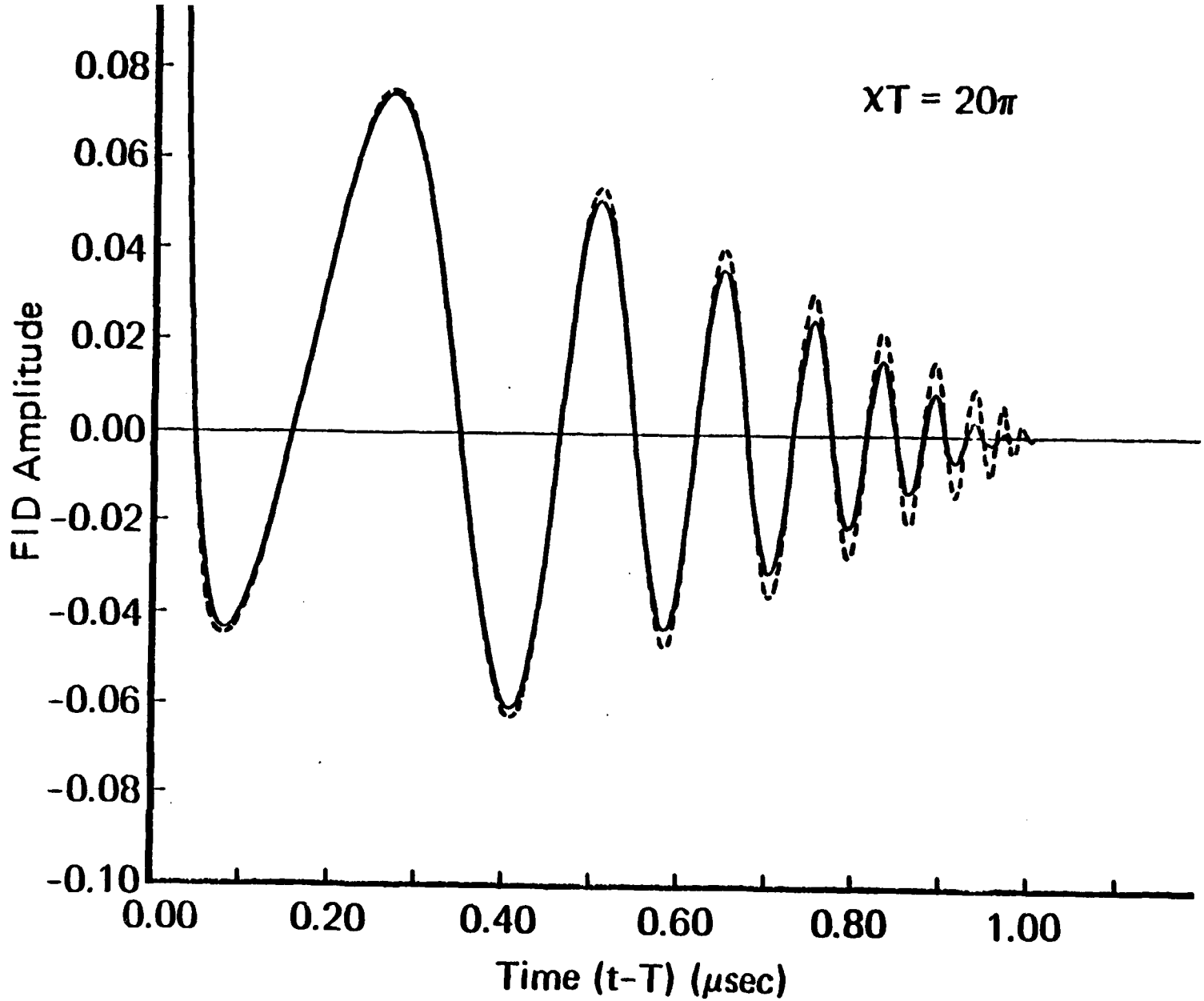


Figure 4. Computer plot of FID versus time for a pulse area $\chi T=20\pi$ μsec^{-1}. Solid curve: Direct numerical integration of Eq. (2.15) where $\sigma=50\pi$ μsec^{-1}, $\chi=20\pi$ μsec^{-1}, and T=1 μsec. Dashed curve: Bessel function sum Eq. (3.37) where the number of terms used in the series is m=90.

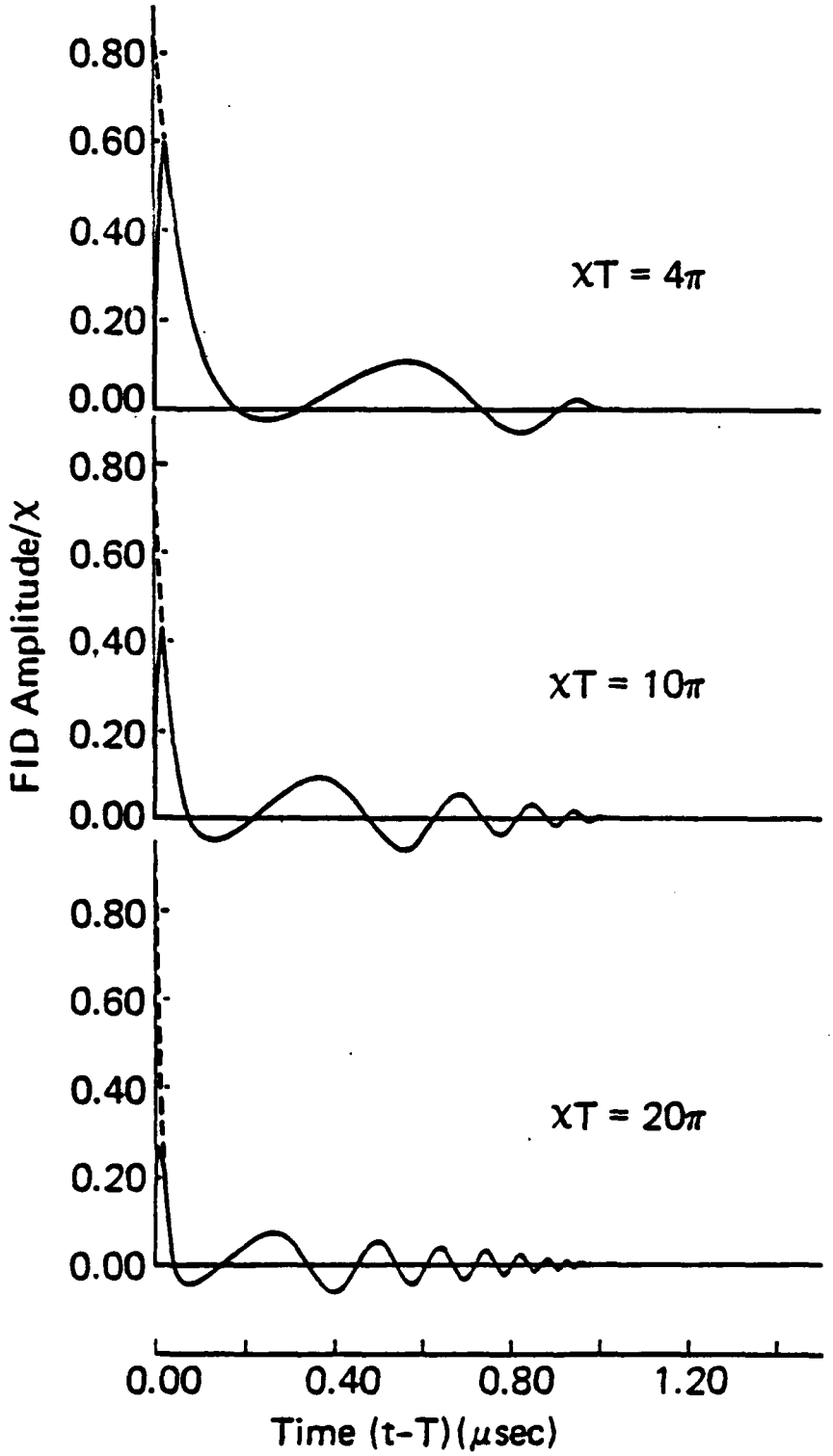


Figure 3. Computer plots of free induction decay amplitude versus time as a function of laser pulse area χT. Solid curves: Direct numerical integration of Eq. (2.15) for a Doppler-broadened lineshape of finite width σ. The following parameters were assumed: $\sigma=50\pi$ μsec^{-1}, T=1 μsec and $\gamma=0$. Dashed curves: Bessel function sum, Eq. (3.37) where $\sigma\to\infty$.

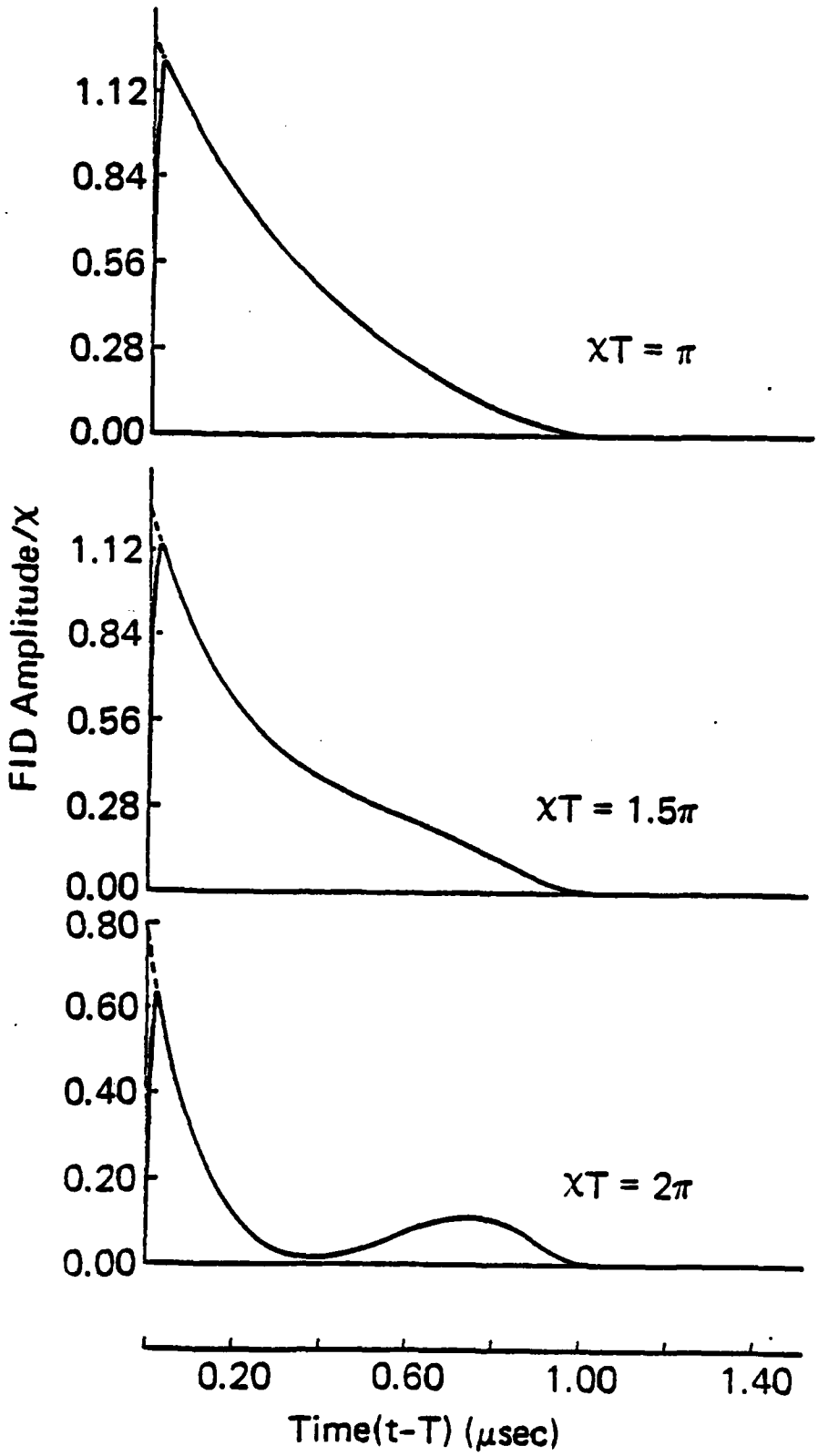


Figure 2. Computer plots of free induction decay amplitude versus time as a function of laser pulse area χT. Solid curves: Direct numerical integration of Eq. (2.15) for a Doppler-broadened lineshape of finite width σ. The following parameters were assumed: $\sigma=50\pi$ μsec^{-1}, T=1 μsec and γ=0. Dashed curves: Bessel function sum Eq. (3.37) where $\sigma\to\infty$.

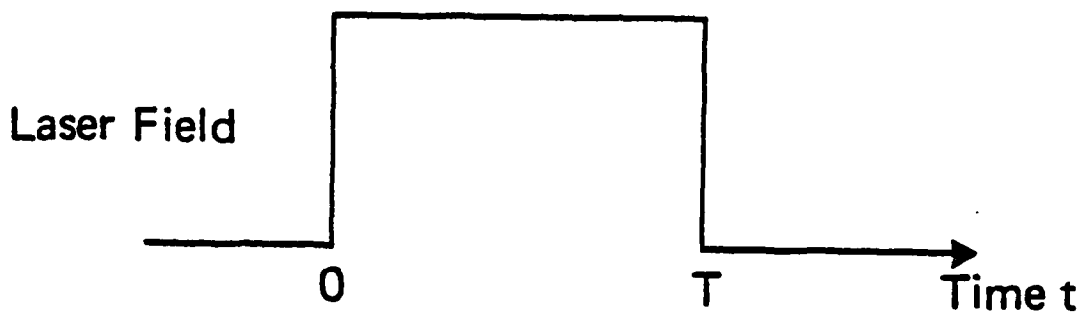


Figure 1. Laser field versus time. The field is nonzero only in the interval $0 \le t \le T$.

15. R. G. Brewer in Frontiers in Laser Spectroscopy, Volume 1 (North-Holland, 1977), p. 341.

16. A. Schenzle, N. C. Wong and R. G. Brewer (to be published).

17. H. C. Torrey, Phys. Rev. 76, 1059 (1949).

18. A. Schenzle and R. G. Brewer, Phys. Rev. A14, 1756 (1976).

19. H. Bateman, Tables of Integral Transforms, Volume I (McGraw-Hill, New York, 1954), p. 248.

20. Handbook of Mathematical Functions, edited by M. Abramowitz and I. A. Stegun (Dover, New York, 1972), p. 355.

21. I. S. Gradshteyn and I. W. Ryzhik, Table of Integrals, Series and Products (Academic Press, New York, 1965), p. 472.

22. G. F. Simmons, Differential Equations (McGraw-Hill, New York, 1972), p. 90.

23. A. Szabo and M. Kroll, Optics Letters 2, 10 (1978).

24. W. B. Mims, Phys. Rev. 141, 499 (1966).

REFERENCES

1. R. G. Brewer and R. L. Shoemaker, Phys. Rev. A6, 2001 (1972).

2. K. L. Foster, S. Stenholm and R. G. Brewer, Phys. Rev. A10 , 2318 (1974).

3. R. G. Brewer and A. Z. Genack, Phys. Rev. Lett. 36, 959 (1976).

4. A. Z. Genack, R. M. Macfarlane and R. G. Brewer, Phys. Rev. Lett. 37, 1078 (1976).

5. H. DeVries, P. DeBree and D. A. Wiersma, Chem. Phys. Lett. 52, 399 (1977).

6. A. Z. Genack and R. G. Brewer, Phys. Rev. A17, 1463 (1978).

7. R. G. DeVoe and R. G. Brewer, Phys. Rev. Lett. 40, 862 (1978); R. G. Devoe and R. G. Brewer, Phys. Rev. A (in press); P. F. Liao, J. E. Bjorkholm and J. P. Gordon, Phys. Rev. Lett. 39, 15 (1977).

8. R. G. DeVoe, A. Szabo, S. C. Rand and R. G. Brewer, Phys. Rev. Lett. 42, 1560 (1979).

9. F. A. Hopf, R. F. Shea and M. O. Scully, Phys. Rev. A7, 2105 (1973).

10. A. Abragam, The Principles of Nuclear Magnetism (Oxford, London, 1961); C. P. Slichter, Principles of Magnetic Resonance (Harper and Row, New York, 1963).

11. S. Haroche in High-Resolution Laser Spectroscopy, edited by K. Shimoda (Springer, Berlin, 1977), p. 253.

12. R. L. Shoemaker and R. G. Brewer, Phys. Rev. Lett. 28, 1430 (1972); R. G. Brewer and E. L. Hahn, Phys. Rev. A11, 1641 (1975).

13. A. L. Bloom, Phys. Rev. 98, 1105 (1955).

14. M. Sargent, M. O. Scully and W. E. Lamb, Jr., Laser Physics (Addison-Wesley, Reading, Massachusetts, 1977).

which can be rearranged to give

$$I_p(T) = 2\pi g(0)\chi \sum_{m=0}^{\infty} \left(\frac{z}{\chi t}\right)^{2m+2} \left[\sum_{j=0}^{2m+1} \sum_{\ell=0}^{j} \frac{(-1)^{j+\ell}(z/2)^{2m+1-\ell} J_{\ell+1}(z)}{(2m+1-j)!\,(j-\ell)!} \right] . \quad \text{(A7)}$$

The limits on the double sum in brackets can be rewritten as

$$\sum_{j=0}^{2m+1} \sum_{\ell=0}^{j} \rightarrow \sum_{\ell=0}^{2m+1} \sum_{j=\ell}^{2m+1} , \quad \text{(A8)}$$

the arguments remaining unaltered. The double sum in brackets then takes the form

$$\sum_{\ell=0}^{2m+1} \left(\frac{z}{2}\right)^{2m+1-\ell} J_{\ell+1}(z) \sum_{j'=0}^{r'} \frac{(-1)^{j'+2\ell}}{(r'-j')!\,j'!}$$

$$= \sum_{\ell=0}^{2m+1} \frac{\left(\frac{z}{2}\right)^{2m+1-\ell} J_{\ell+1}(z)}{(2m+1-\ell)!} \sum_{j'=0}^{r'} (-1)^{j'} C_{j'}^{r'} , \quad \text{(A9)}$$

where

$$r' \equiv 2m+1-\ell , \qquad j' \equiv j - \ell ,$$

$$\sum_{j'=0}^{r'} (-1)^{j'} C_{j'}^{r'} = \delta_{r',0} = \delta_{2m+1,\ell} .$$

In this way the double sum (A9) becomes a single term of $J_{2m+2}(z)$, and (A7) reduces to the remarkably compact form

$$I_p(T) = 2\pi g(0)\chi \sum_{m=1}^{\infty} \left(\frac{z}{\chi t}\right)^{2m} J_{2m}(z) , \quad \text{(A10)}$$

which is the desired result (3.34).

Appendix

We continue the derivation of (3.34) beginning with (3.33),

$$I_p(T) = \frac{2\pi g(0)}{t}\int_0^z \sinh\left(\frac{z^2-z'^2}{2\chi t}\right) z' J_0(z')dz' \ . \tag{A1}$$

Note that

$$\sinh\left(\frac{z^2-z'^2}{2\chi t}\right) = \sum_{m=0}^{\infty}\left(\frac{z^2-z'^2}{2\chi t}\right)^{2m+1}\frac{1}{(2m+1)!}$$

$$= \sum_{m=0}^{\infty}\sum_{j=0}^{2m+1}\frac{(z^2)^{2m+1-j}(-z'^2)^j C_j^{2m+1}}{(2\chi t)^{2m+1}(2m+1)!} \tag{A2}$$

where the second step involves the binomial expansion of $(z^2-z'^2)^{2m+1}$ and $C_j^{2m+1} \equiv \binom{2m+1}{j}$. Then, (A1) is given by

$$I_p(T) = 2\pi\frac{g(0)}{t}\sum_{m=0}^{\infty}\sum_{j=0}^{2m+1}\frac{(-1)^j z^{2(2m+1-j)}}{(2\chi t)^{2m+1}(2m+1-j)!j!}\int_0^z z'^{(2j+1)}J_0(z')dz' \ . \tag{A3}$$

Integration by parts and the relation

$$\frac{d}{dz}\left(z^n J_n(z)\right) = z^n J_{n-1}(z) \tag{A4}$$

yields

$$\int_0^z z'^{2j+1}J_0(z')dz' = \sum_{\ell=0}^{j}(-1)^\ell\frac{j!2^\ell}{(j-\ell)!}z^{2j+1-\ell}J_{\ell+1}(z) \ . \tag{A5}$$

The inclusion of (A5) in (A3) results in a triple sum of Bessel functions,

$$I_p(T) = 2\pi\frac{g(0)}{t}\sum_{m=0}^{\infty}\sum_{j=0}^{2m+1}\sum_{\ell=0}^{j}\frac{(-1)^{j+\ell}2^\ell z^{(4m+3-\ell)}J_{\ell+1}(z)}{(2\chi t)^{2m+1}(2m+1-j)!(j-\ell)!} \tag{A6}$$

decisively using larger pulse areas. Finally, two-pulse echoes having large pulse areas should display oscillations also. However, our numerical calculations show, in agreement with Mims,[24] that the echo shape function is a complicated pattern and does not display the uniform oscillations predicted here for pulsed free induction decay.

$t \mapsto T$: In this limit, $\alpha \mapsto 1$, $r \mapsto 1$ and the sum (3.37) reduces to

$$I(t \mapsto T) = \pi g(0) \chi (1 - J_0(\chi T)) \ , \tag{3.41}$$

which reproduces (3.12) and (3.20) since $w(0) = -1$ and $g(0) = N/\sqrt{\pi}\sigma$ for a Gaussian lineshape.

$t \mapsto 2T$: In this case, $\alpha \mapsto 0$, $r \mapsto 2$ and (3.37) becomes

$$I(t \mapsto 2T) = \frac{\pi}{4} g(0) \chi^3 (2T - t)^2 \ , \tag{3.42}$$

and reproduces (3.13) and (3.21).

Epilogue

This paper predicts an unusual oscillatory FID effect which follows coherent preparation by a resonant square wave electromagnetic pulse. Both numerical and analytic results are obtained from solutions of the Bloch equations. Oscillations are expected when the atomic sample is inhomogeneously broadened ($T_2^* \ll T_2$) and the pulse area satisfies the condition $\chi T \geq 2\pi$. In NMR, the free induction decay measurements of Bloom confirm such oscillations (incorrectly called "edge echoes") where $\chi T = 4\pi$ while in the infrared, the observations of Brewer and Shoemaker support our prediction for the case $\chi T = 1.5\pi$. More recently, Szabo and Kroll[23] have found interferences in optical FID which they attribute to the *edge echo*. However, for their conditions ($\chi T = 4\pi$, $T_2 = 2$ μsec, $T = 7$ μsec, and $\sigma = 1.6\pi$ nsec^{-1}), the envelope formation decays far too rapidly (~30 nsec) to even qualitatively resemble the $\chi T = 4\pi$ curve of Fig. 3. Nevertheless, future optical or NMR experiments might illustrate this phenomenon even more

Limiting Cases

Asymptotic form: For large arguments z, we may use the asymptotic expansion[20]

$$J_{2m}(z) \to (-1)^m \left(\frac{2}{\pi z}\right)^{1/2} \cos(z-\pi/4) \ , \tag{3.38}$$

and obtain a limiting result for the sum (3.37),

$$I(t) = -\sqrt{2\pi}\, g(0)\, \frac{\chi^{1/2}}{t^{1/4}T}\, (2T-t)^{3/4} \cos\left(\chi\sqrt{t(2T-t)}-\pi/4\right) \ , \qquad T<t<2T \ . \tag{3.39}$$

In Fig. 5, a computer plot of the asymptotic expression (3.39) (dashed curve) is overlayed on the numerical integration (2.15) (solid curve). The agreement is quite satisfactory except in the vicinity $t \to T$.

Notice that (3.39) exhibits a number of important characteristics of oscillatory FID. First, the factor $(2T-t)^{3/4}$ reveals that the oscillation envelope decays approximately with a 3/4 power law and reaches a zero amplitude value precisely at $t=2T$. Second, the cosine argument contains an oscillation frequency that increases at $t \to 2T$. Third, since the phase $\chi\sqrt{t(2T-t)}$ advances by χT in the interval $T<t<2T$, the number of oscillations is given by $\sim\chi T/2\pi$. Last, taking only the first term (m=1) in the sum (3.37) and using the asymptotic limit (3.38), we find

$$I(t) = -2\sqrt{2\pi}\, g(0)\, \frac{\chi^{1/2}}{t^{5/4}}\, (2T-t)^{3/4} \cos\left(\chi\sqrt{t(2T-t)}-\pi/4\right) \ , \qquad T<t<2T \ . \tag{3.40}$$

Thus, the asymptotic limit of the first term in the Bessel function sum is the dominant term as it approximates the asymptotic limit of the entire sum to within the factor t/2T. Nevertheless, the factor t/2T is important as it scales the amplitude making (3.39) more precise than (3.40).

$$I(\chi,t,T) = I_p(T)$$

$$= 2\pi g(0)\chi \sum_{m=1}^{\infty} \left(\frac{\alpha}{r}\right)^{2m} J_{2m}(\alpha\chi T) \qquad (3.37)$$

where

$$r \equiv t/T\ , \qquad 2>r>1$$

$$\alpha \equiv \sqrt{r(2-r)}\ , \qquad 0<\alpha<1\ .$$

Returning to the FID computer plots of Figs. 2 and 3, we see that Eq. (3.37) (dashed curve) agrees well with the direct numerical integration (solid curve), Eq. (2.15), for times $(t-T)>T_2^*$. However, there is a disparity in the two cases for short times $(t-T)\sim T_2^*$ since the assumption of infinite Doppler width σ in (3.37) results in a discontinuity at $t=T$ due to the first order FID. We show below for the case of large pulse areas that a good approximation to (3.37) is the first term $(\alpha/r)^2 J_2(\alpha\chi T)$, which gives the same zero crossings as the infinite sum but differs in amplitude. The number of terms m needed to achieve a reasonable fit with direct numerical integration increases with pulse area and in Figs. 2 and 3 follows the sequence m=3,3,5,8,18 and 40 as χT increases. Figure 4 is a blowup for the case $\chi T=20\pi$ and allows the small amplitude oscillations to be seen more clearly as $t\to 2T$. The envelope of the Bessel function sum (dashed curve) damps somewhat less rapidly than the numerical integration. We also notice slight differences in the zero crossings near $t=2T$. Such small differences, as shown in Fig. 4, are due to the finite Doppler width in the numerical integration. From an argument given below, ten periods of oscillation are expected here ($\chi T/2\pi=10$), but only nine are seen due to the relative magnitude and location ($2T-t\simeq 10^{-3}T$) of the tenth oscillation.

It is well known in nuclear magnetic resonance (NMR)[1,2] and quantum optics[3,4] that a two-level quantum system can emit coherent radiation after it is prepared by a pulsed resonant electromagnetic field. This effect, known as free induction decay (FID), has been analyzed over the years through solutions[5,6] of the Maxwell and Schrödinger wave equations and exhibits different properties for transitions which are dominated either by homogeneous or inhomogeneous linebroadening. For the case of strong inhomogeneous broadening, as in the optical regime, particular analytic solutions which are nonlinear in the field amplitude have been found recently[7] and reveal a striking and fundamental characteristic which appears to have gone unnoticed in the previous NMR and optics literature. Earlier studies[6-9] indicate that *when a pulse of finite duration T (interval: $0 \le t \le T$) prepares a sample, the coherent emission which follows lasts only for an additional period T (interval: $T \le t \le 2T$).* An example of a calculation[7] which illustrates this behavior is shown in Fig. 1 where the emission for $t > 2T$ is zero. The oscillatory behavior, which appears for large pulse areas, is also unusual and is discussed elsewhere.[7] These calculations as well as supporting NMR[8] and infrared[6] experiments suggest that the above statement is actually a theorem. We now prove on very general grounds that this is the case without recourse to particular solutions. The theorem holds for arbitrary population (T_1) and dipole (T_2) decay times, arbitrary pulse shapes of finite duration T and can be generalized to multi-level transitions as well. Since the pulse shape is arbitrary, the theorem is equally valid for two or multiple pulse echo sequences.

We assume that an electromagnetic pulse of arbitrary shape

$$E(z,t) = \begin{cases} E_o(t)\cos(\Omega t - kz) , & 0 < t < T \\ 0 , & t < 0 , \; t > T \end{cases} \tag{1}$$

and of duration T coherently prepares an atomic sample. For a two-level quantum system, the atomic density matrix equations of motion take the familiar form

$$\left(\frac{d}{dt} - i\Delta + 1/T_2\right)\tilde{\rho}_{12} = \frac{1}{2} i\chi w \tag{2a}$$

$$\frac{dw}{dt} = - i\chi(\tilde{\rho}_{21} - \tilde{\rho}_{12}) - (w - w^o)/T_1 \tag{2b}$$

where the upper and lower states are $|2\rangle$ and $|1\rangle$, the population difference $w \equiv \rho_{22} - \rho_{11}$, the rapidly oscillating terms in the Schrödinger equation are removed with the substitution $\rho_{12} = \tilde{\rho}_{12} e^{i(\Omega t - kz)}$, and the nonresonant high frequency terms are neglected. Furtherm re, the Rabi frequency $\chi(t) \equiv \mu_{12} E_o(t)/\hbar$ and the tuning parameter $\Delta \equiv -\Omega + \omega_{21} + kv_z$ where μ_{12} is the transition matrix element, ω_{21} is the $1 \leftrightarrow 2$ level splitting and kv_z is a Doppler shift. For an optically thin sample, Maxwell's wave equation yields an emission signal field E(t) which is essentially given by

$$E(t) \sim \langle \tilde{p}(t) \rangle = N \mathrm{Tr} \langle \mu \tilde{\rho}(t) \rangle , \tag{3}$$

where p(t) is the atomic polarization. The bracket denotes an average over the inhomogeneous lineshape, which for an atomic gaseous system is

$$g(\Delta) = \frac{e^{-(\Delta/\sigma)^2}}{\sqrt{\pi}\sigma} , \tag{4}$$

the Doppler width being σ.

By formally integrating (2a) and performing the Doppler average, we obtain the general expression

$$\langle\tilde{\rho}_{12}(t)\rangle = \int_{-\infty}^{\infty} g(\Delta)\tilde{\rho}_{12}(0)e^{(i\Delta-1/T_2)t}d\Delta$$

$$+ \frac{i}{2}\int_{-\infty}^{\infty} d\Delta \int_0^t g(\Delta)w(\Delta,t')\chi(t')e^{(i\Delta-1/T_2)(t-t')}dt' \ . \qquad (5)$$

The first term of (5) can be eliminated with the assumption that coherent preparation does not precede the pulse, i.e., $\tilde{\rho}_{12}(0)=0$.

We now restrict the discussion to physical systems with very large inhomogeneous broadening and will therefore evaluate Eq. (5) in the limit $\sigma\to\infty$ keeping $Ng(0)$ constant. Under the assumption that the order of integration can be interchanged, we first perform the integration over the detuning parameter Δ by closing the path of integration in the upper half plane and find

$$\oint w(\Delta,t')e^{i\Delta(t-t')}d\Delta = 2\pi i\sum R \ (uhp) \qquad (6)$$

where the sum is taken over the residues R in the upper half plane. The contribution to the integral from the half circle contour can be evaluated easily in the limit of infinite radius $|\Delta|\to\infty$ when we recall that the solution of the Bloch equations has the formal structure

$$w(\Delta,t) = \sum_j A_j \exp(z_j t) + \text{constant} \qquad (7)$$

where the quantities z_j are the roots of the characteristic equation

$$(z+1/T_1)(z+1/T_2)^2 + \Delta^2(z+1/T_1) + \chi^2(z+1/T_2) = 0 \ .$$

In the asymptotic limit $|\Delta|\to\infty$ the roots assume the values

$$\lim_{|\Delta|\to\infty} z_j = \begin{cases} -1/T_1 \\ -1/T_2 \pm i\Delta \end{cases} \tag{8}$$

causing the integrand on the circular contour to vanish exponentially when the following relation is satisfied,

$$t > 2t' \ . \tag{9}$$

Notice that (9) appears to be incompatible with the domain $t>t'>0$ defined by the integration limits in (5). This difficulty vanishes however when allowance is made for the finite pulse, Eq. (1), which changes the upper limit of the time integral from $t\to T$ so that (5) becomes

$$\langle\tilde{o}_{12}(t)\rangle = \frac{i}{2\sqrt{\pi}\sigma}\int_{-\infty}^{\infty} d\Delta \int_0^T w(\Delta,t')\chi(t')e^{(i\Delta-1/T_2)(t-t')}dt' \ . \tag{10}$$

The restricted domain $T>t'>0$ of (10) is now consistent with (9) when we assume that

$$t > 2T \geq 2t' \ .$$

Equation (10) is a very compact general expression as it includes the preparation or transient nutation effect for the period $0<t<T$ and FID for the interval $t>T$.

We now evaluate (6). Since the density matrix equations (2) are a set of first order differential equations which depend linearly on the parameter Δ, the solutions according to a theorem of Poincaré[10] are entire

functions and therefore will be analytic in Δ and will contain *no poles* in the finite complex plane. Consequently, the integral (6) vanishes and we conclude that the emission signal (10) is identically zero for t>2T,

$$\langle\tilde{\rho}_{12}(t)\rangle \equiv 0 , \qquad t > 2T . \tag{11}$$

Since the pulse shape according to (1) is arbitrary, this theorem applies equally well to an entire pulse train. For example, in a two-pulse echo experiment where T is the sum of the two pulse widths and the delay time, the echo signal terminates precisely at t=2T.

The above discussion assumes an infinite inhomogeneous linewidth, $\sigma\to\infty$. The effect of finite σ can be seen analytically if we replace the Gaussian lineshape (4) by the Lorentzian $g(\Delta)=(\sigma/\pi)/(\Delta^2+\sigma^2)$ and assume a pulse where in (1) $|E_o(t)|<E_o$. We find an upper bound for the polarization (5) by contour integration in the uhp about the pole $\Delta=i\sigma$, and upon integration over time, we obtain

$$|\langle\tilde{p}(t)\rangle| \le \frac{N}{4\sigma} f(\sigma)\chi e^{-\sigma(t-2T)} , \quad t > 2T \tag{12}$$

where we have used the formal properties[7] of the Bloch equations giving the upper limit $|w(i\sigma,t')|\le f(\sigma)e^{\sigma t'}$ where $f(\sigma)$ is analytic. Hence, a finite inhomogeneous linewidth σ produces a rapid decay for t>2T, in a time $T_2^*\equiv 2/\sigma$.

All of these arguments can be extended to echoes or FID within a multi-level quantum system where the energy spacing, the number of applied

fields and their frequencies are arbitrary. The density matrix Eqs. (2) assume an obvious form given elsewhere.[11] For any one-photon transition i→j, the FID signal is

$$\langle\tilde{\rho}_{ij}(t)\rangle = \int_{-\infty}^{\infty} g(\Delta)\tilde{\rho}_{ij}e^{(i\Delta_{ij}-1/T_{ij})t}d\Delta$$

$$+ \frac{i}{2}\int_{-\infty}^{\infty} d\Delta \sum_k \int_0^t g(\Delta)\tilde{\rho}_{ik}(\Delta,t')\chi_{kj}(t')e^{(i\Delta_{ij}-1/T_{ij})(t-t')}dt'$$

$$+ \text{c.c.} \qquad (13)$$

where

$$\Delta_{ij} = \omega_{ij} - \Omega_{ij} \pm kv_z \ .$$

Since the structure of (13) conforms to (5), the previous arguments apply and the same conclusion follow.

The simplicity of this theorem suggests that a simple physical description of the origin of this effect might exist. Thus far, this approach has proved elusive because the FID or echo depends nonlinearly on the applied field and the inhomogeneous broadening introduces a nonobvious interference among the coherently prepared packets.

It is interesting that the fundamental nature of this phenomenon has escaped attention until now. The theorem should prove useful therefore in interpreting future coherent transient experiments, especially at optical frequencies.

REFERENCES

1. A Abragam, The Principles of Nuclear Magnetism (Oxford, 1961).

2. C. P. Slichter, Principles of Magnetic Resonance (Springer-Verlag, Berlin, 1978).

3. M. Sargent III, M. O. Scully and W. E. Lamb, Jr., Laser Physics (Addison-Wesley, Reading, MA, 1977).

4. L. Allen and J. H. Eberly, Optical Resonance and Two-Level Atoms (Wiley, New York, 1975).

5. E. L. Hahn, Phys. Rev. 77, 297 (1950).

6. R. G. Brewer and R. L. Shoemaker, Phys. Rev. A6, 2001 (1972).

7. A. Schenzle, N. C. Wong and R. G. Brewer, submitted to the Phys. Rev.

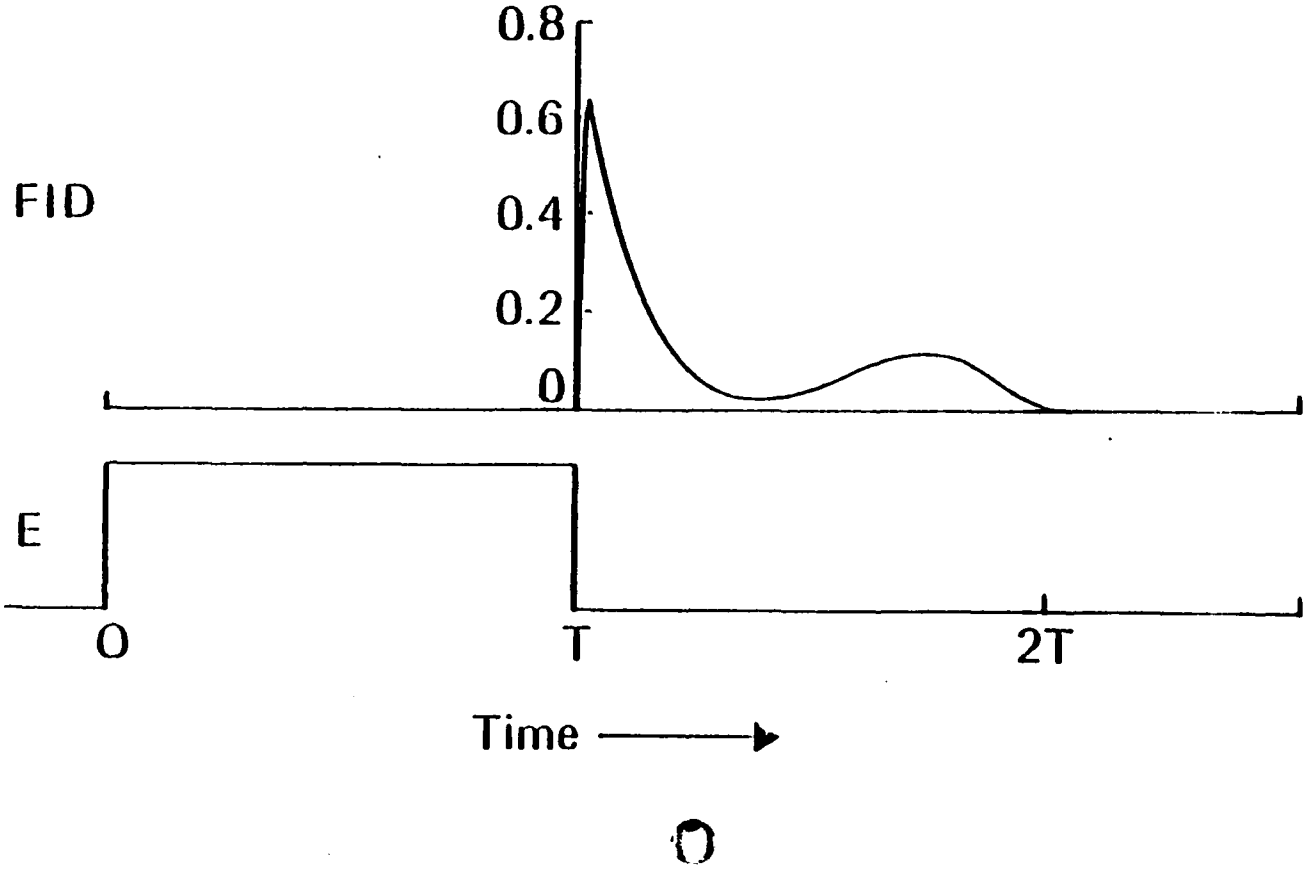
8. A. L. Bloom, Phys. Rev. 98, 1105 (1955).

9. F. Hopf and M. O. Scully, Phys. Rev. 179, 399 (1969).

10. J. H. Poincaré, Les Méthodes Nouvelles de la Mécanique Céleste (Dover, New York, 1957), Vol. 1 p. 48. See also F. R. Moulton, Differential Equations, (Dover, New York, 1958), p. 33.

11. A. Schenzle and R. G. Brewer, Physics Reports 43, No. 12, 455 (1978).

Figure 1. A computer plot is shown of the free induction decay (upper curve following a preparative field pulse (lower curve) of amplitude E, duration T, and pulse area $\chi T=2\pi$. This calculation, which is described in detail in reference 7, follows from a solution of the Bloch equations and a numerical integration over an inhomogeneous lineshape of finite width σ.



Appendix - Item 13

RJ3023 (37388) 1/9/81
Physics

MONTE CARLO THEORY OF OPTICAL DEPHASING IN LaF_3:Pr^{3+} ***

R. G. DeVoe
A. Wokaun*
S. C. Rand**
R. G. Brewer

IBM Research Laboratory
San Jose, California 95193

ABSTRACT: Recent optical free induction decay (FID) measurements of the impurity ion Pr^{3+} in LaF_3 at 2°K reveal optical homogeneous linewidths of only a few kilohertz, considerably narrower than the inhomogeneous broadening due to crystalline strains (5 GHz) or the static local magnetic fields of the ^{19}F nuclei (100 kHz). In this regime, the homogeneous broadening arises from local field fluctuations, as in NMR, and is due to the ^{19}F nuclei which undergo resonant flip-flops and modulate the Pr^{3+} optical transition frequency. We treat the optical response of a two-level quantum system to an intense coherent field and to fluctuating perturbations using a Monte Carlo computer routine that assumes (1) the LaF_3 crystal structure and (2) a sudden fluorine spin flip model. This procedure avoids many of the approximations of previous analytic theories of spectral diffusion in magnetic resonance and extends the calculation specifically to optical FID. The decay behavior is obtained by sampling statistically the Pr^{3+} phase history as subgroups of ^{19}F spins flip randomly in space and time. These fluctuations modify the Bloch equations where the solutions for the preparative and post preparative periods are obtained by numerical integration. In spite of the large lattice size assumed (2250 fluorines), only a few ^{19}F spins contribute substantially to the homogeneous width, a result which shows for the first time that spin flip correlations are not significant. Furthermore, a Pr^{3+} ion polarizes and detunes the nearest fluorines forming a *frozen core* that is incapable of resonant spin flipping with the bulk fluorines. We demonstrate that the core grows radially as the ^{141}Pr ($I=5/2$) magnetic moment increases with I_z, but the Pr optical linewidth changes little, producing essentially one rather than three linewidths. Our calculations utilize no free parameters and predict a Lorenztian lineshape of 8.4 kHz HWHM which compares to the optical FID observation of a

10.1 kHz Lorenztian. The Monte Carlo algorithm is verified further by the static local magnetic broadening of a Pr quadrupole transition which is found to be Gaussian, 82 kHz FWHM, in agreement with a second moment calculation and current observations.

* Present address: Bell Telephone Laboratories, Holmdel, New Jersey 07733.
** Present address: Department of Physics, Stanford University, Stanford, California 94305.
***Work supported in part by the U.S. Office of Naval Research.

I. INTRODUCTION

Optical free induction decay measurements have been performed recently on the praseodymium impurity ion Pr^{3+} in a lanthanum trifluoride host crystal LaF_3 at 2°K yielding a Lorenztian homogeneous linewidth of a few kilohertz - the narrowest optical transition yet observed in a solid.[1,2] Local magnetic dipolar interactions, both homonuclear ^{19}F-^{19}F and heteronuclear ^{141}Pr-^{19}F, are responsible for broadening the line in a way which is reminiscent of past magnetic resonance studies. The optical problem, however, is not identical to previous work because the optical FID effect involves steady state rather than pulse preparation and because optical transitions are usually dominated by inhomogeneous broadening. In this article, we present an optical line broadening theory involving no free parameters that is suitable for describing the current LaF_3:Pr^{3+} FID observations. The calculation utilizes a Monte Carlo technique that avoids some of the assumptions and approximations of past analytic theories in magnetic resonance and furthermore enables us to gain new insight into the dynamic processes occurring in solids.

In optical FID measurements, it is important to realize that a frequency stabilized cw laser beam resonantly excites a two-level quantum transition and thus coherently prepares a *single* homogeneous Pr^{3+} packet under steady state conditions.[1,2] Hence, a narrow hole of a few kilohertz width is burned into the much broader inhomogeneous lineshape which arises from local crystalline Stark fields (width: 5 GHz) and static magnetic fields of the surrounding fluorine nuclei (width: 100 kHz). In addition to the resonantly excited packet, the remaining packets of the inhomogeneous distribution are excited in an off-resonant manner. When the laser frequency is suddenly switched, the Pr^{3+} ions radiate an intense coherent beam of light in the forward direction, the FID signal, where the time dependence is characterized by a fast and a slow regime corresponding to the off-resonant and resonant preparation.

The two time regimes are actually limiting cases of a general analytic solution[3] of optical FID, derived recently for an inhomogeneously broadened two-level quantum system subject to steady state

preparation and relaxation characterized by the phenomenological population and dipole dephasing times T_1 and T_2. In the short time limit, the FID heterodyne beat signal

$$E_b^2(t) \sim \chi^2 e^{-(\sigma t/2)^2}, \quad t << \frac{2\gamma}{\sigma^2}, \tag{1.1}$$

is a Gaussian in time with decay rate $\sigma \equiv 2/T_2^*$ and depends linearly on the laser intensity, χ being the Rabi frequency. This signal reflects the off-resonant preparation of an inhomogeneous lineshape which is itself Gaussian with linewidth σ. In the long time limit, the FID signal

$$E_b^2(t) \sim \chi^4 e^{-(1/T_2+\beta)t}, \quad t >> \frac{1}{\sigma}, \tag{1.2}$$

is an exponential and depends nonlinearly on the laser intensity, the leading term being χ^4 where $\beta = 1/T_2\sqrt{1+\chi^2 T_1 T_2}$. This component corresponds to the resonantly excited packet which is a power broadened Lorentzian of angular linewidth $(1/T_2+\beta)$, the homogeneous width, where in the low power limit

$$\lim_{\chi \to 0} \left(\frac{1}{T_2} + \beta \right) \rightarrow \frac{2}{T_2}. \tag{1.3}$$

The dominant dynamic mechanism contributing to the Pr^{3+} optical dephasing time T_2 is due to the time varying magnetic dipolar interactions where the ^{19}F nuclei undergo resonant flip-flops and impress weak fluctuating magnetic fields on the ^{141}Pr nuclei. The Pr^{3+} optical transition frequency ω is thereby modulated, and as we shall see the low power limit of (1.2) omitting trivial factors, takes the more fundamental form

$$E_b^2(t) \sim \Phi(t) \equiv << \exp\left(i \int_0^t \delta\omega(t')dt' \right) >_{time} >_{lattice}. \tag{1.4}$$

where a time average is to be performed due to the Pr^{3+} frequency fluctuations $\delta\omega(t')$ and a spatial average over the fluorine nuclei surrounding a Pr^{3+} ion. The dipolar mechanism is in fact well substantiated by current optical FID studies where magic angle line narrowing occurs.[2] Thus, when the Pr^{3+}:LaF_3 crystal is irradiated by an appropriate rf field, the ^{19}F nuclei undergo forced precession about an effective field in the rotating frame. The fluctuating ^{19}F-^{19}F dipolar interaction is quenched thereby and the optical linewidth drops from ~10 to ~2 kHz, a behavior which can occur only when the above broadening mechanism prevails.

The central issue is the evaluation of (1.4), a magnetic resonance problem which has attracted theorists for about 30 years. For the purpose of discussion, assume a model where isolated A spins of a lattice are monitored by magnetic resonance and are frequently but weakly perturbed by the more numerous B spins. The resulting frequency fluctuations $\delta\omega(t)$ of the A spins and thus the phase integral (1-4) should then follow Gaussian statistics. With the assumption that $\delta\omega(t)$ follows the Gaussian distribution $P(\delta\omega) = 1/\delta\sqrt{2\pi}\ \exp\left[-1/2(\delta\omega/\delta)^2\right]$, Anderson and Weiss[4] and also Kubo[5] showed that (1.4) reduces to two limiting cases

$$\Phi(t) = e^{-\delta^2 t^2/2}, \quad t << \tau_c . \tag{1.5}$$

$$\Phi(t) = e^{-\delta^2 \tau_c |t|}, \quad |t| >> \tau_c . \tag{1.6}$$

where the depth of modulation $\delta = \langle\delta\omega^2\rangle^{1/2}$ and the correlation time $\tau_c = 1/\delta^2 \int_0^\infty \delta\omega(t')\delta\omega(t' + t)dt'$. Thus, the A spin resonance line exhibits a Gaussian behavior for short times and an exponential decay for long times. As time evolves, the initial linewidth δ narrows to $\delta^2\tau_c$, due either to thermal motion or spin exchange interactions for example. While Eqs. (1.5) and (1.6) superficially resemble the time dependence of the optical problem, Eqs. (1.1) and (1.2), we emphasize that the two theories are unrelated, and as the above discussion indicates, have an entirely different physical origin.

Specific forms for the A spin FID and echo decay were derived initially by Herzog and Hahn[6] using the same model of Gaussian modulation and the Markoff assumption for the correlation function $<\delta\omega(t)\delta\omega(0)> = <\delta\omega(0)^2>e^{-t/\tau_c}$. The leading FID terms in the short and long time limit agree with (1.5) and (1.6). Mims[7] also invoked the Gaussian-Markoff model for the time average but included the spatial average of (1.4) assuming that the dilute A spins are randomly distributed in a lattice of B spins. The resulting echo decay laws are of the form $E(t) = e^{-(2t/T_M)^{3/2}}$ for $t/\tau_c << 1$ and $E(t) = e^{-(2t/T_M)^{1/2}}$ for $t/\tau_c >> 1$ and the FID behavior exhibits similar fractional power laws. This model, therefore, seems inappropriate for optical transients in Pr^{3+}:LaF_3.

Another approach, developed by Klauder and Anderson,[8] assumes a Lorentzian-Markoff model where the abundant B spins execute sudden spin flips randomly in time. The A-B spin dipolar interactions in this case occur less frequently and more violently than the Gaussian modulation described above, and therefore resemble Poisson statistics[5] which also apply in the linebroadening theories of atoms undergoing isolated binary collisions. For a single spin packet, the time and spatial averages, which involve various approximations, yield an exponential FID signal of the form

$$F(t) = e^{-\frac{mt}{R}}, \tag{1.7}$$

where $m = \frac{8\pi^2}{9\sqrt{3}} nr\gamma |\mu|$, n is the B spin density, r is the microscopic B spin flip rate, μ is the B spin moment and γ is the A spin gyromagnetic ratio. The nature of this model and the resulting exponential decay come closer to explaining the optical FID behavior of Pr^{3+}:LaF_3. However, there is a major difficulty because the parameter R is ill-defined for a T_2 process, having been introduced as a device to satisfy stationarity in the Markoffian distribution function.

More recently, Hu and Hartmann[9] obtained analytic results for (1.4) in the case of the one-pulse FID, the two-pulse echo, and the three-pulse stimulated echo. The system again consists of dilute A spins randomly distributed among the B spins which suddenly and randomly flip between two

sonance experiment[17] yields 180±10 kHz FWHM for $I_z = 1/2 \rightarrow 3/2$ and 200±10 kHz FWHM for $= 3/2 \rightarrow 5/2$ whereas an optically detected spin echo measurement[18] gives 230±25 kHz FWHM for $= 3/2 \rightarrow 5/2$. These results are about a factor of two larger than the calculated value because the easurements were conducted in the absence of an external dc magnetic field. However, Erickson[19] s noted that his ~200 kHz linewidth reduces to ~100 kHz when a static field of 16G or larger is plied, bringing the observations into good agreement with the Monte Carlo linewidth of 84.5 kHz. ie theory of line broadening in zero field is more complicated than the calculation presented here as e nonsecular terms of the dipolar interaction must be included. Such a theory, a second moment lculation, was developed by Abragam and Kambe,[20] leading to a similar static dipolar linewidth duction, a factor of 2 or 3, as the magnetic field is increased from its zero field value. We should so note that the observed homogeneous linewidth[1] displays a similar reduction when the static plied field exceeds 19G. The results of this section are summarized in Table I.

We conclude that for static broadening the Monte Carlo result is unambiguous as it agrees curately with the second moment calculation and existing experiments. Furthermore, since the tical and NMR magnetic inhomogeneous linewidths are related trivially by a scale factor, the ratio (3.3) and (4.1), *the second moment calculation itself accurately predicts the optical linewidth arising om a lattice of static dipoles.*

B. Single Packet Case

Rather than deal with the full expression (3.1) immediately, it is possible to use a simplified rm

$$\langle \tilde{\rho}_{12}(t) \rangle \sim \frac{1}{N} \sum_{j=1}^{N} \cos \varphi_j(t) , \qquad (4.3)$$

hich describes many features of the homogeneous broadening problem. Equation (4.3), in fact, is starting point of many line broadening theories. This expression neglects the sine terms as

Let us now compare the Van Vleck[15] method of moments which has been used to calculate the nuclear broadening of EPR lines of dilute paramagnetic crystals[16] or the width of nuclear quadrupole transitions.[11] The second moment

$$\overline{(\Delta\omega_I^2)}_{IS} = \frac{1}{3}\gamma_I''^2\gamma_S^2 S(S+1)\hbar^2 \sum_k \frac{(1-3\cos^2\theta_k)^2}{r_k^6},$$

for a Pr NMR line implies a linewidth

$$\Delta\nu = \frac{1}{2\pi}\sqrt{\overline{\Delta\omega_I^2}} = \frac{1}{2\pi}\gamma_I''\mu_S\sqrt{\sum_k \frac{\overline{(1-3\cos^2\theta_k)^2}}{r_k^6}}. \qquad (4.2)$$

The lattice sum in (4.2) has been evaluated for the nearest 2250 fluorine neighbors and equals 0.0548Å^{-6}, giving a root second moment linewidth $\Delta\nu$=35.8 kHz. The FWHM linewidth is $2\sqrt{2\ln 2}$ larger or $\Delta\nu_{FWHM}$=84.5 kHz.

Figure 2 compares the Monte Carlo lineshape to a Gaussian having a width given by the second moment and the agreement is excellent. Note that there are no adjustable parameters in the comparison except the vertical scale. The Monte Carlo program also calculates a root second moment by

$$\sqrt{\overline{\Delta\omega^2}} = \sqrt{\overline{\frac{1}{N}\sum_{j=1}^{N}[\delta\omega_j(0)]^2}}.$$

giving $\Delta\nu$=34.9 kHz, only 2.5% lower than the Van Vleck result.

In addition to the nearly exact coincidence with the Van Vleck theory, our calculations are supported also by recent Pr ground state linewidth measurements. A steady state rf optical double

IV. RESULTS

A. Magnetic Inhomogeneous Broadening

Due to the ^{141}Pr ($I=5/2$) hyperfine structure, the $^3H_4 \leftrightarrow {}^1D_2$ optical transition is expected to consist of three prominent transitions $(I_z'' \rightarrow I_z') = (1/2 \rightarrow 1/2)$, $(3/2 \rightarrow 3/2)$, and $(5/2 \rightarrow 5/2)$, separated from each other by ~10 MHz but overlapping due to the crystal strain broadening of 5 GHz. The Monte Carlo calculations show that these three lines also are broadened inhomogeneously by the fluorine static magnetic fields; the lineshapes are given by the distribution function G, Eq. (3.5), and are found to be Gaussian with a FWHM linewidth of 42($I_z=1/2$), 126(3/2), and 210(5/2) kHz which are in the ratio of 1:3:5, consistent with (3.3). These calculations assume that the Pr gyromagnetic ratio $\gamma_I''/2\pi = 11.5$ kHz/G, derived from rf optical double resonance,[13] and that $\gamma_I' \sim 0$ since additional experiments[14] indicate that $|\gamma_I'| \leq 1/5 |\gamma_I''|$ where the relative sign of the $^1D_2$ and $^3H_4$ splittings are unknown. L. E. Erickson has kindly informed us that the above value of γ_I'' corrects a numerical error in his previous publication.[13,19]

Because the strain broadening is about 10^4 times larger than the magnetic inhomogeneous broadening, the latter has never been resolved at optical frequencies. The Monte Carlo calculations can be compared, however, to the Pr ground state quadrupole transition linewidth, determined either by second moment calculations or by optically detected NMR measurements. Since rf transitions require that $\Delta I_z = \pm 1$, (3.3) becomes

$$\delta\omega_j(0) = \gamma_I'' \sum_k B_k \frac{S_{kz}^j(0)}{|S_{kz}^j(0)|} . \qquad (4.1)$$

A comparison of (3.3) with (4.1) reveals that the Pr optical and NMR magnetic inhomogeneous linewidths differ only by a scaling factor and are approximately in the ratio of I_z as indicated in Table I. With the aid of (4.1), the Monte Carlo lineshape function is derived for the NMR case and appears in Fig. 2 as a Gaussian profile.

In the fourth step, the preparation $\tilde{\rho}^{j}_{12}(t_{200})$ is computed by numerically integrating the density matrix Eqs. (2.8) or equivalently the Bloch equations

$$\dot{u}_j(t) = -[\Delta_j + \delta\omega_j(t)]v_j(t) - \gamma u_j(t)$$

$$\dot{v}_j(t) = [\Delta_j + \delta\omega_j(t)]u_j(t) + \chi w_j(t) - \gamma v_j(t)$$

$$\dot{w}_j(t) = -\chi v_j(t) - [w_j(t) - w^o]/T_1 \tag{3.6}$$

where

$$\tilde{\rho}^{j}_{12}(t) = u_j(t) + iv_j(t)\,. \tag{3.7}$$

For simplicity, it is assumed that the population difference w is characterized by the single decay time T_1, and the other parameters are defined in Section IIB. The initial conditions are $\rho_{11}(t_0)-\rho_{22}(t_0)=1$, $\tilde{\rho}_{12}(t_0) = 0$, and the preparation is confined to the interval $t_0 \rightarrow t_{200}$.

Finally, the FID signal $\langle\tilde{\rho}_{12}(t)\rangle$ is calculated in (3.1) by iterating the preceding four steps N times to obtain the average $\langle\tilde{\rho}^{j}_{12}(t)\rangle$ in the post preparative period $t>t_{200}$. The effect of inhomogeneous broadening is included by allowing the inhomogeneous shift α_j to vary randomly over its lineshape.

frequency shift $\delta\omega_j(0)$ is computed using (3.3) and its distribution function

$$G \equiv \frac{dN}{d(\delta\omega_j(0))} . \tag{3.5}$$

is plotted in Fig. 2.

The third stage computes the frequency histories $\delta\omega_j(t)$ at 400 discrete times t_l where the fundamental interval $\Delta t \equiv t_{l+1} - t_l$. The time origin $t_0 = 0$ now coincides with the beginning of the preparative period which extends over the initial 200 points ($t_0 \rightarrow t_{200}$) and spans a much longer period than the optical dephasing time. During this period, the laser induces a polarization in the sample which simulates steady state preparation. The second 200 points ($t_{200} \rightarrow t_{400}$), which we consider later, correspond to the free decay period when the laser is out of resonance with the initially prepared packet.

Assumption 5: To calculate $\delta\omega_j(t)$, we assume that the number of fluorine spin flips per unit time n follows a Poisson distribution in time with a mean value

$$n_0 = N_F W ,$$

where N_F is the number of fluorine nuclei and W is the average spin flip rate. Next, a subgroup of fluorine spins, $n(t_l)\Delta t$ in number at time t_l, are chosen randomly in space and undergo a spin flip (sign reversal in B_k) producing a field fluctuation at the Pr^{3+} site and a frequency shift $\delta\omega_j(t_l)$. The calculation is repeated 400 times, generating a new shift for each succeeding time interval Δt so that a frequency history evolves where each shift adds to the previous value. Once a value for W is selected, the temporal distribution in spin flips follows a Poisson distribution and the spatial distribution varies randomly from one time interval to another, producing variations in $\delta\omega_j(t_l)$. The phase histories $\varphi_j(t_l)$ are obtained readily from (3.2).

in terms of the static frequency shift

$$\omega_k = \left|\gamma_I' - \gamma_I''\right| I_z B_k \qquad (3.3')$$

due to the field of the kth fluorine nucleus,

$$B_k = \mu_F \cdot \frac{(3\cos^2\theta_k - 1)}{r_k^3} . \qquad (3.4)$$

Assumption 1: The sudden jump approximation assumes that the fluorine spin $S_{kz}^j(t)$ is restricted to two values, $+1/2$ or $-1/2$, and that the jump occurs instantaneously between these two values at random times with an average rate $W \equiv 1/T$ where T is the mean time between jumps. The pairwise correlation of spin flips implied by (2.4) is ignored. It is possible to write (3.3) because the only dependence on t or j in $\delta\omega_j(t)$ lies in $S_{kz}^j(t)$, and, the various frequency histories differ only in the time evolution of the signs of the fluorine fields.

The first stage in the Monte Carlo program is the calculation of a table of fluorine magnetic fields B_k using (3.4). *Assumption 2*: The angles θ_k and distances r_k of the 2250 fluorines in the nearest 125 unit cells around a Pr site are computed from the LaF_3 crystal structure ($P3Cl - D_{3d}^3$), data of Zalkin, Templeton and Hopkins.[10] *Assumption 3*: The c axis of the LaF_3 crystal is assumed to be parallel to an external magnetic field B_o (z axis), and B_k represents the z component of the fluorine dipolar field where $\mathcal{H}_Q^{Pr} > \mathcal{H}_z^{Pr} > \mathcal{H}_{Pr-F}$. The resulting table of field strengths B_k is used in all subsequent calculations. *Assumption 4*: For simplicity, we assume only one g value for the ground and one for the excited electronic state of Pr^{3+}, avoiding the complexity of the anisotropic g-tensor.

The second stage of the program computes the static magnetic broadening due to a random initial alignment of the fluorine spins $S_{kz}^j(0)$. For each value of j, the fluorine magnetic fields B_k, obtained in the previous step, are summed with a random distribution in their sign. The resulting

III. MONTE CARLO CALCULATION

Outline and Assumptions

We begin by writing the Pr^{3+} density matrix average (2.12) as a sum

$$\langle\tilde{\rho}_{12}(t)\rangle = \frac{1}{N}\sum_{j=1}^{N}\tilde{\rho}_{12}^{j}(0)\exp\left[(-\gamma + i\Delta_j)t + i\int_0^t \delta\omega_j(t')dt'\right], \tag{3.1}$$

over N different Pr^{3+} environments that arise from the local static and fluctuating fluorine spin configuration and the crystalline Stark fields. The index j, therefore, labels a particular ion's preparation $\tilde{\rho}_{12}^{j}(0)$ by a resonant laser field in the presence of a fluctuating Pr^{3+} level spacing $\delta\omega_j(t)$, a specific Pr^{3+} Stark shift α_j in the tuning parameter Δ_j, and a specific Pr^{3+} phase history

$$\varphi_j(t) = \int_0^t \delta\omega_j(t')dt' \tag{3.2}$$

following the preparation. Thus, (3.1) includes both time and spatial averages. The number of Pr^{3+} ions N must be sufficiently large that fluctuations in $\langle\tilde{\rho}_{12}(t)\rangle$ due to finite sample size are negligible. We shall see that this criterion is satisfied for a model where N is in the range 10^3 to 10^6 even though about 10^{15} Pr^{3+} ions are monitored experimentally.

An outline of the numerical evaluation of (3.1) is shown schematically in Fig. 1 and yields (1) the dynamic or homogeneous magnetic broadening due to fluctuations $\delta\omega_j(t)$ in the Pr^{3+} level spacing and (2) a static or inhomogeneous magnetic broadening due to the frequency shift $\delta\omega_j(0)$.

The calculation of the random frequency fluctuation $\delta\omega_j(t)$ can be simplified by writing (2.9)

$$\delta\omega_j(t) = \sum_k \omega_k \frac{S_{kz}^{j}(t)}{\left|S_{kz}^{j}(t)\right|}. \tag{3.3}$$

$$\tilde{\rho}_{12}(t) = \tilde{\rho}_{12}(0) \exp\left[(-\gamma + i\Delta)t + i\int_0^t \delta\omega(t')dt'\right], \tag{2.11}$$

where $\tilde{\rho}_{12}(0)$ expresses the coherent preparation at time t=0. Equation (2.11) involves the phase history of a single Pr^{3+} ion and therefore must be averaged over the distribution of frequency fluctuations occurring at different Pr^{3+} sites both during the preparative period $t \leq 0$ and afterward $t \geq 0$. In addition, averages are to be performed over the local inhomogeneous static magnetic and crystalline Stark fields. Writing all of these averages symbolically by a single bracket, (2.11) becomes

$$\langle\tilde{\rho}_{12}(t)\rangle = \langle\tilde{\rho}_{12}(0) \exp\left[(-\gamma + i\Delta)t + i\int_0^t \delta\omega(t')dt'\right]\rangle . \tag{2.12}$$

Finally, the FID signal expressed as the field amplitude

$$E_{12}(z, t) = \tilde{E}_{12}(z, t)e^{i(\Omega t - kz)} + \text{c.c.}, \tag{2.13}$$

obeys Maxwell's wave equation

$$\frac{\partial\tilde{E}_{12}(t)}{\partial z} = -2\pi ikN\mu_{12}\langle\tilde{\rho}_{12}(t)\rangle . \tag{2.14}$$

for an optically thin sample where N is the Pr^{3+} ion density and μ_{12} is the electric-dipole transition matrix element. Because of the laser frequency shift Ω-Ω', the FID signal F(t) appears as a heterodyne beat due to the cross terms in the total field intensity, i.e.,

$$F(t) = \frac{1}{2}E_o\tilde{E}_{12}(t)e^{i(\Omega - \Omega')t} + \text{c.c.}. \tag{2.15}$$

Thus, the FID signal is determined essentially by the statistical behavior of (2.12) where the fluctuations $\delta\omega(t)$ introduce an additional damping.

$$\chi = \mu_{12}E_o/\hbar, \quad \Delta = -\Omega + \alpha + \omega_{21}, \quad E_i = \hbar\omega_i \ (i = 1,2) ,$$

where α is the shift in the Pr^{3+} transition frequency ω_{21} due to an inhomogeneity in the local static magnetic or crystalline Stark fields.

Fluctuations in the Pr^{3+} transition frequency ω_{21} due to F-F mutual spin flips are included in (2.8a) through the term

$$\delta\omega(t) = -(\gamma_I' - \gamma_I'')\gamma_s\hbar\sum_k \frac{3\cos^2\theta_k - 1}{r_k^3} I_z S_{kz}(t) , \tag{2.9}$$

which follows directly from (2.6). Notice that $\delta\omega$ vanishes when the Pr^{3+} gyromagnetic ratio γ_I of the upper (single prime) and lower (double prime) states are equal.

In (2.8a), the off-diagonal decay parameter $\gamma \equiv 1/2(\gamma_1 + \gamma_2)$ consists of the population decay rates γ_1 and γ_2 of states $|1>$ and $|2>$ while the total dephasing rate

$$\Gamma \equiv \frac{1}{T_2} = \frac{1}{2}(\gamma_1 + \gamma_2) + \gamma_\varphi , \tag{2.10}$$

includes the contribution γ_φ from fluorine spin flips, Eq. (2.9). Note that (2.10) applies only to that part of the decay which is exponential; it is a convenient expression but not an essential one.

Now assume that a narrow packet from the inhomogeneous lineshape is coherently prepared by a cw laser beam under steady state conditions and that FID follows at time t=0 when the laser frequency is switched suddenly by several homogeneous linewidths. The FID solution of (2.8) takes the form

which induces an electric-dipole transition where

$$\mathcal{H}_o^{Pr} = -\vec{\mu} \cdot \vec{E}_x(z, t) ,$$

and $\vec{x}$ and $\vec{z}$ are the polarization and propagation directions.

Because $\mathcal{H}_z^F$ commutes with ρ in (2.1),

$$\left[\mathcal{H}_z^F, \rho\right] = 0 ,$$

Eq. (2.1) reduces to

$$i\hbar\frac{\partial\rho}{\partial t} = \left[\mathcal{H}^{Pr}, \rho\right] + \text{damping terms} . \tag{2.7}$$

B. Optical Free Induction Decay

The time-dependent equations of motion (2.7) now become

$$\dot{\tilde{\rho}}_{12} = [-\gamma + i(\Delta + \delta\omega(t))]\tilde{\rho}_{12} + \frac{1}{2}i\chi(\rho_{22}-\rho_{11}) , \tag{2.8a}$$

$$\dot{\rho}_{22}-\dot{\rho}_{11} = -\gamma_2\rho_{22} + \gamma_1(\rho_{11}-\rho_{11}^o) + i\chi(\tilde{\rho}_{12}-\tilde{\rho}_{21}) . \tag{2.8b}$$

using the definition

$$\rho_{12}(t) \equiv \tilde{\rho}_{12}(t)e^{i(\Omega t-kz)} ,$$

and neglecting nonresonant terms. Here, the Rabi frequency χ, the tuning parameter Δ and the Pr^{3+} eigenenergies in the absence of a light wave are given by

a Zeeman term

$$\mathcal{H}_z^{Pr} = -\vec{I} \cdot \gamma \cdot \vec{B}\hbar ,$$

and the secular part of the Pr-F heteronuclear dipolar interaction of a Pr^{3+} ion with the k surrounding F nuclei of the crystal,

$$\mathcal{H}_{Pr-F} = -\gamma_I \gamma_S \hbar \sum_k \frac{3\cos^2\theta_{kj} - 1}{r_{kj}^3} I_z S_{kz}(t) . \qquad (2.6)$$

Due to the F-F spin flipping, $S_{kz}(t)$ in (2.6) fluctuates in time and wobbles the Pr^{3+} optical transition frequency.

Because of the assumption of a rigid lattice, we neglect certain T_1 processes, i.e., those processes involving phonons or thermal excitation, but not optical spontaneous emission. Furthermore, because the Pr^{3+} ions are dilute, we ignore secular terms such as $I_{kz}I_{jz}$ arising from the dipolar interaction. Finally, in (2.6) the flip-flop terms I^+S^- are omitted because the Larmor frequencies of ^{141}Pr and ^{19}F are so different ($\gamma_I >> \gamma_S$).

The last term of (2.5) expresses the resonant excitation of a Pr^{3+} ion from its lower state $|1>$ to an upper state $|2>$ by a light wave

$$\vec{E}_x(z, t) = \vec{e}_x E_o \cos(\Omega t - kz) .$$

The Hamiltonian

$$\mathcal{H} = \mathcal{H}^{F} + \mathcal{H}^{Pr}, \tag{2.2}$$

contains terms involving either the ^{19}F nuclear spin S or the $^{141}Pr^{3+}$ ion with nuclear spin I. Thus, the fluorine component

$$\mathcal{H}^{F} = \mathcal{H}_{z}^{F} + \mathcal{H}_{F-F}, \tag{2.3}$$

consists of a Zeeman interaction

$$\mathcal{H}_{z}^{F} = -\gamma_{s}\hbar \mathbf{B}\cdot\mathbf{S},$$

the external static magnetic field being B, and a homonuclear magnetic dipolar F-F interaction,[11] the secular part being

$$\mathcal{H}_{F-F} = -\gamma_{s}^{2}\hbar \sum_{k<j} \frac{3\cos^{2}\theta_{kj}-1}{r_{kj}^{3}} \left[S_{kz}S_{jz} - \frac{1}{4}(S_{k}^{+}S_{j}^{-} + S_{k}^{-}S_{j}^{+}) \right]. \tag{2.4}$$

The fluorine raising and lowering opertors $S_{k}^{\pm}S_{j}^{\mp}$ reveal the mutual F-F spin flips which generate local fluctuating magnetic fields that shift the Pr^{3+} transition frequency and broaden the optical transition.

The Pr terms

$$\mathcal{H}^{Pr} = \mathcal{H}_{e}^{Pr} + \mathcal{H}_{Q}^{Pr} + \mathcal{H}_{z}^{Pr} + \mathcal{H}_{Pr-F} + \mathcal{H}_{o}^{Pr}. \tag{2.5}$$

include an electronic component $\mathcal{H}_{e}^{Pr}$, a quadrupolar term,[12] since I=5/2,

$$\mathcal{H}_{Q}^{Pr} = D\left[I_{z}^{2} - \frac{1}{3}I^{2} \right] + \frac{E}{2}(I_{+}^{2} + I_{-}^{2}),$$

LaF_3 crystal structure[10] which contains a dilute concentration of Pr^{3+} ions. Each Pr^{3+} ion replaces a La^{3+} ion where the Pr^{3+} spatial distribution is random. Second, an external magnetic field is assumed causing the fluorine spins to be either in the up or down orientation. Third, because of a low Pr^{3+} concentration, Pr^{3+}-Pr^{3+} interactions are excluded. Fourth, the F spins are assumed to flip suddenly and randomly at a rate W, a quantity which can be calculated from other considerations and compared with experiment. At low temperatures ($T \leq 2°K$), spin lattice relaxation will not induce fluorine spin flips at a significant rate, but fluorine spin pairs can undergo mutual spin flips as described in Eq. (2.4). In Section II, the Pr^{3+} equations of motion are developed in terms of the basic optical field-atom interaction and spin-spin interactions. An expression resembling (1.4) follows for the Pr^{3+} FID signal in the case of coherent preparation by a monochromatic laser field. In Section III, the details of the Monte Carlo calculation are discussed. This step includes the preparation and the sampling procedure for averaging Pr^{3+} phase histories resulting from different fluorine spin distributions. In Section IV, the results of the calculations are described. Thus, the static magnetic inhomogeneous broadening calculation is tested by comparing it to a second moment calculation. For the homogeneous broadening, the nature of a polarized or frozen fluorine core surrounding a local Pr^{3+} ion is analyzed and the dependence of the linewidth on the ^{141}Pr magnetic quantum number is considered.

II. THEORETICAL MODEL

A. Hamiltonian

We seek a solution of the density matrix equations of motion

$$i\hbar \frac{\partial \rho}{\partial t} = [\mathcal{H}, \rho] + \text{damping terms} . \tag{2.1}$$

for the magnetically perturbed Pr^{3+} ions when they are coherently prepared by a laser field and then experience optical FID.

quantum states because of the spin lattice interaction. The FID signal after a spatial and a time average is given by

$$F(t) = \exp\{-\Delta\omega_{1/2}te^{-Wt}[I_o(Wt) + I_1(Wt)]\}, \tag{1.8}$$

and reduces in the short time limit to

$$F(t) = \exp\left[-\Delta\omega_{1/2}t(1-\tfrac{1}{2}Wt)\right], \quad Wt<<1, \tag{1.9}$$

where $\Delta\omega_{1/2} = [16\pi^2/9\sqrt{3}]n\mu_A\mu_B/\hbar$, n is the B spin density, μ is a magnetic moment, W is the B spin flip rate and $I_o(Wt)$ and $I_1(Wt)$ are modified Bessel functions. The leading term $\Delta\omega_{1/2}t$ in (1.9) is independent of the spin flip rate W and therefore represents a static magnetic broadening or first order FID, which is unusual in that it is Lorentzian, and follows directly from the spatial average given initially by Mims.[7] The spatial average assumes a continuum behavior in the A-B internuclear spacing, extending from zero to infinity, and therefore is subject to error, an issue considered by Klauder and Anderson,[8] owing to the neglect of the minimum lattice spacing of real crystals. We shall consider the magnitude of this error later in Appendix A. This model also assumes that the entire inhomogeneous lineshape is uniformly excited with a $\pi/2$ pulse so that the hole burning preparation which occurs in the optical FID problem is ignored.

The A-B spin dipolar interaction for Pr^{3+}:LaF_3 is neither weak enough to fit a Gaussian theory ($\delta\omega\cdot t<<1$), nor strong enough to fit the Klauder-Anderson theory ($\delta\omega\cdot t>>1$). The maximum frequency jump $\delta\omega_{max}$ due to a fluorine spin flip obeys $\delta\omega_{max}\tau\sim 1$, where τ is the observed Pr^{3+} dephasing time. Since neither regime applies, a numerical theory is called for.

In this article, a Monte Carlo line broadening theory is presented with the advantage that many of the assumptions and approximations utilized in the past are avoided, and moreover, the role of the dipolar mechanism in the optical FID problem is treated for the first time. We consider a rigid lattice

discussed in Section IVC. The simplest form of preparation is assumed also, namely, a single homogeneous packet of a two-level quantum system in a 50:50 superposition state. Thus, inhomogeneous and power broadening are ignored.

The use of (4.3) is preferred over the full Monte Carlo program when several parameters are to be varied simultaneously, since it executes at least two orders of magnitude faster. The essential features of dephasing in this case have been demonstrated by studying the variation of the FID decay time $1/\gamma_\varphi$ as a function of a) the number of fluorines in the lattice, b) the fluorine position in the lattice, and c) the fluorine flip rate W.

Our primary result is that a few nearest neighbor fluorines dominate the dephasing of the Pr^{3+} ion. Figure 3 shows the optical linewidth of the $L_z=1/2$ state for a spin flip time T=50 μsec as a function of the number of fluorines permitted to flip. The abscissa counts the number of interacting fluorines, with the strongest taken first, so that as $N\to\infty$, only distant, weakly coupled fluorines remain. Thus, the linewidth of the Pr^{3+} in a lattice in which only the two strongest coupled fluorine nuclei flip is 2/3 that of the whole lattice result, and when 5 fluorines flip, the linewidth is almost indistinguishable from that of the full lattice.

This conclusion is suggested again by Fig. 4 which shows the distribution function $dN/d\omega_k$ of static frequency shifts ω_k, Eq. (3.3′). As expected, most of the 2250 fluorine nuclei interact weakly with a given Pr^{3+} ion and produce very small shifts, which we see are in the range 0 to 3 kHz. The largest shifts, which are discrete at 9, 10, and 20 kHz, result from the five nearest neighbor fluorines which are the main contributors to optical dephasing.

This result has three consequences. *First*, it shows that our lattice size of 2250 fluorines is a few orders of magnitude larger than necessary. *Secondly*, it implies that correlations between adjacent fluorines do not strongly affect the optical linewidth. We do not argue that spin correlations don't

exist, but merely that their effect on the linewidth is small since so few fluorine nuclei are involved. The magnetic resonance theories described above[4-9] have not considered the effect of correlations on the linewidth, and no estimate of its effect has previously been given. From Fig. 3, we see that the flipping of one fluorine provides 30% of the linewidth. With two fluorines we reach 67% of the linewidth but this pair is weakly correlated since the crystal structure shows that these fluorines lie on opposite sides of the Pr ion and are about 5Å apart.

A physical explanation for the weak correlation lies in the strong radial behavior of the individual fluorine magnetic fields B_k, Eq. (3.4), which are proportional to $1/r^3$. If a nearest neighbor and a second nearest neighbor exchange spin orientation, the second nearest neighbor will produce a shift $(1/2)^3$ that of the nearest neighbor, and to current levels of accuracy may be ignored. We note further that the leading role of the nearest neighbors is a familar concept in the theory of moments[11,15] in NMR, where the second moment is proportional to $\Sigma 1/r_k^6$.

We have also studied this question further by introducing correlation in a model calculation using five fluorine spins. An extreme form of correlation is assumed where all five spins flip simultaneously. In one case, we assume that the spins are all parallel so that their fields add to produce the largest frequency jump possible. In the second case, a spin orientation is selected which produces the smallest frequency shift. The first correlation increases the linewidth by 35% while the second case decreases it by 20%. Since any physical correlation would be less extreme, we assert that the effect of correlation on the linewidth is less than ±50%.

The *third* consequence of the leading role of the nearest neighbors in optical dephasing is that perturbations of nearby fluorines by the static Pr^{3+} magnetic moment can cause a large reduction in the linewidth. We call this effect the "frozen core" phenomenon and it has been proposed to explain anomalously narrow linewidths in ESR.[21] The static dipolar magnetic field due to the enhanced nuclear magnetism of the Pr^{3+} ion[22] amounts to several gauss and detunes nearby fluorine nuclei from

the resonance frequency established by the external magnetic field. The flip-flop operators $(S_k^+ S_j^- + S_k^- S_j^+)$ in (2.4) thereby connect states of different energy and for these fluorines spin flips are inhibited. Since those fluorines most strongly coupled to the Pr^{3+} ion are the first to be inhibited, large changes in linewidth result. Furthermore, the three I_z states of Pr^{3+} have different static dipolar fields, in the ratio of 1:3:5. Therefore, the frozen core is "variable", with a size depending on the Pr^{3+} magnetic substate.

This phenomena has been incorporated into the Monte Carlo routine by modifying (2.9) to exclude the detuned fluorines:

$$\delta\omega(t) = -(\gamma_I' - \gamma_I'')\gamma_s\hbar \sum_{k\neq k'}^{2250} \frac{3\cos^2\theta_k - 1}{r_k^3} I_z S_{kz}(t) .$$

Here $\{k'\}$ represents the lattice indices of the detuned fluorines. A fluorine is included in $\{k'\}$ if its detuning by the Pr ion is greater than the fluorine NMR linewidth of 10 kHz.[23]

In Fig. 5 we plot the optical linewidth with and without a frozen core, as a function of the Pr^{3+} magnetic moment $\mu_z^{Pr} = \gamma_I I_z \hbar$ for T=50 μsec. Without the frozen core, the linewidth is approximately proportional to $\left|\mu_z^{Pr}\right|^{1/2}$, in contradiction with our earlier prediction[1,2] that the linewidth should be proportional to $\left|\gamma_I' - \gamma_I''\right|$. We note that although the inhomogeneous magnetic linewidth (4.1) scales as $\left|\gamma_I' - \gamma_I''\right|$, the homogeneous linewidth (3.3) does not depend linearly on this factor because of the time dependence of $S_{kz}^j(t)$.

With the frozen core effect included, the homogeneous linewidth is approximately proportional to $\left|\mu_z^{Pr}\right|^{1/4}$ for $\left|\mu_z^{Pr}\right| \gtrsim 10$kHz/G. For $\left|\mu_z^{Pr}\right| \lesssim 5$kHz/G. the frozen core and no frozen core results are identical, because the radius of the frozen core is less than the nearest neighbor spacing. Instead of our earlier prediction[1,2] of a triexponential decay with decay rates in the ratio of 1:3:5, Fig. 5 shows a ratio of 1:1.4:1.7. A computer plot of this triexponential decay indicates that it is

indistinguishable from a single exponential with a decay rate equal to the average of the $I_z=1/2$, 3/2 and 5/2 values. Our experimental observation[24] of a single exponential decay is therefore explained.

Figure 6 shows the dependence of the optical dephasing time $1/\gamma_\varphi$ on the mean time T between fluorine flips. Based on the previous discussion, γ_φ is the average of the $I_z=1/2$, 3/2 and 5/2 decay rates. The quantity T is the only parameter in our theory that is not directly measurable. We shall first treat it as a free parameter and then use an argument of Bloembergen[25] that predicts T from experimental studies of the fluorine NMR linewidth.[23]

First note that for T between 10 μsec and 1000 μsec, the linewidth is within a factor of two of the experimental value. To this level of accuracy, then, our results are independent of T. Conventional NMR measurements of the fluorine dephasing time in LaF_3 give a value of $T_2=17$ μsec which results from both static and dynamic broadening and does not directly measure the fluorine flip rate. Bloembergen,[25] followed by Lowe and Gade[26] have derived the relationship

$$T \sim 10T_2 ,$$

making use of the method of moments to estimate the flip-flop term in $H_{F\text{-}F}$ (2.4) and deriving a transition probability from it. This approach predicts T=170 μsec, and with the aid of Fig. 6, we see that the Monte Carlo calculation predicts a dephasing time $1/\gamma_\varphi = 19\mu$ sec compared to the experimental value of 15.8 μsec. The agreement to an uncertainty of 15% is unusually good by the standards of previous theories.

C. Hole Burning Preparation and Lineshape Studies

To include the effect of inhomogeneous broadening, we combine (2.15), (3.1) and (3.7) and obtain for the optical FID signal

$$F(t) = \mathrm{Re}\left\{ \frac{1}{N} \sum_{j=1}^{N} [u_j(0) + iv_j(0)] e^{i\varphi_j(t)} \right\}$$

$$= \frac{1}{N} \sum_{j=1}^{N} u_j(0) \cos \varphi_j(t) - \frac{1}{N} \sum_{j=1}^{N} v_j(0) \sin \varphi_j(t) . \qquad (4.4)$$

given in terms of the preparation $u_j(0)$ and $v_j(0)$ at time $t=0$ and the phase $\varphi_j(t)$ where the sum extends over all inhomogeneous environments expressed by the frequency shifts α_j.

Before evaluating (4.4), consider its reduction to the single packet case. In this circumstance, all ions of the packet are in phase at the beginning of the decay $t=0$ and have identical preparative factors so that (4.4) becomes

$$F(t) = \frac{u(0)}{N} \sum_{j=1}^{N} \cos \varphi_j(t) - \frac{v(0)}{N} \sum_{j=1}^{N} \sin \varphi_j(t) .$$

The sum over the sine terms tends to vanish since $\varphi_j(t)$ has equal probability of being positive or negative, and (4.3) results,

$$F(t) = \frac{1}{N} \sum_{j=1}^{N} \cos \varphi_j(t) .$$

where we have set $u(0)=1$. For $LaF_3:Pr^{3+}$, since the maximum frequency jump due to a fluorine spin flip is 10 kHz, the FID sum (4.3) will have Fourier components limited by 10 kHz as well. Furthermore, since the cosine term has zero slope near $t=0$, the first 10 μsec of the decay will be highly *nonexponential.*

We will now see, however, that the effect of inhomogeneous broadening leads to near exponential behavior, in contrast to the single packet case. Thus, in (4.4) the term $\sum_j v_j(0) \sin \varphi_j(t)$ no longer vanishes but is comparable in magnitude to $\sum_j u_j(0) \cos \varphi_j(t)$. This follows since $v_j(0)$ and $\varphi_j(t)$ are correlated and both are odd under frequency inversion so that their product is even. In addition, the frequencies contributing to $\varphi_j(t)$ are no longer limited by the nearest neighbor spin flip value of 10 kHz, but are determined instead by the optical and magnetic *inhomogeneous* broadening. Eventhough the amplitude of the high frequency components is reduced by their off-resonance response, high frequency Fourier components can now appear in (4.4) producing a fast Gaussian response ($T_2^* \sim 100$ psec) near t=0 followed by a slower exponential decay ($1/\gamma_\varphi = 16\ \mu$ sec).

The lineshape of the hole burned into the inhomogeneously broadened line of $LaF_3:Pr^{3+}$ is seen in Fig. 7, the linewidth being 10 kHz HWHM. This is a Monte Carlo calculation of the preparation at time t=0 where the lineshapes correspond to the in-phase $\frac{1}{N}\sum_{j=1}^{N} u_j(0)$ and out-of-phase $\frac{1}{N}\sum_{j=1}^{N} v_j(0)$ contributions which are approximately Lorenztian. Thus, this case differs significantly from the non-Lorenztian behavior of a single packet.

Similarly, Fig. 8 compares the observed optical FID of the $^3H_4 \rightarrow {}^1D_2$ transition of $LaF_3:Pr^{3+}$, which is an exponential, with a Monte Carlo calculation that includes both the preparative and post preparative periods. The calculated quantities $\frac{1}{N}\sum_j u_j(0) \cos \varphi_j(t)$ and $\frac{1}{N}\sum_j v_j(0) \sin \varphi_j(t)$, which assume a preparation time of 200 μsec and $I_z = 3/2$, are plotted separately to show their exponential character. Alternatively, their difference as written in (4.4) leads to a partial cancellation and a numerical result which is far noisier and more difficult to interpret. Note that the two terms of (4.4) as plotted in Fig. 8 agree with the experimental data both in slope and shape, confirming once again the 10 kHz linewidth and the nearly Lorenztian lineshape. Considering there are no free parameters in the theory, except for the vertical scale, the agreement is excellent.

We have so far compared both theory and experiment to an exponential decay law (Fig. 8), but in the Introduction we noted that Pr^{3+}:LaF_3 was an intermediate case, neither Lorentzian nor Gaussian in principle. In fact, both theory and experiment show partially Gaussian decay at short and long times, bracketing the intermediate exponential region. In Fig. 8, for example, for long times ($t>16$ μsec) both theory and experiment decay faster than an exponential. For short times ($t<2$ μsec) Gaussian-like behavior can be inferred from Fig. 7(b) which drops off faster than a Lorentzian for a detuning larger than 20 kHz. Future experiments with increased laser frequency and amplitude stability should clarify this complex decay behavior at short and long times.

The rapid initial response near the time origin arising from the first order FID is not reproduced in these calculations because of the excessive computer time needed to integrate (3.1) over the full strain broadened inhomogeneous linewidth of 5 GHz. Since this feature is well understood by previous analytic arguments,[3] the integration was restricted to $\Delta_j \leq 100$ kHz and consequently the calculated rise time (not shown in Fig. 8 because of the scale) is 5×10^4 times slower than the expected value $T_2^* = 100$ psec.

V. CONCLUSION

The Monte Carlo theory presented has demonstrated in a precise way that the 10 kHz optical homogeneous linewidth recently observed in Pr^{3+}:LaF_3 arises from the magnetic dipolar coupling of the Pr nucleus with the fluorine nuclei which undergo resonant spin flip-flops. The theory accurately predicts, via the variable frozen core argument, the single exponential decay function and gives the decay rate with no free parameters. Not only are the optical[1,2] linewidths predicted but those of nuclear quadrupole resonance[13,17,18] as well.

The Monte Carlo theory possesses several advantages over previous analytic theories. It bypasses an ambiguity present in applying the Klauder-Anderson model.[8] While the

Klauder-Anderson parameter R is clearly defined when the spin flips are caused by spin-lattice relaxation. R has no clear meaning for the T_2 or resonant fluorine flip-flop process considered here.

Also, the Hu-Hartmann theory contains implicitly a spatial integral which cannot be evaluated for our system (Appendix A), so that this theory does not apply to Pr^{3+}:LaF_3 either.

Lastly, we have studied numerically nonlinear solutions of the Bloch equations, in the presence of stochastic phase and frequency fluctuations. Few, if any, analytic solutions to this general problem have been given and we suggest that the Monte Carlo method may have similar applications in gas collision theory as well as other line broadening problems in the solid state.

ACKNOWLEDGMENT

We are indebted to L. E. Erickson for informing us of his unpublished results, the NQR inhomogeneous linewidth of LaF_3:Pr^{3+} and its dependence on the static external magnetic field. We also benefited from the preprint[14] of R. M. Macfarlane and R. M. Shelby. This work was supported in part by the U.S. Office of Naval Research.

APPENDIX A:

Comparison With Hu-Hartmann Theory

An examination of the sudden jump theory of Hu and Hartmann[9] reveals the assumption of a lattice which is continuous rather than discrete. The implication of this assumption and its limits of validity are discussed in this section.

In the Monte Carlo calculation, the linewidth is dominated by the nearest neighbors while in the Hu-Hartmann theory there are no nearest neighbors since the B spins can be infinitesimally close to the A spins. We show that the Hu-Hartmann derivation may be valid for the case of large magnetic

moments encountered in electron spin resonance, but fails for the nuclear spin case of Pr^{3+}:LaF_3. Their approximation lies in the spatial integral, their Eq. (2.10),

$$F(\tau) = \exp\left\{n\alpha\left\langle 1-\exp\left[i\omega_{\alpha\beta}\int_0^\tau h(t)dt\right]\right\rangle\right\} . \tag{A1}$$

The brackets < > represent a spatial average defined in their Eq. (2.8), and

$$\omega_{\alpha\beta} \equiv \frac{2\mu_A\mu_B}{\hbar}\,\frac{(1-3\cos^2\theta_{\alpha\beta})}{r_{\alpha\beta}^3} . \tag{A2}$$

We make their approximation explicit by defining the variable

$$C \equiv \frac{2\mu_A\mu_B}{\hbar}(1-3\cos^2\theta)\int_0^\tau h(t)dt .$$

so that the above expression becomes

$$F(\tau) = \exp\left\{n\alpha\, 2\pi\int_0^\pi \sin\theta d\theta\int_{r_{min}}^{r_{max}} r^2 dr\left[1-e^{iC/r^3}\right]\right\} . \tag{A3}$$

Klauder and Anderson[8] have examined a similar integral and point out that although it is always valid to replace r_{max} by ∞, r_{min} may be replaced by zero only in certain circumstances. Retaining r_{min} in the integral over r we find

$$F(\tau) = \exp\left\{n\cdot 2\pi\cdot\alpha\int_0^\pi \sin\theta d\theta\cdot\frac{C}{3}\int_0^{C/r^3_{min}}\frac{du}{u^2}(1-\cos u)\right\} . \tag{A4}$$

The upper limit of integration has a physical meaning:

$$\frac{C}{r^3_{min}} = 2\pi\nu_{max}\int_0^\tau h(t)dt , \tag{A5}$$

where

$$\nu_{max} \equiv \frac{1}{2\pi} \cdot \frac{2\mu_A\mu_B}{\hbar r^3_{min}}(1-3\cos^2\theta) .$$

is just the frequency jump due to the flipping of the nearest (or most strongly coupled) neighbor. The dimensionless integral

$$\int_0^x (1-\cos u)\frac{du}{u^2}$$

approaches $\pi/2$ for $x>2\pi$, but at small x is linear in x. Note that the integral in (A5) has dimensions of time and is always less than the duration of the experiment, Δt. The Hu-Hartmann theory assumes that $r_{min}=0$, and that the radial integral reduces to $\pi C/6$, whereupon the remaining integration can be easily performed. We have shown, however, that this is true only when

$$\nu_{max} \cdot \Delta t > 1 . \qquad \text{(A6)}$$

When $\nu_{max} \cdot \Delta t < 1$, the radial integral is a linear function of $\nu_{max} \cdot \Delta t$ and therefore depends on the crystal structure via the nearest neighbor interaction so that $F(\tau)$ in (A4) can no longer be integrated analytically. For electron spin resonance, where $\nu_{max} >> 1$ MHz and $\tau > 1$ μsec, this condition is easily satisfied. For the optical dephasing of Pr^{3+}:LaF_3, where ν_{max} is limited by the frozen core effect to 10 kHz and $\Delta t \sim 10$ μsec, it is always violated.[27]

For systems that satisfy this condition more closely than Pr^{3+}:LaF_3 we find the power series technique described in their Eq. (2.15) will fail after a certain number terms, depending on the size of $\nu_{max} \cdot \Delta t$.

REFERENCES

1. R. G. DeVoe, A. Szabo, S. C. Rand and R. G. Brewer, Phys. Rev. Lett. 42, 1560 (1979).
2. S. C. Rand, A. Wokaun, R. G. DeVoe and R. G. Brewer, Phys. Rev. Lett. 43, 1868 (1979).
3. R. G. DeVoe and R. G. Brewer, Phys. Rev. Lett. 40, 862 (1978); R. G. DeVoe and R. G. Brewer, Phys. Rev. A 20, 2449 (1979).
4. P. W Anderson and P. R. Weiss, Rev. Mod. Phys. 25, 269 (1953).
5. R. Kubo in Fluctuation, Relaxation and Resonance in Magnetic Systems (Oliver and Boyd Ltd., Edinburgh, 1962) edited by D. ter Haar, p. 23.
6. B. Herzog and E. L. Hahn, Phys. Rev. 103, 148 (1956).
7. W. B. Mims, Phys. Rev. 168, 370 (1968).
8. J. R. Klauder and P. W. Anderson, Phys. Rev. 125, 912 (1962).
9. P. Hu and S. R. Hartmann, Phys. Rev. B9, 1 (1974).
10. A. Zalkin, D. H. Templeton and T. E. Hopkins, Inorganic Chem. 5, 1466 (1966).
11. A. Abragam, Principles of Nuclear Magnetism (Oxford University Press, Oxford, England, 1961).
12. T. P. Das and E. L. Hahn, Nuclear Quadrupole Resonance Spectroscopy (Academic, New York, 1958).
13. L. E. Erickson, Opt. Commun. 21, 147 (1977).
14. R. M. Macfarlane and R. M. Shelby, (submitted to Optics Letters).
15. J. H. Van Vleck, Phys. Rev. 74, 1168 (1948).
16. N. Laurance, E. C. McIrvine and J. Lambe, J. Phys. Chem. Solids 23, 515 (1962).
17. L. E. Erickson, Phys. Rev. B16, 4731 (1977).
18. R. M. Shelby, C. S. Yannoni and R. M. Macfarlane, Phys. Rev. Lett. 41, 1739 (1978).
19. L. E. Erickson, (private communication).
20. A. Abragam and K. Kambe, Phys. Rev. 91, 894 (1953).
21. W. B. Mims in Electron Paramagnetic Resonance (Plenum, New York, 1972) edited by S. Geschwind, p. 291.

22. M. A. Teplov, Zh. Eksp. Teor. Fiz. 53, 1520 (1967) [Sov. Phys. JETP 26, 872 (1968)]; B. Bleaney, Physica (Utrecht) 69, 317 (1973).

23. K. Lee and A. Shir, Phys. Rev. Lett. 14, 1027 (1965); L. Shen, Phys. Rev. 172, 259 (1968).

24. In our preliminary work, Ref. 1, a biexponential decay was observed at a static magnetic field of 19G, whereas, in the earth's field or at 75G or higher a single exponential was detected. More recently, with improved laser frequency stability, only single exponential decays have been seen.

25. N. Bloembergen, Physica 15, 386 (1949).

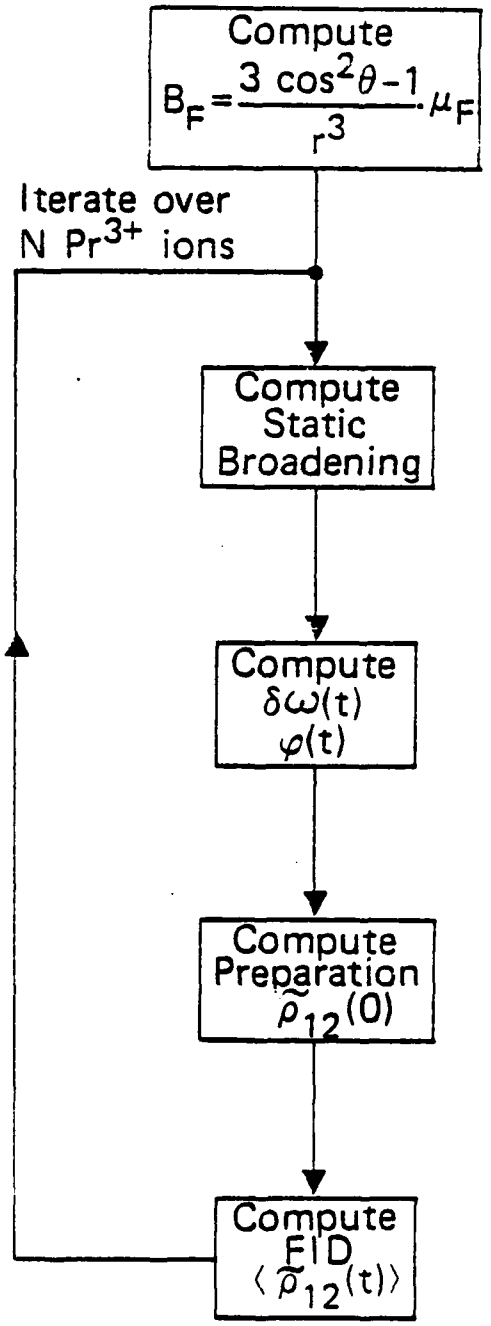
26. I. J. Lowe and S. Gade, Phys. Rev. 156, 817 (1967).

27. In Reference 18, Shelby et al. observe an optically detected echo of a Pr^{3+} quadrupole transition in LaF_3 and attempt to fit their echo envelope function to Eq. (5.7) of the Hu-Hartmann (HH) theory.[9] In view of our discussion, the HH theory does not apply to this case and the apparent fit achieved is invalid. Furthermore, the numerical values of the parameters chosen,[18] $\Delta\omega_{1/2}=50$ kHz and $W=1/17$ μsec^{-1}, are inappropriate.

Table I: Linewidths of ^{141}Pr in LaF_3 Due to Magnetic Inhomogeneous Broadening

Transition	Method	Linewidth FWHM (kHz)
rf($\Delta I''_z = \pm 1$)	Monte Carlo theory*	82
	Van Vleck second moment*	84.5
	cw rf-optical double resonance[17]	
	$I''_z = 1/2 \rightarrow 3/2$	180 ± 10^a (~ 100)^b
	$I''_z = 3/2 \rightarrow 5/2$	200 ± 10^a (~ 100)^b
	Optically detected rf transients[18]	
	$I''_z = 3/2 \rightarrow 5/2$	230 ± 25^a
optical ($^3H_4 \leftrightarrow {}^1D_2$)	Monte Carlo theory*	
	$I''_z \rightarrow I'_z = 1/2 \rightarrow 1/2$	42
	$I''_z \rightarrow I'_z = 3/2 \rightarrow 3/2$	126
	$I''_z \rightarrow I'_z = 5/2 \rightarrow 5/2$	210

This work
Earth's magnetic field
Static external field of ≥ 16G



MONTE CARLO
CALCULATION

ure 1. Schematic diagram of the sequence of operations of the Monte Carlo calculation.

In an experiment, the observable is the square of the total field,

$$< E_T^2 >_{av} = < |E_s + E_x|^2 >_{av} \qquad (2-18)$$

ıere the signal field E_s and the laser field E_x are given by (2-12) and (2-1) and $< >_{av}$ denotes a
ıe average over an optical period. Equation (2-18) contains the cross term

$$I_s = 2E_0 R_e(\tilde{E}_{13} + \tilde{E}_{23}) , \qquad (2-19)$$

ıich is the desired signal intensity where R_e specifies the real part.

It now remains to evaluate $\tilde{E}_{13} + \tilde{E}_{23}$. We solve (2-6) by iteration using the Laplace transform
:thod.[15] First, the wave equation is solved in first order by neglecting the optical interaction $\mathcal{H}_o$.
ith the transformation $c(z) = \int_0^\infty c(t)e^{-zt}dt$, Eqs. (2-6a,b) become

$$(z + \Gamma_1/2)c_1^{(1)}(z) = c_1(0) - iVc_2^{(1)}(z + i\omega_{21}) \qquad (2-20a)$$

$$(z + \Gamma_2/2)c_2^{(1)}(z) = c_2(0) - iV^* c_1^{(1)}(z - i\omega_{21}) \qquad (2-20b)$$

ıere the poles are

$$z_1^{(1)} = \frac{1}{2}[i\omega_{21} - \frac{1}{2}(\Gamma_2 + \Gamma_1)] + \frac{1}{2}[(i\omega_{21} + \frac{1}{2}(\Gamma_2 - \Gamma_1)^2 - 4|V|^2]^{1/2} , \qquad (2-21a)$$

$$z_2^{(1)} = \frac{1}{2}[i\omega_{21} - \frac{1}{2}(\Gamma_2 + \Gamma_1)] - \frac{1}{2}[(i\omega_{21} + \frac{1}{2}(\Gamma_2 - \Gamma_1)^2 - 4|V|^2]^{1/2} , \qquad (2-21b)$$

d $c_{1,2}(0)$ specify the initial conditions at t=0. Equations (2-20) yield

$$c_1(z - i\omega_{21}) = \frac{(z + \Gamma_2/2)c_1(0) - iVc_2(0)}{(z - z_1)(z - z_2)} ,$$

$$c_2(z) = \frac{(z - i\omega_{21} + \Gamma_1/2)c_2(0) - iV^* c_1(0)}{(z - z_1)(z - z_2)} . \qquad (2-22)$$

The two packets corresponding to the 1→3 and 2→3 transitions generate a field amplitude signal

$$E_s(z,t) = [\tilde{E}_{13}(z,t) + \tilde{E}_{23}(z,t)]e^{i(\Omega t - kz)} + c.c. \qquad (2-12)$$

which obeys Maxwell's wave equation

$$\frac{\partial \tilde{E}_{ij'}}{\partial z} = -2\pi ikN\mu_{ij} < < \tilde{\rho}_{ij'}(t) >_{t_o} >_I, \quad (ij = 13,23) \qquad (2-13)$$

for an optically thin sample of length L. Here, the slowly varying part $\tilde{\rho}_{ij}$ of the density matrix $\rho_{ij} = c_i c_j^*$ is defined by

$$\rho_{ij}(z,t) = \tilde{\rho}_{ij}(t)e^{i(\Omega t - kz)}, \quad (ij = 13,23) \qquad (2-14)$$

and N is the Pr^{3+} atomic number density. Because we are interested in steady-state solutions of (2-6), the inner bracket of (2-13) performs the average

$$< \tilde{\rho}_{ij}(t) >_{t_o} = K\int_{-\infty}^{t} \tilde{\rho}_{ij}(t - t_o)dt_o \qquad (2-15)$$

over all times t_o that Pr^{3+} ions enter the absorbing levels i or j and thus commence absorbing laser light. The constant K is the rate that ions enter the absorbing state, due either to optical spontaneous emission or other forms of relaxation.

The outer bracket of (2-13) performs the average

$$< \tilde{\rho}_{ij}(\Delta) >_I = \int_{-\infty}^{\infty} G(\Delta)\tilde{\rho}_{ij}(\Delta)d\Delta \qquad (2-16)$$

over the Pr^{3+} inhomogeneous lineshape function

$$G(\alpha) = \frac{1}{\sqrt{\pi}\sigma}e^{-(\alpha/\sigma)^2}, \qquad (2-17)$$

which is assumed to be Gaussian with $\Delta = \pm\Omega + \omega_{32} + \alpha$ corresponding to (2-10) or (2-11).

The rotating wave approximation has been applied; the zero order eigenenergies are

$$< j | \mathcal{H}_e | j > \; = \; \hbar\omega_j \text{ and } \omega_{ij} \; = \; \omega_i - \omega_j; \qquad (2-7)$$

the Rabi frequencies for the 1-3 and 2-3 transitions are

$$\chi_1 \; = \; \mu_{13}E_0/\hbar \; = \; | < 1 | \mathcal{H}_o | 3 > | /\hbar$$

$$\chi_2 \; = \; \mu_{23}E_0/\hbar \; = \; | < 2 | \mathcal{H}_o | 3 > | /\hbar \; ; \qquad (2-8)$$

and the diagonal damping rates are given by

$$-\frac{i\hbar}{2}\Gamma_j \; = \; < j | \mathcal{H}_d | j > \; . \qquad (2-9)$$

Furthermore, the tuning parameter

$$\Delta \; = \; -\Omega + \omega_{32} + \alpha \text{ for } \omega_3 >> \omega_2 > \omega_1 \; , \qquad (2-10)$$

where α is the shift in the Pr^{3+} transition frequency ω_{32} due to an inhomogeneity in the local crystalline Stark field. When the energy levels of Fig. 4 are inverted, the counter rotating field component is resonant and (2-10) becomes

$$\Delta \; = \; \Omega + \omega_{32} + \alpha \text{ for } \omega_2 > \omega_1 >> \omega_3 \qquad (2-11)$$

and we replace in (2-6) $e^{\mp ikz}$ by $e^{\mp ikz}$.

A set of equations similar to (2-6) is obtained for the transition 1→3 by the index interchange 1→2. We see that the three wave equations of motion offer a simplification over the nine equations of motion arising in a density matrix treatment, but some generality is lost due to the absence of damping in the off-diagonal terms.

also contains an electronic component $\mathcal{H}_e$, a damping term $\mathcal{H}_d$ and the optical interaction

$$\mathcal{H}_o = -\vec{\mu}\cdot\vec{E}_x(z,t) \qquad (2-4)$$

where μ is the induced dipole and we assume that

$$\mathcal{H}_e >> \mathcal{H}_v >> \mathcal{H}_d > \mathcal{H}_o . \qquad (2-5)$$

We further assume that the two transitions 1→3 and 2→3 are strongly inhomogeneously broadened. Because of the perturbation $\mathcal{H}_v$, the two transitions are split, the minimum spacing being $2|V|$ as suggested in Fig. 4. Because of the inequalities (2-5) and inhomogeneous broadening, the laser field excites one packet in the 1→3 transition and a second packet in the 2→3 transition. Hence, a single packet is not excited simultaneously in both transitions as in a double resonance experiment. This situation affords a simplification allowing the two transitions to be treated independently in first approximation.

We seek a solution to the wave equation

$$i\hbar\frac{\partial\psi}{\partial t} = H\psi$$

of the form

$$\psi(t) = c_1(t)e^{-i\omega_1 t}|1> + c_2(t)e^{-i\omega_2 t}|2> + c_3(t)e^{-i\omega_3 t}|3> .$$

Considering first the 2→3 transition, the equations of motion are

$$\dot{c}_1 = -\frac{\Gamma_1}{2}c_1 - iVe^{-i\omega_{21}t}c_2 \qquad (2-6a)$$

$$\dot{c}_2 = -\frac{\Gamma_2}{2}c_2 - iV^*e^{i\omega_{21}t}c_1 + \frac{i\chi_2}{2}e^{-i(\Delta t+kz)}c_3 \qquad (2-6b)$$

$$\dot{c}_3 = -\frac{\Gamma_3}{2}c_3 + i\frac{\chi_2}{2}e^{i(\Delta t+kz)}c_2 . \qquad (2-6c)$$

hyperfine parameters is discussed in Section IV. We also comment on an anomalous modulation of the anticrossing signal which appears when certain experimental conditions are satisfied, and finally, the effect of anticrossing on optical free induction decay is discussed.

II. THEORY OF THE ANTICROSSING SIGNAL

In this section an expression for an optically detected anticrossing signal is derived. The predicted signal applies to the experimental configuration of Fig. 1 where the intensity of a laser beam is monitored after passing through a sample containing resonant Pr^{3+} impurity ions in a $YAlO_3$ host crystal. By application of an external dc magnetic field, certain pairs of Pr^{3+} states approach each other and then exhibit repulsion or anticrossing behavior (Figs. 2 and 3) due to the combined influence of hyperfine and Zeeman interactions. As the magnetic field is swept through the anticrossing region, the anticrossing states mix and under appropriate conditions produce a corresponding intensity variation in the transmitted beam. We wish to show, contrary to some discussions,[8,10,11] that anticrossings can be observed in absorption in solid state laser spectroscopy even in the linear intensity regime. While nonlinear behavior is possible also, it is not essential.

For the purpose of this discussion assume the three-level quantum system of Fig. 4 where a laser field

$$\vec{E}_x(z,t) = \vec{e}_x E_0 \cos(\Omega t - kz) \qquad (2-1)$$

resonantly excites the 1→3 or 2→3 transition and the states $|1\rangle$ and $|2\rangle$ anticross due to the perturbative interaction $\mathcal{H}_v$, the matrix element being

$$V = \langle 1 | \mathcal{H}_v | 2 \rangle / \hbar . \qquad (2-2)$$

The detailed form of this interaction will be considered in Section III. The total Pr^{3+} Hamiltonian

$$\mathcal{H} = \mathcal{H}_e + \mathcal{H}_v + \mathcal{H}_d + \mathcal{H}_o \qquad (2-3)$$

I. INTRODUCTION

The related phenomena of level crossing and anticrossing have proved to be important spectroscopic techniques in atomic physics and constitute an area which predates both optical pumping and lasers. In level crossing, the resonance fluorescence of a suitable pair of degenerate Zeeman levels exhibits spatial interference as an external magnetic field is slowly swept through zero field (Hanle effect)[1] or a crossing at nonzero field.[2] In anticrossing,[3,4] a pair of excited Zeeman levels are subject to a small static interaction, and when an applied magnetic field is swept, the levels first approach and then repel each other rather than cross, causing the emission intensity to vary.

Most level crossings[5] and anticrossings[6] are detected in spontaneous emission although some absorption studies in atoms and molecules have now been performed using laser sources. The signals can then show both a linear or nonlinear[7-11] dependence on laser intensity. A recent example is the optical Hanle effect,[12] a light shift-induced zero field level crossing.

With few exceptions, optical measurements of level crossings and anticrossings in solids are almost nonexistent. One exception is the photon echo study of ruby[13] which reveals a remarkable variation in the decay behavior when the Zeeman levels are tuned through a level crossing region. A related case is the detection of anticrossings and cross relaxation effects in molecular crystals of photo-excited triplet states using microwave spectroscopy[14]

In this article, we apply the level anticrossing technique to solid state laser spectroscopy, choosing the impurity ion crystal $Pr^{3+}:YAlO_3$ as an example. Several anticrossing signals are observed by linear absorption for the Pr^{3+} zero phonon transition $^3H_4(\Gamma_1) \rightarrow {}^1D_2(\Gamma_1)$ where both ground and excited state anticrossings appear. In Section II, we derive an expression for the anticrossing linear absorption signal of a transition subject to strong inhomogeneous broadening. In Section III, the detailed form of the ^{141}Pr nuclear quadrupole and Zeeman interactions, which give rise to anticrossing, is treated by a numerical diagonalization routine. The utility of anticrossings in determining solid state

RJ3073 (38119) 3/5/81
Physics

ANTICROSSINGS IN SOLID STATE LASER SPECTROSCOPY*

A. Wokaun**, S. C. Rand***, R. G. DeVoe and R. G. Brewer

IBM Research Laboratory
San Jose, California 95193

ABSTRACT: We report the first observation of anticrossings in solid state laser spectroscopy. Measurements are performed on the 6105Å zero phonon transition $^3H_4(\Gamma_1) \leftrightarrow {}^1D_2(\Gamma_1)$ of Pr^{3+} in a $YAlO_3$ crystal at 2°K where both ground and excited state anticrossings appear. A perturbation theory of the anticrossing signal is derived from the wave equations of motion for a three-level quantum system subject to a static interaction V between two neighboring levels (1 and 2) while a laser field resonantly excites the inhomogeneously broadened $2 \leftrightarrow 3$ transition. Ground and excited state gyromagnetic ratios $\gamma_i (i = X,Y,Z)$ and the interactions V are obtained by fitting the observed anticrossings to a diagonalized hyperfine-spin Hamiltonian for $^{141}Pr^{3+}$ which includes second-order ligand field corrections in terms containing the electron orbital angular momentum. Under certain conditions, one anticrossing signal develops into a strongly modulated oscillation with a period of ~20 gauss, an unexpected feature which appears to be a nonlinear optical coherence effect. The influence of anticrossing state mixing on optical free induction decay observations is discussed also.

---

*Work supported in part by the U. S. Office of Naval Research

**Present Address: Bell Telephone Laboratories, Holmdel, New Jersey 07733

***Present Address: Department of Physics, Stanford University, Stanford, California 94305

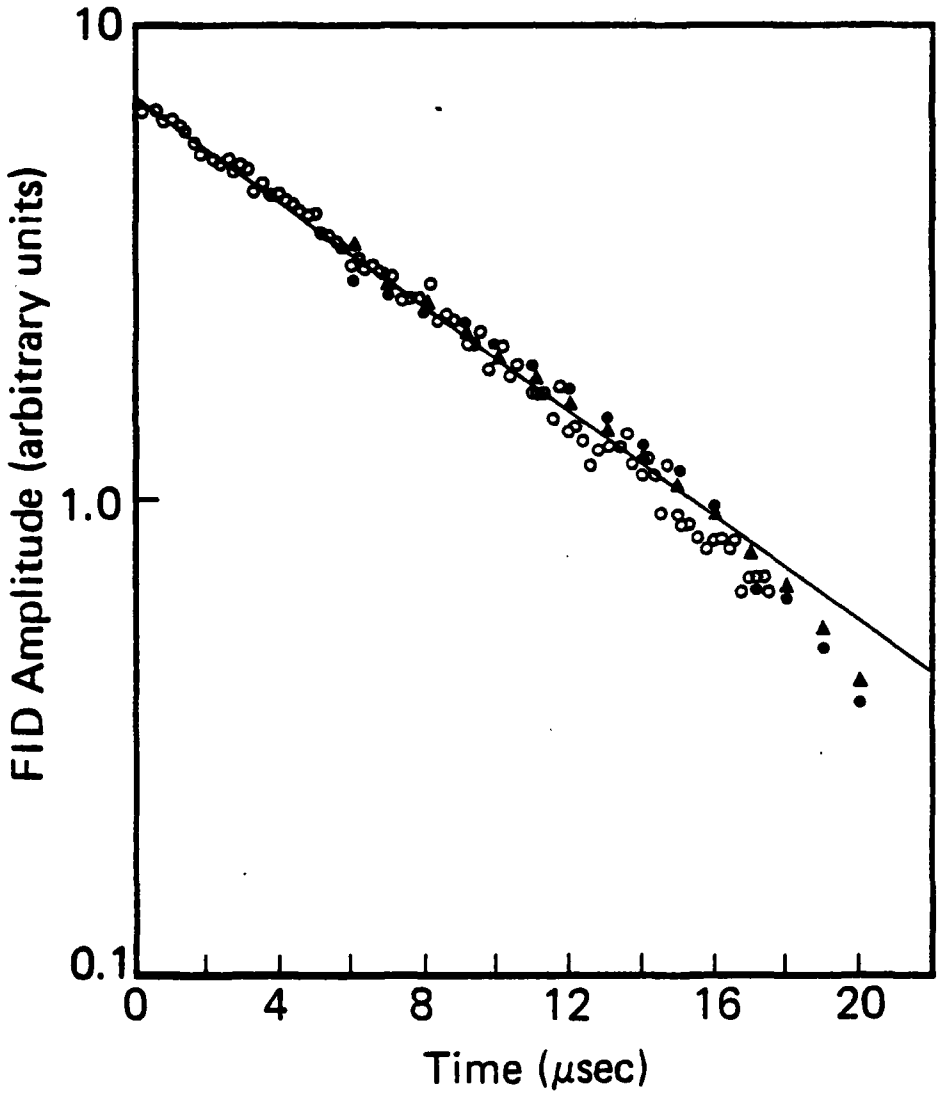


Figure 8. Semi-log plot of the FID signal versus time showing the experimental data: ○ and the Monte Carlo calculation in terms of the out-of-phase Δ: $<v\sin\varphi>$ and the in-phase ●: $<u\cos\varphi>$ components of the Bloch vector where χ=3 kHz. The solid line corresponds to a dephasing time $1/\gamma_\varphi$ = 15.8 μ sec (linewidth: 10.1 kHz).

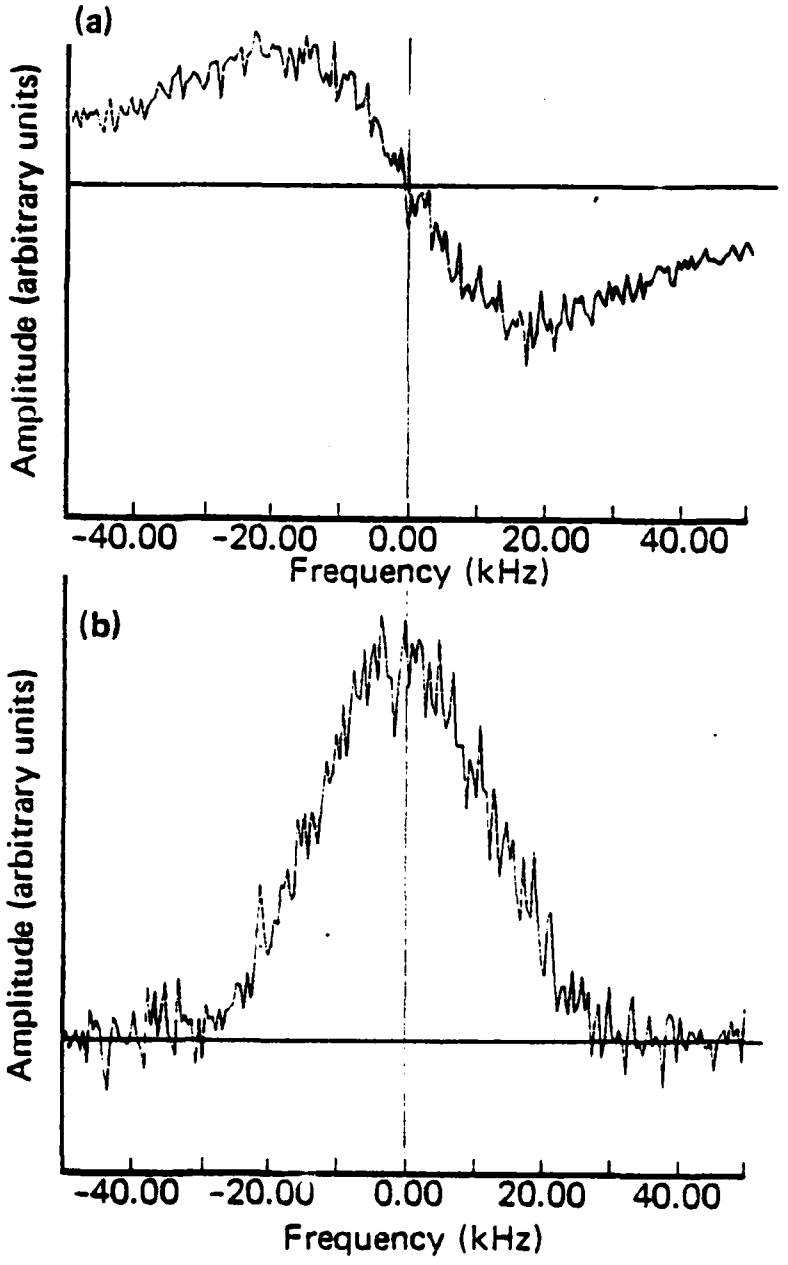


Figure 7. The optical lineshape function of Pr^{3+} during hole burning showing near Lorenztian behavior for the preparative step in terms of (a) the in-phase, u(0), and (b) the out-of-phase, v(0), components of the Bloch vector.

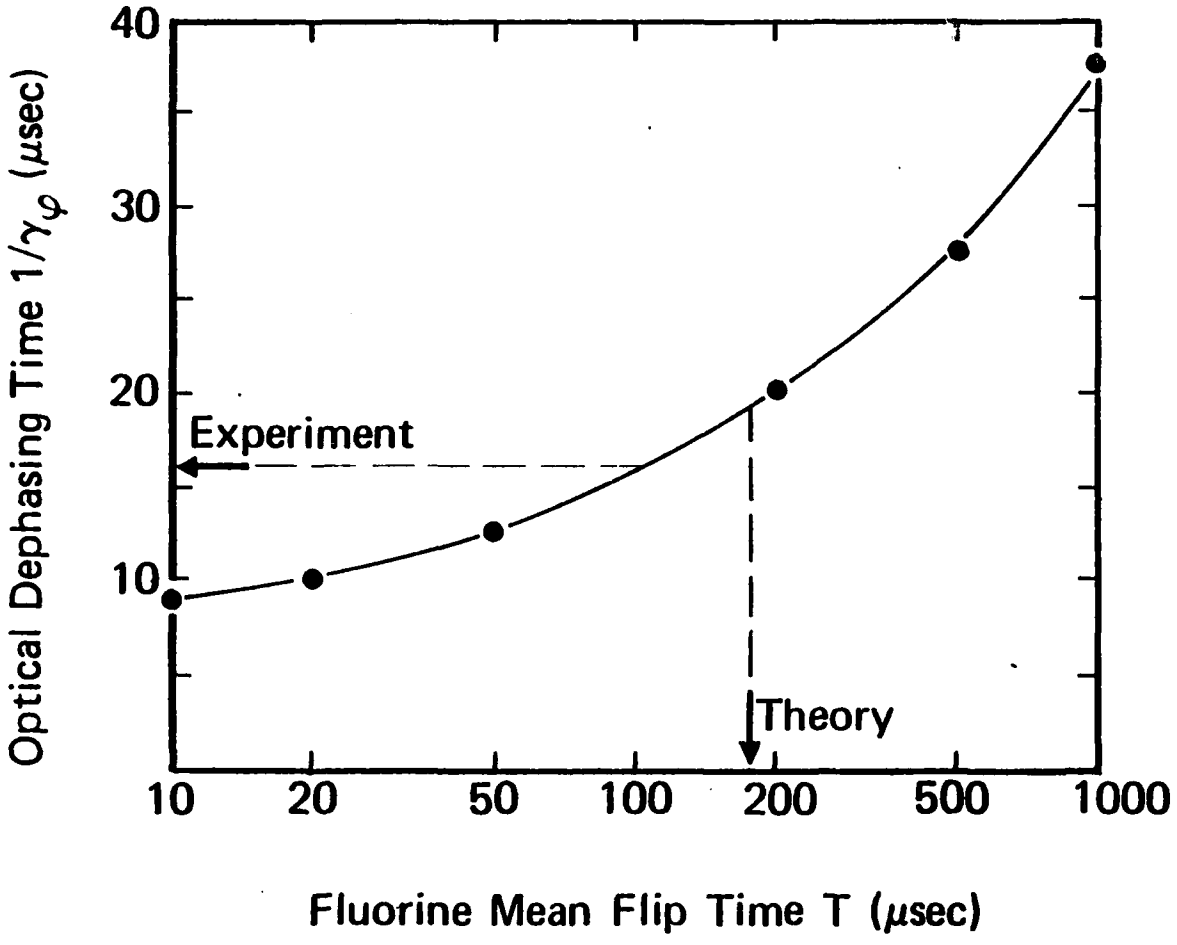


Figure 6. The Pr^{3+} optical dephasing time $1/\gamma_\varphi$ versus the fluorine mean flip time T. The optical FID result is $1/\gamma_\varphi = 15.8\ \mu$ sec and the theoretical fluorine spin flip time T=170 μsec.

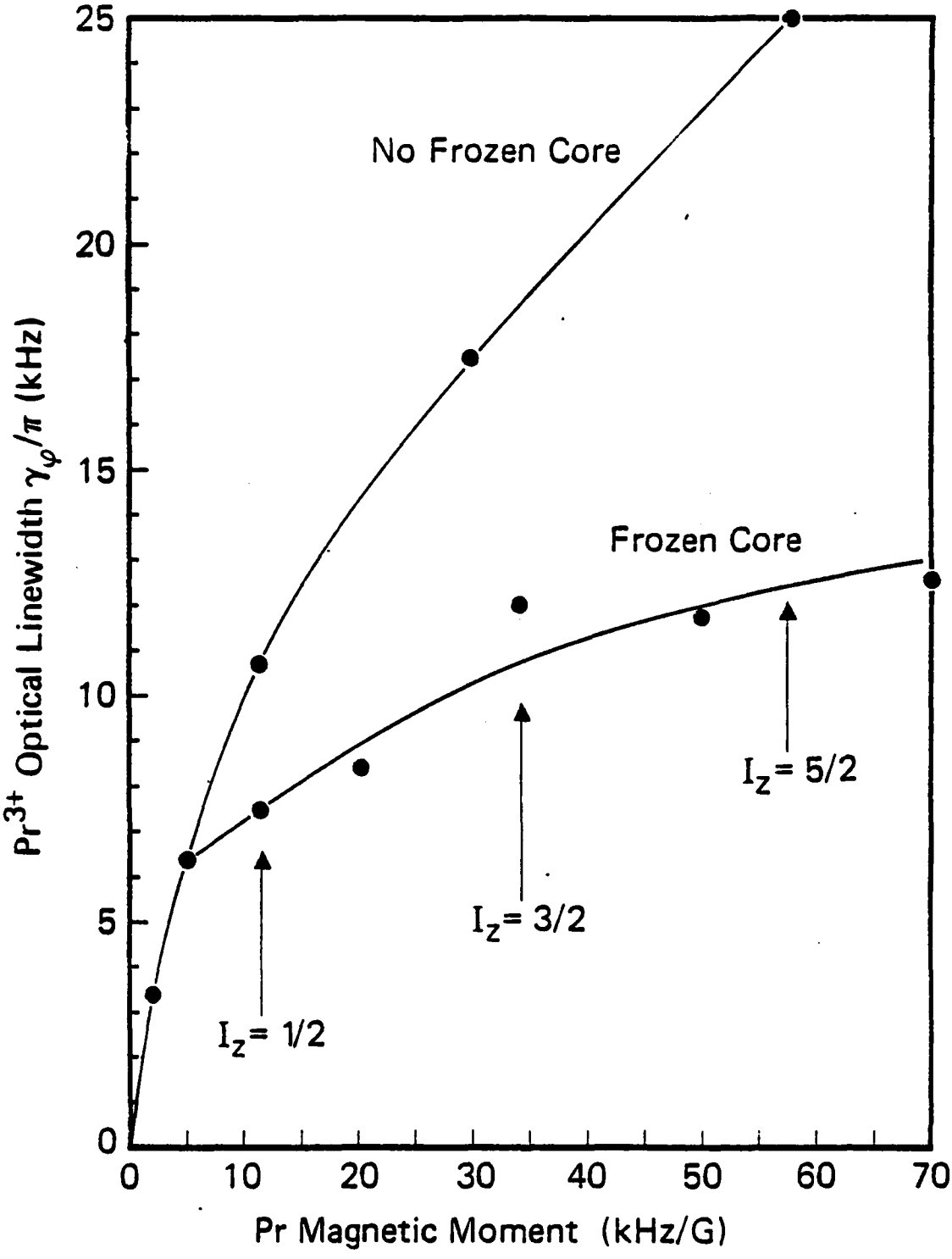


Figure 5. The Pr^{3+} optical linewidth (γ_φ/π FWHM) versus the ^{141}Pr magnetic moment $\mu_z^{Pr} = \gamma_I I_z \hbar$ in units of kHz/G showing the linewidth reduction due to a frozen core where T=50 μsec.

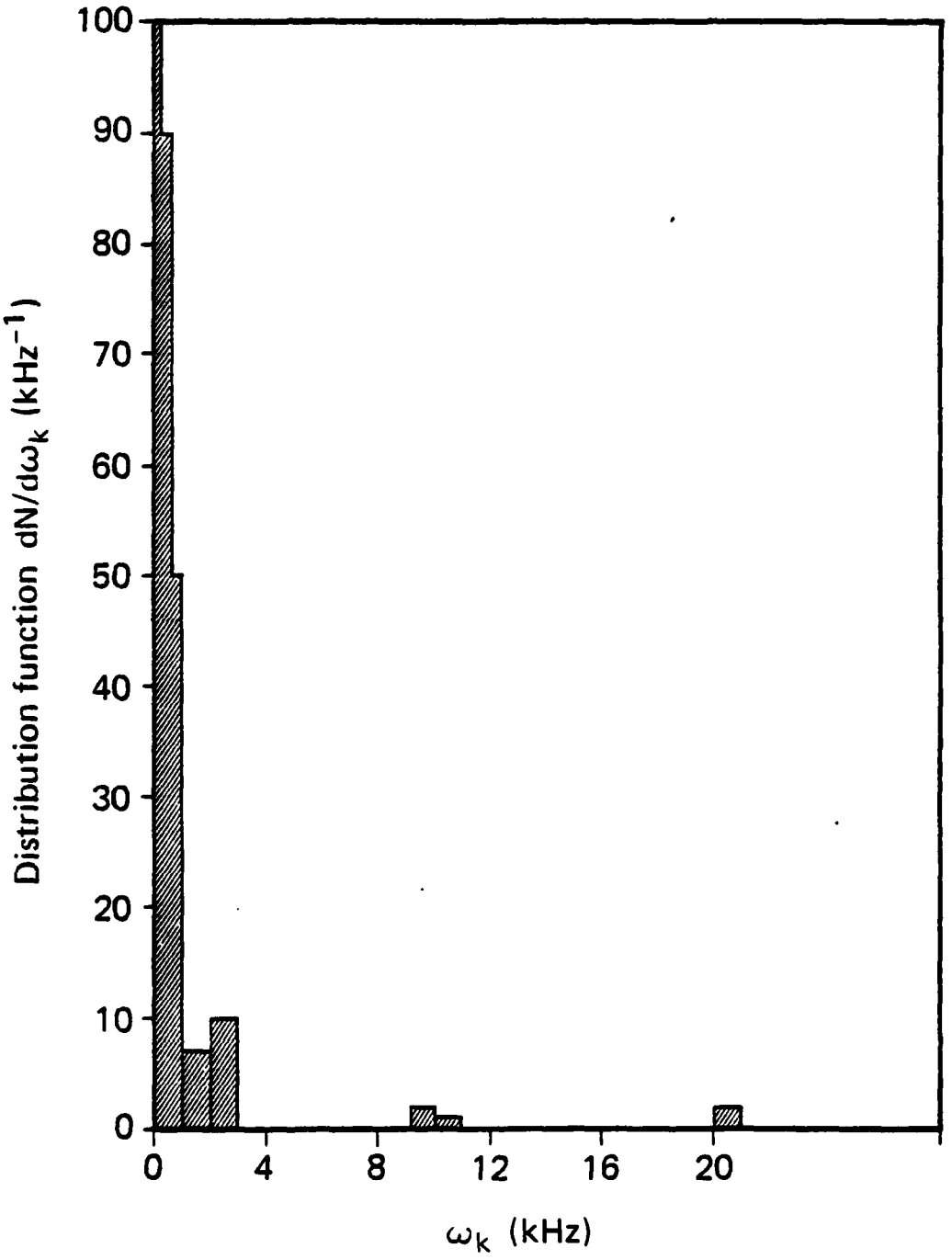


Figure 4. The Pr^{3+} ion distribution function $dn/d\omega_k$ versus the static frequency shift ω_k.

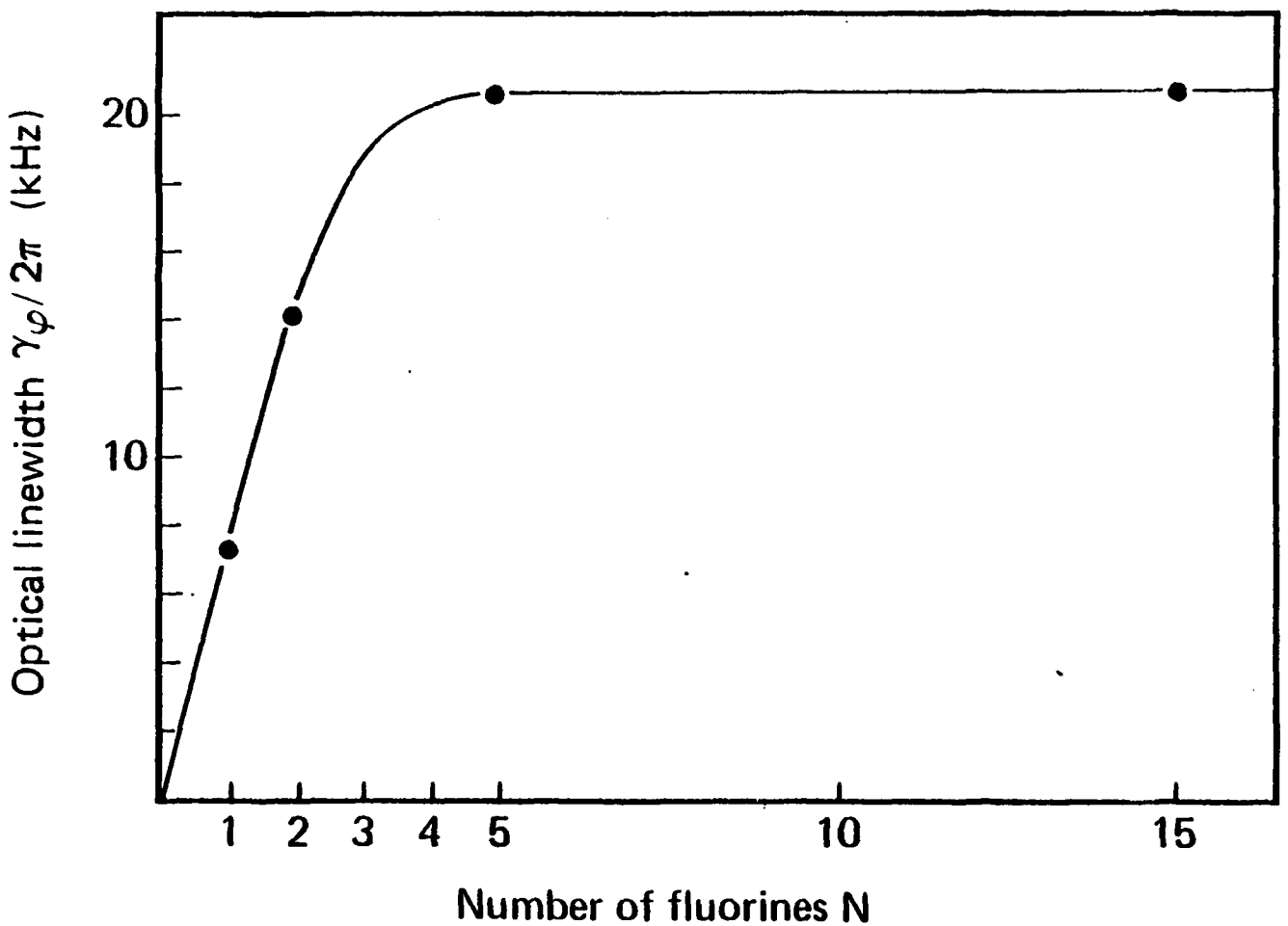


Figure 3. The Pr^{3+} optical linewidth ($\gamma_\varphi/2\pi$ HWHM) of the [illegible] - $^1D_2$ transition for $I_z=1/2$ and the fluorine spin flip time T=50 μsec as a function of the number of fluorine nuclei N where the fluorines closest to the ion are plotted first.

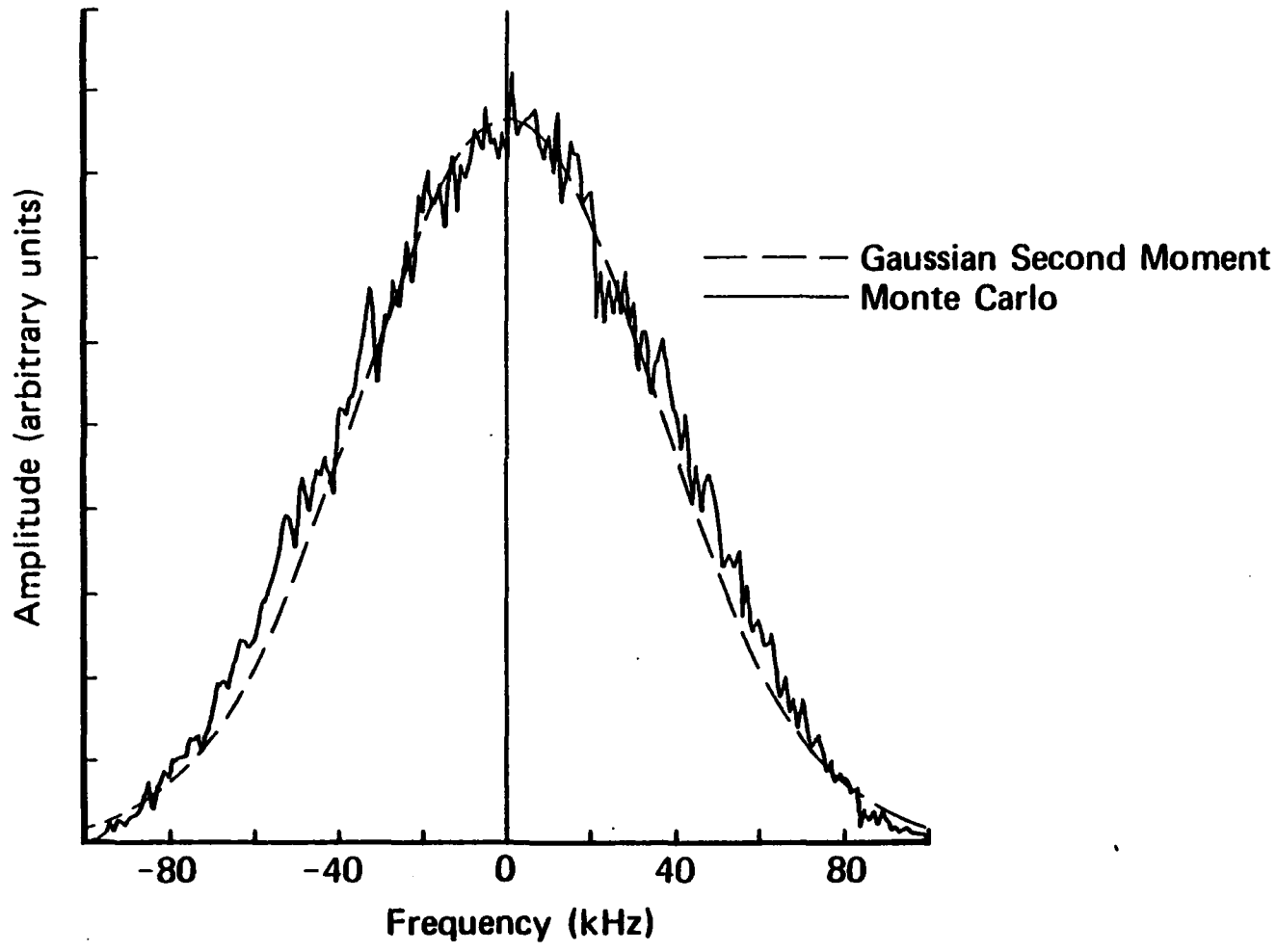


Figure 2. Magnetic inhomogeneous broadening of a ^{141}Pr quadrupole transition showing the Gaussian lineshape of the Monte Carlo calculation (164 kHz FWHM) and an overlapping Gaussian having a width equal to the second moment.

By the inverse transform $c(t) = \frac{1}{2\pi i}\int_{-i\infty+r}^{i\infty+r} e^{zt}c(z)dz$, (2-22) reduces to the first order solutions

$$c_1^{(1)}(t) = \frac{e^{-i\omega_{21}t}}{z_1-z_2}\ \{[(z_1 + \Gamma_2/2)c_1(0)-iVc_2(0)]e^{z_1t}$$

$$-[(z_2 + \Gamma_2/2)c_1(0)-iVc_2(0)]e^{z_2t}\} , \qquad (2-23a)$$

$$c_2^{(1)}(t) = \frac{1}{z_1-z_2}\{[(\Gamma_1/2 + z_1-i\omega_{21})c_2(0)-iV^*c_1(0)]e^{z_1t}$$

$$-[(\Gamma_1/2 + z_2-i\omega_{21})c_2(0)-iV^*c_1(0)]e^{z_2t}\} . \qquad (2-23b)$$

The above derivation simplifies somewhat with the realistic assumption that

$$\Gamma_1 = \Gamma_2 \equiv \Gamma .$$

The poles then become

$$z_1^{(1)} = -\frac{\Gamma}{2} + \frac{i}{2}\left(\omega_{21} + \sqrt{\omega_{21}^2+4|V|^2}\right)$$

$$z_2^{(1)} = -\frac{\Gamma}{2} + \frac{i}{2}\left(\omega_{21} - \sqrt{\omega_{21}^2+4|V|^2}\right) \qquad (2-24)$$

and (2-23) assumes the form

$$c_1^{(1)}(t) = \frac{ie^{-i\omega_{21}t}}{z_1-z_2}(me^{z_1t} + ne^{z_2t}) \qquad (2-25a)$$

$$c_2^{(1)}(t) = \frac{i}{z_1-z_2}(pe^{z_1t} + qe^{z_2t}) \qquad (2-25b)$$

where $m = ac_1(0)-vc_2(0)$, $n = -bc_1(0) + Vc_2(0)$,

$p = -(V^*c_1(0) + bc_2(0))$, $q = V^*c_1(0) + ac_2(0)$,

$$a = \frac{1}{2}(\omega_{21} + \sqrt{\omega_{21}^2+4|V|^2}) \ , \ b = \frac{1}{2}(\omega_{21} - \sqrt{\omega_{21}^2+4|V|^2}) . \qquad (2-26)$$

Note that the wavefunctions (2-23) agree identically with Wieder and Eck[4] who derived the transition probability for the case of spontaneous emission of the anticrossing levels 1 and 2.

We treat the case of absorption for inhomogeneously broadened transitions by formally integrating (2-6c), obtaining the second order result

$$c_3^{(2)}(t) = e^{-\Gamma_3 t/2}\left\{c_3^{(2)}(0) + \frac{i\chi}{2}e^{ikz}\int_0^t c_2^{(1)}(t')e^{(i\Delta+\Gamma_3/2)t'}dt'\right\} \qquad (2-27)$$

in terms of the first order solution $c_2^{(1)}(t)$. Substituting (2-25b) into (2-27) allows us to evaluate the bilinear product

$$c_3(t)c_2^*(t) = \rho_{32}(t) = \tilde{\rho}_{32}(t)e^{i(\Omega t-kz)}, \qquad (2-28)$$

and the superscripts are now dropped. Performing the time average (2.15) of the slowly varying component $\tilde{\rho}_{32}$, we obtain

$$\begin{aligned}
<\tilde{\rho}_{32}(t)>_{t_0} = \frac{i\chi K}{2|z_1-z_2|^2}\Bigg\{ & \frac{-p}{i\Delta+\Gamma_3/2+z_1}\left(\frac{p^*}{-i\Delta-\Gamma_3/2+z_1^*} + \frac{q^*}{-i\Delta-\Gamma_3/2+z_2^*}\right) \\
& - \frac{q}{i\Delta+\Gamma_3/2+z_2}\left(\frac{p^*}{-i\Delta-\Gamma_3/2+z_1^*} + \frac{q^*}{-i\Delta-\Gamma_3/2+z_2^*}\right) \\
& + \frac{1}{i\Delta+\Gamma_3/2+z_1}\left(\frac{pp^*}{z_1+z_1^*} + \frac{pq^*}{z_1+z_2^*}\right) \\
& + \frac{1}{i\Delta+\Gamma_3/2+z_2}\left(\frac{p^*q}{z_1^*+z_2} + \frac{qq^*}{z_2+z_2^*}\right)\Bigg\} \qquad (2-29)
\end{aligned}$$

where it is assumed that the coherent preparation terms $c_3(0)c_2^*(0) = 0$ and $c_3(0)c_1^*(0) = 0$.

To average (2-29) over the inhomogeneous lineshape, we apply (2-16) evaluating the integrals by contour integration under the assumption that the Gaussian is slowly varying and can be factored outside the integral when $\sigma >> \sqrt{\Gamma^2 + 4|V|^2}$. Consider first that the three states are ordered in

energy according to (2-11) so that the decay rates of lower and upper states satisfy $\Gamma_3<\Gamma$. Then the poles of $1/(i\Delta+\Gamma_3/2+z_{1,2})$ in (2-29) reside in the lower half plane (lhp) while the remaining poles lie in the upper half plane (uhp). When the level structure is inverted satisfying (2-10), we similarly assume that $\Gamma<\Gamma_3$ and then all poles are in the uhp. In either case, we find that

$$< < \tilde{\rho}_{32}(t) >_{t_0} >_I = \frac{-i\pi\chi_2 G(|\omega_{32}|-\Omega)K}{2(\omega_{21}^2+4|V|^2)}$$

$$\times\left\{[2|V|^2c_1^2(0)+(\omega_{21}^2+2|V|^2)c_2^2(0)]/\Gamma+\frac{2\Gamma|V|^2[c_2^2(0)-c_1^2(0)]}{\omega_{21}^2+\Gamma^2+4|V|^2}\right\}. \qquad (2-30)$$

For the $1\leftrightarrow3$ transition, the quantity $< < \tilde{\rho}_{31}(t) >_{t_0}) >_I$ is derived from (2-30) by the index interchange $1\leftrightarrow2$.

A trivial integration of (2-13) for both transitions, $1\leftrightarrow3$ and $2\leftrightarrow3$, yields the linear absorption anticrossing signal (2-19),

$$I_s = -2\pi^2 kNL\hbar GK\left\{\frac{c_1^2(0)\chi_1^2+c_2^2(0)\chi_2^2}{\Gamma}\right.$$

$$\left.+\frac{2|V|^2}{\Gamma(\omega_{21}^2+\Gamma^2+4|V|^2)}(\chi_1^2-\chi_2^2)(c_2^2(0)-c_1^2(0))\right\} \qquad (2-31)$$

where it is assumed that $G(|\omega_{32}|-\Omega)\sim G(|\omega_{31}|-\Omega)\equiv G$. As the level splitting ω_{21} is tuned, the first term of (2-31) remains invariant and provides a constant background signal whereas the second term displays anticrossing behavior in the form of a Lorenztian lineshape of angular linewidth

$$\Delta\omega_{1/2} = \sqrt{\Gamma^2+4|V|^2}. \qquad (2-32)$$

We now see that the anticrossing signal vanishes when either the dipole matrix elements or the population difference of the anticrossing states satisfy

$$\chi_1^2-\chi_2^2 = 0 \quad \text{or} \quad c_2^2(0)-c_1^2(0) = 0 . \qquad (2-33)$$

This occurs even though the wavefunction admixture of the anticrossing states varies as ω_{21} is tuned because the gain of light intensity in one transition is just lost by the other. However, linear absorption anticrossing signals can be detected in systems such as Pr^{3+}:LaF_3 or Pr^{3+}:$YAlO_3$ due to the fact that (2-33) is often violated, i.e., $\chi_1^2 \neq \chi_2^2$ and optical pumping redistributes the population among the Zeeman substrates so that $c_2^2(0) \neq c_1^2(0)$. This conclusion seems to disagree with earlier work which states that linear absorption anticrossing signals vanish for inhomogeneously broadened transitions.[8,10,11]

In contrast to anticrossing signals detected by spontaneous emission, the absorption signal predicted by (2-31) is equally valid for anticrossings in lower and upper transition states, consistent with (2-10) and (2-11).

In addition, the anticrossing term goes to zero in the limit $V \to 0$, and therefore, (2-31) does not apply to level crossing which requires that $V=0$. This result is expected since (2-31) fails when $4|V|^2 < \Gamma^2$ as then the two transitions $1 \to 3$ and $2 \to 3$ are coupled and cannot be treated separately.

III. HAMILTONIAN: ZEEMAN AND QUADRUPOLE INTERACTIONS

To predict the magnetic field dependence of anticrossings of Pr^{3+}:$YAlO_3$ in the $^3H_4(\Gamma_1)$ and $^1D_2(\Gamma_1)$ states, it is necessary to diagonalize the Hamiltonian[16,17]

$$\mathcal{H}' = g\beta\vec{B}\cdot\vec{J} + a_J\vec{J}\cdot\vec{I} - g_N\beta_N\vec{B}\cdot\vec{I} + P[I_{Z'}^2 - \tfrac{1}{3}I(I+1) + \tfrac{1}{3}\eta(I_{X'}^2 - I_{Y'}^2)] , \qquad (3-1)$$

which we treat as a perturbation on the ligand field interaction. The first term describes the Zeeman interaction of a Pr^{3+} ion with angular momentum $J\hbar$; the second term is the magnetic hyperfine

interaction of ^{141}Pr with nuclear angular momentum $I\hbar$ where $I=5/2$; and the third term is the nuclear Zeeman interaction. The remaining terms are the nuclear electric quadrupole interaction where P is the quadrupole coupling constant and the asymmetry parameter $\eta = (V_{X'X'}-V_{Y'Y'})/V_{Z'Z'}$ is given in terms of the diagonal tensor components of the electric field gradient at the nucleus in the principal axis system (X',Y',Z').

Following Teplov,[16] we expand (3-1) in the principal axis system (X,Y,Z) of a pseudo-quadrupole tensor Λ_{ii}, defined below, so that

$$\mathcal{H}' = \sum_{i=X,Y,Z} \{ g\beta(B_iJ_i) + a_J(J_iI_i) - g_N\beta_N(B_iI_i) \}$$

$$+ P[I_{Z'}^2 - \frac{1}{3}I(I+1) + \frac{1}{3}\eta(I_{X'}^2 - I_{Y'}^2)] \qquad (3-2)$$

and derive the second order eigenenergy correction

$$W^{(2)} = -\sum_{n\neq 0} \frac{|<n|\mathcal{H}'|0>|^2}{\varepsilon_n - \varepsilon_0} \qquad (3-3)$$

where $|0>$ and $<n|$ represent the lowest state and an excited state of a crystal field Stark split manifold. The only nonvanishing matrix elements of (3-3) are those involving the electron angular momentum operators $J_{X,Y,Z}$ which appear in the first two terms of (3-2). We thus obtain

$$W^{(2)} = -\sum_{i=X,Y,Z} [2g\beta(B_iI_i) + (g\beta B_i)^2/a_J + a_JI_i^2]\Lambda_{ii} \qquad (3-4)$$

where only the diagonal tensors

$$\Lambda_{ii} = \sum_{n\neq 0} \frac{a_J|<0|J_i|n>|^2}{\varepsilon_n - \varepsilon_0} \qquad (3-5)$$

survive in the principal axis system (XYZ). In Eq. (3-4), the first term is a linear Zeeman term which produces an enhanced ^{141}Pr nuclear magnetism,[16,17] and the second term is the quadratic Zeeman effect or Van Vleck paramagnetism. The third term is a pseudo-quadrupole interaction[16,17] that can be cast in the form

$$-\sum_{i=X,Y,Z} a_J I_i^2 \Lambda_{ii} = D_a[I_Z^2 - \tfrac{1}{3}I(I+1)] + E_a(I_X^2 - I_Y^2) \qquad (3-6a)$$

where

$$D_a = a_J[(\Lambda_{XX} + \Lambda_{YY})/2 - \Lambda_{ZZ}] \qquad (3-6b)$$

$$E_a = \frac{a_J}{2}(\Lambda_{YY} - \Lambda_{XX}) \qquad (3-6c)$$

Teplov's Hamiltonian assumes that the Pr^{3+} ion is in a crystal field of orthorhombic symmetry. This symmetry is sufficiently high that all tensors, such as the pseudo-quadrupole tensor Λ_{ij} and the field gradient tensor V_{ij}, can be diagonalized in the same principal axis system, making the above coordinate systems (XYZ) and (X'Y'Z') coincident. For the case of Pr^{3+}:$YAlO_3$, the site symmetry C_{1h} is lower, and rigorously it is no longer always possible to diagonalize Λ_{ij} and V_{ij} in the same coordinate system. This can be seen by first selecting a coordinate system (XYZ) for the C_{1h} symmetry adapted wavefunctions[18]

$$|J,\Gamma_1> = \sum_{J_Z \text{even}} a_{J_Z} |J,J_Z>$$

$$|J,\Gamma_2> = \sum_{J_Z \text{odd}} a_{J_Z} |J,J_Z> ,$$

which is coincident with that of the principal axis (X'Y'Z') of the field gradient tensor V_{ij}. Here, $|J,J_Z>$ is the spherical harmonic Y_{J,J_Z}. Now off-diagonal terms Λ_{ij} appear in (3-4) because the coefficients a_{J_Z}, which are unknown for Pr^{3+}:$YAlO_3$, are not restricted by symmetry. Of course,

when the coordinates (XYZ) are selected so that Λ_{ij} is diagonal, we recover (3-4) but then (XYZ) and (X'Y'Z') are no longer coincident. The reflection operation of C_{1h} only specifies that the coordinate systems (XYZ) and (X'Y'Z') be coincident in one principal axis while the other two axes are related by a rotation.[18a]

A simplification results, however, when we recognize that the Pr^{3+} pseudo-quadrupole moment is expected to be larger than the pure quadrupole moment, $|D_a| >> |P|$. Then, the Λ_{ij} tensor is dominant and with little error we can assume that (XYZ) and (X'Y'Z') are coincident. This approximation is well satisfied by the Pr^{3+} ground state $^3H_4(\Gamma_1)$ and less so by the excited state $^1D_2(\Gamma_1)$. The additional question of the relative orientation of the Λ tensor in the two states $^3H_4(\Lambda_1)$ and $^1D_2(\Lambda_1)$ is discussed in Section IV.

With (3-4) and (3-6), Eq. (3-1) becomes

$$\mathcal{H}' = -\hbar \sum_{i=X,Y,Z} \gamma_i B_i I_i + D[I_Z^2 - \tfrac{1}{3} I(I+1)] + E(I_X^2 - I_Y^2) + \sum_{i=X,Y,Z} (g\beta B_i)^2 \Lambda_{ii}/a_J \qquad (3-7a)$$

where

$$\gamma_i = (g_N \beta_N + 2g\beta\Lambda_{ii})/\hbar \,, \qquad (3-7b)$$

$$D = D_a + P \,, \qquad (3-7c)$$

$$E = E_a + \tfrac{1}{3} P\eta \,. \qquad (3-7d)$$

Note that the g values as defined in (3-1) are positive and that the term $2g\beta\Lambda_{ii}$ of (3-7b) appears with a plus sign, in agreement with Bleaney[17] but not Teplov[16] or Erickson.[19] Since the hyperfine constant for $^{141}Pr^{3+}$ is positive, $a_J = +1093$ MHz,[17] if follows that $\Lambda_{ii} > 0$ and the enhancement of γ_N in (3-7b) is positive.

Considering only the linear Zeeman and quadrupole terms of (3-6a), we rewrite the components of the field B in polar coordinates and obtain

$$\mathcal{H}' = -B_0\hbar[\gamma_X I_X \sin\theta\cos\phi + \gamma_Y I_Y \sin\theta\sin\phi + \gamma_Z I_Z \cos\theta]$$

$$+ D[I_Z^2 - \tfrac{1}{3}I(I+1)] + E(I_X^2 - I_Y^2) \,. \qquad (3-8)$$

The diagonalization of the 6×6 energy matrix arising from (3-8) assumes that the axis of quantization is along the principal Z axis and the operation

$$I_Z\psi = m\psi$$

defines the ^{141}Pr nuclear spin eigenvalue m. The off-diagonal matrix elements of (3-8) are generated by

$$I_X = \tfrac{1}{2}(I_+ + I_-)$$

$$I_Y = \tfrac{1}{2i}(I_+ - I_-)$$

where

$$< m\pm1 \,|\, I_\pm \,|\, m > = [(I\mp m)(I\pm m+1)]^{1/2} \,.$$

The quadratic terms are given by

$$< m' \,|\, I_i^2 \,|\, m > \;=\; < m' \,|\, I_i \,|\, m'' > < m'' \,|\, I_i \,|\, m > \,, \quad (i = X,Y,Z)$$

where $m' = m$ for I_Z and $m' = m, m\pm2$ for $I_{X,Y}$.

The results of this numerical calculation are shown in Fig.s 2, 3 and 5 and Tables I and II.

IV. DETECTION OF ANTICROSSINGS

A. Experimental Technique

Anticrossings are monitored with the experimental arrangement of Fig. 1 which assumes the $YAlO_3$ crystal geometry of Fig. 6. The beam of a single mode cw ring dye laser propagates along the c axis of a crystal of 0.1% Pr^{3+}:$YAlO_3$, immersed in liquid Helium at 1.8°K, and thereby resonantly excites the Pr^{3+} transition $^3H_4(\Gamma_1) \leftrightarrow {}^1D_2(\Gamma_1)$ at a wavelength of 610.5 nm. The laser field is polarized parallel to the crystal a axis, is focussed slightly within the sample to a 200 micron diameter, and has a power in the range 10 to 80 mW. When an external dc magnetic field is applied to the crystal along the b axis and is slowly swept through an anticrossing, in the region 0 to 2 kilogauss, the intensity of the transmitted beam changes. The magnitude of this change is typically 0.1% and is detected with a PIN diode (EGG-SGD160) using phase sensitive detection. For this purpose, the magnetic field is modulated sinusoidally in the range 8 to 25 gauss peak to peak at a frequency of a few kiloHertz, and the anticrossing signals are displayed as a derivative lineshape on an X-Y chart recorder. Signals in quadrature were too small to be detected.

The space group of $YAlO_3$ is D^{16}_{2h}=Pbnm and has an orthorhombic unit cell.[20] The yttrium ions are located in two inequivalent sites, and the praseodymium ion substitutes for yttrium, retaining the original C_{1h} site symmetry. The crystal was cut and polished in the form of a platelet with dimensions $5 \times 5 \times 1.1$ mm^3 parallel to the crystal axes a:b:c. X-ray patterns confirm that the crystal axes are parallel to the faces as in Fig. 6 to an uncertainty of one degree. The crystal can be oriented in either of two orthogonal rotations, through the angles γ or α of Fig. 6, allowing the fixed Zeeman field to make various angles with the crystal axes. In this way, the angular dependence of the magnetic field position of the anticrossing signal can be determined and compared with theory.

The dc magnet (Varian V-4005) was calibrated with a Hall probe (Bell 640) which in turn was calibrated with a reference magnetic (Varian 2100) locked to the proton NMR resonance at 23 MHz. In the range of these measurements, 0 to 2000 gauss, the field is known to an uncertainty of $\pm 1\%$.

As noted previously for the case of Pr^{3+}:LaF_3, optical pumping depletes the population of the hyperfine packets which absorb laser light and reduces the signal to nondetectable levels.[21,22] As in the past,[21,22] we sweep the laser frequency slowly at ~16 MHz/msec so that the optical pumping process is partially reversed and a sizable population is maintained.

Anticrossings were also detected in Pr^{3+}:LaF_3 but were not studied in the same detail as Pr^{3+}:$YAlO_3$.

B. Observations and Results

Figure 7(b) is an example of anticrossings observed in Pr^{3+}:$YAlO_3$ for the case $\alpha=0°$ and $\gamma=0°$ where the signals appear as derivative lineshapes with an intensity that varies approximately linearly with laser intensity. The first signal, labeled "a", is a zero-field level crossing and as the magnetic field increases, four anticrossings appear labeled b, c, d and e. These five signals are in perfect agreement with the number predicted by the diagonalization calculations shown in Fig. 2 for $^3H_4(\Gamma_1)$ and in Fig. 3 for $^1D_2(\Gamma_1)$ where the features are labeled in the same way as in Fig. 7. The calculations assume the hyperfine parameters of Table I and allow us to identify that the b anticrossing occurs in the $^1D_2(\Gamma_1)$ excited state while the c, d and e anticrossings occur in the $^3H_4(\Gamma_1)$ ground state. The characteristics of these anticrossings are summarized in Table II which gives the position of the anticrossing line, the linewidth, and the calculated minimum level spacing at the anticrossing, expressed by a parameter $2|V|$. Note that since the exact diagonalization involves all states, V cannot be correlated rigorously with a matrix element just between two states as in Eq. (2.2).

The fact that the interaction V is nonzero (Table II) proves that features b through e are all anticrossings, i.e., as a pair of levels approach each other, they ultimately repel one another rather than cross. Group theoretical arguments also predict this behavior. Since the symmetry of a general

electric field gradient tensor ($\eta \neq 0$) is D_{2h} and the symmetry of the Zeeman interaction is the one dimensional rotation group SU(1), the symmetry of the combined interaction is

$$D_{2h} \cap C_{\infty} = \begin{cases} C_2 \text{ if magnetic field is along a principal axis ,} \\ \{E\} \text{ otherwise .} \end{cases}$$

The group {E} possesses no symmetry element beyond the identity operation so that all functions transform identically according to one irreducible representation and all basis states can mix or give rise to anticrossings. This is a manifestation of the non-crossing rule where states of the same symmetry do not cross. For the experiments reported here, only anticrossings are expected since the field never lies along a principal axis. Should the magnetic field lie along a principal axis, then the rotation operation $R_z(\phi)\,|\,m\rangle = e^{-im\phi}\,|\,m\rangle$ for C_2 symmetry ($\phi = \pi$) yields two groups of states $\{|\,5/2\rangle, |\,1/2\rangle, |\,-3/2\rangle\}$ and $\{|\,-5/2\rangle, |\,-1/2\rangle, |\,3/2\rangle\}$ which transform according to different irreducible representations. For this case, two eigenstates derived from the same group can anticross while two eigenstates derived from the two different symmetry groups can cross.

The tuning behavior of the anticrossing is dominated by the γ_Z term in the Hamiltonian since it gives rise to a first order Zeeman effect. The γ_X and γ_Y terms, which we consider later, produce a small second order Zeeman effect for fields 0 to 2000 gauss, and while these terms broaden the anticrossing line, they do not result in a noticeable shift of line center. The magnitude of γ_Z is determined from calculations, as shown in Fig. 5, which reproduce the observed line centers listed in Table II. For the $^3H_4(\Gamma_1)$ state, the calculation assumes Erickson's values[19] of the quadrupole parameters D and E and his determination that the principal z axis of the quadrupole tensor lies in the crystal a-b plane and at an angle $\beta = \pm 56.50°$ to the b axis (Fig. 6). It follows that for C_{1h} site symmetry the principal X(Y) axis also lies in the a-b plane while the Y(X) axis is perpendicular to it. The resulting value $\gamma_Z/2\pi = 11.910 \pm 0.10$ kHz/G agrees well with Erickson's low field corrected value[19,23] 11.7 ± 0.04 kHz/G. The precision of our fit, as indicated in Table II, is uncertain by about

0.2% but the absolute error is of the order of ±1% due largely to the limiting signal to noise ratio and the uncertainty in the magnetic field.

The anticrossings also shift in a predictable manner when the $YAlO_3$ crystal is rotated about the a axis through the angle α or about the c axis through the angle γ (see Fig. 6). The angular dependence further corroborates the validity of the diagonalization routine, the choice of parameters, and the existence of two inequivalent Pr^{3+} sites. Figure 7(a) shows the pronounced effect of a small rotation of γ=0.9° (α=0°) on the sharp $^3H_4(\Gamma_1)$ anticrossing c which lies on top of the broader d anticrossing. This feature which is initially at 536.5G when γ=0°, splits into two components at 524 and 550G corresponding to the two inequivalent Pr^{3+} sites indicated in Fig. 6. Table II shows that the calculations agree identically with these results.

In Fig. (8), the rotation angle α is varied (γ=0°) where the observed anticrossing positions agree reasonably well with theory. When α becomes sufficiently large, the calculations reveal that the anticrossings are no longer distinct at which point signals cannot be detected.

For the $^1D_2(\Gamma_1)$ state, the orientation of the principal axis system is unknown although C_{1h} symmetry dictates that one principal axis must be perpendicular to a plane of symmetry, the a-b plane. The α rotation pattern of Fig. 8 shows that the $^1D_2$ anticrossing b changes position very slowly with angle as do the $^3H_4$ anticrossings c and e and can be fit approximately with the $^3H_4$ principal axis system indicated in Fig. 6. A more critical test is the γ rotation pattern where α=0°. We find that the b anticrossing splits into pairs of lines as follows: 200G(γ=0°), 240,170G(γ=10°), and 10,160G(γ=20°). This case can be fit if the principal axis Z lies in the crystal a-b plane as shown in Fig. 6 but β=±40°, instead of ±56.50°, and $\gamma_Z(^1D_2)/2\pi$=2.5 kHz/G. The two-fold symmetry of the two inequivalent sites is required by the $YAlO_3$ crystal symmetry since one yttrium site can be transformed into the other by a glide plane.

In Table I, we note that the only splitting factor that is significantly enhanced is $\gamma_Z(^3H_4)$ as $_i/2\pi$=1.3 kHz/G.

Equation (2-31) predicts that the anticrossing lineshape is a Lorenztian of the form

$$I_s \sim \frac{1}{\omega_{21}^2 + 4|V|^2 + \Gamma^2} \quad . \qquad (4-1)$$

hile the anticrossing line center is determined by γ_Z, the angular linewidth

$$\Delta\omega_{1/2} = \sqrt{4|V|^2 + \Gamma^2}$$

ın be determined by the effect of γ_X and γ_Y on the interaction $|V|$, i.e., one-half the minimum level)acing derived from the Hamiltonian (3.8). The observed linewidths of anticrossings b, d, and e ven in Table II are strongly affected by $|V|$ since $4|V|^2 >> \Gamma^2$ where the population decay rates $(^1D_2)=5.4\times10^3$ sec^{-1} [19] and $\Gamma(^3H_4)\leq 0.02$ sec^{-1}.[24] One wonders why the linewidth should be fluenced by the static interaction V since Lorenztian lineshapes are usually broadened by dynamic ocesses of a stochastic nature. The answer lies in the detection process. As the magnetic field is vept through the anticrossing region, the degree of mixing of the anticrossing states changes and)nsequently the transition probability for optical excitation changes correspondingly. Since the ixing process is confined to the region $|V|$, the optical response is also.

A fit of the linewidth is achieved by replacing $(\omega_{21}^2 + 4|V|^2)$ in (4-1) by the square of the genenergy derived from the diagonalization routine and by varying the parameters γ_X and γ_Y. deed, this fit yields the minimum level spacing parameter $|V|$ given in Table II. Since the adrupole parameter E~0, it follows from (3-5) and (3-6c) that $\gamma_X \sim \gamma_Y$. The resulting γ_X and γ_Y lues are given in Table I and the interactions $|V|/\pi$ in Table II. The calculated peak to peak rivative linewidths for the b, d and e anticrossings are 46, 100 and 52G, respectively. The reement with the observed widths is only suggestive. Instrumental limitations, such as the rf

etic field modulation of 8 to 25G, appear to mask the width of the narrow c anticrossing
/π=9.2 kHz) and the zero field level crossing (| V | /π=0), feature a, which cannot be
ined by the | V | or Γ terms in (4-1). Laser frequency jitter should have no effect on the
idth measurements, and indeed, the anticrossing linewidths were unaffected by laser frequency
ıg.

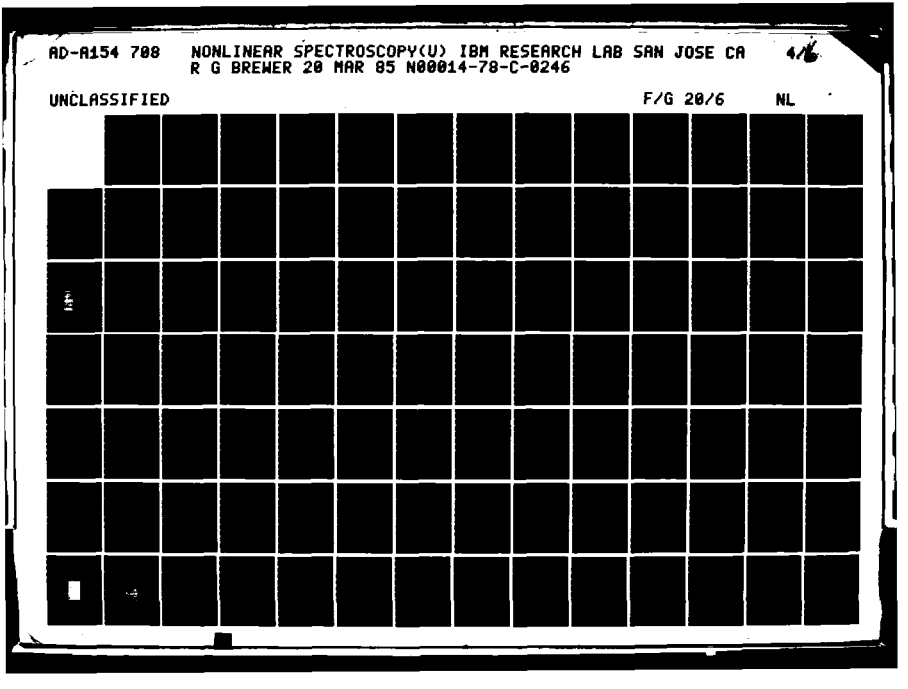
nomalous Wiggle Effect

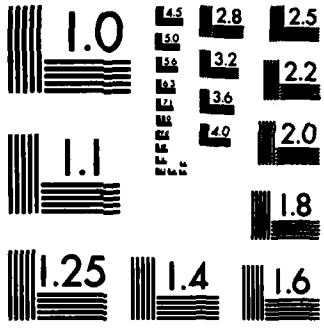
In the region of the c and d anticrossings, an unexpected oscillation (Fig. 9) occurs when
n conditions are satisfied. First, the laser power must exceed 20 mW, and second, the laser
ency sweep rate must be at least 250 MHz/msec corresponding to a ±85 MHz sweep at a
ition rate of 1.5 kHz or higher. The period of oscillation is about 20 gauss and remains invariant
anges in laser power or sweep rate. However, the amplitude of oscillation is remarkably affected
ing a quadratic dependence on laser intensity and a vanishing amplitude when the sweep rate falls
r 0.75 kHz.

The 20 gauss interval appears to be unrelated to hyperfine or superhyperfine splittings or Rabi
ıtions and is probaby a nonlinear coherence phenomenon. Since the $^1D_2(\Gamma_1)$ radiative lifetime is
msec[19] and the hyperfine splittings are of the order of a few megaHertz. the laser frequency
) is large enough and fast enough to coherently prepare packets of three-level quantum systems
4). Thus, the theory of Section II does not apply. The dynamics of coherent two-photon
sses in three-level quantum systems has been investigated previously[25] for certain cases and
ıts a quantum beat effect[26] which produces two sidebands shifted by the 1-2 level spacing
'|. However, this is not an oscillation and the physical origin of these anticrossing oscillations
ıs mysterious.

AD-A154 708 NONLINEAR SPECTROSCOPY(U) IBM RESEARCH LAB SAN JOSE CA 4/6
R G BREWER 20 MAR 85 N00014-78-C-0246

UNCLASSIFIED F/G 20/6 NL




1.0
1.1
1.25
1.4
1.6
1.8
2.0
2.2
2.5
2.8
3.2
3.6
4.0
4.5
5.0
5.6
6.3
7.1
8.0
9.0
10.0
11.2
12.5
14.0
16.0
18.0
20.0
22.4
25.0
28.0
32.0
36.0
40.0
45.0
50.0
56.0
63.0
71.0
80.0
90.0
100.0
112.0
125.0
140.0
160.0
180.0
200.0
224.0
250.0
280.0
320.0
360.0
400.0
450.0
500.0
560.0
630.0
710.0
800.0
900.0
1000.0
1120.0
1250.0
1400.0
1600.0
1800.0
2000.0
2240.0
2500.0
2800.0
3200.0
3600.0
4000.0
4500.0
5000.0
5600.0
6300.0
7100.0
8000.0
9000.0
10000.0
11200.0
12500.0
14000.0
16000.0
18000.0
20000.0
22400.0
25000.0
28000.0
32000.0
36000.0
40000.0
45000.0
50000.0
56000.0
63000.0
71000.0
80000.0
90000.0
100000.0
112000.0
125000.0
140000.0
160000.0
180000.0
200000.0
224000.0
250000.0
280000.0
320000.0
360000.0
400000.0
450000.0
500000.0
560000.0
630000.0
710000.0
800000.0
900000.0
1000000.0
1120000.0
1250000.0
1400000.0
1600000.0
1800000.0
2000000.0
2240000.0
2500000.0
2800000.0
3200000.0
3600000.0
4000000.0
4500000.0
5000000.0
5600000.0
6300000.0
7100000.0
8000000.0
9000000.0
10000000.0
11200000.0
12500000.0
14000000.0
16000000.0
18000000.0
20000000.0
22400000.0
25000000.0
28000000.0
32000000.0
36000000.0
40000000.0
45000000.0
50000000.0
56000000.0
63000000.0
71000000.0
80000000.0
90000000.0
100000000.0
112000000.0
125000000.0
140000000.0
160000000.0
180000000.0
200000000.0
224000000.0
250000000.0
280000000.0
320000000.0
360000000.0
400000000.0
450000000.0
500000000.0
560000000.0
630000000.0
710000000.0
800000000.0
900000000.0
1000000000.0
1120000000.0
1250000000.0
1400000000.0
1600000000.0
1800000000.0
2000000000.0
2240000000.0
2500000000.0
2800000000.0
3200000000.0
3600000000.0
4000000000.0
4500000000.0
5000000000.0
5600000000.0
6300000000.0
7100000000.0
8000000000.0
9000000000.0
10000000000.0
11200000000.0
12500000000.0
14000000000.0
16000000000.0
18000000000.0
20000000000.0
22400000000.0
25000000000.0
28000000000.0
32000000000.0
36000000000.0
40000000000.0
45000000000.0
50000000000.0
56000000000.0
63000000000.0
71000000000.0
80000000000.0
90000000000.0
100000000000.0
112000000000.0
125000000000.0
140000000000.0
160000000000.0
180000000000.0
200000000000.0
224000000000.0
250000000000.0
280000000000.0
320000000000.0
360000000000.0
400000000000.0
450000000000.0
500000000000.0
560000000000.0
630000000000.0
710000000000.0
800000000000.0
900000000000.0
1000000000000.0
1120000000000.0
1250000000000.0
1400000000000.0
1600000000000.0
1800000000000.0
2000000000000.0
2240000000000.0
2500000000000.0
2800000000000.0
3200000000000.0
3600000000000.0
4000000000000.0
4500000000000.0
5000000000000.0
5600000000000.0
6300000000000.0
7100000000000.0
8000000000000.0
9000000000000.0
10000000000000.0
11200000000000.0
12500000000000.0
14000000000000.0
16000000000000.0
18000000000000.0
20000000000000.0
22400000000000.0
25000000000000.0
28000000000000.0
32000000000000.0
36000000000000.0
40000000000000.0
45000000000000.0
50000000000000.0
56000000000000.0
63000000000000.0
71000000000000.0
80000000000000.0
90000000000000.0
100000000000000.0
112000000000000.0
125000000000000.0
140000000000000.0
160000000000000.0
180000000000000.0
200000000000000.0
224000000000000.0
250000000000000.0
280000000000000.0
320000000000000.0
360000000000000.0
400000000000000.0
450000000000000.0
500000000000000.0
560000000000000.0
630000000000000.0
710000000000000.0
800000000000000.0
900000000000000.0
1000000000000000.0
1120000000000000.0
1250000000000000.0
1400000000000000.0
1600000000000000.0
1800000000000000.0
2000000000000000.0
2240000000000000.0
2500000000000000.0
2800000000000000.0
3200000000000000.0
3600000000000000.0
4000000000000000.0
4500000000000000.0
5000000000000000.0
5600000000000000.0
6300000000000000.0
7100000000000000.0
8000000000000000.0
9000000000000000.0
10000000000000000.0
11200000000000000.0
12500000000000000.0
14000000000000000.0
16000000000000000.0
18000000000000000.0
20000000000000000.0
22400000000000000.0
25000000000000000.0
28000000000000000.0
32000000000000000.0
36000000000000000.0
40000000000000000.0
45000000000000000.0
50000000000000000.0
56000000000000000.0
63000000000000000.0
71000000000000000.0
80000000000000000.0
90000000000000000.0
100000000000000000.0
112000000000000000.0
125000000000000000.0
140000000000000000.0
160000000000000000.0
180000000000000000.0
200000000000000000.0
224000000000000000.0
250000000000000000.0
280000000000000000.0
320000000000000000.0
360000000000000000.0
400000000000000000.0
450000000000000000.0
500000000000000000.0
560000000000000000.0
630000000000000000.0
710000000000000000.0
800000000000000000.0
900000000000000000.0
1000000000000000000.0
1120000000000000000.0
1250000000000000000.0
1400000000000000000.0
1600000000000000000.0
1800000000000000000.0
2000000000000000000.0
2240000000000000000.0
2500000000000000000.0
2800000000000000000.0
3200000000000000000.0
3600000000000000000.0
4000000000000000000.0
4500000000000000000.0
5000000000000000000.0
5600000000000000000.0
6300000000000000000.0
7100000000000000000.0
8000000000000000000.0
9000000000000000000.0
10000000000000000000.0
11200000000000000000.0
12500000000000000000.0
14000000000000000000.0
16000000000000000000.0
18000000000000000000.0
20000000000000000000.0
22400000000000000000.0
25000000000000000000.0
28000000000000000000.0
32000000000000000000.0
36000000000000000000.0
40000000000000000000.0
45000000000000000000.0
50000000000000000000.0
56000000000000000000.0
63000000000000000000.0
71000000000000000000.0
80000000000000000000.0
90000000000000000000.0
100000000000000000000.0
112000000000000000000.0
125000000000000000000.0
140000000000000000000.0
160000000000000000000.0
180000000000000000000.0
200000000000000000000.0
224000000000000000000.0
250000000000000000000.0
280000000000000000000.0
320000000000000000000.0
360000000000000000000.0
400000000000000000000.0
450000000000000000000.0
500000000000000000000.0
560000000000000000000.0
630000000000000000000.0
710000000000000000000.0
800000000000000000000.0
900000000000000000000.0
1000000000000000000000.0
1120000000000000000000.0
1250000000000000000000.0
1400000000000000000000.0
1600000000000000000000.0
1800000000000000000000.0
2000000000000000000000.0
2240000000000000000000.0
2500000000000000000000.0
2800000000000000000000.0
3200000000000000000000.0
3600000000000000000000.0
4000000000000000000000.0
4500000000000000000000.0
5000000000000000000000.0
5600000000000000000000.0
6300000000000000000000.0
7100000000000000000000.0
8000000000000000000000.0
9000000000000000000000.0
10000000000000000000000.0
11200000000000000000000.0
12500000000000000000000.0
14000000000000000000000.0
16000000000000000000000.0
18000000000000000000000.0
20000000000000000000000.0
22400000000000000000000.0
25000000000000000000000.0
28000000000000000000000.0
32000000000000000000000.0
36000000000000000000000.0
40000000000000000000000.0
45000000000000000000000.0
50000000000000000000000.0
56000000000000000000000.0
63000000000000000000000.0
71000000000000000000000.0
80000000000000000000000.0
90000000000000000000000.0
100000000000000000000000.0
112000000000000000000000.0
125000000000000000000000.0
140000000000000000000000.0
160000000000000000000000.0
180000000000000000000000.0
200000000000000000000000.0
224000000000000000000000.0
250000000000000000000000.0
280000000000000000000000.0
320000000000000000000000.0
360000000000000000000000.0
400000000000000000000000.0
450000000000000000000000.0
500000000000000000000000.0
560000000000000000000000.0
630000000000000000000000.0
710000000000000000000000.0
800000000000000000000000.0
900000000000000000000000.0
1000000000000000000000000.0
1120000000000000000000000.0
1250000000000000000000000.0
1400000000000000000000000.0
1600000000000000000000000.0
1800000000000000000000000.0
2000000000000000000000000.0
2240000000000000000000000.0
2500000000000000000000000.0
2800000000000000000000000.0
3200000000000000000000000.0
3600000000000000000000000.0
4000000000000000000000000.0
4500000000000000000000000.0
5000000000000000000000000.0
5600000000000000000000000.0
6300000000000000000000000.0
7100000000000000000000000.0
8000000000000000000000000.0
9000000000000000000000000.0
10000000000000000000000000.0
11200000000000000000000000.0
12500000000000000000000000.0
14000000000000000000000000.0
16000000000000000000000000.0
18000000000000000000000000.0
20000000000000000000000000.0
22400000000000000000000000.0
25000000000000000000000000.0
28000000000000000000000000.0
32000000000000000000000000.0
36000000000000000000000000.0
40000000000000000000000000.0
45000000000000000000000000.0
50000000000000000000000000.0
56000000000000000000000000.0
63000000000000000000000000.0
71000000000000000000000000.0
80000000000000000000000000.0
90000000000000000000000000.0
100000000000000000000000000.0
112000000000000000000000000.0
125000000000000000000000000.0
140000000000000000000000000.0
160000000000000000000000000.0
180000000000000000000000000.0
200000000000000000000000000.0
224000000000000000000000000.0
250000000000000000000000000.0
280000000000000000000000000.0
320000000000000000000000000.0
360000000000000000000000000.0
400000000000000000000000000.0
450000000000000000000000000.0
500000000000000000000000000.0
560000000000000000000000000.0
630000000000000000000000000.0
710000000000000000000000000.0
800000000000000000000000000.0
900000000000000000000000000.0
1000000000000000000000000000.0
1120000000000000000000000000.0
1250000000000000000000000000.0
1400000000000000000000000000.0
1600000000000000000000000000.0
1800000000000000000000000000.0
2000000000000000000000000000.0
2240000000000000000000000000.0
2500000000000000000000000000.0
2800000000000000000000000000.0
3200000000000000000000000000.0
3600000000000000000000000000.0
4000000000000000000000000000.0
4500000000000000000000000000.0
5000000000000000000000000000.0
5600000000000000000000000000.0
6300000000000000000000000000.0
7100000000000000000000000000.0
8000000000000000000000000000.0
9000000000000000000000000000.0
10000000000000000000000000000.0
11200000000000000000000000000.0
12500000000000000000000000000.0
14000000000000000000000000000.0
16000000000000000000000000000.0
18000000000000000000000000000.0
20000000000000000000000000000.0
22400000000000000000000000000.0
25000000000000000000000000000.0
28000000000000000000000000000.0
32000000000000000000000000000.0
36000000000000000000000000000.0
40000000000000000000000000000.0
45000000000000000000000000000.0
50000000000000000000000000000.0
56000000000000000000000000000.0
63000000000000000000000000000.0
71000000000000000000000000000.0
80000000000000000000000000000.0
90000000000000000000000000000.0
100000000000000000000000000000.0
112000000000000000000000000000.0
125000000000000000000000000000.0
140000000000000000000000000000.0
160000000000000000000000000000.0
180000000000000000000000000000.0
200000000000000000000000000000.0
224000000000000000000000000000.0
250000000000000000000000000000.0
280000000000000000000000000000.0
320000000000000000000000000000.0
360000000000000000000000000000.0
400000000000000000000000000000.0
450000000000000000000000000000.0
500000000000000000000000000000.0
560000000000000000000000000000.0
630000000000000000000000000000.0
710000000000000000000000000000.0
800000000000000000000000000000.0
900000000000000000000000000000.0
1000000000000000000000000000000.0
1120000000000000000000000000000.0
1250000000000000000000000000000.0
1400000000000000000000000000000.0
1600000000000000000000000000000.0
1800000000000000000000000000000.0
2000000000000000000000000000000.0
2240000000000000000000000000000.0
2500000000000000000000000000000.0
2800000000000000000000000000000.0
3200000000000000000000000000000.0
3600000000000000000000000000000.0
4000000000000000000000000000000.0
4500000000000000000000000000000.0
5000000000000000000000000000000.0
5600000000000000000000000000000.0
6300000000000000000000000000000.0
7100000000000000000000000000000.0
8000000000000000000000000000000.0
9000000000000000000000000000000.0
10000000000000000000000000000000.0
11200000000000000000000000000000.0
12500000000000000000000000000000.0
14000000000000000000000000000000.0
16000000000000000000000000000000.0
18000000000000000000000000000000.0
20000000000000000000000000000000.0
22400000000000000000000000000000.0
25000000000000000000000000000000.0
28000000000000000000000000000000.0
32000000000000000000000000000000.0
36000000000000000000000000000000.0
40000000000000000000000000000000.0
45000000000000000000000000000000.0
50000000000000000000000000000000.0
56000000000000000000000000000000.0
63000000000000000000000000000000.0
71000000000000000000000000000000.0
80000000000000000000000000000000.0
90000000000000000000000000000000.0
100000000000000000000000000000000.0
112000000000000000000000000000000.0
125000000000000000000000000000000.0
140000000000000000000000000000000.0
160000000000000000000000000000000.0
180000000000000000000000000000000.0
200000000000000000000000000000000.0
224000000000000000000000000000000.0
250000000000000000000000000000000.0
280000000000000000000000000000000.0
320000000000000000000000000000000.0
360000000000000000000000000000000.0
400000000000000000000000000000000.0
450000000000000000000000000000000.0
500000000000000000000000000000000.0
560000000000000000000000000000000.0
630000000000000000000000000000000.0
710000000000000000000000000000000.0
800000000000000000000000000000000.0
900000000000000000000000000000000.0
1000000000000000000000000000000000.0
1120000000000000000000000000000000.0
1250000000000000000000000000000000.0
1400000000000000000000000000000000.0
1600000000000000000000000000000000.0
1800000000000000000000000000000000.0
2000000000000000000000000000000000.0
2240000000000000000000000000000000.0
2500000000000000000000000000000000.0
2800000000000000000000000000000000.0
3200000000000000000000000000000000.0
3600000000000000000000000000000000.0
4000000000000000000000000000000000.0
4500000000000000000000000000000000.0
5000000000000000000000000000000000.0
5600000000000000000000000000000000.0
6300000000000000000000000000000000.0
7100000000000000000000000000000000.0
8000000000000000000000000000000000.0
9000000000000000000000000000000000.0
10000000000000000000000000000000000.0
11200000000000000000000000000000000.0
12500000000000000000000000000000000.0
14000000000000000000000000000000000.0
16000000000000000000000000000000000.0
18000000000000000000000000000000000.0
20000000000000000000000000000000000.0
22400000000000000000000000000000000.0
25000000000000000000000000000000000.0
28000000000000000000000000000000000.0
32000000000000000000000000000000000.0
36000000000000000000000000000000000.0
40000000000000000000000000000000000.0
45000000000000000000000000000000000.0
50000000000000000000000000000000000.0
56000000000000000000000000000000000.0
63000000000000000000000000000000000.0
71000000000000000000000000000000000.0
80000000000000000000000000000000000.0
90000000000000000000000000000000000.0
100000000000000000000000000000000000.0
112000000000000000000000000000000000.0
125000000000000000000000000000000000.0
140000000000000000000000000000000000.0
160000000000000000000000000000000000.0
180000000000000000000000000000000000.0
200000000000000000000000000000000000.0
224000000000000000000000000000000000.0
250000000000000000000000000000000000.0
280000000000000000000000000000000000.0
320000000000000000000000000000000000.0
360000000000000000000000000000000000.0
400000000000000000000000000000000000.0
450000000000000000000000000000000000.0
500000000000000000000000000000000000.0
560000000000000000000000000000000000.0
630000000000000000000000000000000000.0
710000000000000000000000000000000000.0
800000000000000000000000000000000000.0
900000000000000000000000000000000000.0
1000000000000000000000000000000000000.0
1120000000000000000000000000000000000.0
1250000000000000000000000000000000000.0
1400000000000000000000000000000000000.0
1600000000000000000000000000000000000.0
1800000000000000000000000000000000000.0
2000000000000000000000000000000000000.0
2240000000000000000000000000000000000.0
2500000000000000000000000000000000000.0
2800000000000000000000000000000000000.0
3200000000000000000000000000000000000.0
3600000000000000000000000000000000000.0
4000000000000000000000000000000000000.0
4500000000000000000000000000000000000.0
5000000000000000000000000000000000000.0
5600000000000000000000000000000000000.0
6300000000000000000000000000000000000.0
7100000000000000000000000000000000000.0
8000000000000000000000000000000000000.0
9000000000000000000000000000000000000.0
10000000000000000000000000000000000000.0
11200000000000000000000000000000000000.0
12500000000000000000000000000000000000.0
14000000000000000000000000000000000000.0
16000000000000000000000000000000000000.0
18000000000000000000000000000000000000.0
20000000000000000000000000000000000000.0
22400000000000000000000000000000000000.0
25000000000000000000000000000000000000.0
28000000000000000000000000000000000000.0
32000000000000000000000000000000000000.0
36000000000000000000000000000000000000.0
40000000000000000000000000000000000000.0
45000000000000000000000000000000000000.0
50000000000000000000000000000000000000.0
56000000000000000000000000000000000000.0
63000000000000000000000000000000000000.0
71000000000000000000000000000000000000.0
80000000000000000000000000000000000000.0
90000000000000000000000000000000000000.0
100000000000000000000000000000000000000.0
112000000000000000000000000000000000000.0
125000000000000000000000000000000000000.0
140000000000000000000000000000000000000.0
160000000000000000000000000000000000000.0
180000000000000000000000000000000000000.0
200000000000000000000000000000000000000.0
224000000000000000000000000000000000000.0
250000000000000000000000000000000000000.0
280000000000000000000000000000000000000.0
320000000000000000000000000000000000000.0
360000000000000000000000000000000000000.0
400000000000000000000000000000000000000.0
450000000000000000000000000000000000000.0
500000000000000000000000000000000000000.0
560000000000000000000000000000000000000.0
630000000000000000000000000000000000000.0
710000000000000000000000000000000000000.0
800000000000000000000000000000000000000.0
900000000000000000000000000000000000000.0
1000000000000000000000000000000000000000.0
1120000000000000000000000000000000000000.0
1250000000000000000000000000000000000000.0
1400000000000000000000000000000000000000.0
1600000000000000000000000000000000000000.0
1800000000000000000000000000000000000000.0
2000000000000000000000000000000000000000.0
2240000000000000000000000000000000000000.0
2500000000000000000000000000000000000000.0
2800000000000000000000000000000000000000.0
3200000000000000000000000000000000000000.0
3600000000000000000000000000000000000000.0
4000000000000000000000000000000000000000.0
4500000000000000000000000000000000000000.0
5000000000000000000000000000000000000000.0
5600000000000000000000000000000000000000.0
6300000000000000000000000000000000000000.0
7100000000000000000000000000000000000000.0
8000000000000000000000000000000000000000.0
9000000000000000000000000000000000000000.0
10000000000000000000000000000000000000000.0
11200000000000000000000000000000000000000.0
12500000000000000000000000000000000000000.0
14000000000000000000000000000000000000000.0
16000000000000000000000000000000000000000.0
18000000000000000000000000000000000000000.0
20000000000000000000000000000000000000000.0
22400000000000000000000000000000000000000.0
25000000000000000000000000000000000000000.0
28000000000000000000000000000000000000000.0
32000000000000000000000000000000000000000.0
36000000000000000000000000000000000000000.0
40000000000000000000000000000000000000000.0
45000000000000000000000000000000000000000.0
50000000000000000000000000000000000000000.0
56000000000000000000000000000000000000000.0
63000000000000000000000000000000000000000.0
71000000000000000000000000000000000000000.0
80000000000000000000000000000000000000000.0
90000000000000000000000000000000000000000.0
100000000000000000000000000000000000000000.0
112000000000000000000000000000000000000000.0
125000000000000000000000000000000000000000.0
140000000000000000000000000000000000000000.0
160000000000000000000000000000000000000000.0
180000000000000000000000000000000000000000.0
200000000000000000000000000000000000000000.0
224000000000000000000000000000000000000000.0
250000000000000000000000000000000000000000.0
280000000000000000000000000000000000000000.0
320000000000000000000000000000000000000000.0
360000000000000000000000000000000000000000.0
400000000000000000000000000000000000000000.0
450000000000000000000000000000000000000000.0
500000000000000000000000000000000000000000.0
560000000000000000000000000000000000000000.0
630000000000000000000000000000000000000000.0
710000000000000000000000000000000000000000.0
800000000000000000000000000000000000000000.0
900000000000000000000000000000000000000000.0
1000000000000000000000000000000000000000000.0
1120000000000000000000000000000000000000000.0
1250000000000000000000000000000000000000000.0
1400000000000000000000000000000000000000000.0
1600000000000000000000000000000000000000000.0
1800000000000000000000000000000000000000000.0
2000000000000000000000000000000000000000000.0
2240000000000000000000000000000000000000000.0
2500000000000000000000000000000000000000000.0
2800000000000000000000000000000000000000000.0
3200000000000000000000000000000000000000000.0
3600000000000000000000000000000000000000000.0
4000000000000000000000000000000000000000000.0
4500000000000000000000000000000000000000000.0
5000000000000000000000000000000000000000000.0
5600000000000000000000000000000000000000000.0
6300000000000000000000000000000000000000000.0
7100000000000000000000000000000000000000000.0
8000000000000000000000000000000000000000000.0
9000000000000000000000000000000000000000000.0
10000000000000000000000000000000000000000000.0
11200000000000000000000000000000000000000000.0
12500000000000000000000000000000000000000000.0
14000000000000000000000000000000000000000000.0
16000000000000000000000000000000000000000000.0
18000000000000000000000000000000000000000000.0
20000000000000000000000000000000000000000000.0
22400000000000000000000000000000000000000000.0
25000000000000000000000000000000000000000000.0
28000000000000000000000000000000000000000000.0
32000000000000000000000000000000000000000000.0
36000000000000000000000000000000000000000000.0
40000000000000000000000000000000000000000000.0
45000000000000000000000000000000000000000000.0
50000000000000000000000000000000000000000000.0
56000000000000000000000000000000000000000000.0
63000000000000000000000000000000000000000000.0
71000000000000000000000000000000000000000000.0
80000000000000000000000000000000000000000000.0
90000000000000000000000000000000000000000000.0
100000000000000000000000000000000000000000000.0
112000000000000000000000000000000000000000000.0
125000000000000000000000000000000000000000000.0
140000000000000000000000000000000000000000000.0
160000000000000000000000000000000000000000000.0
180000000000000000000000000000000000000000000.0
200000000000000000000000000000000000000000000.0
224000000000000000000000000000000000000000000.0
250000000000000000000000000000000000000000000.0
280000000000000000000000000000000000000000000.0
320000000000000000000000000000000000000000000.0
360000000000000000000000000000000000000000000.0
400000000000000000000000000000000000000000000.0
450000000000000000000000000000000000000000000.0
500000000000000000000000000000000000000000000.0
560000000000000000000000000000000000000000000.0
630000000000000000000000000000000000000000000.0
710000000000000000000000000000000000000000000.0
800000000000000000000000000000000000000000000.0
900000000000000000000000000000000000000000000.0
1000000000000000000000000000000000000000000000.0
1120000000000000000000000000000000000000000000.0
1250000000000000000000000000000000000000000000.0
1400000000000000000000000000000000000000000000.0
1600000000000000000000000000000000000000000000.0
1800000000000000000000000000000000000000000000.0
2000000000000000000000000000000000000000000000.0
2240000000000000000000000000000000000000000000.0
2500000000000000000000000000000000000000000000.0
2800000000000000000000000000000000000000000000.0
3200000000000000000000000000000000000000000000.0
3600000000000000000000000000000000000000000000.0
4000000000000000000000000000000000000000000000.0
4500000000000000000000000000000000000000000000.0
5000000000000000000000000000000000000000000000.0
5600000000000000000000000000000000000000000000.0
6300000000000000000000000000000000000000000000.0
7100000000000000000000000000000000000000000000.0
8000000000000000000000000000000000000000000000.0
9000000000000000000000000000000000000000000000.0
10000000000000000000000000000000000000000000000.0
11200000000000000000000000000000000000000000000.0
12500000000000000000000000000000000000000000000.0
14000000000000000000000000000000000000000000000.0
16000000000000000000000000000000000000000000000.0
18000000000000000000000000000000000000000000000.0
20000000000000000000000000000000000000000000000.0
22400000000000000000000000000000000000000000000.0
25000000000000000000000000000000000000000000000.0
28000000000000000000000000000000000000000000000.0
32000000000000000000000000000000000000000000000.0
36000000000000000000000000000000000000000000000.0
40000000000000000000000000000000000000000000000.0
45000000000000000000000000000000000000000000000.0
50000000000000000000000000000000000000000000000.0
56000000000000000000000000000000000000000000000.0
63000000000000000000000000000000000000000000000.0
71000000000000000000000000000000000000000000000.0
80000000000000000000000000000000000000000000000.0
90000000000000000000000000000000000000000000000.0
100000000000000000000000000000000000000000000000.0
112000000000000000000000000000000000000000000000.0
125000000000000000000000000000000000000000000000.0
140000000000000000000000000000000000000000000000.0
160000000000000000000000000000000000000000000000.0
180000000000000000000000000000000000000000000000.0
200000000000000000000000000000000000000000000000.0
224000000000000000000000000000000000000000000000.0
250000000000000000000000000000000000000000000000.0
280000000000000000000000000000000000000000000000.0
320000000000000000000000000000000000000000000000.0
360000000000000000000000000000000000000000000000.0
400000000000000000000000000000000000000000000000.0
450000000000000000000000000000000000000000000000.0
500000000000000000000000000000000000000000000000.0
560000000000000000000000000000000000000000000000.0
630000000000000000000000000000000000000000000000.0
710000000000000000000000000000000000000000000000.0
800000000000000000000000000000000000000000000000.0
900000000000000000000000000000000000000000000000.0
1000000000000000000000000000000000000000000000000.0
1120000000000000000000000000000000000000000000000.0
1250000000000000000000000000000000000000000000000.0
1400000000000000000000000000000000000000000000000.0
1600000000000000000000000000000000000000000000000.0
1800000000000000000000000000000000000000000000000.0
2000000000000000000000000000000000000000000000000.0
2240000000000000000000000000000000000000000000000.0
2500000000000000000000000000000000000000000000000.0
2800000000000000000000000000000000000000000000000.0
3200000000000000000000000000000000000000000000000.0
3600000000000000000000000000000000000000000000000.0
4000000000000000000000000000000000000000000000000.0
4500000000000000000000000000000000000000000000000.0
5000000000000000000000000000000000000000000000000.0
5600000000000000000000000000000000000000000000000.0
6300000000000000000000000000000000000000000000000.0
7100000000000000000000000000000000000000000000000.0
8000000000000000000000000000000000000000000000000.0
9000000000000000000000000000000000000000000000000.0
10000000000000000000000000000000000000000000000000.0
11200000000000000000000000000000000000000000000000.0
12500000000000000000000000000000000000000000000000.0
14000000000000000000000000000000000000000000000000.0
16000000000000000000000000000000000000000000000000.0
18000000000000000000000000000000000000000000000000.0
20000000000000000000000000000000000000000000000000.0
22400000000000000000000000000000000000000000000000.0
25000000000000000000000000000000000000000000000000.0
28000000000000000000000000000000000000000000000000.0
32000000000000000000000000000000000000000000000000.0
36000000000000000000000000000000000000000000000000.0
40000000000000000000000000000000000000000000000000.0
45000000000000000000000000000000000000000000000000.0
50000000000000000000000000000000000000000000000000.0
56000000000000000000000000000000000000000000000000.0
63000000000000000000000000000000000000000000000000.0
71000000000000000000000000000000000000000000000000.0
80000000000000000000000000000000000000000000000000.0
90000000000000000000000000000000000000000000000000.0
100000000000000000000000000000000000000000000000000.0
112000000000000000000000000000000000000000000000000.0
125000000000000000000000000000000000000000000000000.0
140000000000000000000000000000000000000000000000000.0
160000000000000000000000000000000000000000000000000.0
180000000000000000000000000000000000000000000000000.0
200000000000000000000000000000000000000000000000000.0
224000000000000000000000000000000000000000000000000.0
250000000000000000000000000000000000000000000000000.0
280000000000000000000000000000000000000000000000000.0
320000000000000000000000000000000000000000000000000.0
360000000000000000000000000000000000000000000000000.0
400000000000000000000000000000000000000000000000000.0
450000000000000000000000000000000000000000000000000.0
500000000000000000000000000000000000000000000000000.0
560000000000000000000000000000000000000000000000000.0
630000000000000000000000000000000000000000000000000.0
710000000000000000000000000000000000000000000000000.0
800000000000000000000000000000000000000000000000000.0
900000000000000000000000000000000000000000000000000.0
1000000000000000000000000000000000000000000000000000.0
1120000000000000000000000000000000000000000000000000.0
1250000000000000000000000000000000000000000000000000.0
1400000000000000000000000000000000000000000000000000.0
1600000000000000000000000000000000000000000000000000.0
1800000000000000000000000000000000000000000000000000.0
2000000000000000000000000000000000000000000000000000.0
2240000000000000000000000000000000000000000000000000.0
2500000000000000000000000000000000000000000000000000.0
2800000000000000000000000000000000000000000000000000.0
3200000000000000000000000000000000000000000000000000.0
3600000000000000000000000000000000000000000000000000.0
4000000000000000000000000000000000000000000000000000.0
4500000000000000000000000000000000000000000000000000.0
5000000000000000000000000000000000000000000000000000.0
5600000000000000000000000000000000000000000000000000.0
6300000000000000000000000000000000000000000000000000.0
7100000000000000000000000000000000000000000000000000.0
8000000000000000000000000000000000000000000000000000.0
9000000000000000000000000000000000000000000000000000.0
10000000000000000000000000000000000000000000000000000.0
11200000000000000000000000000000000000000000000000000.0
12500000000000000000000000000000000000000000000000000.0
14000000000000000000000000000000000000000000000000000.0
16000000000000000000000000000000000000000000000000000.0
18000000000000000000000000000000000000000000000000000.0
20000000000000000000000000000000000000000000000000000.0
22400000000000000000000000000000000000000000000000000.0
25000000000000000000000000000000000000000000000000000.0
28000000000000000000000000000000000000000000000000000.0
32000000000000000000000000000000000000000000000000000.0
36000000000000000000000000000000000000000000000000000.0
40000000000000000000000000000000000000000000000000000.0
45000000000000000000000000000000000000000000000000000.0
50000000000000000000000000000000000000000000000000000.0
56000000000000000000000000000000000000000000000000000.0
63000000000000000000000000000000000000000000000000000.0
71000000000000000000000000000000000000000000000000000.0
80000000000000000000000000000000000000000000000000000.0
90000000000000000000000000000000000000000000000000000.0
100000000000000000000000000000000000000000000000000000.0
112000000000000000000000000000000000000000000000000000.0
125000000000000000000000000000000000000000000000000000.0
140000000000000000000000000000000000000000000000000000.0
160000000000000000000000000000000000000000000000000000.0
180000000000000000000000000000000000000000000000000000.0
200000000000000000000000000000000000000000000000000000.0
224000000000000000000000000000000000000000000000000000.0
250000000000000000000000000000000000000000000000000000.0
280000000000000000000000000000000000000000000000000000.0
320000000000000000000000000000000000000000000000000000.0
360000000000000000000000000000000000000000000000000000.0
400000000000000000000000000000000000000000000000000000.0
450000000000000000000000000000000000000000000000000000.0
500000000000000000000000000000000000000000000000000000.0
560000000000000000000000000000000000000000000000000000.0
630000000000000000000000000000000000000000000000000000.0
710000000000000000000000000000000000000000000000000000.0
800000000000000000000000000000000000000000000000000000.0
900000000000000000000000000000000000000000000000000000.0
1000000000000000000000000000000000000000000000000000000.0
1120000000000000000000000000000000000000000000000000000.0
1250000000000000000000000000000000000000000000000000000.0
1400000000000000000000000000000000000000000000000000000.0
1600000000000000000000000000000000000000000000000000000.0
1800000000000000000000000000000000000000000000000000000.0
2000000000000000000000000000000000000000000000000000000.0
2240000000000000000000000000000000000000000000000000000.0
2500000000000000000000000000000000000000000000000000000.0
2800000000000000000000000000000000000000000000000000000.0
3200000000000000000000000000000000000000000000000000000.0
3600000000000000000000000000000000000000000000000000000.0
4000000000000000000000000000000000000000000000000000000.0
4500000000000000000000000000000000000000000000000000000.0
5000000000000000000000000000000000000000000000000000000.0
5600000000000000000000000000000000000000000000000000000.0
6300000000000000000000000000000000000000000000000000000.0
7100000000000000000000000000000000000000000000000000000.0
8000000000000000000000000000000000000000000000000000000.0
9000000000000000000000000000000000000000000000000000000.0
10000000000000000000000000000000000000000000000000000000.0
11200000000000000000000000000000000000000000000000000000.0
12500000000000000000000000000000000000000000000000000000.0
14000000000000000000000000000000000000000000000000000000.0
16000000000000000000000000000000000000000000000000000000.0
18000000000000000000000000000000000000000000000000000000.0
20000000000000000000000000000000000000000000000000000000.0
22400000000000000000000000000000000000000000000000000000.0
25000000000000000000000000000000000000000000000000000000.0
28000000000000000000000000000000000000000000000000000000.0
32000000000000000000000000000000000000000000000000000000.0
36000000000000000000000000000000000000000000000000000000.0
40000000000000000000000000000000000000000000000000000000.0
45000000000000000000000000000000000000000000000000000000.0
50000000000000000000000000000000000000000000000000000000.0
56000000000000000000000000000000000000000000000000000000.0
63000000000000000000000000000000000000000000000000000000.0
71000000000000000000000000000000000000000000000000000000.0
80000000000000000000000000000000000000000000000000000000.0
90000000000000000000000000000000000000000000000000000000.0
100000000000000000000000000000000000000000000000000000000.0
112000000000000000000000000000000000000000000000000000000.0
125000000000000000000000000000000000000000000000000000000.0
140000000000000000000000000000000000000000000000000000000.0
160000000000000000000000000000000000000000000000000000000.0
180000000000000000000000000000000000000000000000000000000.0
200000000000000000000000000000000000000000000000000000000.0
224000000000000000000000000000000000000000000000000000000.0
250000000000000000000000000000000000000000000000000000000.0
280000000000000000000000000000000000000000000000000000000.0
320000000000000000000000000000000000000000000000000000000.0
360000000000000000000000000000000000000000000000000000000.0
400000000000000000000000000000000000000000000000000000000.0
450000000000000000000000000000000000000000000000000000000.0
500000000000000000000000000000000000000000000000000000000.0
560000000000000000000000000000000000000000000000000000000.0
630000000000000000000000000000000000000000000000000000000.0
710000000000000000000000000000000000000000000000000000000.0
800000000000000000000000000000000000000000000000000000000.0
900000000000000000000000000000000000000000000000000000000.0
1000000000000000000000000000000000000000000000000000000000.0
1120000000000000000000000000000000000000000000000000000000.0
1250000000000000000000000000000000000000000000000000000000.0
1400000000000000000000000000000000000000000000000000000000.0
1600000000000000000000000000000000000000000000000000000000.0
1800000000000000000000000000000000000000000000000000000000.0
2000000000000000000000000000000000000000000000000000000000.0
2240000000000000000000000000000000000000000000000000000000.0
2500000000000000000000000000000000000000000000000000000000.0
2800000000000000000000000000000000000000000000000000000000.0
3200000000000000000000000000000000000000000000000000000000.0
3600000000000000000000000000000000000000000000000000000000.0
4000000000000000000000000000000000000000000000000000000000.0
4500000000000000000000000000000000000000000000000000000000.0
5000000000000000000000000000000000000000000000000000000000.0
5600000000000000000000000000000000000000000000000000000000.0
6300000000000000000000000000000000000000000000000000000000.0
7100000000000000000000000000000000000000000000000000000000.0
8000000000000000000000000000000000000000000000000000000000.0
9000000000000000000000000000000000000000000000000000000000.0
10000000000000000000000000000000000000000000000000000000000.0
11200000000000000000000000000000000000000000000000000000000.0
12500000000000000000000000000000000000000000000000000000000.0
14000000000000000000000000000000000000000000000000000000000.0
16000000000000000000000000000000000000000000000000000000000.0
18000000000000000000000000000000000000000000000000000000000.0
20000000000000000000000000000000000000000000000000000000000.0
22400000000000000000000000000000000000000000000000000000000.0
25000000000000000000000000000000000000000000000000000000000.0
28000000000000000000000000000000000000000000000000000000000.0
32000000000000000000000000000000000000000000000000000000000.0
36000000000000000000000000000000000000000000000000000000000.0
40000000000000000000000000000000000000000000000000000000000.0
45000000000000000000000000000000000000000000000000000000000.0
50000000000000000000000000000000000000000000000000000000000.0
56000000000000000000000000000000000000000000000000000000000.0
63000000000000000000000000000000000000000000000000000000000.0
71000000000000000000000000000000000000000000000000000000000.0
80000000000000000000000000000000000000000000000000000000000.0
90000000000000000000000000000000000000000000000000000000000.0
100000000000000000000000000000000000000000000000000000000000.0
112000000000000000000000000000000000000000000000000000000000.0
125000000000000000000000000000000000000000000000000000000000.0
140000000000000000000000000000000000000000000000000000000000.0
160000000000000000000000000000000000000000000000000000000000.0
180000000000000000000000000000000000000000000000000000000000.0
200000000000000000000000000000000000000000000000000000000000.0
224000000000000000000000000000000000000000000000000000000000.0
250000000000000000000000000000000000000000000000000000000000.

D. Optical Free Induction Decay

Compaan et al.[13] have reported that the photon echo decay rate of the Cr^{3+} ion in ruby undergoes dramatic changes in the region of a level crossing. The effect is due to the mixing of Cr spin states which modifies its dipolar interaction with the surrounding Al nuclei. We were tempted, therefore, to see if the Pr^{3+}:$YAlO_3$ system exhibits a similar behavior in an anticrossing particularly since the anticrossing curves (Figs. 2 and 3) can exhibit a near zero slope causing the Pr^{3+} magnetic moment and its magnetic interactions to vanish.

Optical free induction decay (FID) measurements were conducted using the method of laser frequency switching a cw ring dye laser that is frequency-locked to an external reference cavity.[22] For nonzero fields either on or off an anticrossing, the optical dephasing time is T_2=76 μsec, corresponding to a 2.1 kHz HWHM linewidth. Using the same experimental set-up and a two-pulse laser frequency switching sequence with optical heterodyne detection, we find that the photon echo yields precisely the same dephasing time as the FID, to within a few percent uncertainty, in contrast to a previous report[27] which asserts that echoes and FID give different results. The absence of a change in the decay rate due to anticrossing has two possible explanations. First, the FID signal arises from all possible optical transitions among the Zeeman substates whereas an anticrossing only involves one pair. This is a dilution effect. And second, the residual linewidth of 2.1 kHz might not be magnetic in origin. At present, it is not possible to decide which explanation prevails.

ACKNOWLEDGMENTS

We thank Marvin J. Weber for his kindly loaning us the Pr^{3+}:$YAlO_3$ crystal used in this study. One of us (RGB) benefited from stimulating conversations with Harold Wieder. The technical assistance of K. L. Foster is appreciated also.

Table I. Hyperfine Parameters of Pr^{3+}:$YAlO_3$ for $^3H_4(\Gamma_1)$ and $^1D_2(\Gamma_1)$

	$^3H_4(\Gamma_1)$	$^1D_2(\Gamma_1)$
$\|D\|$ (MHz)	3.5255 ± 0.0006*	0.3899 ± 0.0057*
$\|E\|$ (MHz)	0.032 ± 0.008*	0.0824 ± 0.0040*
$\gamma_Z/2\pi$(kHz/G)	11.910 ± 0.10	2.50 ± 0.5
$(\gamma_Y=\gamma_X)/2\pi$(kHz/G)	1.75 ± 0.75	2.0 ± 1.0

*L. E. Erickson, Phys. Rev. B 19, 4412 (1979).

Table II. Anticrossing Position, Linewidth and $|V|$ of the $Pr^{3+}:YAlO_3$ Transition $^3H_4(\Gamma_1) \leftrightarrow {}^1D_2(\Gamma_1)$

Anticrossing	State	Angles α,γ(deg)	Field (gauss) observed	Field (gauss) calc'd	Observed Linewidth[1] (gauss)	$\lvert V \rvert/\pi$(kHz)
a [2]	$^3H_4, {}^1D_2$	0,0	0	0	50	0
b	$^1D_2$	0,0	200	200	80	195
c	$^3H_4$	0,0	536.5	536.5	10	9.2
c [3]	$^3H_4$	0,0.9	524 550	524 550	7.8 7.8	9.2
d	$^3H_4$	0,0	535	530	105	866
e	$^3H_4$	0,0	1073	1073	120	442

1. Peak to peak values of derivative lineshape. Due to the field modulation, anticrossings a, b, d, and e are broadened by ~25G while c is broadened by ~8G.

2. This is a zero field level crossing rather than an anticrossing.

3. Because of the γ rotation, two anticrossings appear corresponding to the two inequivalent Pr^{3+} sites.

REFERENCES

1. W. Hanle, Z. Phys. 30, 93 (1924).
2. F. D. Colegrove, P. A. Franken, R. R. Lewis and R. H. Sands, Phys. Rev. Letters 3, 420 (1959); P. A. Franken, Phys. Rev. 121, 508 (1961).
3. T. G. Eck, L. L. Foldy and H. Wieder, Phys. Rev. Letters 10, 239 (1963).
4. H. Wieder and T. G. Eck, Phys. Rev. 153, 103 (1967).
5. C. Cohen - Tannoudji, Frontiers in Laser Spectroscopy, eds. R. Balian, S. Haroche, and S. Liberman (North Holland, Amsterdam, 1977), p. 73; D. R. Crosley and R. N. Zare, Phys. Rev. Letters 18, 942 (1967).
6. G. W. Series, Phys. Rev. Letters 11, 13 (1963); Phys. Rev. 136, A684 (1964).
7. A. C. Luntz, R. G. Brewer, K. L. Foster and J. D. Swalen, Phys. Rev. Letters 23, 951 (1969); A. C. Luntz and R. G. Brewer, J. Chem. Phys. 53, 3380 (1970).
8. K. Shimoda, Japan Journal of Applied Physics 11, 564 (1972).
9. M. S. Feld, A. Sanchez, A. Javan and B. J. Feldman, Proceedings of the Aussois Conference on High Resolution Molecular Spectroscopy, eds. J. C. Pebay-Peyroula and J. C. Lehmann (C.N.R.S., Paris, 1973), p. 87.
10. J. Sakai and M. Katayama, Appl. Phys. Letters, 28, 119 (1976).
11. T. Amano and R. H. Schwendeman, J. Mol. Spectroscopy, 78, 437 (1979).
12. V. P. Kaftandjian, C. Deslart and J. C. Keller, Phys. Rev. A (in press); P. A. Lakshmi and G. S. Agarwal, Phys. Rev. A (in press).
13. A. Compaan, L. Q. Lambert and I. D. Abella, Optics Communications 3, 236 (1971); A. Compaan, Phys. Rev. B11, 4450 (1972); L. Q. Lambert, Phys. Rev. B7, 1834 (1973).
14. W. S. Veeman and J. H. Van der Waals, Chem. Phys. Letters 7, 65 (1970); W. S. Veeman, A. L. J. Van der Poel, and J. H. Van der Waals, Molecular Physics 29, 225 (1975); M. J. Hunt, A. L. Mackay and D. R. Edmonds, Chem. Phys. Letters 34, 473 (1975); G. Kothandaraman, P. F. Brode III and D. W. Pratt, Chem. Phys. Letters 51, 138 (1977); A. Suisalu and P. Avarmaa, Phys. Stat. Sol. (b) 97, 69 (1980).

15. A. Schenzle and R. G. Brewer, Phys. Rev. A14, 1756 (1976).

16. M. A. Teplov, Zh. Eksp. Teor. Fiz. 53, 1510 (1967). [Sov. Phys. JETP 26, 872 (1968)].

17. B. Bleaney, Physica 69, 317 (1973).

18. C. J. Bradley and A. P. Cracknell, The Mathematical Theory of Symmetry in Solids (Clarendon, Oxford, 1972), Chap. II.

18a. In general, the principal axes (X"Y"Z") of the combined pure and pseudo quadrupole tensors will have one axis (the C_{1h} symmetry axis) in common with XYZ and X'Y'Z', but the other two will be related by a rotation. When $|D_a|$ and $|P|$ are of comparable size, the difference between XYZ, X'Y'Z', and X"Y"Z" can affect the magnetic splitting. Let α be the rotation angle around the C_{1h} symmetry axis that transforms X"Y"Z" into XYZ. Then the magnetic splitting term $\vec{B}\cdot\vec{\Lambda}\cdot\vec{I}$ in 3-4 can be transformed into the X"Y"Z" system by a similarity transformation, where $\Lambda''=R^{-1}(\alpha)\Lambda R(\alpha)$. The resultant Λ'' tensor thus contains off-diagonal terms $\Lambda_{X''Y''}\neq 0$ but these do not contribute to the magnetic splitting in first order. The diagonal terms of Λ'' become $\Lambda_{X''X''} = \Lambda_{XX}\cos^2\alpha + \Lambda_{YY}\sin^2\alpha$ and $\Lambda_{Y''Y''} = \Lambda_{YY}\cos^2\alpha + \Lambda_{XX}\sin^2\alpha$. A recent study of the $^1D_2$ magnetic splitting of Pr^{3+} in LaF_3 by R. M. Macfarlane and R. M. Shelby, Optics Lett. 6, 96, 1981 assumes that the Λ tensor has no off-diagonal elements, although the C_2 symmetry permits this and $|D_a| \sim |P|$. We estimate that the angle α can be as large as 20° for Pr^{3+} in LaF_3 although no measurements exist. The magnetic splittings they measure at very high magnetic fields, where the Hamitonian is diagonalized in the XYZ axis system, can thus differ substantially from the low field values, where the Hamiltonian is diagonalized along X"Y"Z". Consequently, this comparison of their high field g values with out low field g values[22] is not justified.

19. L. E. Erickson, Phys. Rev. B19, 4412 (1979).

20. S. Geller and E. A. Wood, Acta. Crystallogr. 9, 563 (1956).

21. A. Z. Genack, R. M. Macfarlane and R. G. Brewer, Phys. Rev. Letters 37, 1078 (1976); R. M. Macfarlane, A. Z. Genack, S. Kano and R. G. Brewer, J. Lumin 18/19, 933 (1979).

22. R. G. DeVoe, A. Szabo, S. C. Rand and R. G. Brewer, Phys. Rev. Letters 42, 1560 (1979); S. C. Rand, A. Wokaun, R. G. DeVoe, and R. G. Brewer, Phys. Rev. Letters 43, 1868 (1979).

23. L. E. Erickson (private communication).

24. We estimate $\Gamma(^3H_4)$ from the observed magnetic substate population recovery time.

25. R. G. Brewer and E. L. Hahn, Phys. Rev. A11, 1641 (1975).

26. R. Haberkorn, H. L. Selzle, W. Dietz, S. H. Lin and E. W. Schlag, Chemical Physics 52, 363 (1980).

27. R. M. Macfarlane, R. M. Shelby, and R. L. Shoemaker, Phys. Rev. Letters 43, 1726 (1979).

FIGURE CAPTIONS

Figure 1. Schematic of the experimental arrangement for detecting anticrossings.

Figure 2. A computer diagonalization of the $^{141}Pr^{3+}$ Zeeman-hyperfine Hamiltonian, Eq. (3-8), showing the ground state $^3H_4(\Gamma_1)$ zero-field level crossings (a) and anticrossings (c, d and e). The parameters of Table I are utilized.

Figure 3. A computer diagonalization of the $^{141}Pr^{3+}$ Zeeman-hyperfine Hamiltonian, Eq. (3-8), showing the excited state $^1D_2(\Gamma_1)$ zero-field level crossings (a) and the anticrossing (b).

Figure 4. Levels 1 and 2 exhibit anticrossing due to the interaction V where ω_{21} is the level-splitting in the absence of an interaction (V=0). A light wave of frequency Ω resonantly excites the 2↔3 transition and thus monitors the anticrossing tuning behavior as the magnetic field is swept. The quantities ω_{21}, V and Ω are in angular units.

Figure 5. Blow-ups of the anticrossings (b, c and e) of Figs. 2 and 3 where the gap spacing or interaction $|V|$, listed in Table II, is more clearly shown. The anticrossing (c) shows a Lorenztian lineshape signal in derivative form which is derived from (4-1); the peak to peak linewidth of ~0.4 gauss, which utilizes the parameters of Table I, does not explain the observed width of ~10 gauss as discussed in the text.

Figure 6. In Zeeman studies, the $YAlO_3$ crystal is rotated either about the c axis through the angle γ or about the a axis through the angle α. When the angles $\alpha=0°$ and $\gamma=0°$, the magnetic

field $B_0 \| b$ axis and the laser beam propagates parallel to the c axis. For the $^3H_4(\Gamma_1)$ state, β=56.50°, and for the $^1D_2(\Gamma_1)$ state, β=40° where the principal nuclear Z axes of the two inequivalent Pr^{3+} sites lie in the a-b plane.

Figure 7. Lower trace: Observed zero-field level crossing and anticrossings of 0.1% Pr^{3+}:$YAlO_3$ at 2°K where the rotation angles are α=0°, γ=0°. Upper trace: The sharp anticrossing c which rides on the broader d anticrossing splits into two well-resolved anticrossings when α=0°, γ=0.9° (See Table II). The scale is in kilogauss.

Figure 8. Zeeman rotation pattern for the anticrossings (b, c and e) where the angle α is varied and γ=0°.

Figure 9. The anomalous modulation effect in the region of anticrossings c and d. The laser frequency is swept through ±85 MHz at a repetition rate of 1.5 kHz and the cw laser power is 80 mW.

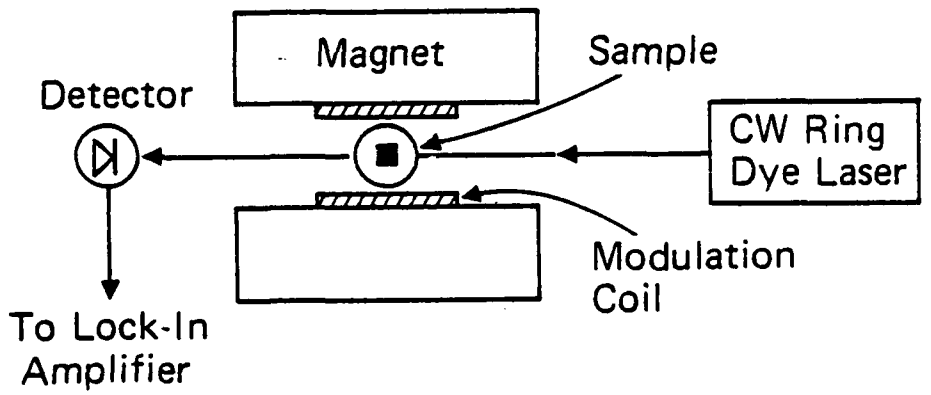

Magnet
Sample
Detector
CW Ring
Dye Laser
Modulation
Coil
To Lock-In
Amplifier

Fig. 1

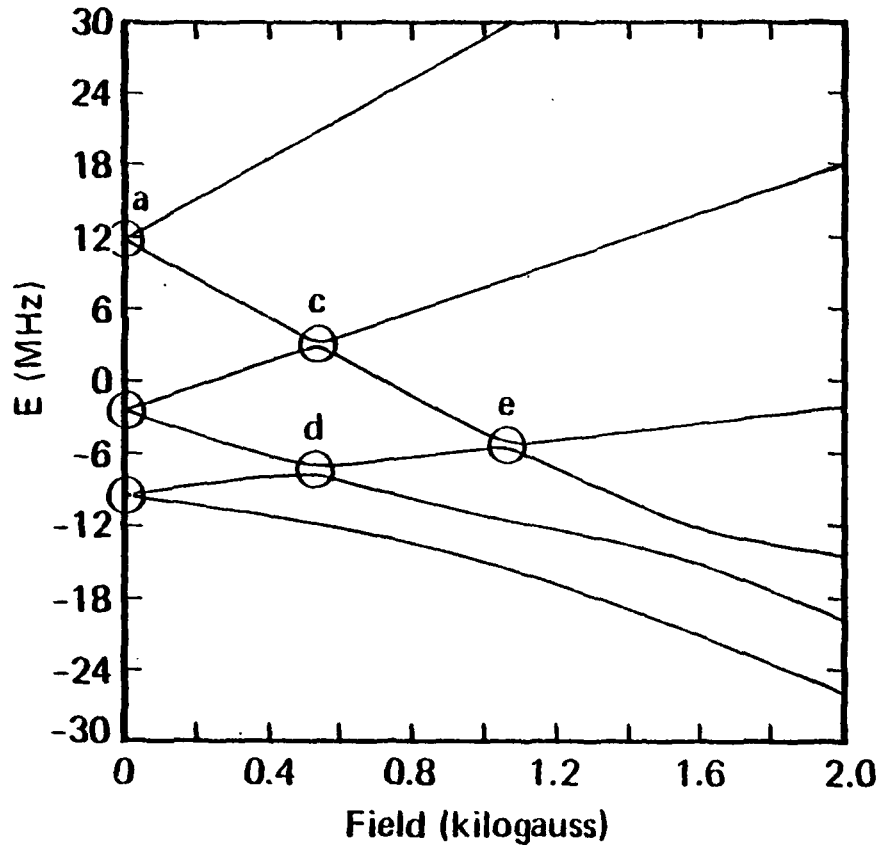

30
24
18
12
6
0
-6
-12
-18
-24
-30
E (MHz)
a
c
d
e
0
0.4
0.8
1.2
1.6
2.0
Field (kilogauss)

Fig. 2

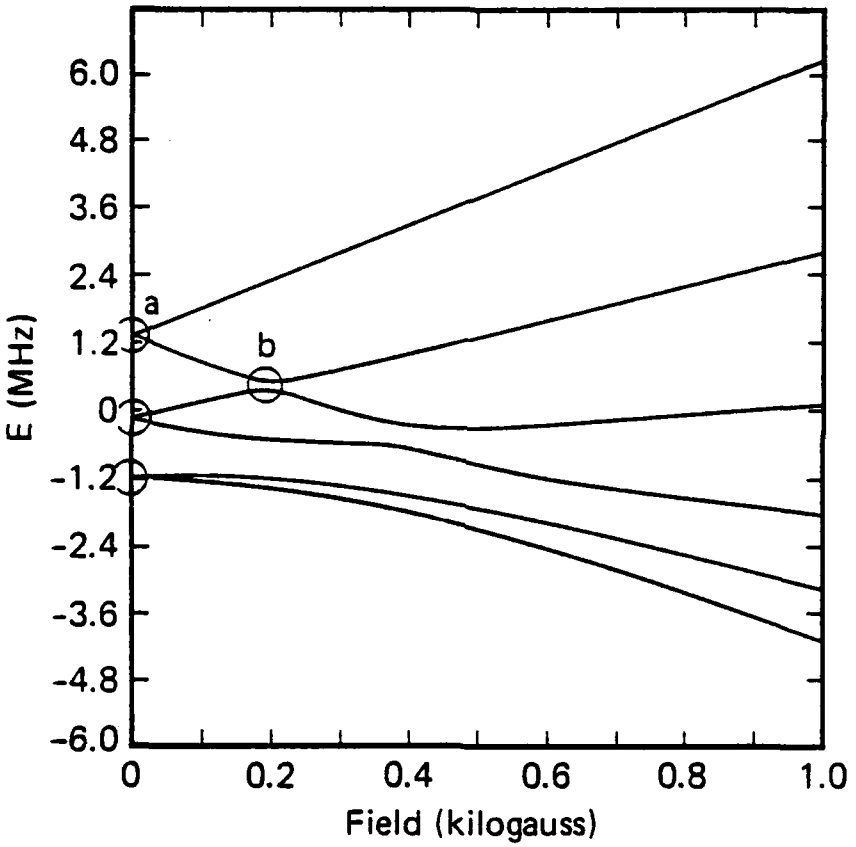

6.0
4.8
3.6
2.4
1.2
0
-1.2
-2.4
-3.6
-4.8
-6.0
E (MHz)
a
b
0
0.2
0.4
0.6
0.8
1.0
Field (kilogauss)

Fig. 3

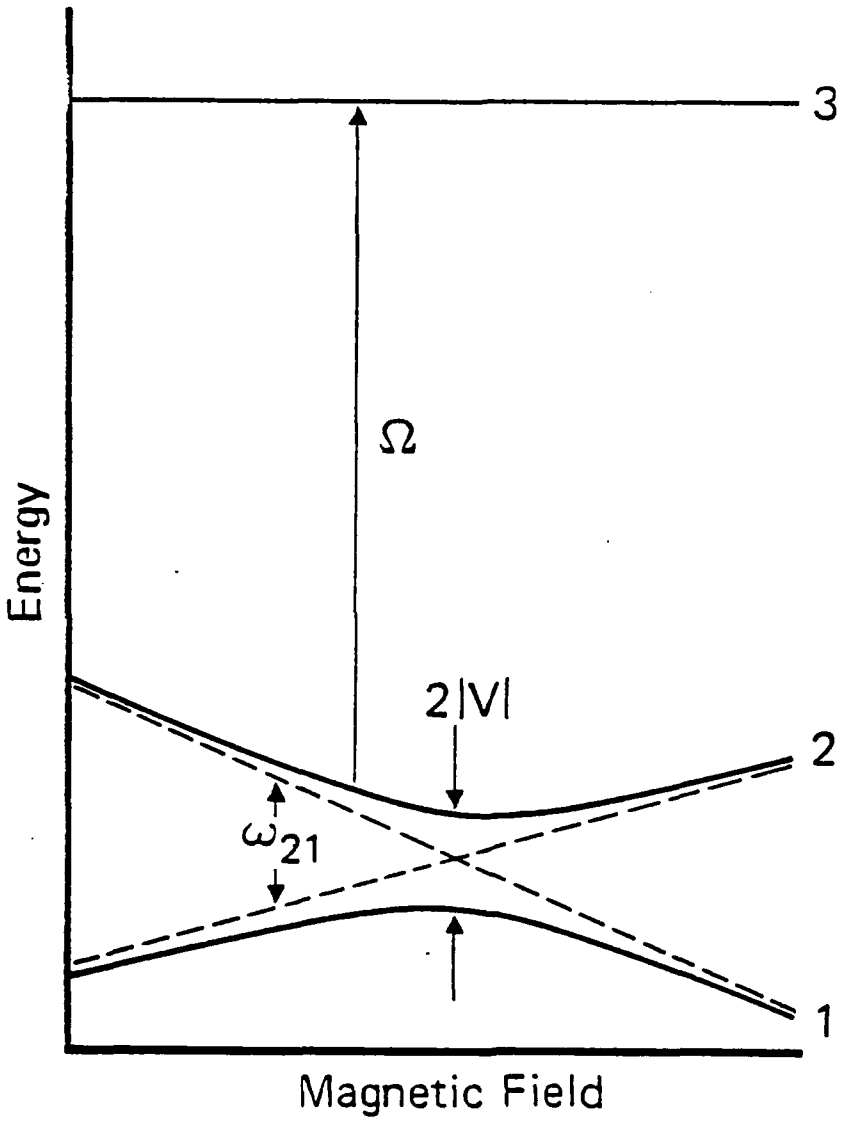


Fig. 4

NEW PHENOMENA IN COHERENT OPTICAL TRANSIENTS

R. G. Brewer
R. G. Devoe
S. C. Rand
A. Schenzle
N. C. Wong
S. S. Kano
A. Wokaun

IBM Research Laboratory
San Jose, California 95193

It is often stated, and with justification, that the concepts underlying coherent optical transient phenomena can be found in the literature of spin transients. For example, the Bloch vector [1] description of spin echoes [2] and free precession [3] applies equally well to photon echoes [4] and optical free induction decay [5]. While this conclusion remains largely true, it is not equally valid to say that the techniques are the same or to prophesy that the applications of optical and rf transients are identical also. In fact, the decay channels of optically excited atoms, molecules and solids usually involve a variety of interactions which contrast with the magnetic interactions encountered in spin resonance. This is a major distinction, one which has permitted new studies at optical frequencies. Moreover, it is also true that some of the practioners of magnetic resonance are beginning to learn a few lessons from quantum optics as well. In this paper, I have selected some of the new developments which are representative of the field of coherent optical transients.

PHENOMENA

Scientific discoveries sometimes proceed in the following stages [6]:

Prehistoric age	Might have been discovered, but wasn't
Stone age	Discovered, but not noticed
Ice age	Noticed, but not believed
Bronze age	Believed, but not interesting
Iron age	Wow!

I am not sure where the new phenomena I wish to discuss stand, perhaps between the bronze and iron age. They are: (1) oscillatory free induction decay; (2) stimulated photon echo effect; and (3) molecular spin-rotation effect.

Oscillatory Free Induction Decay [7]

Imagine that a square pulse of coherent electromagnetic radiation of duration T resonantly excites an inhomogeneously broadened two-level quantum system. We ask what is the nature of the coherent emission, free induction decay, following the pulse. It is remarkable that anything new is to be discovered here since all coherent transient effects involve some form of pulse preparation. However, analytic and numerical solutions of the Bloch equations reveal new features which are shown in Fig. 1. In particular, large amplitude oscillations appear as the pulse area χT

Appendix - Item 16

RJ3178 (38984) 7/7/81
Physics

NEW PHENOMENA IN COHERENT OPTICAL TRANSIENTS *

R. G. Brewer
R. G. Devoe
S. C. Rand
A. Schenzle
N. C. Wong
S. S. Kano
A. Wokaun

IBM Research Laboratory
San Jose, California 95193

ABSTRACT: This article reviews certain aspects of recent studies in coherent optical transients. Included are new phenomena and applications to the study of atomic collisions and solids.

*Work supported in part by the U.S. Office of Naval Research.

REFERENCES

1. T. W. Mossberg and S. R. Hartmann, Phys. Rev. A (preceding paper).
2. A. Schenzle, N. C. Wong, and R. G. Brewer, Phys. Rev. A 22, 635 (1980).
3. R. G. Brewer and R. L. Shoemaker, Phys. Rev. A 6, 2001 (1972).
4. A. L. Bloom, Phys. Rev. 98, 1105 (1955).
5. M. Kunitomo, T. Endo, S. Nakanishi, and T. Hashi (to appear in Phys. Lett.).
6. M. Kunitomo, and T. Hashi, Phys. Lett. 81A, 299 (1981).
7. V. P. Chebotayev, N. M. Dyuba, M. I. Skvortov, and L. S. Vasilenko, Appl. Phys. 15, 319 (1978); R. Kachru, T. W. Mossberg, E. Whittaker, and S. R. Hartmann, Opt. Commun. 31, 223 (1979).
8. J.-L. LeGouët, and P. R. Berman, Phys. Rev. A 20, 1105 (1979).
9. T. W. Mossberg, R. Kachru, S. R. Hartmann, and A M. Flusberg, Phys. Rev. A. 20, 1976 (1979).
10. M. Aihara and H. Inaba, J. Phys. A 6, 1709 (1973); 6 1725 (1973).
11. T. Mossberg, A. Flusberg, R. Kachru, and S. R. Hartmann, Phys. Rev. Lett. 39, 1523 (1977).
12. I. Solomon, Phys. Rev. 110, 61 (1958).

tri-level echo,[11] in which counter-propagating waves are used, also occurs within the interval $T \leq t \leq \left(1 + \frac{\Omega_{max}}{\Omega_{min}}\right)T$. Theoretical[9,10] predictions of noncollinearly excited tri-level echoes also fall within the same interval.

Another exception to the theorem cited by MH is the multiple nuclear spin echoes in solids observed by Solomon.[12] However, this spin system does not satisfy the essential requirement of being strongly inhomogeneously broadened, and therefore has no relevance.

In conclusion, we have delineated more explicitly the limits of validity of the theorem. The generalized form of the theorem states that an optically thin multi-level quantum system subject to a multi-frequency radiation pulse of duration T and extreme inhomogeneous broadening, ceases to radiate coherent emission for times longer than $t = \left(1 + \frac{\Omega_{max}}{\Omega_{min}}\right)T$. This assumes the rotating wave approximation and is valid only if all excitation fields propagate collinearly in the same direction and there exists at most one combination of excitation frequencies which is resonant with a particular transition. Within these restrictions, the number of fields, their frequencies and the pulse shape remain arbitrary.

The same analysis as in SWB follows. We have

$$\tilde{\rho}_{i\ell}(v_z,t') = \sum_m A_m e^{z_m t'} \tag{3}$$

where z_m are the roots of the characteristic equation for the multi-level generalized Bloch equations. In the asymptotic limit $|v_z| \to \infty$, the roots assume the values

$$\lim_{|v_z| \to \infty} z_m = \text{constants}, \ \pm ik_{ij}v_z, \ \text{for all } i \neq j \text{ pairs.}$$

The constants are simply combinations of the population relaxation rates. Substitution of (3) into (2) followed by contour integration in the upper half plane results in the condition that for times

$$t_{ij} \geq \left(1 + \frac{k_{max}}{k_{ij}}\right)T \tag{4}$$

coherent emission for the i-j transition vanishes. Hence, *all* coherent emission should terminate for times

$$t \geq \left(1 + \frac{\Omega_{max}}{\Omega_{min}}\right)T \tag{5}$$

where we now neglect dispersion and Ω_{max} and Ω_{min} correspond to the maximum and minimum values of the set $\{\Omega_{\ell m}\}$. Note that (4) reduces to the two-level case, $t_{ij} \geq 2T$, when $\Omega_{max} = \Omega_{ij}$.

Theoretical[9,10] predictions of tri-level echoes prepared by uni-directional excitation confirm the new result, Eq. (5). Furthermore, although Eq. (5) is valid only for uni-directional excitation, we note that the observed rephasing time of the sum-frequency

realizing that the density matrix has velocity dependent components of the form $(k_{ij}v_z)$ for all i-j pairs. This change leads to a new result which is applicable when the excitation frequencies are different and also when multi-photon transitions occur.

The generalized theorem in its new form is derived in the same spirit as for the two-level case. A multi-level quantum system is assumed which is excited by a pulse of arbitrary shape consisting of traveling wave components all propagating in the same direction with different frequencies. The rotating wave approximation and the assumption of an optically thin sample are maintained in addition to that of strong inhomogeneous broadening. We further assume that for each n-photon i-j transition, there is at most one combination of n excitation fields which is resonant, as is usually the case in an experiment. This enables us to perform a generalized rotating frame transformation by excluding any atomic structure which allows its energy levels to be coupled in more than one way. We denote the i-j transition frequency by ω_{ij} and the corresponding frequency of the resonant combination of excitation fields by Ω_{ij}. The quantities ω_{ij} and Ω_{ij} are elements of corresponding sets $\{\omega_{\ell m}\}$ and $\{\Omega_{\ell m}\}$ which embrace all possible transitions consistent with the fields applied. The coherent emission at time t>T when averaged over the inhomogeneous lineshape is given by

$$\langle \tilde{\rho}_{ij}(t) \rangle = \frac{i}{2}\int_{-\infty}^{\infty} g(\Delta_{ij})d\Delta_{ij} \sum_{\ell} \int_{o}^{T} dt' e^{(i\Delta_{ij}-1/T_{ij})(t-t')}$$

$$\times \left[\tilde{\rho}_{i\ell}(v_z,t')\chi_{\ell j}(t')-\chi_{i\ell}(t')\tilde{\rho}_{\ell j}(v_z,t')\right] \qquad (2)$$

where Δ_{ij} is defined by (1) and where we take $\tilde{\rho}_{ij}(0) = 0$.

The subsequent discussion by SWB extends the theorem to a multi-level quantum system where the energy spacing, the number of fields and their frequencies are arbitrary. However, we still assumed, though not explicitly stated, that all waves propagate collinearly in the forward direction as indicated in the formal structure of Eq. (13) of SWB. Any deviation from uni-directional excitation may result in spatial hole-burning and may lead to the possibility of temporal rephasing of the spatial coherence created by such excitation. This kind of rephasing occurs in the standing wave echo where the spatial coherence lasts for times $t>2T$, as demonstrated both experimentally[7] and theoretically.[8] Obviously, the theorem doesn't apply in this case because the waves are no longer uni-directional.

Now consider the first example of MH, the inverted-difference frequency tri-level echo,[9] where the excitation is uni-directional, and the rephasing time satisfies $t>2T$ for a suitable choice of frequencies. This example has caused us to realize that Eq. (13) of SWB is oversimplified and, thanks to their suggestion, we now introduce a modification. The difficulty lies in the definition of the tuning parameter

$$\Delta_{ij} = \omega_{ij} - \Omega_{ij} + kv_z ,$$

which asserts that the Doppler shift kv_z is the same for all transitions $i \rightarrow j$, making the SWB conclusion invalid for multi-frequency excitation.

We now replace this definition by

$$\Delta_{ij} = \omega_{ij} - \Omega_{ij} + k_{ij}v_z \; ; \; k_{ij} \equiv \Omega_{ij}/c , \qquad (1)$$

Mossberg and Hartmann (MH)[1] comment on a "theorem of coherent transients" developed by Schenzle, Wong, and Brewer (SWB)[2], citing examples which are not covered. Objection to the theorem's applicability arises when standing waves are used or when the excitation frequencies are different. In this comment, we further clarify the limits of validity of our theorem.

The theorem applies to nuclear magnetic resonance (NMR) and quantum optics, and is derived, within the rotating wave approximation, for an optically thin atomic system subject to extreme inhomogeneous broadening and to coherent preparation by a pulsed electromagnetic field. The initial discussion of SWB considers a fundamental problem, the resonant excitation of a two-level quantum system by a single-frequency *traveling wave* pulse of arbitrary shape, which is clearly defined in our Eq. (1).[2] The theorem states that when a pulse of finite duration T (interval $0 \leq t \leq T$) prepares a sample, the coherent emission which follows lasts only for an additional period T (interval $T \leq t \leq 2T$).

The validity of this theorem has already been demonstrated by experiments in the infrared[3] and radio frequency[4] regions where the condition of strong inhomogeneous broadening is maintained. More recently, NMR measurements by Kunitomo et al.[5] confirm that the free decay signal for an inhomogeneously broadened transition terminates precisely at $t=2T$. Moreover, Kunitomo and Hashi[6] observe for the same inhomogeneously broadened system that spin locked echoes, notched echoes, and new types of spin echoes are all confined to the time interval $T \leq t \leq 2T$. We emphasize that the theorem at this stage rests on the following assumptions: (1) extreme inhomogeneous broadening of a two-level quantum transition, (2) excitation by a single-frequency traveling wave pulse of arbitrary shape, and (3) the rotating wave approximation.

RJ3183 (38989) 7/15/81
Physics

THEOREM ON COHERENT TRANSIENTS: RESPONSE TO A COMMENT **

Axel Schenzle*
N. C. Wong
Richard G. Brewer

IBM Research Laboratory
San Jose, California 95193

and

Department of Applied Physics
Stanford University,
Stanford, California 94305

ABSTRACT: The limits of validity of a theorem on coherent transients are discussed with reference to a recent comment.

---

*Normally at the Department of Physics, Universität Essen, Gesamthochschule, Essen, West Germany.

**Work supported in part by the U.S. Office of Naval Research.

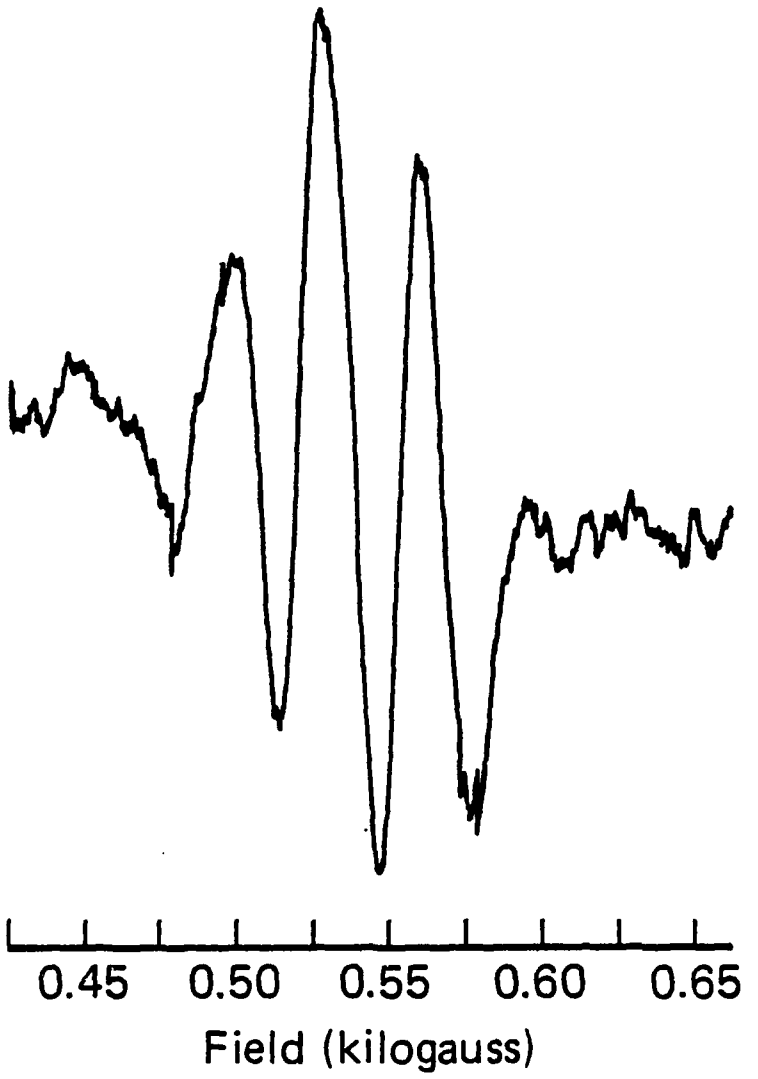


Fig. 9

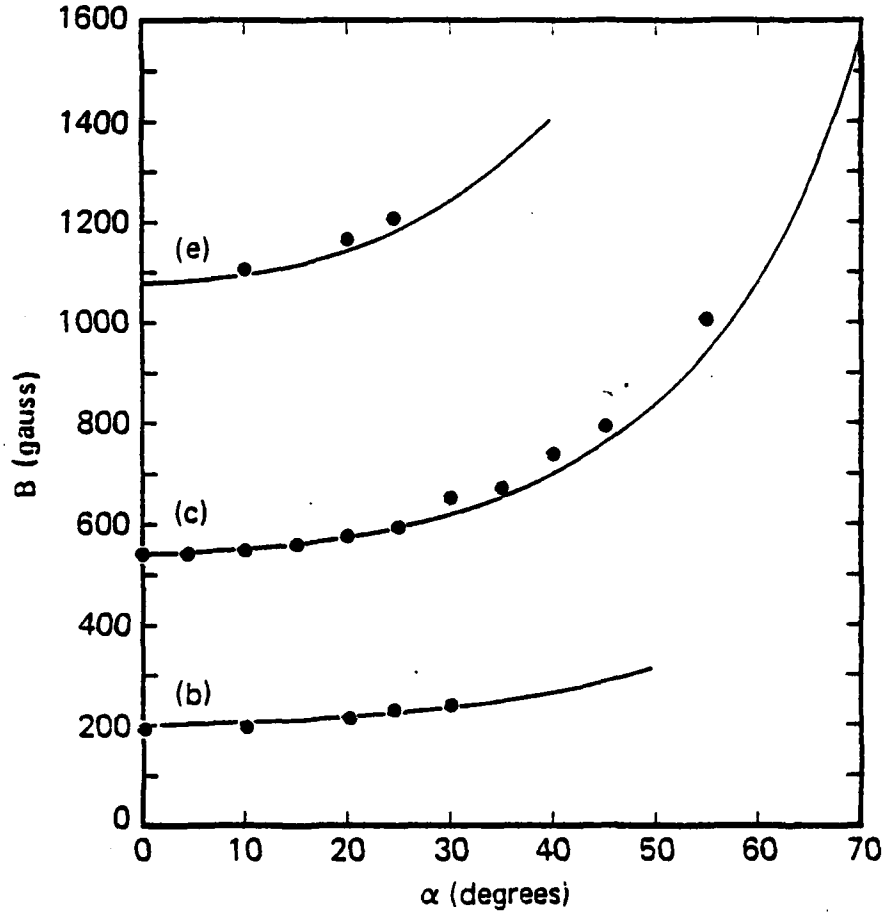

1600
1400
1200
1000
800
600
400
200
0
B (gauss)
(e)
(c)
(b)
0
10
20
30
40
50
60
70
α (degrees)

Fig. 8

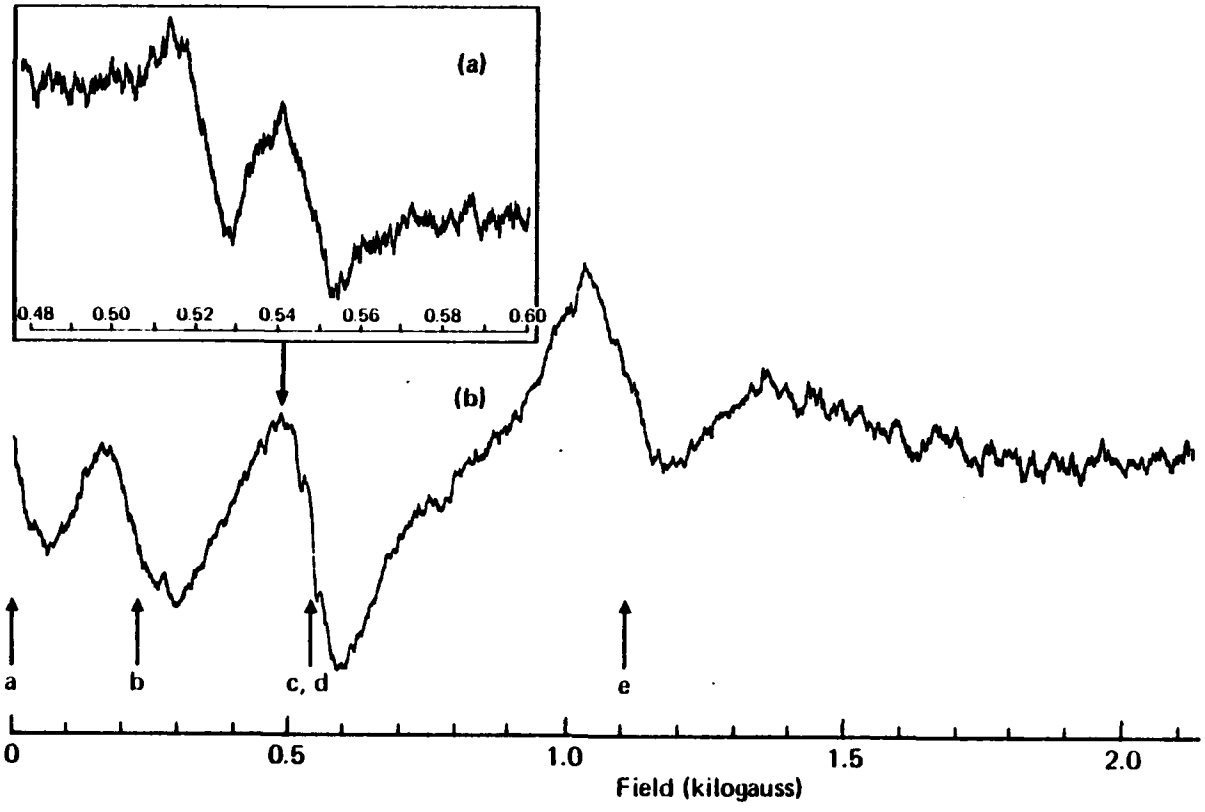

(a)
0.48
0.50
0.52
0.54
0.56
0.58
0.60
(b)
a
b
c, d
e
0
0.5
1.0
1.5
2.0
Field (kilogauss)

Fig. 7

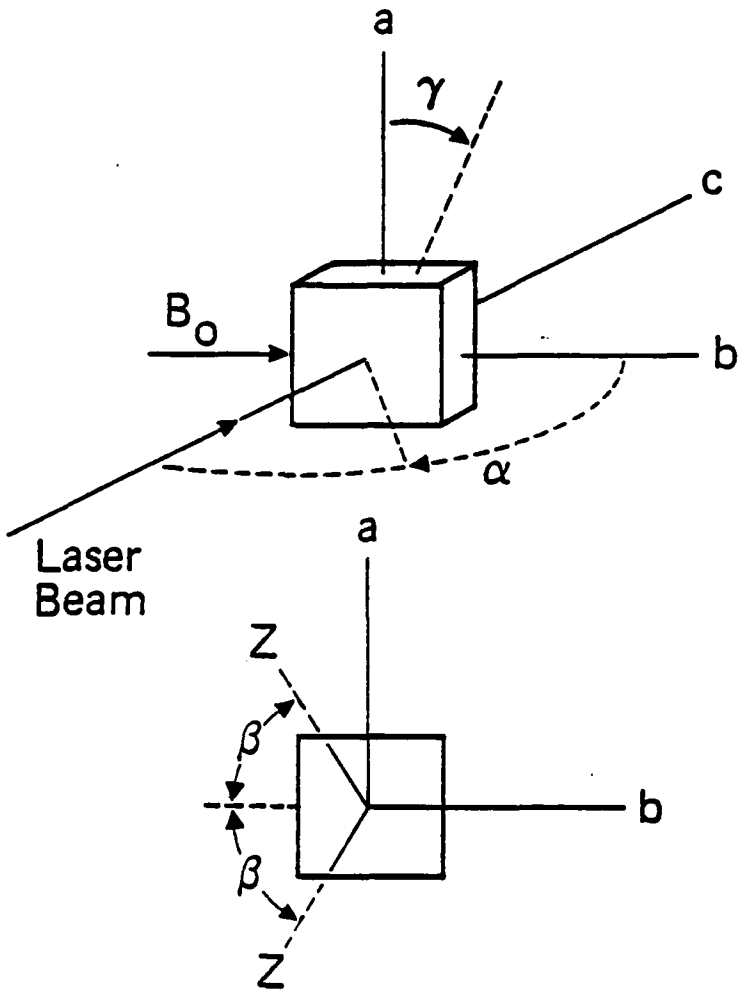


Fig. 6

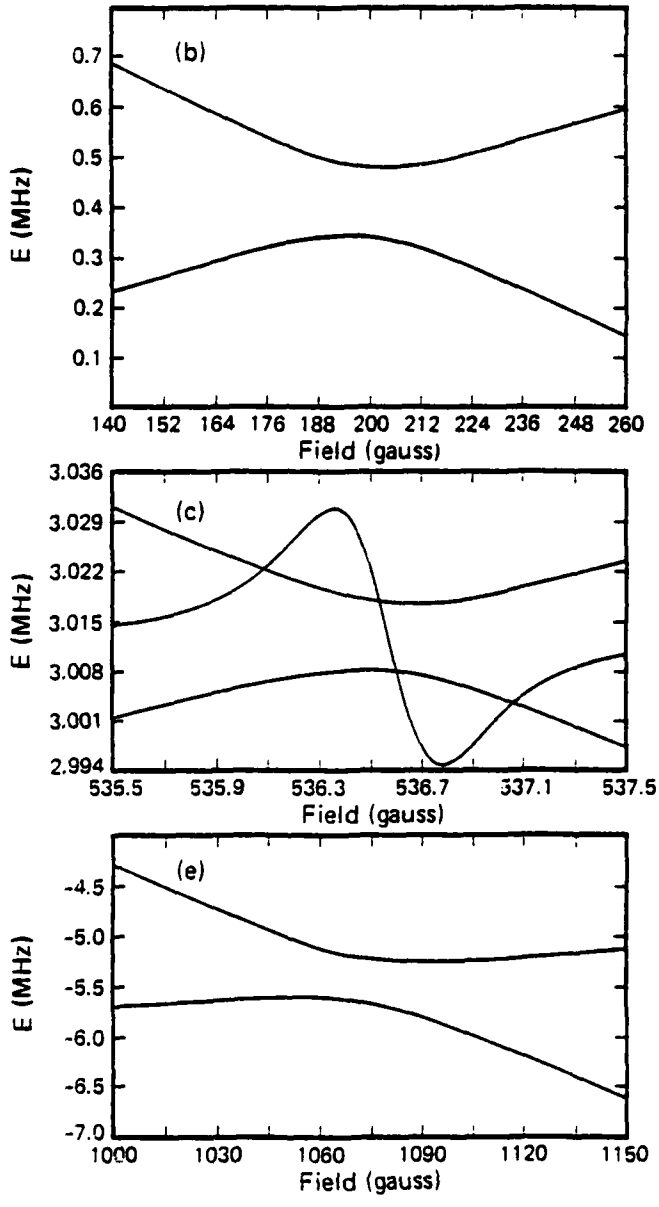

(b)
E (MHz)
0.7
0.6
0.5
0.4
0.3
0.2
0.1
140 152 164 176 188 200 212 224 236 248 260
Field (gauss)
(c)
E (MHz)
3.036
3.029
3.022
3.015
3.008
3.001
2.994
535.5 535.9 536.3 536.7 337.1 537.5
Field (gauss)
(e)
E (MHz)
-4.5
-5.0
-5.5
-6.0
-6.5
-7.0
1000 1030 1060 1090 1120 1150
Field (gauss)

Fig. 5

increases, χ being the Rabi frequency. Physically, Rabi sidebands introduced in the preparative period are preserved in the polarization following the pulse and give rise to the predicted oscillations. The oscillation frequency is not constant, but increases with time due to interference among the packets of the inhomogeneously broadened lineshape. As the packets get out of phase, due to differences in their frequency, an interference results and causes the transient to vanish precisely at time 2T, i.e., one pulse width following the pulse [8]. The initial rapid rise near time t=T arises from the first order FID, discussed elsewhere [9]. Hence, there are three time scales: the initial rapid response (T_2^*), the period of oscillation ($\sim 1/\chi$), and the duration of the emission ($T \leq t \leq 2T$). The uniqueness of the phenomenon is due to a combination of nonlinear behavior, which becomes evident at elevated intensities, and a transition that is strongly inhomogeneously broadened.

These predictions have been fully confirmed in the radio frequency region recently (Fig. 1) [10] and in the future should be readily detectable at optical frequencies as well.

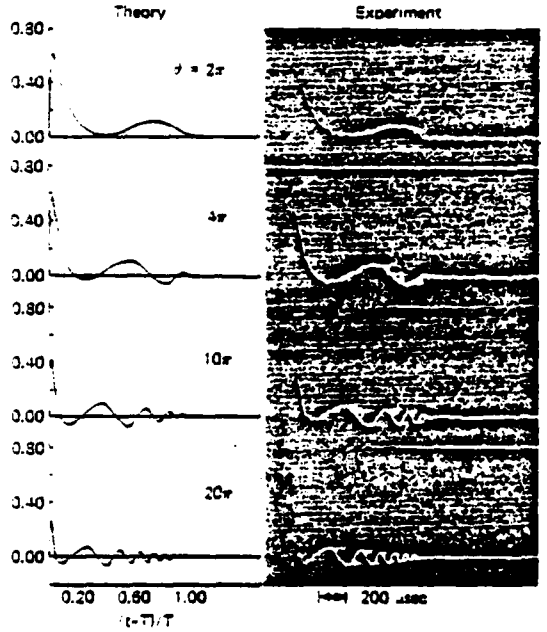


Figure 1. Oscillatory free induction decay. Left: theory of Schenzle et al. (Ref. 7); right: FID of protons in water by Hashi et al. (Ref. 10).

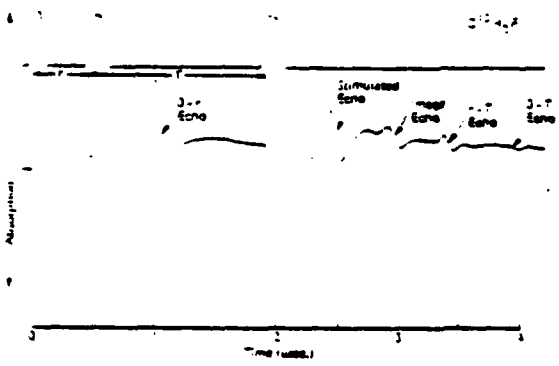


Figure 2. Stimulated and two-pulse infrared photon echoes in $C^{13}H_3F$ (lower trace) resulting from Stark switching pulses (upper trace).

Stimulated Echo Effect

Hahn's discovery of the spin echo or two-pulse echo of a two-level spin system also lead to the discovery of the stimulated or three-pulse echo [2] (Fig. 2). In the latter, two rf pulses at times t=0 and t=T produce the normal spin echo at t=2T, while a third pulse at t=T+τ creates a stimulated echo at t=T+2τ (and subsequent two-pulse echoes which can be ignored here). The first pulse prepares two-level spin packets in quantum mechanical superposition which thereafter dephase. The second pulse reverses their phase relationship so that they come back into phase to produce the spin-echo pulse. In addition, a modulated population distribution among the upper and lower spin states results with a modulation frequency 1/τ, the inverse of the time between the two initial pulses. The modulated population possesses a precise phase in the frequency domain, within the

inhomogeneous lineshape, a property that can persist long after the temporal coherence of the superposition state has vanished. Finally, the third pulse reads out the precise phase information contained in the modulated population of both upper and lower spin states by again introducing a two-level coherent superposition that interferes in such a way as to produce an echo, the stimulated echo. The new aspect of this subject is that the frequency of the third pulse can differ from the first two pulses, allowing either the lower or upper initial spin states to participate in a second transition which similarly produces a stimulated echo [11,12]. Thus, population relaxation, which washes out the modulation pattern, can be examined selectively in either initial spin state - a point not realized in the NMR literature. The recent optical studies in gases [11] and solids [12] support these conclusions. In some solids at liquid helium temperature, for example, the ground state population modulation persists for 30 minutes or more [12].

Spin-Rotation Effect [13]

The optical Stark switching technique [14] has permitted observing many of the optical analogs of spin transients and also some new effects as well. Consider one of these, the two-pulse photon echo of $^{13}CH_3F$ gas which shows a pronounced interference or modulation behavior in the echo amplitude as the pulse delay time is advanced [13]. The modulation arises from the molecular spin-rotation interaction $\mathcal{H}=C\vec{I}\cdot\vec{J}$, where I and J are the spin and molecular rotation quantum numbers. The smallness of the interaction constant $C\lesssim 20$ kHz suggests that a significant modulation is unlikely, but rather surprisingly, a depth of modulation of 35% or more is readily detectable. To understand the phenomenon, we imagine that two Stark pulses switch $^{13}CH_3F$ molecules twice into resonance with a fixed frequency (9.66 μm) CO_2 laser so as to produce an infrared photon echo. The Stark pulse amplitudes are sufficiently large that the laser drives only one pair of levels in a given molecule. When the pulses are switched off, the formerly driven level pair (still in superposition) mixes with the neighboring undriven levels through the spin-rotation interaction. It can be shown that four levels are now in superposition in place of the original two, and because of the small spin-rotation splitting, transitions of slightly different frequency interfere. Even though the splitting is small and normally difficult to detect, a large modulation in the echo envelope function results. Spin-rotation modulation in $^{13}CH_3F$ has been monitored for the ^{13}C nucleus and the ^{19}F nucleus in both ground and excited vibrational states. Precise determinations of the interaction parameter C should be possible in future measurements.

ELASTIC COLLISIONS

Any process that introduces random phase changes in an ensemble of coherently prepared atomic dipoles will produce damping. One example is the subtle effect of elastic collisions of atoms in a coherent two-level superposition state. It is the optical superposition state that distinguishes this elastic scattering problem from previous work. Is it possible to predict in general whether the two states which are in superposition behave in the same way or not during elastic scattering? I think that the answer is no, and we must, at least for the present, be guided by observations.

Initial photon echo studies [15] in the infrared region involving the superposition of a pair of vibration-rotation states of $^{13}CH_3F$ show that the elastic collisions are of the velocity changing type. Here, the two states are described by the same scattering trajectory. Experiments can be interpreted by the following simplified agrument. The dipolar phase change corresponding to a change in velocity Δv along the optic axis direction is given by $\Delta\phi = k\Delta v t$, where $k = 2\pi/\lambda$, λ is the optical wavelength and t is the time. In a two-pulse echo experiment with pulse delay time τ, such random phase changes will cause the molecular dipoles to get out of step, and the echo amplitude will shrink by the phase factor

$$S \sim \langle e^{ik\Delta v\tau} \rangle_{\text{collision}} . \tag{1}$$

Eq. (1) takes limiting forms in the short- and long-time regimes,

$$S \sim \exp[-k^2 \Delta u^2 \Gamma \tau^3/4] \ , \quad k\Delta v\tau << 1$$

$$S \sim \exp[-\Gamma\tau] \ , \qquad k\Delta v\tau >> 1 \tag{2}$$

where Γ is an average rate of a binary collision and Δu is a characteristic change in velocity per collision. The nonexponential decay at short times followed by an exponential decay is the signature for the velocity changing collision mechanism (Fig. 3). In addition to the $^{13}CH_3F$ results, recent infrared echo measurements [16] in SF_6 obey (2) also, in support of the velocity changing collision mechanism. It may be that all molecules prepared in coherent superposition in the infrared exhibit elastic velocity changing collisions in this way.

In the visible region, however, the superposition involves two electronic states which may behave quite differently during an elastic collision. State-dependent elastic collisions can produce phase interruptions of the form $\Delta\phi = \Delta\omega t_c$, where $\Delta\omega$ is the angular shift in the transition frequency and t_c is the collision duration. The decay law for this model is exponential (Fig. 4). Optical free induction decay of the visible transition of I_2 vapor does indeed reveal an exponential decay [17], and recently measurements [18] have been extended to times as short as 10 nsec with no evidence for an $\exp(-Kt^3)$ decay law. Photon echo studies in helium, neon and argon plasmas also obey exponential behavior [19]. In contrast to the above, it is claimed [20] that photon echoes of the sodium D lines display both velocity changing and phase interrupting character in different time regimes. This interpretation, if correct, raises the issue of a need for a more general treatment of the effect of elastic scattering of atoms in superposition states, rather than the limiting cases of velocity changing and phase interrupting collisions considered here.

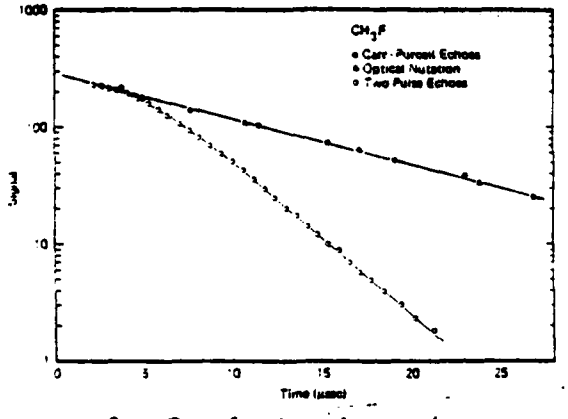


Figure 3. Population decay (upper curve) and dipole dephasing (lower curve) in CH_3F, detected by infrared coherent transients, where the difference in the two results from velocity changing collisions.

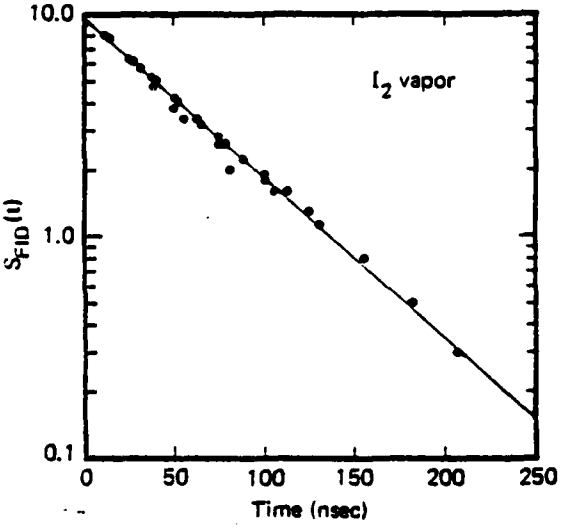


Figure 4. Optical FID in a visible transition of I_2. This shows exponential decay down to ~10 nsec due to phase interrupting collisions in contrast to Fig. 3.

SOLIDS

Remarkably narrow optical homogeneous linewidths of the order of 1 kHz have now been observed in the low temperature zero-phonon transition $^3H_4 \longleftrightarrow {}^1D_2$ of the impurity ion Pr^{3+} in LaF_3 and other host crystals using optical free induction decay [21,22]. A cw ring dye laser that is frequency-locked to a stable external reference cavity coherently prepares a single Pr^{3+} packet within its homogeneous width, producing a narrow hole within the strain-broadened inhomogeneous lineshape (~5 GHz width). When the exciting laser beam is frequency-switched a few megaHertz, using an external Bragg modulator [21], the free precession commences and the usual FID heterodyne beat signal results as seen with a P-I-N photodiode in transmission (Fig. 5). In the absence of power-broadening, the decay of this signal is one-half the dipole dephasing time ($T_2/2$).

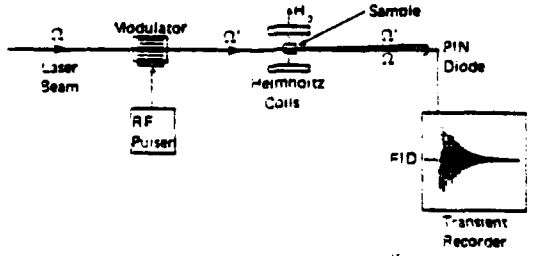


Figure 5. Laser frequency switching technique for observing coherent optical transients such as FID.

For Pr^{3+}:LaF_3, the homogeneous linewidth can be no narrower than 160 Hz, due to the 0.5 msec radiative lifetime of the $^1D_2$ state. At 2°K, phonon processes contribute at most a few Hertz. Laser power broadening is estimated to be less than 100 Hz. The dominant dynamic process arises from the magnetic-dipolar spin interactions, due first to the fluctuating

resonant flip-flops among pairs of ^{19}F spins and second to the resulting nonresonant heteronuclear ^{141}Pr-^{19}F interaction which reflects the time dependence of the homonuclear events. That such a mechanism determines the optical homogeneous width follows first from the magnitude of the broadening which is comparable to that encountered in NMR. Secondly, the linewidth or dephasing time depends on the strength of the applied external magnetic field. For example, in the Earth's field, T_2=3.6 usec, but when the external field exceeds the local field of ~20G, T_2=15.8 usec corresponding to a 10 kHz HWHM linewidth. Obviously, when the external field exceeds the local field, the induced precession rate is fast enough to time average the slower chaotic motions associated with the field fluctuations along the external field direction. Magnetic fluctuations in the transverse directions are unaffected, however, and thus the linewidth narrows but does not vanish.

An even more dramatic and unambiguous demonstration of the dipolar line-broadening mechanism is found in the application of the magic angle line-narrowing technique of NMR to optical spectroscopy [22]. The optical FID experiment is repeated, but now in the presence of an rf and a static magnetic field (Fig. 6). By transforming the Bloch formalism and the homonuclear (F-F) and the heteronuclear (Pr-F) dipolar interactions into a suitable rotating frame, it can be shown [22] that the optical linewidth in the presence of an rf field is given by

$$\Delta\nu(\beta) = \Delta\nu(0)|\cos\beta \cdot 1/2(3\cos^2\beta-1)| \quad . \qquad (3)$$

Here, β is the angle the effective field makes with the applied static magnetic field and $\Delta\nu(0)$ is the optical linewidth in the absence of the rf field. Note that in the rotating frame the $1/2(3\cos^2\beta-1)$ term takes the form of a secular dipolar interaction and we see that the linewidth vanishes when $\beta=\pi/2$, the fluorine resonance condition, and $\beta=54.7°$, the magic angle condition. Physically, the induced precession resulting from the applied static and oscillating magnetic fields provides a time averaging mechanism which tends to eliminate the chaotic motions arising from the local ^{19}F field fluctuations. The argument therefore is similar to the time averaging achieved with a static field, as described above, but in the magic angle case, the averaging is more effective.

The form of (3) has been verified in detail by FID studies of Pr^{3+}:LaF_3, and furthermore shows that the linewidth narrows from ~10 to ~2 kHz [22] (Fig. 7). The source of the residual broadening is still being examined.

Finally, a Monte Carlo theory [23] of optical dephasing in Pr^{3+}:LaF_3 has been developed to explain the current FID observations. A numerical approach was attempted since the heteronuclear dipolar interaction is neither weak enough to fit a Gaussian theory ($\delta\omega t<<1$) nor strong enough to fit the Klauder-Anderson theory [24] ($\delta\omega t>>1$). Instead, $\delta\omega_{max}T\sim1$, where $\delta\omega_{max}$ is the maximum Pr^{3+} frequency jump, due to a fluorine spin flip, and T is the observed Pr^{3+} dephasing time. A Monte Carlo computer routine was utilized that assumed: (1) the LaF_3 crystal structure and (2) a sudden fluorine spin-flip model, thus avoiding many of the approximations of past analytic theories in magnetic resonance. The Pr^{3+} decay behavior is obtained by sampling statistically the Pr^{3+} phase history as subgroups of ^{19}F spins flip randomly in space and time. Only a few ^{19}F spins contribute significantly to the homogeneous width, a result which shows for the first time that spin-flip correlations are not significant. Furthermore, a Pr^{3+}

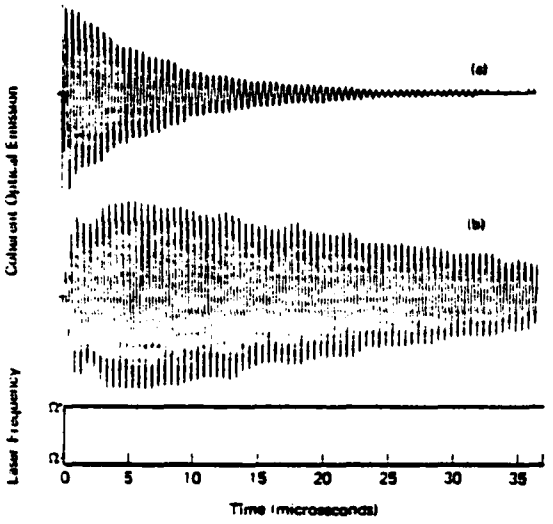


Figure 6. Optical FID in Pr^{3+}:LaF_3 with (a) no rf and (b) with rf at the magic angle condition.

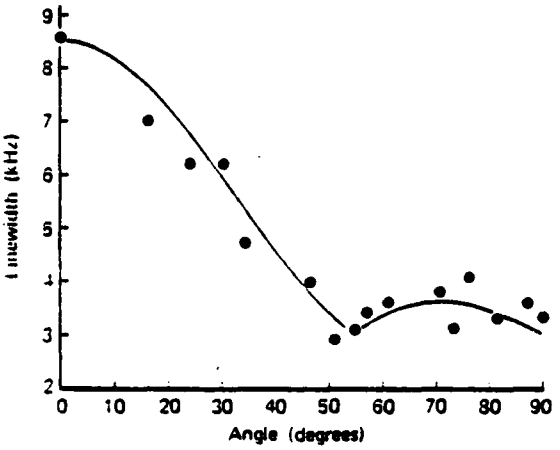


Figure 7. Optical linewidth of $Pr^{3+}LaF_3$ versus the angle β expressed in degrees. Solid circles: experimental points. Solid line: Eq. (3).

ion polarizes and detunes the nearest fluorines, forming a frozen core that is incapable of spin flipping with the bulk fluorines. Although the core grows radially as the ^{141}Pr (I=5/2) magnetic moment increases with I_z, the optical linewidth changes little since the fluorines which participate in spin flipping become more distant. Using no free parameters, a Lorentzian lineshape of 8.4 kHz HWHM is calculated which compares very well to the optical FID observation of a 10.1 kHz Lorentzian. (See Figs. 8 and 9.)

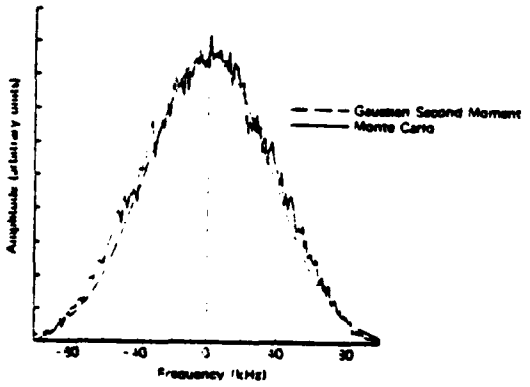


Figure 8. Magnetic inhomogeneous linewidth of a ^{141}Pr quadrupole transition of Pr^{3+}:LaF_3 showing the Gaussian lineshape of a Monte Carlo calculation and also a second moment calculation.

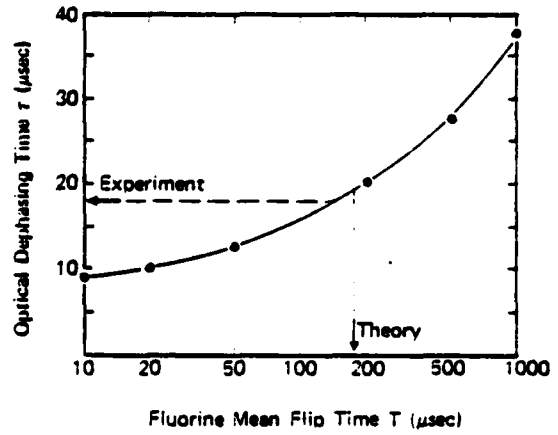


Figure 9. The Pr^{3+} optical dephasing time $1/\gamma_0$ versus the fluorine mean flip time T. The optical FID result is $1/\gamma_0$=15.9 μsec and the theoretical fluorine spin-flip time T=170 μsec.

CONCLUSION

There exist many other cases of coherent optical transients and their applications which have not been mentioned due to lack of space. For example, long optical dephasing times have been observed for the first time in stoichiometric EuP_5O_{14} which appears to exhibit a weak delocalized excitation among the Eu^{3+} ions [25]. Dephasing studies in the picosecond range [26] are also attracting considerable attention for exploring very fast processes in condensed matter. All of these investigations make use of the selectivity and precision inherent in the coherence techniques which lasers now provide.

REFERENCES

1. F. Bloch, Phys. Rev. 70, 460 (1946).
2. E. L. Hahn, Phys. Rev. 80, 580 (1950).
3. E. L. Hahn, Phys. Rev. 77, 297 (1950).
4. N. A. Kurnit, I. D. Abella and S. R. Hartmann, Phys. Rev. Lett. 13, 567 (1964).
5. R. G. Brewer and R. L. Shoemaker, Phys. Rev. A 6, 2001 (1972).
6. Variations on a theme of H. J. Lipkin in The Mossbauer Effect, edited by H. Frauenfelder (W. A. Benjamin Inc., New York, 1962), p. 13.
7. A. Schenzle, N. C. Wong and R. G. Brewer, Phys. Rev. A 21, 887 (1980).
8. See the theorem A. Schenzle, N. C. Wong and R. G. Brewer, Phys. Rev. 22, 635 (1980).
9. R. G. DeVoe and R. G. Brewer, Phys. Rev. A. 20, 2449 (1979).
10. M. Kunitomo, T. Endo, S. Nakanishi and T. Hashi, Phys. Lett. 80A, 84 (1980).
11. T. Mossberg, A. Flusberg, R. Kachru and S. R. Hartmann, Phys. Rev. Lett. 42, 1665 (1979).
12. J. B. Morsink and D. A. Wiersma in Laser Spectroscopy IV, edited by H. Walther and K. W. Rothe (Springer-Verlag, New York, 1979), p. 404.
13. J. A. Kash and E. L. Hahn (to be published).
14. R. G. Brewer and R. L. Shoemaker, Phys. Rev. Lett. 27, 631 (1971).
15. J. Schmidt, P. R. Berman and R. G. Brewer, Phys. Rev. Lett. 31, 1103 (1973); P. R. Berman, J. M. Levy and R. G. Brewer, Phys. Rev. A 11, 1668 (1975).
16. B. Comaskey, R. E. Scotti and R. L. Shoemaker; Optics Letters 6, 45 (1981).
17. R. G. Brewer and A. Z. Genack, Phys. Rev. Lett. 36, 959 (1976).
18. R. G. Brewer and S. S. Kano in Nonlinear Behavior of Molecules and Ions in Electric, Magnetic or Electromagnetic Fields (Elsevier, Amsterdam, 1979), p. 45.
19. M. Woodworth and I. D. Abella, J. Opt. Soc. Am. 70, 1567 (1980).
20. T. W. Mossberg, R. Kachru and S. R. Hartmann, Phys. Rev. Lett. 44, 73 (1980).
21. R. G. DeVoe, A. Szabo, S. C. Rand and R. G. Brewer, Phys. Rev. Lett. 42, 1560 (1979).
22. S. C. Rand, A. Wokaun, R. G. DeVoe and R. G. Brewer, Phys. Rev. Lett. 43, 1868 (1979).
23. R. G. DeVoe, A. Wokaun, S. C. Rand and R. G. Brewer, Phys. Rev. B 23, 3125 (1981).
24. J. R. Klauder and P. W. Anderson, Phys. Rev. 125, 912 (1962).
25. R. M. Shelby and R. M. Macfarlane, Phys. Rev. Lett. 45, 1098 (1980).
26. D. A. Wiersma, Advances in Chemical Physics (to be published in 1981).

RJ3324 (40081) 11/30/81
Physics

PHASE MODULATION LASER SPECTROSCOPY **

Axel Schenzle*
Ralph G. DeVoe
Richard G. Brewer

IBM Research Laboratory
San Jose, California 95193

ABSTRACT: A novel phase modulation technique which permits subkilohertz laser stability and new levels of precision in laser spectroscopy was reported recently. For spectroscopy, the basic arrangement consists of a combination of an optical pump and a probe field which is phase modulated. The pump prepares the atomic sample by burning a narrow hole within the atom's inhomogeneous lineshape, and the probe beam samples the prepared hole when its modulation sidebands are swept into resonance. Off resonance, the probe is balanced as pairs of sidebands produce heterodyne beat signals of opposite phase which just cancel. On resonance, the balance is upset and yields a nonvanishing beat signal with a Lorentzian absorption or dispersion lineshape and with residual noise approaching the shot noise limit. Here, we investigate the theory of phase modulation spectroscopy. We treat the nonlinear response of an atomic two-level quantum system subject to an intense pump and a weak copropagating or counterpropagating phase-modulated probe beam. The density matrix equations of motion are solved by a Laplace transform method and by the novel use of a translation operator which allows the infinite hierarchy of coupled equations to close. A solution equivalent to the rate

---

*On leave from the Department of Physics, Universität Essen, Gesamthochschule, Essen, West Germany

**Work supported in part by the U.S. Office of Naval Research.

equation result is developed and coherence corrections are found which predict new resonances, as yet observed. The delayed pump-probe technique encountered in solid state laser spectroscopy is analyzed in this context for two and three-level quantum systems. The response of a Fabry-Perot cavity to a phase-modulated light wave is examined also and reveals an unexpected absorption feature.

I. INTRODUCTION

An elegant phase modulation method for detecting optical atomic resonances, particularly in the nonlinear regime, has been devised recently[1-3] and applied to phase locking a laser to a reference cavity with unsurpassed precision.[2-4] Laser phase locking has produced a laser linewidth as narrow as 100 Hertz in the case of a dye laser[2] and is also being used in an attempt to detect gravity waves with optical interferometers.[5] While these detection ideas are new in the optical region, far earlier developments at longer wavelengths exist. Thus, Smaller[6] demonstrated some thirty years ago the advantages of phase modulation in (linear) magnetic resonance spectroscopy. Even earlier, Pound[7] proposed that microwave oscillators could best be stabilized by phase locking. Phase modulation spectroscopy also resembles the heterodyne detection utilized in coherent optical transients where laser frequency switching is employed.[8]

The basic spectroscopic arrangement considered here consists of a combination of optical pump and probe fields which appear either simultaneously or in sequence. The pump is typically a single frequency cw laser field that prepares an atomic sample, for example, by burning a hole within its inhomogeneous lineshape. The probe, which can be derived from the pump or another laser source, is phase modulated and therefore contains a Bessel function distribution of sidebands that appear symmetrically in pairs about the unmodulated laser frequency.

In the absence of attenuation, each pair of sidebands generates with the central frequency component at a photodetector a pair of heterodyne beat signals of opposite phase which just cancel. This balance is upset and a nonvanishing beat signal remains when the probe frequency is swept, bringing a sideband into resonance with the prepared

hole. The background signal and its noise are therefore eliminated automatically. Moreover, since the beat frequency can be made arbitrarily high (radio or microwave), the desired beat signal can be detected in a spectral region where the residual noise spectrum is falling off. The resulting high sensitivity, which will ultimately be limited by shot noise, promises new levels of precision in laser spectroscopy.

In this article, we investigate the theory of phase modulation laser spectroscopy, extending the work of Bjorklund[1(a)] and Hall et al.[3] Our analysis treats the nonlinear optical response of a two-level atomic quantum system subject to copropagating or counterpropagating laser beams where at least one of the fields is phase modulated. The counterpropagating beam case resembles the Lamb-dip effect but is more complex due to the multimode character of the phase modulated probe. Solutions equivalent to a rate equation result are developed and the effect of coherence corrections are examined, revealing in certain cases new resonances. The delayed pump-probe measurement frequently encountered in solid state optical hole burning studies is analyzed where it is found that the two and three-level quantum systems behave differently. Finally, the (linear) response of a Fabry-Perot cavity to a phase modulated light wave is considered because of its relevance to phase locking a laser.

II. BASIC THEORY

A. Equations of Motion: Counterpropagating Beams

We treat the nonlinear optical response of an atomic two-level quantum system subject to two colinear light fields that propagate in opposite directions along the laboratory z axis. The one field,

$$E_1(z,t) = \tilde{E}_1 e^{i(\omega_o t+kz)} + c.c., \quad (2.1)$$

we designate the pump field. The counterpropagating component, the probe field

$$E_o(z,t) = \tilde{E}_o e^{i(\omega_o t-kz)} e^{i\varphi(t)} + c.c., \quad (2.2)$$

is phase modulated at frequency Ω where

$$\varphi = M \cos\Omega t$$

and therefore possesses sidebands according to the Fourier decomposition

$$e^{i\varphi(t)} = \sum_{n=-\infty}^{\infty} a_n e^{in\Omega t} . \quad (2.3a)$$

Here, $a_n = i^n J_n(M)$, J_n is the nth order Bessel function,

$$a_n = a_{-n} \text{ and } a_n^* = (-1)^n a_n . \quad (2.3b)$$

Both fields are assumed polarized along the x axis. To account for the atom's motion with velocity v_z, and hence its time dependence, we transform from the laboratory (z) to the atom's moving coordinate (z') by

$$z = z' + v_z t .$$

The total field can then be written in the compact form

$$E(z',t) = E_o(z',t) + E_1(z',t) = e^{i(\omega_o - kv_z)t} \sum_{n,m} A_n^m e^{i\Omega_n^m t} + c.c. \quad (2.4)$$

where the pump field is specified by m=1,

$$A_0^1 = \tilde{E}_1 e^{ikz'} \text{ and } \Omega_0^1 = 2kv_z , \; n = 0 , \quad (2.5)$$

and the probe field by m=0,

$$A_n^0 = \tilde{E}_o\, e^{-ikz'} a_n \text{ and } \Omega_n^0 = n\Omega\,, \qquad n = 0, \pm 1, \pm 2\ldots\,. \tag{2.6}$$

Thus, it is assumed that the two fields are present simultaneously whereas in Section III the simpler problem of pump and probe occupying different time intervals is considered. We ignore the slight difference in pump and probe k vectors ($\Delta k = \Omega/c$) arising from phase modulation and assume in (2.5) and (2.6) that $k \equiv k_0^1 = k_n^0$. Also, the slowly varying components of (2.4) are given by

$$\tilde{E}^+(t) = \sum_{n,m} A_n^m\, e^{i\Omega_1^m t} \text{ and } \tilde{E}^- = (\tilde{E}^+)^*\,. \tag{2.7}$$

In addition, (2.4) is sufficiently general to allow phase modulation in each of the counterpropagating beams, a case we treat later.

The density matrix equations of motion

$$i\hbar \frac{\partial \rho}{\partial t} = [H,\rho] + \text{damping terms}$$

for a two-level quantum system, with upper level 2 and lower level 1, can now be written[9] as

$$\dot{\tilde{\rho}}_{12}(t) = (i\Delta - 1/T_2)\tilde{\rho}_{12} - 2igw \sum_{n,m} A_n^m\, e^{i\Omega_n^m t} \tag{2.8a}$$

$$\dot{w}(t) = -ig\left[\tilde{\rho}_{12} \sum_{n,m} A_n^{m*}\, e^{-i\Omega_n^m t} - \tilde{\rho}_{21} \sum_{n,m} A_n^m\, e^{i\Omega_n^m t}\right] - (w - w^o)/T_1\,. \tag{2.8b}$$

Here, the atomic unperturbed energy eigenvalues are

$$H_{11} = \hbar\omega_1 \, , \; H_{22} = \hbar\omega_2 \text{ and } \omega_{21} \equiv \omega_2 - \omega_1$$

while the off-diagonal optical-atom dipole interaction is

$$H_{12} = g\hbar E(z,t) \tag{2.9}$$

with

$$g = -\mu_{12}/\hbar \, , \tag{2.10}$$

μ_{12} being the dipole matrix element. In (2.8), we have applied the rotating wave approximation and retained the slowly varying off-diagonal component $\tilde{\rho}_{12}$ with the substitution

$$\rho_{12} = \tilde{\rho}_{12} \, e^{i(\omega_o - kv_z)t} \, . \tag{2.11}$$

The tuning parameter is defined as

$$\Delta = \omega_{21} - \omega_o + kv_z \, , \tag{2.12}$$

the population difference as

$$w = \frac{1}{2}(\rho_{22} - \rho_{11}) \, , \tag{2.13}$$

and the phenomenological dipole (T_2) and population (T_1) decay times have been introduced.

The pump and probe fields generate a signal field

$$\tilde{E}_s^+ \sim ig\langle\tilde{\rho}_{12}(z',t)\rangle \tag{2.14}$$

where the directionality of the beam, as we shall see, appears in the solution $\tilde{\rho}_{12}(z',t)$ due to the $e^{\pm ikz'}$ phase factors of (2.5) and (2.6). Equation (2.14) is valid for an optically

Proceeding as in Section IIC, the signal field

$$\tilde{E}_s^+ \sim ig\tilde{\rho}_{12}$$

appears in the heterodyne beat expression

$$B(t) = \tilde{E}^+\tilde{E}_s^- + \tilde{E}^-\tilde{E}_s^+ \tag{2.59}$$

where we see that the pump field

$$\tilde{E}^+(t) = A_0^1 e^{2ikv_z t}$$

cancels the $e^{2ikv_z t}$ factor of (2.58).

Upon Doppler integration of (2.59) and with the manipulations (2.35) and (2.36) to extract beats oscillating at $e^{i\Omega t}$, we find that

$$\langle B(t)\rangle = -8\pi g^4 w^o N \frac{T_1}{\sqrt{1+(\Omega T_1)^2}} |A_0^1|^2 e^{i(\Omega t+\varphi)}$$

$$\times \sum_\ell A_{\ell-1}^* A_\ell \delta \frac{\delta^2 - \left(\frac{\Omega}{2}(\ell+1)\right)^2 + 1/T_2^2 + i\frac{\Omega(\ell+1)}{T_2}}{\left[\left(\delta - \frac{\Omega}{2}(\ell+1)\right)^2 + 1/T_2^2\right]\left[\left(\delta + \frac{\Omega}{2}(\ell+1)\right)^2 + 1/T_2^2\right]} + \text{c.c.} \tag{2.60}$$

where $\tan\varphi = 1/(\Omega T_1)$. To see the behavior of (2.60) in lowest order, we again select terms in $\ell = 0$ and $\ell = +1$ with the result

E. The Backward Wave

Now consider beat signals that propagate in the backward direction, the direction of the pump field. Analysis shows that case (2.46c) is qualitatively similar to the coherence correction of the beat signal propagating in the forward direction, (2.46a), and is of higher order being proportional to $|A_0^1|^4$. The dominant beat signal in the backward direction corresponds to (2.46b) which we now discuss in detail. The starting point is (2.44) and takes the form

$$\tilde{\rho}_{12}(Z) = \frac{8ig^3w^o/T_1}{Z-i\Delta+1/T_2} \sum_{n',n''}{}' A_0^1 A_{n'}^{0*} A_{n''}^0$$

$$\times\left(Z - 2ikv_z + 1/T_1 + 4g^2|A_0^1|^2\Lambda_{00}^{11}(Z - i2kv_z)\right)^{-1} \Lambda_{n'n''}^{00}(Z - 2ikv_z)$$

$$\times\left(Z - i(2kv_z - \Omega(n'-n''))\right)^{-1}$$

$$\times\left(Z - i(2kv_z - \Omega(n'-n'')) + 1/T_1 + 4g^2|A_0^1|^2\Lambda_{00}^{11}(Z - i(2kv_z - \Omega(n'-n''))\right)^{-1} \quad (2.57)$$

under the condition (2.46b).

To the lowest order of approximation, we drop the power broadening $|A_0^1|^2$ terms in the above denominators and perform the Laplace transform at the pole $Z=2ikv_z - i\Omega(n'-n'')$ to obtain

$$\tilde{\rho}_{12}(t) = -4g^3w^oA_0^1 \sum_{n',n''} A_{n'}^{0*}A_{n''}^0 \frac{1}{\Omega(n'-n'')+i/T_1}$$

$$\times\, e^{2ikv_zt - i(n'-n'')\Omega t}(kv_z - \delta - (n'-n'')\Omega - i/T_2)^{-1}$$

$$\times\left((kv_z + \delta - n''\Omega + i/T_2)^{-1} - (kv_z + \delta - n'\Omega - i/T_2)^{-1}\right). \quad (2.58)$$

We find

$$\langle B_0\rangle = -2\bar{\delta}\frac{x}{\sqrt{1+x}}\left\{\frac{\bar{\Gamma}\bar{\Omega}+i(\bar{\delta}^2+\bar{\Gamma}^2-(\bar{\Omega}/2)^2)}{\left[(\bar{\delta}-\bar{\Omega}/2)^2+\bar{\Gamma}^2\right]\left[(\bar{\delta}+\bar{\Omega}/2)^2+\bar{\Gamma}^2\right]}-\frac{i}{\bar{\delta}^2+\bar{\Gamma}^2}\right\}, \quad (2.55)$$

and

$$\langle B_1\rangle = -\frac{1}{2}\frac{x^2}{\sqrt{1+x}(1+\sqrt{1+x})}\left\{F(\bar{\Omega})-F^*(-\bar{\Omega})-F(0)+F^*(0)\right\},$$

where

$$F(\bar{\Omega}) = \frac{\bar{\delta}-\frac{\bar{\Omega}}{2}+2i\bar{\Gamma}}{\bar{\delta}-\frac{\bar{\Omega}}{2}+i\bar{\Gamma}}\left(\bar{\delta}-\frac{\bar{\Omega}}{2}+i\bar{\Gamma}+i\bar{\alpha}\right)$$

$$\times\left[\left(\bar{\delta}-\frac{\bar{\Omega}}{2}+i\bar{\Gamma}\right)\left(\bar{\delta}-\frac{\bar{\Omega}}{2}+i\bar{\Gamma}+i\bar{\alpha}\right)\left(\bar{\delta}-\frac{\bar{\Omega}}{2}+i\bar{\alpha}+i\right)-\frac{1}{2}\left(\bar{\delta}-\frac{\bar{\Omega}}{2}+i\bar{\Gamma}+i\frac{\bar{\alpha}}{2}\right)\right]^{-1}. \quad (2.56)$$

The coherence correction $\langle B_1\rangle$ to the rate equation result $\langle B_0\rangle$ is illustrated in Fig. 1 and is reminiscent of Lamb-dip theories[14] when coherence contributions are included.

For weak fields, the ratio of the coherence correction to the rate equation contribution is

$$\frac{\langle B_1\rangle}{\langle B_0\rangle} \sim \frac{T_2}{T_1}4g^2T_1T_2\left|A_0^1\right|^2.$$

Thus, the rate equations are valid only when $T_2 << T_1$ and the fields are weak, $4g^2T_1T_2\left|A_0^1\right|^2 << 1$.

The appearance of $2kv_z$ and $3kv_z$ in the above resonance denominators suggests higher order resonances. However, these effects disappear on Doppler integration and would be observed only in the presence of a third field as witnessed in previous studies.[12,13]

By contour integration, the Doppler integral of $B_1(t)$ is

$$\langle B_1(t)\rangle = -\frac{2\pi}{\Gamma\alpha} N g^6 w^o \frac{T_1}{T_2} |A_0^1|^4 e^{i\Omega t} \sum_\ell A_{\ell-1}^* A_\ell$$

$$\times \left\{ \left(\frac{\delta - \ell\Omega/2 + 2i\Gamma}{\delta - \ell\Omega/2 + i\Gamma} \right) (\delta - \ell\Omega/2 + i\Gamma + i\alpha) \right.$$

$$\times \left[\left(-\frac{\ell\Omega}{2} + \delta + i\alpha + i/2T_1 \right) \left(\delta - \frac{\ell\Omega}{2} + i\Gamma \right) \left(\delta - \frac{\ell\Omega}{2} + i\alpha + i\Gamma \right) \right.$$

$$\left. \left. - g^2 |A_0^1|^2 \left(\delta - \frac{\ell\Omega}{2} + i\Gamma + i\alpha/2 \right) \right]^{-1} - \text{c.c. } (\ell \to -\ell) \right\} + \text{c.c.} . \qquad (2.52)$$

The final result is the sum of (2.39) and (2.52),

$$\langle B(t)\rangle = \langle B_0(t) + B_1(t)\rangle . \qquad (2.53)$$

Let us treat the case $\ell = 0$ and $\ell = +1$ again using the reduced variables and definitions

$$x = 4g^2 T_1 T_2 |A_0^1|^2 , \quad \bar{\alpha} = \sqrt{1+x}$$

$$\bar{\Gamma} = \frac{1}{2}(1 + \sqrt{1+x}) , \quad T_2 = 2T_1 \qquad (2.54)$$

$$\bar{\Omega} = T_2 \Omega , \qquad \bar{\delta} = T_2 \delta .$$

Equation (2.47) then becomes

$$D_\ell = \frac{32ig^6(T_1/T_2)w^o\,|A_0^1|^4 A_\ell^0}{\Delta-\ell\Omega+i/T_2}\Lambda_{0\ell}^{10}(i\ell\Omega - i2kv_z)$$

$$\times\left[i\ell\Omega-i2kv_z + 1/T_1 + 4g^2|A_0^1|^2\Lambda_{00}^{11}(i\ell\Omega-i2kv_z)\right]^{-1}$$

$$\times\left[(\delta-kv_z)^2 + 1/T_2^2 + 4g^2|A_0^1|^2T_1/T_2\right]^{-1}. \qquad (2.49)$$

The remaining steps follow the rate equation calculation.

The coherence correction to the heterodyne beat signal, (2.37), takes the form

$$B_1(t) = \frac{32g^6(T_1/T_2)w^o\,e^{i\Omega t}|A_0^1|^4}{(\delta-kv_z)^2 + 1/T_2^2 + 4g^2|A_0^1|^2T_1/T_2}\sum_\ell A_{\ell-1}^* A_\ell$$

$$\times\left\{\frac{\Lambda_{0\ell}^{10}(i\ell\Omega-i2kv_z)}{\Delta-\ell\Omega+i/T_2}\left[-\ell\Omega + 2kv_z + i/T_1 + 4ig^2|A_0^1|^2\Lambda_{00}^{11}(i\ell\Omega - 2ikv_z)\right]^{-1}\right.$$

$$\left. - (\ell\to-\ell)^*\right\} + \text{c.c.} \qquad (2.50)$$

where

$$\Lambda_{0\ell}^{10}(i\ell\Omega - i2kv_z) = \frac{i}{2}\left(\frac{1}{-\ell\Omega+\Delta+i/T_2} + \frac{1}{kv_z-\delta+i/T_2}\right),$$

$$\Lambda_{00}^{11}(i\ell\Omega - i2kv_z) = \frac{i}{2}\left(\frac{1}{-\ell\Omega+\Delta+i/T_2} + \frac{1}{-\ell\Omega+3kv_z-\delta+i/T_2}\right). \qquad (2.51)$$

$$e^{i(k^m - k^{m'} + k^{m''})z'} \text{ where } k^m = \begin{cases} k & m = 1 \\ -k & m = 0 \end{cases} \tag{2.45}$$

as indicated in (2.5) and (2.6). Eight possible combinations of the values exist but only three are relevant:

$$m = 1\,,\ m' = 1\,,\ m'' = 0 \Rightarrow e^{-ikz'} \tag{2.46a}$$

$$m = 1\,,\ m' = 0\,,\ m'' = 0 \Rightarrow e^{ikz'} \tag{2.46b}$$

$$m = 0\,,\ m' = 0\,,\ m'' = 1 \Rightarrow e^{ikz'} \tag{2.46c}$$

where $m = 1 \Rightarrow n = 0$ and $m = 0 \Rightarrow n = \pm 1, \pm 2, \ldots$. Considering the case (2.46a) where the signal field propagates in the direction of the probe beam, the Laplace transform of (2.44) evaluated at the pole $Z = i\ell\Omega$ gives the signal field $\tilde{E}_s^+$, (2.32), where

$$D_\ell = \frac{-8ig^4 w^o}{\Delta - \ell\Omega + i/T_2} \,|A_0^1|^2 A_\ell^0 \left[i\ell\Omega - i2kv_z + 1/T_1 + 4g^2|A_0^1|^2 \Lambda_{00}^{11}(i\ell\Omega - i2kv_z)\right]^{-1}$$

$$\times \Lambda_{0\ell}^{10}(i\ell\Omega - i2kv_z)\left[1 + 4g^2|A_0^1|^2 \frac{T_1}{T_2} \frac{1}{(\delta - kv_z)^2 + 1/T_2^2}\right]^{-1} . \tag{2.47}$$

Notice that the Doppler integral of (2.47) vanishes when the $|A_0^1|^2$ term of the last line of (2.47) is neglected. This observation causes us to rewrite the last bracket as

$$[\ ]^{-1} = 1 - \frac{4g^2|A_0^1|^2 T_1/T_2}{(\delta - kv_z)^2 + 1/T_2^2 + 4g^2|A_0^1|^2 T_1/T_2} , \tag{2.48}$$

$$\langle B(t)\rangle = -8i\pi Ng^4 w^o T_1 \sum_{nn'} |A_{n'}^1|^2 A_{n-1}^{0*} A_n e^{i\Omega t}$$

$$\times \delta \frac{\delta^2 + 1/T_2^2 - \left(\frac{n-n'}{2}\Omega\right)^2 - i(n-n')\frac{\Omega}{T_2}}{\left[\left(\delta - \left(\frac{n-n'}{2}\Omega\right)\right)^2 + 1/T_2^2\right]\left[\left(\delta + \frac{n-n'}{2}\Omega\right)^2 + 1/T_2^2\right]} + \text{c.c.},$$

which resembles (2.39).

D. Coherence Effects

The rate equation result (2.39) ignores coherence effects, i.e., sideband terms that coherently modulate the population at frequency $n\Omega$. When coherence is included, beat signals appear in both forward and backward directions and new resonances are found. We, therefore, return to (2.28) and consider for the moment only those terms omitted in the rate equation calculation. With (2.28) and (2.22a), we now obtain

$$\tilde{\rho}_{12}(Z) = \frac{8ig^3 w^o/T_1}{Z - i\Delta + 1/T_2} \sum_{n,m}{}' A_n^m \left[Z - i\Omega_n^m + 1/T_1 + 4g^2 |A_0^1|^2 \Lambda_{00}^{11}(Z - i\Omega_n^m)\right]^{-1}$$

$$\times \sum_{\{n',m'\}}{}' A_{n'}^{m'*} A_{n''}^{m''} \Lambda_{n',n''}^{m',m''}(Z - i\Omega_n^m) T\left(\Omega_{n'}^{m'} - \Omega_{n''}^{m''} - \Omega_n^m\right)$$

$$\times \frac{1}{Z}\left(Z + 1/T_1 + 4g^2 |A_0^1|^2 \Lambda_{00}^{11}(Z)\right)^{-1}. \qquad (2.44)$$

In anticipating the Laplace transform, we first notice that $T(\Omega_{n'}^{m'} - \Omega_{n''}^{m''} - \Omega_n^m)\frac{1}{Z}$ provides the only pole that is not damped in the long-time limit. Secondly, our interest is restricted to terms that oscillate at $\ell\Omega$ so that in (2.44) the operator $T = T(-\ell\Omega)$. Thirdly, the amplitude product $A_n^m A_{n'}^{m'*} A_{n''}^{m''}$ contains the phase factors

Equation (2.43) displays dispersive (in-phase) and absorptive (out of phase) power-broadened Lorentzian lineshapes of width Γ as shown in Fig. 1. The central resonance $\omega_{21}=\omega_o$, which occurs when the laser is tuned to the peak of the Doppler lineshape, is purely dispersive. To understand the sideband resonance $\omega_o=\omega_{21}-\Omega/2$, note that the pump must burn a hole in a packet shifted from the Doppler peak by $\Omega/2$ in order that the counterpropagating high frequency sideband at $\omega_{21}+\Omega/2$ can come into resonance with the same packet. Similarly, the resonance at $\omega_o=\omega_{21}+\Omega/2$ occurs when the pump is displaced by $-\Omega/2$ from the Doppler peak. In contrast to the central feature, the sidebands show both absorptive and dispersive lineshapes, the latter being opposite in sign from the central line.

Consideration of other terms in (2.39) results in a correction of (2.43) as well as higher order resonances at

$$\delta = \pm\frac{\ell\Omega}{2} .$$

Finally, the rate equations predict a beat signal only in the forward direction, the direction of the probe beam, as indicated by the $e^{-ikz'}$ factor contained in the signal field (2.33).

The absence of a beat in the backward direction is easily understood as the rate equation approximation completely neglects the coherent oscillations of the population. Therefore, the backward travelling pump remains a single frequency field which is incapable of producing a heterodyne beat. In Section IIE, this case is treated.

Finally, an experimental situation might arise where both the forward and backward waves are phase modulated. A similar calculation to the above reveals that

equivalent to that of the rate equations,

$$\langle B_0(t)\rangle = -8i\pi Ng^4 w^o |A_0^1|^2 \frac{T_1}{T_2} \frac{e^{i\Omega t}}{\alpha}$$

$$\times \sum_\ell A^*_{\ell-1} A_\ell \delta \frac{\delta^2 - (\ell\Omega/2)^2 + \Gamma^2 - i\Gamma\ell\Omega}{\left[\left(\delta - \frac{\ell\Omega}{2}\right)^2 + \Gamma^2\right]\left[\left(\delta + \frac{\ell\Omega}{2}\right)^2 + \Gamma^2\right]} + \text{c.c.} \qquad (2.39)$$

with

$$\alpha = \frac{1}{T_2}\left(1 + 4g^2 T_1 T_2 |A_0^1|^2\right)^{1/2}, \qquad (2.40)$$

$$\Gamma = \frac{1}{2}(\alpha + 1/T_2)\,, \qquad (2.41)$$

$$\delta = \omega_{21} - \omega_o\,, \qquad (2.42)$$

and $N = 1/(\sqrt{\pi}ku)$ is the normalization factor of (2.15).

The behavior of (2.39) is easily seen by considering only the central component with $\ell = 0$ and the two sidebands at $\omega_o \pm \Omega$ with $\ell = +1$, which yields

$$\langle B_0(t)\rangle = -16\pi Ng^4 \tilde{E}_o^2 \tilde{E}_1^2 w^o \frac{T_1}{T_2} \frac{J_0(M)J_1(M)}{\alpha}$$

$$\times \delta\left\{\left(\frac{1}{\delta^2 + \Gamma^2} - \frac{\delta^2 - (\Omega/2)^2 + \Gamma^2}{\left[\left(\delta - \frac{\Omega}{2}\right)^2 + \Gamma^2\right]\left[\left(\delta + \frac{\Omega}{2}\right)^2 + \Gamma^2\right]}\right)\cos\Omega t\right.$$

$$\left. - \frac{\Gamma\Omega}{\left[\left(\delta - \frac{\Omega}{2}\right)^2 + \Gamma^2\right]\left[\left(\delta + \frac{\Omega}{2}\right)^2 + \Gamma^2\right]} \sin\Omega t\right\}. \qquad (2.43)$$

and we have omitted the unsaturated term anticipating that it vanishes upon Doppler integration. To this order of approximation, $\tilde{E}_s^+$ is emitted in the direction of the probe beam as the above term $D_\ell \sim A_\ell^0 = \tilde{E}_o\, e^{-ikz'} a_\ell$ indicates.

The heterodyne beat signal (2.16) then follows from the signal field (2.32) and the probe field (2.7) with m=0 where

$$B(t) = \sum_{n,\ell} A_n^0\, e^{in\Omega t}\, D_\ell^*\, e^{-i\ell\Omega t} + \text{c.c.}\,. \tag{2.34}$$

Selecting those terms in the double sum which give the fundamental beat term $e^{\pm i\Omega t}$, we find that

$$B(t) = \sum_{\ell} \left(A_{\ell-1}^* A_\ell f(\ell) + A_{\ell+1} A_\ell^* f^*(\ell)\right) e^{i\Omega t} + \text{c.c.} \tag{2.35}$$

where $f(\ell)$ consists of the remaining terms of D_ℓ. The relations (2.3b) allow us to prove that the index interchange $\ell \to -\ell$ results in

$$A_{\ell+1} A_\ell^* \to -A_{\ell-1}^* A_\ell \tag{2.36}$$

and thus the terms can be combined as

$$B(t) = \sum_{\ell} A_{\ell-1}^* A_\ell \left(f(\ell) - f^*(-\ell)\right) e^{i\Omega t} + \text{c.c.} \tag{2.37}$$

or

$$B_0(t) = \frac{-8ig^4 (T_1/T_2) w^o \,|\, A_0^1 \,|^2}{(\Delta - 2kv_z)^2 + 1/T_2^2 + 4g^2 (T_1/T_2) \,|\, A_0^1 \,|^2}$$

$$\times \sum_{\ell} A_{\ell-1}^* A_\ell \left\{ \frac{1}{\Delta - \ell\Omega + i/T_2} + \frac{1}{\Delta + \ell\Omega - i/T_2} \right\} + \text{c.c.}\,. \tag{2.38}$$

The Doppler integral (2.15) of B(t) can be carried out by contour integration to give a result

leading term of (2.28),

$$w(Z) = \frac{w^o}{T_1}\frac{1}{Z}\,(Z + 1/T_1 + 4g^2\,|\,A_0^1\,|^2\Lambda_{00}^{11}(Z))^{-1}\,, \tag{2.29}$$

which we now consider, generates a result equivalent to the rate equations. The remaining higher order Σ' terms of (2.28), the coherence terms, modulate the population at the sideband frequencies $\Omega_{n'}^{m'}-\Omega_{n''}^{m''}$ and will be treated later as a correction. With the aid of (2.19a) and (2.29), we have

$$\tilde{\rho}_{12}(Z) = -\frac{2igw^o/T_1}{Z-i\Delta+1/T_2}$$

$$\times \sum_{n,m} A_n^m(Z - i\Omega_n^m)^{-1}(Z - i\Omega_n^m + 1/T_1 + 4g^2\,|\,A_0^1\,|^2\Lambda_{00}^{11}(Z - i\Omega_n^m))^{-1}\,. \tag{2.30}$$

The inverse Laplace transform, (2.18), applied to (2.30) yields

$$\tilde{\rho}_{12}(t) = -\sum_\ell \Big(\frac{2igw^o/T_1}{i(\ell\Omega-\Delta)+1/T_2}\Big)\Big(\frac{A_\ell^0\, e^{i\ell\Omega t}}{1/T_1 + 4g^2\,|\,A_0^1\,|^2\Lambda_{00}^{11}(0)}\Big)\,, \tag{2.31}$$

where we have considered only the poles $Z=in\Omega$ as the others with decay time T_2 or shorter are strongly damped in the long time limit $t>>T_2$.

Notice that $\tilde{\rho}_{12}$ generates the signal field (2.14)

$$\tilde{E}_s^+(z',t) = \sum_\ell D_\ell\, e^{i\ell\Omega t} \tag{2.32}$$

where

$$D_\ell = \frac{-8ig^4(T_1/T_2)w^o\,|\,A_0^1\,|^2A_\ell^0}{\Delta-\ell\Omega+i/T_2}\,\Big[(\Delta-2kv_z)^2 + 1/T_2^2 + 4g^2(T_1/T_2)\,|\,A_0^1\,|^2\Big]^{-1}\,, \tag{2.33}$$

C. Rate Equations

At this point, it becomes necessary to introduce approximations as the general analytic treatment developed thus far cannot be sustained for all fields having arbitrary intensity. As an initial approximation, we assume that the probe field $|A_n^0|$ is weak while the pump field $|A_0^1|$ is of arbitrary strength. Next, the leading term (m=1, m'=1, n=0, n'=0) in (2.23), which yields an exact solution, is extracted from the sum so that

$$w^o/ZT_1 = \{Z + 1/T_1 + 4g^2|A_0^1|^2\Lambda_{00}^{11}(Z) + 4g^2{\sum}'\Lambda_{nn'}^{mm'}(Z)A_n^{m*}A_{n'}^{m'}T(\Omega_n^m-\Omega_{n'}^{m'})\}w(Z) \quad (2.25)$$

where the prime on the summation denotes that the leading term of the sum (m=m'=1) is omitted. Equation (2.25) now has the form

$$[a(Z) + T)]w(Z) = f(Z)\,, \quad (2.26)$$

or equivalently we can invert the transformation to obtain

$$w(Z) = (1 + a^{-1}T)^{-1}a^{-1}f(Z)\,. \quad (2.27)$$

A perturbation expansion of $(1+a^{-1}T)^{-1}$ in powers of the smaller terms $A_n^{m*}A_{n'}^{m'}$ of (2.25) where m, m' $\neq$ 1 yields

$$w(Z) = \frac{w^o}{T_1}\{1 - 4g^2(Z + 1/T_1 + 4g^2|A_0^1|^2\Lambda_{00}^{11}(Z))^{-1} \times {\sum_{\{n,m\}}}' A_{n'}^{m'*}A_{n''}^{m''}\Lambda_{n'n''}^{m'm''}(Z)T(\Omega_{n'}^{m'}-\Omega_{n''}^{m''}) \times Z^{-1}(Z + 1/T_1 + 4g^2|A_0^1|^2\Lambda_{00}^{11}(Z))^{-1}\} \quad (2.28)$$

where the translation operator T operates on all terms to the right of it that depend on Z. The

$$\tilde{\rho}_{12}(Z) = \frac{-2ig}{Z - i\Delta + 1/T_2} \sum_{n,m} A_n^m w(Z - i\Omega_n^m) \tag{2.19a}$$

$$w(Z)(Z + 1/T_1) = \frac{w^o}{ZT_1} - ig \sum_{n,m} A_n^{m*} \tilde{\rho}_{12}(Z + i\Omega_n^m) + ig \sum_{n,m} A_n^m \tilde{\rho}_{21}(Z - i\Omega_n^m) . \tag{2.19b}$$

Here, the initial conditions are not retained as only the long-time behavior ($t >> T_2$) is of interest. Notice that Eqs. (2.19) do not close on one another but instead form an infinite hierarchy of coupled equations involving terms of the type $\tilde{\rho}_{12}(Z \pm i\Omega_n^m)$, $\tilde{\rho}_{12}(Z \pm 2i\Omega_n^m)$, $\tilde{\rho}_{12}(Z \pm 3i\Omega_n^m)$,.... . This difficulty is formally avoided by introducing the translation operator[11]

$$T(X)f(Z) = f(Z + iX) , \tag{2.20}$$

where $T(X) = \sum_n \frac{(iX)^n}{n!} \frac{\partial^n}{\partial Z^n}$, and it is evident that

$$T(X)T(Y) = T(X + Y) . \tag{2.21}$$

The hierarchy of Eqs. (2.19) can now be written in a compact from which closes, namely,

$$\tilde{\rho}_{12}(Z) = \frac{-2ig}{Z - i\Delta + 1/T_2} \sum_{n,m} A_n^m T(-\Omega_n^m) w(Z) \tag{2.22a}$$

$$w(Z)(Z + 1/T_1) = \frac{w^o}{ZT_1} - ig \sum_{n,m} A_n^{m*} T(\Omega_n^m) \tilde{\rho}_{12}(Z) + ig \sum_{n,m} A_n^m T(-\Omega_n^m) \tilde{\rho}_{21}(Z) . \tag{2.22b}$$

However, the problem of dealing with noncommuting operators must be faced. We find from (2.22b), after inserting $\tilde{\rho}_{12}(Z)$ and $\tilde{\rho}_{21}(Z)$ from (2.22a) and then using (2.21), that

$$w^o/ZT_1 = \left\{ Z + 1/T_1 + 4g^2 \sum_{\substack{n,n' \\ m,m'}} \Lambda_{nn'}^{mm'}(Z) A_n^{m*} A_{n'}^{m'} T\left(\Omega_n^m - \Omega_{n'}^{m'}\right) \right\} w(Z) \tag{2.23}$$

where

$$\Lambda_{n,n'}^{m,m'}(Z) = \frac{1}{2}\left[(Z - i\Delta + i\Omega_n^m + 1/T_2)^{-1} + (Z + i\Delta - i\Omega_{n'}^{m'} + 1/T_2)^{-1} \right] . \tag{2.24}$$

thin sample and follows from Maxwell's wave equation in the slowly varying envelope approximation. The bracket of (2.14) indicates an average

$$\langle\tilde{\rho}_{12}\rangle = \int_{-\infty}^{\infty} G(v_z)\tilde{\rho}_{12}(v_z)d(kv_z) \tag{2.15}$$

over the inhomogeneous lineshape where

$$G(v_z) = e^{-(v_z/u)^2}/(\sqrt{\pi}ku)$$

for an atomic system, u being the most probable velocity. Equation (2.15) is to be evaluated in the limit of infinite Doppler width, an assumption which is valid in optical hole burning experiments.

However, the observable is a heterodyne beat of the signal field (2.14) and the total field (2.4) where the cross terms of the intensity $|E(t)+E_s(t)|^2$ are

$$B(t) = \tilde{E}^{+}\tilde{E}_s^{-} + \tilde{E}^{-}\tilde{E}_s^{+} . \tag{2.16}$$

B. Laplace Transform

The equations of motion (2.8) constitute a set of three linear differential equations with time-dependent coefficients. These can be solved by use of the Laplace transform[10]

$$\rho(Z) = \int_0^{\infty} e^{-Zt}\rho(t)dt \tag{2.17}$$

where the inverse transform is given by

$$\rho(t) = \frac{1}{2\pi i}\int_{-i\infty+r}^{i\infty+r} e^{Zt}\rho(Z)dZ . \tag{2.18}$$

By application of (2.17), Eqs. (2.8) become

$$\langle B(t)\rangle = -16\pi g^4 w^o N \frac{T_1}{\sqrt{1+(\Omega T_1)^2}} |A_0^1|^2 J_0(M)J_1(M)$$

$$\times\delta\left\{\left[\frac{\Omega/T_2}{\left[\left(\delta-\frac{\Omega}{2}\right)^2+1/T_2^2\right]\left[\left(\delta+\frac{\Omega}{2}\right)^2+1/T_2^2\right]}\right.\right.$$

$$\left.-\frac{2\Omega/T_2}{[(\delta-\Omega)^2+1/T_2^2][(\delta+\Omega)^2+1/T_2^2]}\right]\cos(\Omega t+\varphi)$$

$$+\left[\frac{\delta^2-(\Omega/2)^2+1/T_2^2}{\left[\left(\delta-\frac{\Omega}{2}\right)^2+1/T_2^2\right]\left[\left(\delta+\frac{\Omega}{2}\right)^2+1/T_2^2\right]}\right.$$

$$\left.\left.-\frac{\delta^2-\Omega^2+1/T_2^2}{[(\delta-\Omega)^2+1/T_2^2][(\delta+\Omega)^2+1/T_2^2]}\right]\sin(\Omega t+\varphi)\right\}. \qquad (2.61)$$

Thus, the backward wave displays Lorentzian lineshapes of width $1/T_2$ in absorption and dispersion when the resonance conditions $\delta=\pm\Omega/2$ and $\delta=\pm\Omega$ are satisfied. A plot of (2.61) in Fig. 2 reveals that the $\Omega/2$ and Ω resonances are of opposite sign but are equal in absolute magnitude. Unlike the beat signal of the forward wave, (2.43), the $\delta=\pm\Omega$ resonances are new and the $\delta=0$ resonance is missing. The beats expected in the forward direction have indeed been observed[1(b),3] but the prediction (2.61) has yet to be confirmed.

III. SOLIDS

A. Two-Level Problem

A number of hole burning experiments have been reported recently in solid state laser spectroscopy.[15] A pump field burns a hole which resides in the ground state population

distribution long after the field is removed. A weaker probe field then follows and monitors the memory of the hole in one or more transitions, revealing hyperfine structure and potentially dynamic line broadening effects. Since phase modulation is useful in this application,[16] we present the relevant theory.

The previous two-level formalism can be adopted except that the pump field

$$E_1(z,t) = \tilde{E}_1 e^{i(\Omega_1 t - k_1 z)} + \text{c.c.}, \tag{3.1}$$

which replaces (2.1), propagates in the same direction as the probe field (2.2),

$$E_2(z,t) = \tilde{E}_2 e^{i(\Omega_2 t - k_2 z)} e^{i\varphi(t)} + \text{c.c.} \tag{3.2}$$

where the indices are changed for convenience, $k \equiv k_1 \sim k_2$, $A_0^1 = \tilde{E}_1 e^{-ikz'}$ and $\Omega_0^1 = 0$. Since the pump and probe occupy different time intervals, the treatment is significantly simpler than Section II. For the preparative stage, the equations of motion (2.8) are now

$$\dot{\tilde{\rho}}_{12} = (i\Delta_1 - 1/T_2)\tilde{\rho}_{12} - 2igw\tilde{E}_1 \tag{3.3a}$$

$$\dot{w} = -(w-w^o)/T_1 - ig\tilde{E}_1(\tilde{\rho}_{12} - \tilde{\rho}_{21}) \tag{3.3b}$$

where

$$\Delta_i = \omega_{21} - \Omega_i + kv_z, \quad i = 1,2. \tag{3.4}$$

The steady-state solution, $\dot{\tilde{\rho}}_{12} = \dot{w} = 0$, is

$$w_{ss} = w^o\left(1 - \frac{4g^2|\tilde{E}_1|^2 T_1/T_2}{\Delta_1^2 + 1/T_2^2 + 4g^2|\tilde{E}_1|^2 T_1/T_2}\right). \tag{3.5}$$

For the probing stage, we obtain a perturbation solution of

$$\dot{\tilde{\rho}}_{12} = (i\Delta_2 - 1/T_2)\tilde{\rho}_{12} - 2igw_{ss}\sum_n A_n e^{in\Omega t} \tag{3.6}$$

in the long time limit $t>>T_2$ with

$$\tilde{\rho}_{12}(t) = -2igw_{ss}\sum_n A_n e^{in\Omega t}/(-i\Delta_2 + in\Omega + 1/T_2)\,, \tag{3.7}$$

w_{ss} being given by (3.5). Contour integration of the Doppler integral of $\tilde{\rho}_{12}(t)$ followed by the manipulations (2.35) and (2.36) yields the beat signal

$$\langle B(t)\rangle = -8i\pi w^o N g^4 |\tilde{E}_1|^2 \frac{T_1}{T_2\alpha} e^{i\Omega t}$$

$$\times \sum_\ell A^*_{\ell-1}A_\ell \delta' \frac{\delta'^2 - (\ell\Omega/2)^2 - i\Gamma\ell\Omega + \Gamma^2}{[(\delta' - \ell\Omega/2)^2 + \Gamma^2][(\delta' + \ell\Omega/2)^2 + \Gamma^2]} + \text{c.c.} \tag{3.8}$$

where

$$\delta' = (\Omega_1 - \Omega_2)/2\,,$$

and α and Γ are defined by (2.40) and (2.41). This result has precisely the same form as the case of the counterpropagating pump and probe beams, Eq. (2.39), except that the tuning parameter changes from the off-resonance parameter $\delta = \omega_{21} - \omega_o$ to the laser frequency difference $\delta' = (\Omega_1 - \Omega_2)/2$. Hence, the beat signals will have the appearance of Fig. 1.

B. Three-Level Problem

In the spirit of the previous section, we now treat a three-level quantum system where two optical transitions 1→3 and 1→2 share a common lower level. In the preparation, the pump field (3.1) first excites one of the transitions, and thereafter, the probe field (3.2) samples the residual

hole in the population distribution of level 1 in either transition. At first sight, it would appear that the three-level case offers nothing new. However, careful analysis shows that the two transitions, as seen by the probe, do not exhibit the same response.

For the preparative stage, the density matrix equations of motion can be written as

$$\dot{\tilde{\rho}}_{21} = i\Delta_{21}\tilde{\rho}_{21} - ig_1\tilde{E}_1^-(\rho_{11}-\rho_{22}) + ig_2\tilde{E}_1^-\rho_{23} - \Gamma\tilde{\rho}_{21} ,$$

$$\dot{\tilde{\rho}}_{31} = i\Delta_{31}\tilde{\rho}_{31} - ig_2\tilde{E}_1^-(\rho_{11}-\rho_{33}) + ig_1\tilde{E}_1^-\rho_{32} - \Gamma\tilde{\rho}_{31} ,$$

$$\dot{\tilde{\rho}}_{23} = i\Delta_{23}\tilde{\rho}_{23} - ig_1\tilde{E}_1^-\tilde{\rho}_{13} + ig_2\tilde{E}_1^+\tilde{\rho}_{21} - \Gamma'\rho_{23} ,$$

$$\dot{\rho}_{11} = \gamma_2\rho_{22} + \gamma_3\rho_{33} + ig_1(-\tilde{E}_1^+\tilde{\rho}_{21} + \tilde{E}_1^-\tilde{\rho}_{12}) + ig_2(-\tilde{E}_1^+\tilde{\rho}_{31} + \tilde{E}_1^-\tilde{\rho}_{13}) ,$$

$$\dot{\rho}_{22} = ig_1(-\tilde{E}_1^-\tilde{\rho}_{12} + \tilde{E}_1^+\tilde{\rho}_{21}) - \gamma_2\rho_{22} ,$$

$$\dot{\rho}_{33} = ig_2(-\tilde{E}_1^-\tilde{\rho}_{13} + \tilde{E}_1^+\tilde{\rho}_{31}) - \gamma_3\rho_{33} . \qquad (3.9)$$

The following matrix elements and definitions apply

$$H_{ii} = \hbar\omega_i , \quad \omega_{ij} = \omega_i - \omega_j , \quad i \text{ or } j = 1,2,3 ,$$

$$H_{12} = g_1\hbar E_1 , \quad H_{13} = g_2\hbar E_1 , \quad H_{23} = 0 ,$$

$$\rho_{ij} = \tilde{\rho}_{ij}\, e^{i(\Omega_1 - kv_z)t} , \quad ij = 12, \text{ or } 13 ,$$

$$\Delta_{21} = \Omega_1 - \omega_{21} - kv_z ,$$

$$\Delta_{31} = \Omega_1 - \omega_{31} - kv_z ,$$

$$\Delta_{23} = \omega_{32} . \qquad (3.10)$$

We also assume that the system is isolated so that

$$1 = \rho_{11} + \rho_{22} + \rho_{33} ,$$

and that the pump field resonantly excites one transition or the other, but not both simultaneously so that we expect that

$$\tilde{\rho}_{23} \sim 0 .$$

For simplicity, we assume that

$$g \equiv g_1 = g_2 \text{ and } \gamma \equiv \gamma_2 = \gamma_3 .$$

In steady state, the solutions are

$$w_{12}^{ss} = \frac{(\Delta_{31}^2 + \Gamma^2)(\Delta_{21}^2 + \Gamma^2) + a^2(\Delta_{21}^2 + \Gamma^2)}{(\Delta_{31}^2 + \Gamma^2)(\Delta_{21}^2 + \Gamma^2) + 2a^2(\Delta_{31}^2 + \Delta_{21}^2 + 2\Gamma^2) + 3a^4} \tag{3.11}$$

$$w_{13}^{ss} = \frac{(\Delta_{21}^2 + \Gamma^2)(\Delta_{31}^2 + \Gamma^2) + a^2(\Delta_{31}^2 + \Gamma^2)}{(\Delta_{31}^2 + \Gamma^2)(\Delta_{21}^2 + \Gamma^2) + 2a^2(\Delta_{31}^2 + \Delta_{21}^2 + 2\Gamma^2) + 3a^4} \tag{3.12}$$

where

$$a^2 = \frac{2g^2}{\gamma} \Gamma |E_1|^2 .$$

For the probing period, lowest order perturbation theory yields the equation of motion

$$\dot{\tilde{\rho}}_{21} = i\bar{\Delta}_{21}\tilde{\rho}_{21} - ig\sum_n A_n^* e^{-in\Omega t} w_{12}^{ss} - \Gamma\tilde{\rho}_{21} ,$$

which has the long-time ($t >> T_2$) solution

$$\tilde{\rho}_{21}(t) = -ig\sum_n w_{12}^{ss} A_n^* e^{-in\Omega t} \frac{1}{-in\Omega - i\bar{\Delta}_{21} + \Gamma} .$$

Similarly,

$$\tilde{\rho}_{31}(t) = \tilde{\rho}_{21}(2 \longleftrightarrow 3)$$

where

$$\bar{\Delta}_{21} = \Omega_2 - \omega_{21} - kv_z ,$$

$$\bar{\Delta}_{31} = \Omega_2 - \omega_{31} - kv_z .$$

Proceeding as before, the signal field is

$$\tilde{E}_s^- \sim -ig(\tilde{\rho}_{21} + \tilde{\rho}_{31}) ,$$

and the heterodyne beat is of the form

$$B(t) = -g^2 \sum_\ell e^{i\Omega t} A_{\ell+1} A_\ell^* \times \left[\frac{w_{12}^{ss}}{-i\ell\Omega - i\bar{\Delta}_{21} + \Gamma} - \frac{w_{12}^{ss}}{-i\ell\Omega + i\bar{\Delta}_{21} + \Gamma} + \frac{w_{13}^{ss}}{-i\ell\Omega - \bar{\Delta}_{31} + \Gamma} - \frac{w_{13}^{ss}}{-i\ell\Omega + i\bar{\Delta}_{31} + \Gamma} \right] . \tag{3.13}$$

To carry out the Doppler integration, we consider the weak field case

$$w_{12}^{ss} = 1 - a^2 \frac{(\Delta_{21}^2 + \Gamma^2) + 2(\Delta_{31}^2 + \Gamma^2)}{(\Delta_{31}^2 + \Gamma^2)(\Delta_{21}^2 + \Gamma^2)} ,$$

$$w_{13}^{ss} = (W_{12}^{ss})(2 \longleftrightarrow 3) \tag{3.14}$$

where power broadening is ignored by neglecting the a^2 and a^4 terms in the denominators of (3.11) and (3.12).

Upon the Doppler integration of (3.13), the final result is

$$\langle B(t)\rangle = 4\pi i \frac{g^4 |E_1|^2}{\gamma} e^{i\Omega t} \sum_{\ell} A_{\ell+1} A_{\ell}^{*}$$

$$\times [4F_{\ell}(\Delta) + F_{\ell}(\Delta-\delta) + F_{\ell}(\Delta+\delta)] + \text{c.c.} \qquad (3.15)$$

with

$$F_{\ell}(\Delta) = \frac{-(\ell\Omega)^2 + \Delta^2 + 4\Gamma^2 + 4i\Gamma\ell\Omega}{[(\ell\Omega+\Delta)^2 + 4\Gamma^2][(\ell\Omega-\Delta)^2 + 4\Gamma^2]} ,$$

$$\Delta = \Omega_2 - \Omega_1 ,$$

$$\delta = \omega_{23} .$$

Equation (3.15) is shown in Fig. 3 for the case $\ell=0$ and $\ell=-1$ and shares common features with the copropagating beam two-level case (3.8). The dispersion spectrum consists of a central triplet feature at $\Omega_2=\Omega_1$ and $\Omega_2=\Omega_1\pm\omega_{23}$, while one sideband appears as a triplet at $\Omega_2=\Omega_1-\Omega$ and $\Omega_2=\Omega_1-\Omega\pm\omega_{23}$ and the other sideband at $\Omega_2=\Omega_1+\Omega$ and $\Omega_2=\Omega_1+\Omega\pm\omega_{23}$. The absorption spectrum shows two triplets centered at $\Omega_2=\Omega_1\pm\Omega$, corresponding to the dispersion spectrum but now the central feature is missing as in the two-level case of Fig. 1. Also, the Lorentzian lineshape has a width of 2Γ due to the separate contributions of pump and probe absorption.

Note that the central absorption components at $\Omega_2=\Omega_1\pm\Omega$ are four times as intense as the satellite lines at $\Omega_2=\Omega_1\pm\Omega\pm\omega_{23}$. Two factors contribute to this ratio. First, the central component is due to two transitions 1→3 and 1→2 which are excited at the same frequency due to the inhomogeneous broadening whereas the satellite lines are single transitions. This effect contributes a factor of two. Second, the nonlinear response of a transition is proportional to the incremental change in population (see Eq. (2.8a)). If the population change arising form hole burning is $-\delta$ for the lower state and $+\delta$ for the upper state, the central component intensity will be proportional to 2δ. However, the satellite line involves a common lower state with its contribution of $+\delta$ while the excited state is not prepared and therefore doesn't contribute. This effect provides the remaining factor of two.

IV. FABRY-PEROT

We now calculate the response of a plane mirror Fabry-Perot cavity to a phase-modulated laser beam. This linear problem, which contrasts with the nonlinear atomic case, is the basis of an important method for precision laser frequency (phase) locking.[2-4]

The incident field, which strikes the mirrors at normal incidence, is again given by (2.2), and the transmitted and reflected field amplitudes are well known[17] to be

$$E_t = \frac{1-R}{1-Re^{i\delta}}\,E_o\,, \tag{4.1}$$

$$E_r = \sqrt{R}\,\frac{1-e^{i\delta}}{1-Re^{i\delta}}\,E_o \tag{4.2}$$

where R is the mirror's reflectivity and the phase change for a double traversal of a cavity of spacing d is

$$\delta = 2nd\omega_o/c\,. \tag{4.3}$$

For a high reflectivity cavity satisfying the condition $1-R<<1$, we approximate the phase factor by

$$e^{i\delta} \sim 1 + i\delta\,. \tag{4.4}$$

Recognizing that the cavity resonance condition is

$$\delta_r = 2nd\omega_r/c = m2\pi \ (m = 0,1,2,...)\,, \tag{4.5}$$

we rewrite (4.4) as

$$e^{i\delta} = e^{i(\delta-\delta_r)} \sim 1 + i2nd\Delta/c \tag{4.6}$$

where the tuning parameter

$$\Delta = \omega_o-\omega_r\,. \tag{4.7}$$

Substitution of (4.6) into (4.1) and (4.2) gives

$$E_t = \frac{\Gamma(\Gamma+i\Delta)}{\Delta^2+\Gamma^2}\,E_o\,, \tag{4.8}$$

$$E_r = \frac{\Delta(\Delta-i\Gamma)}{\sqrt{R}(\Delta^2+\Gamma^2)}\,E_o\,, \tag{4.9}$$

with the linewidth defined by

$$\Gamma = \left(\frac{1-R}{R}\right)\left(\frac{c}{2nd}\right).$$

The transmitted intensity then assumes the form

$$|E_t|^2 = \Gamma^2\sum_\ell A^*_{\ell-1}A_\ell\, e^{i\Omega t}\left(\frac{\Gamma+i\Delta_\ell}{\Gamma^2+\Delta_\ell^2}\right)\left(\frac{\Gamma-i\Delta_{\ell-1}}{\Gamma^2+\Delta_{\ell-1}^2}\right) + c.c. \tag{4.10}$$

where E_0 has been expanded into its sidebands through (2.3a) and we have retained in the sum only the beat terms containing $e^{i\Omega t}$. For the case $\ell=0$ and $\ell=+1$, Eq. (4.10) reduces to

$$|E_t|^2 = -2\Omega\Gamma^2 A_0 A_1 e^{i\Omega t}$$

$$\times \Delta \frac{\Gamma^2+\Delta^2-\Omega^2+2i\Gamma\Omega}{(\Gamma^2+\Delta^2)(\Gamma^2+(\Delta+\Omega)^2)(\Gamma^2+(\Delta-\Omega)^2)} + \text{c.c.} . \tag{4.11}$$

Thus, three linear resonances appear (Fig. 4) at $\omega_0=\omega_r$ and $\omega_0=\omega_r\pm\Omega$, both in absorption and dispersion. In contrast to the nonlinear atomic response, (2.43) for example, the central line provides a nonvanishing absorption signal, an effect which apparently has gone unnoticed.[1-3] This central feature can disappear, however, when the absorption spectrum is not pure and contains a dispersive component when the phase angle θ is given by

$$\tan\theta = \frac{\Gamma^2-\Omega^2}{2\Gamma\Omega} .$$

A similar calculation for the intensity of the reflected component shows that

$$|E_r|^2 = \frac{2\Omega}{R} A_0 A_1 e^{i\Omega t}$$

$$\times \Delta \frac{i\Omega\Gamma(\Gamma^2-\Delta^2+\Omega^2)+\Gamma^2(\Gamma^2+\Delta^2+\Omega^2)}{(\Gamma^2+\Delta^2)(\Gamma^2+(\Delta+\Omega)^2)(\Gamma^2+(\Delta-\Omega)^2)} + \text{c.c.} \tag{4.12}$$

where we see that (4.11) and (4.12) are related by

$$|E_r|^2 = -\frac{2}{R}\cos\phi\sqrt{\Omega^2/\Gamma^2+1}\,|E_t|^2 \tag{4.13}$$

and $\tan\phi=\Omega/\Gamma$.

CONCLUSIONS

Calculations for several different cases that arise in phase modulation laser spectroscopy have been developed. Various predictions are made including the role of higher order coherence effects and the appearance of resonances which have yet to be observed.

ACKNOWLEDGMENTS

We are pleased to acknowledge enlightening conversations with G. C. Bjorklund, S. A. Lee, J. L. Hall, R. W. P. Drever, and M. Levenson. This work was supported in part by the U.S. Office of Naval Research.

REFERENCES

1. (a) G. C. Bjorklund, Optics Letters 5, 15 (1980); (b) G. C. Bjorklund and M. D. Levenson, Phys. Rev. A 24, 166 (1981); (c) G. C. Bjorklund, K. Jain, and J. D. Hope, Appl. Phys. Lett. 38, 747 (1981).
2. R. W. P. Drever, J. L. Hall, F. V. Kowalski, J. Hough, G. M. Ford, and A. Munley (to be published).
3. J. L. Hall, L. Hollberg, T. Baer, and H. G. Robinson (to be published).
4. R. G. DeVoe and R. G. Brewer (unpublished).
5. R. W. P. Drever et al., in Laser Spectroscopy V, Proceedings of the Fifth International Laser Spectroscopy Conference, Jasper, Canada, 1981 (Springer-Verlag, in press), edited by B. P. Stoicheff and T. Oka.
6. B. Smaller, Phys. Rev. 83, 812 (1951).
7. R. V. Pound, The Review of Scientific Instruments 17, 490 (1946).
8. R. G. Brewer, Physics Today 30, No. 5, 50 (1977).
9. R. G. Brewer in, Frontiers in Laser Spectroscopy, Vol. 1 (North-Holland, 1977), p. 341, edited by R. Balian, S. Haroche, and S. Liberman.
10. A. Schenzle and R. G. Brewer, Phys. Rev. A 14, 1756 (1976).
11. A. Schenzle and R. G. Brewer, Physics Reports (Section C of Physics Letters) 43, No. 12, 455 (1978).
12. J. Reid and T. Oka, Phys. Rev. Lett. 38, 67 (1977).
13. S. Haroche and F. Hartmann, Phys. Rev. A6, 1280 (1972).
14. V. S. Letokhov and V. P. Chebotayev, V. P. Chebotayev, Nonlinear Laser Spectroscopy (Springer-Verlag, N.Y., 1977), p. 78.

15. T. Muramoto, S. Nakaniski, and T. Hashi, Opt. Comm. 21, 139 (1977); R. M. Macfarlane and R. M. Shelby, Optics Letters 6, 96 (1981), and references therein.

16. W. Lenth, C. Ortiz, and G. C. Bjorklund, Optics Letters 6, 351 (1981).

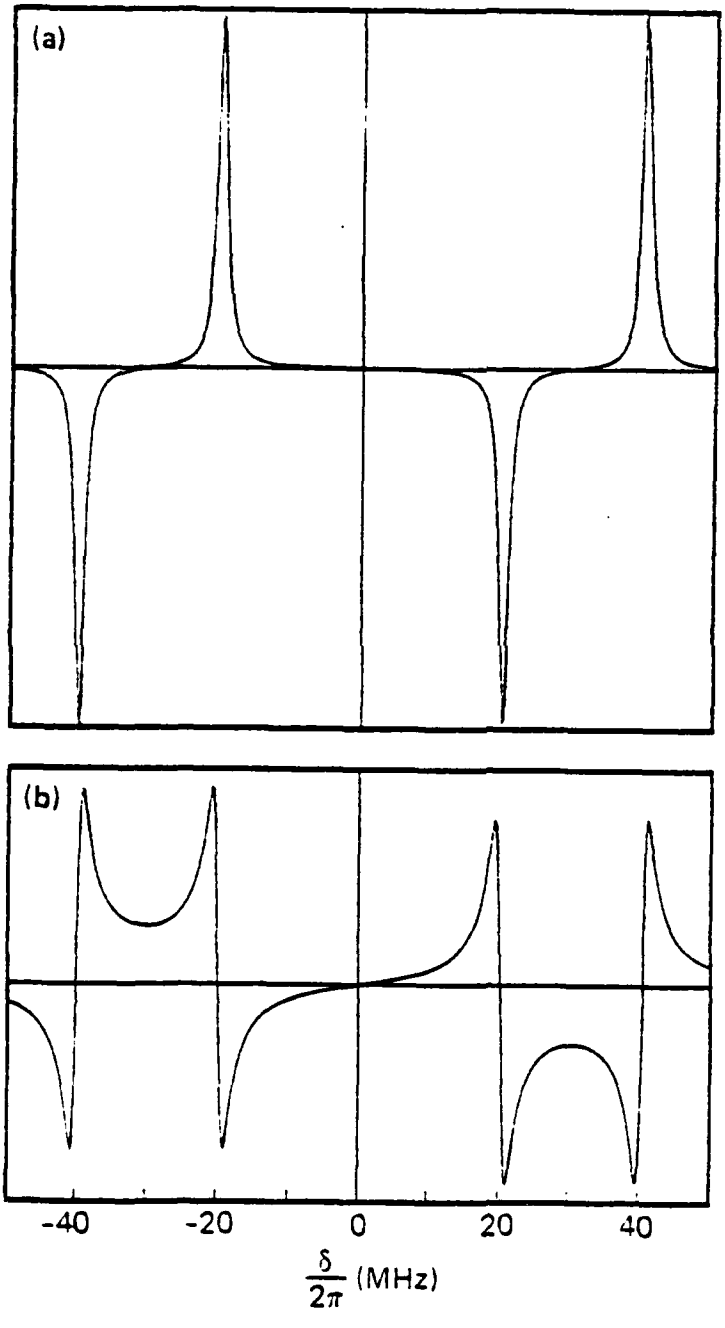
17. M. Born and E. Wolf, Principles of Optics, 5th ed. (Pergamon, Oxford, 1975).

FIGURE CAPTIONS

Figure 1. Theoretical absorption (upper curves) and dispersion (lower curves) lineshapes for a two-level atom interacting simultaneously with a pump field and a counterpropagating phase modulated probe field which is detected. The frequency axis $\delta=\omega_{21}-\omega_0$. Solid curve: Eq. (2.55) which is equivalent to a rate equation result. Dashed curve: the sum of (2.55) and the coherence correction (2.56). Parameters: $T_2=1$ μsec, x=5, $\Omega=30$ (2π radians$\cdot\mu$sec^{-1}), and $\bar{\Gamma}=1.72$.

Figure 2. Theoretical absorption (upper curve) and dispersion (lower curve) lineshapes for a two-level atom interacting simultaneously with a pump field and a counterpropagating phase modulated probe field, Eq. (2.61). In this case, the pump beam is detected, and besides the $\delta=\pm\Omega/2$ resonances, new resonances appear at $\delta=\pm\Omega$ due to the inclusion of coherence corrections. Parameters: $T_2=1$ μsec and $\Omega=30$ (2π radians$\cdot\mu$sec^{-1}).

Figure 3. Theoretical absorption (upper curves) and dispersion (lower curve) lineshapes for a three-level atom interacting initially with a pump field of frequency Ω_1 and subsequently with a probe field of frequency Ω_2, Eq. (3.15). The frequency axis $\Delta=\Omega_2-\Omega_1$. Triplet features appear where the central line is four times the intensity of either satellite line. Parameters: $\Omega=50$ (2π radians$\cdot\mu$sec^{-1}), $\Gamma=0.25$ μsec^{-1}, and $\omega_{23}=10$ (2π radians$\cdot\mu$sec^{-1}).



gure 2. Computer plots of Eq. (4) for (a) absorption and (b) dispersion lineshapes of the mp beam where $\Omega/2\pi=40.2$ MHz and $\Gamma/2\pi=0.8$ MHz HWHM.

Figure 2. R.G. DEVOE et al

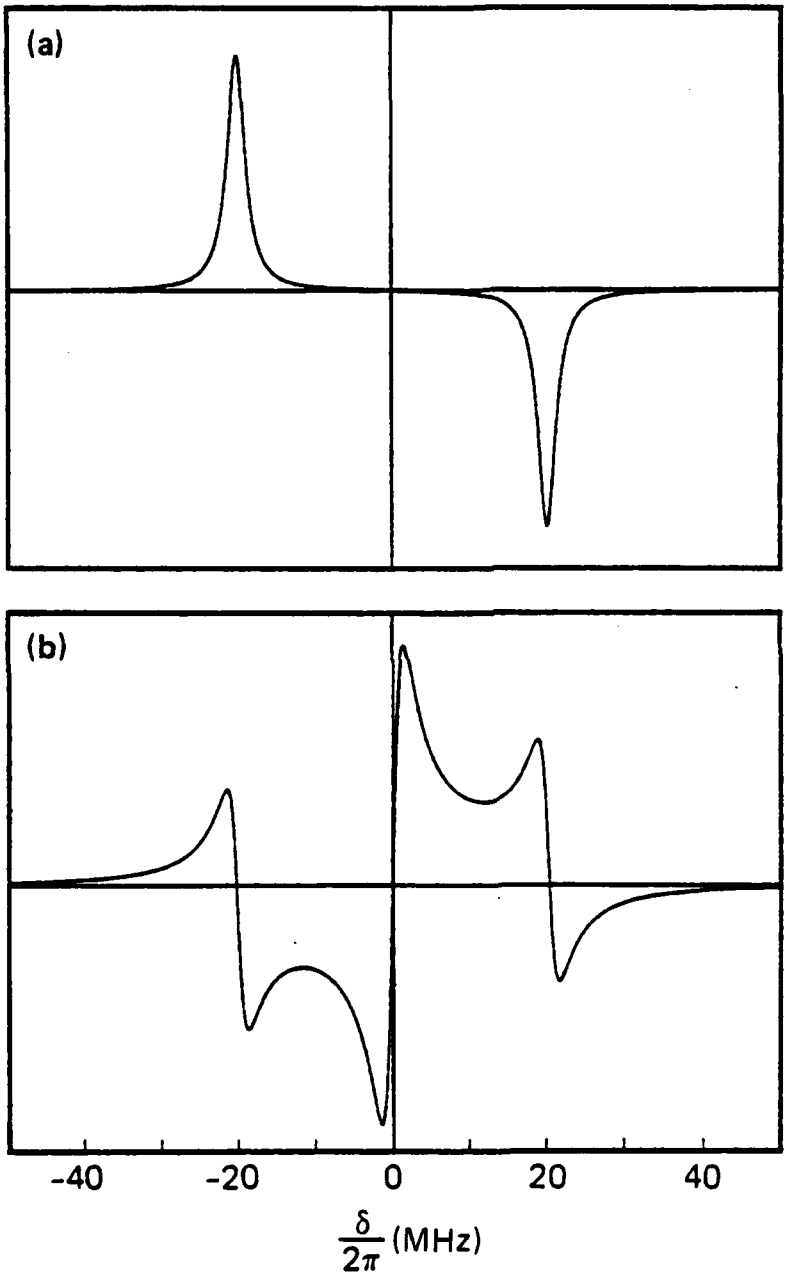


Figure 1. Computer plots of Eq. (3) for (a) absorption and (b) dispersion lineshapes of the phase modulated probe beam where $\Omega/2\pi$=40.2 MHz and $\Gamma/2\pi$=0.8 MHz HWHM.

Figure 1. R.G. DEVOE et al

REFERENCES

1. G. C. Bjorklund, Optics Letters 5, 15 (1980).
2. G. C. Bjorklund and M. D. Levenson, Phys. Rev. A 24, 166 (1981).
3. J. L. Hall, L. Hollberg, T. Baer and H. G. Robinson, Appl. Phys. Lett. 39, 680 (1981).
4. R. W. P. Drever, J. L. Hall, F. V. Kowalski, J. Hough, G. M. Ford and A. Munley (to be published).
5. S. E. Whitcomb and R. W. P. Drever (private communication).
6. R. G. DeVoe and R. G. Brewer (unpublished).
7. A. Schenzle, R. G. DeVoe and R. G. Brewer, Phys. Rev. A (in press).
8. R. K. Raj, D. Bloch, J. J. Snyder, G. Camy and M. Ducloy, Phys. Rev. Lett. 44, 1251 (1980).
9. J. L. Hall (private communication).

amplitude and linewidth. In particular, the characteristic spectrum of the pump beam uniquely identifies the coherent interaction predicted by Eq. (4).

The disparity in the signal-to-noise ratio of Figs. (3) and (4) also follows from Eqs. (3) and (4) which predict an absorption intensity ratio of probe to pump of $R=\Omega T_1$ at $\delta=\pm\Omega/2$. For $\Omega/2\pi=40.2$ MHz, R~50 which compares to an observed ratio of 60. This crude comparison assumes that $T_1 \sim T_2$, where we recognize that T_1 does not describe population decay accurately for the transition levels of I_2 when collisional broadening occurs. An additional test of (4) arises when we note that the pump signal scales as $1/\Omega$ in the limit $\Omega T_1 >> 1$. This behavior is also verified when the modulation frequency is changed from 40.2 to 10.4 MHz causing the observed pump signal intensity to increase 4×.

Finally, it should be mentioned that the four-wave process described here overlaps to some extent an earlier study[8] in this area. Thus, Raj et al.[8] detected a similar Doppler-free two-line spectrum of I_2 resulting from the application of three collinear fields of different frequency, two copropagating in one direction and a third in the opposite direction (the direction for detection). In contrast, the phase modulated light wave case constitutes a balanced system involving pairs of sidebands where the larger number of Fourier components reveals resonances in a new way, as the present article demonstrates.

This work was supported in part by the U.S. Office of Naval Research. We are also pleased to acknowledge that coherent four-wave resonances of the type reported here have just been observed in the laboratory of J. L. Hall.[9]

remain unmodulated. An alternative point of view is that the probe modulates the population which in turn modulates the pump field, a coherent process. We see in Fig. 2 that the pump signal spectra are characteristically different from that of the probe beam and consist of four equally intense lines in absorption. In dispersion, the central feature of Fig. 1(b) is missing and the four lines appear in pairs of opposite phase and with inversion symmetry about the origin.

To observe these resonances, the output of a cw ring dye laser of linear polarization was divided into two counterpropagating beams which are expanded to a diameter of 2 mm and overlap throughout the length of a 60 cm cell containing I_2 vapor (pressure: 30 mTorr). The probe beam has a power of 8 mW and is phase modulated by an AD*P crystal either at $\Omega/2\pi$=40.2 or 10.4 MHz (modulation index: 1.0). The pump beam has a power of 28 mW and is frequency shifted by $\Delta/2\pi$=80 MHz using an acousto-optic modulator to avoid undesirable feedback into the laser; accordingly, the probe and pump resonances are all shifted by $-\Delta/2$. The ring dye laser is phase-locked to a reference cavity at a wavelength of ~5790Å and possesses a 300 Hertz rms laser linewidth in short term.[6] The laser tracks the reference cavity as it is swept, producing at resonance heterodyne beat signals at two PIN diodes which monitor probe and pump beams simultaneously. The detector output is demodulated with a double balanced mixer.

Oscilloscope traces of the probe and pump signals for an isolated I_2 transition are shown in Figs. (3) and (4) both in absorption and dispersion for the case $\Omega/2\pi$=40.2 MHz. These observations clearly reproduce our theoretical predictions[7] (which assume $\Omega/2\pi$=40.2 MHz, T_2=0.2 μsec, and $\Gamma/2\pi=1/2\pi T_2$=0.8 MHz HWHM) in the number of features which appear and their spacing and in the lineshapes including their phase, relative

What resonances then are to be expected when the pump beam is monitored instead of the probe? The solution[7] in this case also takes the form of a heterodyne beat signal,

$$< B(t) > = -16\pi N g^4 \tilde{E}_o^2 \tilde{E}_1^2 w^o \frac{T_1}{\sqrt{1+(\Omega T_1)^2}} J_0(M) J_1(M)$$

$$\times \delta \left\{ \left[\frac{\Omega/T_2}{[(\delta-\Omega/2)^2 + 1/T_2^2][(\delta+\Omega/2)^2 + 1/T_2^2]} \right.\right.$$

$$\left. - \frac{2\Omega/T_2}{[(\delta-\Omega)^2 + 1/T_2^2][(\delta+\Omega)^2 + 1/T_2^2]} \right] \cos(\Omega t + \Phi)$$

$$+ \left[\frac{\delta^2 - (\Omega/2)^2 + 1/T_2^2}{[(\delta-\Omega/2)^2 + 1/T_2^2][(\delta+\Omega/2)^2 + 1/T_2^2]} \right.$$

$$\left.\left. - \frac{\delta^2 - \Omega^2 + 1/T_2^2}{[(\delta-\Omega)^2 + 1/T_2^2][(\delta+\Omega)^2 + 1/T_2^2]} \right] \sin(\Omega t + \Phi) \right\}, \qquad (4)$$

where $\tan\Phi = 1/(\Omega T_1)$. Nonlinear resonances, which interestingly occur to the same order E^4 as in (3), appear in absorption (Fig. 2a) and dispersion (Fig. 2b) at $\delta = \pm\Omega/2, \pm\Omega$. We can decompose, for example, one of these four-wave interactions into a resonant one-wave process where $\omega_o - kv_z = \omega_{21}$ and a resonant three-wave process for the same velocity group v_z where three of the applied fields stimulate absorption twice at frequency ω_o and emission at $\omega_o + \Omega$ such that $(\omega_o - kv_z) - (\omega_o + \Omega - kv_z) + (\omega_o + kv_z) = \omega_{21}$. The four-wave resonance $\delta = -\Omega/2$ follows from these two conditions. Similarly, a second four-wave interaction requires that $(\omega_o + \Omega - kv_z) = \omega_{21}$ and $(\omega_o + \Omega - kv_z) - (\omega_o - kv_z) + (\omega_o + kv_z) = \omega_{21}$ to yield the four-wave resonance $\delta = \Omega$. These are coherent four-wave interactions that are responsible for generating a heterodyne beat signal in a pump beam which otherwise would

Phase modulation produces pairs of sidebands of opposite phase that are balanced in the absence of absorption or phase shifts. However, when a sideband is partially absorbed, the probe beam displays a heterodyne beat signal of the form[7]

$$< B_0(t) > = -16\pi N g^4 \tilde{E}_0^2 \tilde{E}_1^2 w^o (T_1/T_2) J_0(M) J_1(M)/\alpha$$

$$\times \delta \Bigg\{ \Bigg[\left(\frac{1}{\delta^2+\Gamma^2} - \frac{\delta^2-(\Omega/2)^2+\Gamma^2}{[(\delta-\Omega/2)^2+\Gamma^2][(\delta+\Omega/2)^2+\Gamma^2]} \right) \cos \Omega t$$

$$- \frac{\Gamma\Omega}{[(\delta-\Omega/2)^2+\Gamma^2][(\delta+\Omega/2)^2+\Gamma^2]} \sin \Omega t \Bigg\} \qquad (3)$$

where the bracket $< >$ denotes an average over the inhomogeneous Doppler lineshape, $\delta=\omega_{21}-\omega_o$, $\Gamma=\frac{1}{2}(\alpha+1/T_2)$, $\alpha = \frac{1}{T_2}(1 + 4g^2 T_1 T_2 \tilde{E}_1^2)^{1/2}$, T_1 and T_2 are the population and dipole dephasing times, $g=-\mu_{12}/\hbar$, μ_{12} is the transition matrix element, N is the population density, w^o is the population difference of levels 1 and 2 in the absence of the applied fields, and J_n is a Bessel function of order n. Equation (3) is derived from the density matrix equations of motion using perturbation theory and is equivalent to a rate equation solution. Equation (3) exhibits nonlinear resonance features as the laser frequency ω_o is tuned, either in absorption (Fig. 1a) at $\delta=\pm\Omega/2$ or in dispersion (Fig. 1b) at $\delta=0$, $\pm\Omega/2$. The resonance conditions for absorption also follow simply by noting that at resonance a particular velocity packet v_z interacts simultaneously with the pump field (satisfying $\omega_o=\omega_{21}\mp kv_z$) and the appropriate sideband (satisfying $\omega_o\pm\Omega=\omega_{21}\pm kv_z$). Thus, the probe sideband samples the hole burned by the pump, and to this order of approximation, coherence effects do not enter.

An optical phase modulation technique[1] was introduced recently that allows sharp nonlinear atomic resonances to be detected with low noise.[2,3] The method also has been applied successfully to phase locking a laser to a reference cavity, providing laser linewidths as narrow as ~100 Hertz.[4-6] These two developments in combination set the stage for establishing new levels of precision in optical spectroscopy. There is interest, therefore, in fully characterizing the basic nonlinear optical interactions which occur when atoms are subjected to phase modulated light waves.

In a previous article,[7] we developed a theory of phase modulation spectroscopy that predicts two classes of nonlinear atomic resonances. One can be described in terms of rate equations or hole burning arguments and indeed was observed and discussed previously.[2,3] Another emerges from coherent interactions which are now verified in this communication.

Our previous theoretical model[7] assumes a collection of two-level atoms, with frequency splitting ω_{21}, capable of undergoing an electric-dipole transition 1↔2 under the action of an intense pump field

$$E_1(z,t) = \tilde{E}_1 \, e^{i(\omega_o t + kz)} + \text{c.c.} \tag{1}$$

and a weak counter propagating collinear probe field

$$E_o(z,t) = \tilde{E}_o \, e^{i(\omega_o t - kz)} \, e^{i\varphi(t)} + \text{c.c.} \tag{2}$$

that is phase modulated at frequency Ω where the phase

$$\varphi(t) = M \cos \Omega t \, .$$

RJ3414 (40680) 3/8/82
Physics

COHERENCE PHENOMENA IN PHASE MODULATION LASER SPECTROSCOPY *

Ralph G. DeVoe
Richard G. Brewer

IBM Research Laboratory
San Jose, California 95193

ABSTRACT: The technique of phase modulation laser spectroscopy is used to detect a coherent four-wave interaction in I_2 vapor. A phase modulated probe beam induces in the sample an oscillating population which in turn modulates a counterpropagating pump beam that reveals a characteristic two resonance spectrum. The observations fully confirm an earlier density matrix calculation.

*Work supported in part by the U.S. Office of Naval Research.

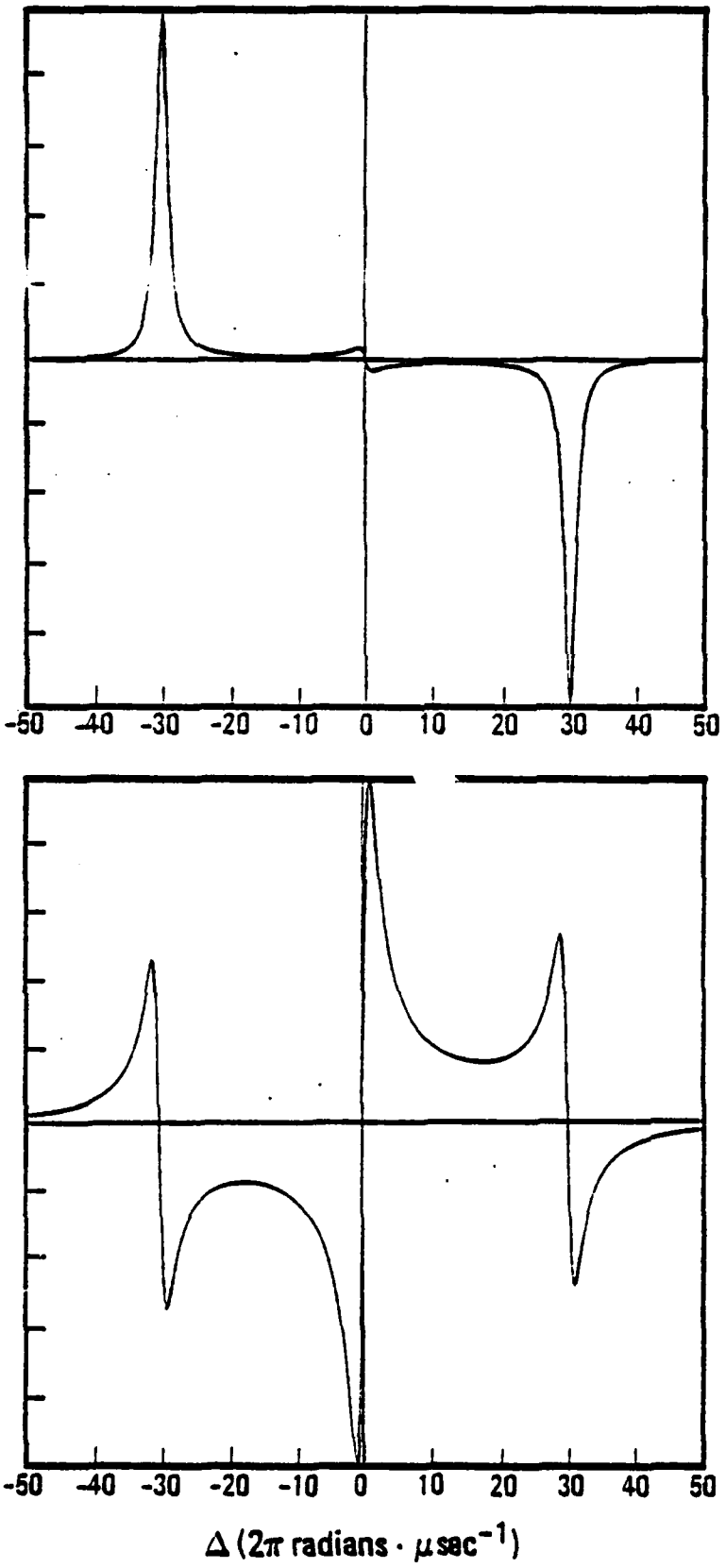

-50 -40 -30 -20 -10 0 10 20 30 40 50
-50 -40 -30 -20 -10 0 10 20 30 40 50
Δ (2π radians · μsec⁻¹)

Figure 4.

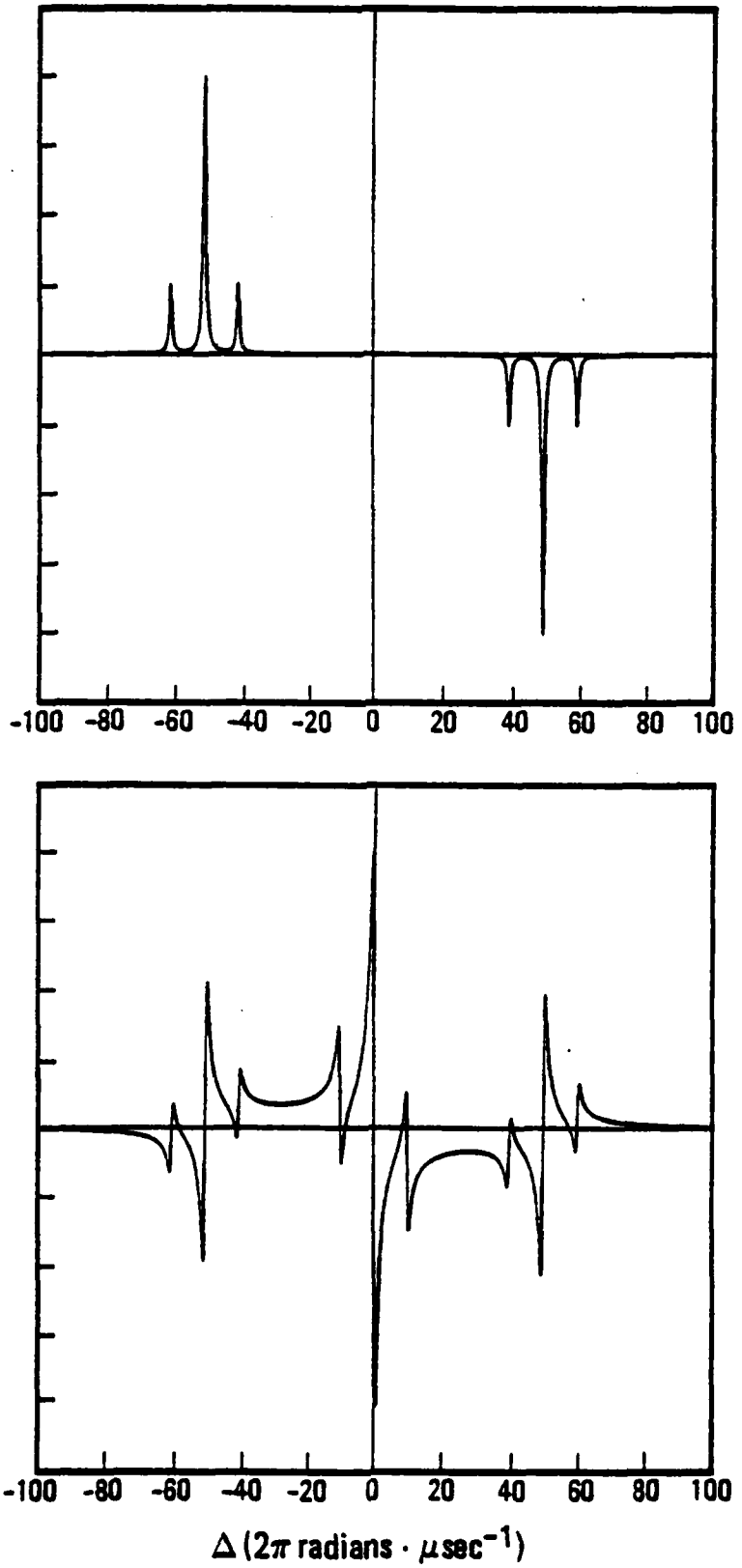

-100 -80 -60 -40 -20 0 20 40 60 80 100
-100 -80 -60 -40 -20 0 20 40 60 80 100
Δ (2π radians · μsec⁻¹)

Figure 3.

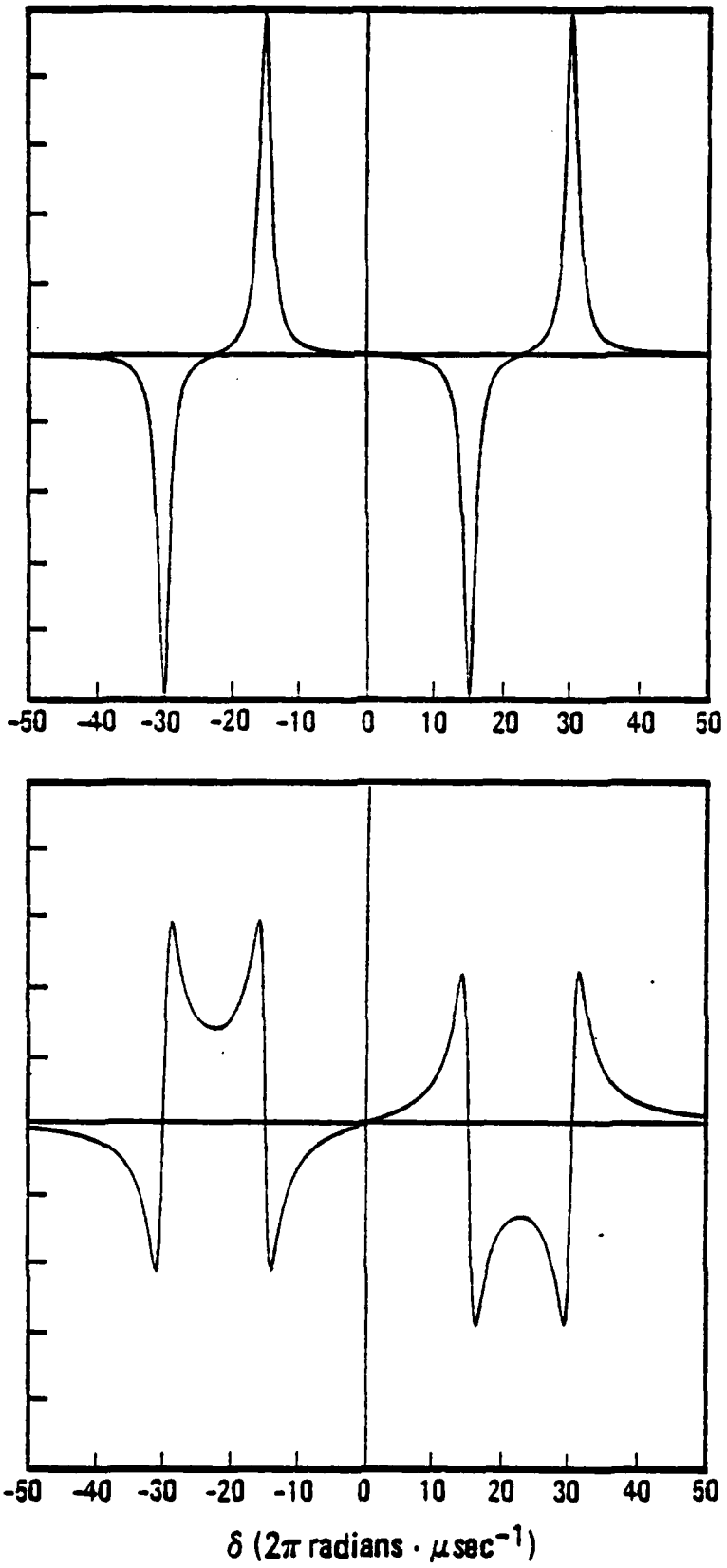

-50 -40 -30 -20 -10 0 10 20 30 40 50
-50 -40 -30 -20 -10 0 10 20 30 40 50
δ (2π radians · μsec⁻¹)

Figure 2.

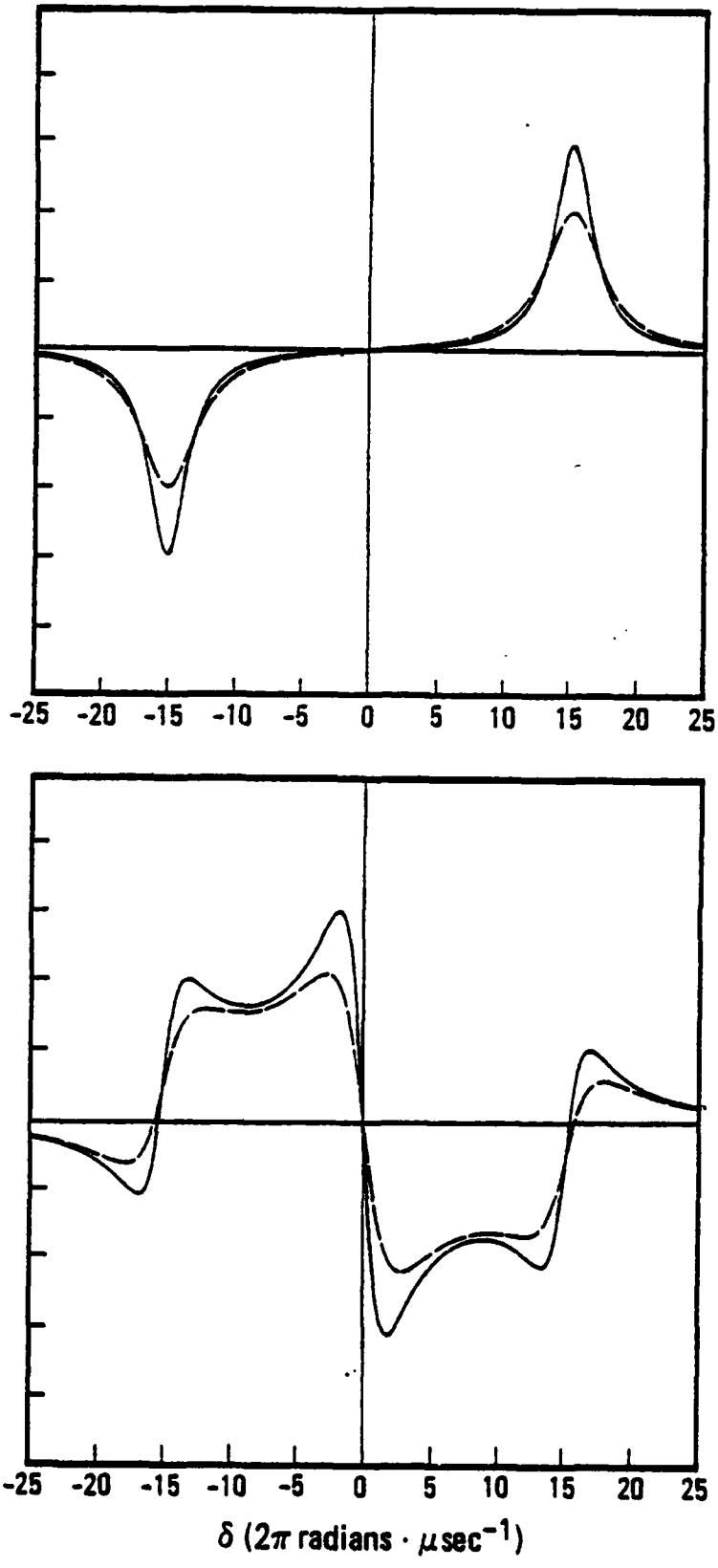

-25 -20 -15 -10 -5 0 5 10 15 20 25
-25 -20 -15 -10 -5 0 5 10 15 20 25
δ (2π radians · μsec⁻¹)

Figure 1.

Figure 4. Theoretical absorption (upper curve) and dispersion (lower curve) lineshapes for a Fabry-Perot cavity subjected to a phase-modulated laser beam where detection is in reflection, Eq. (4.12). The frequency axis $\Delta=\omega_o-\omega_r$. The transmission lineshape simply reverses sign as (4.13) indicates. Parameters: $\Omega=30$ (2π radians$\bullet\mu$sec^{-1}), and $\Gamma=1$ μsec^{-1}.

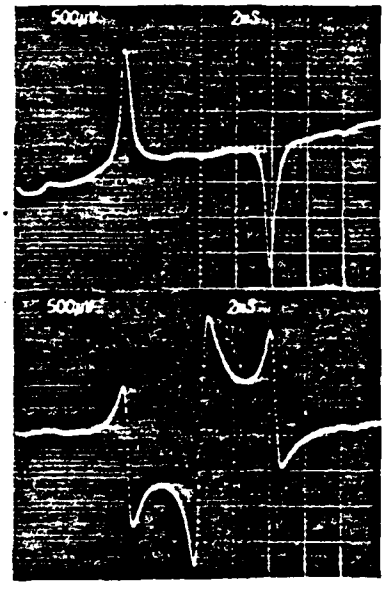


Figure 3. Observed I_2 absorption (upper) and dispersion (lower) lineshapes of the phase modulated probe beam. Compare Fig. 1.

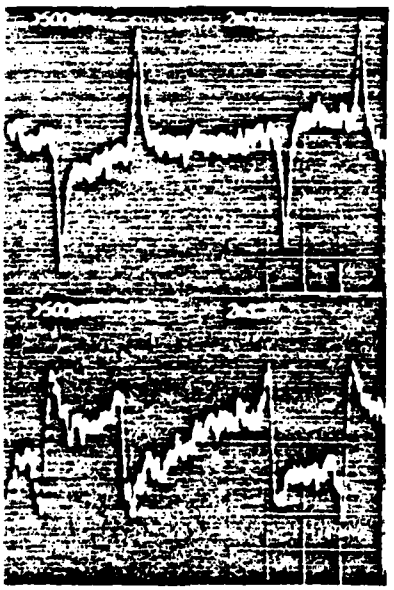


Figure 4. Observed I_2 absorption (upper) and dispersion (lower) lineshapes of the pump beam for the same transition shown in Fig. 3. Compare Fig. 2.

RJ 3597 (42143) 9/8/82
Physics

LASER SPECTROSCOPY OF SOLIDS*

Richard G. Brewer
Ralph G. DeVoe

IBM Research Laboratory
San Jose, California 95193, U.S.A.

ABSTRACT: Remarkably narrow optical homogeneous linewidths of the order of 1 kHz have now been observed in low temperature zero-phonon transitions of dilute impurity ion crystals, such as Pr^{3+} in LaF_3. Novel nonlinear optical resonance techniques have been devised for this purpose using ultrastable phase locked cw dye lasers where the measurements are performed either in the frequency domain (hole burning) or in the time domain (coherent optical transients). These studies effectively bring the Mossbauer effect into the optical region. Hence, the observed linewidths are no longer limited by inhomogeneous strain broadening (~5 GHz) or even by static local fields due to neighboring spins (~100 kHz). However, weak magnetic field fluctuations from local spins are readily detected. As an example, spin decoupling and line narrowing, which are well known in NMR, are observed in an optical transition of Pr^{3+}:LaF_3 at 2°K where the ^{19}F-^{19}F dipolar interaction is quenched and the optical linewidth drops from 10 to 2 kHz, clearly demonstrating the spin broadening mechanism. Results will be discussed in terms of a Monte Carlo line broadening theory.

---

*This work is supported in part by the U.S. Office of Naval Research.

INTRODUCTION

Solids have long played an important role in the development of laser physics. Indeed, the first laser was a solid state device, namely, Maiman's ruby laser.[1] Shortly thereafter the field of nonlinear optics commenced when Franken et al.[2] transformed a ruby laser beam into its second harmonic by passing it through a quartz crystal. And the first coherent optical transient effect, the photon echo, was detected later in ruby by Hartmann et al.[3]

Laser spectroscopy,[4] on the other hand, has been concerned largely with atomic and molecular systems in the gas phase, and it is only recently that the new techniques of laser spectroscopy have been applied to solids. Within the last three years, for example, it has become clear that the optical homogeneous linewidths of certain rare earth impurity ion crystals can be exceedingly narrow, the order of 1 kilohertz or less.[5-7] These zero phonon transitions are the optical analogs of the Mossbauer effect. Such narrow linewidths suggest a number of new precision measurements, either in the time or frequency domain. In the time domain, coherent transients can be examined to reveal new aspects of the dynamic interactions occurring in solids. In the frequency domain, the structural details of solids can be probed as in nuclear magnetic resonance. Also, the possibility of developing solid state optical clocks exists and with it the potential for testing fundamental theories, such as the general theory of relativity.

In this article, I will restrict the discussion to recent dynamic studies of the optically active impurity ion Pr^{3+} in a host crystal of LaF_3 at ~2°K. This study tests our understanding of the Pr^{3+} optical linebroadening and dephasing mechanisms, which are largely magnetic in origin, through such experimental optical techniques as free induction decay[5] and magic angle line narrowing.[6] This work has advanced recently to a new level of precision due to the development of a highly stable tunable ring dye laser that possesses a

linewidth of about 300 Hertz.[8] On the theoretical side, our success with Monte Carlo calculations of linebroadening in Pr^{3+}:LaF_3 will be reviewed.[9] Even more recently, we have been encouraged by an analytic treatment which explains the main features of linebroadening in this impurity ion solid and reveals as well limitations in the use of the optical Bloch equations for the case of solids.[10]

FREE INDUCTION DECAY THEORY

The two most important methods for measuring optical dephasing times have been the photon echo[3] and free induction decay (FID),[11] which we now consider. The simplest model is that of a collection of two-level atoms which are resonantly excited (prepared) by a coherent light wave. The atoms thereby are transformed from an initial stationary state to a superposition or mixed state which displays a time-dependent behavior both during the preparation stage and afterwards. Once the excitation is removed, the system freely radiates a coherent beam of light in the forward direction–the free induction decay effect. The atoms are perturbed of course by various time-dependent interactions which get them out of phase and produce a damped emission. An example of FID in Pr^{3+}:LaF_3 is shown in Figure 1.

BLOCH EQUATIONS

To interpret the observed decay rate, various theoretical models can be applied. We begin with the Schrödinger equation of motion in density matrix form

$$i\hbar\dot{\rho} = [H,\rho] + \text{relaxation terms} \qquad (1)$$

which will be used to derive Bloch equation solutions[12] for a two-level atomic system before proceeding to more advanced cases. The Hamiltonian

$$H = H_0 + H_1$$

contains the free atom part H_0 with eigenenergies

$$E_i = \hbar\omega_i \quad (i = 1,2)$$

where $\omega_{21} = \omega_2 - \omega_1$ and the index 2 labels the upper state and 1 the lower state. In the presence of a light wave

$$E(z,t) = E_0 \cos(\Omega t - kz),$$

the atom undergoes a transition $1 \leftrightarrow 2$ due to the atom-field interaction

$$H_1 = -\mu \cdot E(z,t)$$

where the electric dipole matrix element is

$$\mu_{12} = \langle 1 | \mu | 2 \rangle .$$

The equations of motion for the slowly varying terms become

$$\dot{\tilde{\rho}}_{12} = (-1/T_2 + i\Delta)\tilde{\rho}_{12} + \frac{1}{2} i\chi(\rho_{22} - \rho_{11}) \tag{2a}$$

$$\dot{\rho}_{22} - \dot{\rho}_{11} = -(\rho_{22} - \rho_{11})/T_1 + (\rho^{\circ}_{22} - \rho^{\circ}_{11})/T_1 + i\chi(\tilde{\rho}_{12} - \tilde{\rho}_{21}) \tag{2b}$$

with the definition

$$\rho_{12} = \tilde{\rho}_{12} e^{i(\Omega t - kz)}$$

and neglecting nonresonant terms. Here, the Rabi frequency χ and the tuning parameter Δ are defined by

$$\chi = \mu_{12} E_0/\hbar \text{ and } \Delta = -\Omega + \alpha + \omega_{21}$$

where α is a shift in the transition frequency ω_{21} due to an inhomogeneity in the local environment, i.e., static magnetic or crystalline Stark fields in the case of Pr^{3+}:LaF_3.

In the optical Bloch model, the decay behavior is introduced in (2) by phenomenological population and dipole decay times T_1 and T_2 as in NMR. Thus, with the definitions

$$u = \tilde{\rho}_{12} + \tilde{\rho}_{21}\ ,\ v = i(\tilde{\rho}_{21} - \tilde{\rho}_{12}),\ \text{and}\ w = \rho_{22} - \rho_{11}\ ,$$

we cast (2) into the Bloch equation[13]

$$\frac{dB}{dt} = \beta \times B$$

which describes a precessional motion of the Bloch vector B about an effective field β with components

$$B = iu + jv + kw\ ,$$

$$\beta = i\chi + k\Delta\ .$$

This is mathematically equivalent to a spin precessing in a magnetic field.[14]

Bloch equation solutions are derived from (2) using a Laplace transform technique[15] and yield for the steady-state preparation

$$\tilde{\rho}_{12}(0) = \frac{i\chi(-i\Delta + 1/T_2)(\rho^{\circ}_{22} - \rho^{\circ}_{11})/2}{\Delta^2 + 1/T_2^2 + \chi^2 T_1/T_2}\ . \qquad (3)$$

At time t=0, the excitation ends and the FID begins because the laser frequency is switched suddenly to a new value ($\Omega \rightarrow \Omega'$). The FID solution follows from (2a) as

$$\tilde{\rho}_{12}(t) = \tilde{\rho}_{12}(0)e^{(-1/T_2 + i\Delta)t}\ ,\quad t>0\ . \qquad (4)$$

The FID expressed as a field amplitude

$$E_{12}(z,t) = \tilde{E}_{12}(z,t)e^{i(\Omega t - kz)} + \text{c.c.}$$

obeys Maxwell's wave equation

$$\frac{\partial \tilde{E}_{12}}{\partial z} = -2\pi ikN\mu_{12}\langle\tilde{\rho}_{12}(t)\rangle \tag{5}$$

where the bracket

$$\langle\tilde{\rho}_{12}(t)\rangle = \frac{1}{\sqrt{\pi}\sigma}\int_{-\infty}^{\infty} g(\Delta)\rho_{12}(\Delta,t)d\Delta \tag{6}$$

denotes an average over a Gaussian inhomogeneous lineshape $g(\Delta) = e^{-(\Delta/\sigma)^2}$. The observed FID signal appears as a heterodyne beat

$$F(t) = \frac{1}{2}E_0\tilde{E}_{12}e^{i(\Omega-\Omega')t} + \text{c.c.} \tag{7}$$

due to the laser frequency switch $\Omega\rightarrow\Omega'$ at t=0, a process which terminates the excitation of the initially prepared packet and allows sensitive detection of the free precession signal with low noise. Omitting trivial factors, the resulting FID Bloch solution is of the form

$$F(t) \sim \chi^2\Big(1-\frac{1}{\sqrt{1+\chi^2T_1T_2}}\Big)e^{-(t/T_2)(1+\sqrt{1+\chi^2T_1T_2})}\cos(\Omega-\Omega')t\,. \tag{8}$$

The preexponential factor displays a nonlinear intensity dependence in contrast to NMR where FID is a first order process due to the small inhomogeneous broadening. Similarly, the damping term in (8) exhibits power broadening through the term $\chi^2T_1T_2$ where $T_1>>T_2$ in Pr^{3+}:LaF_3. In the limit $\chi^2T_1T_2<<1$, the decay time becomes $\frac{1}{2}T_2$.

While the Bloch theory has played an important role in NMR and quantum optics, it also is limited in that it ignores the details of the basic dipolar interactions such as Pr^{3+}–F and F–F which broaden the Pr^{3+} optical transition. It also ignores the presence of a frozen core of fluorine nuclei surrounding each Pr^{3+} ion, the LaF_3 crystal structure, and the dependence of linewidth on the Pr^{3+} (I=5/2) magnetic substrate. Before considering the

Monte Carlo calculation which overcomes these difficulties, let us consider the current status of the experiments.

FREE INDUCTION DECAY EXPERIMENTS

The optical Pr^{3+} transition of interest is $^3H_4 \rightarrow {}^1D_2$ which lies conveniently in the yellow region at 5925Å. Due to the low electric field site symmetry (C_2), all electronic degeneracy is removed. Thus, for the ground electronic state $^3H_4$, there are $2J+1=9$ Stark split *singlet* states with splittings of order 50 cm^{-1}. Consequently, as noted by Bleaney[16] and by Teplov,[17] all first order magnetic hyperfine interactions vanish in the absence of an external magnetic field. The nuclear quadrupole interaction and the second order magnetic dipole hyperfine interaction generate three doubly degenerate hyperfine states for each Stark split singlet ($I_z = \pm 5/2$, $\pm 3/2$ and $\pm 1/2$ since $I=5/2$) with splittings of the order of 10 MHz. Only the lowest crystal field Stark split states of $^3H_4 \rightarrow {}^1D_2$, the zero phonon line, are examined. Hence, three equally intense optical transitions occur, $I''_z \leftrightarrow I'_z = \pm 5/2 \leftrightarrow \pm 5/2$, $\pm 3/2 \leftrightarrow \pm 3/2$, and $\pm 1/2 \leftrightarrow \pm 1/2$, and overlap because of the large inhomogeneous strain broadening of ~5 GHz.

The technique for observing optical FID relies on laser frequency switching[18] as shown in Figure 2.[5] The external beam of a phase-locked cw ring dye laser of high frequency stability passes through an acousto-optic modulator prior to exciting a 0.1 at.% $Pr^{3+}:LaF_3$ crystal which is immersed in liquid helium at ~1.6°K. A single packet of Pr^{3+} ions within the inhomogeneous lineshape is coherently prepared by a laser beam (~5 mW at the crystal) when the modulator is driven by a 110 MHz rf source which is gated on for a 400 μsec period. FID follows when the rf frequency is switched suddenly from 110 to 108 MHz and is detected by a photodiode as a 2 MHz heterodyne beat signal in transmission.

LASER PHASE LOCKING

To detect ultraslow dephasing times by FID, the laser frequency must remain fixed within the Pr^{3+} homogeneous linewidth for the preparation interval ~T_2, otherwise the observed decay merely reflects laser frequency jitter. Figure 3 shows a phase modulation technique for phase/frequency locking a ring dye laser to a reference cavity. The method, which was proposed by Drever, has yielded laser linewidths as narrow as ~100 Hertz.[19,8] A part of the external beam of the laser is phase modulated by passing it through an electro-optic crystal that is driven continuously by a 40 MHz rf generator, and the beam then strikes an acoustically isolated 50 cm confocal reference cavity having a 1.5 MHz bandwidth. The laser field now contains pairs of sidebands located symmetrically about the center frequency. When the center frequency coincides with a mode of the reference cavity, the central component will be stored in the cavity for its ringing time while the sidebands will be reflected at the end mirror. For this condition, the reflected light and some of the stored light which leaks out of the cavity will produce at a photodiode two heterodyne beats of opposite phase which just cancel. If, however, the laser phase or frequency fluctuates, this balanced condition will be upset because the stored light retains memory of the laser's frequency at a previous instant while the reflected light monitors the instantaneous laser frequency. In this circumstance, the two heterodyne beat signals no longer cancel but produce an error signal in a fast high gain servo loop that drives the laser frequency to a stable operating point.

Important advantages of this method are (1) Laser amplitude noise can be reduced to the shot noise limit because the beat frequency can be selected in a region where the laser noise is low and because the balancing technique automatically eliminates laser noise not associated with the error signal. (2) The response time of the optical cavity is fast in the

reflection mode allowing a large servo loop bandwidth and thus a narrow laser linewidth. (3) The heterodyne beat error signal can be monitored in a dispersion mode (Figure 4) which offers a sharp discriminant and locates the lock point at zero amplitude, independent of the size of the error signal. In Figure 4, the phase-locked laser beam is monitored with a second 50 cm confocal cavity and shows that the laser linewidth is no larger than 300 Hertz rms.

The phase modulation technique can be used also for detecting low amplitude noise lineshapes (hole-burning) under steady-state conditions as demonstrated initially by Bjorklund.[20,21] In combination with a laser of high frequency stability, extraordinarily high resolution optical studies can now be performed in solids.

DATA ACQUISITION

The realization of tunable lasers of high frequency stability, assures that FID or other coherent transients with long optical dephasing times can be monitored reproducibly with high precision. Figure 1 shows the excellent fit of a damped cosine function which is overlayed on 400 experimental points of the Pr^{3+}:LaF_3 data. In fact, the two curves cannot be distinguished and the residuals indicate that the decay time can be determined to an uncertainty of less than 1%. The experimental points were acquired from an analog signal using a transient digitizer, and the data was stored in an IBM Personal Computer and then transferred to an IBM 3033 computer for least squares analysis, graphics or other data handling.

MAGIC ANGLE LINE NARROWING

The FID technique offers a way of measuring the optical homogeneous linewidths of a solid such as Pr^{3+}:LaF_3 without the influence of inhomogeneous broadening. Thus, in

Figure 1 the linewidth is about 10 kHz HWHM, i.e., about the same magnitude as that encountered in NMR. What is the broadening mechanism? The $^1D_2$ radiative lifetime of 0.5 msec sets a limiting value of 160 Hertz HWHM; phonon-ion interactions at 1.6°K are negligible at this point in time as are $Pr^{3+}-Pr^{3+}$ interactions in the dilute samples studied. The dominant effect is the fluctuating part of the Pr–F magnetic dipolar interaction.

The dipolar mechanism has been demonstrated convincingly by an optical magic angle line narrowing experiment[6] which we now discuss. The pulse sequence is shown in Figure 5 and involves not only laser frequency switching for producing FID but the simultaneous application of an rf pulse in near resonance with ^{19}F nuclei. The basic idea is that pairs of F nuclei throughout the crystal undergo mutual spin flips which produce a fluctuating magnetic field at each Pr^{3+} site. The $^1D_2$ and $^3H_4$ states of Pr^{3+} fluctuate in energy correspondingly and thus the optical transition broadens. With a suitable rf field applied, the F precessional motion about its effective field tends to average out the F–F dipolar interaction and as a result the Pr–F dipolar interaction is quenched (see Figure 6). This effect can be viewed as a kind of motional narrowing. A detailed theory, which is given elsewhere,[6] predicts that the Pr^{3+} linewidth is given by

$$\Delta\nu(\beta) = \Delta\nu(0) \cos\beta \cdot \frac{1}{2}(3\cos^2\beta - 1) \qquad (9)$$

where $\beta=\tan^{-1}(\gamma_F B_x/\Delta_F)$ is the angle that the effective field of the F nucleus makes with the z axis in its rotating frame, B_x being the rf field amplitude. From (9), we see that the Pr^{3+} linewidth should drop to zero when $\beta=\pi/2$, the F resonance condition, and $\beta=\cos^{-1}\left(\frac{\sqrt{3}}{3}\right)$, the magic angle condition. In practice, the linewidth drops from 10 to 2 kHz, but the measurements should be repeated using the improved phase locked laser to determine the origin of the residual width. Figure 7 shows that the experimental results

gree rather well with Eq. (9) and thus unequivocally verifies the magnetic dipolar roadening mechanism.

ONTE CARLO THEORY[9]

We now require a more detailed theory of linebroadening than the simplistic T_1, T_2 lescription of the Bloch equations. We first replace Eq. (2a) by

$$\dot{\tilde{\rho}}_{12} = (-\gamma + i(\Delta + \delta\omega(t))\tilde{\rho}_{12} + \frac{1}{2} i\chi(\rho_{22}-\rho_{11}) \tag{10}$$

where the Pr^{3+} transition frequency fluctuates as

$$\delta\omega(t) = -(\gamma_I'-\gamma_I'')\gamma_s\hbar\sum_k \frac{3\cos^2\theta_k - 1}{r_k^3} I_k S_{kz}(t) \tag{11}$$

lue to random flipping of the fluorine spin $S_z(t)$ arising from F−F mutual spin flips which ıffect the secular part of the Pr−F dipolar interaction. Here, the F spin is labeled S and the ³r spin I, the population decay term $\gamma = \frac{1}{2}(\gamma_1 + \gamma_2)$, and the gyromagnetic ratio of the $^1D_2$ ınd $^3H_4$ states are γ_I' and γ_I''. The FID solution of (10) now assumes the form

$$\langle\tilde{\rho}_{12}(t)\rangle = \langle\tilde{\rho}_{12}(0) \exp\left[(-\gamma + i\Delta)t + i\int_0^t \delta\omega(t')dt'\right]\rangle . \tag{12}$$

The quantity $\tilde{\rho}_{12}(t)$ involves the phase history of a single Pr^{3+} ion and therefore must be ıveraged over the distribution of frequency fluctuations occurring at different Pr^{3+} sites both luring the preparative period $t\leq 0$ and afterward $t\geq 0$. In addition, averages are to be ɔerformed over the local inhomogeneous static magnetic and crystalline Stark fields.

The following assumptions enter into the calculation. (1) The sudden jump ıpproximation of the kth fluorine spin $S_{kz}(t)$ assumes that it can have only two values $+1/2$ ınd $-1/2$ and that it jumps instantaneously between these two values at random times and

itions in the lattice at an average rate W. (2) The LaF_3 crystal structure ($P3Cl-D_{3d}^3$) is umed for the nearest 125 unit cells (2250 fluorines) surrounding a Pr site. (3) The c axis the LaF_3 crystal is parallel to an external magnetic field. (4) The number of fluorine spin s per unit time follows a Poisson distribution.

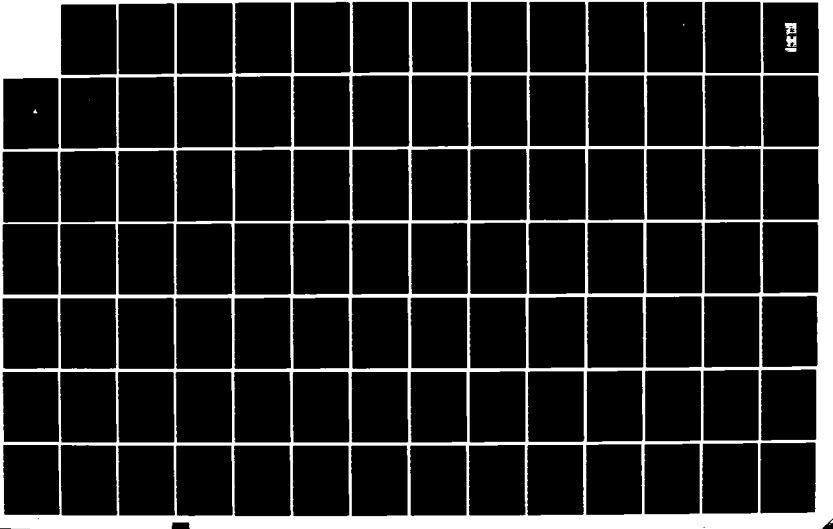
The resulting computer program is not only capable of generating the Pr^{3+} optical nogeneous linewidth but the static magnetic inhomogeneous linewidth as well. Table 1 nmarizes these calculations and the current experimental results. For an rf transition of $^3H_4$ Pr^{3+} ground state, a value of 82 kHz is obtained for the inhomogeneous magnetic adening which compares favorably to a Van Vleck second moment calculation and to tically detected rf measurements for external fields in excess of the local field of 16G.

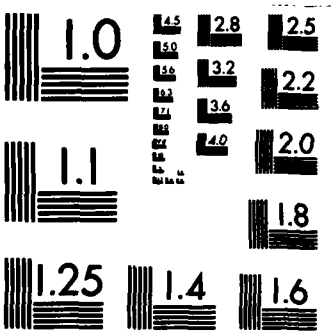
Notice in Figure 8 that the optical dephasing time is rather insensitive to the assumed orine mean flip time T. Actually, the parameter T need not be assumed, but rather it can calculated from the method of moments[24] to be $T \sim 10T_2 = 170$ μsec which yields a μsec (16.8 kHz) dephasing time compared to the experimental value 15.8 μsec).1 kHz). The agreement is unusually good by the standards of previous theories nsidering that the discrepancy is only 15%.

Other conclusions emerge from these studies largely due to the fact that only a few orine nuclei, those close to the Pr^{3+} site, are found to contribute to optical dephasing. r example, our lattice size of 2250 fluorine is about two orders of magnitude larger than essary. Secondly, the small number of fluorines required implies that correlations ween nearby fluorines do not strongly affect the optical linewidth. Thirdly, the static $^{3+}$ magnetic moment can polarize the nearest neighbor fluorines and detune them from the k fluorines so that they are incapable of undergoing spin flips. This frozen core effect,

AD-A154 708 NONLINEAR SPECTROSCOPY(U) IBM RESEARCH LAB SAN JOSE CA 5/6
R G BREWER 20 MAR 85 N00014-78-C-0246

UNCLASSIFIED F/G 20/6 NL





MICROCOPY RESOLUTION TEST CHART
NATIONAL BUREAU OF STANDARDS-1963-A

which is well known in ESR, reduces the Pr^{3+} linewidth from the value it would have if the nearest neighbors were also flipping. Inclusion of the frozen core model in the Monte Carlo calculation shows, contrary to intuition, that the optical linewidth varies slowly with the Pr^{3+} magnetic moment $\mu_z^{Pr} = \gamma_I I_z \hbar$ or magnetic substrate I_z.

GAUSSIAN MODULATION MODEL

Very recently, we have attempted to obtain analytic solutions for the optical dephasing problem using a Gaussian modulation model. This approach, which will be reported elsewhere,[10] has enjoyed some success and should be a useful method in the future for describing the nature of optical dephasing in these many body systems.

TABLE 1. Linewidths of ^{141}Pr in LaF_3 Due to Magnetic Broadening

Transition	Method	Linewidth FWHM (kHz)
		Inhomogeneous
rf($\Delta I''_z = \pm 1$)	Monte Carlo theory	82
	Van Vleck second moment	84.5
	cw rf-optical double resonance[22]	
	$I''_z = 1/2 \rightarrow 3/2$	$180 \pm 10^a (\sim 100)^b$
	$I''_z = 3/2 \rightarrow 5/2$	$200 \pm 10^a (\sim 100)^b$
	Optically detected rf transients[23]	
	$I''_z = 3/2 \rightarrow 5/2$	230 ± 25^a
		Homogeneous
optical ($^3H_4 \leftrightarrow {}^1D_2$) ($\Delta I_z = 0$)	Monte Carlo theory	16.8
	FID experiment[5]	20.2^b

[a]Earth's magnetic field
[b]Static external field ≥16G

REFERENCES

1. T. H. Maiman, Nature 187, 493 (1960).
2. P. A. Franken, A. E. Hill, C. W. Peters and G. Weinrich, Phys. Rev. Lett. 7, 118 (1961).
3. N. A. Kurnit, I. D. Abella and S. R. Hartmann, Phys. Rev. Lett. 13, 567 (1964).
4. See for example Laser Spectroscopy V, edited by A. R. W. McKeller, T. Oka and B. P. Stoicheff (Springer-Verlag, New York, 1981).
5. R. G. DeVoe, A. Szabo, S. C. Rand and R. G. Brewer, Phys. Rev. Lett. 42, 1560 (1979).
6. S. C. Rand, A. Wokaun, R. G. DeVoe and R. G. Brewer, Phys. Rev. Lett. 43, 1868 (1979).
7. R. M. Macfarlane, R. M. Shelby and R. L. Shoemaker, Phys. Rev. Lett. 43, 1726 (1979).
8. R. G. DeVoe and R. G. Brewer (unpublished).
9. R. G. DeVoe, A. Wokaun, S. C. Rand and R. G. Brewer, Phys. Rev. B23, 3125 (1981).
10. E. Hanamura, R. G. DeVoe and R. G. Brewer (to be published).
11. R. G. Brewer and R. L. Shoemaker, Phys. Rev. A6, 2001 (1972).
12. R. G. Brewer in Frontiers in Laser Spectroscopy, Les Houches Lectures (North-Holland, New York, 1977), p. 341.
13. F. Bloch, Phys. Rev. 70, 460 (1946).
14. R. P. Feynman, F. L. Vernon and R. W. Hellwarth, J. Appl. Phys. 28, 49 (1957).
15. A. Schenzle and R. G. Brewer, Phys. Rev. A14, 1756 (1976).
16. B. Bleaney, Physica (Utrecht) 69, 317 (1973).

17. M. A. Teplov, Zh. Eksp. Teor. Fiz. 53, 1510 (1967) [Sov. Phys. JETP 26, 872 (1968)].

18. A. Z. Genack and R. G. Brewer, Phys. Rev. A17, 1463 (1978); R. G. Brewer and A. Z. Genack, Phys. Rev. Lett. 36, 959 (1976).

19. R. W. P. Drever, J. L. Hall, F. V. Kowalski, J. Haugh, G. M. Ford and A. Munley (unpublished).

20. G. C. Bjorklund, Opt. Lett. 5, 15 (1980); G. C. Bjorklund and M. D. Levenson, Phys. Rev. A24, 166 (1981).

21. The theory of phase modulation laser spectroscopy is described in A. Schenzle, R. G. DeVoe and R. G. Brewer, Phys. Rev. A25, 2606 (1982).

22. L. E. Erickson, Phys. Rev. B16, 4731 (1977).

23. R. M. Shelby, C. S. Yannoni and R. M. Macfarlane, Phys. Rev. Lett. 41, 1739 (1978).

24. N. Bloembergen, Physica (Utrecht) 15, 386 (1949); I. J. Lowe and S. Gade, Phys. Rev. 156, 817 (1967).

FIGURE CAPTIONS

Figure 1. A computer plot of 400 points of optical FID of 0.1 at.% Pr^{3+}:LaF_3 at 1.6°K. The experimental data are overlayed on a damped cosine, and the residuals indicate that the dephasing time of 5.10 μsec has an uncertainty of less than 1%. The signal is power broadened.

Figure 2. Acousto-optic modulator laser frequency switching technique for observing coherent optical transients such as FID and photon echoes.

Figure 3. Schematic of apparatus for phase-locking a cw ring dye laser. The sample and detection circuit to the right show how narrow hole burning signals can be detected by phase modulation spectroscopy with basically the same apparatus.

Figure 4. Top two traces: Experimental dispersive lineshape of a phase-locked laser beam (40 MHz modulation frequency) as seen by a frequency swept 50 cm confocal cavity in reflection. The laser beam is phase locked to a second 50 cm cavity and exhibits in the third trace, where the first cavity is not swept, a 300 Hz rms laser linewidth.

Figure 5. Magic angle pulse sequence showing the laser field frequency shift and the F spin decoupling radio frequency field with time. The Pr^{3+} ions are coherently prepared by the laser field in the initial 200 μsec interval and then exhibit optical FID when the laser frequency is suddenly switched 2 MHz at t=200 μsec.

Figure 6. Optical FID in 0.1% Pr^{3+}:LaF_3 at 1.8°K in the presence of a static magnetic field B_0=130G±c axis: (a) with no rf field where T_2=15.6 μsec (10.2 kHz) and (b) under magic angle conditions with an rf field B_x=25G where T_2=66 μsec (2.4 kHz).

Figure 7. Pr^{3+} optical linewidth versus angle β expressed in degrees. Solid circles: experimental points for the case B_0 = 130G ∥ c axis and B_x = 25G. Solid curve: Eq. (9) with frequency offset of 3 kHz included for residual broadening.

Figure 8. The Pr^{3+} optical dephasing time versus the fluorine mean flip time T. The optical FID result is 15.8 μsec and the theoretical fluorine spin flip time T=170 μsec.

FIGURE CAPTIONS

Figure 1. A computer plot of 400 points of optical FID of 0.1 at.% Pr^{3+}:LaF_3 at 1.6°K. The experimental data are overlayed on a damped cosine, and the residuals indicate that the dephasing time of 5.10 μsec has an uncertainty of less than 1%. The signal is power broadened.

Figure 2. Acousto-optic modulator laser frequency switching technique for observing coherent optical transients such as FID and photon echoes.

Figure 3. Schematic of apparatus for phase-locking a cw ring dye laser. The sample and detection circuit to the right show how narrow hole burning signals can be detected by phase modulation spectroscopy with basically the same apparatus.

Figure 4. Top two traces: Experimental dispersive lineshape of a phase-locked laser beam (40 MHz modulation frequency) as seen by a frequency swept 50 cm confocal cavity in reflection. The laser beam is phase locked to a second 50 cm cavity and exhibits in the third trace, where the first cavity is not swept, a 300 Hz rms laser linewidth.

Figure 5. Magic angle pulse sequence showing the laser field frequency shift and the F spin decoupling radio frequency field with time. The Pr^{3+} ions are coherently prepared by the laser field in the initial 200 μsec interval and then exhibit optical FID when the laser frequency is suddenly switched 2 MHz at t=200 μsec.

Figure 6. Optical FID in 0.1% Pr^{3+}:LaF_3 at 1.8°K in the presence of a static magnetic field B_0=130G$\pm$c axis: (a) with no rf field where T_2=15.6 μsec (10.2 kHz) and (b) under magic angle conditions with an rf field B_x=25G where T_2=66 μsec (2.4 kHz).

Figure 7. Pr^{3+} **optical linewidth versus angle** β **expressed in degrees. Solid circles: experimental points for the case** $B_0 = 130G \parallel$ **c axis and** $B_x = 25G$**. Solid curve: Eq. (9) with frequency offset of 3 kHz included for residual broadening.**

Figure 8. The Pr^{3+} **optical dephasing time versus the fluorine mean flip time T. The optical FID result is 15.8** μ**sec and the theoretical fluorine spin flip time T=170** μ**sec.**

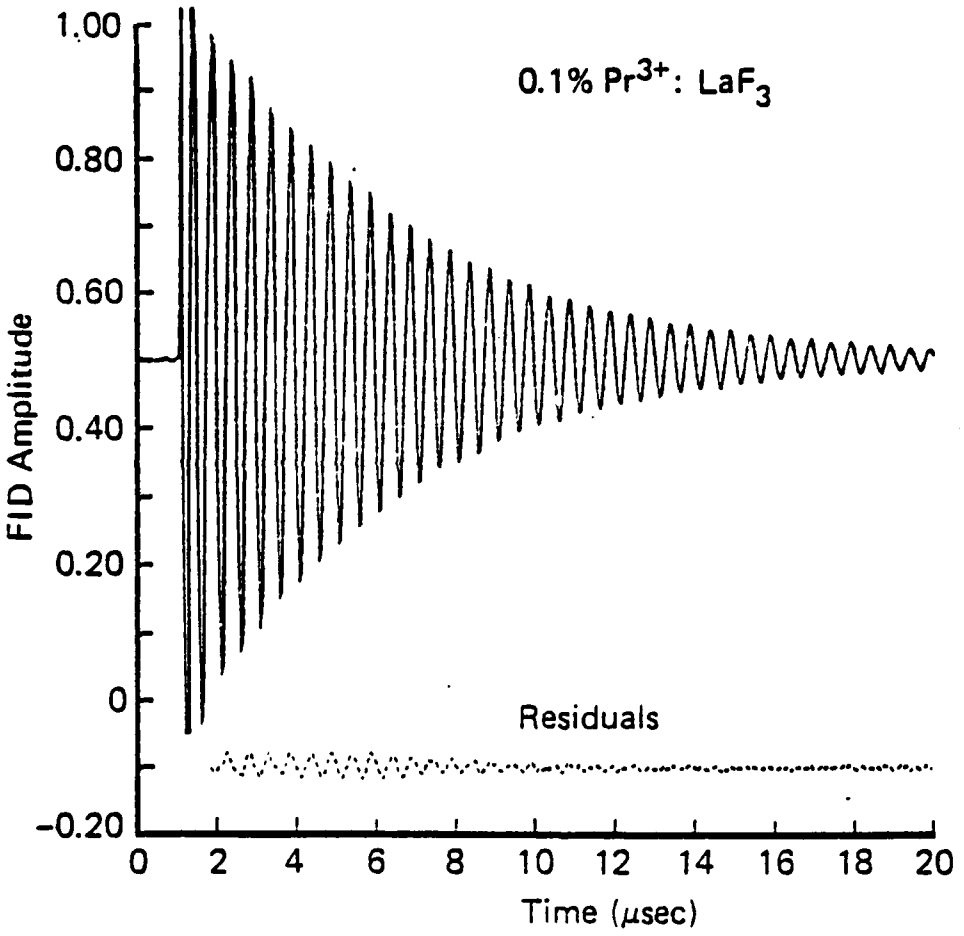

1.00
0.80
0.60
0.40
0.20
0
-0.20
FID Amplitude
0.1% Pr^{3+}: LaF_3
Residuals
0
2
4
6
8
10
12
14
16
18
20
Time (μsec)

Figure 1

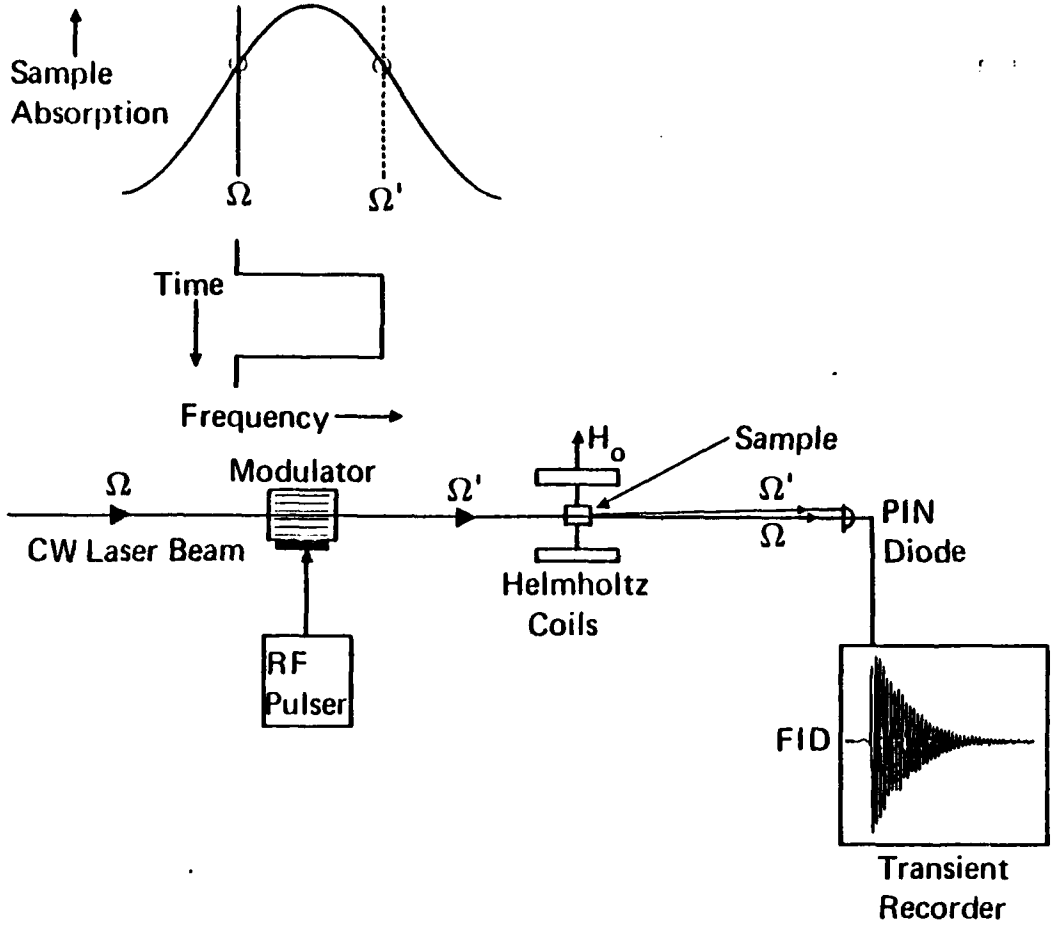


Figure 2
(Brewer)

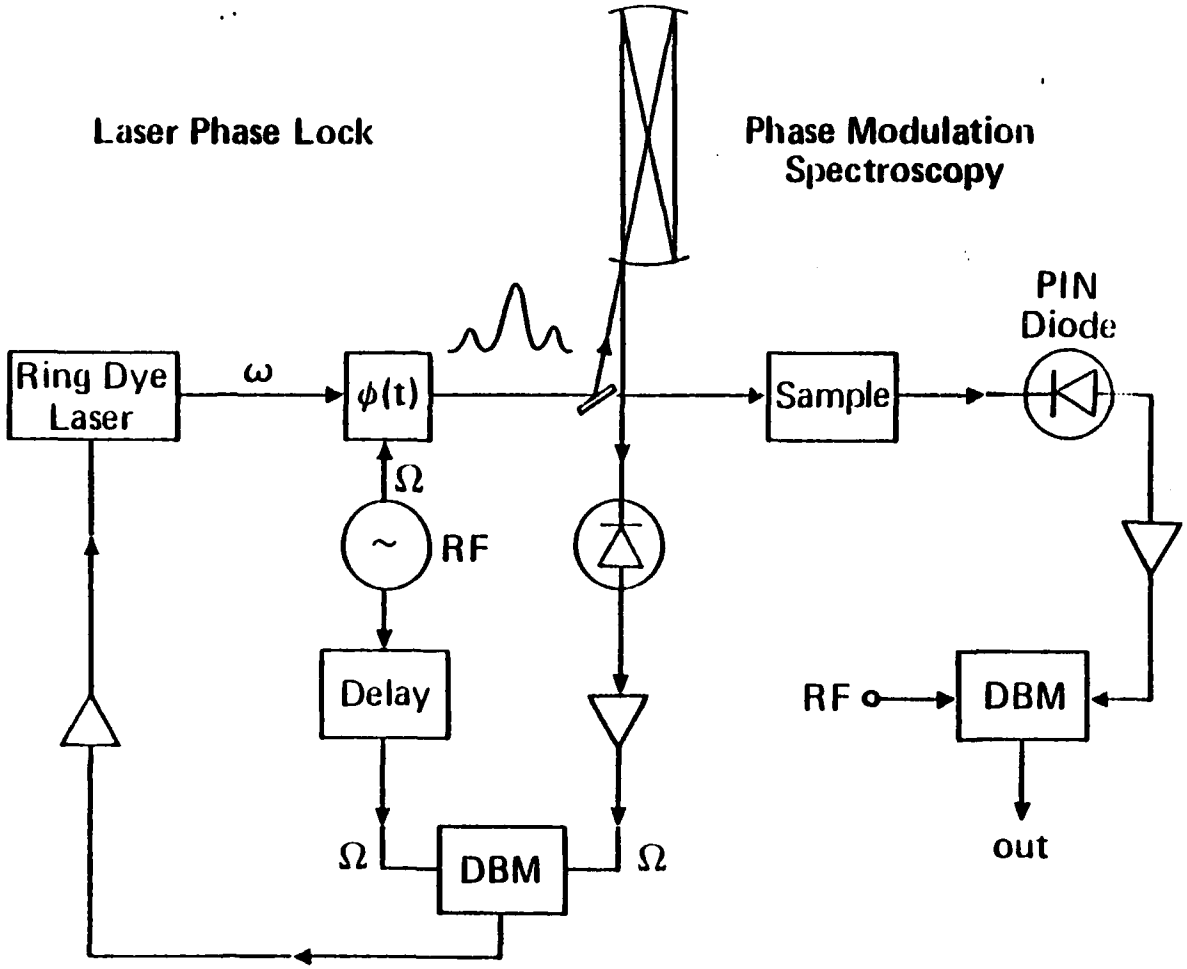


Figure 3 (Brewer)

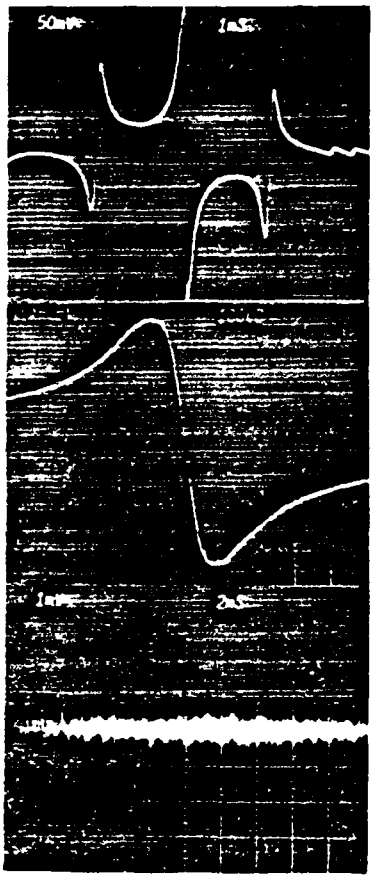


Figure 4
(Brewer)

FIGURE CAPTIONS

Figure 1. Raman heterodyne NMR signals of the Pr^{3+}:LaF_3 $^3H_4$ ground state spin transitions (a) I_z=1/2↔3/2 in absorption and (b) 3/2↔5/2 in absorption and dispersion for H_0~0G.

Figure 2. Schematic of the experimental arrangement for Raman heterodyne detection of cw or pulsed NMR.

Figure 3. Computer plot of Raman heterodyne detection of spin echoes for (a) the $^3H_4$ (3/2↔5/2) spin transition where H_0≃0G, H_1=12G, the pulsed delay time τ=15 μsec, and the rf pulse widths are 1.8 and 3.0 μsec and (b) the $^1D_2$ (3/2↔5/2) spin transition where H_0=43G, H_1=23G, τ=50 μsec, and the rf pulse widths are 3 and 4 μsec. In (b), the echo envelope is amplified ~10× and an arrow marks its center.

REFERENCES

* On leave from the Institute für Angewandte Physik, Universität Hannover, Hannover, West Germany.

1. R. G. Brewer and R. L. Shoemaker, *Phys. Rev. Lett.* **27**, 631 (1971); R. G. Brewer and A. Z. Genack, *Phys. Rev. Lett.* **36**, 959 (1976).
2. R. L. Shoemaker and R. G. Brewer, *Phys. Rev. Lett.* **28**, 1430 (1972); R. G. Brewer and E. L. Hahn, *Phys. Rev. A* **8**, 464 (1973).
3. M. D. Levenson, Introduction to Nonlinear Laser Spectroscopy (Academic Press, New York, 1982), p. 17 and references therein.
4. B. S. Mathur, H. Tang, R. Bulos and W. Happer, *Phys. Rev. Lett.* **21**, 1035 (1968).
5. K. Chiang, E. A. Whittaker and S. R. Hartmann, *Phys. Rev. B* **23**, 6142 (1981); E. A. Whittaker and S. R. Hartmann, *Phys. Rev. B* **26**, 3617 (1982).
6. S. R. Hartmann, *IEEE J. Quantum Electron* **4**, 802 (1968); P. Hu, S. Geschwind and T. M. Jedju, *Phys. Rev. Lett.* **37**, 1357 (1976).
7. L. E. Erickson, *Optics Communications* **21**, 147 (1977); K .K. Sharma and L. E. Erickson, *Phys. Rev. Lett.* **45**, 294 (1980).
8. R. M. Shelby, C. S. Yannoni and R. M. Macfarlane, *Phys. Rev. Lett.* **41**, 1739 (1978).
9. L. E. Erickson, *Phys. Rev. B* **16**, 4731 (1977).
10. Handbook of Mathematical Functions, edited by M. Abramowitz and I. Stegun (U.S. Government Printing Office, Washington D.C., 1968), p. 297; R. G. DeVoe and R. G. Brewer, *Phys. Rev. A* **20**, 2449 (1979).
11. R. G. DeVoe, A. Wokaun, S. C. Rand and R. G. Brewer, *Phys. Rev. B* **23**, 3125 (1981).
12. R. M. Macfarlane, R. M. Shelby and R. L. Shoemaker, *Phys. Rev. Lett.* **43**, 1726 (1979).
13. J. Mlynek, (to be published).

TABLE I

Raman detected quadrupole splittings (ν) and linewidths ($\nu_{1/2}$) for the lowest Stark split states of $^3H_4$ (ground state) and $^1D_2$ of Pr^{3+} (0.1 at %):LaF_3 in the earth's magnetic field.

$I_z \leftrightarrow I_z$	ν (MHz)	$\nu_{1/2}$ (kHz, FWHM)
$^3H_4$ (1/2↔3/2)	8.470±0.005	159±5
$^3H_4$ (3/2↔5/2)	16.677±0.003	160.5±1
$^3H_4$ (1/2↔5/2)	25.150±0.003	259±8
$^1D_2$ (1/2↔3/2)	3.724±0.006	46.5±1
$^1D_2$ (3/2↔5/2)	4.783±0.001	45.3±2.6

and 20±2 kHz for the $^1D_2$ (3/2↔5/2) and (1/2↔3/2) lines (H_0>30G). By comparison, rf-optical double resonance gives 19 kHz for the 16.7 MHz transition[8] and photon echo measurements[12] for $^3H_4 \leftrightarrow {}^1D_2$ yield 14 kHz. Furthermore, we can conclude using Table I that the magnetic homogeneous and inhomogeneous widths are comparable in the $^1D_2$ state whereas the inhomogeneous width dominates in the $^3H_4$ state. Very crudely, the excited and ground state inhomogeneous linewidths scale as γ_z. However, to understand these comparisons more fully and to relate them in a self-consistent way, we plan to extend our earlier Monte Carlo line broadening theory.[11]

This brief article touches but a few examples. It is clear, however, that the full range of cw and pulsed NMR experiments can now be explored with equal facility in normal and optically excited low temperature impurity ion solids. In addition to Pr^{3+}:LaF_3, similar measurements have been conducted on Pr^{3+}:$YAlO_3$ and atomic gases.[13]

We are indebted to D. Horne and K. L. Foster for technical aid. One of us (N.C.W.) acknowledges support of a Hertz Foundation Graduate Fellowship. This work was supported in part by the U.S. Office of Naval Research.

seems to depend in a complicated way on the optical pumping cycle, the rf sweep rate (range: 1 MHz/10 msec to 1 MHz/60 sec) and whether one or two hyperfine transitions are excited in the same sweep.

Table I summarizes the Pr^{3+} quadrupole splittings and amplitude linewidths observed in the earth's magnetic field. These values are uncertain by at most a few kHz and thus reduce the error in previous measurements[5,7-9] by a factor of 5 or more. The $^1D_2$ linewidths, compare favorably with Whittaker et al.[5] (60±20 kHz FWHM) and are significantly smaller than that of Erickson's (200±50 kHz)[9] which is limited by laser frequency stability. The $^3H_4$ values of Erickson[7] (180±10 kHz) and that of Shelby et al.[8] (230 kHz) appear to be power broadened. We find that the Table I linewidths decrease by ~30% when a dc field H_0>50G is applied, bringing them into closer agreement with our $^3H_4$ Monte Carlo (82 kHz) and second moment (84.5 kHz) calculations.[11] From the splittings and numerical eigenenergy solutions of the Pr^{3+} quadrupole Hamiltonian $\mathcal{H}_Q = D[I_z^2 - I(I+1)/3] + E(I_x^2 - I_y^2)$, we obtain for the $^3H_4$ state D=4.1795±0.0013 MHz and E=0.154±0.004 MHz (η=0.111±0.003) while for $^1D_2$ D=1.2921±0.0009 MHz and E=0.305±0.001 MHz (η=0.708±0.002).

We also have detected two-pulse spin echoes, as well as nutation and free induction decay, in each of the four quadrupole transitions. Figure 3 shows spin echoes for the $^3H_4$ (3/2↔5/2) transition in a dc magnetic field H_0~0G and for the $^1D_2$ (3/2↔5/2) line in a field H_0~50G that enhances the signal ~10× and produces interferences among the Zeeman split lines in the free induction decay following the initial two pulses and in the echo. *The $^1D_2$ excited state spin echoes are the first observations of this kind.* For a field H_0 parallel to the crystal a axis, the homogeneous linewidths ($1/\pi T_2$) FWHM derived from the spin echo dephasing times T_2 are 21±2 kHz for the $^3H_4$ (3/2↔5/2) line (H_0~0G) and 15±2

The experimental configuration of Fig. 2 can be used for both cw and pulsed NMR experiments. The cw beam of a Coherent 599 dye laser oscillating in the locked mode (linewidth: 4 MHz pp) at 5925Å excites the Pr^{3+} $^3H_4 \rightarrow {}^1D_2$ transition by propagating along the c axis of a 0.1 at % Pr^{3+}:LaF_3 crystal ($3.5 \times 3.5 \times 2$ mm^3) with a beam diameter of ~100 microns and power in the range 3 to 50 mW. Population loss by optical pumping is circumvented by laser frequency sweeping (sweep rate: 400 MHz/0.5 sec) within the 5 GHz optical inhomogeneous lineshape. Radio frequency fields up to 30 Gauss and in the range $\omega/2\pi = 3$ to 17 MHz are applied by a pair of small Helmholtz coils surrounding the crystal, as in Fig. 2, where both are immersed in a liquid helium cryostat at 1.6°K. The coherently generated Stokes and anti-Stokes fields result in a heterodyne beat signal of frequency $\omega = |\Omega - \Omega'|$ that is detected with a P-I-N diode and demodulated in a double balanced mixer to yield absorption or dispersion lineshapes, Fig. 1(b), according to the rf phase setting ϕ. Since the signals are large, video detection is feasible, and furthermore the noise level is *shot noise limited* because the heterodyne detection process, unlike previous optical-rf methods, selects a frequency window where the laser noise is $10^8\times$ lower than the dc level.

Most of the features predicted by Eq. (1) are verified for the $^3H_4$ and $^1D_2$ quadrupole transitions. Consider first the 16.7 MHz transition of Fig. 1(b) where (1) the $H_1E_1^2$ field dependence is obeyed in the region of negligible power broadening, (2) the predicted (open circles) and observed (solid line) linehapes are essentially Gaussian, and (3) both absorptive and dispersive lineshapes appear. The three-level model does not include, however, the effects of optical pumping and laser frequency sweeping which dramatically increase the Pr^{3+} population difference ($\rho_{22} - \rho_{11}$) above the unperturbed value of Eq. (1) and improve the signal strength. In contrast, the lineshape of Fig. 1(a) is not strictly Gaussian due largely to the appearance of a symmetrical pair of lobes in the wings of the line. This curious effect

corresponding to the 1↔3 and 2↔3 transitions. This action generates coherent Stokes and anti-Stokes fields which in lowest order yield a heterodyne beat signal of the form

$$|E|^2_{beat} = -a\chi\chi_1\chi_2(\rho^o_{22}-\rho^o_{11})$$

$$\times e^{-(\Delta/\sigma_\alpha)^2}\left[\cos\omega t \cdot \mathrm{Im}w\left(\frac{\Delta_{21}+i\gamma_{21}}{\sigma_\beta}\right)-\sin\omega t \cdot \mathrm{Re}w\left(\frac{\Delta_{21}+i\gamma_{21}}{\sigma_\beta}\right)\right] \qquad (1)$$

where $a=\pi^2 kNL\hbar/$ $_{\beta})$, $\vec{k}$ being the optical propagation vector, N the atomic number density and L the atomic optical path length. The function[10] $w(z) = (i/\pi)\int_{-\infty}^{\infty} e^{-t^2}\,dt/(z-t)$ represents a convolution of an inhomogeneous Gaussian and a Lorentzian lineshape, with σ_α the strain-broadened Gaussian linewidth for the optical transition, σ_β the Gaussian linewidth of the rf transition arising from static local magnetic fields, γ_{21} the homogeneous linewidth of the spin transition, $\Delta=\Omega-\omega_{31}$ the optical tuning parameter and $\Delta_{21}=\omega-\omega_{21}$ the rf tuning parameter. The Rabi frequencies are $\chi=\mu_{12}H_1/\hbar$, $\chi_1=\mu_{13}E_1/\hbar$ and $\chi_2=\mu_{23}E_1/\hbar$ where μ_{ij} is the transition matrix element. Thus, the beat signal scales as the product of the rf magnetic field amplitude H_1 and the laser intensity E_1^2 where the two photon process requires the product H_1E_1 and the heterodyne beat introduces an additional E_1 factor. To this order of approximation, the signal varies as the unperturbed population difference $(\rho^o_{22}-\rho^o_{11})$.

The beat Eq. (1) displays in and out of phase components of the beat frequency ω and a Gaussian rf lineshape, as in Fig. 1(b), when $\gamma_{21}/\sigma_\beta << 1$. When the laser frequency is tuned far off resonance, (1) predicts that the heterodyne beat vanishes even though the Stokes and anti-Stokes sidebands can remain strong. Physically, the optically resonant case corresponds to the Stokes and anti-Stokes sidebands being of the same phase (AM modulation) and thus add whereas in the nonresonant case the two sidebands are of opposite phase (FM modulation) and cancel. This suggests that the nonresonant Raman detection of NMR should be possible with FM detection.

In Fig. 2, we see that when the two optical fields (Ω and Ω') strike a photodetector a heterodyne beat signal of frequency $\omega = |\Omega - \Omega'|$ appears, a feature which enhances detection sensitivity. The heterodyne process occurs automatically as part of the basic interaction and thus is closely related to Stark or laser frequency switching experiments[1] which produce in two photon processes coherent Raman beats[2] or heterodyne beats in one photon coherent transients.[1]

The present case differs from earlier studies of the stimulated Raman effect[3] where two optical fields drive two coupled electric dipole transitions and the remaining third transition is radiatively inactive or is not monitored. Here, all three fields appear corresponding to the three possible transitions, a three wave mixing effect. It also differs in that both electric and magnetic dipole transitions are employed, and it is for this reason that NMR can be observed readily for the first time in a stimulated Raman process, either under cw or pulsed conditions. Note also that the technique can be generalized to any three level system where all three transitions are active, allowing detection of NMR, ESR or even infrared transitions.

Our work thus extends previous coherent techniques as in optical pumping double resonance,[4] coherent Raman beats,[2] photon echo modulation and nuclear double resonance[5] and Raman echoes[6] or those methods which rely on incoherent detection using optical spontaneous emission, for example, in rf-optical double resonance experiments[7,8] or in enhanced and saturated absorption.[9] However, the present precision and sensitivity greatly surpass these techniques.

To predict the characteristics of the Raman heterodyne beat signal, we have performed a steady-state perturbation calculation for an inhomogeneously broadened three-level atom where the rf magnetic field drives the $1 \leftrightarrow 2$ transition and the laser field drives packets

This Letter reports a new way of detecting nuclear magnetic resonance in solids using a coherent optical and radio frequency induced Raman effect. The technique, which employs heterodyne detection, is capable of monitoring coherent spin transients or nuclear resonances under cw conditions, both in ground and excited electronic states. Due to the high sensitivity and precision, dilute systems in the gas phase or solid state can now be examined which are inaccessible by conventional NMR. Furthermore, the method surpasses previous optical-rf measurements, especially for excited electronic states which have remained elusive. We illustrate the versatility of the method in a dilute rare earth impurity ion crystal, Pr^{3+}:LaF_3, where Pr^{3+} spin echoes of nuclear quadrupole transitions are detected not only in the $^3H_4$ ground electronic state but also for the first time in the $^1D_2$ excited state, thus allowing a critical test of current line broadening theory. From the cw spectrum, the Pr^{3+} hyperfine splittings in these electronic states, as well as the magnetically broadened inhomogeneous lineshapes and widths, are determined with kilohertz precision, about a five-fold improvement over earlier measurements.

In Fig. 1(b), the Pr^{3+} (I=5/2) electron-hyperfine energy level diagram reveals the basic stimulated Raman process where two coherent fields, one at the optical frequency Ω (solid arrow) and the other at the rf frequency ω (squiggle arrow) drive two coupled transitions resonantly. The electric dipole allowed optical transition $^3H_4$ (I_z=5/2)$\rightarrow$$^1D_2$ (I_z=5/2) and the magnetic dipole allowed quadrupole transition $^3H_4$ (I_z=3/2$\leftrightarrow$5/2) combine in a two photon process to generate a coherent optical field at the sum frequency $\Omega'=\Omega+\omega$ (dashed arrow). This transition is also electric dipole allowed due to the fact that the $^1D_2$ hyperfine states are mixed by the nuclear quadrupole interaction. In addition, a Stokes field at the difference frequency $\Omega-\omega$ (not shown), due to a second resonant packet, accompanies the above anti-Stokes field.

RJ 3824 (43791) 3/14/83
Physics

RAMAN HETERODYNE DETECTION OF NMR *

J. Mlynek*
N. C. Wong
R. G. DeVoe
E. S. Kintzer
R. G. Brewer

IBM Research Laboratory
San Jose, California 95193

and

Department of Applied Physics
Stanford University
Stanford, California 94305

ABSTRACT: An optical heterodyne technique based on the coherent Raman effect is demonstrated for detecting nuclear magnetic resonance (NMR) and coherent spin transients in normal and optically excited impurity ion solids at low temperature. Initial measurements on Pr^{3+}:LaF_3 provide the first spin echo studies of an electronically excited state, and cw resonances yield NMR line centers and shapes with kilohertz precision.

*Work supported in part by the U.S. Office of Naval Research.

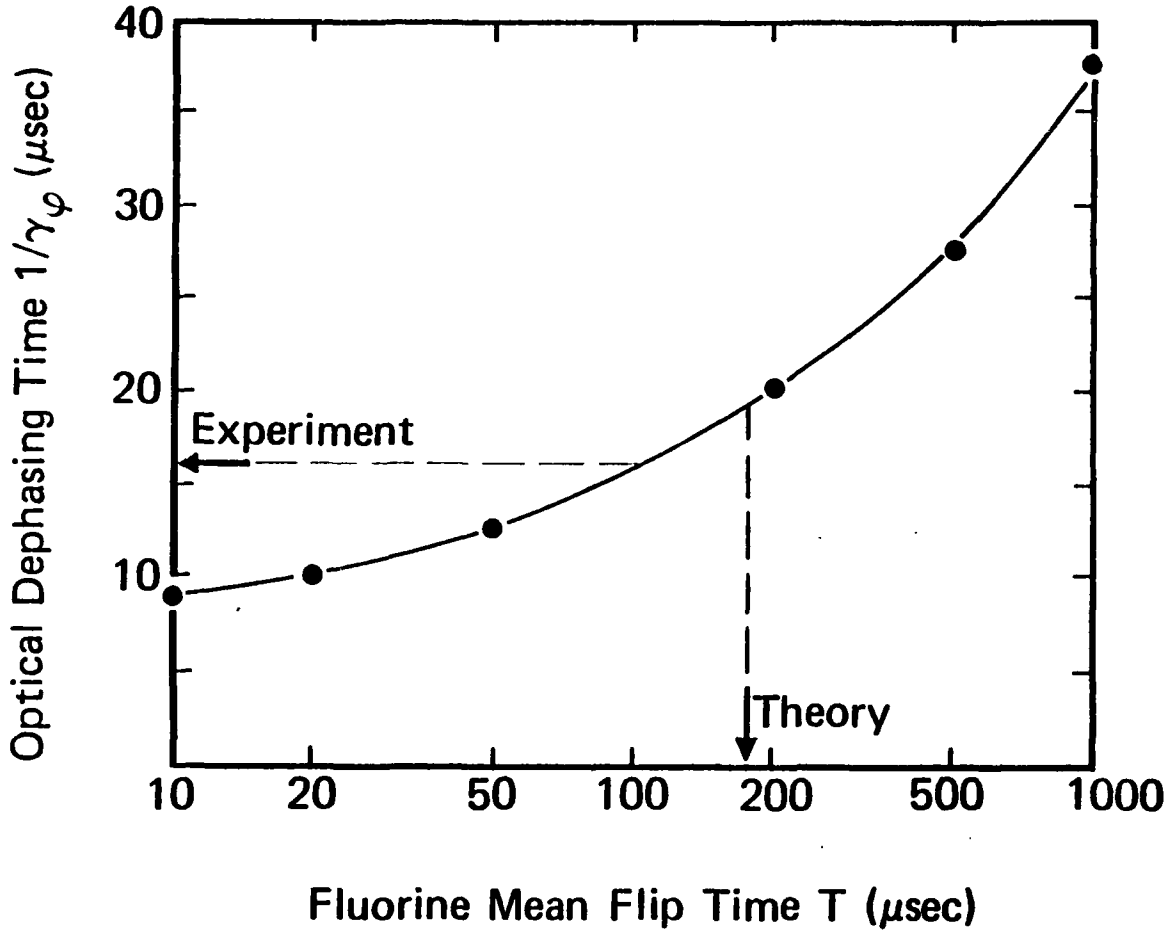


Figure 8
(Brewer)

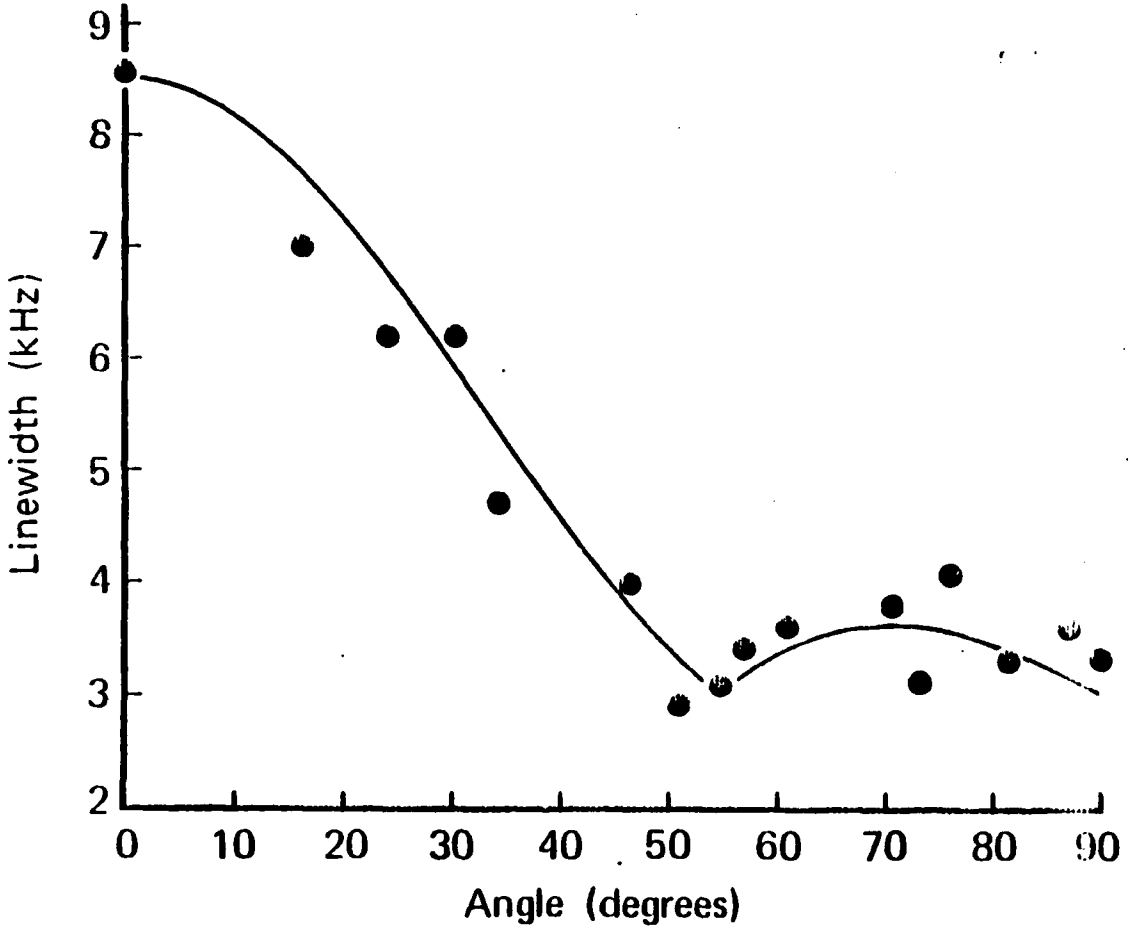


Figure 7
(Brewer)

D

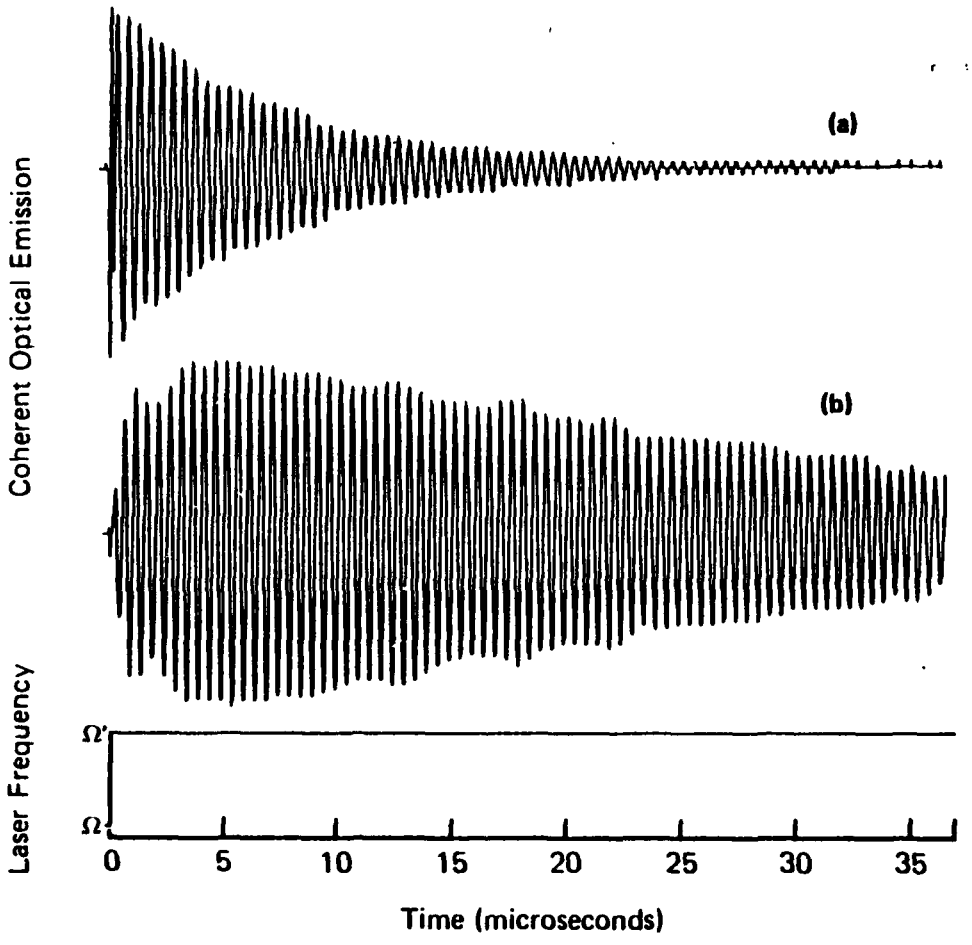


Figure 6
(Brewer)

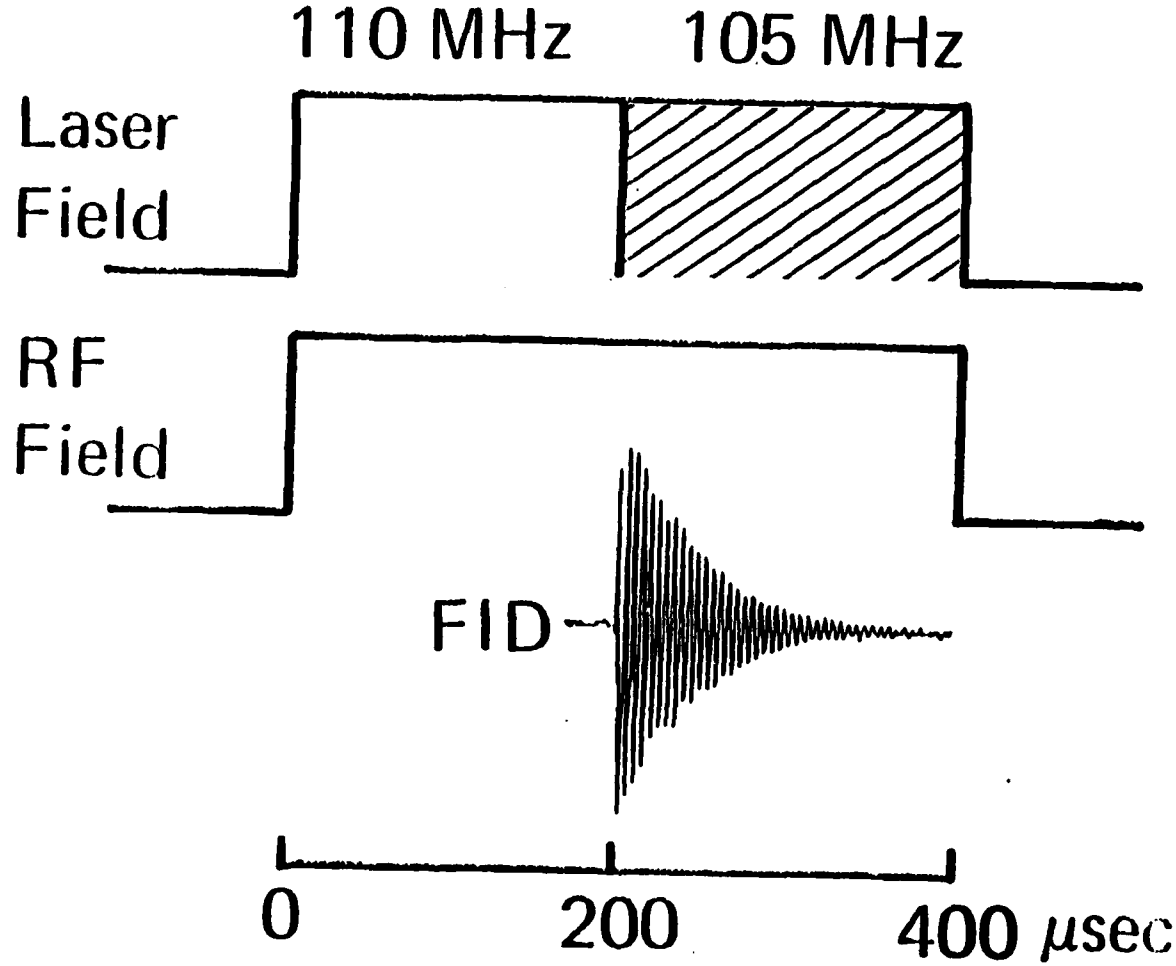


Figure 5
(Brewer)

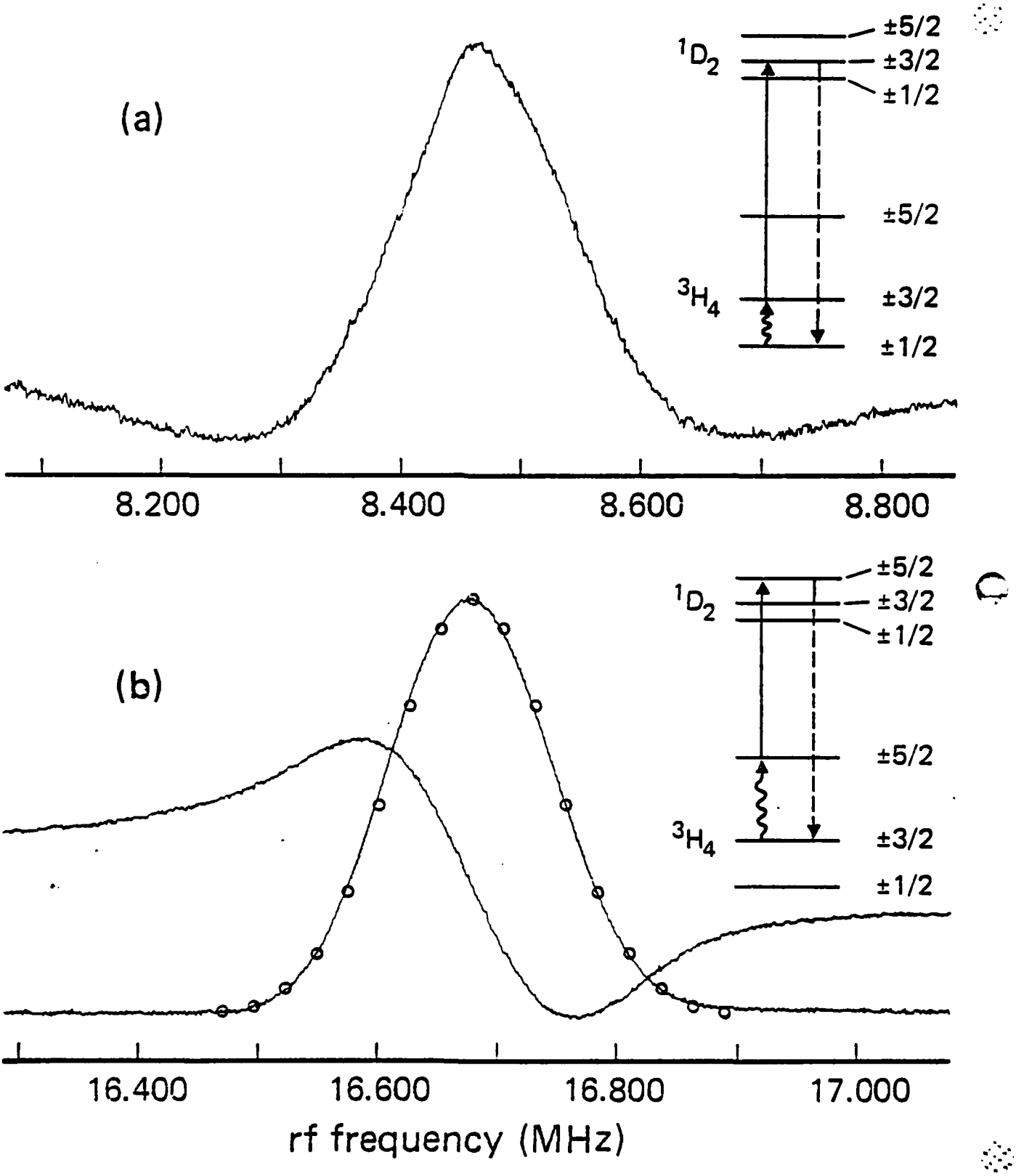

(a)
$^1D_2$
±5/2
±3/2
±1/2
±5/2
$^3H_4$
±3/2
±1/2
8.200
8.400
8.600
8.800
(b)
$^1D_2$
±5/2
±3/2
±1/2
±5/2
$^3H_4$
±3/2
±1/2
16.400
16.600
16.800
17.000
rf frequency (MHz)

Figure 1.

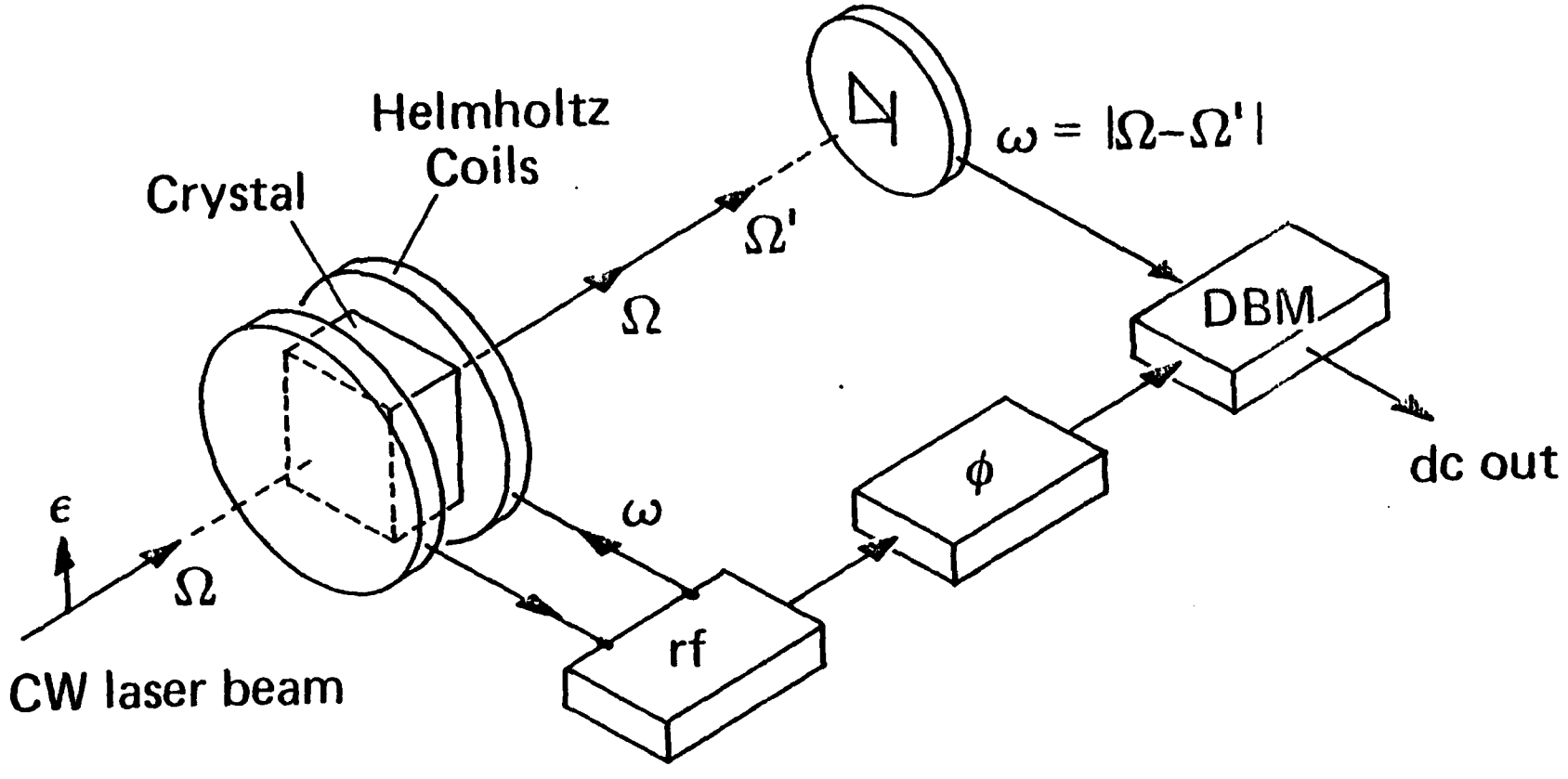

Helmholtz
Coils
Crystal
Ω'
Ω
ω = |Ω−Ω'|
DBM
dc out
ϕ
ω
ϵ
Ω
rf
CW laser beam

Figure 2.

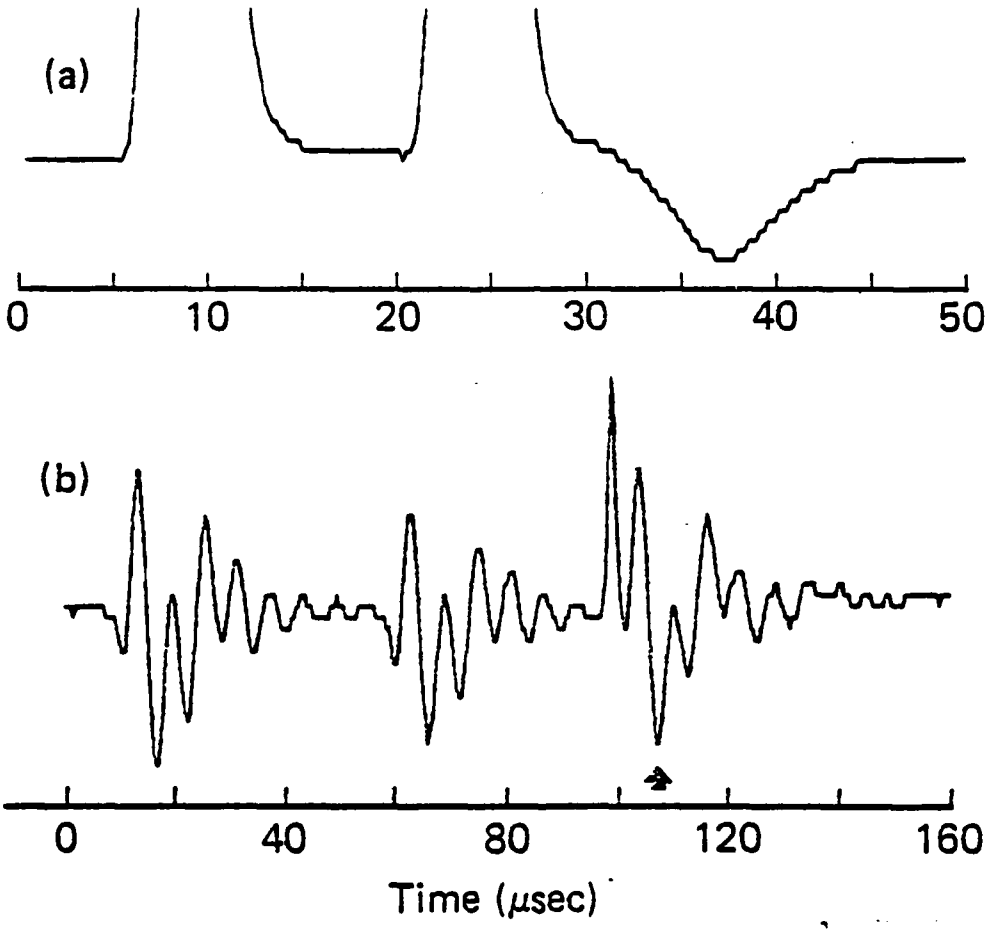


Figure 3.

RJ 3844 (43911) 4/4/83
Physics

EXPERIMENTAL TEST OF THE OPTICAL BLOCH EQUATIONS FOR SOLIDS*

Ralph G. DeVoe
Richard G. Brewer

IBM Research Laboratory
San Jose, California 95193

ABSTRACT: This paper provides the first experimental test of the Bloch equations for an optical transition in a low temperature impurity ion solid, Pr^{3+}:LaF_3, where the condition $T_1 >> T_2$ applies. Intensity-dependent optical FID measurements are performed using an ultrastable cw dye laser (linewidth: 300 Hz) and reveal an $\exp(-2t/T_2)$ decay law at low Rabi frequency (χ), as predicted by the Bloch equations, and an $\exp(-\chi t)$ decay at high χ, which violates the Bloch prediction but agrees with Redfield's characterization of NMR saturation in solids.

*Work supported in part by the U.S. Office of Naval Research.

It is commonly assumed in quantum optics and laser spectroscopy that the optical Bloch equations[1,2] provide a fundamental starting point for the quantum description of nonlinear optical phenomena such as saturation and coherent optical transients. The Bloch equations incorporate relaxation processes in the two-level density matrix equations by two phenomenological parameters, the (diagonal) population decay time T_1 and the (off-diagonal) dipole dephasing time T_2. Implicit in their use is the assumption that T_1 and T_2 are independent of laser intensity. In gas phase atomic or molecular systems, where $T_1 \sim T_2$, this premise appears to be justified.[3] However, in low temperature solids, where $T_1 >> T_2$, the assumption that T_2 is independent of laser intensity may break down in a manner resembling Redfield's description[4,5] of nuclear magnetic resonance saturation in solids. In fact, it is surprising in view of the extensive number of earlier laser studies of solids that the validity of the optical Bloch equations in the saturation regime has gone unchallenged.

In this Letter,[6] we report the first detailed study of saturation behavior in a coherently excited low temperature impurity ion solid, $Pr^{3+}:LaF_3$, and show using measured values of T_1 and T_2 that the Bloch prediction becomes invalid at elevated laser intensities. Instead, we find agreement with Redfield's saturation theory.[4]

Our technique examines the intensity-dependence of optical free induction decay (FID). The Pr^{3+} ions are coherently prepared in a narrow packet of the inhomogeneously broadened line by an ultrastable cw dye laser, and FID follows when the excitation is suddenly removed, the decay time being dependent on the Pr^{3+} saturation behavior and hence the laser intensity in the preparative period.

Consider now the optical FID solution[7] of the Bloch equations

$$\dot{u} + \Delta v + u/T_2 = 0 \tag{1a}$$

$$\dot{v} - \Delta u - \chi w + v/T_2 = 0 \tag{1b}$$

$$\dot{w} + \chi v + (w - w^0)/T_1 = 0 . \tag{1c}$$

and also the prediction which results from Redfield's modification[4] of these equations. Equation (1) follows from the 2×2 density matrix equations of motion for a two-level quantum system, with frequency splitting ω_{21}, interacting with an electromagnetic field of frequency Ω. The Bloch vector amplitudes u, v, and w are related to the density matrix elements by $\rho_{12} = \frac{1}{2}(u + iv)e^{i\Omega t}$, the dipole term, and $\rho_{22} - \rho_{11} = w$, the population difference term. We also define the tuning parameter $\Delta = -\Omega + \omega_{21}$ and the Rabi frequency as χ. With the assumption of steady-state preparation of an inhomogeneously broadened transition, the Bloch decay law for the heterodyne FID signal,[7] derived from (1), is of the form

$$F_B(t) \sim \exp\left\{-t\left[1/T_2 + \sqrt{1/T_2^2 + \chi^2 T_1/T_2}\ \right]\right\} \tag{2a}$$

$$\rightarrow \begin{cases} \exp(-2t/T_2) , & \chi^2 T_1 T_2 << 1 \quad (2b) \\ \exp\left\{-t\left[1/T_2 , + \chi\sqrt{T_1/T_2}\ \right]\right\} , & \chi^2 T_1 T_2 >> 1, \quad (2c) \end{cases}$$

where (2b) and (2c) express the low and high power limits respectively. Note in (2a) that the $1/T_2$ term is the dephasing contribution of the FID period whereas the square root term is the hole burning contribution of the preparative stage.

Redfield's modification[4] of the Bloch equations involves substituting for T_2 in (1a) an effective dephasing time T_{2e} which is power-dependent with limiting values of T_2 at low power and T_1 at high power. At intermediate powers, the behavior is more complex and has

not been described analytically. The FID solution becomes

$$F_R(t) \sim \exp\left\{-t\left[1/T_2 + \sqrt{1/(T_2T_{2e}) + \chi^2 T_1/T_{2e}}\right]\right\} \tag{3a}$$

$$\rightarrow \exp\{-t(1/T_2 + \chi)\}, \quad \chi^2 T_1 T_2 >> 1 \tag{3b}$$

where (3b) expresses the high power limit, and the low power limit coincides with (2b). By comparing (2c) and (3b), it will be apparent that in a solid where $T_1 >> T_2$ the Bloch model saturates as $\chi\sqrt{T_1/T_2}$, considerably faster than the Redfield result χ. We now demonstrate that the FID measurements support the Redfield prediction (3b) and not the Bloch result (2c).

The Pr^{3+} transition examined, the lowest crystal field split components of the $^1D_2 \leftrightarrow {}^3H_4$ states at 5925Å was chosen because the quantities T_1 and T_2 are well known. In addition, a Monte Carlo calculation[8] and a magic angle line narrowing experiment[9] have precisely defined the line broadening mechanism: the Pr^{3+} ion dephases due to ^{19}F-^{19}F nuclear spin flip-flops which modulate the Pr^{3+} optical transition frequency via the Pr-F dipolar interaction.

To monitor saturation and FID of a single Pr^{3+} packet, we have actively stabilized a cw ring dye laser to a linewidth narrower than any presently known optical transition in a solid. An RMS stability of <300 Hz, corresponding to a fractional linewidth of 6×10^{-13}, has been achieved by an FM sideband phase-locking technique.[10] This technique is far superior to an earlier method of locking to the side of a transmission fringe of a reference cavity for two reasons. First, it utilizes a frequency-locking signal that is shot-noise limited due to the noise cancellation property of FM detection.[11] Secondly, it permits a faster servo response time with consequently higher servo gain because the laser error signal is instantaneously reflected off the reference etalon rather than undergoing a 100 nsec delay in transmission.

A pair of identical 50 cm confocal invar etalons, acoustically and thermally isolated, serve as the frequency reference and as an independent stability monitoring system.

Optical FID and nutation are observed by laser frequency switching as described previously.[12] The frequency stabilized beam first enters an acousto-optic Bragg modulator which acts as an optical gate and a laser frequency switch. The beam then passes through a pair of lenses of 5 and 10 cm focal length that produce beam diameters in the range 0.08 to 1 mm and with neutral density filters intensities in the sample from 50 mW/cm^2 to 50 W/cm^2. The generally elliptical beam cross sections are measured with a Reticon diode array to an accuracy of 0.015 mm. The linearly polarized laser field propagates along the c axis of a $5\times6\times7$ mm^3 crystal of 0.1 at. % Pr^{3+}:LaF_3 at 1.6°K before striking a p-i-n photodiode. An external dc magnetic field of 500G is applied perpendicular to the c axis. The Pr^{3+} ions are coherently prepared when the modulator is driven by a 400 μsec rf pulse at 95 MHz. At the end of the pulse, the laser frequency is abruptly switched from 95 to 97 MHz for a 100 μsec period, causing FID to occur in the initially prepared packet and nutation in the newly excited packet. Since the sample is illuminated for only 500 μsec every 2 sec, optical pumping is minimized.

The FID signals, which are not averaged, exhibit excellent reproducibility and signal to noise as indicated in Fig. 1, a computer plot of 400 experimental points overlaid on an exponentially damped cosine function. The two curves appear to be indistinguishable, and the residuals show that the dephasing time can be determined with an uncertainty of less than 1%.

In Fig. 2 is plotted the linewidth of the prepared hole $\Delta\nu$ *versus* the Rabi frequency $\chi/2\pi$. For the Bloch theory, $\Delta\nu = (1/2\pi)\sqrt{1/T_2^2 + \chi^2 T_1/T_2}$ HWHM, and for the FID

experiments, $\Delta\nu = (1/2\pi)(1/\tau - 1/T_2)$ where τ is the observed dephasing time. Here, T_1=0.5 msec[13] and χ is obtained directly from the fit of nutation signals to Bloch theory below saturation, which yields 4.7×10^{-4} Debye for the transition moment. Above saturation, the nutation signals deviate from Bloch predictions and are not used. A heterodyne photon echo measurement gives T_2=21.7 μsec in agreement with an extrapolation of the FID data to zero power, Eq. (2b), and a previous value.[14] Scatter in the data is due to the uncertainty in χ.

We see that the two curves of Fig. 2 agree in the low power regime up to $\chi/2\pi$=3 kHz and thereafter diverge rapidly. At elevated power, the Bloch prediction approaches $(\chi/2\pi)\sqrt{T_1/T_2}$ while the experimental linewidths approach $\chi/2\pi$, the ratio of the two being 4.8. The observations, therefore, are in striking agreement with the Redfield prediction (3b).

To establish that the deviation from Bloch saturation behavior, Fig. 2, represents a fundamental effect and not an artifact of our technique, we have examined the effect on FID of (a) finite duration *versus* steady-state preparation pulses, (b) spin double resonance processes arising from fortuitous Zeeman tuning, (c) the intensity dependence of the heterodyne probe pulse, and (d) a theoretical model that incorporates a multi-level instead of a two-level quantum system.

(a) Numerical FID solutions of Eq. (1) show that a 400 μsec pulse preparation time (the experimental value) yields a dephasing time that falls less than 20% below the steady-state value (2a). Furthermore, experiments with pulses in the range 400 μsec to 1 msec also reveal a 20% variation in τ in agreement with the numerical solutions. Hence, our transient excitation technique permits a valid comparison with steady-state Bloch theory.

(b) By increasing the external magnetic field from 100 to 5000G in 6 steps at two fixed Rabi frequencies, $\chi/2\pi=10$ and 20 kHz, we noted no change in the dephasing time to within 5%. This test rules out the possibility of chance coincidences of the Zeeman split F and Pr^{3+} hyperfine states that could produce a double resonance effect. (c) By varying the heterodyne probe pulse in the range 1 μW to 1 mW while keeping the preparation pulse intensity fixed ($\chi/2\pi=20$ kHz), we find that the FID dephasing time remains unchanged to within 5%. Hence, the anomalous dephasing effect seen in heterodyne photon echoes is excluded.[14] (d) As is well known, the Bloch equations (1) apply only to a two-level quantum system, and yet population relaxation in Pr^{3+}:LaF_3 involves three or more levels as evidenced by a strong optical pumping cycle. We have numerically calculated the influence of optical pumping and hence a multi-level system on FID by assuming a two-level system ($1 \rightleftharpoons 2$) that is now in contact with an n level reservoir.[15] With this model, the branching ratio of the optically excited state was varied by five orders of magnitude, and yet the dephasing time changed by less than 20%. It should also be noted that a preparation pulse of 400 μsec duration prevents more than 30% of the population from leaking out of the optically excited two-level system. Hence, optical pumping of a multi-level configuration does not play an important role.

We have shown that optical saturation in Pr^{3+}:LaF_3 is consistent with Redfield's predictions.[4] It is possible, however, that while our result resembles Redfield's effect phenomenologically, it could have a different physical origin. We briefly sketch which concepts used to understand this phenomenon in NMR are likely to be valid in the optical region. First, Redfield's explanation for the replacement of T_2 by T_1 in Eq. (1a) arises because the decay of u is partially forbidden by energy and entropy considerations above saturation, an effect that can create local spin order in neighboring nuclei. In the optical

case, this mechanism would explain the lengthening of T_2 for Pr^{3+} at high χ since the fluorine spin fluctuations would be reduced due to local F spin order. We plan to test this hypothesis by Raman heterodyne detection of NMR.[16] A second possibility is that the fluorine nuclei are not ordered by the laser, but rather that their coupling to the Pr^{3+} optical transitions via the Pr^{3+}-F dipolar interaction is averaged out by the high optical Pr^{3+} Rabi frequency. We note that the related effect, Pr^{3+} optical line-narrowing by applied rf fields which are resonant with the F nuclei, has already been observed in this system.[9] On the other hand, the concept of spin temperature in the rotating frame is not applicable to Pr^{3+}:LaF_3 since at 0.1% concentration, the Pr^{3+} ions do not exchange optical energy, and hence cannot come to equilibrium as in a pure solid.

These studies thus emphasize that the optical dephasing parameter T_2 is not necessarily appropriate for coherently excited solids when saturation conditions prevail. Secondly, it seems plausible that other impurity ion solids should behave similarly to Pr^{3+}:LaF_3 in obeying Redfield behavior. Finally, we note that a detailed microscopic theory of optical saturation in solids awaits development.

We acknowledge with pleasure stimulating conversations with E. L. Hahn and A. G. Redfield. This work was supported in part by the U.S. Office of Naval Research.

REFERENCES

1. F. Bloch, *Phys. Rev.* **70**, 460 (1946).
2. M. Sargent III, M. O. Scully, and W. E. Lamb, Jr., *Laser Physics* (Addison-Wesley, Reading, MA, 1974), p. 91.
3. P. R. Berman, J. M. Levy, and R. G. Brewer, *Phys. Rev.* A11, 1668 (1975).
4. A. G. Redfield, *Phys. Rev.* **98**, 1787 (1955).
5. C. P. Slichter, *Principles of Magnetic Resonance* (Springer-Verlag, New York, 1978), p. 188.
6. For a preliminary report see R. G. DeVoe, E. Hanamura, and R. G. Brewer, *Bull. Am. Phys. Soc.* **28**, No. 3, 550, March 1983 (Los Angeles Meeting).
7. R. G. Brewer in *Frontiers in Laser Spectroscopy*, Les Houches Lectures, edited by R. Balian, S. Haroche, and S. Liberman (North Holland, New York, 1977), p. 341.
8. R. G. DeVoe, A. Wokaun, S. C. Rand, and R. G. Brewer, *Phys. Rev. B* **23**, 3125 (1981).
9. S. C. Rand, A. Wokaun, R. G. DeVoe, and R. G. Brewer, *Phys. Rev. Lett.* **43**, 1868 (1979).
10. R. W. P. Drever, J. L. Hall, F. V. Kowalski, J. Hough, G. M. Ford, and A. Munley (unpublished); R. G. DeVoe and R. G. Brewer (unpublished).
11. G. C. Bjorklund, *Opt. Lett.* **5**, 15 (1980).
12. R. G. DeVoe, A. Szabo, S. C. Rand, and R. G. Brewer, *Phys. Rev. Lett.* **42**, 1560 (1979).
13. M. J. Weber, *J. Chem. Phys.* **48**, 4774 (1978).
14. R. M. Macfarlane, R. M. Shelby, and R. L. Shoemaker, *Phys. Rev. Lett.* **43**, 1726 (1979).
15. A. Schenzle and R. G. Brewer, *Phys. Rev. A* **14**, 1756 (1976).

16. J. Mlynek, N. C. Wong, R. G. DeVoe, E. S. Kintzer, and R. G. Brewer, *Phys. Rev. Lett.* **50**, 993 (1983).

FIGURE CAPTIONS

Figure 1. A computer plot of 400 points of optical FID of 0.1 at. % Pr^{3+}:LaF_3 at 1.6°K. The experimental data are overlaid on a damped cosine, and the residuals indicate that the dephasing time of 5.10 μsec has an uncertainty of less than 1%. The signal is power broadened.

Figure 2. Optical linewidth $\Delta\nu$(HWHM) of the prepared hole *versus* the Rabi frequency $\chi/2\pi$ according to the Bloch theory (upper curve) and FID experiments of Pr^{3+}:LaF_3 (filled circles) where the solid curve is a best fit to the data. The point $\Delta\nu=1/(2\pi T_2)$ at $\chi=0$ results from a photon echo experiment.

the second term, and (ii) the magnetic inhomogeneous linewidth (~100 kHz) is orders of magnitude smaller than the optical inhomogeneous linewidth (~5 GHz).

Therefore, denoting the portion of the second order stationary solutions (2.19) which contribute to the Raman signal by $\tilde{\rho}^{s}_{13}$ and $\tilde{\rho}^{s}_{23}$, we have

$$\tilde{\rho}^{s}_{13} = \frac{\alpha_2 \beta\, e^{i\omega_H t}}{i(\Delta_E + \Delta_H) - \gamma_{13}} \frac{\rho^{o}_{22} - \rho^{o}_{11}}{i\Delta_H - \gamma_{12}} , \tag{2.20a}$$

$$\tilde{\rho}^{s}_{23} = \frac{\alpha_1 \beta^{*}\, e^{-i\omega_H t}}{i(\Delta_E + \omega_H) - \gamma_{23}} \frac{\rho^{o}_{22} - \rho^{o}_{11}}{i\Delta_H + \gamma_{12}} . \tag{2.20b}$$

Note that in cases where the Raman energy separation $\hbar\omega_{21}$ is larger than the Boltzmann factor kT, as in infrared transitions, the population differences in (i) are also comparable even without optical pumping.

C. Raman Heterodyne Signal

To obtain the Raman signal field $\tilde{E}_s$ (2.6), one averages the signal matrix elements $\tilde{\rho}^{s}_{13}$ and $\tilde{\rho}^{s}_{23}$ (2.20) over the Gaussian crystal strain and magnetic inhomogeneous lineshapes, $g_E(\Delta_E)$ and $g_H(\Delta_H)$, respectively, given by

$$g_E(\Delta_E) = \frac{1}{\sqrt{\pi}\,\sigma_E} e^{-\left(\frac{\Delta_E - \bar{\Delta}_E}{\sigma_E}\right)^2} , \tag{2.21a}$$

and

$$g_H(\Delta_H) = \frac{1}{\sqrt{\pi}\,\sigma_H} e^{-\left(\frac{\Delta_H - \bar{\Delta}_H}{\sigma_H}\right)^2} , \tag{2.21b}$$

$$\tilde{\rho}_{13}^{(2)}(t\to\infty) = \frac{\alpha_2\beta\, e^{i\omega_H t}}{i(\Delta_E+\Delta_H)-\gamma_{13}} \frac{\rho_{22}^o-\rho_{11}^o}{i\Delta_H-\gamma_{12}} - \frac{\rho_{33}^o-\rho_{22}^o}{i\Delta_E-\gamma_{23}}$$

$$\times \left[\frac{\alpha_2\beta\, e^{i\omega_H t}}{i(\Delta_E+\Delta_H)-\gamma_{13}} + \frac{\alpha_2\beta^*\, e^{-i\omega_H t}}{i(\Delta_E+\omega_{21}+\omega_H)-\gamma_{13}} \right], \qquad (2.19a)$$

$$\tilde{\rho}_{23}^{(2)}(t\to\infty) = \frac{\alpha_1\beta^*\, e^{-i\omega_H t}}{i(\Delta_E+\omega_H)-\gamma_{23}} \frac{\rho_{22}^o-\rho_{11}^o}{i\Delta_H+\gamma_{12}} - \frac{\rho_{33}^o-\rho_{11}^o}{i(\Delta_E+\omega_{21})-\gamma_{13}}$$

$$\times \left[\frac{\alpha_1\beta\, e^{i\omega_H t}}{i(\Delta_E-\omega_H)-\gamma_{23}} + \frac{\alpha_1\beta^*\, e^{-i\omega_H t}}{i(\Delta_E+\omega_H)-\gamma_{23}} \right]. \qquad (2.19b)$$

The first order solutions for $\tilde{\rho}_{13}$ and $\tilde{\rho}_{23}$ in (2.18c) and (2.18d) are proportional to E_o, oscillate at the laser frequency ω_E in the laboratory frame, and reflect the forced oscillation of the dipoles due to the driving field $\bar{E}_o$. The second order solutions (2.19) are proportional to $E_o|H_1|$, oscillate at $\omega_E \pm \omega_H$ in the laboratory frame, and reflect the two-quantum transitions.

The first term of the solutions (2.19a) and (2.19b) contribute to the Raman signal of the rf transition $1 \longleftrightarrow 2$. This is also evident from the formal solution for $\tilde{\rho}_{13}$ (2.13e) and $\tilde{\rho}_{23}$ (2.13f), where the Raman signal, be it cw or transient, can only come from the terms $\alpha_2\tilde{\rho}_{12}$ in (2.13e) and $\alpha_1\tilde{\rho}_{21}$ in (2.13f).

The second term in (2.19a) and (2.19b) can be dropped because after it is averaged over the optical inhomogeneous lineshape, its contribution is orders of magnitude smaller than the first term and it does not depend on the rf tuning parameter Δ_H. This is so because (i) due to optical pumping, the normally near-zero Raman population difference $\rho_{22}^o-\rho_{11}^o$ in the first term of (2.19) is comparable to the population difference $\rho_{33}^o-\rho_{22}^o$ (or $\rho_{33}^o-\rho_{11}^o$) in

$$\tilde{\rho}_{ij} = \sum_{n=0} \tilde{\rho}_{ij}^{(n)} \ , \text{ and } \rho_{ii} = \sum_{n=0} \rho_{ii}^{(n)} \ , \tag{2.16}$$

where n denotes the order of perturbation. The zeroth order field-free solution given by

$$\rho_{ii}^{(0)}(t) = \rho_{ii}^{o} \ , \ i = 1,2,3 \ , \tag{2.17a}$$

$$\tilde{\rho}_{ij}^{(0)}(t) = 0 \ , \ i \neq j \ , \tag{2.17b}$$

and the initial conditions (2.14) are used to obtain the first order n=1 solution

$$\rho_{ii}^{(1)}(t) = 0 \ , \tag{2.18a}$$

$$\tilde{\rho}_{12}^{(1)}(t) = \frac{-i\beta(\rho_{22}^{o}-\rho_{11}^{o})}{i\Delta_H-\gamma_{12}} \left(1 - e^{(i\Delta_H-\gamma_{12})t}\right) \ , \tag{2.18b}$$

$$\tilde{\rho}_{13}^{(1)}(t) = \frac{-i\alpha_1(\rho_{33}^{o}-\rho_{11}^{o})}{i(\Delta_E+\omega_{21})-\gamma_{13}} \left(1 - e^{[i(\Delta_E+\omega_{21})-\gamma_{13}]t}\right) \ , \tag{2.18c}$$

$$\tilde{\rho}_{23}^{(1)}(t) = \frac{-i\alpha_2(\rho_{33}^{o}-\rho_{22}^{o})}{i\Delta_E-\gamma_{23}} \left(1 - e^{(i\Delta_E-\gamma_{23})t}\right) \ . \tag{2.18d}$$

Substituting the first order solution (2.18) into the formal solution (2.13), and letting $t \to \infty$ so that damping terms go to zero and only oscillatory terms remain, we obtain the stationary second order n=2 solution for $\tilde{\rho}_{13}$ and $\tilde{\rho}_{23}$:

$$\rho_{11}(t) = \rho_{11}^{o} + \int_0^t dt' \, e^{-\gamma_1(t-t')}[i\beta\tilde{\rho}_{21}(t') + i\alpha_1\tilde{\rho}_{31}(t') + c.c.] , \tag{2.13a}$$

$$\rho_{22}(t) = \rho_{22}^{o} + \int_0^t dt' \, e^{-\gamma_2(t-t')}[i\beta^* \, \tilde{\rho}_{12}(t') + i\alpha_2 \, \tilde{\rho}_{32}(t') + c.c.] , \tag{2.13b}$$

$$\rho_{33}(t) = \rho_{33}^{o} + \int_0^t dt' \, e^{-\gamma_3(t-t')}[i\alpha_1^* \, \tilde{\rho}_{13}(t') + i\alpha_2^* \, \tilde{\rho}_{23}(t') - c.c.] , \tag{2.13c}$$

$$\tilde{\rho}_{12}(t) = \int_0^t dt' \, e^{(i\Delta_H-\gamma_{12})(t-t')}\{i\beta[\rho_{22}(t')-\rho_{11}(t')]$$

$$+ [i\alpha_1 \, \tilde{\rho}_{32}(t')-i\alpha_2^* \, \tilde{\rho}_{13}(t')] \, e^{-i\omega_H t'}\} , \tag{2.13d}$$

$$\tilde{\rho}_{13}(t) = \int_0^t dt' \, e^{[(i\Delta_E+\omega_{21})-\gamma_{13}](t-t')}\{i\alpha_1[\rho_{33}(t')-\rho_{11}(t')]$$

$$- i\alpha_2\tilde{\rho}_{12}(t')e^{i\omega_H t'} + i\tilde{\rho}_{23}(t')(\beta \, e^{i\omega_H t'} + c.c.)\} , \tag{2.13e}$$

$$\tilde{\rho}_{23}(t) = \int_0^t dt' \, e^{(i\Delta_E-\gamma_{23})(t-t')}\{i\alpha_2[\rho_{33}(t')-\rho_{22}(t')]$$

$$- i\alpha_1\tilde{\rho}_{21}(t') \, e^{-i\omega_H t'} + i\tilde{\rho}_{13}(t')(\beta \, e^{i\omega_H t'} + c.c.)\} , \tag{2.13f}$$

with the initial conditions

$$\rho_{ii}(0) = \rho_{ii}^{o} \quad \text{and} \quad \tilde{\rho}_{ij}(0) = 0 , \qquad i \neq j . \tag{2.14}$$

In the weak field limit,

$$\alpha_1, \, \alpha_2, \, \beta \to 0 , \tag{2.15}$$

we obtain a perturbative solution from the formal solution (2.13) in orders of α_1, α_2, and β, thus excluding power broadening effects. We write

$$\tilde{\rho}_{23} = (i\Delta_E - \gamma_{23})\tilde{\rho}_{23} + i\alpha_2(\rho_{33} - \rho_{22}) - i\alpha_1 \tilde{\rho}_{21} e^{-i\omega_H t}$$

$$+ i(\beta e^{i\omega_H t} + c.c.)\tilde{\rho}_{13} . \qquad (2.12f)$$

Here the tuning parameters Δ_H and Δ_E are defined by

$$\Delta_H \equiv \omega_{21} - \omega_H , \quad \Delta_E \equiv \omega_{32} - \omega_E , \qquad (2.12g)$$

and $\omega_{ij} \equiv \omega_i - \omega_j$ is the frequency separation between states $|i\rangle$ and $|j\rangle$. ρ_{ii}^o is the field-free population for state $|i\rangle$ at thermal equilibrium.

The RWA assumes that $\tilde{\rho}_{ij}(t)$ is slowly varying with respect to the corresponding frequency $|\omega_{ij}|$. This implies that $\tilde{\rho}_{13}(t)$ and $\tilde{\rho}_{23}(t)$ are allowed to have components which vary at the rate ω_H since we have assumed $\omega_E >> \omega_H$ (2.2). Despite the presence of $e^{-i\omega_H t}$ in Eq. (2.12d),[24] the primary signal of ρ_{12} (2.18b) indeed satisfies the RWA assumption.

We should mention that in the equations of motion (2.12), optical pumping effects are not taken into account partly because of the complexity in modeling them, but also because they occur on a much longer time scale than that of the experiment. Although optical pumping can significantly affect the population levels ρ_{ii}^o, we show in Sec. VA that even when the time scale of the experiment approaches that of optical pumping, the essential features remain unchanged.

B. Perturbation Solution

Within the RWA we seek a perturbative stationary solution to the equations of motion (2.12) by assuming that the excitation fields $\vec{E}_o$ and $\vec{H}_1$ are weak. In Sec. IIE, we relax the weak field condition on $\vec{H}_1$ to obtain a more general time dependent solution. Formally integrating Eqs. (2.12), we obtain

From the total intensity $I_T = E_T E_T^*$, one obtains the observable heterodyne beat signal

$$I_s = \frac{1}{2}\,\tilde{E}_s E_o^* + \text{c.c.} \tag{2.10}$$

We introduce phenomenologically the population decay rates γ_i for state $|i\rangle$, and the transverse decay rates $\gamma_{ij}=\gamma_{ji}$ between states $|i\rangle$ and $|j\rangle$. By defining

$$\rho_{12}(t) = \tilde{\rho}_{12}\, e^{i\omega_H t}\,, \tag{2.11a}$$

$$\rho_{13}(z,t) = \tilde{\rho}_{13}(t)\, e^{i(\omega_E t - k_E z)}\,, \tag{2.11b}$$

$$\rho_{23}(z,t) = \tilde{\rho}_{23}(t)\, e^{i(\omega_E t - k_E z)}\,, \tag{2.11c}$$

and applying the rotating wave approximation (RWA) which neglects the nonresonant terms, the equations of motion (2.3) become

$$\dot{\rho}_{11} = -\gamma_1(\rho_{11}-\rho_{11}^o) + (i\beta\,\tilde{\rho}_{21} + i\alpha_1\,\tilde{\rho}_{31} + \text{c.c.})\,, \tag{2.12a}$$

$$\dot{\rho}_{22} = -\gamma_2(\rho_{22}-\rho_{22}^o) + (i\beta^*\,\tilde{\rho}_{12} + i\alpha_2\,\tilde{\rho}_{32} + \text{c.c.})\,, \tag{2.12b}$$

$$\dot{\rho}_{33} = -\gamma_3(\rho_{33}-\rho_{33}^o) + (i\alpha_1^*\,\tilde{\rho}_{13} + i\alpha_2^*\,\tilde{\rho}_{23} + \text{c.c.})\,, \tag{2.12c}$$

$$\dot{\tilde{\rho}}_{12} = (i\Delta_H-\gamma_{12})\tilde{\rho}_{12} + i\beta(\rho_{22}-\rho_{11}) + (i\alpha_1\,\tilde{\rho}_{32} - i\alpha_2^*\tilde{\rho}_{13})\, e^{-i\omega_H t}\,, \tag{2.12d}$$

$$\dot{\tilde{\rho}}_{13} = [i(\Delta_E + \omega_{21})-\gamma_{13}]\tilde{\rho}_{13} + i\alpha_1(\rho_{33}-\rho_{11}) - i\alpha_2\,\tilde{\rho}_{12}\, e^{i\omega_H t}$$
$$+ i(\beta\, e^{i\omega_H t} + \text{c.c.})\tilde{\rho}_{23}\,. \tag{2.12e}$$

$$\beta \equiv \frac{H_1}{2\hbar} \langle 1 | \vec{\mu}_H \cdot \hat{e}_2 | 2 \rangle \equiv \frac{H_1 \mu_{12}}{2\hbar} , \tag{2.4c}$$

and μ_{ij} is assumed real. The parameters are related to the Rabi frequencies by

$$\alpha_1 = \frac{1}{2} \chi_1 , \ \alpha_2 = \frac{1}{2} \chi_2 , \ \beta = \frac{1}{2} \chi . \tag{2.5}$$

For an optically thin sample, the optical signal field

$$\vec{E}_s(z,t) = \hat{e}_1 \tilde{E}_s(z,t) e^{i(\omega_E t - k_E z)} + \text{c.c.} \tag{2.6}$$

obeys Maxwell's wave equation

$$\frac{\partial \tilde{E}_s}{\partial z} = - 2\pi i k_E \langle \tilde{P}_s \rangle , \tag{2.7}$$

where the tilde denotes the slowly varying part. The Raman signal polarization

$$\langle \tilde{P}_s(t) \rangle = N(\mu_{31} \langle \tilde{\rho}_{13}(t) \rangle + \mu_{32} \langle \tilde{\rho}_{23}(t) \rangle) \tag{2.8}$$

is to be averaged over the crystal strain and magnetic inhomogeneous lineshapes which are assumed Gaussian. The angular brackets in (2.7) and (2.8) denote this average, and N is the number density.

The signal field $\vec{E}_s$ (2.6) and the input laser field $\vec{E}_o$ (2.1a) give rise to the total field

$$\vec{E}_T = \vec{E}_o + \vec{E}_s$$

$$= \hat{e}_1 \tilde{E}_T e^{i(\omega_E t - k_E z)} + \text{c.c.} \tag{2.9a}$$

where

$$\tilde{E}_T = \frac{1}{2} E_o + \tilde{E}_s . \tag{2.9b}$$

Although we assume $\vec{H}_1$ is a magnetic field, our formulation is applicable for any electromagnetic wave. The frequencies of $\vec{E}_o$ and $\vec{H}_1$ are assumed to satisfy the condition

$$\omega_E >> \omega_H \,. \tag{2.2}$$

In Eq. (2.1b) the spatial dependence of $\vec{H}_1$ is ignored because the wavelength of $\vec{H}_1$ is much larger than the interaction region.

The density matrix equations of motion are given by

$$i\hbar \frac{\partial \rho}{\partial t} = [\mathscr{H},\rho] + \text{damping terms} \tag{2.3}$$

where the Hamiltonian $\mathscr{H} = \mathscr{H}_o + \mathscr{H}'$ consists of the field-free Hamiltonian $\mathscr{H}_o$ and the dipole interactions

$$\mathscr{H}' = -\vec{\mu}_E \cdot \vec{E}_o - \vec{\mu}_H \cdot \vec{H}_1$$

satisfying the usual conditions

$$\langle i | \mathscr{H}_o | j \rangle = \hbar\omega_i \delta_{ij} \,,$$

$$\langle i | \mathscr{H}' | i \rangle = 0 \,, \quad i,j = 1,2,3 \,.$$

Here $\vec{\mu}_E$ and $\vec{\mu}_H$ are the electric and magnetic dipole moment operators, respectively. The dipole coupling strengths are given by the parameters

$$\alpha_1 \equiv \frac{E_o}{2\hbar} \langle 1 | \vec{\mu}_E \cdot \hat{e}_1 | 3 \rangle \equiv \frac{E_o \mu_{13}}{2\hbar} \,, \tag{2.4a}$$

$$\alpha_2 \equiv \frac{E_o}{2\hbar} \langle 2 | \vec{\mu}_E \cdot \hat{e}_1 | 3 \rangle \equiv \frac{E_o \mu_{23}}{2\hbar} \,, \tag{2.4b}$$

II. THEORY

In this section we present a new theory for the interaction of two resonant electromagnetic fields with a three-level system using a density matrix perturbation method. Our theory differs from previous three-level calculations[11,18,23] involving Raman scattering or two-photon transitions in that we assume all three transitions are dipole allowed. This introduces additional terms in the equations of motion with new solutions. This assumption is satisfied in the Pr^{3+}:LaF_3 $^1D_2 \leftrightarrow {}^3H_4$ transition because of hyperfine state mixing in the $^1D_2$ excited state. In lowest order, our theory predicts a three-wave mixing effect while the usual stimulated Raman scattering and two-photon transitions are four-wave mixing processes.[11] When the condition of a weak rf excitation is relaxed, we show that both linear and nonlinear processes of the NMR transition can be optically monitored.

A. Equations of Motion

In Fig. 3, the energy level diagram shows that the Raman levels 1 and 2 are close lying states whose energy separation may be radio frequency as in NMR, microwave as in ESR, or infrared as in molecular ro-vibrational levels, and level 3 is separated from them by a much larger energy in the optical frequency range. Level 3 may lie higher than the Raman levels, as shown in Fig. 3, or lower such that the Raman levels may be hyperfine states of an electronic ground or excited state.

A laser field

$$\vec{E}_o(z,t) = \hat{e}_1 \frac{E_o}{2} e^{i(\omega_E t - k_E z)} + \text{c.c.} \tag{2.1a}$$

connects level 3 optically to the Raman levels, which are coupled by an rf magnetic field

$$\vec{H}_1(t) = \hat{e}_2 \frac{H_1}{2} e^{i\omega_H t} + \text{c.c.} \tag{2.1b}$$

Unlike the usual stimulated Raman effect,[11] this is a resonant process in which all three transitions are either electric or magnetic dipole allowed. The technique can be generalized to any three level systems where all three transitions are active, allowing sensitive detection of NMR, ESR, or even infrared transitions. In addition to Pr^{3+}:LaF_3, similar measurements have been performed on Pr^{3+}:$YAlO_3$[12] and samarium vapor.[13]

Our work thus extends previous coherent techniques as in optical pumping double resonance,[14] coherent optical double resonance,[15] coherent Raman beats,[16] photon echo modulation,[17] photon echo nuclear double resonance,[4] and Raman echoes,[18,19] or those methods which rely on incoherent detection as in enhanced and saturated absorption,[20] and rf-optical double resonance.[2,3]

There is currently considerable interest in the impurity ion solid Pr^{3+}:LaF_3. Optical dephasing (T_2) measurements on the $^1D_2 \leftrightarrow {}^3H_4$ transition have been carried out using different laser techniques[5-7] and very narrow optical homogeneous linewidths of a few kHz have been obtained. The dominant optical line broadening mechanism has been determined to be the ^{19}F-^{19}F dipolar interaction, where spin flip fluctuations of the ^{19}F nuclei impress weak fluctuating magnetic fields on the ^{141}Pr nuclei and perturb the Pr^{3+} optical transition frequency through the Pr-F nuclear dipole-dipole interaction. This has been confirmed by a Monte Carlo calculation[9] and by magic angle line narrowing experiments.[5,7] In addition, a recent experiment[8] shows that at high laser intensities the system Pr^{3+}:LaF_3 is no longer adequately described by the optical Bloch equations[21] and exhibits a Redfield-type saturation behavior[22] in the optical T_2. A full understanding of these measurements requires establishing a link between the optical dephasing measurements and the NMR line broadening mechanisms of each hyperfine transition, a task that can be accomplished by the present technique.

I. INTRODUCTION

Recently we reported a preliminary account of Raman heterodyne detection,[1] a new way of observing nuclear magnetic resonance (NMR). The purpose of this paper is to relate a number of the details of this technique, its theory, its advantages and some applications. This method, which utilizes a coherent optical and radio frequency (rf) induced Raman effect, is capable of monitoring coherent spin transients or nuclear resonances under cw conditions in both ground and optically excited states with high sensitivity and precision. Dilute systems in the gas phase or solid state can now be examined which are inaccessible by conventional NMR. The method, which surpasses previous rf-optical techniques,[2-4] has been demonstrated in a dilute rare earth impurity ion crystal Pr^{3+}:LaF_3, where the first spin echo measurements of an electronic excited state are made, and cw resonances yield NMR line centers and shapes with kilohertz precision. Here we report further measurements which allow us to compare for the first time NMR and optical dephasing studies[5-8] and to test current line broadening theory.[9]

In Fig. 1, the Pr^{3+} (I=5/2) hyperfine energy level diagram reveals the basic stimulated Raman effect where an optical field at the frequency ω_E (solid arrow) and an rf field at the frequency ω_H (squiggle arrow) drive two coupled transitions resonantly, which combine in a two photon process to generate a coherent anti-Stokes field at the sum frequency $\omega_E' = \omega_E + \omega_H$. In addition, a Stokes field at the difference frequency $\omega_E - \omega_H$, due to a second resonant packet, accompanies the above anti-Stokes field. In Fig. 2, the two optical fields, ω_E and ω_E', produce at the photodetector a heterodyne beat signal of frequency $\omega_H = |\omega_E - \omega_E'|$. This optical heterodyne process enhances detection sensitivity, and is closely related to that used in Stark or laser frequency switching experiments.[10]

RJ 3951 (44629) 7/6/83
Physics

RAMAN HETERODYNE DETECTION OF NUCLEAR MAGNETIC RESONANCE***

N. C. Wong*
E. S. Kintzer
J. Mlynek**
R. G. DeVoe
R. G. Brewer

IBM Research Laboratory
San Jose, California 95193

and

Department of Applied Physics
Stanford University,
Stanford, California 94305

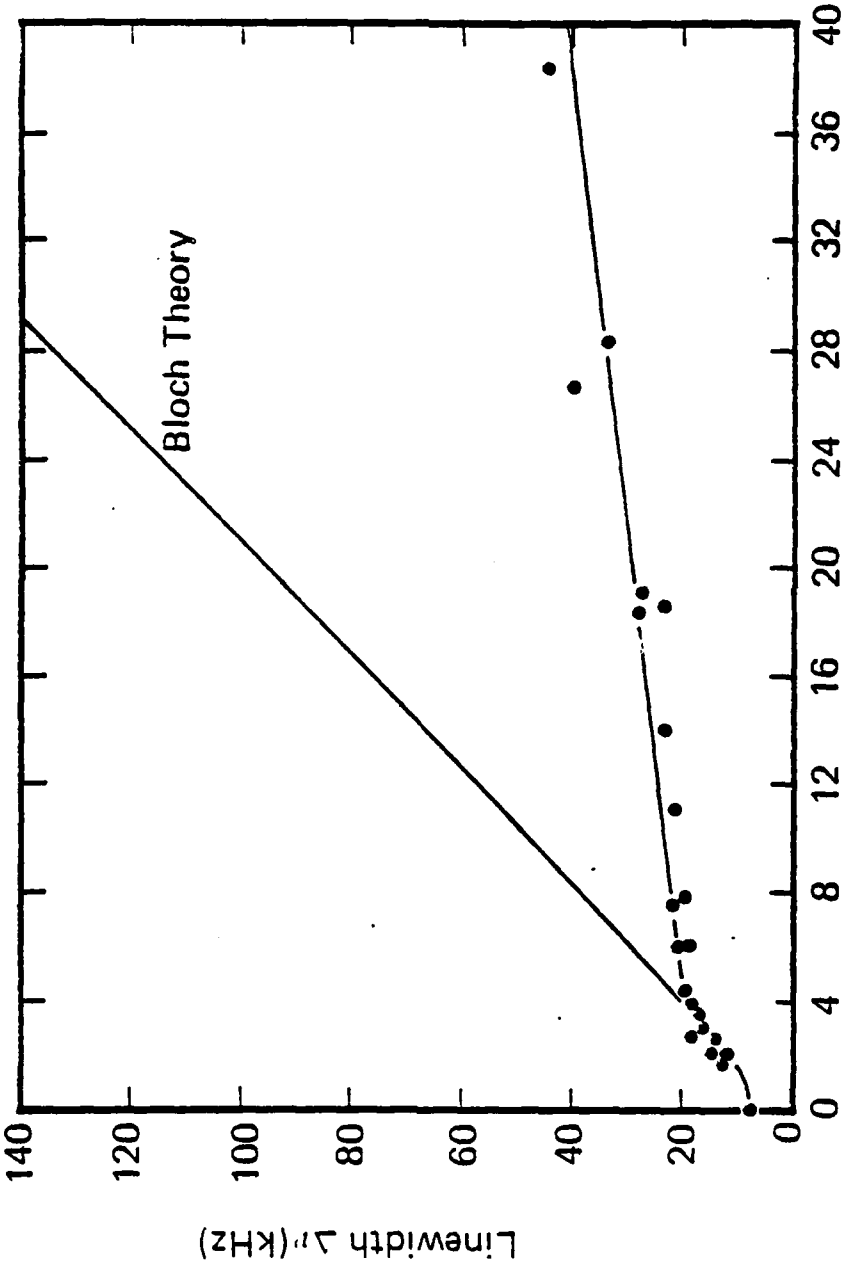
ABSTRACT: A novel coherent Raman effect induced by a laser and a radio frequency (rf) field is used to detect cw and pulsed nuclear magnetic resonance (NMR) in ground and excited electronic states. The effect is illustrated in the impurity ion solid Pr^{3+}:LaF_3 at 1.6°K utilizing the Pr^{3+} optical transition $^3H_4(\Gamma_1) \rightarrow {}^1D_2(\Gamma_1)$. The laser field of frequency ω_E and the rf field (ω_H) induce a light wave at the sum $\omega_E+\omega_H$ (anti-Stokes) and difference $\omega_E-\omega_H$ (Stokes) frequencies, generating an absorptive or dispersive heterodyne beat signal (ω_H) with the laser field at a photodetector. The theory of this effect is characteirzed in a new three-level perturbation calculation which requires, unlike the usual stimulated Raman effect, that all three transitions be electric or magnetic dipole allowed. Detailed predictions are confirmed by cw measurements of the Pr^{3+}:LaF_3 hyperfine splittings where the optical heterodyne signals are shot noise limited. The Pr^{3+} nuclear quadrupole parameters are obtained for the $^3H_4$ and $^1D_2$ states where the line centers are determined with kilohertz precision. The corresponding wave functions show significant hyperfine state mixing, as required for all three transitions to be dipole allowed. The cw lineshapes are narrow (30 to 160 kHz), inhomogeneously broadened by nuclear magnetic interactions, and reveal either a Gaussian or an anomalous second-derivative-like lineshape. The spin echo measurements for the $^3H_4$ and $^1D_2$ hyperfine transitions yield homogeneous lineshapes, which are Lorentzian, and rather surprisingly, linewidths in the narrow range 10 to 20 kHz, a result which tests current line broadening theories.

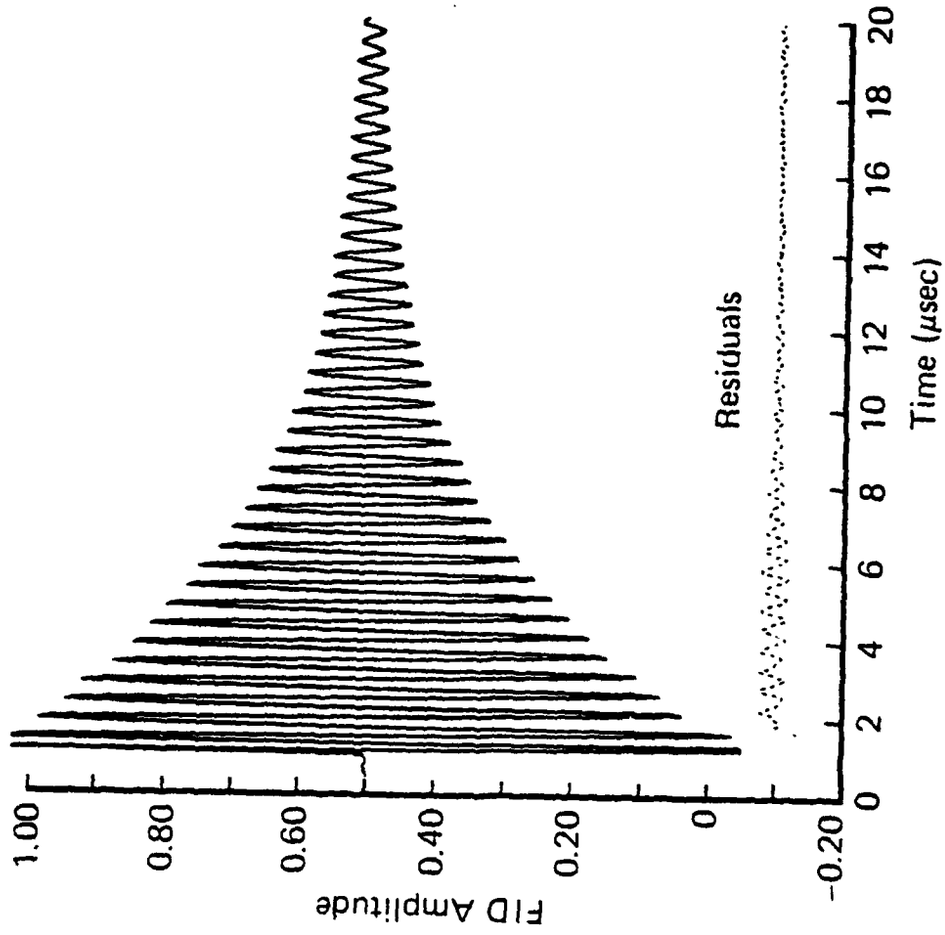
---

*From the thesis of N. C. Wong, June 1983, in partial fulfillment of the requirements for the Ph.D. degree, Stanford University.

**On leave from the Institut für Angewandt Physik, Universität Hannover, Hannover, West Germany.

***Work supported in part by the U.S. Office of Naval Research.


Linewidth $\Delta\nu$ (kHz)
140
120
100
80
60
40
20
0
Bloch Theory
0
4
8
12
16
20
24
28
32
36
40
$\chi/2\pi$ (kHz)


FID Amplitude
1.00
0.80
0.60
0.40
0.20
0
-0.20
Residuals
0
2
4
6
8
10
12
14
16
18
20
Time (μsec)

where $\bar{\Delta}_E \equiv \omega_{32}^o - \omega_E$, $\bar{\Delta}_H \equiv \omega_{21}^o - \omega_H$ are the laser and rf frequency offsets from the center frequencies ω_{32}^o and ω_{21}^o of the inhomogeneously broadened transitions 3↔2 and 2↔1, respectively. σ_E and σ_H are the respective half widths at the 1/e points of the lineshapes g_E and g_H. We assume that the strain broadening is very large and satisfies

$$\sigma_E >> \sigma_H, \gamma_{i3} , \quad i = 1,2 . \tag{2.22}$$

Making use of the *w* function[25]

$$w(z) = \frac{i}{\pi} \int_{-\infty}^{\infty} \frac{e^{-t^2} dt}{z - t} , \quad \text{Im } z > 0 \tag{2.23a}$$

and its property

$$w(-z^*) = w(z)^* . \tag{2.23b}$$

we compute the average of the signal matrix elements

$$\langle \tilde{\rho}_{i3} \rangle = \int_{-\infty}^{\infty} \int_{-\infty}^{\infty} d\Delta_E d\Delta_H g_E(\Delta_E) g_H(\Delta_H) \tilde{\rho}_{i3} , \quad i = 1,2 . \tag{2.24}$$

Noting that the optical inhomogeneous width is large (2.22), the integration over Δ_E is simplified and one obtains

$$\langle \tilde{\rho}_{13} \rangle = \frac{\pi}{\sigma_E \sigma_H} \alpha_2 \beta (\rho_{22}^o - \rho_{11}^o) e^{i\omega_H t} w\left(\frac{\bar{\Delta}_E}{\sigma_E} \right) w\left(\frac{\bar{\Delta}_H + i\gamma_{12}}{\sigma_H} \right) , \tag{2.25a}$$

$$\langle \tilde{\rho}_{23} \rangle = - \frac{\pi}{\sigma_E \sigma_H} \alpha_1 \beta^* (\rho_{22}^o - \rho_{11}^o) e^{-i\omega_H t} w\left(\frac{\bar{\Delta}_E + \omega_H}{\sigma_E} \right) w^*\left(\frac{\bar{\Delta}_H + i\gamma_{12}}{\sigma_H} \right) . \tag{2.25b}$$

The Raman signal polarization $\langle\tilde{P}_s\rangle$ (2.8) consists of an anti-Stokes component $N\mu_{31}\langle\tilde{\rho}^s_{13}\rangle$ and a Stokes component $N\mu_{32}\langle\tilde{\rho}^s_{23}\rangle$. In the case that the strain broadening σ_E is large compared with the rf frequency ω_H, we have

$$w\left(\frac{\bar{\Delta}_E+\omega_H}{\sigma_E}\right) \simeq w\left(\frac{\bar{\Delta}_E}{\sigma_E}\right), \quad \sigma_E >> \omega_H, \tag{2.26}$$

and the Stokes and anti-Stokes components have equal amplitude. If $\sigma_E>>\omega_H$ is not valid, the Raman signal is dominated by either the anti-Stokes component $N\mu_{31}\langle\tilde{\rho}^s_{13}\rangle$ Eq. (2.25a) or the Stokes component $N\mu_{32}\langle\tilde{\rho}^s_{23}\rangle$ Eq. (2.25b), depending on the optical frequency offset $\bar{\Delta}_E$.

For Pr^{3+}:LaF_3, the optical inhomogeneous width is large, and (2.26) is satisfied. Then, one obtains from Eqs. (2.7) and (2.8), and the signal matrix elements (2.25), the Raman signal field Eq. (2.6)

$$\tilde{E}_s = -\frac{4\pi^2 i\hbar k_E L N}{\sigma_E\sigma_H E_o^*}(\rho^o_{22}-\rho^o_{11})\, w\left(\frac{\bar{\Delta}_E}{\sigma_E}\right)$$

$$\times\left[\alpha_1^*\alpha_2\beta\, w\left(\frac{\bar{\Delta}_H+i\gamma_{12}}{\sigma_H}\right) e^{i\omega_H t}-\text{c.c.}\right], \tag{2.27}$$

where L is the length of an optically thin sample. The Raman heterodyne beat signal I_s Eq. (2.10) is given by

$$I_s = a|E_o|^2|H_1|(\rho^o_{22}-\rho^o_{11})\,\text{Re}\left[w\left(\frac{\bar{\Delta}_E}{\sigma_E}\right)\right]\text{Im}\left[w\left(\frac{\bar{\Delta}_H+i\gamma_{12}}{\sigma_H}\right)e^{i\omega_H t}\right] \tag{2.28}$$

where the constant

$$a = \frac{\pi^2 k_E L N}{\sigma_E \sigma_H \hbar^2} \mu_{12}\mu_{23}\mu_{31} \cdot \tag{2.29}$$

In Eqs. (2.28) and (2.29) the definitions (2.4) of the dipole coupling parameters α_1, α_2, and β are used, and the overall phase of the coupling product $\alpha_1^*\alpha_2\beta$ is set to zero.

For on-resonance optical excitation $\sigma_E >> \bar{\Delta}_E$, one can use the expansion[25]

$$w(z) \simeq e^{-z^2}\left(1 + \frac{2iz}{\sqrt{\pi}}\right), \quad z \to 0 \tag{2.30}$$

to recover the usual Gaussian factor

$$w\left(\frac{\bar{\Delta}_E}{\sigma_E}\right) \simeq e^{-\left(\frac{\bar{\Delta}_E}{\sigma_E}\right)^2}, \quad \sigma_E >> \bar{\Delta}_E \cdot \tag{2.31}$$

One then obtains

$$I_s = a' \chi \chi_1 \chi_2 (\rho_{22}^o - \rho_{11}^o)\, e^{-\left(\frac{\bar{\Delta}_E}{\sigma_E}\right)^2}$$

$$\times \left[\cos \omega_H t \ \mathrm{Im}\, w\left(\frac{\bar{\Delta}_H + i\gamma_{12}}{\sigma_H}\right) + \sin \omega_H t \ \mathrm{Re}\, w\left(\frac{\bar{\Delta}_H + i\gamma_{12}}{\sigma_H}\right)\right] \tag{2.32}$$

where $a' \equiv \pi^2 k_E N L \hbar / \sigma_E \sigma_H$. We have again used the coupling parameter definitions (2.4) and their relation with the Rabi frequencies Eq. (2.5). Equation (2.32) is identical[26] with the expression we have obtained earlier.[1]

D. Results of Theory

Within the assumptions of the RWA (2.11), weak fields (2.15), and a large optical inhomogeneous width, (2.22) and (2.26), we have obtained the steady-state Raman heterodyne signal I_s (2.28). From Eq. (2.28) we note that the Raman signal is linear in laser power $|E_o|^2$, and in the magnetic field amplitude $|H_1|$, where a factor $|E_oH_1|$ is required by the two photon process and heterodyning introduces the second $|E_o|$. It is also linear in each of the three dipole moments $\mu_{12}\mu_{23}\mu_{31}$, Eq. (2.29). This shows clearly that the effect is a three-wave mixing process and that no Raman heterodyne signal is observed unless all three transitions are dipole allowed.

The factor $\rho^o_{22}-\rho^o_{11}$ in Eq. (2.28) indicates that a population difference between the Raman levels is required in order to have a non-zero Raman signal. Its actual magnitude is determined by optical pumping which occurs on a slow time scale.

The Raman signal I_s can be reduced to a simple expression when we assume large inhomogeneous widths σ_E and σ_H. For a large optical inhomogeneous width one obtains the Gaussian approximation (2.31). For a large magnetic inhomogeneous width $\sigma_B >> \bar{\Delta}_B$ and also $\gamma_{12} \to 0$, the expansion (2.30) enables one to obtain

$$\mathrm{Im}\left[w\left(\frac{\bar{\Delta}_H + i\gamma_{12}}{\sigma_H} \right) e^{i\omega_H t} \right] \simeq e^{-\left(\frac{\bar{\Delta}_H}{\sigma_H}\right)^2} \left(\sin \omega_H t + \frac{2\bar{\Delta}_H}{\sqrt{\pi}\,\sigma_H} \cos \omega_H t \right) . \qquad (2.33)$$

With rf phase sensitive detection, one can therefore select the in-phase dispersive signal $I_s(0^o)$ or the out-of-phase absorptive signal $I_s(90^o)$ of I_s, Eq. (2.28), given by

$$I_s(0^o) = I_s(90^o) \frac{2}{\sqrt{\pi}} \left(\frac{\bar{\Delta}_H}{\sigma_H} \right) , \qquad (2.34a)$$

$$I_s(90^\circ) = a\,|E_0|^2\,|H_1|\,(\rho_{22}^0-\rho_{11}^0)\; e^{-\left(\frac{\bar{\Delta}_E}{\sigma_E}\right)^2}\; e^{-\left(\frac{\bar{\Delta}_H}{\sigma_H}\right)^2}, \qquad (2.34b)$$

where the approximations (2.31) and (2.33) are used and the constant a is given by Eq. (2.29). The absorptive and dispersive signals display the overall magnetic inhomogeneous Gaussian lineshape, and one is able to measure the line centers and linewidths of the inhomogeneously broadened rf transition alone.

When the conditions $\sigma_B >> \bar{\Delta}_B$, $\gamma_{12} \to 0$ are relaxed, the overall absorptive and dispersive lineshapes are a convolution of a Gaussian and a Lorentzian lineshape, but the essential features of the signals Eq. (2.34) remain the same.

One can write the total field $\tilde{E}_T$ (2.9b) in a manner which reveals explicitly the amplitude modulation (AM) and frequency modulation (FM) sideband structure. If ω_o and ω_m are the carrier and modulation frequencies, respectively, and c and d are the AM and FM modulation depths, we can represent AM by

$$E_{AM} = E_o[1 + c\cos(\omega_m t + \phi)]\, e^{i\omega_o t}, \qquad (2.35a)$$

and FM by

$$E_{FM} = E_o\, e^{i\omega_o t}\, e^{id\cos(\omega_m t+\phi)}. \qquad (2.35b)$$

They can be written as

$$E_{AM} = E_o(1 + u\, e^{i\omega_m t} + u^*\, e^{-i\omega_m t})\, e^{i\omega_o t}, \qquad (2.36a)$$

and, for small FM modulation depth $d<<1$,

$$E_{FM} = E_o(1 + v\, e^{i\omega_m t} - v^*\, e^{-i\omega_m t})\, e^{i\omega_o t}, \qquad (2.36b)$$

where the respective complex AM and FM sideband amplitudes are given by

$$u = \frac{1}{2} c\, e^{i\phi} , \tag{2.36c}$$

and

$$v = \frac{1}{2} d\, e^{i\phi} . \tag{2.36d}$$

Equations (2.36) show that in AM the sidebands at frequencies $\pm\omega_m$ have the same phase, while those in FM have opposite phase. Hence AM and FM can be distinguished by the phase relationship of the sideband complex amplitudes. The total field $\tilde{E}_T$ (2.9b) can be written as

$$\tilde{E}_T = \frac{1}{2} E_o(1 + x\, e^{i\omega_H t} + y\, e^{-i\omega_H t}) \tag{2.37a}$$

and decomposed into

$$\tilde{E}_T = \frac{1}{2} E_o[1 + (u\, e^{i\omega_H t} + c.c.) + (v\, e^{i\omega_H t} - c.c.)] , \tag{2.37b}$$

with

$$u = \frac{1}{2} (x + y^*) \text{ and } v = \frac{1}{2} (x - y^*) , \tag{2.37c}$$

thus showing the AM (second term) and FM (last term) sideband structure. We can, therefore, obtain from the Raman signal field $\tilde{E}_s$ (2.27) the AM and FM sideband complex amplitudes

$$u(AM) = q\ \mathrm{Re}\ w\left(\frac{\bar{\Delta}_E}{\sigma_E}\right) , \tag{2.38a}$$

$$v(FM) = iq\ \mathrm{Im}\ w\left(\frac{\bar{\Delta}_E}{\sigma_E}\right) , \tag{2.38b}$$

$$q = \frac{-i\pi^2 k_E L N}{\sigma_E \sigma_H \hbar^2} (\rho_{22}^o - \rho_{11}^o)(\mu_{12}\mu_{23}\mu_{31}) H_1 \; w\left(\frac{\bar{\Delta}_H + i\gamma_{12}}{\sigma_H}\right) . \qquad (2.38c)$$

Equations (2.37) and (2.38) show clearly the simultaneous presence of AM and FM in the total field. In a square law detector, the FM signal cancels out and only the AM signal (the real part) remains, from which one obtains the absorptive and dispersive signals Eq. (2.34).

When the laser is off-resonant with the optical transition such that $\bar{\Delta}_E >> \sigma_E$, we obtain[25]

$$\lim_{\bar{\Delta}_E >> \sigma_E} w\left(\frac{\bar{\Delta}_E}{\sigma_E}\right) \to \frac{i\sigma_E}{\sqrt{\pi}\,\bar{\Delta}_E} . \qquad (2.39)$$

The AM signal (2.38a) is weak, while the FM signal (2.38b) which contains Im $w(\bar{\Delta}_E/\sigma_E)$ is dominant and therefore can be monitored using an FM detection scheme. The loss in signal due to the large optical frequency offset can be compensated with an increase in laser power. Hence our results predict that the Raman signal can be detected using resonant or nonresonant light in either an AM or FM mode, making it a very versatile technique.

E. A More General Solution

Here we seek a time-dependent solution to the equations of motion (2.12) in the limits of a weak optical field

$$\alpha_1, \alpha_2 \to 0 , \qquad (2.40a)$$

and a large optical inhomogeneous width

$$\sigma_E \to \infty , \qquad (2.40b)$$

with arbitrary rf field strength H_1. From the formal solution for $\tilde{\rho}_{23}(t)$ Eq. (2.13f), the part which contributes to the Raman heterodyne signal is given by

$$\tilde{\rho}^{s}_{23}(t) = \int_0^t dt' \; e^{(i\Delta_E - \gamma_{23})(t-t')} \; e^{-i\omega_H t'} [-i\alpha_1 \tilde{\rho}_{21}(t')] \,, \tag{2.41}$$

with the RWA being the only assumption. Averaging over the inhomogeneous lineshapes (2.21), one obtains

$$\langle \tilde{\rho}^{s}_{23}(t) \rangle = -i\alpha_1 \; e^{-i\omega_H t} \int g_H(\Delta_H) d\Delta_H \int_0^t dt' \tilde{\rho}_{21}(t')$$

$$\times \left[e^{(i\omega_H - \gamma_{23})(t-t')} \int g_E(\Delta_E) d\Delta_E \; e^{i\Delta_E (t-t')} \right] . \tag{2.42}$$

In Eq. (2.42) the matrix element $\tilde{\rho}_{21}(t')$ is assumed to have no Δ_E dependence, which is valid in the limit of a weak optical field (2.40a). This is evident from the structure of the formal solutions Eqs. (2.13a), (2.13b), and (2.13d) which show that $\tilde{\rho}_{12}$ has no zeroth or first order terms in α_1 and α_2. This implies that the primary signal of $\tilde{\rho}_{12}$ comes from the interaction of the Raman levels 1 and 2 with the magnetic field $\vec{H}_1$.

Integrating over $g_E(\Delta_E)$ (2.21a) gives

$$\int_{-\infty}^{\infty} \frac{e^{-\left(\frac{\Delta_E - \bar{\Delta}_E}{\sigma_E}\right)^2}}{\sqrt{\pi}\,\sigma_E} \; e^{i\Delta_E (t-t')} d\Delta_E = e^{-\left[\frac{\sigma_E}{2}(t-t')\right]^2} \; e^{i\bar{\Delta}_E (t-t')} \tag{2.43}$$

and Eq. (2.42) becomes

$$\langle\tilde{\rho}_{23}(t)\rangle = -i\alpha_1\, e^{-i\omega_H t}\int d\Delta_H g_H(\Delta_H)\int_0^t dt'\,\tilde{\rho}_{21}(t')$$

$$\times\, e^{[i(\bar{\Delta}_E+\omega_H)-\gamma_{23}](t-t')}\, e^{-\left[\frac{\sigma_E}{2}(t-t')\right]^2} \qquad (2.44)$$

Invoking the assumption of a large optical inhomogeneous width σ_E (2.40b), the Gaussian factor $\exp\left(-\left[\frac{\sigma_E}{2}(t-t')\right]^2\right)$ is zero unless $t'=t$, thus allowing us to write it as a delta function $\delta(t-t')$. Hence

$$\int_0^t dt'\,\tilde{\rho}_{21}(t')\, e^{[i(\bar{\Delta}_E+\omega_H)-\gamma_{23}](t-t')}\, e^{-\left[\frac{\sigma_E}{2}(t-t')\right]^2}$$

$$= \int_0^t dt'\,\rho_{21}(t') e^{[i(\bar{\Delta}_E+\omega_H)-\gamma_{23}](t-t')}\,\delta(t-t')$$

$$= \tilde{\rho}_{21}(t)\,, \qquad \sigma_E \to \infty\,. \qquad (2.45)$$

One then obtains

$$\langle\tilde{\rho}_{23}(t)\rangle = -i\alpha_1\, e^{-i\omega_H t}\int g_H(\Delta_H)\tilde{\rho}_{21}(\Delta_H,t)d\Delta_H\,, \qquad (2.46a)$$

and similarly

$$\langle\tilde{\rho}_{13}(t)\rangle = -i\alpha_2\, e^{i\omega_H t}\int g_H(\Delta_H)\tilde{\rho}_{12}(\Delta_H,t)d\Delta_H\,. \qquad (2.46b)$$

Substituting (2.46) into (2.8), one obtains from Eqs. (2.6) and (2.7) the time-dependent Raman signal field $\tilde{E}_s$:

$$\tilde{E}_s(t) = \frac{-2\pi\, k_E LN}{\hbar}\,\mu_{13}\mu_{32}E_o\,\mathrm{Re}\langle\rho_{12}(t)\rangle_H\,, \qquad (2.47)$$

where

$$\langle \rho_{12}(t) \rangle_H \equiv \int g_H(\Delta_H) \rho_{12}(\Delta_H, t) d\Delta_H \,, \tag{2.48}$$

and the relation (2.11a) for ρ_{12} is used.

The Raman signal (2.47) thus obtained is derived within the RWA and in the limits of a weak optical field (2.40a) and a large optical inhomogeneous width (2.40b). It is valid for cw or transient excitations and arbitrary magnetic field strength H_1. Since there is no constraint imposed on the Raman excitation, multiple rf fields with arbitrary field strengths and frequencies can be applied. The laser field acts as a faithful probe which reproduces coherently cw or transient phenomena in the Raman spin levels.

III. CW MEASUREMENTS

A. Review

We present the results of Raman heterodyne measurements made on the lowest (Γ_1) crystal field states of the zero-phonon $^1D_2 \leftrightarrow {}^3H_4$ transition in Pr^{3+}:LaF_3 at 5925Å. These electronic singlet states, where the $2J+1$ degeneracy is lifted by the crystal field because of the low C_2 Pr^{3+} site symmetry,[27] are each split into three doublets ($\pm I_z$) by the second order hyperfine interaction[28,29] and the nuclear electric quadrupole interaction[30] of Pr^{3+} ($I=5/2$), as shown in Fig. 1. There are six magnetically inequivalent Pr^{3+} sites.[27]

Hyperfine interactions in Pr^{3+}:LaF_3 have been studied by various techniques such as rf-optical double resonance,[2,3] enhanced and saturated absorption,[20,31] photon echo nuclear double resonance (PENDOR),[4] and photon echo modulation.[32] In the present study, the level splittings as well as the magnetic inhomogeneous lineshapes and widths of the rf hyperfine transitions ($I_z=1/2 \leftrightarrow 3/2$) and ($I_z=3/2 \leftrightarrow 5/2$) in both $^3H_4$ ground and $^1D_2$ excited states are determined with kilohertz precision, about a five-fold improvement over earlier measurements.

The high sensitivity of the Raman heterodyne technique has yielded narrower inhomogeneous linewidths (Table I) than previous measurements[2-4,17,20,32] which appear to have been instrument limited. The hyperfine splittings (Table I) are fit with the total nuclear quadrupole Hamiltonian[29] (3.1) to obtain the quadrupole parameters D and E (Table II) and the eigenstate amplitudes of the hyperfine levels (Table III), where the $^1D_2$ excited state is found to be strongly mixed (Sec. IIID). The observed lineshape in Fig. 4(b) is compared to the predictions of our three level calculation (Sec. II) and a Monte Carlo line broadening theory,[9] where agreement is found in both cases. Anomalous lineshapes resembling second derivatives are also observed, as shown in Figs. 4(a) and 5, where a pair of symmetrical side lobes appear.

B. Apparatus

A schematic diagram of the apparatus for the cw Raman heterodyne experiment is shown in Fig. 6. A Coherent 599 single mode, linearly polarized cw dye laser oscillating in the locked mode (linewidth 4 MHz pp) at 5925Å excited the Pr^{3+} $^3H_4 \leftrightarrow {}^1D_2$ transition by propagating along the c axis (also the C_3 axis) of a 0.1 at. % Pr^{3+}:LaF_3 crystal ($4\times4\times5$ mm^3) with a beam diameter of ~100 microns and power in the range 3–50 mW. Radio frequency magnetic fields H_1, polarized along the crystal c axis, were applied by a small pair of Helmholtz coils surrounding the crystal, where both were immersed in a liquid helium cryostat at 1.6K. Fields up to 3 Gauss in the frequency range $\omega_H/2\pi$=2–20 MHz were supplied by an HP 3325A frequency synthesizer and an ENI 400AP broadband rf amplifier. In addition, a static magnetic field H_0 up to 160 Gauss was applied normal to the crystal c axis. The forward scattered laser light was incident upon an E.G.&G. FND-100 photodiode.

The ac component of the photodiode signal was amplified by a low noise 47 dB broadband rf amplifier Q-bit QB-256 which was then mixed with the HP 3325A local oscillator using a Microcircuits Laboratories ZLW-1-1 double balanced mixer (DBM). The phase of the local oscillator was adjusted to give an absorptive or dispersive Raman signal. An unequal time delay between the Raman signal and the reference at the DBM was avoided as it could distort the signal lineshape, caused by a frequency dependent phase difference between the two inputs.

The mixer output voltage was amplified 100× with a two-stage 500 kHz bandwidth dc amplifier, then filtered and amplified again by a Tektronix 7A22 differential amplifier which had a variable bandwidth, set large enough to give an undistorted lineshape for a given rf sweep rate. The signal was averaged by a Data Precision 6000 Waveform Analyzer and model 610 module with 100 kHz 14-bit analog digital conversion. The averaged signal was sent to an IBM Personal Computer for storage and further analysis.

The Raman signal from the $^1D_2$ excited state hyperfine transitions could be observed only if one modified the $^3H_4$ ground state optical pumping. This was achieved by externally sweeping the laser frequency (Sec. VB) at a rate ~250 MHz/0.25 sec, well within the ~5 GHz optical inhomogeneous lineshape. A slower sweep rate reduced the signal size implying that the optical pumping cycle was completed within a time ~10 ms. Furthermore, we had the option of gating the signal averager so that data could be taken during the positive or negative frequency sweep or both. Laser frequency sweeping was not required for the $^3H_4$ hyperfine transitions.

In cases where it was necessary to achieve high accuracy for the line centers and widths, the experiment was performed under the following conditions. Optical power in the

range 3-10 mW was employed so that the Raman signal was in the linear low-power regime according to Eq. (2.28). Saturation of the rf transition was avoided by utilizing low rf magnetic fields (0.08-0.16G peak), so that the linewidths were not power broadened and the line centers remained unshifted. Under these conditions, the Raman signal was easily detected as a result of averaging (~1,000 sweeps) and the high sensitivity of the technique. We note that the (I_z=3/2⟷5/2) transition frequencies of both $^3H_4$ ground and $^1D_2$ excited states were shifted by −10 kHz at higher rf power (H_1~1G), whereas the 8.47 MHz and 3.7 MHz resonances did not show any frequency shift.

C. Confirmation of Theory

We have confirmed the predictions of the three-level calculations (Sec. IID) in each of the four hyperfine transitions. (i) In the low power limit, the Raman heterodyne signal is found to depend linearly on the rf field amplitude H_1 and the laser intensity $|E_o|^2$, Eq. (2.32). (ii) The absorptive and dispersive components of the signal can be obtained by properly adjusting the rf phase ϕ (Fig. 2), as shown in Fig. 4(b), where (iii) the observed absorptive lineshape (solid line) of the 16.7 MHz transition is essentially a Gaussian (open circles) Eq. (2.34b), implying that the transition is indeed inhomogeneously broadened.

Table I shows that the two hyperfine transitions (I_z=1/2⟷3/2) and (I_z=3/2⟷5/2) have the same low field linewidths within an electronic level ($^3H_4$ or $^1D_2$). The linewidths of the $^3H_4$ ground state (160 kHz) and $^1D_2$ excited state (32 kHz) scale (~5) approximately as the ratio of the gyromagnetic ratios $|\vec{\gamma}(^3H_4)|/|\vec{\gamma}(^1D_2)|$. This is expected from theory[33] for a $|\Delta I_z| = 1$ magnetic dipole transition in an inhomogeneous magnetic local field where $|\vec{z}|(^3H_4)/(2\pi)| = 11.6$ kHz/G is a low field result[27] but $|\vec{z}(^1D_2)/2\pi| = 3.6$ kHz/G is obtained in the high field regime,[31] the ratio being 3.2.

At a dc field H_o=30-150G, the $^3H_4$ ground state inhomogeneous widths have been observed to narrow from the zero field values of 160 kHz to ~100 kHz, in agreement with Monte Carlo (82 kHz) and second moment (84.5 kHz) line broadening calculations.[9] Such a reduction in the static dipolar linewidth when H_o is increased from its zero value agrees with a second moment calculation by Abragam and Kambe.[34]

). Nuclear Quadrupole Interaction

In Pr^{3+}:LaF_3, each electronic level ($^3H_4$ or $^1D_2$) is split into three doublets ($\pm I_z$) by the dominant second order hyperfine interaction[28,29] and the nuclear electric quadrupole interaction[30] of Pr^{3+} (I=5/2). The second order hyperfine interaction, which is determined by the crystal field splittings and the hyperfine coupling constant, enhances the effective Pr^{3+} nuclear magnetic moment.[28] Since the strength of this enhanced, second order hyperfine interaction differs for each electronic level, the enhanced gyromagnetic tensors of the $^3H_4$ ground and $^1D_2$ excited states can vary in magnitude and orientation. The pure nuclear quadrupole interaction and the hyperfine-induced nuclear pseudoquadrupole interaction can be described by a single total nuclear quadrupole Hamiltonian[29]

$$\mathcal{H}_Q = D\left[I_z^2 - I(I+1)/3\right] + E\left(I_x^2 - I_y^2\right) , \qquad (3.1)$$

where each crystal field state has a different set of quadrupole parameters D and E. We also define an overall asymmetry parameter $\eta \equiv |3E/D|$.

The quadrupole splittings in the earth's field (Table I) obtained by the Raman heterodyne technique can be fit[30] with the Pr^{3+} nuclear quadrupole Hamiltonian (3.1), and supply the quadrupole parameters D and E and the asymmetry parameter η for each electronic state. The value of η allows the determination of the amount of state mixing of

ıen the optical transition $^3H_4$ I_z=1/2 (3/2)→$^1D_2$ I_z=1/2 (3/2) is swept immediately after
e transition $^3H_4$ I_z=5/2→$^1D_2$ I_z=5/2. This implies that the Raman signal is generated
ly when the laser is positively swept (or negatively) but not in the other direction.
hether the signal appears on the positive or negative sweep depends on the absolute
dering of the ground state hyperfine levels.

We have observed at H_o=0G that the $^1D_2$ (I_z=1/2↔3/2) resonance is stronger
·5×) when the laser is in a positive sweep, while that of the $^1D_2$ (I_z=3/2↔5/2) transition
stronger (~5×) when the laser is in a negative sweep. This observation should allow us to
:termine the absolute ordering of the $^3H_4$ ground state hyperfine manifold, thus determining
e sign of the quadrupole parameter D. A mathematical model of the optical pumping cycle
modified by the laser frequency sweeping is now under investigation.

I. SENSITIVITY

The ability of the Raman heterodyne technique to detect both cw and pulsed NMR in
ound or optically excited state is due to the high sensitivity afforded by the shot noise
nited performance of the heterodyne process. Here we show a signal to noise (S/N)
ıalysis using the cw Raman heterodyne signal of Fig. 4(a).

The total optical power incident on a photodetector is

$$P = P_o(1 + |u|^2 + 2|u| \sin\omega_H t) , \qquad (6.1)$$

here $P_o = AcE_o^2/8\pi$ is the input laser power, A and c being the laser beam cross section
ıd the speed of light, respectively, and $|u| = |2\tilde{E}_s/E_o|$ is the AM sideband amplitude
q. (2.38a). The factor of 2 in $|u|$ is due to the definitions of $\tilde{E}_s$ and E_o in Eqs. (2.6) and
.1a). For $|u|<<1$, the dc power $P_o \approx P$ is much greater than either tne heterodyne power

nd 16.7 MHz transitions, respectively, and the lineshape of the 16.7 MHz transition also tarts to change more.

Figure 11 shows that the lineshape depends quite critically on the optical pumping ycle, as modified by the rf sweep times. However, we note that the basic features of the laman signal, as described in Sec. II, remain the same. We should mention that within the ptical inhomogeneous line, optical pumping can modify the population difference $\rho^{o}_{22}-\rho^{o}_{11}$ in :q. (2.20) differently, in sign and magnitude, depending on the laser frequency detuning. herefore, in the integration over the optical inhomogeneous lineshape Eq. (2.24), one annot assume that $\rho^{o}_{22}-\rho^{o}_{11}$ is constant, and the effect is that the Raman signal phase and nagnitude in Eq. (2.28) are modified.

3. Laser Frequency Sweeping

In Sec. IIIB and IVB, it was mentioned that laser frequency sweeping was used to edistribute the ground state population resulting from optical pumping, and this allowed letection of excited state Raman heterodyne signals.

In a sweep cycle, the hole that is burned in a particular frequency packet within the ·5 GHz optical inhomogeneous lineshape during the positive sweep is refilled in the negative weep. As a concrete example, consider the $^1D_2$ (I_z=1/2↔3/2) transition at 3.7 MHz. If here is no laser sweeping, the optical transition connecting the transitions $^3H_4$ I_z=1/2 3/2)→$^1D_2$ I_z=1/2 (3/2) pumps the ground state population into the $^3H_4$ I_z=5/2 level, hereby quenching the excited state (I_z=1/2↔3/2) Raman signal.

When the laser is swept to excite the $^3H_4$ (I_z=5/2)↔$^1D_2$ (I_z=5/2) transition, the H_4 (I_z=1/2) and (I_z=3/2) levels are re-populated, thus providing population to the excited tate and a Raman signal is generated. We note that this re-population is effective only

transition should be stronger than that of the 8.5 MHz transition. Such a difference in signal size has been observed. Based on this model, one can make the following predictions.

(i) An increase in the 8.5 MHz transition Raman signal (H_0=0G) should occur upon the application of a 16.7 MHz rf field which transfers the optically pumped population in $I_z=\pm 5/2$ to the Raman level $I_z=\pm 3/2$. (ii) A similar signal increase of the 8.5 MHz transition (H_0=0G) should also occur if both ground state hyperfine transitions are excited in a single rf frequency sweep, which re-distributes the hyperfine population within a time equal to the rf sweep time ($<T_1^*$).

In the present study, observations have been made which agree with the predictions (i) and (ii). At H_0=0G, the 8.5 MHz cw Raman signal increases by ~5x, when (i) a 16.7 MHz rf field (~1G) is applied, or when (ii) both ground state hyperfine transitions (8.5 and 16.7 MHz) are excited in a single rf sweep (sweep time=10 ms). In addition, a similar increase is observed when (iii) a dc field H_0>10G is applied, which quenches the Pr-La cross relaxation process[37] and mixes the ground state hyperfine states.

In (ii) as we vary the rf sweep time from 10 ms to 10s, the signal size decreases and its phase changes. Figure 11 shows four cw Raman signals each with a different sweep time. When the sweep time varies from (a) 10 ms to (b) 100 ms, the relative size of the 8.5 MHz side lobes changes slightly due to a phase change of the signal. As the sweep time is increased to (c) 1 sec, the order of T_1^* of the 8.5 MHz transition, the signal size of both transitions is reduced ~50% and ~20% for the 8.5 MHz and 16.7 MHz transitions, respectively. The 8.5 MHz signal has a larger reduction and its lineshape changes more dramatically. When the sweep time approaches the relaxation time of the 16.7 MHz transition (d) 10 sec, the signal size decreases further by ~70% and ~50% for the 8.5 MHz

V. OPTICAL PUMPING

Optical pumping[2,20] occurs in $Pr^{3+}:LaF_3$ when the population of a ground state Pr^{3+} hyperfine level is transferred to other hyperfine levels in the $^3H_4$ ground state via excitation to the $^1D_2$ hyperfine levels with subsequent relaxation ($\Delta I_z \neq 0$). This action creates a nonthermal ground state nuclear population distribution that yields nonvanishing Raman signals Eq. (2.28) of the ground state, as discussed in the theoretical treatment, Sec. III. On the other hand, the $^1D_2$ excited state Raman signals are observed only when this optical pumping cycle is modified by laser frequency sweeping.

A. Effect of Ground State Spin Lattice Relaxation

According to the studies of Shelby, Macfarlane, and Yannoni,[37] for a 0.1 at. % $Pr^{3+}:LaF_3$ sample, the experimentally deduced spin lattice relaxation times T_1^* of the ground state 8.5 MHz and 16.7 MHz transitions at 1.6K in the earth's magnetic field are, respectively, 5 sec and 100 sec. The faster T_1^* time for the 8.5 MHz ($I_z = 1/2 \leftrightarrow 3/2$) transition is attributed to a Pr-La cross relaxation energy-conserving process involving simultaneous spin flips of a Pr nucleus and three surrounding La nuclei. The long spin-lattice relaxation time of the 16.7 MHz ($I_z = 3/2 \leftrightarrow 5/2$) transition is assumed to be due to Pr-Pr interaction.

In a cw measurement at $H_0 = 0G$ for the $^3H_4$ 8.5 MHz ($I_z = \pm 1/2 \leftrightarrow \pm 3/2$) transition, population in these levels is optically pumped to the $^3H_4$ ($I_z = \pm 5/2$) hyperfine states and remains there due to the long ($I_z = \pm 5/2$) relaxation time ($T_1^* \sim 100s$), thus reducing the Raman signal. Similarly in a cw measurement of the $^3H_4$ 16.7 MHz ($I_z = \pm 3/2 \leftrightarrow \pm 5/2$) transition, population is optically pumped to the $^3H_4$ ($I_z = \pm 1/2$) states. But here the relaxation from ($I_z = \pm 1/2$) to ($I_z = \pm 3/2$) is faster due to the shorter relaxation time ($T_1^* \sim 5s$) of the 8.5 MHz transition, and therefore the Raman signal of the 16.7 MHz

The oscillation in Fig. 9(b) occurs because the FID is modulated due to the Zeeman splitting at H_0=30G. The much longer-lived FID-echo interference in Fig. 9(b) (H_0=30G) suggests a longer T_2 dephasing time of the FID, which is confirmed by the narrowing of the linewidth from 21 kHz (H_0=0G) to 11 kHz (30G).

F. Optical Effects in Spin Echo Measurements

To test how the NMR linewidth measurement is affected by the presence of the optical field, we have used an acousto-optic modulator to gate the laser amplitude with different gating sequences. (i) An echo signal is observed when the laser field is turned off just before the first rf pulse and on just before the echo, indicating that the laser is not required for the formation of the spin echo. (ii) Similarly, when the laser field is turned off just after the first rf pulse and on just before the echo, T_2 measurements of the 3.7 MHz transition at H_0=30G and the 16.7 MHz transition at H_0=0G (Table IV) show no change in the linewidths. This implies for these two transitions that when the laser is on during an rf pulse sequence, there is no optical power broadening in the NMR homogeneous widths. This procedure (see Sec. IVB) was also used for echo amplitude calibration.

(iii) We have made linewidth measurements on the $^1D_2$ excited state hyperfine transitions with the laser turned on 200 μs before and off 200 μs after the rf pulse sequence, at a repetition rate of 30 Hz. Table IV shows that there is no change in linewidth for the 3.7 MHz (I_z=1/2$\leftrightarrow$3/2) transition with optical gating, but the 4.8 MHz (I_z=3/2$\leftrightarrow$5/2) linewidth is reduced from 15$\pm$2 kHz to 10$\pm$2 kHz. The present results are preliminary, and further studies in this system and other impurity ion solids are planned to determine the nature of this line narrowing effect.

Due to hyperfine state mixing, it is necessary to compute the expectation value $\langle I_x \rangle$ for the 16.7 MHz, 4.8 MHz, and 3.7 MHz transitions, using the eigenstate amplitudes $a(I_z)$ in Table III, in order to obtain from Eq. (4.1) $\gamma_x/2\pi(^3H_4)=4.55$ kHz/G, and $\gamma_x/2\pi(^1D_2)=1.3$ kHz/G. The uncertainty (~10%) of γ_x is due to the accuracy of the determination of the Rabi frequencies and the rf field amplitudes. Therefore, the Pr^{3+} nuclear dipole moment in the $^3H_4$ ground state is enhanced ~3.5× relative to that in the $^1D_2$ excited state, which is approximately the same as the bare Pr^{3+} nuclear moment.[29,36]

Within experimental error our $\gamma_x/2\pi(^3H_4)$ value is consistent with Erickson's 4.98±0.04 kHz/G obtained by a measurement of the ground state Zeeman splitting,[27] and that of Macfarlane and Shelby (4.2 kHz/G) by nutation at $H_0=0$G.[3,31] In contrast, our measured $\gamma_x/2\pi(^1D_2)=1.3$ kHz/G differs from that (2.2±0.1 kHz/G) of Macfarlane and Shelby obtained from a high field study.[31]

E. Interference Effect in Spin Echo Measurements

In Fig. 9(a), the natural logarithm of the echo amplitude of the 16.7 MHz transition at $H_0=0$G is plotted as a function of the pulse delay time τ. Note that the signal "bends" over near the time origin. Similarly, the same effect occurs at $H_0=30$G in Fig. 9(b), where the "bending" extends to a longer delay time (~30 μs). This feature is due to an interference between the echo and the FID of the second pulse when they overlap in time. This interference limits the minimum delay time between the two excitation pulses, and has been observed in echoes of the other hyperfine transitions. To reduce this interference for echoes measurements, the dc field is made inhomogeneous by placing a small bar magnet near the sample, creating a field gradient at the crystal. We note that Shelby et al. have observed a similar structure in the 16.7 MHz transition echo measurement using a different rf-optical detection scheme.[3]

$^3H_4$ NMR linewidths (~10-20 kHz). There is clearly a close link between the optical and NMR measurements, but a proper theory has yet to be developed to make such a connection.

D. Nutation and FID

The gyromagnetic ratio $\vec{\gamma}$ for the ground and excited electronic states can be obtained from spin nutation measurements. They can be compared to reveal the amount of enhancement of the Pr^{3+} nuclear magnetic moment due to the second order hyperfine interaction.[28]

Spin nutation and FID are observed when a single rf pulse H_1 at the transition frequency is applied along the crystal c axis, which coincides with the C_3 axis. From the Rabi frequency χ one can measure the magnetic dipole moment $\mu_x = \hbar\chi/H_1$ and deduce the gyromagnetic ratio γ_x from the relation

$$\mu_x \equiv \gamma_x \hbar \langle I_x \rangle . \tag{4.1}$$

Here we follow Erickson's convention that the Pr^{3+} site axis, which coincides with the crystal C_3 axis, is the x axis.[27]

Figure 8 shows a nutation and FID signal of the ground state 16.7 MHz transition at H_0=0G when a single 100 μs rf pulse with H_1=6.4G is applied. The nutation is fit with a zero order Bessel function $J_0(\chi t)$[21] to obtain the Rabi frequency $\chi/2\pi = \mu_x H_1/h$ (33 kHz) to within 5%. From nutation measurements at H_0=0G with different rf field strength H_1 (5-20G), we obtain the magnetic dipole moments $\mu_x/h = \chi/2\pi H_1$ ~5.2 kHz/G, ~1.6 kHz/G, and ~2.0 kHz/G for the 16.7 MHz, 4.8 MHz, and 3.7 MHz transitions, respectively. Measurements at $H_0 \neq 0$G show a variation in the dipole moments of less than 10% for H_0 up to 110G.

under different experimental conditions (dc field strength and gating of laser field). Figure 9 compares the homogeneous linewidths (FWHM) $\Delta f_H = 1/\pi T_2$ of the 16.7 MHz transition at (a) H_0=0G (21±2 kHz) and (b) H_0=30G (11±2 kHz), showing a factor of two difference in the linewidth. The linewidth of 21±2 kHz at H_0=0G agrees with that of Shelby and coworkers[3] (19 kHz, H_0=0G). We have found no variation in the 16.7 MHz transition linewidth when dc fields in the range 30-70G are applied in the echo measurements. This implies that H_0=30G is sufficient for the linewidth reduction.

In a dc field $H_0 \geq 30$G, the ^{19}F nuclei are quantized along $H_0 \perp c$ axis, rather than the local fields due to the ^{141}Pr and other ^{19}F nuclei. Under such a condition, the nonsecular terms of the ^{19}F-^{141}Pr dipolar Hamiltonian are small[34] and therefore there is a corresponding reduction in the ^{19}F-^{141}Pr dipolar interaction. This in turn narrows the homogeneous linewidth, as is demonstrated in the 16.7 MHz transition (Fig. 9).

Table I shows that the inhomogeneous widths of the hyperfine transitions for H_0=0G are the same within an electronic level (160 kHz for $^3H_4$ and 32 kHz for $^1D_2$), but spin echo measurements at H_0=30G (Table IV) show narrower linewidths for the (I_z=3/2↔5/2) transitions (11 kHz for $^3H_4$ and 15 kHz for $^1D_2$) than the (I_z=1/2↔3/2) transitions (20 kHz for both $^3H_4$ and $^1D_2$). It is also noted that while the $^3H_4$ and $^1D_2$ inhomogeneous widths scale approximately as their gyromagnetic ratios (Sec. IIIC), there is no such relationship in the homogeneous linewidth measurements. The Monte Carlo calculation[9] points out that such a linear scaling is not expected.

Last of all, it is noted that photon echo measurements at H_0=80G⊥c axis on the $^1D_2 \leftrightarrow {}^3H_4$ optical transition by gated heterodyne detection gives an optical homogeneous linewidth (FWHM) of ~14 kHz.[6,8] This value of ~14 kHz is in agreement with the $^1D_2$ and

oscilloscope (bandwidth: 10 MHz). The averaged signal was sent to the computer for further analysis.

The pulse nature of the transient signal required a large detection bandwidth (~500 kHz) so that signal averaging was often necessary. In the excited state measurements, laser frequency sweeping was required as described in Sec. IIIB. The FID and echo were observed to be out of phase with the nutation, as predicted by theory,[21] which is shown in a spin echo of the 8.5 MHz transition (Fig. 7(a)) and in the nutation and FID of the 16.7 MHz transition (Fig. 8).

In a spin echo experiment, an rf pulse sequence of $\sim\pi/2$ and $\sim\pi$ was applied with field strength H_1=25-65G $\parallel$ c axis. The two rf pulses had variable widths (1-4 μs) and were separated by a digitally controlled delay time (4-70 μs). When a dc field $H_0 \perp$ c axis of >15G was applied, the optical pumping cycle was modified and the transients of the 3.7 MHz, 4.8 MHz, and 8.5 MHz transitions were enhanced by ~5-10×. At H_0=0G, spin echoes were observed only in the 16.7 MHz transition.

Figure 7(b) shows an echo signal of the 16.7 MHz transition at a high dc field H_0=67G, where both the FID and echo are modulated at the Zeeman frequency 390±10 kHz. A cw spectrum of the 16.7 MHz transition in the same field reveals that one of the three pairs of Pr^{3+} sites is Zeeman split by ±390 kHz. Contribution to the echo signal from the other Zeeman lines was suppressed due to the narrow Fourier frequency range of excitation (pulse width of 1-4 μs) and the site-selective laser polarization.[27,35]

C. Homogeneous Linewidth Results

Table IV summarizes the results of spin echo measurements for the two hyperfine transitions (I_z=1/2↔3/2) and (I_z=3/2↔5/2) in both $^3H_4$ ground and $^1D_2$ excited states

(Sec. IVD), and (ii) observe an interference effect of the echo amplitude when the delay time is small (Fig. 9).

B. Apparatus

For the transient Raman measurements, the optical arrangement of Fig. 6 remained the same while a different electronics configuration was required, as shown in Fig. 10. Proper impedance matching of the rf input to the resonant Helmholtz coils yielded up to 65 Gauss of pulsed rf fields which were derived from a gated HP 3325A frequency synthesizer and followed by a broadband rf power amplifier ENI 350L. The gate was a home-built multiple pulse generator capable of producing pulses of variable widths (1-100 μs) with digitally controlled pulse separations, and was also used in the detection process described below.

The ac component of the photodiode signal was filtered with a bandpass filter centered at the rf transition frequency (3-17 MHz) with ~1 MHz full width at -3 dB, and was amplified by an rf amplifier Q-bit QB-256. In spin echo measurements, the nutation signal was attenuated by a gated current controlled DBM but the echo was not, providing an effective ~10× gain on the echo. This put the nutation and echo on the same vertical scale so that in the analysis the echo amplitude could be calibrated with respect to the first pulse nutation, a procedure that was required due to the laser power fluctuation from one pulse sequence to the next. The rf signal was then amplified by a Q-bit QB-188 amplifier before being mixed with a local oscillator derived from a second HP 3325A frequency synthesizer (FS2), which was phased locked to the first one (FS1) and was used here as a convenient and accurate phase shifter. The relative phase of the two synthesizers was adjusted to yield the in-phase or out-of-phase component of the mixer signal, which was then fed through the 500 kHz bandwidth dc amplifier and averaged with a Tektronix 468 digital storage

minimum (~5× smaller) at H_0=3.3G (> earth's field of ~0.5G). Further increase of H_0 reverses the phase of the signal, which starts to increase in magnitude. At H_0=6.2G, it reaches a signal size about the same as that at H_0=0G. A similar behavior in the 8.47 MHz resonance has also been observed. This observation suggests that the anomalous lineshapes in Figs. 4(a) and 5 may be related in a complicated way to the local magnetic fields due to the ^{19}F nuclei, which are modified by the application of a small dc field. Further studies in this system and other impurity ion solids should illuminate the exact nature of these side lobes.

IV. COHERENT SPIN TRANSIENTS

A. Motivation

As is well known, coherent spin transients[33] are useful for the study of nuclear time dependent phenomena. In Pr^{3+}:LaF_3, the ^{19}F-^{19}F spin flip fluctuations[5,7] are responsible for the dephasing of both the optical and hyperfine transitions. Therefore, it is of interest to obtain homogeneous widths of the hyperfine transitions not only in the ground state but also in the optically excited state, thus allowing a comparison with the optical homogeneous linewidth.[5-8]

Previous transient studies of Pr^{3+} hyperfine transitions have been confined to the ground state.[3] The Raman heterodyne technique has enabled us to observe spin echoes (Fig. 7), free induction decay (FID) and nutation (Fig. 8) of each hyperfine transition in both $^3H_4$ ground and $^1D_2$ excited electronic levels. Spin echo measurements have yielded homogeneous linewidths for the four rf transitions (Table IV), which are compared for the first time with the homogeneous width of the $^3H_4 \leftrightarrow {}^1D_2$ optical transition. Coherent spin transients have also allowed us to (i) measure the gyromagnetic ratio γ_x by spin nutation

The present ground state 8.47 MHz and 16.7 MHz transition linewidths (Table I) are in agreement with our previous values[1] (160 kHz), which are also narrower than earlier measurements.[2,3,17] The weak excited state sum frequency ($I_z = 1/2 \leftrightarrow 5/2$) 8.51 MHz resonance observed in photon echo modulation[32] does not appear in the ground state 8.47 MHz lineshape of Fig. 4(a). This is because the laser is not swept during the ground state measurement and optical pumping greatly reduces the population in the excited state, thus making the 8.51 MHz resonance too weak to be detected.

The $^3H_4$ 8.47 MHz transition in Fig. 4(a) and the $^1D_2$ 3.7 MHz transition in Fig. 5 do not conform to a Gaussian lineshape but more closely resemble a second derivative due to the presence of a pair of symmetrical side lobes. Although the nature of the side lobes is not understood, we have determined some of their characteristics, in particular those of the 8.47 MHz transition. In contrast, the 4.8 MHz lineshape exhibits, to a lesser degree, a similar side lobe structure, but the 16.7 MHz resonance of Fig. 4(b) exhibits a pure Gaussian lineshape with no side lobes whatsoever.

We have tried unsuccessfully to eliminate the 8.47 MHz side lobes in Fig. 4(a) by (1) applying 3.7 MHz and/or 4.8 MHz rf fields (to check the presence of the excited state sum frequency 8.51 MHz resonance), (2) applying a 16.7 MHz rf field (0-3G, to modify the optical pumping cycle), (3) applying a static magnetic field (0-20G), (4) changing the rf sweep rate (0.01-1 sec), (5) rf power (0.08-5G), and (6) laser power (3-40 mW). These tests modify the anomalous lineshape only to the extent of a change in the signal size or an overall phase shift.

An interesting effect has been observed in the $^1D_2$ 4.8 MHz resonance when a small dc field is applied. As H_0 is increased from zero, the signal decreases initially and reaches a

$$|I_z> = \sum_{I_z=-5/2}^{5/2} a(I_z)\,|I_z^o>\,, \tag{3.2}$$

where from Eq. (3.1), $\eta \equiv |3E/D| = 0$ implies that there is no mixing of the hyperfine states. The coefficients $a(I_z)$ are given in Table III. Due to the large asymmetry parameter $\eta(^1D_2)=0.706$, the significance of state mixing in $^1D_2$ is apparent. The mixing of $|I_z^o>$ in the excited state therefore makes possible the electric dipole $^1D_2 \leftrightarrow {}^3H_4$ optical transition when $\Delta I_z \neq 0$, and gives rise to the Raman heterodyne signal, which requires that all three transitions be active Eq. (2.29).

We note that the present ground state quadrupole parameters (Table II) and eigenstate amplitudes $a(I_z)$ (Table III) are in agreement with those obtained by Erickson.[2] However, Erickson has chosen the other set of $|D|$ and $|E|$ values for the $^1D_2$ excited state ($\eta>1$).[20]

E. Inhomogeneous Linewidths and Shapes

Table I compares the present measurements with previous values of the inhomogeneous widths of the ground and excited state hyperfine transitions in the earth's field. The $^1D_2$ excited state linewidths (FWHM) of 32 ± 3 kHz are much narrower than Erickson's measurement[20] (200 ± 50 kHz) which presumably is limited by laser frequency stability. They are also narrower than our previous Raman heterodyne measurement[1] (46 ± 3 kHz) and those of Whittaker and Hartmann[32] (60 ± 20 kHz). Our current linewidths are obtained by using lower rf fields ($H_1=0.16$G) to avoid saturation, and by synchronizing the averaging process to the direction of the laser frequency sweep so that either positive or negative frequency sweep signals are averaged but not both. The procedure is important because laser sweeping prepares the $^1D_2$ populations differently depending on the sweep direction (Sec. VB) and asynchronous signal averaging can contribute a few kHz to the linewidth.

the hyperfine levels within an electronic state ($^3H_4$ or $^1D_2$), which is important for an understanding of the Raman heterodyne effect.

For the $^1D_2$ excited state 3.724 and 4.791 MHz splittings (Table I), one finds two possible sets of D and E values. One set, where $\eta<1$, assigns the 3.7 MHz splitting to the ($I_z=1/2\leftrightarrow3/2$) transition, while the other set, with $\eta>1$, assigns it to the ($I_z=3/2\leftrightarrow5/2$) transition.

The correct set of D and E values can be deduced when one examines the Zeeman splittings under a static magnetic field $H_0\sim150G\perp c$ axis. The ($I_z=\pm3/2\leftrightarrow\pm5/2$) transition is expected to split into two Zeeman lines under H_0, while the ($I_z=\pm1/2\leftrightarrow\pm3/2$) transition should split into four lines due to the admixture of the $\pm1/2$ states induced by the dc field.[30,33] Note that the six inequivalent Pr^{3+} sites[27] can be grouped into three pairs, where the two sites in each pair are indistinguishable in this study ($H_0\leq150G\perp c$ axis). Thus, we have observed 6 lines from the $^1D_2$ 4.8 MHz transition and 12 lines from the 3.7 MHz transition, corresponding to the respective 2 and 4 Zeeman lines of each of the 3 pairs of Pr^{3+} sites. This observation enables us to assign the 3.7 MHz splitting to the $^1D_2$ ($I_z=\pm1/2\leftrightarrow\pm3/2$) transition. Similarly in the ground state, we correlate the 8.5 MHz splitting with the ($I_z=\pm1/2\leftrightarrow\pm3/2$) transition. The assignments indicate that $\eta<1$ for both ground and excited states and determine the correct values of $|D|$ and $|E|$ which are summarized in Table II. Note that the sign of D (or E) cannot be determined from the splittings.

With the values of $|D|$ and $|E|$ from Table II the quadrupole Hamiltonian (3.1) is diagonalized to yield the zero field ($H_0=0G$) eigenstates $|I_z>$ in terms of the pure states ($\eta=0$) $|i_z^o>$:

$$P_h = 2|u|P_o \tag{6.2}$$

or the Raman power

$$P_R = |u|^2 P_o \equiv (P_h/2P_o)^2 P_o . \tag{6.3}$$

The signal in Fig. 4(a) is obtained with an incident power P_o=2.65 mW, a detection bandwidth Δf=10 kHz, signal averaging of $M=2^{12}$ events, a detection impedance R=50Ω, and a photodetector sensitivity η=0.4 A/W. Signal averaging improves the signal to noise (rms) ratio S/N to a measured value (Fig. (4a)) of

$$S/N = 110 . \tag{6.4}$$

The noise output voltage

$$\bar{v}_o' = 3.86 \text{ mV rms} \tag{6.5a}$$

corresponds to a noise voltage $\bar{v}_o$ at the detector

$$\bar{v}_o = \frac{\sqrt{M}}{G} \bar{v}_o' = 145 \text{ nV rms} , \tag{6.5b}$$

where $\sqrt{M} = 64$ is the noise reduction due to averaging and $G=1.7\times10^6$ is the gain of the detection electronics.

The dc photocurrent

$$i = \eta P_o = 1.06 \text{ mA} \tag{6.6}$$

gives rise to a shot noise voltage

$$\bar{v}_{SN} = R\sqrt{2ei\Delta f} = 92 \text{ nV rms} . \tag{6.7}$$

At room temperature, the thermal noise voltage is

$$\bar{v}_{TN} = \sqrt{4kTR\Delta f} = 91 \text{ nV rms} , \tag{6.8}$$

which combines with $\bar{v}_{SN}$ to give a total noise voltage of

$$\bar{v}_N = \left(\bar{v}_{TN}^2 + \bar{v}_{SN}^2\right)^{1/2} = 130 \text{ nV rms} , \tag{6.9}$$

in agreement with the measured noise $\bar{v}_o = 145$ nV rms (6.5b), thus demonstrating that the technique is shot noise limited.

The detected heterodyne power Eq. (6.2) is given by

$$P_h = 2\,|u|\,P_o$$

$$= (S/N)\bar{v}_o'/(GR\eta) = 12.5 \text{ nW} , \tag{6.10}$$

corresponding to an AM sideband amplitude

$$|u| = P_h/2P_o = 2.4\times10^{-6} .$$

We define the heterodyne power with unity S/N (6.10) as the minimum detectable heterodyne power

$$P_h^{min} = 1.1 \times 10^{-10}\text{W} ,$$

which is equivalent to a minimum detectable Raman power, Eq. (6.3),

$$P_R^{min} = \left(P_h^{min}/2P_o\right)^2 P_o$$

$$= 1.2 \times 10^{-18}\text{W} , \tag{6.11}$$

$\leftrightarrow$ 4 Raman photons/ sec .

With higher rf and optical powers and a smaller detection bandwidth, this minimum detectable Raman power can easily approach $P_R^{min} \sim 1 \times 10^{-20}$W!

In contrast, previous rf-optical techniques[2,3] which rely on optical hole burning require a substantial change of at least several percent in either fluorescence or transmitted laser power in order to obtain a satisfactory S/N ratio. Here, heterodyne detection enhances the signal in two ways, by (i) detecting the heterodyne power $P_h = 2|u|P_o$ rather than the Raman power $P_R = |u|^2 P_o$, and (ii) allowing detection at a frequency window outside the laser amplitude noise spectrum, which in our case is from dc to ~1 MHz. Furthermore, the technique is not limited by laser frequency jitter, in first order, or the radiative lifetime of the third level.

VII. SUMMARY AND DISCUSSION

We have described the theory and experimental results of Raman heterodyne detection, a new laser spectroscopic technique for observing NMR. It is shown in theory and practice that the full range of cw or pulsed NMR can now be explored in either ground or excited electronic states with high precision and sensitivity. We have presented new results on the hyperfine transitions in the $^3H_4$ ground or $^1D_2$ excited states of Pr^{3+}:LaF_3, allowing a comparison with optical dephasing measurements and current or future line broadening theories. Anomalous lineshapes and homogeneous NMR linewidths should stimulate further work in NMR line broadening theory and in experimental studies in this system and other impurity ion solids.

This technique can be extended in various ways. Its high sensitivity should allow studies of dilute systems in gases and solid state, and of weakly allowed transitions, *e.g.*, in parity violation experiments.[38] In principle, it is applicable to microwave and infrared

transitions. The possibility of nonresonant FM detection makes it more versatile and offers the possibility of generating optical FM sidebands at high frequencies (>1 GHz). It seems clear that this technique has many potential applications.

ACKNOWLEDGMENT

One of us (N.C.W.) was supported by a Hertz Foundation Graduate Fellowship and the other (E.S.K.) an IBM Graduate Fellowship. We acknowledge partial support from the U.S. Office of Naval Research.

Table I

Quadrupole splittings f and comparison of inhomogeneous linewidths Δf (FWHM) for the hyperfine transitions of $^3H_4$ ground and $^1D_2$ excited states of 0.1 at. % Pr^{3+}:LaF_3 in the earth's magnetic field.

$L_z \leftrightarrow L_z$	f(MHz)	Δf(kHz)				
		present study	previous work			
$^3H_4$ (1/2↔3/2)	8.470±0.005	166±2	159±5[a]	220±30[b]	200±10[d]	
$^3H_4$ (3/2↔5/2)	16.688±0.003	158±2	160.5±1[a]	200±30[b]	180±10[d]	230±25[f]
$^1D_2$ (1/2↔3/2)	3.724±0.006	32±3	46.5±1[a]	70±20[c]	200±50[e]	
$^1D_2$ (3/2↔5/2)	4.791±0.004	33±3	45.3±2.6[a]	60±30[c]	200±50[e]	

[a]Reference 1, using the Raman heterodyne technique.

[b]Reference 17.

[c]Reference 32.

[d]Reference 2.

[e]Reference 20.

[f]Reference 3.

Table II

Quadrupole parameters $|D|$, $|E|$, and the asymmetry parameter η of the Pr^{3+}:LaF_3 nuclear quadrupole Hamiltonian $\mathscr{H}_Q$ Eq. (3.1) of the Pr^{3+} $^3H_4$ ground and $^1D_2$ excited states.

State	$\|D\|$ (MHz)	$\|E\|$ (MHz)	η
$^3H_4$	4.1819±0.0013	0.151±0.004	0.108±0.003
$^1D_2$	1.2938±0.0009	0.305±0.001	0.706±0.002

Table III

Amplitudes $a(I_z)$ of eigenstates $|I_z\rangle$ in terms of pure states ($\eta=0$) $|I_z^o\rangle$ of Pr^{3+}:LaF_3 $^3H_4$ ground and $^1D_2$ excited states.

		$\|I_z^o\rangle$		
	$\|I_z\rangle$	$\|\pm 5/2^o\rangle$	$\|\pm 1/2^o\rangle$	$\|\mp 3/2^o\rangle$
	$\|\pm 5/2\rangle$	0.99982	0.01902	0.00073
$^3H_4$	$\|\pm 1/2\rangle$	−0.01891	0.99695	−0.07575
	$\|\mp 3/2\rangle$	−0.00217	0.07573	0.99713
	$\|\pm 5/2\rangle$	0.99154	0.12613	0.03076
$^1D_2$	$\|\pm 1/2\rangle$	−0.10588	0.92275	−0.37058
	$\|\mp 3/2\rangle$	−0.07512	0.36419	0.92829

Table IV

Homogeneous linewidths Δf_H (FWHM) of hyperfine transitions with quadrupole splittings f for the $^3H_4$ ground and $^1D_2$ excited states of 0.1 at. % Pr^{3+}:LaF_3 in a dc magnetic field $H_o \perp c$ axis.

$L_z \leftrightarrow L_z'$	f(MHz)	Δf_H(kHz)[a]	$H_o \perp c$ axis(Gauss)
$^3H_4$ (1/2$\leftrightarrow$3/2)	8.470	19.5±2	~30
$^3H_4$ (3/2$\leftrightarrow$5/2)	16.688	21±2[b]	0
$^3H_4$ (3/2$\leftrightarrow$5/2)	16.688	11±1	~30-70
$^1D_2$ (1/2$\leftrightarrow$3/2)	3.724	20±2[b,c]	~30-70
$^1D_2$ (3/2$\leftrightarrow$5/2)	4.791	15±2	~30
$^1D_2$ (3/2$\leftrightarrow$5/2)	4.791	10±2[d]	~30

[a]Measurements made with no optical gating as described in Sec. IVB, unless otherwise noted.

[b]Identical results achieved with or without gating sequence (ii) of the laser amplitude as described in Sec. IVF.

[c]Identical results achieved with or without gating sequence (iii) of the laser amplitude, as described in Sec. IVD.

[d]With gating sequence (iii) of the laser amplitude, as described in Sec. IVD.

REFERENCES

1. J. Mlynek, N. C. Wong, R. G. DeVoe, E. S. Kintzer, and R. G. Brewer, *Phys. Rev. Lett.* **50**, 993 (1983).
2. L. E. Erickson, *Opt. Commun.* 21, 147 (1977).
3. R. M. Shelby, C. S. Yannoni, and R. M. Macfarlane, *Phys. Rev. Lett.* 41, 1739 (1978).
4. K. Chiang, E. A. Whittaker, and S. R. Hartmann, *Phys. Rev.* B23, 6142 (1981).
5. S. C. Rand, A. Wokaun, R. G. DeVoe, and R. G. Brewer, *Phys. Rev. Lett.* 43, 1868 (1979); see also R. G. DeVoe, A. Szabo, S. C. Rand, and R. G. Brewer, *Phys. Rev. Lett.* 42, 1560 (1979).
6. R. M. Macfarlane, R. M. Shelby, and R. L. Shoemaker, *Phys. Rev. Lett.* 43, 1726 (1979).
7. R. M. Macfarlane, C. S. Yannoni, and R. M. Shelby, *Opt. Commun.* 32, 101 (1980).
8. R. G. DeVoe and R. G. Brewer, *Phys. Rev. Lett.* **50**, 1269 (1983).
9. R. G. DeVoe, A. Wokaun, S. C. Rand, and R. G. Brewer, *Phys. Rev.* B23, 3125 (1981), and references therein.
10. R. G. Brewer and R. L. Shoemaker, *Phys. Rev. Lett.* 27, 631 (1971); R. G. Brewer and A. Z. Genack, *Phys. Rev. Lett.* 36, 959 (1976).
11. M. D. Levenson, *Introduction to Nonlinear Laser Spectroscopy* (Academic Press, New York, 1982), p. 17, and references therein.
12. N. C. Wong, E. S. Kintzer, and R. G. Brewer, to be published.
13. J. Mlynek, to be published.
14. B. S. Mathur, H. Tang, R. Bulos, and W. Happer, *Phys. Rev. Lett.* 21, 1035 (1968).
15. J. Mlynek, et al., *Opt. Lett.* 6, 87 (1981).
16. R. L. Shoemaker and R. G. Brewer, *Phys. Rev. Lett.* 28, 1430 (1972); R. G. Brewer and E. L. Hahn, *Phys. Rev.* A8, 464 (1973).

17. Y. C. Chen, K. Chiang, and S. R. Hartmann, *Phys. Rev.* **B21**, 40 (1980).

18. S. R. Hartmann, *IEEE J. Quantum Electron.* **QE-4**, 802 (1968).

19. P. Hu, S. Geschwind, and T. M. Jedju, *Phys. Rev. Lett.* **37**, 1357 (1976).

20. L. E. Erickson, *Phys. Rev.* **B16**, 4731 (1977).

21. R. G. Brewer, in *Frontiers in Laser Spectroscopy*, Proceedings of the Les Houches Summer School, Session XXVII, edited by R. Balian, S. Haroche, and S. Liberman (North-Holland, Amsterdam, 1977), p. 341; L. Allen and J. H. Eberly, *Optical Resonance and Two-Level Atoms* (Wiley-Interscience, New York, 1975).

22. A. G. Redfield, *Phys. Rev.* **98**, 1787 (1955).

23. R. G. Brewer and E. L. Hahn, *Phys. Rev.* **A11**, 1641 (1975); V. P. Chebotayev, in *High Resolution Laser Spectroscopy, Topics in Applied Physics*, edited by K. Shimoda (Springer, New York, 1976), Vol. 13, and references therein; A. Schenzle and R. G. Brewer, *Phys. Report* **43**, 455 (1978).

24. The last term in Eq. (2.12d) contributes to a second order dc term to ρ_{12}, due to a two-photon transition via level 3, which does not appear in the optical heterodyne signal. The nonresonant term of ρ_{12} that is neglected by the RWA adds a weak, third harmonic term to the heterodyne signal and therefore is not detected.

25. *Handbook of Mathematical Functions*, edited by M. Abramowitz and I. A. Stegun (U.S. GPO, Washington, DC, 1972), p. 297; R. G. DeVoe and R. G. Brewer, *Phys. Rev.* **A20**, 2449 (1979).

26. Aside from some obvious notational differences, the only definitional change is $\bar{\Delta}_H = -\omega_{21}$ (as defined in Ref. 1).

27. B. R. Reddy and L. E. Erickson, *Phys. Rev.* **B27**, May (1983).

28. B. Bleaney, *Physica*, **69**, 317 (1973).

29. M. A. Teplov, *Zh. Eksp. Teor. Fiz.* **53**, 1510 (1967) [*Sov. Phys. JETP* **26**, 872 (1968)]; see also A. Wokaun, S. C. Rand, R. G. DeVoe, and R. G. Brewer, *Phys. Rev.* **B23**, 5733 (1981).

30. T. P. Das and E. L. Hahn, *Nuclear Quadrupole Resonance Spectroscopy* (Academic, New York, 1958).

31. R. M. Macfarlane and R. M. Shelby, *Opt. Lett.* **6**, 96 (1981).

32. E. A. Whittaker and S. R. Hartmann, *Phys. Rev.* **B26**, 3617 (1982).

33. A. Abragam, *The Principles of Nuclear Magnetism* (Oxford University Press, London, 1961); C. P. Slichter, Principles of Magnetic Resonance (Harper and Row, New York, 1963).

34. A. Abragam and K. Kambe, *Phys. Rev.* **91**, 894 (1953).

35. R. M. Shelby and R. M. Macfarlane, *Opt. Commun.* **27**, 399 (1978).

36. R. M. Macfarlane, D. P. Burum, and R. M. Shelby, *Phys. Rev. Lett.* **49**, 636 (1982).

37. R. M. Shelby, R. M. Macfarlane, and C. S. Yannoni, *Phys. Rev.* **B21**, 5004 (1980).

38. E. D. Commins and P. H. Bucksbaum, *Annu. Rev. Nucl. Part. Sci.* **30**, 1 (1980).

FIGURE CAPTIONS

Figure 1. Hyperfine energy level diagram for the 5925Å $^3H_4$-$^1D_2$ transition of Pr^{3+}:LaF_3, showing the coherent Raman process. The squiggle arrow indicates the rf driving field, while the solid arrow represents the optical driving field. The coherently generated anti-Stokes field is shown as a dashed line.

Figure 2. Simplified schematic of the experimental arrangement for Raman heterodyne detection of cw or pulsed NMR.

Figure 3. Energy level diagram for the stimulated Raman process in a three-level atom. $\vec{H}_1$ excites the 1↔2 rf transition and E_o excites the 2↔3 optical transition.

Figure 4. Raman heterodyne NMR signals of the Pr^{3+}:LaF_3 $^3H_4$ ground state hyperfine transition (a) I_z=1/2↔3/2 in absorption for H_1=0.8G, and (b) I_z=3/2↔5/2 in absorption and dispersion for H_1=0.16G in the earth's magnetic field. The open circles represent the Gaussian fit of Eq. (2.34b).

Figure 5. Raman heterodyne NMR absorptive signal of the Pr^{3+}:LaF_3 $^1D_2$ excited state hyperfine transition I_z=1/2↔3/2 in the earth's magnetic field. To avoid rf power broadening, H_1=0.16G.

Figure 6. Schematic of the experimental configuration for cw Raman heterodyne measurements.

ure 7. Raman heterodyne detected spin echoes for (a) the $^3H_4$ (I_z=1/2↔3/2) spin nsition where H_0=30G, H_1=36G, pulse delay time τ=30 μs, and the rf pulse widths are and 2.5 μs, and (b) the $^3H_4$ (I_z=3/2↔5/2) spin transition where H_0=67G, H_1=27G, 38 μs, and the rf pulse widths are 1.3 and 1.3 μs. In (b) the FID and echo are dulated at the Zeeman frequency 390±10 kHz. The echoes in (a) and (b) are amplified 0×.

ure 8. Raman detected spin nutation and FID for the $^3H_4$ (I_z=3/2↔5/2) 16.69 MHz n transition where H_0=0G, H_1=6.4G, rf pulse width=100 μs, with a measured Rabi quency $\chi/2\pi=\mu_x H_1/h$=33 kHz. The arrow marks the end of the applied rf pulse and refore the beginning of the FID.

ure 9. Natural log of the Raman detected spin echo amplitude as a function of the pulse lay time τ for the $^3H_4$ (I_z=3/2↔5/2) spin transition for (a) H_0=0G indicating a mogeneous linewidth (FWHM) Δf_H=21±2 kHz and (b) H_0=30G with Δf_H=11±1 kHz. e signal "bending over" in (a) $\tau \lesssim 30$ μs and (b) $\tau \lesssim 30$ μs is due to an interference effect tween the echo and FID of the second pulse.

ure 10. Schematic of the experimental configuration for coherent spin transient asurements using Raman heterodyne detection.

ure 11. Raman heterodyne signals of the Pr^{3+}:LaF_3 $^3H_4$ (I_z=1/2↔3/2) and $^3H_4$ =3/2↔5/2) spin transitions at H_0=0G when both transitions are excited in a single rf quency sweep (7-18 MHz) with the sweep time of (a) 10 ms, (b) 100 ms, (c) 1s, and) 10s. In (d) the signal is amplified 2×.

$Pr^{3+}: LaF_3$

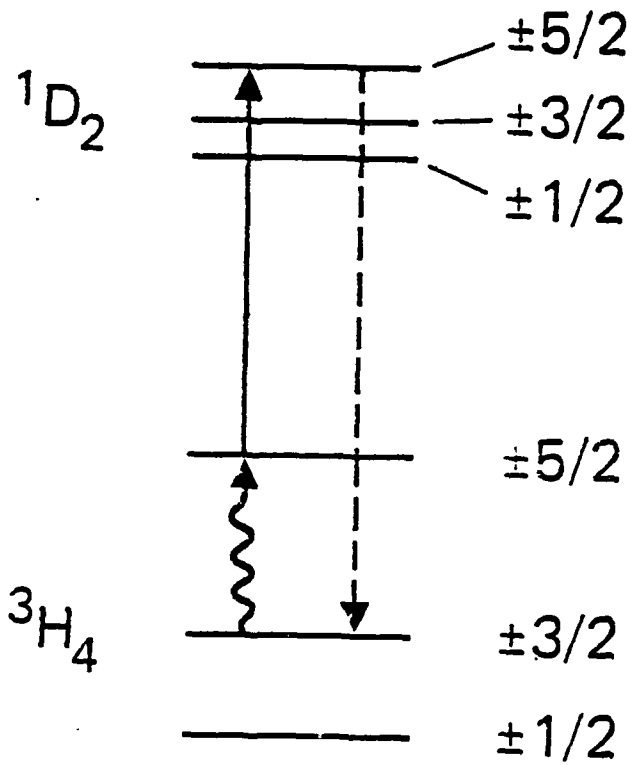
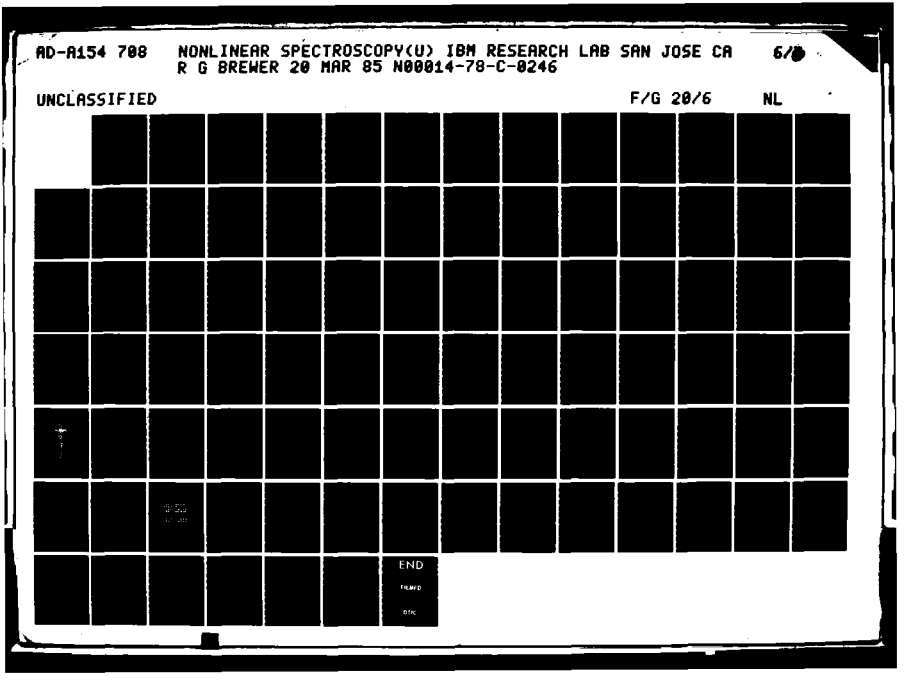
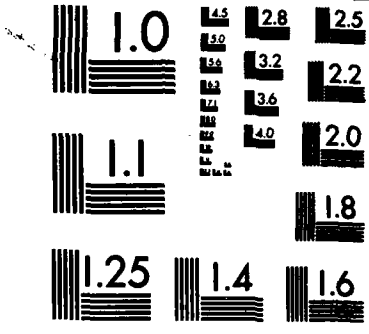


Fig. 1.

AD-A154 708 NONLINEAR SPECTROSCOPY(U) IBM RESEARCH LAB SAN JOSE CA 6/
R G BREWER 20 MAR 85 N00014-78-C-0246

UNCLASSIFIED F/G 20/6 NL





MICROCOPY RESOLUTION TEST CHART
NATIONAL BUREAU OF STANDARDS-1963-A

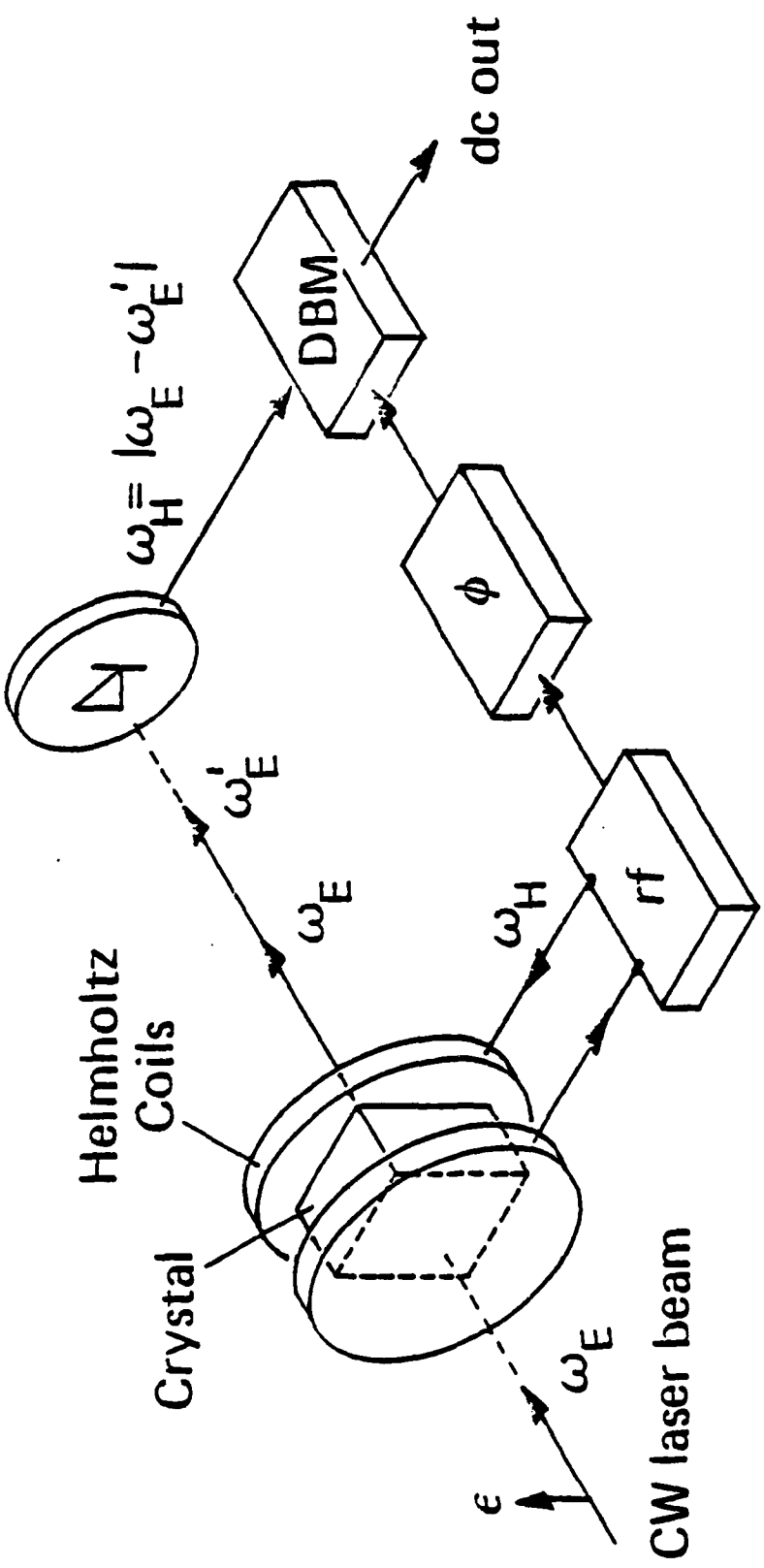

dc out
DBM
$\omega_H = |\omega_E - \omega'_E|$
Δ
ϕ
rf
ω'_E
ω_E
ω_H
ω_E
Helmholtz Coils
Crystal
ϵ
CW laser beam

Fig. 2.

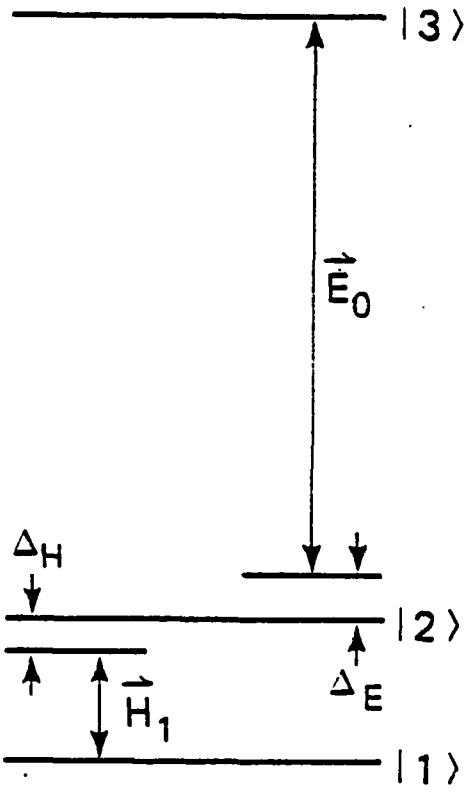


Fig. 3.

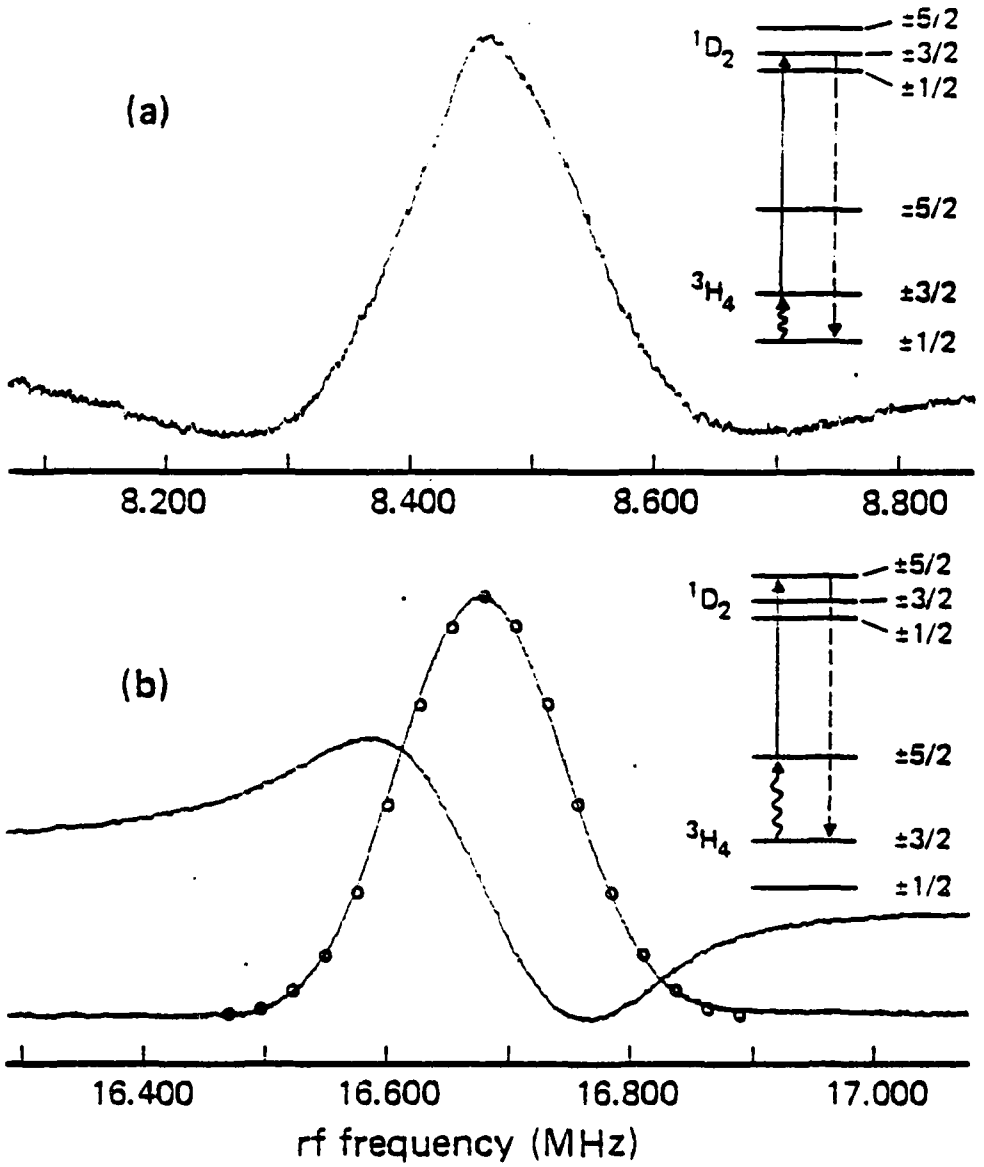

(a)
$^1D_2$
±5/2
±3/2
±1/2
±5/2
$^3H_4$
±3/2
±1/2
8.200
8.400
8.600
8.800
(b)
$^1D_2$
±5/2
±3/2
±1/2
±5/2
$^3H_4$
±3/2
±1/2
16.400
16.600
16.800
17.000
rf frequency (MHz)

Fig. 4.

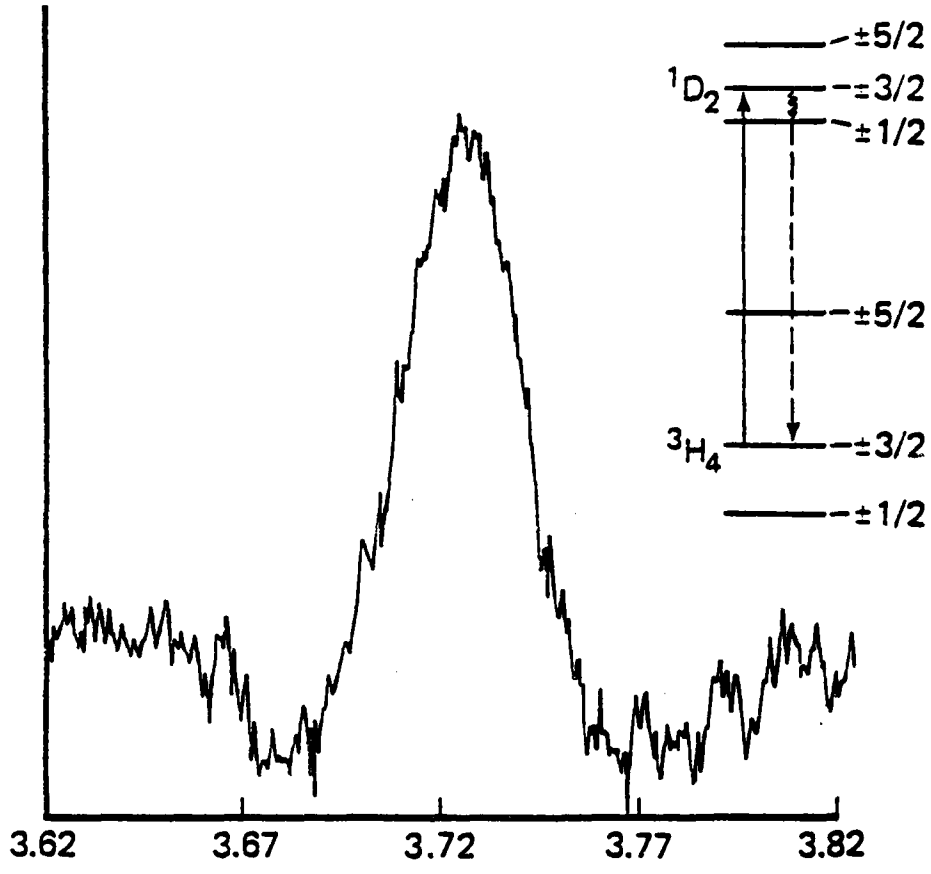


Fig. 5.

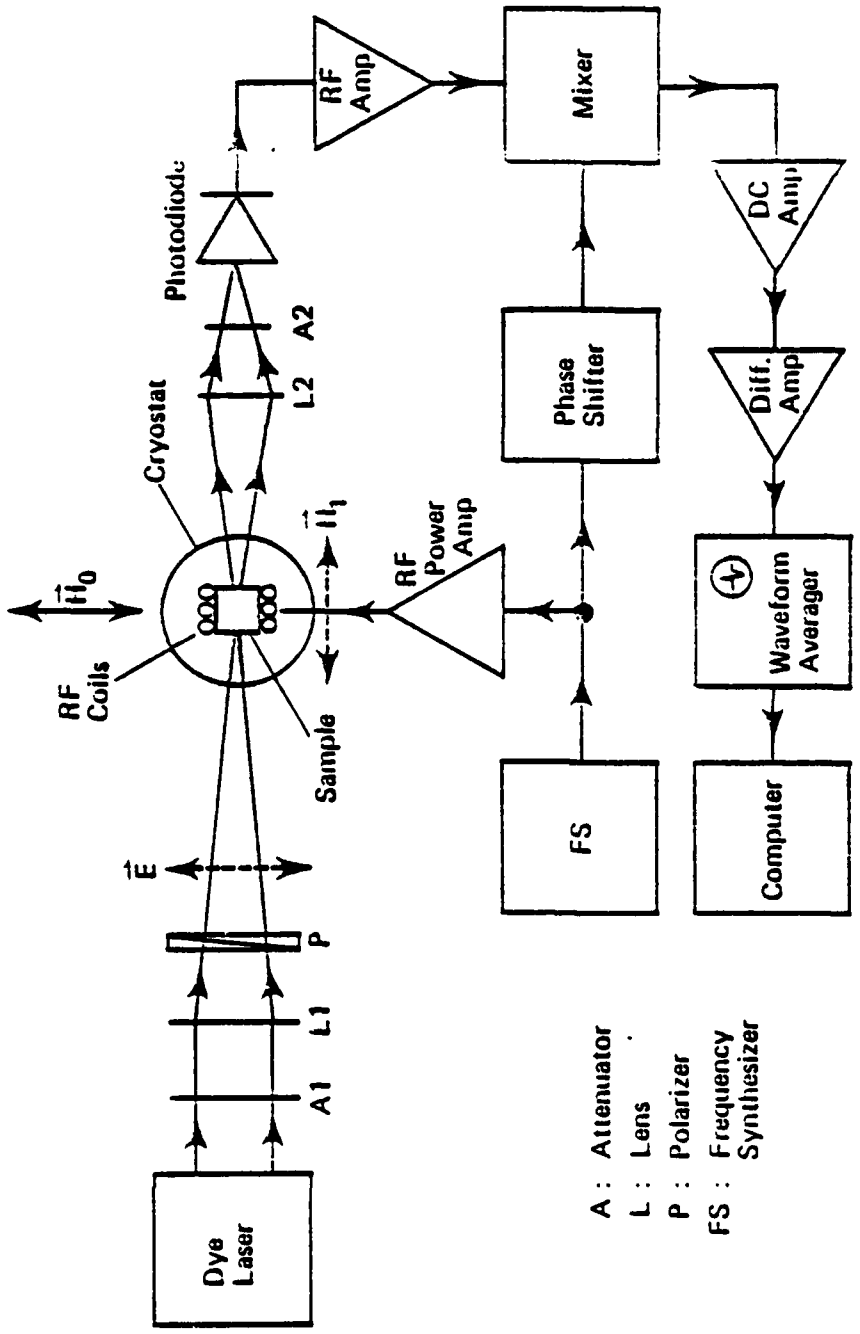

Dye Laser
A1
L1
P
$\vec{E}$
RF Coils
$\vec{H}_0$
Sample
$\vec{H}_1$
Cryostat
L2
A2
Photodiode
RF Amp
RF Power Amp
Mixer
Phase Shifter
FS
DC Amp
Diff. Amp
Waveform Averager
Computer
A : Attenuator
L : Lens
P : Polarizer
FS : Frequency Synthesizer

Fig. 6.

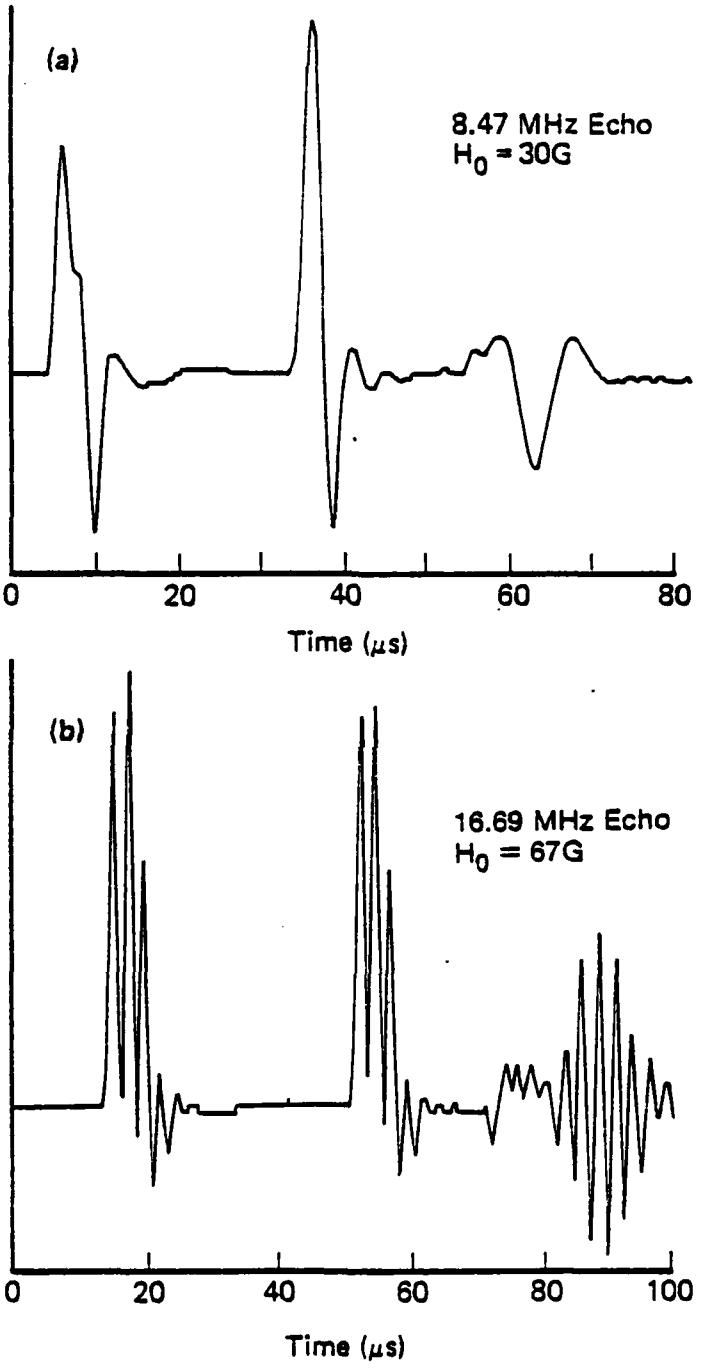

(a)
8.47 MHz Echo
H_0 = 30G
0
20
40
60
80
Time (μs)
(b)
16.69 MHz Echo
H_0 = 67G
0
20
40
60
80
100
Time (μs)

Fig. 7.

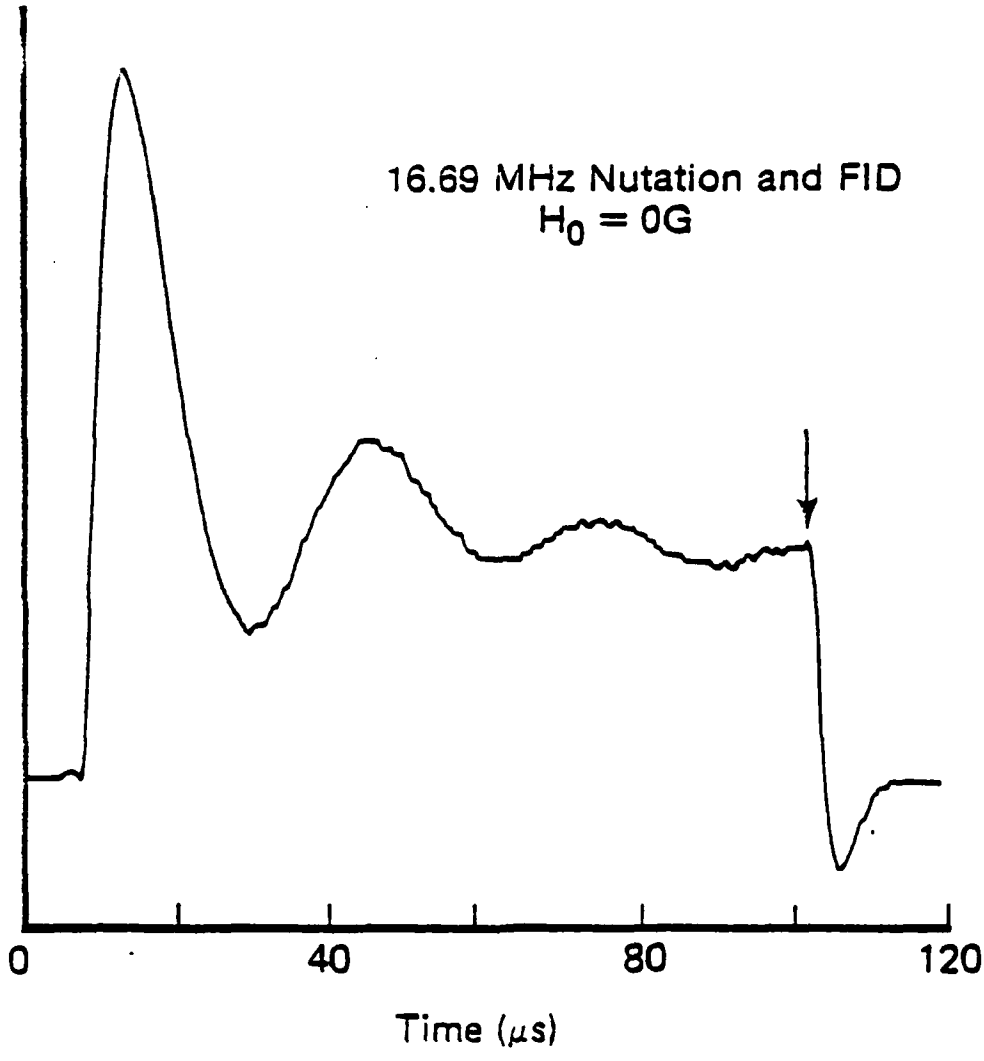


Fig. 8.

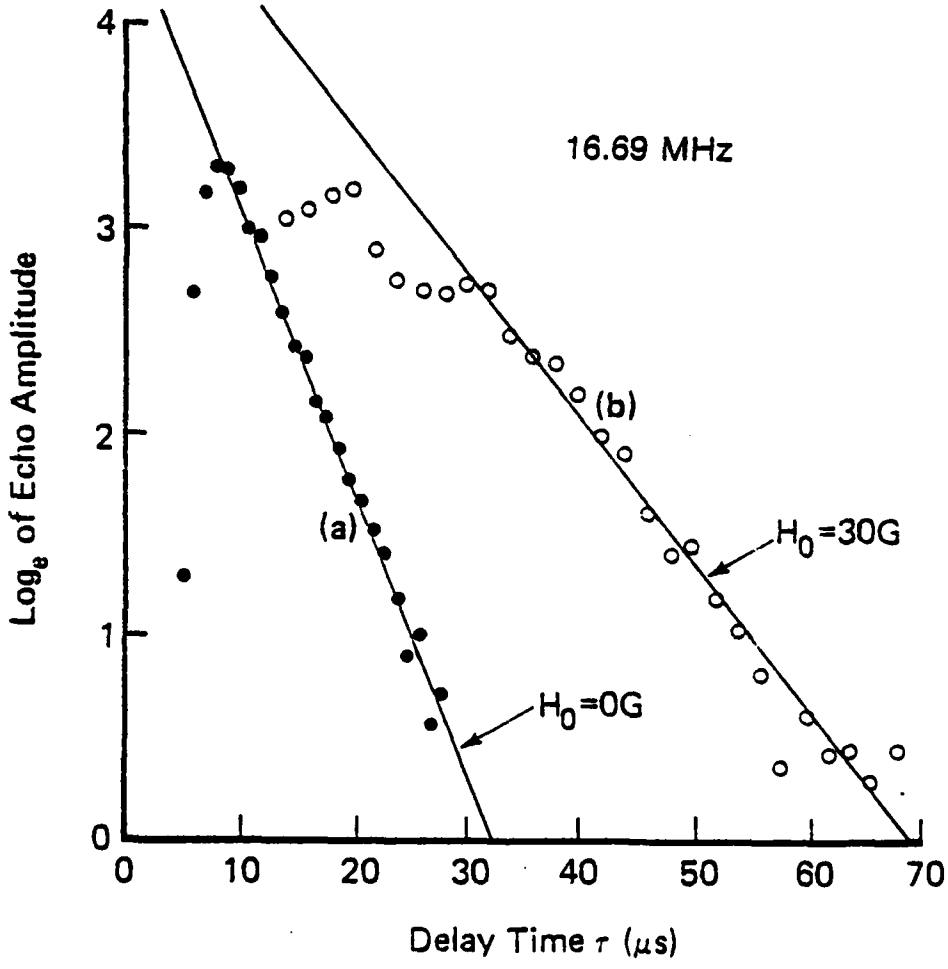

16.69 MHz
(a)
(b)
H_0=0G
H_0=30G
$\log_e$ of Echo Amplitude
Delay Time τ (μs)
0
1
2
3
4
0
10
20
30
40
50
60
70

Fig. 9.

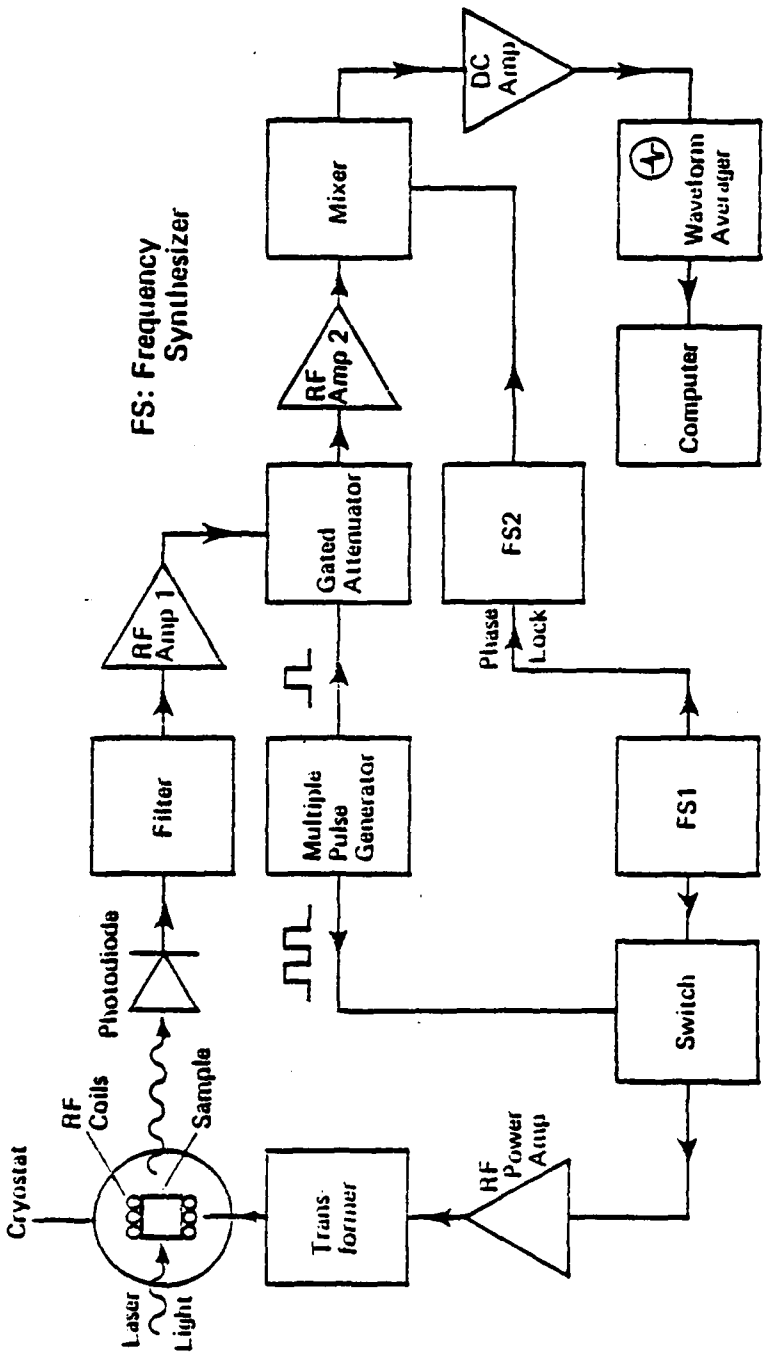

Cryostat
RF Coils
Sample
Photodiode
Laser Light
Filter
RF Amp 1
Trans-former
Multiple Pulse Generator
Gated Attenuator
RF Amp 2
RF Power Amp
Switch
FS1
FS2
Phase Lock
FS: Frequency Synthesizer
Mixer
DC Amp
Waveform Averager
Computer

Fig. 10.

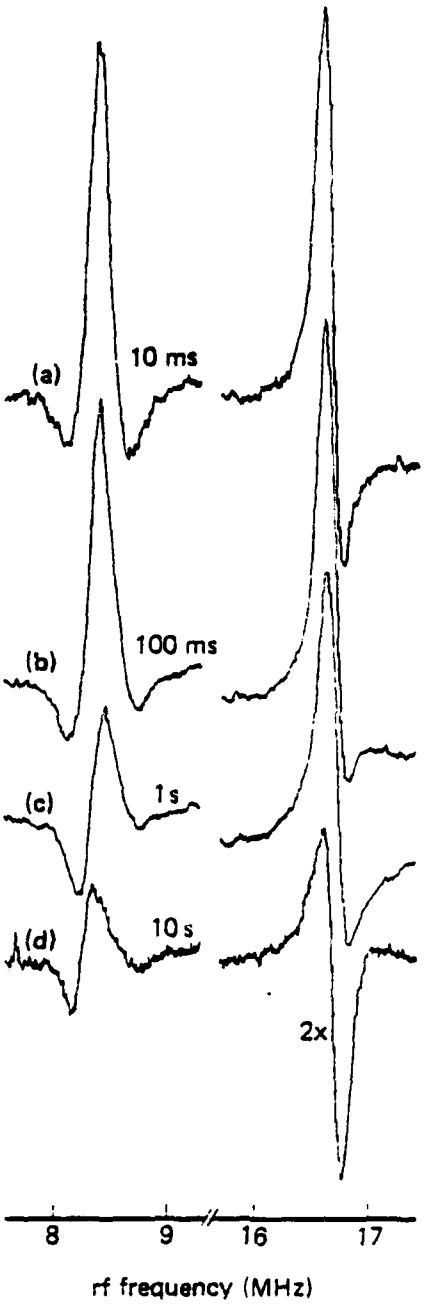


Fig. 11.

RJ 4217 (46295) 3/8/84
Physics

MICROSCOPIC THEORY OF OPTICAL LINE NARROWING** OF A COHERENTLY DRIVEN SOLID

A. Schenzle*
R. G. DeVoe
M. Mitsunaga
R. G. Brewer

IBM Research Laboratory
San Jose, California 95193

ABSTRACT: It was shown recently that the optical Bloch equations are violated when a coherent optical field drives an impurity ion system, Pr^{3+}:LaF_3, causing an intensity-dependent line narrowing effect where the nuclear Pr-F spin-spin interaction is quenched. This article clarifies the physical origin of this phenomenon by developing modified Bloch equations of a new form based on a microscopic model where the damping depends not only on the optical field strength but on the finite bandwidth σ of the fluorine spin reservoir.

---

*On leave from the Department of Physics, Universität Essen, Gesamthochschule, Essen, West Germany

**Work supported in part by the U.S. Office of Naval Research.

The Bloch equations,[1] which can be viewed as the two-level density matrix equations of motion, have enjoyed a profound success over the years, first in explaining nuclear magnetic resonance (NMR) and then in quantum optics and laser spectroscopy.[2] Relaxation is included through the two well-known phenomenological parameters, the (diagonal) population decay time T_1 and the (off-diagonal) dipole dephasing time T_2. A serious difficulty arises, however, in the case of solids when the condition $T_1 >> T_2$ applies, as appreciated by Redfield[3,4] in the NMR saturation of metals and more recently in the optical free induction decay (FID) measurements[5] of the impurity ion solid $Pr^{3+}:LaF_3$. In this circumstance, T_2 is not a constant but depends on the strength of the resonant oscillatory field applied or equivalently the Rabi frequency χ. An important consequence is that at sufficiently high χ, the limit $T_2 \to T_1$ is reached because the dephasing mechanism is quenched, and thus the linewidth appears *narrower* than the Bloch prediction.

In this Letter, we derive the first microscopic theory of the optical line narrowing effect for an impurity ion solid, an effect that has escaped detection by NMR and whose physical origin has been obscure.[5] We specifically consider the $Pr^{3+}:LaF_3$ system to illustrate the nature of the solutions, which depart from Redfield's concept[3] of a spin temperature in the rotating fra[illegible] to allow a comparison with the initial optical experiment[5] in this area. Here, the Pr^{3+} opt[illegible] broadening process is known from optical-rf magic angle line narrowing studies[6] and Monte Carlo calculations;[7] it arises from the F-F nuclear spin flip-flops that weakly modulate the Pr^{3+} optical transition frequency via the nuclear Pr-F dipolar interaction. The theory provides a simple yet general physical interpretation of why the magnetic line broadening mechanism effectively vanishes when the Pr^{3+} ions are coherently driven by a sufficiently intense laser field, even though the transition is of the electric dipole type. Predictions for the behavior at arbitrary field strengths are obtained, not

$$\langle \tilde{m}_1 | \tilde{m}_3(\beta) \rangle = \sum_{m',m} a_{m'} c_m D(\beta)_{m'm} , \qquad m',m = 5/2,1/2,-3/2 \tag{7}$$

$$\langle \tilde{m}_2 | \tilde{m}_3(\beta) \rangle = \sum_{m',m} b_{m'} c_m D(\beta)_{m'm} , \qquad -m',m = 5/2,1/2,-3/2 . \tag{8}$$

Equation (7) contains matrix elements $D(\beta)_{m'm}$ where $m-m' = 0, \pm 2, \pm 4$ and thus have the property as (6) shows of being even functions of the angle β. The elements of (8), on the other hand, satisfy $m-m' = \pm 1, \pm 3, +5$ which are odd functions of β. Since μ_{12} is independent of β, we conclude that the Raman heterodyne signal

$$S(\beta) \sim \mu_{12} | \langle \varphi_1 | \mu | \varphi_3 \rangle |^2 \langle m_2 | m_3(\beta) \rangle \langle m_3(\beta) | m_1 \rangle \tag{9}$$

is an odd function of β. It follows that the two signals $S_{1,2}$ associated with sites 1 and 2 will be of opposite sign since the transformation angles for sites 1 and 2 are $+\beta$ and $-\beta$, respectively. The resulting signal $S_1 + S_2$ will then vanish since the rf transition frequencies of the two sites are equal in a zero external field.

Furthermore, should the quadrupole axes of upper and lower electronic states be congruent so that $Z_{1,2} = Z'_{1,2}$ making $\beta = 0$, we then find from (6) that $D(\pi/2,0,-\pi/2)_{m'm} = \delta_{m'm}$. This has the consequence that $| m_3 \rangle = \sum_m c_m \psi_m$ with $m = 5/2, 1/2, -3/2$ and hence $\mu_{23} = 0$ causing the Raman heterodyne signal to vanish. We conclude that for $H_0 = 0$ the Raman heterodyne signal of a hyperfine transition vanishes when either (1) $\beta = 0$ because for $H_{rf} \perp Z$ one of the three required matrix elements is zero or when (2) $\beta \neq 0$ as then the two sites generate signals of opposite sign which just cancel.

Upon application of a static magnetic field H_0, the two-fold degeneracy of $| \pm m \rangle$ in (3) is lifted. In this 2×2 problem, the eigenvalues are

are mixed in the axial basis set ψ_m where m_i=-5/2, -1/2 and 3/2 since the quadrupole Hamiltonian connects only the states differing by $\Delta m=2$. The rf magnetic dipole transition $1\leftrightarrow 2$ imposes for $H_{rf}\perp Z$ the I_z selection rule $\Delta m=\pm 1$ which is satisfied by the eigenvectors

$$|m_1\rangle = \sum_m a_m \psi_m , \qquad m = 5/2, 1/2, -3/2 \tag{4a}$$

$$|m_2\rangle = \sum_m b_m \psi_m , \qquad m = -5/2, -1/2, 3/2 , \tag{4b}$$

or their conjugates ($m\rightarrow -m$) and can now be applied to (2a).

The excited state nuclear wavefunction $|m_3\rangle$ requires special care, however, since its $Z'_{1,2}$ axes are rotated by the angles $\pm\beta$ relative to the $Z_{1,2}$ ground state orientation as in Fig. 2. For $|m_3\rangle$ to be represented in the same basis set as the ground state wavefunctions (3), we perform an Eulerian rotation transformation[5] $P(\alpha,\beta,\gamma)$ on (3),

$$|m_3\rangle = P(\alpha,\beta,\gamma)\sum_m c_m \psi_m , \qquad m = 5/2, 1/2, -3/2 \tag{5a}$$

$$= \sum_{m,m'} c_m \psi_{m'} D^{(j)}(\alpha,\beta,\gamma)_{m'm} , \qquad m' = \pm 5/2, \pm 3/2, \pm 1/2 . \tag{5b}$$

The general angular momentum transformation matrix element[5] is

$$D^{(j)}(\alpha,\beta,\gamma)_{m'm} = e^{-im'\alpha} e^{-im\gamma} \sum_k \frac{(-1)^k [(j+m)!(j-m)!(j+m')!(j-m')!]^{1/2}}{k!(j+m-k)!(j-m'-k)!(k+m'-m)!}$$

$$\times (\cos\beta/2)^{2j-2k-m'+m} (-\sin\beta/2)^{2k+m'-m} , \tag{6}$$

and for Pr^{3+}:$YAlO_3$, j=5/2 with $\alpha=\pi/2$, $\gamma=-\pi/2$ assuming rotations about a space-fixed right hand coordinate system (X,Y,Z), the principal quadrupole axes of the ground state. Thus, the nuclear overlap integrals of (2a) become

In contrast to most other optical spectroscopic methods where the signal is a function of the *square* of the relevant transition matrix elements $|\mu_{ij}|^2$, the Raman heterodyne beat signal

$$S \sim \mu_{12}\mu_{23}\mu_{31} \tag{1}$$

exhibits a *linear* dependence in each of the three transition matrix elements associated with Fig. 1.[1,2] A consequence of (1), which has gone unnoticed until now, is that such a detection scheme has a potential for measuring the phase of a matrix element as well as its magnitude. Thus, the sign of the Raman heterodyne signal can vary among inequivalent impurity ion sites even if they are related by rotational symmetry. As a clear example, we discuss the case of Pr^{3+}:$YAlO_3$ which undergoes the optical transition $^3H_4 \rightarrow {}^1D_2$ of Fig. 1 and possesses two Pr^{3+} sites with two-fold rotational symmetry as shown in Fig. 2, Z being the principal nuclear quadrupole axis of quantization of Pr (I=5/2). We now show that the two sites corresponding to the $Z_{1,2}$ axes yield Raman signals of opposite sign as well as interference phenomena as observed in Fig. 3.

First, consider the case of a zero static external magnetic field, $H_0=0$. The three relevant transition matrix elements are given by

$$\mu_{ij} = \langle \varphi_i m_i | \mu | \varphi_j m_j \rangle = \begin{cases} \langle \varphi_{1,2} | \mu | \varphi_3 \rangle \langle m_{1,2} | m_3 \rangle & (2a) \\ \langle m_1 | \mu | m_2 \rangle , & (2b) \end{cases}$$

assuming the Pr^{3+} electronic $|\varphi\rangle$ and nuclear $|m\rangle$ wavefunctions are separable where μ is an electric (2a) or a magnetic (2b) dipole operator and $\varphi_1=\varphi_2$. For the case of a nonaxial electronic field gradient at the Pr nucleus, the nuclear quadrupole functions[4]

$$|\pm m_i\rangle = \sum_m a_m^{(i)} \psi_m , \qquad m = \pm 3/2, \mp 1/2, \mp 5/2 , \tag{3}$$

An optical heterodyne technique based on the coherent Raman effect was demonstrated recently for detecting nuclear magnetic resonance (NMR) and coherent spin transients of impurity-ion solids.[1,2] The Raman process, indicated in Fig. 1, employs a coherent radio frequency field (ω) that resonantly excites the nuclear transition 1↔2 and an optical frequency field (Ω) that excites the electronic transition 2↔3. An optical field at the sum frequency ($\Omega' = \Omega + \omega$) is thereby created and generates with the incident optical field at a photodetector a heterodyne beat signal of frequency $\omega = |\Omega - \Omega'|$, that reflects the NMR transition. The method is extremely sensitive and has the virtue of yielding NMR spectra and coherent spin transients in both ground and excited electronic states with kilohertz precision.

While the basic Raman heterodyne technique can be understood by a three-level perturbation calculation, two fundamental characteristics have been puzzling.[1,2] First, in the crystals studied thus far, $Pr^{3+}:LaF_3$ and $Pr^{3+}:YAlO_3$, the signals only appear in the presence of an external Zeeman field, and second, the lineshapes are anomalous, resembling the second derivative of a Gaussian. This Letter identifies that both phenomena are a manifestation of inequivalent nuclear sites that generate Raman signals of opposite sign and thus can interfere when their frequencies match, as they do at low magnetic fields. For this to occur, we show that for nuclei possessing an electric quadrupole moment, such as Pr, the principal quadrupole axes in ground and excited electronic states must be incongruent, a condition easily satisfied in practice. While this Letter describes a Raman interference due to inequivalent nuclear sites, it may be only one of a broad class of Raman coherence phenomena. For example, interference of Raman detected nuclear Zeeman transitions is observed for the case of a single site as well and will be covered elsewhere.[3] This work therefore reveals a new aspect of coherent Raman scattering of solids.

RJ 4267 (46855) 4/17/84
Physics

RAMAN HETERODYNE INTERFERENCE OF INEQUIVALENT NUCLEAR SITES *

M. Mitsunaga
E. S. Kintzer
R. G. Brewer

IBM Research Laboratory
San Jose, California 95193

and

Department of Applied Physics
Stanford University
Stanford, California 94305

ABSTRACT: A novel interference effect that is unique to the recently introduced technique of Raman heterodyne detection of NMR is illustrated for the impurity ion crystal Pr^{3+}:$YAlO_3$. Experiments confirm theoretical arguments that the two inequivalent Pr nuclear sites in the host lattice generate coherent Raman signals of opposite sign that interfere. A necessary requirement, which can now be examined in detail, is that the principal nuclear quadrupole Z axis of Pr be incongruent in the ground and optically excited electronic states.

*Work supported in part by the U.S. Office of Naval Research.

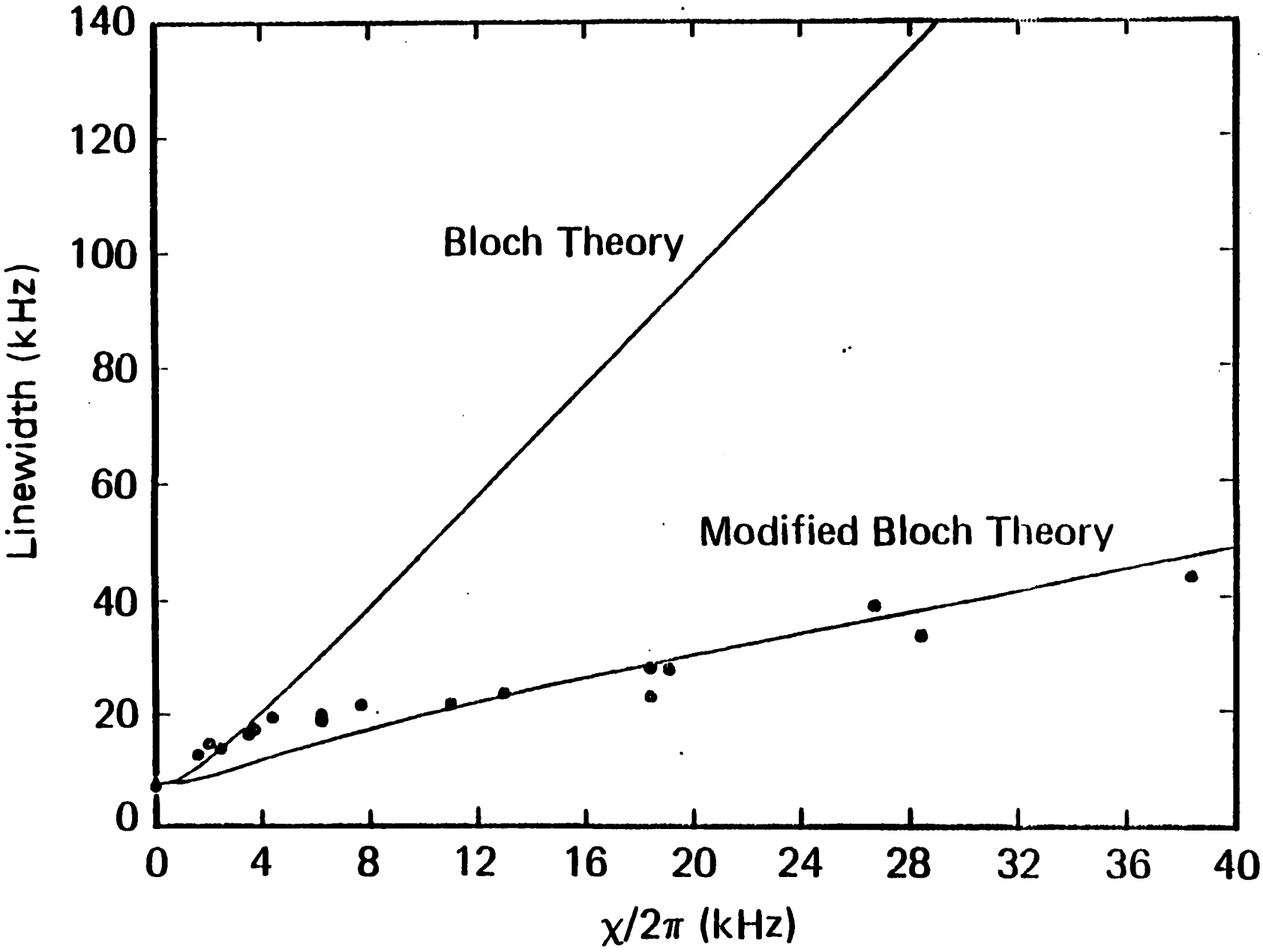


Figure 1. Optical linewidth (HWHM) of the prepared hole *vs.* the Rabi frequency $\chi/2\pi$ according to the Bloch theory Eq. (12) (upper curve), the modified Bloch theory Eqs. (9) and (10) (lower curve) and the optical FID experiments[5] of Pr^{3+}:LaF_3 (filled circles). A photon echo experiment[5] yields the intercept $1/2\pi T_2$ at $\chi=0$ (filled circle).

REFERENCES

1. F. Bloch, *Phys. Rev.* 70, 460 (1946).
2. M. Sargent III, M. O. Scully and W. E. Lamb, Jr., *Laser Physics* (Addison-Wesley, Reading, MA, 1974), p. 91.
3. A. G. Redfield, *Phys. Rev.* 98, 1787 (1955).
4. See also C. P. Slichter, *Principles of Magnetic Resonance* (Springer-Verlag, New York, 1978), pp. 174, 188.
5. R. G. DeVoe and R. G. Brewer, *Phys. Rev. Lett.* 50, 1269 (1983).
6. S. C. Rand, A. Wokaun, R. G. DeVoe and R. G. Brewer, *Phys. Rev. Lett.* 43, 1868 (1979).
7. R. G. DeVoe, A. Wokaun, S. C. Rand and R. G. Brewer, *Phys. Rev.* B23, 3125 (1981).
8. R. G. Brewer, in *Frontiers in Laser Spectroscopy*, Proceedings of the Les Houches Summer School, Session XXVII, edited by R. Balian, S. Haroche and S. Liberman (North-Holland, Amsterdam, 1977), p. 341.
9. See for example, S. Stenholm and D. ter Haar, *Physica* 32, 1361 (1966), and references therein.
10. L. Shen, *Phys. Rev.* 172, 259 (1968) report an rf FID value of $\sigma/2\pi = 9.7$ kHz which deviates slightly from our best fit value of 8.0 kHz in Fig. 1.
11. M. J. Weber, *J. Chem. Phys.* 48, 4774 (1978).
12. A. Schenzle, R. G. DeVoe, M. Mitsunaga and R. G. Brewer (to be published).

Monte Carlo calculations also reproduce the main features of the line narrowing effect and will be reported later along with additional details of the theory developed here.[12]

In conclusion, Redfield's theory[3] of NMR saturation of a pure solid also exhibits line narrowing but is a more complicated case than that of an impurity ion solid since the relaxing system and the thermal bath are one and the same. Another distinction is that the u and v components in this paper have the same line narrowing behavior whereas in Redfield's treatment there is an asymmetry. And finally, our model does not rely on the concept of a spin temperature in the rotating frame.

The stimulating comments of A. G. Redfield, E. L. Hahn and F. Bloch are appreciated. This work was supported in part by the U.S. Office of Naval Research.

mentioned, when $\sigma \to \infty$ the normal Bloch equations are recovered in (6), thus causing the first order FID to vanish. Hence, for this model the Bloch equations are violated not only at high χ but at low χ as well.

Our findings are summarized in Fig. 1 which gives the dependence of the steady-state linewidth of the prepared hole on χ. Equation (9) is evaluated numerically in the range $\chi=0$ to 40 kHz using parameters appropriate for Pr^{3+}:LaF_3: $\sigma/2\pi=8.0$ kHz,[10] $T_1=0.5$ msec[11] and $T_2=21.7$ μsec. [5] At elevated χ, the modified Bloch theory, (9) and (10), are in excellent agreement with the FID observations,[5] where both are far narrower than the Bloch theory (12). At low χ, (9) falls slightly below the observations, the agreement being perhaps fortuitous since the intercept at $\chi=0$ predicted by (12) is $1/2\pi T_2=7.3$ kHz and by (13) is $\sigma/2\pi=8.0$ kHz. Current observations[5] are incapable of distinguishing which FID intercept is correct, and in the future a more stringent test of the low-field prediction should be made in a system where $\sigma \sim 1/T_2$ is avoided.

The physical interpretation of this effect resides in the intensity-dependent damping term Γ_β, Eq. (7b). Here, the resonance condition $\delta(\omega_q-\omega_{q'}-\beta)$ requires that a pair of fluorine nuclei undergoing a flip-flop conserve energy with a Pr^{3+} pseudo-spin in its rotating frame. Equation (8) shows that when β becomes large compared to the fluorine linewidth σ, the number of fluorine nuclei that can participate diminishes, $\Gamma_\beta \to 0$, and then the Pr^{3+} optical linewidth is modified. Thus, the optical field introduces Rabi sidebands that detune the Pr^{3+} ions, its low frequency Fourier components, from the fluorine spin reservoir. This view is perhaps equivalent to the time averaging behavior suggested in the beginning of this article.

commences at t=0 when the field is suddenly turned off. Both periods contribute to the decay where the e^{-t/T_2} term in (9) originates solely in the second interval $t \geq 0$. The intensity-dependent damping arises from the steady-state solutions of (6)

$$u(0) = v(0)(\Gamma_{uw}\chi T_1 - \Delta)/\Gamma_{uv} - w_0\Gamma_{uw}/\Gamma_{uv}$$

$$v(0) = w_0(\chi - \Delta\Gamma_{uw}/\Gamma_{uv})/(\Delta^2/\Gamma_{uv} - \chi\Delta T_1\Gamma_{uw}/\Gamma_{uv} + \Gamma_{uv} + \chi^2 T_1) \qquad (10)$$

where $\Gamma_{uv} = [(\Delta^2+\sigma^2)/T_2 + \chi^2/T_1]/(\Delta^2+\chi^2+\sigma^2)$, $\Gamma_{uw} = (1/T_2 - 1/T_1)\Delta\chi/(\Delta^2+\chi^2+\sigma^2)$, and for convenience assuming that $\gamma = 1/T_1$.

In the high field limit $\chi >> \sigma(T_1/T_2)^{1/2}$, (10) yields $J^+(0)/\hbar \tilde{=} -w_0\chi(\Delta - i/T_1)/(\Delta^2+\chi^2)$ and disregarding trivial factors, we find from (9) the free precession decay law

$$\langle J^+(t) \rangle \sim e^{-(\chi + 1/T_2)t} . \qquad (11)$$

This is the principal result of our calculation and demonstrates that the high field decay rate $\sim\chi$ is considerably narrower than the Bloch result $\sim\chi(T_1/T_2)^{1/2}$ when $T_1 >> T_2$ where the FID Bloch theory[8] is given by

$$\langle J^+(t) \rangle \sim \exp\{-t[(\chi^2 T_1/T_2 + 1/T_2^2)^{1/2} + 1/T_2]\} . \qquad (12)$$

Similarly, in the low field limit $\chi << \sigma$, (9) reduces to

$$\langle J^+(t) \rangle \sim \chi e^{-(\sigma + 1/T_2)t} . \qquad (13)$$

This is an unanticipated first order FID with decay rate $\sigma + 1/T_2$ that doesn't reduce to the Eq. (12) Bloch value $2/T_2$ as $\chi \to 0$. It is a consequence of our adopting a model which imposes a thermal reservoir having a finite bandwidth σ and of our treating relaxation and the field dependence simultaneously, in contrast to previous theories[9] where the relaxation is treated separately and then added to the field dependent equations of motion. As already

where slowly varying population decay terms in γ and $1/T_1$ have been added. The primary damping constants are given by

$$\Gamma = \pi \sum_{qq'} h_{qq'}^2 \, \bar{n}_{q'}(\bar{n}_q + 1)\delta(\omega_q - \omega_{q'}) \tag{7a}$$

$$\Gamma_\beta = \pi \sum_{qq'} h_{qq'}^2 \bar{n}_{q'}(\bar{n}_q + 1)\delta(\omega_q - \omega_{q'} - \beta) \, , \tag{7b}$$

$\bar{n}_q$ being the fluorine thermal population average of the qth nucleus and ω_q its Zeeman frequency. Note that the δ functions impose resonance conditions on pairs of fluorine nuclei. Thus, Γ represents the zero-field limit when $\omega_q = \omega_{q'}$, with $1/T_2 = \Gamma + \gamma$, γ being bounded by $1/2T_1 \le \gamma \le 1/T_1$. On the other hand, interestingly, Γ_β is field-dependent where the resonance condition requires $\omega_q = \omega_{q'} + \beta$.

The useful relation

$$\Gamma_\beta = \Gamma\sigma^2/(\beta^2 + \sigma^2) \tag{8}$$

follows by converting the sums in (7) to integrals and with the assumption that the fluorine spectral lineshape is a Lorentzian with angular width σ. Hence, Γ_β depends on a finite fluorine bandwidth σ as well as β. By comparison, the usual Bloch equations with damping times T_2 and T_1 are recovered from (6) in the limits $\chi = 0$ or when $\sigma \to \infty$ as then $\Gamma_\beta \to \Gamma$.

We now obtain solutions for the optical FID signal, essentially given by

$$\langle J^+(t) \rangle = \langle J^+(0) \, e^{i\Delta t} \rangle \, e^{-t/T_2} \, , \tag{9}$$

which follows from (6) where $J^\pm/\hbar = (u \pm iv)/2$ and the bracket denotes an average over the Pr^{3+} optical inhomogeneous lineshape. The initial condition $J^+(0)$ constitutes the steady-state hole burning preparation of Pr^{3+} ions by a laser field, and free-precession

The equations of motion now become

$$\dot{I}'_x = -\frac{1}{\beta}(\Delta I'_y + \chi I'_z \sin\beta t)\sum_{qq'} h_{qq'} b_q^+ b_{q'}$$

$$\dot{I}'_y = \frac{1}{\beta}(\Delta I'_x - \chi I'_z \cos\beta t)\sum_{qq'} h_{qq'} b_q^+ b_{q'}$$

$$\dot{I}'_z = \frac{\chi}{\beta}(I'_x \sin\beta t + I'_y \cos\beta t)\sum_{qq'} h_{qq'} b_q^+ b_{q'} . \qquad (4)$$

These expressions when averaged over the heat bath are of the form $\dot{I}'_i = \langle D_{ij}(t)\rangle I'_j(t)$ and vanish in the absence of fluorine pair correlations since $\langle b_q^+\rangle\langle b_{q'}\rangle = 0$ for $q \neq q'$. However, by means of second order perturbation theory, Eqs. (4) reduce to the form

$$\dot{I}'_i(t) = \int_0^\infty \langle D_{ij}(t) D_{jk}(t-\tau)\rangle I'_k(t)\,d\tau \qquad (i,j,k = 1,2,3) \qquad (5)$$

where the upper limit has been extended from t to ∞ assuming a short correlation time, $1/\sigma < t$. The approximation $I'_k(t-\tau) = I'_k(t)$ has also been made in (5), which allows it to be factored outside the integral, and implies that this quantity is slowly varying compared to the correlation function $\langle D_{ij}(t) D_{jk}(t-\tau)\rangle$ which may now be evaluated. The transformation of (3) back to the untilted rotating frame results in the modified Bloch equations

$$\dot{u} = -\Delta v - \frac{1}{\beta^2}(\Delta^2\Gamma + \chi^2\Gamma_\beta)u + \frac{\Delta\chi w}{\beta^2}(\Gamma_\beta - \Gamma) - \gamma u$$

$$\dot{v} = \Delta u + \chi w - \frac{1}{\beta^2}(\Delta^2\Gamma + \chi^2\Gamma_\beta)v - \gamma v \qquad (6)$$

$$\dot{w} = -\chi v - (w - w_0)/T_1$$

physical picture where a high rate of optical excitation could yield a zero time-averaged magnetic interaction.

From the quantum mechanical equation of motion $\dot{J}_i = i/\hbar[\mathcal{H}, J_i]$, Eq. (1) and the angular momentum commutation relations, it follows that

$$\dot{J}^{\pm} = \pm i\left(\Delta + \sum_{qq'} h_{qq'} b_q^{+} b_{q'}\right) J^{\pm} \pm i\chi J_z \tag{2a}$$

$$\dot{J}_z = i\chi(J^{+} - J^{-})/2 \,. \tag{2b}$$

It is evident in (2a) that the Pr-F dipolar damping term modulates the Pr^{3+} energy level splitting ω_{21} since it is imaginary whereas in the Bloch equations the T_2 damping term is real. The time dependence of all terms in (2), except the dipolar term, can be removed by the rotation transformations[3]

$$\begin{pmatrix} J_x' \\ J_y' \\ J_z' \end{pmatrix} = R_{z'}(\beta t) R_y(\theta) \begin{pmatrix} J_x \\ J_y \\ J_z \end{pmatrix} . \tag{3}$$

Beginning with the initial rotating frame (x,y,z), the z axis is rotated about the y axis through the angle $\theta = \cos^{-1}\Delta/\beta$, making it coincident with the effective field β. In this tilted frame (x',y,z'), the x'-y plane is then rotated about z' through the precession angle βt.

just in the high field limit, and rather surprisingly, it is found that the Bloch equations can be violated even in the low field regime.

Our model assumes that the Pr^{3+} ions can be idealized by a two-level quantum system and in the absence of damping obeys the Bloch torque equation $\frac{d\vec{J}}{dt}=\vec{\beta}\times\vec{J}$ under the influence of an optical field $\epsilon(t)=\epsilon_0\cos\Omega t$.[8] The pseudo-angular momentum operator $\vec{J}=\hbar(\vec{i}u+\vec{j}v+\vec{k}w)/2$, expressed in terms of the Bloch vector [u,v,w] in the optical rotating frame, corresponds to that of a spin 1/2 particle and contains the components $J_z=\hbar(a_2^+a_2-a_1^+a_1)/2$, $J^+=\hbar a_2^+a_1$, and $J^-=\hbar a_1^+a_2$ using raising and lowering operators for the ground $|1\rangle$ and excited $|2\rangle$ states. The effective field $\vec{\beta}=-\vec{i}\chi+\vec{k}\Delta$ contains the Rabi frequency $\chi=-g\epsilon_0$, g being the optical coupling constant, and the tuning parameter $\Delta=\omega_{21}-\Omega$, ω_{21} being the Pr^{3+} level frequency splitting.

To include damping, we modify the Bloch equations starting with the Hamiltonian

$$\mathcal{H} = \Delta J_z - \chi(J^+ + J^-)/2 + \sum_q \hbar\omega_q b_q^+ b_q + \sum_{qq'} h_{qq'} J_z b_q^+ b_{q'} \qquad (1)$$

where the first term is the energy of the Pr^{3+} ion and the second is the Pr^{3+} optical electric dipole interaction. The third term is the Zeeman energy of q fluorine nuclei in a local or applied magnetic field, $b_q^{\pm}$ being the F spin raising and lowering operators. The fourth term is the dynamic part of the nuclear Pr-F dipolar interaction which causes the Pr^{3+} energy splitting ω_{21} to fluctuate in time and to broaden the line. It arises because pairs of fluorine spins undergoing random flip-flops $b_q^+b_{q'}$ magnetically shift the Pr^{3+} states $|1\rangle$ and $|2\rangle$ by different amounts. It is derived from the complete dipolar Hamiltonian assuming that F-F flip-flops act as a perturbation. This term links the optical excitation, suggested by the Pr^{3+} pseudo spin operator J_z, to the magnetic perturbation $b_q^+b_{q'}$ and already begins to imply a

$$W_{\pm m_i}(H_0) = W_{\pm m_i}(0) \pm (\hbar H_0/2)(\gamma_z^2 A_i^2 \cos^2\theta + \gamma_y^2 B_i^2 \sin^2\theta)^{1/2}, \quad (10)$$

and the eigenvectors display mixing of the basis states $|\pm m_i\rangle$ of the form

$$|\pm m_i\rangle = \cos\alpha_i(\theta)\,|\pm m_i\rangle - i\sin\alpha_i(\theta)\,|\mp m_i\rangle\,. \quad (11)$$

Here, $\theta = H_0 \forall Z$ for the $^3H_4$ state (Fig. 2), $\tan 2\alpha_i = (B_i\gamma_y/A_i\gamma_z)\tan\theta$, $\gamma_{z,y}$ are components of the Pr gyromagnetic ratio and B and A are functions[4] of the mixing coefficients $a_m^{(i)}$ in (3). Taking the upper signs of (11) and using (4) and (5), we obtain for the nuclear overlap integrals

$$\langle\tilde{m}_1|\tilde{m}_3\rangle = a_m c_{m'}\{D_{mm'}(\beta)\cos(\alpha_1-\alpha_3) + iD_{m-m'}\sin(\alpha_1-\alpha_3)\} \quad (12a)$$

$$\langle\tilde{m}_1|\tilde{m}_3\rangle = b_m c_{m'}\{D_{-mm'}(\beta)\cos(\alpha_2-\alpha_3) + iD_{mm'}\sin(\alpha_2-\alpha_3)\} \quad (12b)$$

where $m,m' = 5/2, 1/2, -3/2$. Consider now the symmetrical case where H_0 points along the crystal b axis ($\theta_1 = -\theta_2$) or a axis ($\theta_1 = \pi - \theta_2$) of Fig. 2 and produces a sign reversal in α_i for the two sites. Since $D_{mm'}$ is even and $D_{-mm'}$ is odd in β, it follows that the sign of (12a) is preserved and the sign of (12b) is reversed in the two sites. Similarly, we find that μ_{12} is independent of β and invariant to a sign change in α. Consequently, for this symmetrical case the overall signal S_1+S_2 vanishes. However, for arbitrary angles θ_1, θ_2 and β, analytic and numerical calculations show that for certain choices of $|\tilde{m}_1\rangle$, $|\tilde{m}_2\rangle$ and $|\tilde{m}_3\rangle$, S_1 and S_2 are again of opposite sign, but in general sign reversal is not a universal property when the symmetry is broken.

The origin of the interference phenomenon is illustrated in Fig. 3 where absorption Raman heterodyne beat spectra are given for a 0.1 at.% Pr^{3+}:$YAlO_3$ platelet with dimensions $5\times5\times1.1$ mm^3 parallel to the crystal axes a:b:c, the temperature being 1.51°K.

With the experimental arrangement of references 1 and 2, the $^3H_4 \rightarrow {}^1D_2$ transition is excited by a Coherent 599 dye laser beam, 25 mW in a 100 micron diameter at a wavelength of 610.5 nm, propagating with linear polarization along the crystal c axis. The $^3H_4$ $|\pm 1/2\rangle \rightarrow |\pm 3/2\rangle$ transitions, two strong and two weak ones for each site, are excited by sweeping a 0.3G rf magnetic field, oriented along the crystal c axis, over the range 6 to 8 MHz. The static field H_0 lies in the a-b plane at an angle of 33.6° to the b axis, and as it increases from 0 to 69G, the signal evolves into the four-line spectrum predicted by (10). For $H_0 \sim 0$, the interference effect predicted by (9) is observed as the signal amplitude approximates zero due to the cancellation of S_1 and S_2. For $H_0 = 4G$, the anomalous second derivative-like lineshape observed previously[1,2] appears, and above 32G all four strong lines are fully resolved and display sign reversal in the two sites. In addition, the signal is found to vanish due to interference when $H_0 \neq 0$ is oriented symmetrically so that $\theta_1 = -\theta_2$ or $\theta_1 = \pi - \theta_2$. Furthermore, interference is independent of the polarization direction of the light beam.

Since the Raman interference effect hinges on $\beta = |Z_{1,2} \not\forall Z'_{1,2}|$ being nonzero, it is important to determine the magnitude of this angle. By rotating the field H_0 about the c axis to different angles $\theta_{1,2}$ relative to $Z_{1,2}$ in the a-b plane, the angular dependence of the Zeeman spectrum is found and hence the Z orientation $\beta_0 = b \not\forall Z$. Figure 4 shows a least squares fit, using Eq. (10), to the observed points for the excited state $^1D_2$ transition $|\pm 3/2\rangle \rightarrow |\pm 5/2\rangle$ which is an 8-line spectrum, 4 lines for each site, where the zero-field splitting is 1.569 MHz. These data and similar measurements for the ground state $^3H_4$ transitions $|\pm 1/2\rangle \rightarrow |\pm 3/2\rangle$ (zero-field splitting: 7.062 MHz) yield

$$^1D_2: \ \beta_0 = 69.2° \pm 1°, \qquad ^3H_4: \ \beta_0 = 56.4° \pm 1° .$$

The result for $^3H_4$ is in good agreement with a previous value.[6] The $^1D_2$ measurement of β_0 represents the first solid state determination of the nuclear quadrupole orientation in an excited electronic state. For this specific angle of $\beta = 69.2° - 56.4° = 12.8°$, sign reversal is obeyed for arbitrary H_0 orientation.

It is possible to generalize these ideas further. Clearly, the Raman heterodyne interference effect is a general phenomenon that will occur in any impurity ion crystal possessing two or more inequivalent nuclear quadrupole sites when $\beta \neq 0$. For the interference signal to vanish, site symmetry is required, and must be preserved upon application of a static field H_0. The crucial requirement is that ground and excited electronic state quadrupole axes be incongruent, a property that can now be examined quantitatively by Raman heterodyne detection. Finally, Raman interference is expected for other kinds of transitions, besides hyperfine, and even for a single site as in the recently observed Zeeman transitions.[3]

We are indebted to K. L. Foster for technical aid. One of us (E.S.K.) acknowledges an IBM Graduate Fellowship. This work was supported in part by the U.S. Office of Naval Research.

REFERENCES

1. J. Mlynek, N. C. Wong, R. G. DeVoe, E. S. Kintzer and R. G. Brewer, *Phys. Rev. Lett.* **50**, 993 (1983).

2. N. C. Wong, E. S. Kintzer, J. Mlynek, R. G. DeVoe and R. G. Brewer, *Phys. Rev.* **B28**, 4993 (1983).

3. E. S. Kintzer, M. Mitsunaga, J. Mlynek, N. C. Wong and R. G. Brewer (to be published). This experiment requires that $H_{rf} \perp Y$; see the discussion following Eq. (3).

4. T. P. Das and E. L. Hahn, Nuclear Quadrupole Resonance Spectroscopy (Academic, New York, 1958).

5. M. Tinkham, Group Theory and Quantum Mechanics (McGraw-Hill, New York, 1964), p. 101.

6. L. E. Erickson, *Phys. Rev.* **B19**, 4412 (1979); L. E. Erickson, *Phys. Rev.* **B24**, 5388 (1981).

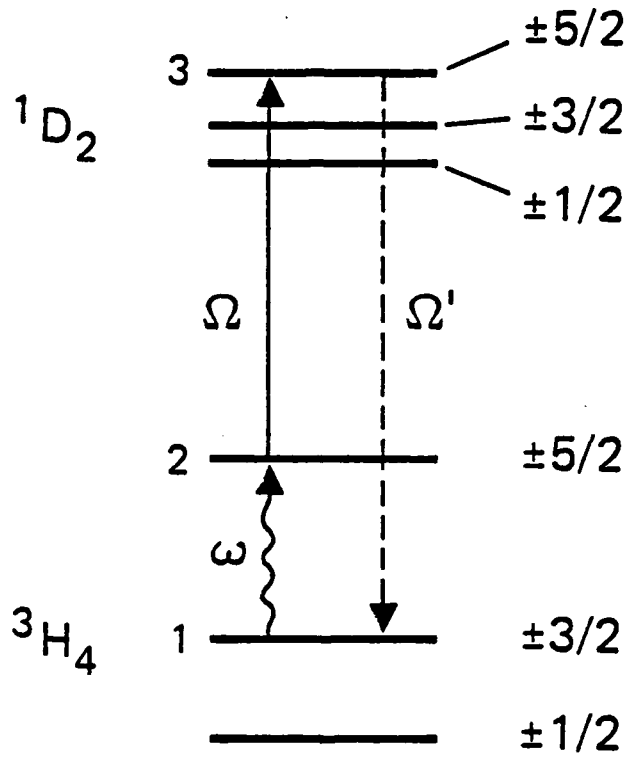


Fig. 1. Hyperfine energy level diagram in the absence of state mixing for the 610.5 nm $^3H_4 \rightarrow {}^1D_2$ transition of Pr^{3+}:$YAlO_3$ showing the coherent Raman process (not to scale) for levels labeled 1, 2 and 3.

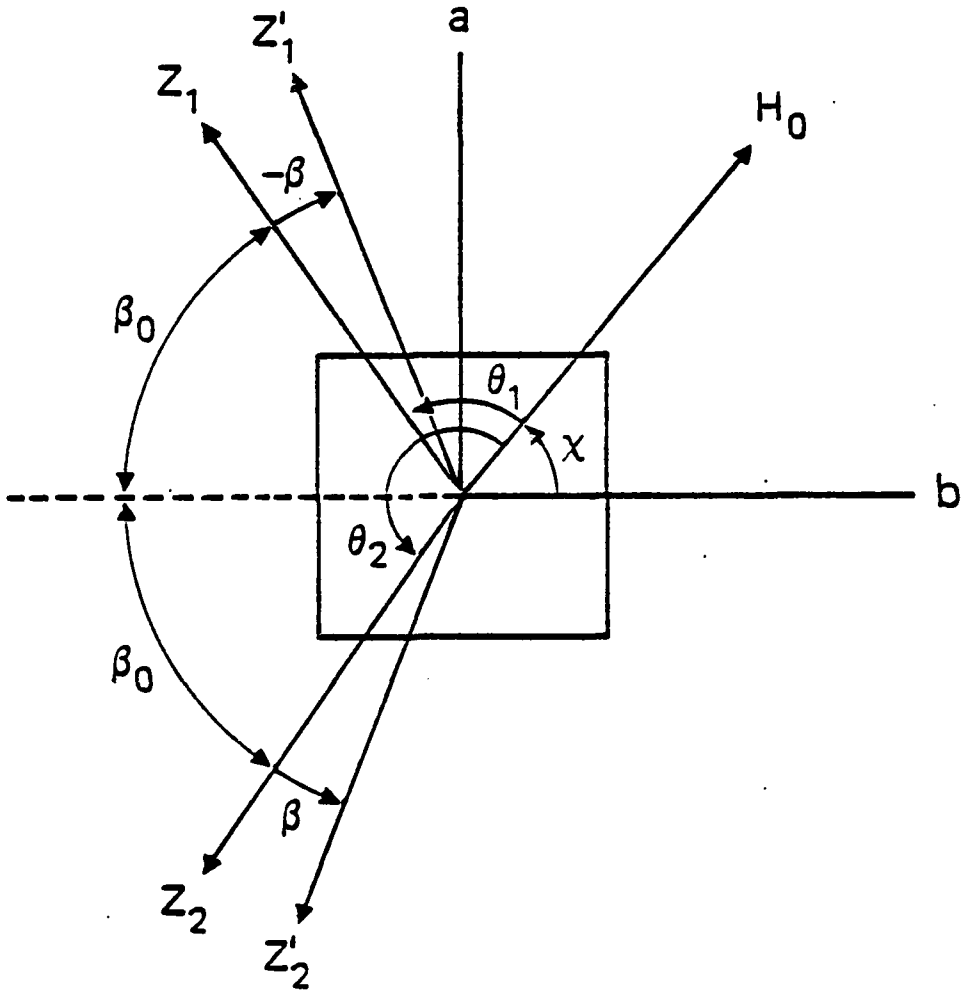


Fig. 2. The principal nuclear quadrupole Z axis of Pr lies in the a-b plane of $YAlO_3$ where the two inequivalent sites for $^3H_4(Z_{1,2})$ or $^1D_2(Z'_{1,2})$ make equal angles with the b axis. A static magnetic field H_0 also in the a-b plane deviates by the angle χ from the b axis, by θ_1 from Z_1 and by θ_2 from Z_2.

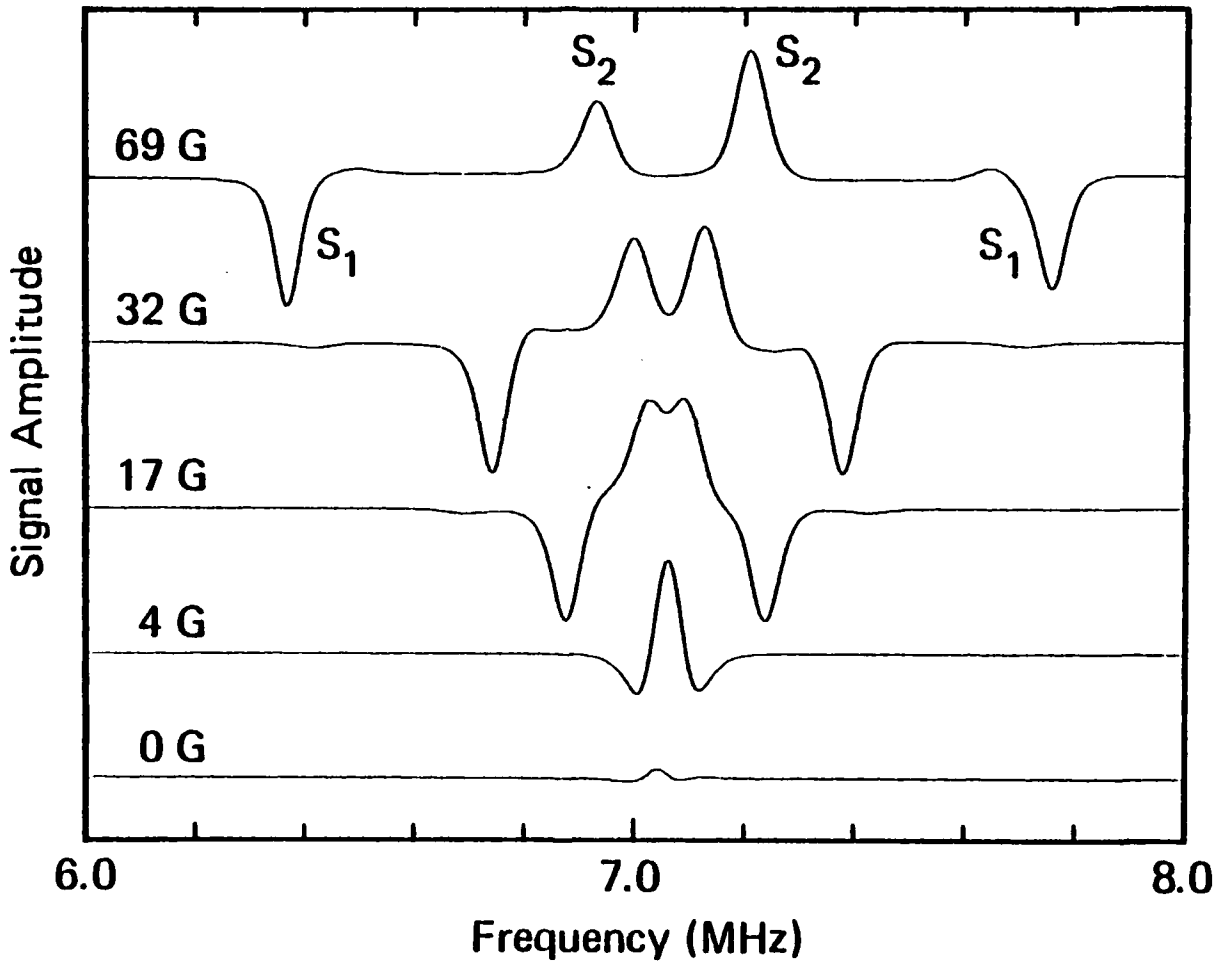


Fig. 3. Observed Raman heterodyne beat spectrum in absorption for the $^3H_4$ $|\pm 3/2> \leftrightarrow |\pm 1/2>$ transitions of 0.1 at.% Pr^{3+}:$YAlO_3$ as a function of H_0 (χ=33.6°) where the sign reversal in S_1, S_2 for the two sites is evident.

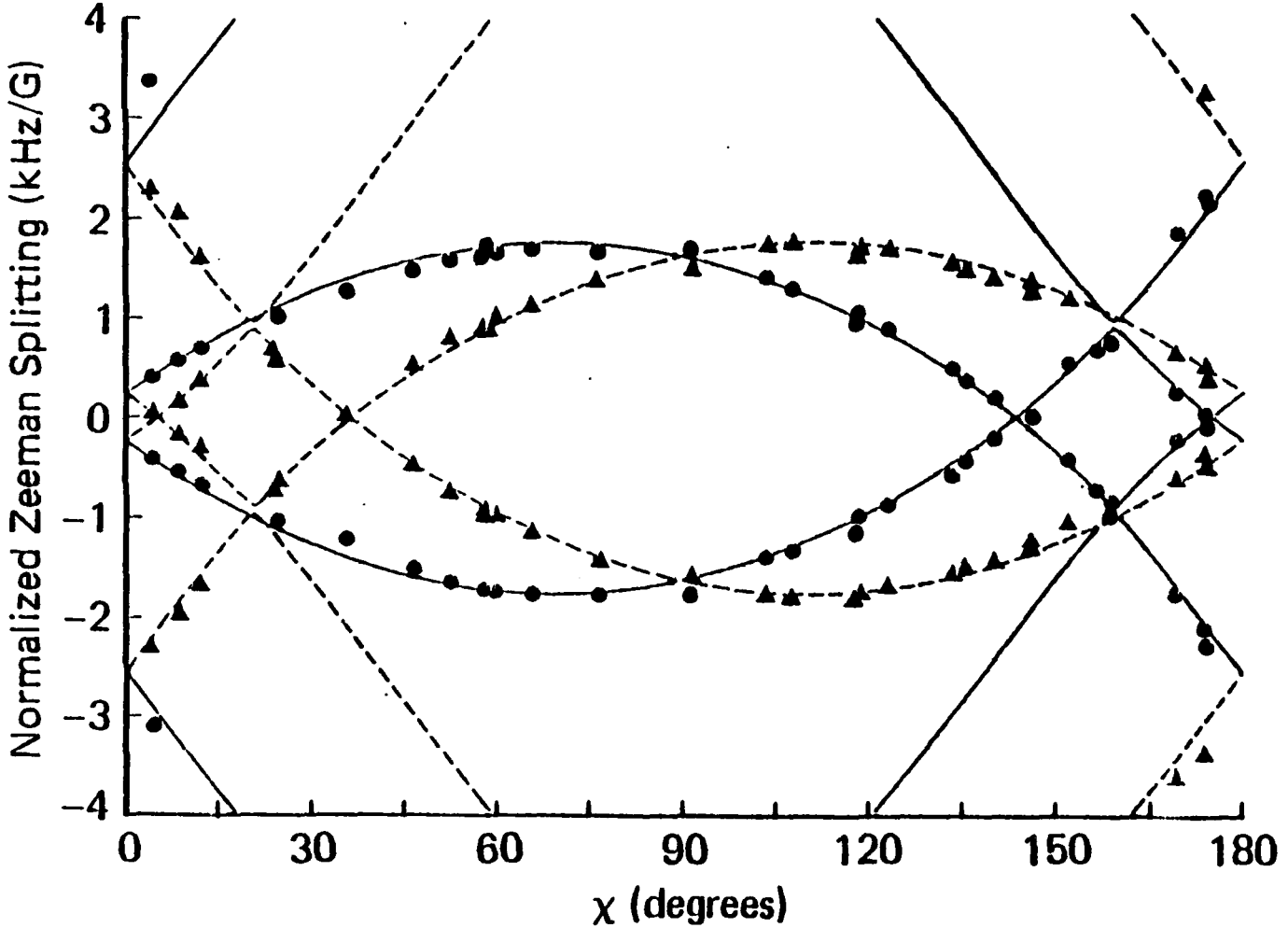


Fig. 4. Zeeman absorption spectrum of the excited state $^1D_2$ | ±5/2>↔| ±3/2> transition of 0.1 at.% Pr^{3+}:$YAlO_3$ as a function of the angle χ that H_0~50G makes with the crystal b axis. Experimental points for sites 1 (●) and 2 (▲). Theoretical curves for sites 1 (solid) and 2 (dashed). The angle γ=20.8° locates the Z' axis angle $\beta_z=\pi/2-\gamma=69.2°$

RJ 4337 (47285) 6/26/84
Physics

Appendix - Item 25

CUMULATIVE TWO-PULSE PHOTON ECHOES**

A. Schenzle*
R. G. DeVoe
R. G. Brewer

IBM Research Laboratory
San Jose, California 95193

ABSTRACT: This paper reports an unusual photon echo phenomenon where a train of echoes, generated by a repeating two-pulse sequence, exhibits growth rather than damping. The effect, which is observed in the impurity ion crystal $Pr^{3+}:YAlO_3$, results from an electronic ground state population grating that is created by the two-pulse sequence and is stored coherently as a modulation in the frequency domain. The depth of modulation increases with increasing n where n is the number of the two-pulse sequence, a result which is predicted in a three-level density matrix theory. The effect is closely related to previous stimulated or three-pulse photon echoes but differs in that growth is observed directly for the first time in the simpler two-pulse sequence.

**Work supported in part by the U.S. Office of Naval Research.

I. INTRODUCTION

Following the initial work of Carr and Purcell,[1] a number of multi-pulse spin[2-5] and photon echo[6-8] experiments have been reported. In liquids, the technique has allowed measurement of the spatial diffusion of spins which are dominated either by inhomogeneous static[1,3] or radio frequency (rf)[2] magnetic fields. In solids, with more elaborate rf multi-pulse sequences,[4,5] spin dipolar line broadening has been reduced dramatically. In gases, the optical analog of the Carr-Purcell method has permitted the detection of long-range velocity-changing collisions,[6] and more recently, a train of stimulated three-pulse photon echoes has been used to monitor optical dephasing times in solids on a picosecond time scale.[7]

In this article, we report that photon echoes generated by a repetitive two-pulse sequence, Fig. 1, can actually exhibit growth, contrary to intuition and past experience where the echo envelope invariably damps. This growth phenomenon is displayed clearly in Fig. 2 for the case of the impurity ion crystal $Pr^{3+}:YAlO_3$ at 1.6°K where the echo amplitude increases linearly with time. Since the interval T between neighboring pulse sequences is much greater than the optical dephasing time T_2, the only possibility for a *memory* effect which leads to echo growth resides in the optically excited population distribution. The physical origin of this effect arises from a population distribution or grating of the form

$$w \sim a \cos \Delta\tau + b \sin \Delta\tau \qquad (1.1)$$

that is modulated in the frequency domain Δ due to a two-pulse delay time τ. Successive two-pulse sequences increase the depth of modulation, the coefficients a and b, where (1.1) contains the required Fourier components for two-pulse echo formation leading to echo growth.

A population memory effect also arises in the three-pulse stimulated photon echo, either in a single[9,10] or multi-pulse[7] sequence, although past observations have not revealed the growth pattern directly in contrast to Fig. 2.

We show here that a two-pulse echo growth pattern can be explained in principle using a two-level quantum system as a model. However, the numerical values of the decay parameters and the conditions of our experiment argue in favor of a three-level model where the population is stored in a bottleneck or third level. The bulk of the paper is concerned with these two calculations.

Finally, we note that since the optical homogeneous linewidth $Pr^{3+}YAlO_3$ is but a few kilohertz, reproducible echo growth measurements are made possible only through the use of a (gated) ultrastable cw dye laser having a linewidth of 300 Hertz or less.

II. TWO-LEVEL MODEL

We assume that two-level atoms are repetitively excited by the square-wave optical two-pulse sequence of Fig. 1 where τ is the delay time of the second pulse and T is the repetition time of the two-pulse sequence. We further assume that (1) the laser frequency remains fixed within the sample's homogeneous width, (2) the optical pulse area $\theta = (\mu_{12}/\hbar)\int_{-\infty}^{\infty} \varepsilon(z,t)dt$ is small, satisfying $\theta << \pi/2$ and (3) the repetition period is much longer than the optical dephasing time, $T >> T_2$. Condition (1) guarantees that the same packets within the inhomogeneous lineshape are interrogated throughout the pulse train and thus will faithfully generate the desired echo envelope. In Section IV, the complication resulting from an unstable laser is discussed. Condition (2) is required if echo growth is to occur. Condition (3) assures that phase memory is retained in the frequency domain rather than in the time domain.

The 2×2 density matrix equations of motion,[11] the Bloch equations,

$$\begin{aligned}
\dot{\tilde{\rho}}_{12} &= (i\Delta - 1/T_2)\tilde{\rho}_{12} + (i\chi/2)w \\
\dot{\tilde{\rho}}_{21} &= \dot{\tilde{\rho}}_{12}^{*} \\
\dot{w} &= -(w-w_o)/T_1 - i\chi(\tilde{\rho}_{21}-\tilde{\rho}_{12})
\end{aligned} \tag{2.1}$$

are to be solved during pulse excitation and between pulses with the added complication that the pulse sequence is repetitive. Here, the tilde signifies the optical rotating frame, the population difference of levels 2 and 1 is defined by $w=\rho_{22}-\rho_{11}$, the Rabi frequency is $\chi=\mu_{12}E_0/\hbar$ and the tuning parameter $\Delta=\omega_{21}-\Omega$ where μ_{12} is the optical transition matrix element, E_0 the optical field amplitude, ω_{21} the energy level splitting and Ω the optical frequency.

The pulses are assumed to be sufficiently short that damping can be neglected and $\Delta=0$. On the other hand, if Δ is retained, the simplicity of the treatment given below vanishes. For the initial condition

$$[\tilde{\rho}_{12}(0),\tilde{\rho}_{21}(0),w(0)] \tag{2.2}$$

at time $t=0$ the pulse solutions of (2.1) are

$$\begin{aligned}
\tilde{\rho}_{12}(t) &= (1/2)\tilde{\rho}_{12}(0)(1+\cos\chi t) + (1/2)\tilde{\rho}_{21}(0)(1-\cos\chi t) + (i/2)w(0)\sin\chi t\,, \\
\tilde{\rho}_{21}(t) &= (1/2)\tilde{\rho}_{12}(0)(1-\cos\chi t) + (1/2)\tilde{\rho}_{21}(0)(1+\cos\chi t) - (i/2)w(0)\sin\chi t\,, \\
w(t) &= i\tilde{\rho}_{12}(0)\sin\chi t - i\tilde{\rho}_{21}(0)\sin\chi t + w(0)\cos\chi t\,.
\end{aligned} \tag{2.3}$$

Between pulses, $\chi=0$ and (2.1) yields

$$\begin{aligned}\tilde{\rho}_{12}(t) &= \tilde{\rho}_{12}(0)e^{(i\Delta-1/T_2)t}\ ,\\ \tilde{\rho}_{21}(t) &= \tilde{\rho}_{21}(0)e^{-(i\Delta+1/T_2)t}\ ,\\ w(t) &= w(0)e^{-t/T_1} + w_0(1-e^{-t/T_1})\ .\end{aligned} \tag{2.4}$$

We now cast the problem in matrix form, writing the state vector as

$$X(t) = \begin{pmatrix} \tilde{\rho}_{12}(t) \\ \tilde{\rho}_{21}(t) \\ w(t) \\ w_0 \end{pmatrix}\ . \tag{2.5}$$

A time evolution matrix $\Pi(t)$ then transforms an initial value $X_j(0)$, the jth component of the state vector, into the i th component

$$X_i(t) = \Pi_{ij}(t)X_j(0) \tag{2.6}$$

at the later time t. From (2.3) and $w_0=1$, the Π matrix during a pulse is

$$F(t) = \begin{pmatrix} \frac{1}{2}(1+\cos\chi t) & \frac{1}{2}(1-\cos\chi t) & \frac{i}{2}\sin\chi t & 0 \\ \frac{1}{2}(1-\cos\chi t) & \frac{1}{2}(1+\cos\chi t) & -\frac{i}{2}\sin\chi t & 0 \\ i\sin\chi t & -i\sin\chi t & \cos\chi t & 0 \\ 0 & 0 & 0 & 1 \end{pmatrix}\ . \tag{2.7}$$

The Π matrix between pulses follows from (2.4) and is given by

$$D(t) = \begin{pmatrix} e^{(i\Delta-1/T_2)t} & 0 & 0 & 0 \\ 0 & e^{-(i\Delta+1/T_2)t} & 0 & 0 \\ 0 & 0 & e^{-t/T_1} & (1-e^{-t/T_1}) \\ 0 & 0 & 0 & 1 \end{pmatrix} . \tag{2.8}$$

Successive application of (2.7) and (2.8) for the two-pulse sequence of Fig. 1 generates the echo operator

$$E(t) = D(t)F(t_2)D(\tau)F(t_1) \tag{2.9}$$

where t is the time interval measured from the end of the second pulse, t_1 and t_2 are the first and second pulse widths and τ is the second pulse delay time.

For the n-pulse sequence of Fig. 1, repeated application of (2.9) results in

$$X(t) = E(t)[E(T)]^{n-1}X(0) \tag{2.10}$$

where the initial condition

$$X(0) = \begin{pmatrix} 0 \\ 0 \\ 1 \\ 1 \end{pmatrix} w_0 . \tag{2.11}$$

Here, the time dependence of the element X(t) appears only in E(t) corresponding to the nth or last two-pulse sequence.

The echo matrix E(T) simplifies considerably with the assumption $T>>T_2$, allowing us to ignore the damping terms e^{-T/T_2}. For a single sequence, detailed evaluation of (2.9) gives

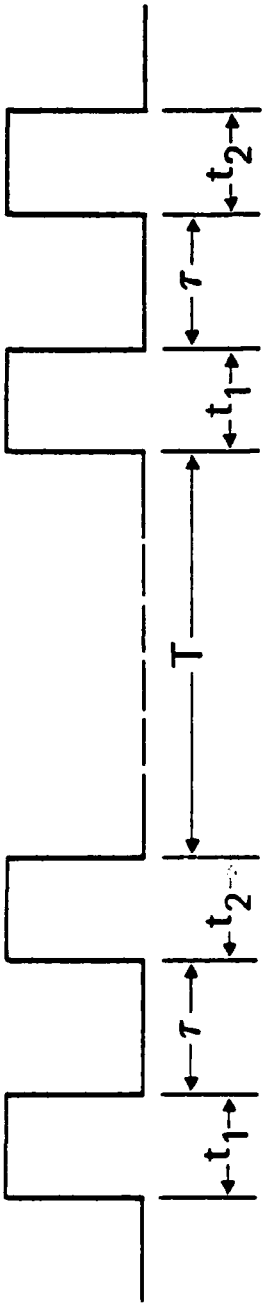


Figure 1. R.G. Brewer

FIGURE CAPTIONS

Figure 1. A repetitive two-pulse echo sequence where n is the number of times the sequence repeats.

Figure 2. Cumulative two-pulse photon echoes observed in 0.1 at % Pr^{3+}:$YAlO_3$ at 1.6°K. The echo amplitude grows as the two-pulse sequence n increases.

Figure 3. Population decay rates γ_i(i=1,2,3) are indicated for the three-level model where level 3 is the bottleneck.

Figure 4. Echo amplitude *versus* two-pulse sequence number n showing near linear behavior. The data are taken from Fig. 2.

REFERENCES

1. H. Y. Carr and E. M. Purcell, *Phys. Rev.* 94, 630 (1954).
2. I. Solomon, *Phys. Rev. Lett.* 2, 301 (1959).
3. S. Meiboom and D. Gill, *Rev. Sci. Instr.* 29, 688 (1958).
4. J. S. Waugh, L. M. Huber and U. Haeberlen, *Phys. Rev. Lett.* 20, 180 (1968); E. D. Ostroff and J. D. Waugh, *Phys. Rev. Lett.* 16, 1097 (1966).
5. C. P. Slichter, *Principles of Magnetic Resonance* (Springer-Verlag, New York, 1978) for additional discussion and references.
6. J. Schmidt, P. R. Berman and R. G. Brewer, *Phys. Rev. Lett.* 31, 1103 (1973); P. R. Berman, J. M. Levy and R. G. Brewer, *Phys. Rev. A*11, 1668 (1975).
7. W. H. Hesselink and D. A. Wiersma, *Phys. Rev. Lett.* 43, 1991 (1979); W. H. Hesselink and D. A. Wiersma, *J. Chem. Phys.* 75, 4192 (1981).
8. W. S. Warren and A. H. Zewail, *J. Chem. Phys.* 75, 5956 (1981).
9. J. B. W. Morsink and D. A. Wiersma in *Laser Spectroscopy IV* (Springer-Verlag, New York, 1979), edited by H. Walther and K. W. Rothe, p. 404.
10. T. W. Mossberg, R. Kachru, S. R. Hartmann and A. M. Flusberg, *Phys. Rev. A*20, 1976 (1979).
11. R. G. Brewer in *Frontiers in Laser Spectrosocpy*, Proceedings of the Les Houches Summer School, Session XXVII, edited by R. Balian, S. Haroche and S. Liberman (North-Holland, Amsterdam, 1977), p. 341.
12. F. Rohart and B. Macke, *Appl. Phys. B*26, 23 (1981).

Due to the damping terms $e^{-n\gamma_3 T}$ and $e^{-\gamma_3 T}$ in (3.25), growth will begin to taper off when $n\gamma_3 T \sim 1$, and in principle this behavior would permit a measurement of γ_3, the decay rate of the bottleneck. For $Pr^{3+}:YAlO_3$, the bottleneck population decay must certainly be leakage among the $^3H_4$ hyperfine states with decay times exceeding one second. Attempts to see this saturation effect by lengthening T failed because the modulator scatters $\sim 10^{-6}$ of the incident light through the aperture during the "dark periods", and the attendant optical pumping provides an additional path for erasing the population grating.

As a final comment, we emphasize that echo growth could not be observed in $Pr^{3+}:YAlO_3$ without using an ultrastable dye laser. If the laser frequency shifts from one pulse sequence to the next, the echo amplitude will not necessarily grow but may vary randomly as the laser samples new packets within the inhomogeneous lineshape. Growth can occur only when the same packets are excited repeatedly. The problem is especially critical in impurity ion solids such as $Pr^{3+}:YAlO_3$ since the population grating spans a narrow frequency range of tens of kilohertz. Indeed, when the laser was not frequency/phase locked, the echo amplitude fluctuated wildly. It is clear that previous photon echo decay time measurements of these narrow line systems are subject to these amplitude fluctuations, which perhaps can be reduced to some extent by averaging.[12]

ACKNOWLEDGMENT

This work was supported in part by the U.S. Office of Naval Research.

IV. OBSERVATIONS AND CONCLUSIONS

Photon echoes were monitored in the impurity ion crystal 0.1 at % Pr^{3+}:$YAlO_3$. The crystal was in the form of a platelet with dimensions $5 \times 5 \times 1.1$ mm^3 parallel to the crystal axes a:b:c and was immersed in liquid helium at 1.6°K. The beam of an ultrastable cw ring dye laser, possessing a linewidth of 300 Hertz rms short term, passed through an acousto-optic modulator driven by a train of radio frequency pulses and then propagated with a focused diameter of 76 microns along the c axis of the crystal before striking a P-I-N diode photodetector.

The laser beam was tuned to 610.5 nm to resonantly excite the Pr^{3+} transition $^3H_4(\Gamma_1) \leftrightarrow {}^1D_2(\Gamma_1)$ and had a power in the sample of 2.5 mW. When the modulator was driven by a 95 MHz radio frequency pulse, the beam was deviated and passed through an opening in an aperture and then through the sample. Between pulses, the undeviated beam was blocked by the aperture. The pulse generator was programmed to produce a repetitive three-pulse sequence of adjustable width, frequency, delay and amplitude. The first two pulses of equal amplitude and of 95 MHz frequency generate the echo signal while the third (probe) pulse of reduced amplitude and of 97 MHz frequency overlaps the echo pulse in time to produce a readily detected 2 MHz heterodyne beat echo signal. To lengthen the Pr^{3+} dephasing time and to increase the echo amplitude, a static field of 500 Gauss was applied parallel to the crystal b axis.

The evolution of echo signals shown in Fig. 2 clearly reveals the growth behavior for a series of two-pulse sequences up to n=6, all applied pulses being activated by an electronic clock. Here, the pulse widths are $t_1 = t_2 = 2.5$ μsec, the pulse delay time $\tau = 6$ μsec and the pulse sequence repetition time T=2 msec. In Fig. 4, we see that the echo amplitude varies linearly with n as predicted by (3.21b).

For the case of arbitrary $\gamma_3 T$, we consider (3.19) again using the small area approximation and write

$$\tilde{\rho}_{12}(t)_n = (i/8)\theta_1\theta_2^2\, e^{i\Delta(t-\tau)}\, e^{-(t+\tau)/T_2}$$

$$\times\left\{ne^{-(n-1)\gamma_3 T} + (1-e^{-\gamma_3 T})\sum_{\ell=0}^{n-2}(1+\ell)e^{-\ell\gamma_3 T}\right\}. \tag{3.23}$$

Since the sum in (3.23) can be expressed as the derivative of a geometric series,

$$\sum_{\ell=0}^{n-2}\ell e^{-a\ell} = -\frac{\partial}{\partial a}\sum_{\ell=0}^{n-2}e^{-a\ell} = -\frac{\partial}{\partial a}\left(\frac{1-e^{-(n-1)a}}{1-e^{-a}}\right) \tag{3.24}$$

where $a=\gamma_3 T$, it follows that

$$\tilde{\rho}_{12}(t)_n = (i/8)\theta_1\theta_2^2\, e^{i\Delta(t-\tau)}\, e^{-(t+\tau)/T_2}\left(\frac{1-e^{-n\gamma_3 T}}{1-e^{-\gamma_3 T}}\right). \tag{3.25}$$

The function

$$F(n) = \left(\frac{1-e^{-n\gamma_3 T}}{1-e^{-\gamma_3 T}}\right)$$

has the limiting values

$$\lim_{\gamma_3 T\to 0} F(n) = n, \tag{3.26}$$

$$\lim_{\gamma_3 T\to \infty} F(n) = 1 \tag{3.27}$$

where (3.26) exhibits growth with increasing n in agreement with (3.21b) and (3.27) shows no growth as predicted by (3.22).

It is now possible to rewrite (3.15) as

$$\tilde{\rho}_{12}(t)_n = E_{13}(t)\left\{(1-\alpha)^{n-1}e^{-(n-1)\gamma_3 T} + (1-e^{-\gamma_3 T})\sum_{\ell=0}^{n-2}(1-\alpha)^{\ell}e^{-\ell\gamma_3 T}\right\} \qquad (3.19)$$

where in the small area approximation (2.20),

$$\alpha = (1/4)\theta_1\theta_2 e^{-(i\Delta - 1/T_2)\tau} . \qquad (3.20)$$

In the limit $\gamma_3 T \to 0$ and $n\gamma_3 T \to 0$, (3.19) reduces to

$$\tilde{\rho}_{12}(t)_n = E_{13}(t)(1-\alpha)^{n-1} \qquad (3.21a)$$

$$= n(i/8)\theta_1\theta_2^2\, e^{i\Delta(t-\tau)}\, e^{-(t+\tau)/T_2}\, e^{-(n-1)\gamma_3 T} . \qquad (3.21b)$$

This expression resembles that of the two-level model (2.24) with the factor n replacing (2n-1), and thus at large n the echo amplitude (3.21) is one-half that of (2.24). The reason is that in the three-level case the population transfers rapidly from level 2 to the bottleneck level 3, reducing the grating population difference of levels 1 and 2 to one-half that of the two-level model.

On the other hand, for delay times T long compared to the bottleneck storage time, $\gamma_3 T >> 1$, memory of the population grating is lost. In the limit $\gamma_3 T \to \infty$ and $n\gamma_3 T \to \infty$, (3.19) becomes

$$\tilde{\rho}_{12}(t)_n = E_{13}(t) , \qquad (3.22)$$

and the echo is due to the last pulse sequence n alone.

Since

$$[E(T)]^{n-1}\begin{pmatrix}0\\0\\1\\0\\1\end{pmatrix} = \begin{pmatrix}0\\0\\[E_{33}(t)]^{n-1} + E_{35}(T)\sum_{\ell=0}^{n-2} E_{33}^{\ell}\\0\\1\end{pmatrix}, \tag{3.14}$$

(3.10) becomes

$$\tilde{\rho}_{12}(t)_n = E_{13}(t)\left[(E_{33}(T))^{n-1} + E_{35}(T)\sum_{\ell=0}^{n-2} E_{33}^{\ell}(T)\right]. \tag{3.15}$$

Here, $E_{15}(t)=0$,

$$\begin{aligned} E_{13}(t) = {} & -(i/4)\sin\chi t_1(1+\cos\chi t_2)e^{(i\Delta-1/T_2)(t+\tau)} \\ & +(i/4)\sin\chi t_1(1-\cos\chi t_2)e^{(i\Delta-1/T_2)t}e^{-(i\Delta+1/T_2)\tau} \\ & -(i/4)\sin\chi t_2(1+\cos\chi t_1)e^{(i\Delta-1/T_2)t} \\ & +(i/4)\sin\chi t_2(1-\cos\chi t_1)e^{(i\Delta-1/T_2)t}e^{-\gamma_0\tau} \end{aligned} \tag{3.16}$$

$$\begin{aligned} E_{33}(T) = e^{-\gamma_3 T}\{ & -(1/4)\sin\chi t_1\sin\chi t_2 e^{(i\Delta-1/T_2)\tau} \\ & -(1/4)\sin\chi t_1\sin\chi t_2 e^{-(i\Delta+1/T_2)\tau} \\ & +(1/4)(1+\cos\chi t_1)(1+\cos\chi t_2)e^{-\gamma_3\tau} \\ & +(1/4)(1-\cos\chi t_1)(1-\cos\chi t_2)e^{-\gamma_0\tau}\} \end{aligned} \tag{3.17}$$

$$E_{35}(T) = (1/2)e^{-\gamma_3 T}(1+\cos\chi t_2)(1-e^{-\gamma_3\tau}) + (1-e^{-\gamma_3\tau}). \tag{3.18}$$

The echo signal for the nth pulse sequence now assumes the form

$$\tilde{\rho}_{12}(t)_n = E_{1j}(t)[E(T)]^{n-1}_{jk}\begin{pmatrix}0\\0\\1\\0\\1\end{pmatrix} \tag{3.10}$$

where the column vector specifies the initial condition. The echo matrix E(T), (2.10), is evaluated using the approximations

$$T>>T_2,\ |\lambda|<<1,\ \gamma_0 T>>1 \text{ and } \gamma_3 T<<1 \tag{3.11}$$

where the first inequality was introduced in the two-level model, the second follows from (3.3), the third assumes the decay time of level 2 is rapid compared to the time T between two successive pulse sequences, and the fourth guarantees that the population grating is not erased during the experiment. For a single pulse sequence, evaluation of the echo matrix (2.9) gives

$$E(T) = \begin{pmatrix} 0 & 0 & 0 & 0 & 0 \\ 0 & 0 & 0 & 0 & 0 \\ E_{31} & E_{32} & E_{33} & E_{34} & E_{35} \\ 0 & 0 & 0 & 0 & 0 \\ 0 & 0 & 0 & 0 & 0 \end{pmatrix}. \tag{3.12}$$

For an n-pulse sequence

$$E^n(T) = \begin{pmatrix} 0 & 0 & 0 & 0 & 0 \\ 0 & 0 & 0 & 0 & 0 \\ E_{33}^{n-1}E_{31} & E_{33}^{n-1}E_{32} & E_{33}^{n} & E_{33}^{n-1}E_{34} & E_{35}\sum_{\ell=0}^{n-1}E_{33}^{\ell} \\ 0 & 0 & 0 & 0 & 0 \\ 0 & 0 & 0 & 0 & 0 \end{pmatrix}. \tag{3.13}$$

Proceeding as in the two-level model, we define a state vector

$$X(t) = \begin{pmatrix} \tilde{\rho}_{12}(t) \\ \tilde{\rho}_{21}(t) \\ \rho_{11}(t) \\ \rho_{22}(t) \\ 1 \end{pmatrix} . \tag{3.7}$$

The time evolution matrix during a pulse

$$F(t) = \begin{pmatrix} \frac{1}{2}(1+\cos\chi t) & \frac{1}{2}(1-\cos\chi t) & -\frac{i}{2}\sin\chi t & \frac{i}{2}\sin\chi t & 0 \\ \frac{1}{2}(1-\cos\chi t) & \frac{1}{2}(1+\cos\chi t) & \frac{i}{2}\sin\chi t & -\frac{i}{2}\sin\chi t & 0 \\ -\frac{i}{2}\sin\chi t & \frac{i}{2}\sin\chi t & \frac{1}{2}(1+\cos\chi t) & \frac{1}{2}(1-\cos\chi t) & 0 \\ \frac{i}{2}\sin\chi t & -\frac{i}{2}\sin\chi t & \frac{1}{2}(1-\cos\chi t) & \frac{1}{2}(1+\cos\chi t) & 0 \\ 0 & 0 & 0 & 0 & 1 \end{pmatrix} \tag{3.8}$$

follows from (3.5). Between pulses, the matrix

$$D(t) = \begin{pmatrix} e^{(i\Delta - 1/T_2)t} & 0 & 0 & 0 & 0 \\ 0 & e^{-(i\Delta+1/T_2)t} & 0 & 0 & 0 \\ 0 & 0 & e^{-\gamma t} & \lambda(e^{-\gamma_3 t}-e^{-\gamma_0 t}) & (1-e^{-\gamma_3 t}) \\ 0 & 0 & 0 & e^{-\gamma_0 t} & 0 \\ 0 & 0 & 0 & 0 & 1 \end{pmatrix} \tag{3.9}$$

follows from (3.6).

During pulse excitation, we again neglect Δ and damping so that the two-level solutions (2.3) apply but with the additional condition

$$\rho_{22}(t) + \rho_{11}(t) = \rho_{22}(0) + \rho_{11}(0) . \tag{3.4}$$

We obtain for pulse excitation

$$\begin{aligned}
\tilde{\rho}_{12}(t) &= (1/2)\tilde{\rho}_{12}(0)(1 + \cos \chi t) + (1/2)\tilde{\rho}_{21}(0)(1 - \cos \chi t) \\
&\quad -(i/2)\rho_{11}(0) \sin \chi t + (i/2)\rho_{22}(0) \sin \chi t , \\
\tilde{\rho}_{21}(t) &= \tilde{\rho}_{12}(t)^* , \\
\rho_{11}(t) &= -(i/2)\tilde{\rho}_{12}(0) \sin \chi t + (i/2)\tilde{\rho}_{21}(0) \sin \chi t \\
&\quad + (1/2)\rho_{11}(0)(1 + \cos \chi t) + (1/2)\rho_{22}(0)(1 - \cos \chi t) , \\
\rho_{22}(t) &= (i/2)\tilde{\rho}_{12}(0) \sin \chi t - (i/2)\tilde{\rho}_{21}(0) \sin \chi t \\
&\quad + (1/2)\rho_{11}(0)(1 - \cos \chi t) + (1/2)\rho_{22}(0)(1 + \cos \chi t) .
\end{aligned} \tag{3.5}$$

The solutions between pulses are found from (3.1) with $\chi = 0$,

$$\begin{aligned}
\tilde{\rho}_{12}(t) &= \tilde{\rho}_{12}(0)\, e^{(i\Delta - 1/T_2)t} , \\
\rho_{21}(t) &= \tilde{\rho}_{12}(t)^* , \\
\rho_{11}(t) &= \rho_{11}(0)\, e^{-\gamma_3 t} + \rho_{22}(0)\lambda(e^{-\gamma_3 t} - e^{-\gamma_0 t}) + (1 - e^{-\gamma_3 t}) , \\
\rho_{22}(t) &= \rho_{22}(0) e^{-\gamma_0 t}
\end{aligned} \tag{3.6}$$

where

$$\begin{aligned}
\lambda &= (\gamma_3 - \gamma_1)/(\gamma_3 - \gamma_0) , \\
\gamma_0 &= \gamma_1 + \gamma_2 ,
\end{aligned}$$

and small terms have been dropped through the inequality (3.3).

where (2.22) is readily expanded in (n-1) because of the smallness of $\theta_1\theta_2$. The echo signal derived from (2.15) now takes the form

$$\tilde{\rho}_{12}(t)_n = (2n-1)\frac{i}{8}\,\theta_1\theta_2^2\, e^{i\Delta(t-\tau)}\, e^{-(t+\tau)/T_2} \tag{2.24}$$

where only the echo rephasing terms are retained. In contrast to (2.19), the echo amplitude increases linearly as 2n-1=1,3,5... as the pulse sequence number n increases.

III. THREE-LEVEL MODEL

The density matrix equations of motion for the two-level problem (2.1) are extended by adding level 3 as in Fig. 3 which allows the population transfer 2→3 at the rate γ_2, 3→1 (γ_3) as well as 2→1 (γ_1). The reverse processes are considered improbable and are ignored. We then have

$$\begin{aligned}
\dot{\tilde{\rho}}_{12} &= (i\Delta - 1/T_2)\tilde{\rho}_{12} + (i\chi/2)(\rho_{22}-\rho_{11})\,, \\
\dot{\tilde{\rho}}_{21} &= \dot{\tilde{\rho}}_{12}^{\,*}\,, \\
\dot{\rho}_{11} &= (i\chi/2)(\tilde{\rho}_{21}-\tilde{\rho}_{12}) + \gamma_1\rho_{22} + \gamma_3\rho_{33}\,, \\
\dot{\rho}_{22} &= -(i\chi/2)(\tilde{\rho}_{21}-\tilde{\rho}_{12}) - \gamma_0\rho_{22}\,,
\end{aligned} \tag{3.1}$$

where

$$\gamma_0 = \gamma_1 + \gamma_2$$

and population is conserved among the three states satisfying

$$\rho_{11} + \rho_{22} + \rho_{33} = 1\,. \tag{3.2}$$

For a significant population bottleneck, we assume that

$$\gamma_2 >> \gamma_1, \gamma_3\,. \tag{3.3}$$

Equation (2.15) is to be averaged over the inhomogeneous lineshape, but this procedure doesn't alter the results to be discussed and will be ignored.

Inspection of (2.17) and (2.18) reveals that in the limit $T/T_1 \to \infty$, $\sum_{\ell=0}^{n-2} E_{33}^{\ell}(T) = 1$, $E_{34}(T) = 1$ and consequently

$$\tilde{\rho}_{12}(t)_n = E_{13}(t) \,. \tag{2.19}$$

That is to say that the population grating or memory is erased for times longer than the population decay time T_1 and the echo signal (2.19) has its origin only in the last pulse sequence $E_{13}(t)$. For the experiment of Fig. 2, $T/T_1 \sim 2$ and here numerical evaluation of (2.15) shows that $\tilde{\rho}_{12}(t)_n$ is essentially given by (2.19). This model, therefore is in disagreement with the observations, making it clear that a population bottleneck is needed so that the population grating isn't filled in. In the next section, a three-level model satisfies this requirement.

To complete this section, we next consider the other extreme when $T/T_1 \ll 1$ and assume that small area pulses are applied where

$$\theta_1 = \chi t_1 \ll \pi/2 \quad \text{and} \quad \theta_2 = \chi t_2 \ll \pi/2 \,. \tag{2.20}$$

We then have

$$E_{13}(t) = (i/2)e^{(i\Delta - 1/T_2)t}\left[\theta_1 e^{(i\Delta - 1/T_2)t} - (1/4)\theta_1\theta_2^2\, e^{-(i\Delta + 1/T_2)\tau} + \theta_2\right] \tag{2.21}$$

$$[E_{33}(T)]^{n-1} = [1-(1/2)\theta_1\theta_2\, e^{-\tau/T_2}\,(e^{i\Delta\tau} + e^{-i\Delta\tau})]^{n-1}$$

$$\sim [1-((n-1)/2)\theta_1\theta_2 e^{-\tau/T_2}(e^{i\Delta\tau} + e^{-i\Delta\tau})] \tag{2.22}$$

$$E_{34}(T) \sim 0 \tag{2.23}$$

$$E(T) = \begin{pmatrix} 0 & 0 & 0 & 0 \\ 0 & 0 & 0 & 0 \\ E_{31} & E_{32} & E_{33} & E_{34} \\ 0 & 0 & 0 & 1 \end{pmatrix} \tag{2.12}$$

while for n sequences

$$[E(T)]^n = \begin{pmatrix} 0 & 0 & 0 & 0 \\ 0 & 0 & 0 & 0 \\ E_{33}^{n-1}E_{31} & E_{33}^{n-1}E_{32} & E_{33}^{n} & E_{34}\sum_{\ell=0}^{n-1} E_{33}^{\ell} \\ 0 & 0 & 0 & 1 \end{pmatrix} . \tag{2.13}$$

The echo signal for an n-pulse sequence is essentially given by the polarization or off-diagonal element

$$\tilde{\rho}_{12}(t)_n = E_{1j}(t)[E(T)]^{n-1}_{j\ell}\, X_\ell(0) \tag{2.14}$$

$$= E_{13}(t)\Big(E_{33}^{n-1} + E_{34}\sum_{\ell=0}^{n-2} E_{33}^{\ell}\Big)W_0 \tag{2.15}$$

where (2.14) follows from (2.10), the initial condition $X_\ell(0)$ is given by (2.11), and matrix multiplication of (2.11) and (2.13) produces (2.15). Here,

$$E_{13}(t) = (i/2)e^{(i\Delta - 1/T_2)t}\big[(1/2)(1 + \cos \chi t_2) \sin \chi t_1 e^{(i\Delta - 1/T_2)\tau}$$
$$- (1/2)(1 - \cos \chi t_2) \sin \chi t_1 e^{-(i\Delta + 1/T_2)\tau} + \cos \chi t_1 \sin \chi t_2 e^{-\tau/T_1}\big] , \tag{2.16}$$

$$E_{33}(T) = e^{-T/T_1}\big[\cos \chi t_2 \cos \chi t_1 e^{-\tau/T_1} - (1/2) \sin \chi t_2 \sin \chi t_1 e^{-(i\Delta + 1/T_2)\tau}$$
$$- (1/2) \sin \chi t_2 \sin \chi t_1 e^{(i\Delta - 1/T_2)\tau}\big] , \tag{2.17}$$

$$E_{34}(T) = \cos \chi t_2 e^{-T/T_1}(1 - e^{-\tau/T_1}) + (1 - e^{-T/T_1}) . \tag{2.18}$$

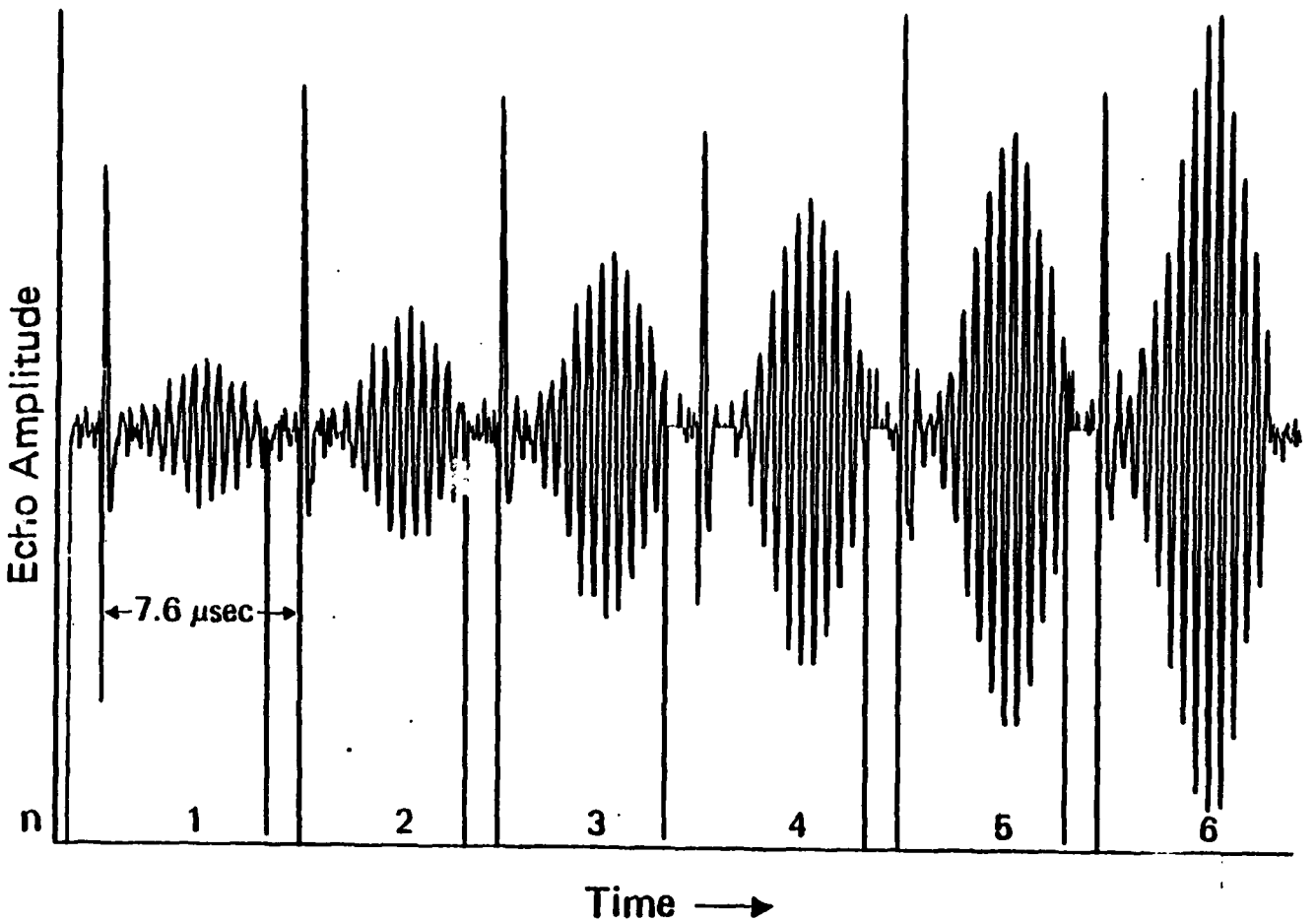


Figure 2. R.C. Brewer

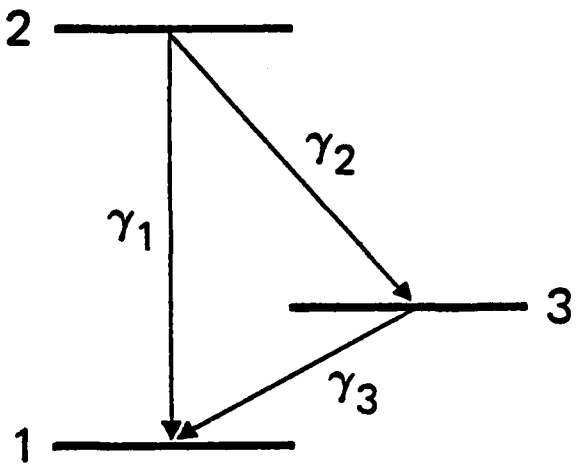


Figure 3. R.G. Brewer

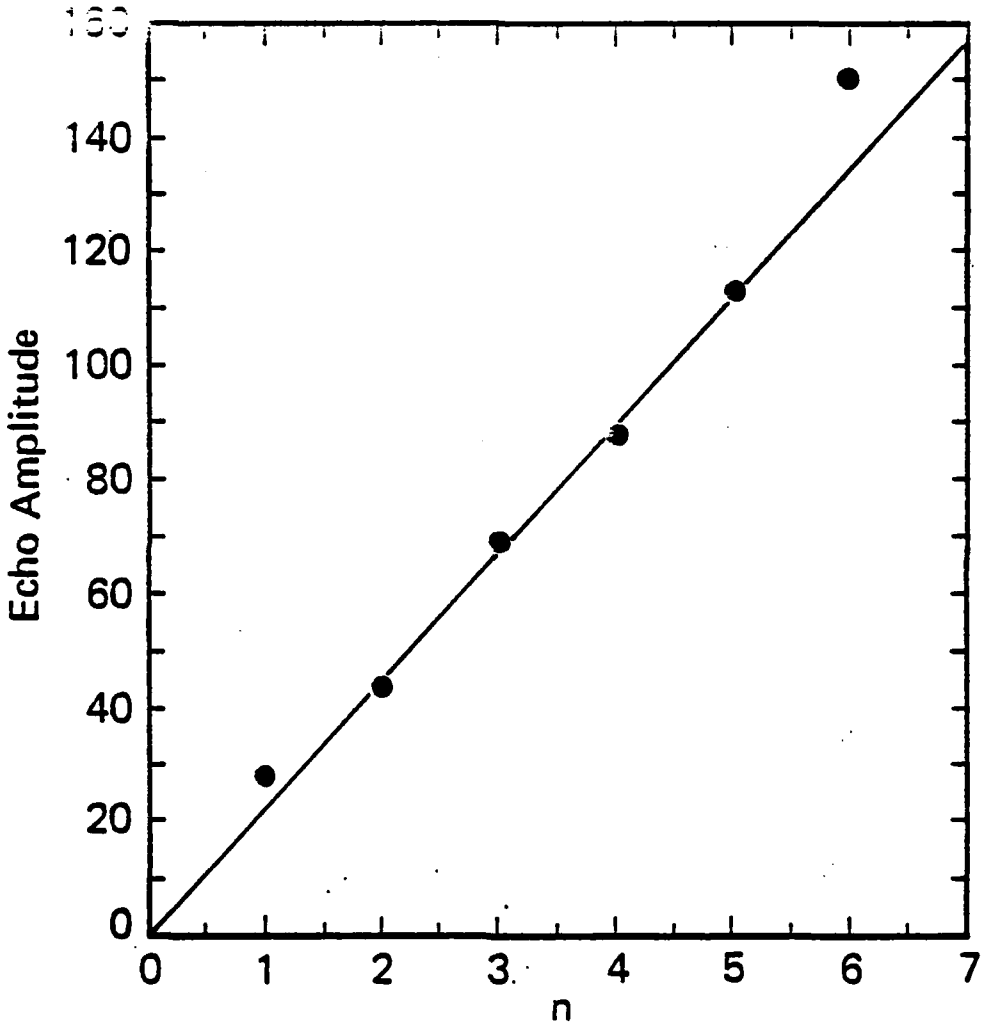


Figure 4. R.G. Brewer

RJ 4381 (47639) 8/1/84
Physics

LASER FREQUENCY DIVISION AND STABILIZATION *

R. G. DeVoe
R. G. Brewer

IBM Research Laboratory
San Jose, California 95193

ABSTRACT: A novel optical interferometric technique is proposed for stabilizing and measuring a laser frequency in terms of a radio frequency (rf) standard. In preliminary studies, a sensitive optical dual frequency modulation scheme (DFM) allows locking a laser to an optical cavity and the cavity in turn to a radio frequency reference with a noise level of 60×10^{-3} Hertz or 2 parts in 10^{10}. In principle, the laser frequency ω_0 can acquire the stability of the rf standard and being locked to a high order multiple n of the rf frequency ω_1 facilitates the optical-rf division $\omega_0/n=\omega_1$.

*Work supported in part by the U.S. Office of Naval Research.

The current method for measuring an optical frequency relative to the primary time standard, the cesium beam standard at ~9.2 GHz, utilizes a complex frequency synthesis chain involving harmonics of laser and klystron sources. The method has been extended recently to the visible region,[1] to the 633 nm He-Ne laser locked to a molecular iodine line, with an impressive accuracy of 1.6 parts in 10^{10}. With the new definition of the meter, the distance traversed by light in vacuum during the fraction 1/299 792 458 of a second, the speed of light is now fixed and both time and length measurements can be realized with the same accuracy as an optical frequency measurement. In view of the complexity of optical frequency synthesis, these developments set the stage for originating complementary techniques for stabilizing and measuring laser frequencies which are more convenient.

This paper reports a sensitive optical interferometric technique *dual frequency modulation* (DFM) for measuring and stabilizing a laser frequency by comparison, in a single step, to a radio frequency (rf) standard. Conversely, a low-noise rf source can be stabilized by a laser frequency reference. Preliminary measurements discussed below give a resolution of 2 parts in 10^{10}, but optimized devices should have a resolution between 10^{-12} and 10^{-15}. The method may be competitive with the optical frequency synthesis chain in accuracy and its simplicity suggests its convenient use in metrology, high-precision optical spectroscopy, and gravity wave detection.[2]

The principle of the technique rests on phase-locking the mode spacing $c/2L$ of an optical cavity to a radio frequency standard and simultaneously phase-locking a laser to the n-th order of the same cavity. When these two conditions are satisfied, the optical frequency ω_0 and the radio frequency ω_1 are simply related,

$$\omega_0 = n\omega_1 , \qquad (1)$$

neglecting for the moment diffraction and phase-shift corrections. The idea of locking a laser to a cavity is of course a well-established subject,[3,4] but the concept of phase-locking an optical cavity to a radio frequency source is new. Interferometric rf-optical frequency comparisons of lower sensitivity have previously been performed by Bay *et al.*[5] using a related idea based on amplitude modulation (AM) rather than frequency modulation, as will be discussed below.

To introduce the DFM technique, first consider a single frequency modulation scheme. An electrooptic phase modulator driven at ω_1 generates a comb of optical frequencies $\omega_0 \pm m\omega_1$ which are compared to cavity modes of frequency $n\sigma$, where σ is the cavity free spectral range, m=0,1,2,... and n is a large integer $\sim 10^6$ (see Fig. 1). The cavity response perturbs the balanced phase relationships between the sidebands and transforms frequency modulation into intensity modulation at ω_1. A photodetector, viewing the cavity either in reflection or transmission, then generates an error signal at the heterodyne beat frequency ω_1. This signal yields a null when the laser frequency ω_0 equals $n\sigma$ and the radio frequency ω_1 matches the mode spacing σ. In this circumstance, the comb of optical frequencies all resonate with their corresponding cavity modes. The difficulty with this approach is that the error signal depends not only on the rf detuning $\delta = \omega_1 - \sigma$ but also on the optical detuning $\Delta = \omega_0 - n\sigma$. Detailed analysis as well as experiment show that the error signal is proportional to $\delta\Delta$ and thus vanishes when $\Delta = 0$, independent of δ, a feature which prevents direct locking of the cavity to the rf source and realizing Eq. (1).

The DFM technique (Fig. 1) overcomes this problem by using two phase modulators, driven at frequencies ω_1 and ω_2 respectively. Dual frequency modulation creates, in lowest order, sidebands at $\omega_0 \pm \omega_1$, $\omega_0 \pm \omega_2$, and $\omega_0 \pm \omega_1 \pm \omega_2$. A photodetector views the cavity in reflection and two error signals are derived, one at ω_2 and the other at the *intermodulation* frequency $\omega_1 \pm \omega_2$. The first signal at ω_2 allows locking the laser to the reference cavity as described elsewhere[3,4] and is independent of ω_1 tuning. The second signal at $\omega_1 \pm \omega_2$ allows locking the cavity to the rf reference. This signal varies directly with the rf detuning $\delta = \omega_1 - \sigma$ and provides the desired null at the rf resonance condition $\omega_1 = \sigma$, while being independent of laser detuning Δ. To derive this result, we write for the double phase modulated light wave incident on the cavity

$$E_i = E_0 \, e^{i\omega_0 t + i\beta_1 \sin\omega_1 t + i\beta_2 \sin\omega_2 t} . \tag{2}$$

Taking only the zeroth and first order sidebands of the Fourier decomposition

$$e^{i\beta\sin\omega t} = \sum_{n=-\infty}^{\infty} J_n(\beta) e^{i\omega t} \sim J_0(\beta) + J_1(\beta) 2i \sin\omega t , \tag{3}$$

the reflected light waves

$$E_r(\omega) = g(\Delta) E_i \tag{4}$$

take the form

$$E_r = E_0\, e^{i\omega_0 t}\{J_0(\beta_1)J_0(\beta_2)g(\Delta) + 2iJ_0(\beta_1)J_1(\beta_2)\sin\omega_2 t$$

$$+ e^{i\omega_1 t}[J_0(\beta_2)J_1(\beta_1)g(\Delta+\delta) + 2iJ_1(\beta_1)J_1(\beta_2)\sin\omega_2 t]$$

$$-e^{-i\omega_1 t}[J_0(\beta_2)J_1(\beta_1)g(\Delta-\delta) + 2iJ_1(\beta_1)J_1(\beta_2)\sin\omega_2 t]\} \qquad (5)$$

where $g(\Delta)$ is the cavity lineshape function.

Equation (5) assumes that $\omega_2 >> \Gamma$ so that light at $\omega_0 \pm \omega_2$ and $\omega_0 \pm \omega_1 \pm \omega_2$ falls outside the fringe linewidth Γ and is totally reflected with $g=1$. The detected heterodyne beat signal at $\omega_1 \pm \omega_2$ is given by

$$E_r E_r^*(\omega_1 \pm \omega_2) = 4|E_0|^2 J_0(\beta_1)J_1(\beta_1)J_0(\beta_2)J_1(\beta_2)\sin\omega_2 t$$

$$\times \{\mathrm{Im}[g(\Delta+\delta)-g(\Delta-\delta)]\cos\omega_1 t + \mathrm{Re}[g(\Delta+\delta)+g(\Delta-\delta)-2g(\Delta)]\sin\omega_1 t\}\,. \qquad (6)$$

Since the coefficient of $\sin\omega_1 t$ in (6) is ~0, only the $\cos\omega_1 t$ term contributes and the DFM signal is directly proportional to the difference in cavity phase shifts of the $\omega_0+\omega_1$ and $\omega_0-\omega_1$ sidebands. With the further assumption that the lineshape function g can be approximated by a Lorentzian[6]

$$g(\Delta) = \frac{\Delta(\Delta - i\Gamma)}{\sqrt{R}(\Delta^2+\Gamma^2)}\,, \qquad (7)$$

the error signal simplifies to

$$E_r E_r^*(\omega_1 \pm \omega_2) = -4|E_0|^2 J_0(\beta_1)J_0(\beta_2)J_1(\beta_1)J_1(\beta_2)$$

$$\times \frac{\delta}{\Gamma}\,[\sin(\omega_1+\omega_2)t + \sin(\omega_1-\omega_2)t]\,. \qquad (8)$$

By detecting the beat either at $\omega_1+\omega_2$ or $\omega_1-\omega_2$ in a double balanced mixer, an error signal proportional to the rf detuning δ can be derived for locking an optical cavity to an rf standard, or conversely an rf source to a cavity. Second, the error signal is independent of laser detuning Δ and thus optical frequency jitter. Third, there is no background signal. Fourth, the DFM signal has excellent signal-to-noise ratio since $4J_0(\beta_1)J_1(\beta_1)J_0(\beta_2)J_1(\beta_2)=.45$ at $\beta_1=\beta_2=1$.

A prototype DFM standard (Fig. 2) has been constructed to verify the principle and study resolution and systematic errors. A home-made cw dye ring laser containing an intracavity ADP crystal for laser phase-locking to an external cavity emits 30 mW of light at 5900Å. The beam is focused through a home-made $LiTaO_3$ traveling wave electrooptic phase modulator,[7] which generates FM sidebands at $\omega_1=298.667120$ MHz$=c/2L$. The rf at ω_1 is generated by a Fluke 6071A synthesizer locked to a Vectron CO-247 10 MHz quartz oscillator with a stability of one part in 10^{10} per day. The beam then passes through a second phase modulator, an ADP crystal resonantly driven at $\omega_2=19.400$ MHz. The mode-matched cavity is a 50 cm confocal interferometer with an invar spacer, is acoustically and thermally isolated, and has a measured linewidth HWHM $\Gamma/2\pi=75$ kHz (finesse=2000). An optical circulator both isolates the laser from the cavity and directs the reflected light, the signal, to a high-speed photodiode (Motorola MRD-510). The detector photocurrent contains rf beats at ω_2 and $\omega_1\pm\omega_2$ which are amplified and then separately filtered. The error signal at ω_2 is sent to an FM sideband servo which locks the dye laser to the n-th cavity fringe so that $\omega_0=n\sigma$ with a short-term error $\Delta/2\pi\sim300$ Hz RMS.[4] The DFM signal at $\omega_1-\omega_2=279.267$ MHz is coherently detected in a double-balanced mixer. The error signal, Eq. (8), controls the cavity length L via a piezo so that the resonance

ondition $\sigma=\omega_1$ is satisfied. Ignoring mirror phase shifts and diffraction, the esonances $\omega_0=n\sigma$ and $\sigma=\omega_1$ yield $\omega_1=\omega_0/n$, and an optical-rf frequency divider is ealized.

The resolution or short-term frequency stability of the prototype has been neasured by opening the cavity-rf servo-loop, integrating the error signal with a 0.1 sec ime constant, and recording it on an oscilloscope. Figure 3 shows a peak-to-peak ioise level of ~0.4 Hz or an RMS noise level $\Delta\nu_{RMS}$~60 mHz (60×10^{-3} Hz). This epresents an RMS fractional frequency deviation (Allan variance) $\sigma_y=2\pi\Delta\nu_{RMS}/\omega_1=2\times10^{-10}$. For comparison, the earlier AM technique of Bay *et al.*[5] leveloped noise levels $\Delta\nu_{RMS}\approx100$ Hz for a 100 sec integration time, which implies hat our signal-to-noise ratio is 50,000 times greater.

The theoretical shot-noise-limited resolution of the DFM technique can be stimated as $\Delta\nu_{RMS}=\Gamma/(2\pi\sqrt{N\tau})$ where N is the number of photoelectrons/sec and τ s the integration time. For $N=10^{15}$ sec^{-1} and $\tau=0.1$ sec $\Delta\nu_{RMS}=10^{-7}\Gamma/2\pi$ or .5 millihertz. Our prototype is thus within a factor of 10 of the shot-noise limit.

Optimized DFM standards can be expected to have a resolution 10^2 to 10^5 higher. 'or example, the rf sideband spacing ω_1 can be increased to equal an integral multiple f the cavity mode spacing c/2L. Because of the periodicity of the cavity lineshape unction g, the short-term stability $\Delta\nu_{RMS}$ will be unchanged, but the fractional requency stability improves with increasing ω_1. Operating at $\omega_1=29.8667$ GHz so hat the sidebands interact with the (n+100th) and (n-100th) cavity modes would give shot-noise limited resolution $\sigma_y=\Delta\nu_{RMS}/(29.9\ GHz)=2.5\times10^{-13}$ for $\tau=0.1$ sec. his value far exceeds the stability of current commercial standards. Secondly,

superpolished mirrors developed for ring laser gyros can increase the finesse from 2,000 to >20,000, reducing Γ and $\Delta\nu_{RMS}$ by another factor of 10. Third, increasing the cavity length L reduces Γ proportionality. Use of a gravitational wave interferometer would reduce Γ by several additional factors of 10. Optimization of the DFM technique thus offers the possibility of microwave frequency standards with microHertz linewidths or Hertz stability in the optical region.

Systematic errors that can affect the accuracy of rf-optical frequency comparisons fall into two classes: (1) instrumental effects that shift the lock point of the DFM system off the center of the cavity resonance, and (2) corrections to Eq. (1) due to cavity mirror reflection and diffraction phase shifts. Residual AM in the phase modulator is well known to introduce an instrumental offset in FM servo systems. FM polarization spectroscopy[8] and AM servo techniques[9] can reduce the offset but the DFM technique solves this problem more decisively, in a new way. Because AM at the intermodulation frequency $\omega_1 \pm \omega_2$ is the *product* of the AM factors at ω_1 and ω_2, AM in our system can be only $(10^{-4})^2$ or 10^{-8}, a negligible level. A second kind of instrumental offset arises from the interference of light scattered off pairs of optical surfaces between the laser and detector. Fringes of low contrast result which cause significant offsets that are easily recognized, measured, and corrected in the DFM technique because they are periodic in laser tuning and generate a background rf signal at $\omega_1 \pm \omega_2$.

The second class of systematic errors due to cavity mirror reflection and diffraction phase shifts has been analyzed by Bay *et al.*[5] 12 years ago and by Layer *et al.*[10] They suggest that these optical frequency corrections can be measured to ~10^{-10} to 10^{-11}. Recent improvements in mirror quality indicate that these limits can

now be exceeded, and new methods of measuring the phase shift correction are also being examined. The DFM technique should therefore have a systematic error comparable to the current accuracy of 1.6×10^{-10} of the optical frequency synthesis chain.[1]

We conclude that both the long- and short-term stability of the optical frequency divider can be made competitive with, if not superior to, current techniques. In view of the large effort currently directed at optical frequency synthesis and new microwave frequency standards, we propose that the relatively simple and promising technique of DFM should now be pursued.

We are indebted to K. L. Foster for technical aid. This work was supported in part by the U.S. Office of Naval Research.

REFERENCES

1. D. A. Jennings, C. R. Pollack, F. R. Peterson, R. E. Drullinger, K. M. Evenson, and J. S. Wells, *Optics Letters* 8, 136 (1983).
2. R. W. P. Drever *et al.* in *Laser Spectroscopy V* (Springer-Verlag, New York, 1981), edited by A. R. W. McKellar, T. Oka, and B. Stoicheff, p. 33.
3. R. W. P. Drever, J. L. Hall, E. V. Kowalski, H. Hough, G. M. Ford, A. J. Munley, and H. Ward, *Appl. Phys.* B31, 97 (1983).
4. R. G. DeVoe and R. G. Brewer, *Phys. Rev. Lett.* 50, 1269 (1983).
5. Z. Bay, G. G. Luther, and J. A. White, *Phys. Rev. Lett.* 29, 189 (1972).
6. A. Schenzle, R. G. DeVoe, and R. G. Brewer, *Phys. Rev.* A25, 2606 (1982).
7. R. G. DeVoe and R. G. Brewer, *Phys. Rev.* A20, 2449 (1979).
8. M. Romagnoli, M. D. Levenson, and G. C. Bjorklund, *Optics Letters* 8, 635 (1983).
9. J. L. Hall, L. Hollberg, Ma Long-Sheng, T. Baer, and H. G. Robinson, *Journal de Physique* 42, Colloque C-8, Supplement 12, page C8-59 (1981).
10. H. P. Layer, R. D. DesLattes, and W. G. Schweitzer, *Appl. Optics* 15, 734 (1976).

FIGURE CAPTIONS

Figure 1. Schematic representation (not to scale) of the dual frequency modulation sidebands of a laser relative to the dispersive part of the interferometer lineshape function g, Eq. (7).

Figure 2. Block diagram of an optical frequency divider showing two servo loops where the laser is locked to a reference cavity and the cavity to a radio frequency standard. The $LiTaO_3$ modulator is driven at ω_1 and the ADP modulator at ω_2. LSB denotes a mixer and filter which generates the difference frequency ω_1-ω_2 for the double balanced mixer (DBM) in the cavity-rf servo.

Figure 3. Oscilloscope photograph of the experimental DFM error signal at ω_1-ω_2 corresponding to Eq. (8). The vertical scale was calibrated at 1 Hz/div by detuning ω_1 by 5 Hz.

till align approximately with the other runners as they cross the starting line, because he vill not have deviated very far from his "ordered" position in the short time between hots.

This multiple-reversal sequence has an even more dramatic effect. Suppose that a ertain runner's speed has been increased slightly by a collision. He will thus run a reater distance per unit time than he would have if the group of runners had been ollision-free. However, since he repeatedly reverses his direction he deviates from his rdered position, first in one direction and then in the other, by equal amounts. The listance by which he deviates from his ordered position will therefore average out to ero. He will stay roughly in alignment with the other runners. In a sense, it is as hough the collision never happened.

In the same way, if a gaseous sample were excited with many closely-spaced pulses, hen the Doppler shifts caused by elastic collisions would be averaged out to zero: each tom that had changed velocity due to collisions would have alternating higher and lower mission frequencies than the average atom; thus, on average, the atoms will be excited in nison. Since the atoms thus stay synchronized, the effect of elastic collisions is inimized.

After each of the many pulses the atoms will come back into alignment, as the unners do between the multiple gunshots, and each time the atoms realign they emit nother echo pulse. The chain of many pulses thus produces a chain of many echoes, one cho between each pair of pulses.

extended to the optical region by Jan Schmidt of the University of Leiden, Paul R. Berman of New York University and one of us (Brewer). We shall describe an optical case, a photon echo experiment performed on a gaseous sample.

The photon echo effect is, in principle, very similar to the nuclear-spin echo. In the spin echo, an incident rf pulse resonates with precessing proton axes to align them in a state of dynamic order; this order seems to decay but is recalled by a second resonant rf pulse, which reverses the relative phase angles of the protons, causing them to realign and produce an echo pulse. The photon echo is analogous, except the incident radiation is provided by a laser beam (that is, in the optical region), and it resonates with oscillations of the electron cloud surrounding each gaseous atom to produce an echo pulse.

The gaseous molecules of a typical photon echo experiment are in a state of chaotic thermal motion and behave like billiard balls, undergoing elastic collisions which change their velocities but not their internal states. If the molecules are elastically scattered after being excited by the first laser pulse, they experience slightly altered trajectories and velocities and, because of the Doppler effect, each affected atom's emission frequency (which is analogous to the precession rate of a proton axis) is changed. The ensemble of atoms is no longer in a state of hidden order. In the racetrack analogy, it is as though collisions between the runners had changed each runner's velocity. In the NMR case, the same sort of decay occurs because some molecules of the liquid sample, in diffusive motion, move randomly to regions of differing magnetic field strength.

Returning to the racetrack analogy, imagine that the starter fires his gun many times in rapid succession, each time causing the runners to reverse their motions. Even if the runner's speed has changed slightly (because of a collision) between gunshots, he will

of such random processes in matter as thermal agitation, internal motion and the fluctuation of local fields.

With the development of coherent laser light, the echo concept was extended in 1964 to optical frequencies by Norman A. Kurnit, Isaac D. Abella and Sven R. Hartmann of Columbia University (see "Proton Echoes" by Sven R. Hartmann; *Scientific American*, April 1968). The physical principles underlying the spin and photon echoes are the same, both being examples of hidden order produced and revealed by coherent radiation, although the spin echo involves atomic nuclei, while the photon echo usually involves atomic electrons. In fact, as Richard P. Feynman, Frank L. Vernon and Robert W. Hellwarth, then at the California Institute of Technology, were able to show, both situations can be described by the same mathematical formalism, which is a generalization of Bloch's original gyroscopic equations.

The above experiments show that the hidden order within seemingly disordered systems can sometimes be revealed. It has also been shown that certain phenomena, such as molecular collisions, can introduce elements of disorder into this hidden order, causing the echo strength to decay. Can echo experiments be devised that will negate even such randomly-occurring, seemingly irreversible effects?

The suggestion seems to contradict one's intuition that the large-scale consequences of such random events as collisions between molecules are, in principle, irreversible. In this instance intuition is misleading, because it is sometimes possible to eliminate even the disordering effects of elastic molecular collisions. This result is achieved by applying a large number of incident pulses spaced closely together. These multipulse experiments were first performed in NMR by Herman Y. Carr, now at Rutgers, and Purcell, and later

frequency of precession. This spin-flipping property of resonant radiation is the cornerstone of the nuclear magnetic resonance (NMR) technique discovered independently in 1946 by Edward M. Purcell of Harvard and the late Felix Bloch, then at Stanford. In nuclear magnetic resonance spectroscopy, a sample is excited to see which frequency of radiation will induce spin-flipping, where each resonant frequency corresponds to a unique nuclear spin in a particular nuclear environment. For example, the strength of the local magnetic field can vary in different parts of a molecule because an electron cloud partially shields its nucleus from an external field. Once an NMR technician knows the spin-flipping frequencies, he or she can determine the chemical makeup of the sample. Spin echoes are among the most useful of NMR imaging techniques. The externally-applied fields can be controlled to determine the occurrence of a given precession frequency over a large sample, even one as large as a human body. The response of protons from regions of the body can be recorded electronically and processed to produce an internal image of a living organ.

There is another way that spin echo effects can be used to study the properties of various substances. In our racetrack analogy, the runners will not all finish simultaneously if some of them have tired and reduced their speeds during the race; in a sense, any change of speed introduces a disorder within the hidden order. A corresponding disorder in an atomic sample could involve collisions between the atoms, magnetic interactions between neighboring atoms or movement of an atom from a region where the external magnetic field is high to one where it is lower, thus changing its rate of precession. If the delay between the two rf pulses is lengthened, then the random disorder introduced between pulses will increase and the echo signal will be weaker. A physicist or chemist can thus use the strength of the echo, or its decay time, as a measure

characteristic of a large collection of dipoles rotating together. The sample is now in a state of apparent chaos.

After the protons' free induction decay, the sample is excited with the second rf pulse, which acts like the second firing of the starter's gun. This pulse is at the same frequency as the first but in a typical experiment it lasts twice as long; consequently the plane in which the proton spin axes lie is flipped through a full 180°, ending once again in an orientation perpendicular to the constant field. It is as though the plane in which the spin axes lie has been turned upside down or reflected in a mirror.

Following the first rf pulse, the phase angles between faster- and slower-precessing spins had gradually grown larger. Just after the second pulse, which turns over the plane in which the axes lie, the phase angles between the various axes are the same as before, but the relative positions of the faster- and slower-precessing axes are reversed. In other words, prior to the second pulse the faster-precessing axes had gradually come to point slightly ahead of the direction that the slower-precessing axes pointed; after the second pulse, the plane in which the axes lie has been turned upside down or mirror-reflected, the slower-precessing axes point slightly ahead of the faster-precessing axes (see illustration on page 00). The faster-precessing proton spins are now behind the lower ones, just as the faster runners were behind after the starter's second signal. As in the race, rapidly precessing spin axes will catch up with the slower ones so that realignment is achieved; at that moment the atoms will emit another burst of radiation, the echo pulse, showing that the seemingly lost order has been recovered.

In the spin echo effect the applied rf bursts are said to be in resonance with the proton spins, because the frequency of the bursts exactly matches the protons' natural

field and the constant field. The combination of these two precessions is a downward spiral, traced by the spin axis of each proton.

The angle through which the protons tip is determined by the strength and duration of the rf pulse. In a typical spin echo experiment, this first pulse might be timed so that it tilts the proton spins exactly 90° from the vertical; in other words, they come to lie on a plane perpendicular to their original orientation. If the constant magnetic field is left on, the proton spins will precess in unison in this new plane; in a sense, they will resemble one giant spinning magnet. Like such a spinning magnet, the protons emit an oscillating electromagnetic pulse, the free induction decay signal, so named because the synchronized free precession of spins induces a decaying electromagnetic signal. This corresponds to the start of the race, when the spin axes are in a state of dynamic order.

One reason for the decay of the free induction signal may be that the static magnetic field does not have exactly the same strength throughout the sample. Since the protons' precession frequency depends upon the strength of the external field, a proton is a region where the magnetic field is stronger will precess more rapidly than the others, just as some runners are faster than others. As some protons precess rapidly and others slowly, the spin axes no longer point in exactly the same direction. They gradually fan out, like the runners on the track; the spin axes of those protons which precess rapidly will point ahead of the axes of the more slowly precessing protons (see illustration on page 00). The angle formed between any two spin axes that come to point in different directions is called the phase angle; the magnitude of the phase angle is a measure of how far the two spin axes are out of synchronization. As they desynchronize the protons no longer emit the oscillating electromagnetic field, the free induction decay, that is

the angular momentum of a gyroscope. The spin axis of a proton is a constant magnetic field, like that of a gyroscope in a constant gravitational field, precesses; that is, it traces a circle about a line parallel to the force field (see illustration on page 00). The precession frequency, the rate at which the proton's axis goes around its circle, depends in part upon the strength of the external magnetic field. This tendency of the proton's spin axis to precess about an applied constant field is the basis of the spin echo effect.

In a spin echo experiment, the constant components of the spin axes of the protons in the sample are initially aligned parallel to a constant external magnetic field. Since they are exactly parallel to the field, they do not precess (as a perfectly vertical gyroscope would not precess). The first radio-frequency pulse is then applied. This rf pulse contains a circularly-polarized component - that is, a small rotating magnetic field - which rotates at rate with which the protons' spin axes would precess if they were not of alignment with the constant field and if it were the only field present.

The rf pulse causes the ensemble of protons to execute a complicated motion, best described as a combination of two less complex precessional motions (see illustration on page 00). The simpler of these two motions is a precession about the static external field: the rf pulse tilts the spin axes out of alignment with the constant field (although they remain essentially in alignment with each other during the short pulse time) and they begin to precess about the static field lines at their normal rate of precession. Since the direction of the rf magnetic field contained in the pulse also rotates at this rate, the angle between the rotating rf field and any proton spin axis remains constant as the proton spins precess, and thus from this vantage point of the protons the pulse field seems constants in direction. Consequently the proton spins precess about both the pulse

analog, called the free induction decay effect, which has found wide use in both ratio- and optical-frequency regions.

A more concrete example of a memory effect can actually be demonstrated by mechanical means (see illustration on page 00). A viscous fluid is placed in the ring-shaped space between two concentric plastic cylinders. Whereas the outer cylinder is stationary, the inner one is free to rotate about its axis. A streak of colored dye, representing an initial alignment of particles, is injected into the fluid. When the inner cylinder is turned the dye disperses throughout the liquid. If one were to show the volume between the cylinders to a thermodynamicist, he or she would say that the dye is completely disordered (that is, that the entropy is at a maximum), and that the mixing process is complete and irreversible. In fact, the liquid is in a state of hidden order (or constant entropy): reversal of the rotation of the inner cylinder reverses the mixing process; after an equal number of reverse rotations the dye streak reappears.

In 1950 one of us (Hahn), then at the University of Illinois, discovered a memory effect similar in principle to the cases of the runners and the dye, which operates on the atomic scale. A sample of glycerin was placed in a magnetic field and exposed to two short bursts of electromagnetic radio-frequency (rf) radiation, separated by an interval T of a few hundredths of a second. The sample retained a memory of the pulse sequence, and at time 2T seconds after the first rf pulse the sample itself emitted a third pulse, an echo. This phenomenon is known as the nuclear-spin echo.

The nuclear-spin echo is a consequence of the gyromagnetic properties of atomic nuclei, such as the proton that makes up a hydrogen nucleus. Because the proton spins and is electrically charged, it has a magnetic moment, which is similar in some ways to

systems we shall discuss, this hidden order is provided by exposing samples (which may be solid, liquid or gaseous) to coherent electromagnetic radiation of various types, including radio waves, microwaves and laser beams. Sound waves can also play this role. The reemergence of an ordered state in such systems becomes evident when the sample emits its own coherent electromagnetic pulse, an echo of the earlier radiation. Apart from their inherent interest, these echo pulses and related forms of coherent emission provide novel ways to study the fundamental behavior of atomic interactions.

The concept of hidden order can be demonstrated by analogy. Imagine a group of runners poised on the starting line of a circular track (see illustration on page 00). The starter fires his gun, the race begins, and the runners spread out along the course, each running at a different fixed speed. Once they have circled the track a few times, some runners will have lapped others and there will be no obvious visible correlation between the runners' relative positions and their various speeds. Someone who had not seen the start of the race could be led to assume that there was no particular order in the disposition of the runners - that they represented a disordered system. Now suppose that the runners have contrived to turn around and retrace their paths at some prearranged signal (perhaps a second firing of the starter's gun) which is given T minutes into the race. If each runner maintains his speed, albeit in the opposite direction, they will come together and cross the starting line in unison exactly 2T minutes after the beginning of the race. They will have recovered their initial order (this order will, of course, disappear once again after the runners cross the line)

The even simpler case of all runners traveling together at the same radial speed is not to be ignored either. Here, the initial order is preserved and there is no need to reverse the runners' direction. As we shall see, this example has an electromagnetic

In 1872 Ludwig Boltzmann, a founder of modern thermodynamics, gave a lecture in which he said that the entropy, or disorder, of isolated systems increases irreversibly as time passes. On hearing this the physicist Joseph Loschmidt rose to protest. He said that the laws governing the motions of all particles are symmetric with respect to time. Thus any system which had decayed from order to chaos could be made orderly once again simply by reversing the momentum of each particle, without affecting the total kinetic energy of the system. In defiance Boltzmann pointed his finger at Loschmidt and said, "*You* reverse the momenta."

This scholarly conflict illustrates the paradoxial nature of the second law of thermodynamics. This law says that systems tend toward maximum entropy. Yet Loschmidt's argument remains cogent. If one were able to film the motions of any small group of particles and show that film to a physicist, he or she would have no way of telling, in principle, whether the projector were running forward or backward. Consequently, according to Loschmidt's criticism (which has come to be called the Loschmidt paradox), any law that governs the behavior of large collections of particles should be symmetric with respect to time. While the meaning and implications of the second law are still active topics of research and disagreement (see "The Arrow of Time," by David Layzer; *Scientific American*, December 1975), there now exist several methods by which Loschmidt's time reversal can be realized. In other words, a system of particles which has apparently decayed from a highly ordered state can be returned to that state by reversing the motions (or some other degree of freedom) of its constituent particles. In effect, an assembly of atoms is able to exhibit a kind of memory of its earlier condition.

If a system is to display this kind of atomic memory, it must be prepared so that it has some sort of order, often hidden in its apparently disordered state. In the atomic

RJ 4508 (48516) 11/15/84
Physics

ATOMIC MEMORY*

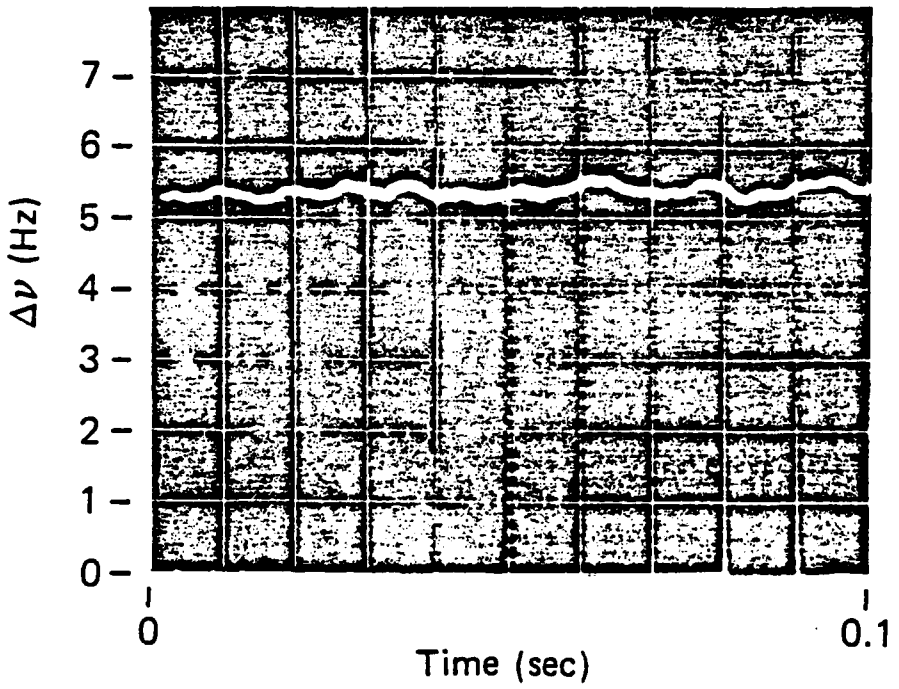
Richard G. Brewer
Erwin L. Hahn

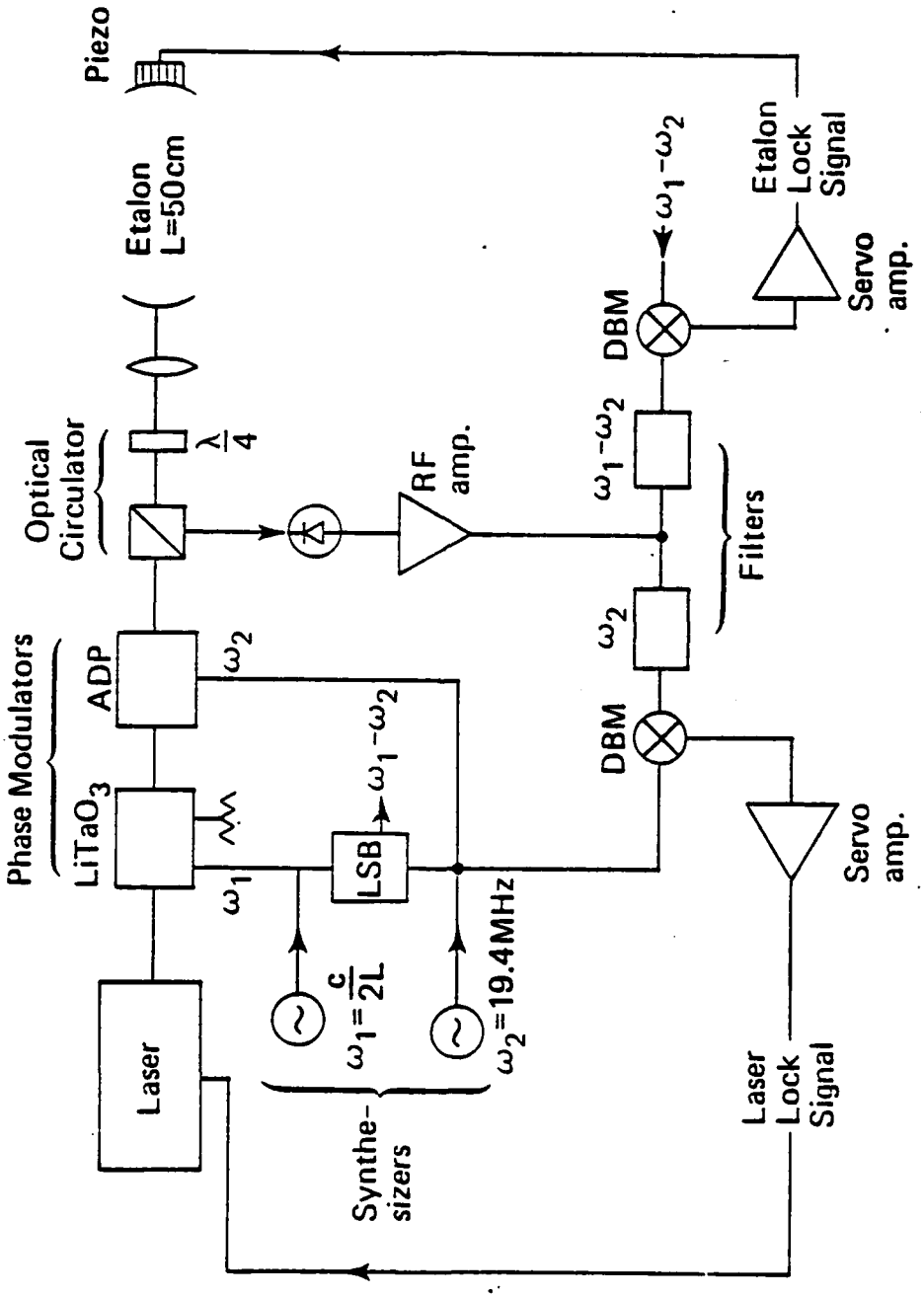
IBM Research Laboratory
San Jose, California 95193

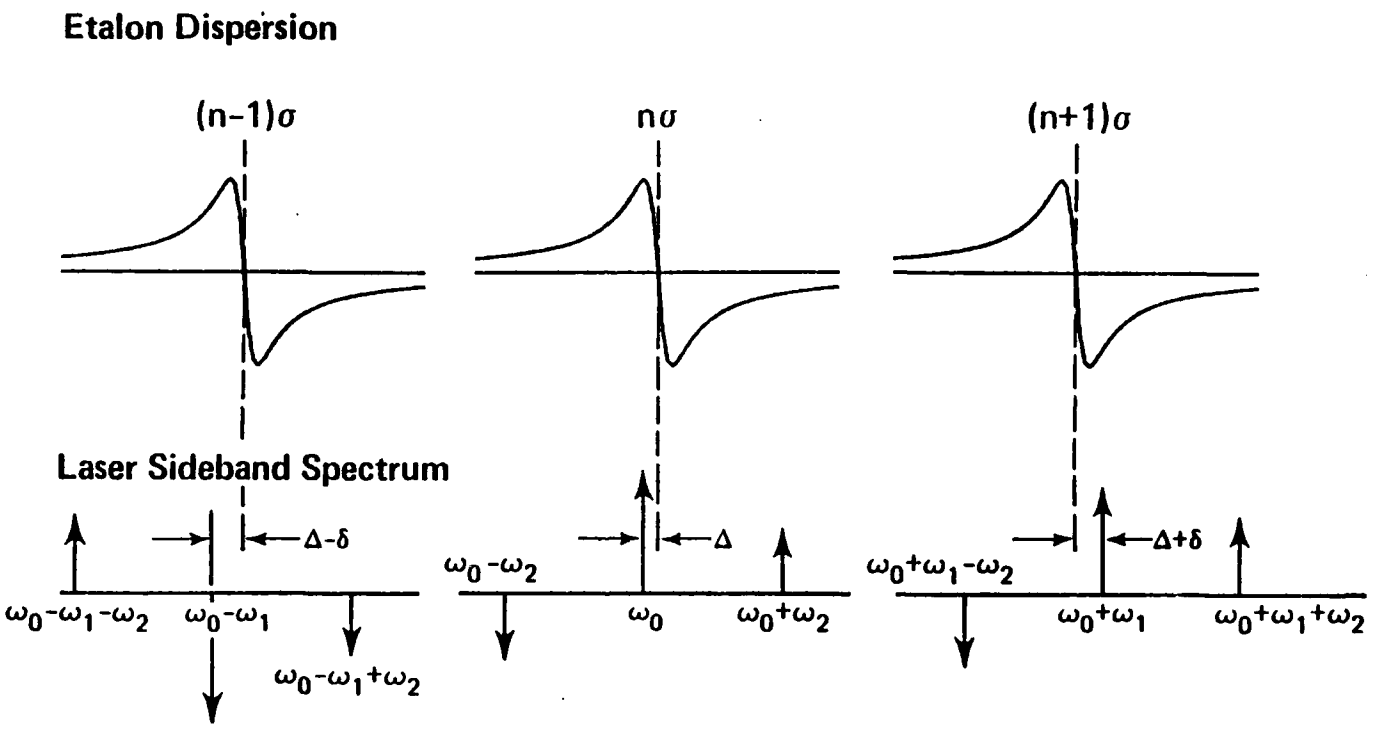
ABSTRACT: Atomic systems which have decayed from highly ordered states can be manipulated to recover their initial order. The degree to which order is restored allows investigation of atomic interactions.

REVISED VERSION OF RJ 2764

*Work supported in part by the U.S. Office of Naval Research.


7
6
5
4
3
2
1
0
Δν (Hz)
0
0.1
Time (sec)


Piezo
Etalon
L=50cm
Optical
Circulator
λ/4
RF
amp.
Phase Modulators
ADP
LiTaO3
ω2
ω1
LSB
ω1-ω2
Laser
Synthe-
sizers
ω1=c/2L
ω2=19.4MHz
DBM
ω1-ω2
Filters
ω2
DBM
ω1-ω2
Etalon
Lock
Signal
Servo
amp.
Servo
amp.
Laser
Lock
Signal


Etalon Dispersion
(n-1)σ
nσ
(n+1)σ
Laser Sideband Spectrum
Δ-δ
Δ
Δ+δ
ω0-ω2
ω0+ω1-ω2
ω0-ω1-ω2
ω0-ω1
ω0-ω1+ω2
ω0
ω0+ω2
ω0+ω1
ω0+ω1+ω2

This Carr-Purcell multipulse experiment is really a way of enhancing the ordinary echo effect; the experimenter applies many pulses in order to produce many echoes, prolonging the sample's state of order.

There is another type of multiple-pulse experiment which is even more striking than the Carr-Purcell effect. The "magic sandwich echo" effect was first demonstrated by John S. Waugh, along with Won-Kyu Rhim and Alex Pines, then students of his at the Massachusetts Institute of Technology. The effect involves subjecting a sample to a long series of specially-processed pulses in order to produce just one echo. What is special about the magic sandwich is that it can be performed on a sample which would ordinarily not produce any echo at all. Without the application of this unusual train of pulses, that sample's earlier state of order could never be recovered.

In a typical magic sandwich experiment a calcium fluoride crystal is placed in a constant magnetic field. As in the spin echo experiment, an rf pulse that tips the spin axes of the fluorine nuclei by 90° is applied to the sample. The crystal then emits a free induction decay signal, like the free induction decay signal emitted by the liquid sample in a spin echo experiment. After the free induction decay has died out another 90° pulse is applied, followed immediately by a long series of 180° pulses in rapid succession and then by another 90° pulse. This is the sandwich; in it the two 90° pulses represent the bread and the series of 180° pulses are the filling.

There is still no simple pictorial model for describing what happens during the magic sandwich effect. It can only be said (according to the currently accepted mathematical description) that the magic sandwich actually changes the sign of the

equation of motion for the fluorine nuclei; in other words, it performs precisely the momentum reversal that Loschmidt described to Boltzmann.

Even in an experiment involving multiple pulses, there is still some decay of the echo signal: in a Carr-Purcell experiment succeeding echoes grow weaker. This decay, in the case of a gas, is due primarily to inelastic collisions, collisions violent enough to produce irreversible quantum changes in the energy levels of the atoms involved. The echo decay in a multipulse experiment is therefore a measure of the rate of inelastic collisions and diffusion in a sample. This means that a multipulse experiment can be used to select specific types of atomic interactions for study without the complication of competing dynamic processes.

There is yet another way of producing atomic memory, one in which time reversal is not required. The basic idea appears in the racetrack analogy. It is possible to have all the runners travel at the same radial speed, preserving their initial alignment. This is the simplest case of all, but how can it be achieved?

In a gaseous sample, it is possible to select all the atoms having one specific velocity by exciting the sample with a nearly monochromatic (single-frequency) continuous wave (cw) laser beam of the appropriate resonant frequency. Because of the Doppler effect, an atom moving at one velocity will absorb light at a slightly different frequency than will an identical atom moving at a different velocity. If the laser frequency is spectrally pure, that is, if it is essentially a single frequency, then only the atoms having one particular velocity can be selected and prepared coherently. To revert to the racetrack analogy, it is as if only runners of one specific speed were selected to start the race.

The alignment of these coherently prepared atoms is demonstrated in a laser frequency-switching apparatus (see illustration on page 00). After a long excitation period the frequency of the laser beam is suddenly switched to a new value so that it is no longer in resonance with the prepared group of atoms. This switching ends the excitation. However, the coherently prepared atoms now act like a set of identical tuning forks that have been struck simultaneously; since they all have the same resonant frequency they reinforce each other and radiate, in unison, an intense, coherent beam of light in the forward direction. This signal has all the properties of laser light (coherence, directionality and a single frequency) because the atoms retain a memory of their initially ordered state. This is the optical analog of the free induction decay emission associated with magnetic resonance. The free induction decay effect was first discovered in NMR in the radio frequency region by one of us (Hahn) and in the optical region by the other of us (Brewer) and Richard L. Shoemaker, now at the University of Arizona. Like the echo effect, free induction decay allows the physicist or chemist to measure difficult to observe properties of materials. By studying the decay times of various emission frequencies under different conditions, one can achieve a better understanding of the interactions within and between the molecules of a sample.

Laser frequency switching, introduced at IBM Research, San Jose by one of us (Brewer) in collaboration with Azriel Z. Genack, now at Xerox, has been used to observe not only free induction decay, but a whole class of atomic memory phenomena. The process of tuning the laser into and out of resonance with an atomic sample is equivalent, in a sense, to applying pulses of laser light; thus, switching a laser into resonance with a sample for two short periods of time is essentially equivalent to applying two short laser bursts, and will produce the same echo phenomena. The

frequency switching technique has the advantage that switching processes can be more precisely timed and controlled by electro-optic devices. In addition, interference between the sample's emission and the laser light (at its new frequency) produces a strong (heterodyne) beat signal that can be used to distinguish the sample's emission from any background noise.

One of us (Brewer), along with Ralph G. DeVoe of IBM, has recently used the laser frequency-switching technique to examine the fundamental gyroscopic equations used by Bloch in his first description of NMR. According to Bloch's equations, the nuclear memory decay time should not depend on the strength of the applied fields. In 1955 A. Redfield showed, using thermodynamic arguments, that these equations required modification. He observed the nuclear magnetic resonance of a pure metal, and found that an intense radio frequency field can actually lengthen the memory lifetime (that is, reduce the rate of decay) through a time-averaging effect which is similar in some ways to a time reversal.

DeVoe and Brewer have extended Redfield's argument into the optical region by using one of the most stable tunable lasers in existence (the laser's emission frequency can be adjusted and, when set, is stable to five parts in 10 million million) in a free induction decay experiment. The sample examined was a crystal of lanthanum trifluoride containing praseodymium impurity ions, and the memory decay was due to a nuclear magnetic interaction between the praseodymium and the neighboring fluorine nuclei.

Like a proton, a fluorine nucleus behaves as a spinning charge, creating its own magnetic field. The fields of fluorine nuclei are strong enough to flip over neighboring fluorine nuclei in the same way that an rf pulse can flip over a proton. When a fluorine

nucleus flips, the resulting change in the local magnetic field is sometimes strong enough to flip over yet another neighboring fluorine nucleus. Such random sequences of spin flipping are common in the lanthanum trifluoride crystal.

When a lanthanum trifluoride crystal is exposed to coherent laser radiation of the correct resonant frequency, the praseodymium ions become synchronized and emit their own coherent radiation, a free induction decay signal. Fluorine nuclei that undergo random spin flipping can desynchronize the neighboring praseodymium ions, causing the coherent optical emission to die out.

DeVoe and Brewer measured this decay time using the laser frequency switching technique described above. They excited a sample of lanthanum trifluoride with a tunable dye laser and then switched the frequency of the laser so that it no longer resonated with the praseodymium impurity ions. This requires an extraordinarily frequency-stable laser in order to excite an extremely small range of frequencies (the linewidth of praseodymium is only 10 kilohertz, roughly 10 million times narrower than previous optical measurements in solids). Once the laser frequency had been switched, the praseodymium ions emitted the free induction decay signal, which decayed in about 17 microseconds.

Even this magnetic interaction can be quenched, (?) simply by increasing the intensity of the laser that was used to excite the crystal. An increase in laser intensity drives the praseodymium ions more rapidly between higher and lower quantum states, as they absorb and reemit photons. Each time the praseodymium ion goes through an absorption-emission cycle, the nuclear magnetic interaction between it and the neighboring fluorine nuclei changes sign; that is to say, the interaction that had been

acting between a praseodymium ion and a fluorine nucleus will act in the opposite direction after the praseodymium ion has absorbed and reemitted a photon. Thus a fluorine nucleus which had been causing a praseodymium ion to desynchronize from the others will effectively reverse its effect on that ion and force it back into synchronization. This is similar to the reversal of phase order produced by the laser in a multipulse Carr-Purcell experiment. If the time between phase reversals is shorter than the time between the desynchronizing events (in this case random fluorine flips), then the disturbances caused by the fluorine nuclei are compensated because its interaction with the praseodymium is reversed. Together with Axel Schenzle of the University of Essen, West Germany and Masaharu Mitsunaga of IBM, DeVoe and Brewer have developed a general microscopic quantum theory of this phenomenon that extends, for the first time, the thermodynamic argument of Redfield.

The techniques of pulsed radio-frequency radiation, the principles of which have been known for nearly 40 years, are a great boon to science and medicine, primarily in NMR body imaging and the structural analysis of chemical compounds and the solid state. With the development of extremely pre(?) and stable lasers, these methods are just now being made possible in the optical region.

These atomic memory phenomena would have delighted Loschmidt because they show that some types of decay, even decay caused by random collisions, can be reversed. Beyond their philosophical charm, however, atomic memory phenomena can be very useful. By eliminating the decay effects of some processes, they allow physicists to study other processes in greater detail, giving us a clearer view into the structure and interactions of materials on the atomic level.

END

FILMED

7-85

DTIC